Modelling Framework for In-Vivo Knee Joint Contact Analysis

Lauren Mai Swain

BEng (Hons)

A thesis submitted for the degree of

Doctor of Philosophy

Cardiff University

October 2025

ABSTRACT

Understanding the relationship between knee joint mechanics and disease is essential for improving the prevention and treatment of conditions such as osteoarthritis (OA). This work developed a comprehensive framework to investigate tibiofemoral (TF) joint contact mechanics by integrating accurate in-vivo biplane videoradiography (BVR) kinematics with musculoskeletal (MSM) and finite element (FEM) modelling. By combining the complementary strengths of these techniques, the framework provides a more comprehensive understanding of knee biomechanics, capturing joint kinematics, loading, and internal tissue mechanics during dynamic functional activities.

A protocol was established for the simultaneous acquisition and processing of BVR and marker-based motion capture data, enabling accurate calculation of 6 degree of freedom TF kinematics during gait, stair ascent, and lunging tasks. These datasets were used to evaluate MSM predictions of TF kinematics and contact pressures, comparing models with generic and MRI-derived personalised contact geometries. Incorporating subject-specific bone and cartilage geometries improved MSM estimates during gait, particularly in the anterior-posterior direction, however the limitations of the modelling approach for higher flexion activities were highlighted.

The BVR-derived kinematics were then used to drive a fully kinematically driven FEM of the knee, enabling investigation of articular cartilage contact pressures, stresses, and strains during the stance phase of gait. The model produced loading patterns consistent with previous literature, with peak contact pressures, stresses and strains coinciding with the loading peaks during gait. The model demonstrated the feasibility and value of combining high-fidelity imaging with FEM to explore in-vivo internal cartilage mechanics.

Overall, this research presents a novel, integrated approach for studying in-vivo knee biomechanics. The framework delivers both methodological and practical advances, providing a foundation for future work investigating pathological cohorts, surgical interventions, and the biomechanical mechanisms underlying disease onset and progression.

ACKNOWLEDGEMENTS

This research was supported by the Engineering and Physical Sciences Research Council (EPSRC) doctoral training grant (EP/T517951/1).

I would like to thank my supervisors for all their support throughout my PhD. Firstly, thanks to Dr David Williams for his constant help and support over the years, and for always being there to answer my (many) questions. Also, thank you to Dr Hayley Wyatt for all the modelling and pastoral support through both my undergrad and PhD, and to Prof. Ilse Jonkers for providing her expertise and guidance. A huge thanks to Prof. Cathy Holt for always having my back, challenging me to become a better researcher, and for always reminding me of the bigger picture.

I would also like to thank Dr Bryce Killen and Dr Miel Willems from the team at KU Leuven for taking the time to teach me their OpenSim pipeline and for all their help troubleshooting.

A big thank you to everyone who has been part of the MSKBRF team over my PhD. In particular, thanks to Dionne Shillabeer for fun lab days and supporting data collection, and to Dr James Cowburn for our modelling chats, as well as Jenny Williams, Katie Prentice, Rebecca Reddiough and Saumiyaah Nimalakumaran for keeping me company in the office, and to my fellow PhD buddies, Dr Marina De Vecchis, Alonso Soto Rosales and Janine Flohr for your friendship, but especially to Dr Polly Blaikie, my unofficial PhD mentor, for all the writing days, tea and jigsaws.

I would also like to thank all my friends and family, to my parents who have got me to where I am today, and to my brothers, Alistair and Joe (sorry, Joe, for beating you to “Dr Swain”, it’s the privilege of being the oldest sibling!). Also, to Gemma, Lizzy and Lucy for putting up with living with me during the busiest year of my life.

The final thank you goes to Tom, my wonderful husband and best friend, for everything you did to keep me going, particularly towards the end of this process. I couldn’t have done it without you.

TABLE OF CONTENTS

LIST OF ABBREVIATIONS

AA	Abduction-Adduction
ACL	Anterior Cruciate Ligament
ACS	Anatomical Coordinate System
AIM	Automatic Identification of Markers
AP	Anterior-Posterior
ASIS	Anterior Superior Iliac Spine
BVR	Biplane Videoradiography
BW	Body Weight
CD	Compression-Distraction
CISS-3D	Three-Dimensional Constructive Interference in Steady State
COM	Centre of Mass
COP	Centre of Pressure
CT	Computed Tomography
CUBRIC	Cardiff University Brain Research Imaging Centre
DESS-3D	Three-Dimensional Dual Echo Steady State
DOF	Degree Of Freedom
DRR	Digitally Reconstructed Radiograph
EMG	Electromyography
FC	femoral cartilage
FE	Flexion-Extension
FEM	Finite Element Model(ling)
FP	Force plate
GCS	Global Coordinate System
HS	Heel-strike
IE	Internal-External (Rotation)
ISB	International Society of Biomechanics
JAM	Joint Articular Mechanics
JCS	Joint Coordinate System
KOOS	Knee injury and Osteoarthritis Outcome Score
KOS	Knee Outcome Survey
LCL	Lateral Collateral Ligament

MBIR	Model-Based Image Registration
MCL	Medial Collateral Ligament
ML	Medial-Lateral
MPRAGE	Magnetisation-Prepared Rapid Acquisition Gradient Echo
MRI	Magnetic Resonance Imaging
MSKBRF	Musculoskeletal Biomechanics Research Facility
MSM	Musculoskeletal Model(ling)
MVC	Maximum Voluntary Contractions
OA	Osteoarthritis
OBB	Oriented Bounding Box
OKS	Oxford Knee Score
OT	Object Transform
PACS	Pain Audit Collection System
PCL	Posterior Cruciate Ligament
PD	Proximal-Distal
PF	Patellofemoral
QTM	Qualysis Track Manager
r	Pearson's coefficient
r^2	Coefficient of determination
RMS	Root Mean Squared
RSA	Roentgen Stereophotogrammetric Analysis
SENIAM	Surface Electromyography for the Non-invasive Assessment of Muscle
SPM	Statistical Parametric Mapping
STA	Soft Tissue Artefact
std	Standard deviation
TC	tibial cartilage
TF	Tibiofemoral
TKR	Total Knee Replacement
TL	Transverse Ligament
TO	Toe-off
TTL	Transistor-Transistor Logic
UKA	Unicompartmental Knee Arthroplasty

V3D	Visual3D
VIBE	Volume-Interpolated Breath hold Examination
W	Wilcoxon signed-rank test statistic
WOMAC	Western Ontario and McMaster Universities Osteoarthritis Index
z*	Critical threshold for significance
α	Statistical significance level

CHAPTER 1: INTRODUCTION AND LITERATURE REVIEW

1.1 INTRODUCTION

The knee is the largest joint in the human body. It plays a key role in controlling the body's centre of mass and posture during activities of daily living, facilitating movement through a large range of motion (ROM) and its ability to withstand high forces (Standring 2021). As a weight-bearing joint, it provides both mobility and stability, enabling efficient and controlled movement. The knee consists of two articulating joints, the tibiofemoral (TF) and patellofemoral (PF) joints, which together form a complex synovial structure essential for locomotion. Because it is involved in many daily activities, sustains high mechanical loads, and is inherently unstable, the knee is particularly susceptible to injury and disease, both of which are commonly associated with pain. Although the relationships between mechanical factors, altered joint biomechanics, and pain have been explored (Wyndow et al. 2016; Seeley et al. 2022; Hutchison et al. 2023), they remain poorly understood. Knee pain accounts for around 5% of general practice consultations (Frese et al. 2013), highlighting its widespread impact and the need for a deeper understanding of the biomechanical mechanisms linked to pain.

Osteoarthritis (OA) is the most common chronic joint disease (Mukherjee et al. 2020). 60% of all OA cases affect the knee, making it the most frequently affected joint (Prieto-Alhambra et al. 2014; Long et al. 2022). OA is a degenerative disease of the whole joint, causing loss of articular cartilage and abnormal remodelling of bone (Arden and Nevitt 2006; Mukherjee et al. 2020), resulting in symptoms of pain, reduced mobility and joint instability (Hunter and Bierma-Zeinstra 2019). As with knee pain more broadly, alterations in joint loading, such as increased medial loading and higher knee adduction moments, have been linked to the development and progression of OA (Baliunas et al. 2002; Miyazaki et al. 2002; Andriacchi and Mündermann 2006), with uneven load distribution accelerating structural joint deterioration (Sharma et al. 2001). Factors such as malalignment, previous injury, and altered neuromuscular control also contribute to abnormal joint mechanics and accelerate cartilage degeneration (Griffin and Guilak 2005; Felson 2013). With knee OA affecting around 16% of the global population (≥ 16 years old) (Cui et al. 2020), it is important to understand the altered biomechanics that can lead to disease

progression, as OA cannot currently be prevented effectively (Mukherjee et al. 2020).

Although radiographic changes are commonly used to diagnose OA, the relationship between structural damage and symptoms is weak (Bensalma et al. 2022). Increasing evidence shows that mechanical factors such as altered joint loading, malalignment, and dynamic instability are more closely related to pain and functional impairment than static radiographic images (Bensalma et al. 2022; Hutchison et al. 2022). For example, greater medial knee loading and the presence of varus thrust have been linked to higher pain levels and disease progression (Hutchison et al. 2022), but limited knee flexion during loading is associated with poorer function (Bensalma et al. 2022). These findings highlight the importance of considering joint mechanics in both research and clinical management, as understanding how biomechanical alterations relate to pain may help identify modifiable targets for intervention (Allen et al. 2025). Assessing both healthy and pathological joints is therefore essential to understanding the altered biomechanics associated with musculoskeletal disease, injury, and interventions (Postolka et al. 2020; Ulbricht et al. 2020).

To fully understand these changes, all aspects of knee biomechanics must be considered. Combining information about bone kinematics from accurate imaging, with joint contact pressures, loading, soft tissue stresses and strains from personalised models, provides a comprehensive picture of in-vivo knee biomechanics. Using complementary imaging and modelling techniques brings together the strengths of multiple methodologies to enhance insight, providing a deeper understanding of an individual's joint behaviour during functional activities. Analysing in-vivo knee kinematics and loading in this way can provide better insight into OA characteristics, including how it progresses, ultimately aiming to improve prevention and treatment strategies for those suffering from this disease.

The remainder of Chapter 1 provides an overview of existing methods in literature for measuring in-vivo joint kinematics, with particular focus on biplane videoradiography (BVR) and its application to quantifying knee motion during dynamic activities. Current approaches to musculoskeletal modelling (MSM) and finite element modelling (FEM) of the knee are also reviewed, with emphasis on their use in

investigating cartilage mechanics. Together, this literature is used to identify limitations and gaps in current methodologies, providing the rationale for the approaches taken in this thesis, particularly the incorporation of BVR-derived kinematics in knee modelling.

1.2 MEASURING IN-VIVO JOINT KINEMATICS

In-vivo assessments form an important part of human motion analysis which aims to assist with identification, prevention and rehabilitation of musculoskeletal diseases, disabilities and injuries by investigating altered movement patterns (Hausdorff et al. 2000; Salarian et al. 2004; Astephen et al. 2008; Heesen et al. 2008; Sawacha et al. 2012; Pavao et al. 2013; Franklyn-Miller et al. 2017; Wade et al. 2022).

For the knee in particular, in-vivo imaging is key to understanding the small changes in TF kinematics caused by diseases like OA (Mills et al. 2013; Farrokhi et al. 2014; Yamagata et al. 2021), injury (Moglo and Shirazi-Adl 2005; Ali et al. 2017) or interventions (Schwechter and Fitz 2012; Clary et al. 2013b; Heyse et al. 2017). Accurately determining in-vivo knee joint kinematics, including all six degrees of freedom (DOFs) including rotations and translations (Figure 1-1), is necessary to understand complex joint movement in both healthy and pathological cohorts (Astephen et al. 2008; Giphart et al. 2012).

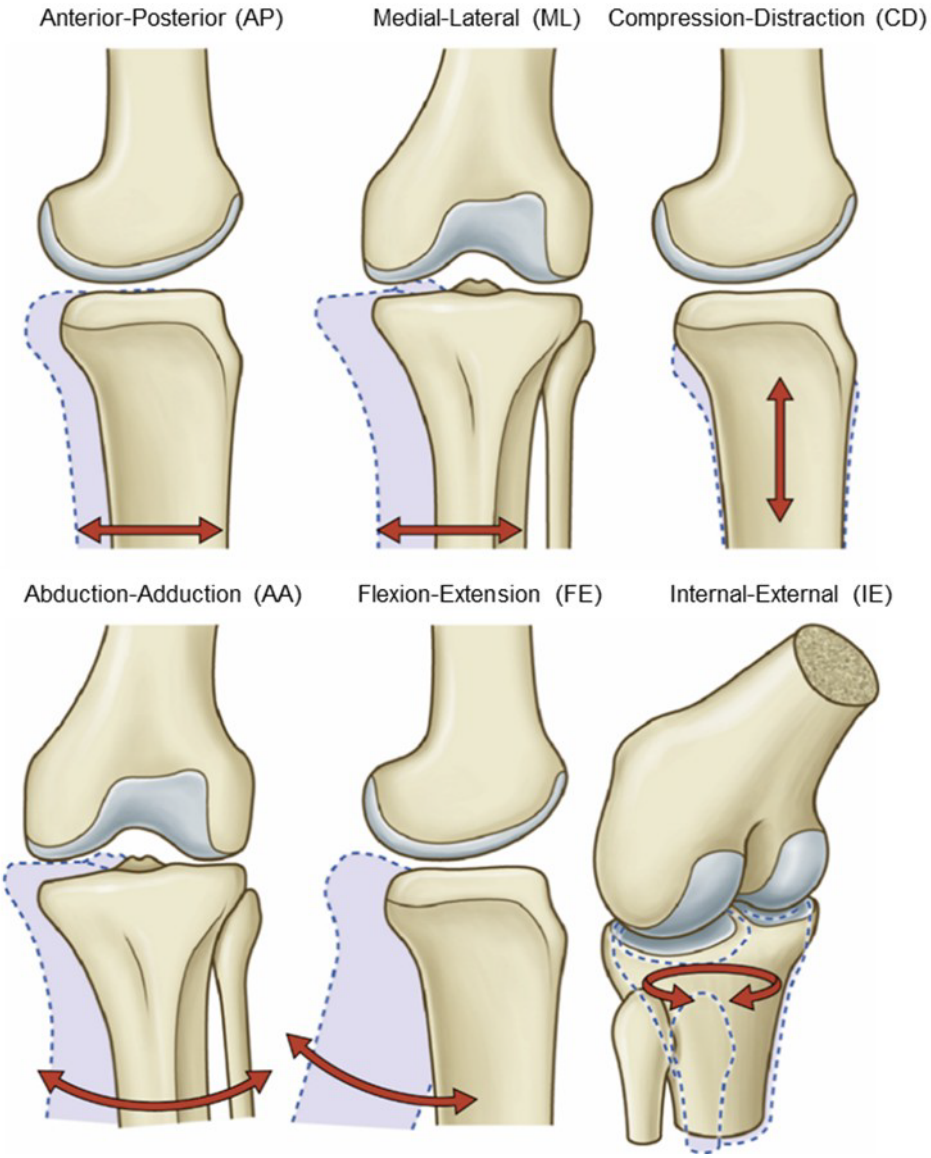

Figure 1-1 – The six DOFs of the TF joint with the three translational DOFs in the top row and the three rotational DOFs in the bottom row. Image from Standring (2021).

Multiple methods for calculating in-vivo kinematics exist, which capture the 6 DOFs of the both the TF and PF joints to varying levels of accuracy, a few of which are described in the following sections.

1.2.1 MARKER-BASED MOTION CAPTURE

Marker-based motion capture is the established standard for quantifying human joint motion (Hume et al. 2018). This typically involves a set of infrared cameras which are used to identify the positions of retro-reflective markers in three-dimensional (3D) space (Figure 1-2). These markers are placed on specific locations on the body, including palpated anatomical landmarks and marker clusters, and are used for joint

definitions and tracking body segment motion. The identified markers are then used to define body segment position and orientation and calculate relative joint kinematics (Taylor et al. 1982; Kadaba et al. 1990).

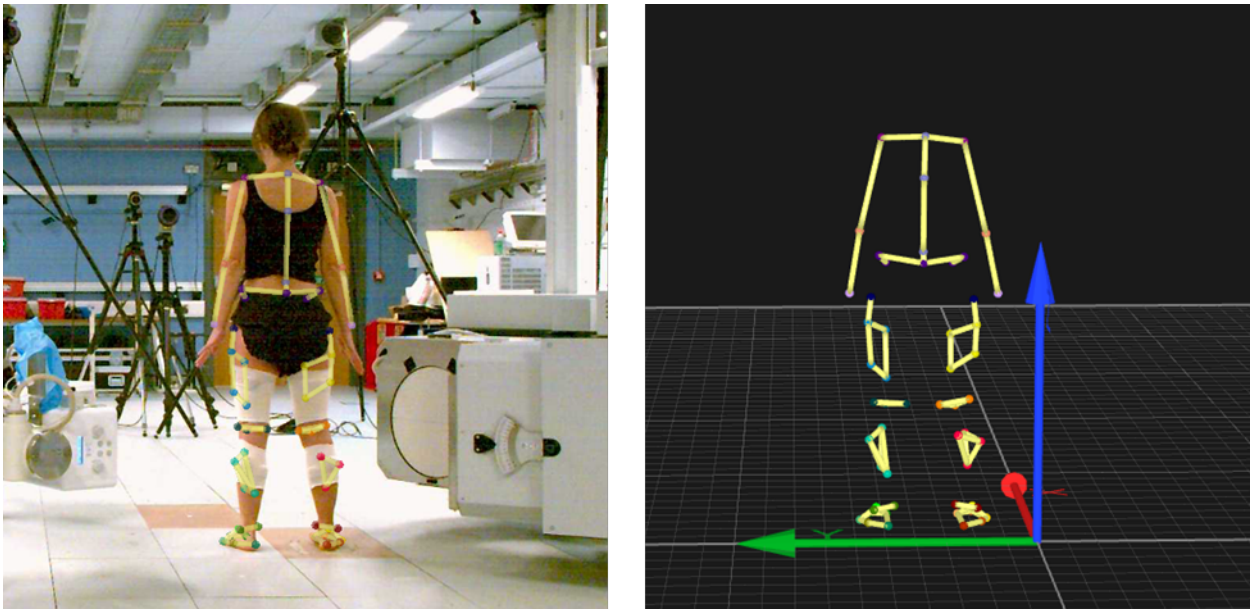

Figure 1-2 – Identified markers overlayed on a single camera view (left) reconstructed in 3D from all camera views (right).

This technique can quantify whole body kinematics, providing high repeatability in the sagittal plane for the lower limb (Mackey et al. 2005). However, it has insufficient accuracy in the other planes (Ramsey and Wretenberg 1999) as it suffers from errors caused by inaccurate marker placement on anatomical landmarks, as well as soft tissue artefact (STA) (Ramsey and Wretenberg 1999; Gorton et al. 2009; Akbarshahi et al. 2010). The quantification of the accuracy of this technique is discussed in more detail in Section 1.4.2.

1.2.2 FLUOROSCOPY AND BIPLANE VIDEORADIOGRAPHY

Another technique used for measuring in-vivo joint kinematics is X-ray fluoroscopy, also known as videoradiography. Fluoroscopy is the process of real-time dynamic imaging using X-rays (Cowen et al. 2008) and has been used to image joints in-vivo since the 1970s (Gray et al. 2018). An X-ray source-detector pair is used to sample images of the human body as it passes through the X-ray beam, producing a series radiographs containing the bone poses (the six DOF rotations and translations) of the desired joint at each point in time. Model-based image registration is then performed, matching a 3D geometry (Section 1.3.2) to the outline of the bone on a radiograph to define the pose at each frame.

Originally, fluoroscopy was performed using a single plane system, sampling radiographs from a continuous X-ray beam. Single-plane fluoroscopy has limited accuracy as it is difficult to determine any motion out-of-plane due to having only the perspective of a single 2D image at each timepoint (Fregly et al. 2005; Lin et al. 2014).

To overcome this, Biplane Videoradiography (BVR) systems were introduced, using two synchronised source-detector pairs to obtain simultaneous images at each frame from two different orientations to allow for more accurate 3D reconstruction of bone positions (Gray et al. 2018). Another advancement of BVR was utilising pulsed X-rays instead of a continuous beam, which reduces the radiation dose to the participant by emitting a series of short pulses, reducing the total X-ray exposure time (Mahesh 2001); this also reduces blur, improving output image quality (Williams 2018).

BVR is currently the gold-standard for accurately measuring in-vivo kinematics during physiological loading (Li et al. 2012; Gray et al. 2018; Setliff and Anderst 2024). Unlike marker-based motion capture, BVR has been shown to produce highly accurate 3D arthrokinematics of the knee joint in all planes (Li et al. 2008; Anderst et al. 2009; Guan et al. 2016; Gray et al. 2017; Pitcairn et al. 2018) (Section 1.4.1). It is not affected by STA or marker misplacement as it does not require placement of external devices or markers which may interfere with natural movement (Kozanek et al. 2009; Setliff and Anderst 2024).

However, a limitation of BVR is that there is only a relatively small capture volume when compared to other imaging modalities. This means it is very difficult to capture the entire motion path of the knee through the whole of an activity, so capture is limited to certain sections of the movement (e.g., stance phase) (Kozanek et al. 2009). For this reason, BVR may be captured simultaneously with alternative imaging methods (e.g. marker-based motion capture) to provide (less accurate) whole body motion, along with highly accurate kinematics of the joint(s) of interest.

1.2.3 INTRACORTICAL BONE PINS

Although BVR is highly accurate, greater accuracy can be achieved by rigidly attaching a trackable object directly to the bone. This ensures only bone motion is

recorded and is not affected by inaccuracies in the model segmentation and registration.

Levens et al. (1948) were the first to use intracortical bone pins to investigate in-vivo human motion by surgically implanting threaded stainless-steel pins into bony landmarks on the lower limb with attached retroreflective markers to track body segment motion. This approach allowed for accurate joint kinematic calculations since, unlike skin-mounted markers (Section 1.2.1), those fixed to bone pins did not move relative to the underlying bone they were tracking. This technique has subsequently been used by other researchers to investigate knee joint kinematics (McClay 1990; Koh et al. 1992; Lafortune et al. 1992b; Lafortune et al. 1994; Reinschmidt et al. 1997b; Ramsey and Wretenberg 1999; Benoit et al. 2006).

Despite the highly accuracy of this technique, the involvement of invasive surgical methods makes it unsuitable for larger scale studies due to the complexity, risks and ethical considerations associated with surgical implantation of the rods. Complications can also arise with the pins and their insertion sites, including the pins vibrating, bending, or loosening during data collection, as well as the potential for impingement of soft tissues (Levens et al. 1948; Ramsey et al. 2003).

1.2.4 ROENTGEN STEREOPHOTOGRAMMETRIC ANALYSIS

An alternative method for determining bone motion with high accuracy is roentgen stereophotogrammetric analysis (RSA) (Kärrholm et al. 1997; Valstar et al. 2005; Bragdon et al. 2006). RSA involves the surgical implantation of small tantalum beads into the desired bone, with at least three beads per bone to allow for 3D pose reconstruction. The radiopaque beads are then visible when imaged using videoradiography, enabling tracking of the bead centroids across a dynamic activity. These data, along with the 3D relationship between the bead positions and the bone anatomical coordinate system (ACS), enable accurate calculation of TF kinematics (Nilsson et al. 1990; Anderst et al. 2009; Tranberg et al. 2011; Cardinale et al. 2020).

Similarly to intracortical bone pins (Section 1.2.3), RSA requires invasive surgery, which limits its use to small-scale cohorts, usually as part of an already planned procedure (e.g. total knee replacement, TKR, or anterior cruciate ligament, ACL, repair).

Whereas model-based image registration can be affected by inaccuracies in the model geometry or unclear bone edges on the radiographs (Anderst et al. 2009), bead positions can be defined more precisely, providing greater accuracy despite using the same imaging techniques (Section 1.2.2). For these reasons, RSA is often used to determine the accuracy of a standard model-based BVR pipeline (Setliff and Anderst 2024) as the two methods can be directly compared using the same images.

1.3 BIPLANE VIDEORADIOGRAPHY

1.3.1 BVR SYSTEM AT CARDIFF

The bespoke BVR system at Cardiff (Figure 1-3) was designed for easy and consistent positioning of the two source-detectors pairs, both relative to each other and to the global coordinate system (GCS) of the laboratory (Williams 2018). This was achieved by a custom-built ceiling-mounted pair of mechanical arms, which are fixed to ensure each source and corresponding detector are always aligned on the horizontal plane. This, along with 16 controllable axes, enables quick, repeatable positioning of the system to ensure X-ray quality. With ten of the 16 axes computer-controlled, this again speeds up equipment positioning, allowing multiple setups within a single data collection session; a capability most BVR systems lack due to requiring manual setup of separate source and detector equipment. The ease of the Cardiff BVR system repositioning allows for a wider range of movements to be captured in one session, as different activities require adjustment to the X-ray arm positioning, for example, in height or angle, to optimise for bone tracking. The specific definition and controls of these axes, along with their positions for the activities included in the pilot protocol and created as part of the initial development of the system, are discussed in more detail in Section 2.3.1.

Figure 1-3 – Bespoke BVR system at Cardiff University.

An important feature of the BVR system at Cardiff is the capacity for both continuous (at up to 1000 fps) and pulsed X-ray imaging (up to 125 fps). As discussed in Section 1.2.2, the use of pulsed X-rays contributes to minimising the ionising radiation dose. The source-detector pairs are synchronised to capture images of short X-ray pulses, instead of sampling images from a continuous X-ray beam, thus reducing the overall time the X-ray beam is firing during a given movement.

1.3.2 3D BONE MODEL GENERATION

To calculate kinematics from two-dimensional (2D) BVR images, 3D models of bone geometry are matched with radiograph pairs during image registration (Kim et al. 2011). There are two main imaging modalities used for generating 3D geometries for this application: computed tomography (CT) and magnetic resonance imaging (MRI).

CT is the gold standard for generating 3D bone models (Moro-oka et al. 2007; Lee et al. 2008; Rathnayaka et al. 2012) because it produces clear, defined bone boundaries. However, as CT requires increasing the ionising radiation dose, alternative imaging modalities, e.g., MRI, may be more appropriate, particularly when imaging healthy volunteers. Studies have shown that 3T MRI provides sufficient

accuracy for model-based image registration, making it a viable alternative to CT (Neubert et al. 2017; Williams 2018). Additionally, MRI can image soft-tissue joint structures, such as the articular cartilage and menisci, which are not visible on CT scans without a contrast agent. Inclusion of soft tissue imaging enables further analysis of joint contact, including cartilage contact areas or ligament elongation, when combined with BVR image registration outputs, (Setliff and Anderst 2024).

The specific structures of interest can then be segmented from the 3D imaging to create 3D geometries which are used to generate the digitally reconstructed radiographs (DRRs) required for image registration (Section 2.4.2).

1.3.3 DEFINING TIBIOFEMORAL KINEMATICS

6 DOF kinematics of the tibiofemoral joint, calculated for the bone pose maps generated from model-based image registration, fully define the position and orientation of the bone ACS at each frame. The most common approach for calculating these kinematics is the method proposed by Grood and Suntay (1983) (Figure 1-4), as recommended by the International Society of Biomechanics (ISB) (Wu et al. 2002).

This describes the three rotations of the knee as follows: flexion around the fixed body of the femur (medial-lateral, ML, axis through the femoral condyles), external rotation around the fixed body axis of the tibia (superior-inferior, SI, axis, perpendicular to the tibial plateau), and adduction around the floating axis (the cross-product of the two fixed body axes). These conventions can also be used to define TF joint translations, but their magnitudes are highly dependent on the positioning of the bone origins chosen (Grood and Suntay 1983).

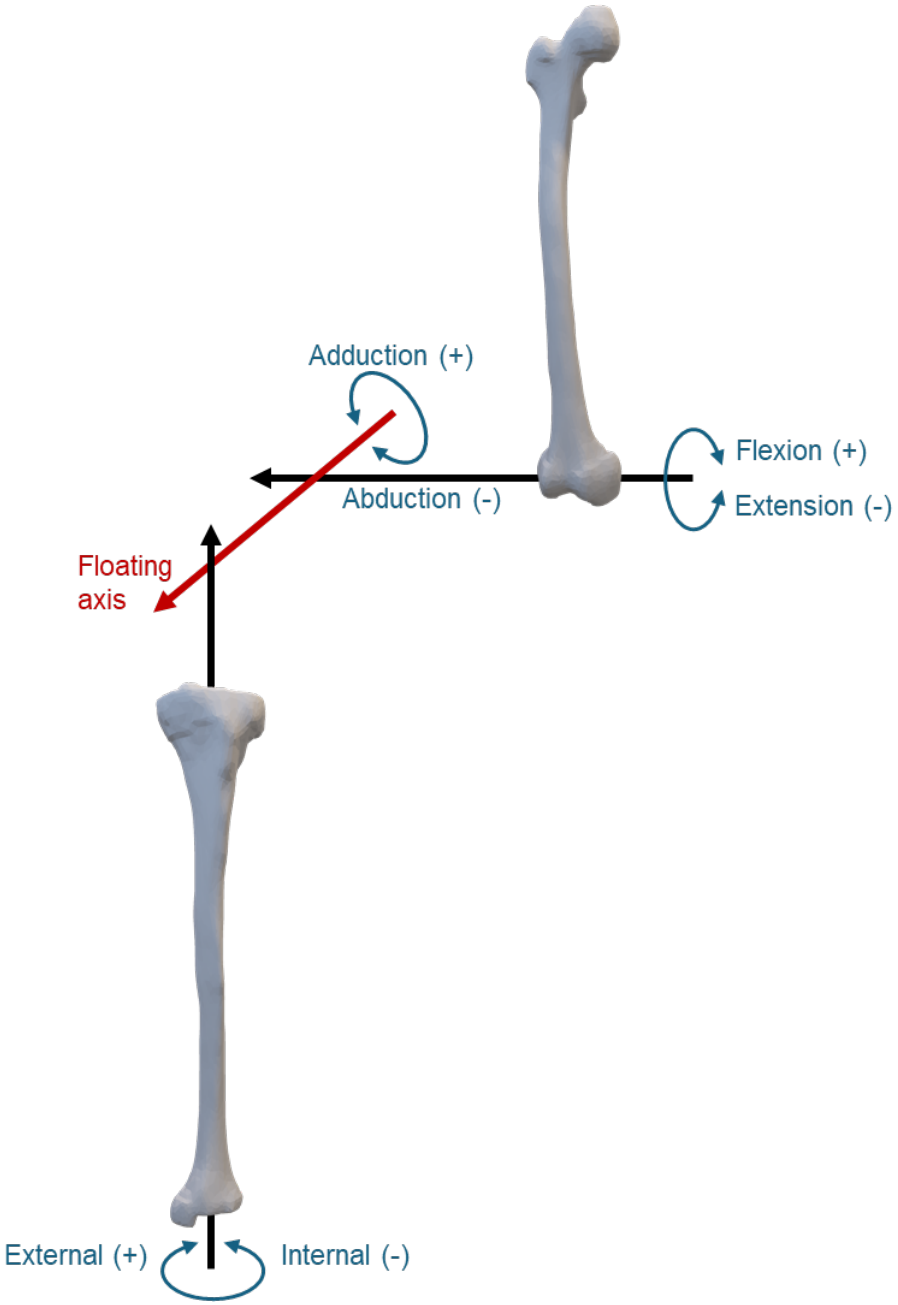

Figure 1-4 – Joint coordinate system angle definitions, recreated from Grood and Suntay (1983).

One limitation of comparing TF translations across a cohort using these conventions is that knee size affects translation magnitude, making it difficult to average results across a cohort. For example, in SI axis translations, the offset in distraction magnitude is highly dependent on knee size because larger bones result in greater separation between bone origins, making it challenging to detect variations in movement over large offsets. For this reason, alternative approaches have been used, such as defining only compression-distraction (CD) or all three knee joint translations relative to an initial coincident origin (usually the femoral origin located

between the condyles) (Kefala et al. 2017; Gray et al. 2019; Thomeer et al. 2021; Kour et al. 2022) or expressing the translations of one bone in the coordinate system of the other (Tashman et al. 2004; Li et al. 2012). Using a single, coincident origin also has the benefit of being consistent with the typical joint definition in marker-based motion capture kinematics, for example, in an OpenSim model (Lenhart et al. 2015), allowing for direct comparison between translation outputs.

1.3.4 PREVIOUS BVR STUDIES

A number of previous studies have used BVR to obtain in-vivo kinematics for a variety of joints, including up to six DOFs of the TF and PF joints. A scoping review by Setliff and Anderst (2024), that investigated the usage of BVR for in-vivo human skeletal kinematics, found that nearly half of all in-vivo BVR studies (180/379 studies included) looked at knee kinematics.

Setliff and Anderst (2024) also found that the average in-vivo BVR study cohort size (across all joints, not just the knee) was small (mean = 16, median = 11). This reflects the time required to process BVR data (which they estimated at 40-80 hrs per data collection), as well as the high cost associated with this technique.

BVR has been used to study knee kinematics across various dynamic activities. Table 1-1 provides examples of movements investigated in literature, illustrating the range of activities studied, although this is not an exhaustive list.

Table 1-1 – Examples of the activities used with BVR to investigate knee motion.

Activity	**Studies**
Level gait (overground)	(Myers et al. 2012; Guan et al. 2016; Guan et al. 2017; Kefala et al. 2017; Pitcairn et al. 2018; Gray et al. 2019; Gray et al. 2020; Gray et al. 2021; Thomeer et al. 2021; Ganapam et al. 2022; Hamilton et al. 2022; Kour et al. 2022; Thomeer et al. 2022; Hamilton et al. 2023; Guan et al. 2024)
Treadmill level gait	(Kozanek et al. 2009; Liu et al. 2010; Barre et al. 2013; Guan et al. 2016; Guan et al. 2017; Yang et al. 2018; Gale and Anderst 2019; Koo and Koo

	2019; Nagai et al. 2019; Gale and Anderst 2020; Byrapogu et al. 2022)
Downhill gait (overground or treadmill)	(Farrokhi et al. 2014; Gustafson et al. 2015; Gray et al. 2021; Gustafson et al. 2021; Thomeer et al. 2021; Ganapam et al. 2022; Thomeer et al. 2022)
Running (treadmill)	(Li et al. 2012; Nagai et al. 2019; Tanaka et al. 2023)
Downhill running (treadmill)	(Tashman et al. 2004; Tashman et al. 2007; Anderst et al. 2009; Hoshino and Tashman 2012; Hoshino et al. 2013; Nagai et al. 2018; Yang et al. 2018)
Stair ascent/step up	(Li et al. 2012; Suzuki et al. 2012; Li et al. 2013; Pitcairn et al. 2018; Gray et al. 2021; Thomeer et al. 2021; Byrapogu et al. 2022; Kour et al. 2022; Thomeer et al. 2022; Guan et al. 2024)
Stair decent/step down	(Kefala et al. 2017; Gray et al. 2021; Thomeer et al. 2021; Byrapogu et al. 2022; Kour et al. 2022; Thomeer et al. 2022; Guan et al. 2024)
Non-weightbearing flexion (or extension)	(Myers et al. 2011; Myers et al. 2012; Kefala et al. 2017; Shih et al. 2020; Gray et al. 2021; Thomeer et al. 2021; Thomeer et al. 2022; Hamilton et al. 2023)
Continuous lunge (dynamic, weightbearing)	(Kernkamp et al. 2019; Hamilton et al. 2022)
Quasi-static lunge (weightbearing)	(Defrate et al. 2006; Bingham et al. 2008; Nha et al. 2008; Van de Velde et al. 2009a; Van de Velde et al. 2009b; Hosseini et al. 2012; Kobayashi et al. 2013; Qi et al. 2013; Van de Velde et al. 2016)
Sit-to-stand	(Shih et al. 2020; Byrapogu et al. 2022; Kour et al. 2022; Guan et al. 2024)
Stand-to-sit	(Kour et al. 2022; Guan et al. 2024)
Drop landing	(Myers et al. 2011; Torry et al. 2011a; Torry et al. 2011b; Myers et al. 2012; Tanaka et al. 2023)
Pivot (90° direction change)	(Kefala et al. 2017)

Due to variations in BVR equipment, different configurations are often used for the same activity. Physical limitations in the arrangement of the X-ray source-detector pairs may prevent them from being positioned in certain configurations. For example, with the Cardiff BVR system, with source-detector pairs mounted on machine arms, it is not possible to stack the detectors directly on top of one another, and there will always be a slight offset. Currently, no standard exists for collecting data across activities, leaving BVR protocol design up to user discretion. This lack of standardisation makes it challenging to compare results across research studies (Setliff and Anderst 2024).

BVR has been used to investigate many clinically relevant questions, highlighting its ability to provide accurate, useful in-vivo data. It has not only been utilised to investigate changes in joint kinematics due to diseases, such as OA (Farrokhi et al. 2014; Gustafson et al. 2015; Gustafson et al. 2021), but also the efficacy of interventions for such diseases, including TKR (Barre et al. 2013; Guan et al. 2016; Guan et al. 2017; Gray et al. 2020; Shih et al. 2020; Kour et al. 2022; Guan et al. 2024), UKA (Byrapogu et al. 2022), and ACL injury and subsequent repairs (Defrate et al. 2006; Tashman et al. 2007; Van de Velde et al. 2009a; Hosseini et al. 2012; Van de Velde et al. 2016; Nagai et al. 2018; Pitcairn et al. 2018; Ganapam et al. 2022).

As well as studying six DOF kinematics, BVR has also been used to investigate cartilage deformation (Liu et al. 2010; Thomeer et al. 2022) and contact location (Liu et al. 2010; Hamai et al. 2013; Gray et al. 2019; Thomeer et al. 2021; Thomeer et al. 2022), as well as TF centre of rotation location changes (Gray et al. 2019; Postolka et al. 2020) and joint space distances (Byrapogu et al. 2022).

1.4 DATA COLLECTION TECHNIQUE ACCURACY

1.4.1 ACCURACY OF BIPLANE VIDEORADIOGRAPHY

The accuracy of BVR for calculating in-vivo bone motion and kinematics has been quantified across a range of joints, with studies typically reporting an accuracy of around 1-2° or better for rotational DOFs, and 0.5-1.0 mm or better for translational DOFs (Bey et al. 2006; Anderst et al. 2009; Anderst et al. 2011; Pitcairn et al. 2018; Akhbari et al. 2019; Pitcairn et al. 2020).

RSA is typically used as the benchmark for BVR accuracy (Setliff and Anderst 2024) as the implanted beads can be tracked from the same X-ray images used in standard model-based image registration. The accuracy of BVR is dependent on several factors, including the joint of interest, source-detector equipment and configuration, X-ray generator settings, and type of dynamic activity being imaged. Therefore, the accuracy of a specific protocol must be determined individually.

Anderst et al. (2009) investigated BVR accuracy during in-vivo treadmill running (2.5 m/s) in three ACL-reconstruction patients who had three tantalum beads implanted into their ACL-intact leg during the reconstruction surgery. They found femur and tibia tracking precision to be similar, with no significant bias in model-based tracking compared to bead-based tracking. The rotations were shown to be generally well predicted by the model-based image registration with root mean squared (RMS) errors of 1.75° (FE), 1.44° (IE) and 0.54° (AA). The translations were also calculated accurately, with ML and CD both having RMS errors of 0.69 mm. AP translation had the highest RMS error of the TF translations (1.54 mm), suggested to be due to the orientation of the source-detectors relative to the direction of travel, reinforcing the dependence of BVR accuracy on equipment configuration.

Another study looking at BVR TF tracking accuracy was Guan et al. (2016) who investigated the accuracy of their mobile biplane X-ray imaging system during simulated walking of an intact human cadaveric knee compared to a TKR implanted into sawbones. Again, they compared model-based tracking to the ‘gold-standard’ bead-based tracking. They found greater accuracy for the TKR knee measurements, likely because the implant edges were more clearly defined in the X-ray images and the precisely known TKR component geometry facilitated more accurate model-matching. The RMS errors for the intact knee ranged from 0.30-0.77° for the rotations and 0.35-0.78 mm for the translations. The highest errors were found in the IE rotation and ML translation and were attributed to the inter-axis angle of the X-ray setup (60°) and their position relative to the imaged knee.

Li et al. (2008) also investigated the accuracy of their (static) BVR system using human cadavers, comparing model-based image registration-derived to RSA-derived kinematics. The mean difference between RSA and model-based TF rotations during

dynamic flexion-extension (of the full knee ROM) were found to be between -0.16-0.37°, and the translations were found to be between -0.13-0.24 mm.

These studies show that BVR is an accurate method for determining in-vivo kinematics of the TF joint during dynamic movements, although specific protocol and equipment accuracy can vary.

1.4.2 MARKER-BASED MOTION CAPTURE ACCURACY

As discussed briefly in Section 1.2.1, marker-based motion capture is widely used for assessing joint kinematics, but its accuracy is affected by several factors, including anatomical landmark identification, STA, and movement dynamics. Various studies have evaluated these limitations across different activities to understand their effects on TF joint kinematics.

STA is one of the main contributing factors to marker-based motion capture errors. To investigate this, several studies have employed single-plane fluoroscopy to assess STA during various dynamic tasks, including Stagni et al. (2005) who used retroreflective, radiopaque markers to compare skin-marker motion capture with single-plane fluoroscopy in TKR patients. The skin markers moved significantly relative to the underlying implant components (and therefore bones), with deviations reaching 31 mm for the thigh and 21 mm for the shank, with the largest errors (up to 42 mm) occurring in the distal thigh. AA and IE rotations were found to be most affected, indicating that STA could substantially compromise kinematic interpretation, particularly in clinical gait analysis.

Akbarshahi et al. (2010) investigated STA across multiple activities, including open-chain knee flexion, hip axial rotation, walking, and step-ups, by comparing marker-based motion capture results with single-plane fluoroscopy. Their results highlighted the subject-, task-, and location-dependent nature of STA magnitudes. They also showed greater STA for the thigh than the shank, with marker movement RMS errors reaching 29.3 mm and kinematic errors peaking in open-chain flexion (FE: 24.3°, IE: 17.9°, AA: 14.5°). Using a similar method, Tsai et al. (2011) examined STA during stair ascent, again finding greater soft tissue movement in the thigh than the shank. They also found knee joint centre translations to be significantly larger from motion-capture data. Earlier work by Sati et al. (1996) also explored skin-bone movement using single-plane fluoroscopy and skin-mounted radio-opaque markers, during

dynamic knee flexion, revealing substantial variability in marker displacement over the medial and lateral femoral condyles (2.5–17 mm RMS), with maximum marker movement reaching 44 mm. Collectively, these studies support the current belief that STA is a major source of error in marker-based TF kinematics, particularly in dynamic and high-flexion tasks.

Reinschmidt et al. (1997b) presented similar findings when comparing skin-marker motion capture with intracortical bone pin data (Section 1.2.3) during running, attributing the main differences between external and skeletal motion to thigh STA. These differences resulted in FE errors that averaged 21% of the ROM during stance, while IE and AA errors were much larger, at 63% and 70% of the ROM, respectively. Joint angles were consistently overestimated, with errors varying considerably between subjects.

Ramsey and Wretenberg (1999) also utilised intracortical bone pins to investigate marker-based motion capture accuracy. They found skin-mounted marker kinematics exhibited translational errors of 2-15 mm and rotational errors of 2-10° compared to bone pin measurements, again stating STA as the primary source of error.

STA errors lead to incorrectly calculated bone axes positions as demonstrated by Miranda et al. (2013), who explored motion capture errors during a dynamic jump-cut manoeuvre. Discrepancies in femoral ACS axes rotation and translation peaked at 18.18° and 33.70 mm, respectively; tibial ACS axes errors were similarly high, at 13.43° and 29.11 mm. These axes errors had a subsequent effect on the calculated six DOF kinematics with maximum rotational differences of 9.28° in FE, 11.80° in AA, and 14.76° in IE. Translations were found to be poorly predicted with maximum errors of 16.84 mm in the ML direction, 21.62 mm for AP, and 27.60 mm for CD. Notably, the secondary rotational and translational errors often exceeded 100% of the measurement magnitude. The largest errors occurred post-ground contact, where soft tissue and muscle oscillations amplified motion capture errors.

Hume et al. (2018) compared motion capture-derived kinematics to BVR using both a standard three DOF Visual3D (V3D, HAS-Motion, Canada) pipeline and a six DOF OpenSim MSM across a range of activities – including seated knee extension, gait, step-down, and pivot turns. For the V3D results, large errors in translation were seen in all three planes, consistent with the findings from Miranda et al. (2013). The

largest error was found in the AP (20.9 mm), followed by CD (19.7 mm) and ML (7.0 mm) directions, highlighting why translations are rarely reported from marker-based V3D pipelines. Rotational errors were smaller but still reached 5.9° for AA and 7.0° for IE rotation. Hume et al. (2018) also found that the differences between the V3D and BVR secondary kinematics increased as knee flexion increased. An alternative approach, using the OpenSim MSM with spline functions to relate secondary kinematics to flexion produced improved kinematic prediction accuracy but did not fully resolve subject-specific discrepancies (Hume et al. 2018).

Marker-based motion capture derived kinematics have also been compared to the more accurate method, RSA (Section 1.2.4). Using RSA as the comparator, Tranberg et al. (2011) found relatively good agreement of flexion during active knee extension, but motion capture slightly overestimated flexion, with errors increasing from 2° at full extension to 5° at higher flexion angles. IE rotation was found to be reasonably accurate at lower flexion angles but diverged significantly at higher flexion (up to 11° at 50°). AA displayed systematic mean differences of 2-4° across all flexion angles. These results highlight that while FE data derived from motion-capture is likely reliable, errors in secondary kinematics are more pronounced, due to STA and the small true motion in these planes.

As well as STA, marker placement variability also contributes to kinematic errors. Della Croce et al. (1999) examined intra- and inter-examiner reliability in anatomical landmark identification, reporting root mean square (RMS) errors of 6-21 mm for intra-examiner assessments and 13-25 mm for inter-examiner comparisons. These variations affect bone ACS definitions, introducing systematic inaccuracies.

Together, these studies illustrate the challenges of using marker-based motion capture for precise kinematic analysis. The main sources of error include marker placement variation and STA, with inaccuracies worsening at higher flexion angles and during dynamic tasks.

1.5 BIPLANE VIDEORADIOGRAPHY HEALTHY IN-VIVO TIBIOFEMORAL KINEMATICS FROM LITERATURE

From literature, a description of the 6 DOF kinematics of the TF joint for healthy volunteers participating in in-vivo BVR studies is summarised below for the three activities in the protocol described in Chapter 2 (Section 2.3.6). These activities were chosen for a pilot study protocol. They were created as part of the Cardiff BVR system development (Section 1.3.1) to provide data on a range of functional knee movements, for everyday activities (level gait and stair ascent) and high flexion (lunge) to give a picture of healthy TF joint motion.

1.5.1 LEVEL GAIT

As shown in Table 1-1 in Section 1.3.4, level gait is the most studied activity when using BVR to investigate TF kinematics. This key activity of daily living is often used as an indicator of knee joint health (Minns 2005; Kumar et al. 2013; Mills et al. 2013), hence why it is an important activity to study.

The TF joint was found to have little flexion at heel-strike (HS); some studies reported small degrees of flexion at HS (Gray et al. 2019; Gale and Anderst 2020), whereas others reported slight extension (Kozanek et al. 2009; Thomeer et al. 2021). After HS, the knee then began to flex, reaching its first flexion peak during early stance. The knee then extended again until approximately 70% stance, where it rapidly flexed until toe-off (TO), reaching its maximum value for stance phase. There was some disagreement regarding the value of the maximum flexion peak at TO. Some studies predicting a lower peak, around 15° (Gray et al. 2019), while others predicted up to around 50° (Thomeer et al. 2020). Although all studies described a similar flexion pattern, this difference arose from the timing of the second flexion peak in the entire gait cycle, which was predicted to occur close to TO. This timing difference also explains the variations in the ROM observed across the studies.

Little AA rotation was found during stance phase (Kefala et al. 2017; Gray et al. 2019; Gale and Anderst 2020; Thomeer et al. 2021), with it having the smallest ROM of the three rotations (Kozanek et al. 2009; Myers et al. 2012; Kefala et al. 2017; Gale and Anderst 2020; Hamilton et al. 2023). Most studies found the average knee adduction angle to remain positive throughout stance phase (Kefala et al. 2017; Gray

et al. 2019; Gale and Anderst 2020; Thomeer et al. 2021), however, some studies found the knee to be abducted instead (Kozanek et al. 2009; Myers et al. 2012). There was also disagreement over whether the abduction angle correlates with flexion; Kozanek et al. (2009) found adduction to be moderately correlated with flexion, whereas Thomeer et al. (2021) and Gray et al. (2019) found weak correlation.

Most studies found the tibia was found to be externally rotated at HS, then internally rotated throughout the majority of the rest of stance phase, with this internal rotation overall increasing in value throughout stance phase until reaching peak internal rotation at terminal stance (Kozanek et al. 2009; Kefala et al. 2017; Gray et al. 2019; Thomeer et al. 2020; Thomeer et al. 2021). However, one study found the mean angle remained externally rotated throughout the majority of stance phase (Gale and Anderst 2020), although it found a similar rotation pattern to the other studies. External rotation was found to be moderately correlated with flexion (Kozanek et al. 2009; Thomeer et al. 2021).

The largest translational ROM during stance phase was AP (Kozanek et al. 2009; Gale and Anderst 2020; Hamilton et al. 2023). Most studies found the tibia to be anteriorly translated relative to the femur during the whole of stance phase (Kozanek et al. 2009; Gray et al. 2019; Gale and Anderst 2020; Thomeer et al. 2021). Some studies found a peak anterior translation around the point of contralateral TO, then a decrease in anterior translation, followed by a final increase to maximum anterior translation during the latter portion of stance phase (Gray et al. 2019; Thomeer et al. 2020; Thomeer et al. 2021). Increased anterior translation was found to be linked with flexion (Kozanek et al. 2009; Gray et al. 2019; Thomeer et al. 2021).

Overall, the knee was found to begin stance phase laterally translated, with minimal change until the latter part of stance, where the knee shifted medially reaching its peak medial translation at TO (Gray et al. 2019; Thomeer et al. 2020; Thomeer et al. 2021). The differences in pattern found in other studies (Kozanek et al. 2009; Gale and Anderst 2020) can be attributed to the different methods used to define the translations. Medial shift was found to be correlated with increasing flexion (Gray et al. 2019; Thomeer et al. 2021).

CD was found to have the smallest translational ROM, with minimal change during stance, often with a non-descript profile (Kozanek et al. 2009; Thomeer et al. 2020; Thomeer et al. 2021; Hamilton et al. 2023). The TF joint was found to be in compression throughout stance (Gray et al. 2019; Thomeer et al. 2020; Thomeer et al. 2021). It was also found to be coupled with flexion (Gray et al. 2019; Thomeer et al. 2021).

1.5.2 STAIR ASCENT

Stair ascent (or an equivalent step-up activity) was included in fewer BVR studies than level gait (Section 1.3.4), with only a handful of studies presenting TF kinematics in healthy individuals (Suzuki et al. 2012; Li et al. 2013; Thomeer et al. 2021). Suzuki et al. (2012) and Li et al. (2013) only presented TF flexion out of the six DOFs, as they looked at PF kinematics and TF joint contact location, respectively. Therefore, to better understand the expected kinematic profiles in healthy knees for this activity, studies using single-plane fluoroscopy (Tsai et al. 2011) and involving intact knees – compared to an injured contralateral limb – (Li et al. 2012) were also included.

The flexion profiles of the stance phase of stair ascent all began at a high degree of flexion (ranging from ~50-70°), increasing slightly to peak flexion (at around 10-20% stance phase), before steadily decreasing to reach minimum flexion (Tsai et al. 2011; Li et al. 2012; Suzuki et al. 2012; Li et al. 2013; Thomeer et al. 2021). The end of stance phase differed between studies, with some finding the mean flexion angle to increase again in the last ~10% stance phase after reaching its minimum (Tsai et al. 2011; Thomeer et al. 2021), whereas others only found a steady decrease, reaching slight joint extension at the end of stance (Suzuki et al. 2012; Li et al. 2013). This may be due to these studies using a single step-up activity, as opposed to a multiple-step stair ascent, so stance ends with both feet on the floor in a neutral standing position, rather than the participant continuing on to the next stair.

The knee displayed a small ROM of a few degrees throughout stance phase (Tsai et al. 2011; Li et al. 2012; Thomeer et al. 2021). Thomeer et al. (2021) found the mean knee adduction to remain around 4-5° throughout all of stance phase. Li et al. (2012) similarly found the knee to be slightly adducted (between 0-2° adduction) throughout, with an overall slight trend of increasing adduction through to the end of the recorded

period of the activity (0.3s from HS). Unlike the other two, Tsai et al. (2011) found the knee to be abducted during stance phase, finding the largest abduction angles toward the start and end of the activity, with it tending to 0° at around 50% stance.

All three studies found the knee to be internally rotated by ~10-18° at the start of stance, followed by a decrease reaching a minimum of approximately 4-8° at the end of stance phase (Tsai et al. 2011; Li et al. 2012; Thomeer et al. 2021). Tsai et al. (2011) and Thomeer et al. (2021) found a similar IE rotation ROM, with a similar profile of a steeper decrease at the start, followed by a short period of minimal change around 60% stance, then another period of decrease.

AP was found to have the largest ROM out of the three translations (Tsai et al. 2011; Thomeer et al. 2021). Thomeer et al. (2021) found the tibia to be translated anteriorly throughout the whole of stance phase, with initial increasing anterior motion at HS, peaking early in stance phase (approximately 7 mm at around 15-20% stance), followed by decreasing anterior drawer. Tsai et al. (2011) found a similar initial peak of anterior motion (at around 20-30% stance), then the tibia moved posteriorly, reaching slight posterior translation during 80-90% stance (the end of recorded motion). Li et al. (2012), however, reported posterior translation of the knee at HS (starting at around 20 mm), with a slight anterior movement for the rest of the recorded period (reaching around 10mm posterior translation). The overall magnitude of translation reported by Li et al. (2012) appears comparable to that of the other two studies, though in the opposite direction. As the authors did not specify the sign convention used in their graphs (labelled only as ‘AP translation’), negative values were assumed to represent posterior translation.

There was little ML translation ROM during the stance phase of stair ascent, with all studies showing this translation to fluctuate around 0 mm (Tsai et al. 2011; Li et al. 2012; Thomeer et al. 2021). Tsai et al. (2011) and Thomeer et al. (2021) found a similar profile of a small lateral peak in the first half of stance, followed by the tibia moving medially, reaching an overall medial translation in the second half of stance, whereas Li et al. (2012) found the tibia to be translated laterally by less than 1 mm throughout, with little variation.

Tsai et al. (2011) predicted very little change in CD translation during stance phase of stair ascent, with slight proximal translation in the first half, followed be even

smaller distal translation in the second half, all fluctuating around 0 mm translation. Thomeer et al. (2021) also found a small ROM, but the tibia was proximally translated (around 2 mm) all through stance. Li et al. (2012) found larger distal translation of the knee of around 15-25 mm, likely due to the joint definition offset, and found a trend of increasing distal translation from HS onwards.

Only Thomeer et al. (2021) reported on correlation between flexion angle and the other five secondary TF DOFs during stair ascent. Coupling was found between flexion and abduction, external rotation, and lateral shift (r^2 = 0.76, 0.80, and 0.83, respectively). Moderate correlation was found between flexion and the other two rotations.

Due to the limited number of studies investigating stair ascent TF kinematics using BVR, it is difficult to know the extent of the range of variation expected across participants when completing this activity.

1.5.3 LUNGE

A dynamic weightbearing lunge was included in the pilot study protocol to investigate knee kinematics during deeper knee flexion. As there is demand for deep flexion amongst OA and TKR patients to allow them to perform a range of daily activities such as kneeling, squatting, gardening, yoga and getting into a bath (Weiss et al. 2002; Huddleston et al. 2009; Galvin et al. 2018). Understanding healthy TF kinematics during deeper flexion becomes necessary to bring patients closer to ‘typical’ movement, improving knee ROM in all six DOFs, not just FE.

As only one study presented healthy TF kinematics during a dynamic, weightbearing lunge using BVR (Hamilton et al. 2022), studies that used single-plane radiography (Leszko et al. 2011; Hamai et al. 2013), a quasi-static lunge (Qi et al. 2013), or a non-weightbearing flexion-extension activity (Myers et al. 2012; Kefala et al. 2017; Thomeer et al. 2021) are also used to describe kinematic profiles of the TF joint during a high-flexion activity.

A large variation was found in the flexion ROM between activities. Some studies only measured kinematics from 0° flexion (Myers et al. 2012; Thomeer et al. 2021), whereas others measured from full joint extension (Leszko et al. 2011; Qi et al. 2013). The range of peak flexion was large as some studies stopped the knee flexing

at 90° (Myers et al. 2012), whereas others altered the activity to increase the maximum flexion angle; for example, Leszko et al. (2011) got their participants to lean forward at the peak lunge, and Hamai et al. (2013) made participants lunge onto a 25 cm step, reaching 150° knee flexion.

The tibia was consistently reported as adducted relative to the femur during flexion activities (Leszko et al. 2011; Hamai et al. 2013; Qi et al. 2013; Kefala et al. 2017; Thomeer et al. 2021; Hamilton et al. 2022). Some studies also showed an overall trend of increasing adduction as flexion increased (Leszko et al. 2011; Hamai et al. 2013; Qi et al. 2013), however this was not observed consistently across studies.

For IE rotation, a consistent trend of increasing internal rotation of the tibia relative to the femur was observed in multiple studies, reaching around ~20° internal rotation at 100° flexion (Leszko et al. 2011; Hamai et al. 2013; Kefala et al. 2017; Hamilton et al. 2022). Generally, the knee was found to remain internally rotated throughout (Hamai et al. 2013; Kefala et al. 2017; Thomeer et al. 2021; Hamilton et al. 2022), however some recorded slight external rotation at very low flexion angles (into joint extension) (Leszko et al. 2011; Qi et al. 2013) which was attributed to the screw-home mechanism (Barnett 1953; Hallen and Lindahl 1966).

For the translations, increasing knee flexion angle resulted in increasing anterior translation of the tibia relative to the femur (Qi et al. 2013; Kefala et al. 2017; Thomeer et al. 2021; Hamilton et al. 2022). ML translation was presented with less consistency, with some studies presenting a lateral to medial shift of the tibia as flexion increased (Thomeer et al. 2021; Hamilton et al. 2022). In contrast, Qi et al. (2013) showed higher lateral translations (6-8 mm) at higher and lower flexion angles, with a lower lateral translation between 30-120° flexion (3.0-4.5 mm). Kefala et al. (2017) found variation in the magnitude of ML translation between participants, with some showing medial translation and others showing lateral translation. CD was not presented by many studies, but Thomeer et al. (2021) found the joint to be in compression throughout, beginning at around 1 mm of compression with minimal change during early flexion, then increasing to reach a peak compression of around 4 mm at peak flexion and Hamilton et al. (2022) presented CD translation that decreased as flexion increased (with an average ROM of 4.5 mm).

Thomeer et al. (2021) found all five secondary DOFs to be coupled with flexion angle, with r^2 values ranging from 0.81 to 0.99. This shows the value of activities that achieve high flexion angles in understanding the relationship between flexion and the other TF DOFs.

1.6 MUSCULOSKELETAL MODELLING

Musculoskeletal modelling (MSM) is used to investigate parameters that are unable to be measured directly from in-vivo methods, such as musculo-tendon and joint contact forces during movement (Erdemir et al. 2007; Pandy and Andriacchi 2010; Cheze et al. 2015; Moissenet et al. 2017). By modelling the skeleton as a series of rigid bodies connected by joints and actuated by muscle and ligament forces, MSM allows for non-invasive estimations of in-vivo joint kinematics, muscle activation patterns and joint forces during dynamic motion. This makes it a useful tool for both research and clinical applications (Cardona and Garcia Cena 2019; Luis et al. 2022).

MSM provides a method for quantifying muscle forces, joint torques, and tissue loading during movement, providing a tool to investigate pathologies affecting neuromuscular control, such as stroke (Lin and Yan 2011; Giarmatzis et al. 2022; Wang et al. 2022), or joint specific pathologies, such as OA (Kumar et al. 2013; Dzialo et al. 2019; Price et al. 2020; Ghazwan et al. 2022; Bowd et al. 2023).

MSMs designed to focus on knee movement typically represent the lower limb joints with varying DOFs of movement depending on the specific joint and the complexity required to replicate joint movement. The upper body can also be included to model full body movement.

The MSM bones and joints are articulated using spring bundles, representing the muscles and ligaments, to replicate body positions. The equations of motion are then solved to match input marker trajectories and ground reaction forces (GRFs), typically from marker-based motion capture, as frequently used inputs (Sylvester et al. 2021). Together, the ligament and muscle forces are balanced, through the process of inverse dynamics, to solve the resultant forces required to generate movement of the model that matches the measured in-vivo body movements from motion-capture. This then allows further analysis of muscle coordination strategies or joint contact throughout a dynamic motion.

The most widely used muscle model for MSM is the Hill-type muscle model (Miller 2018; Andersen 2021; Yeo et al. 2023). It made up of three elements (Figure 1-5): a contractile element that accounts for activation dynamics (including force-length-velocity relationships), a series elastic element representing tendon elasticity and energy storage, and a parallel elastic element modelling passive tissue stiffness at extreme lengths (Zajec 1989; Scovil and Ronsky 2006; Miller 2018; Cardona and Garcia Cena 2019; Luis et al. 2022; Zhao et al. 2022). Although the Hill-type model suffers from numerical instabilities, it is still widely used due to its computational simplicity and suitability for large-scale simulations (Yeo et al. 2023).

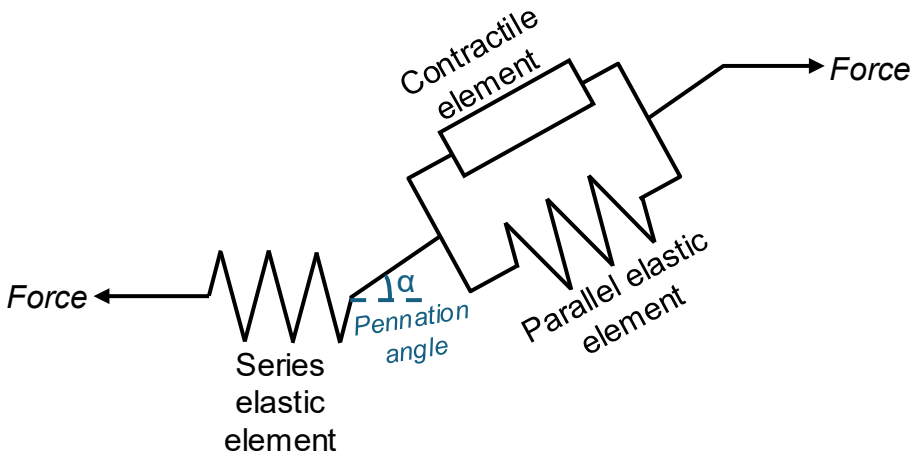

Figure 1-5 – Hill-type muscle model diagram showing the three model elements.

Ligaments are usually modelled as nonlinear springs that act in a straight line between defined bony insertion points. This has the benefit of a low computational cost and easy integration, but neglects the anisotropy and viscoelasticity of the tissue (Kiapour et al. 2014b).

One open-source platform used for MSM is OpenSim (Delp et al. 2007). It is widely used for dynamic simulations and biomechanical analysis as it is flexible, powerful and freely available. It provides tools for creating subject-specific models, importing experimental data, conducting inverse and forward dynamics analyses, and generating muscle-driven simulations, as well as allowing customisable workflows through a scripting interface (Hicks 2013). This makes it suitable for investigating muscle function, movement dynamics, and designing medical interventions. It has been used extensively for a range of applications including rehabilitation, orthopaedics, ergonomics, performance and robotics (Petrucci 2024).

1.6.1 JOINT CONTACT MODELLING

As well as joint kinematics and muscle forces, MSMs can also be used to investigate joint contact mechanics, including predicting tissue loading and cartilage wear, during movement. Understanding healthy and pathological knee contact mechanics is important as abnormalities in TF contact pressure distributions have been correlated with cartilage degeneration and subchondral bone remodelling in osteoarthritic knees (Khot and Guttal 2021; Mohout et al. 2023). As well as native knee contact analysis, these techniques can also be expanded to investigate surgical interventions by simulating how implants distribute joint loading (Eskinazi and Fregly 2016).

There are several approaches to investigating joint contact mechanics using MSMs, including Hertzian contact models, elastic foundation models, surrogate contact models and hybrid MSM-FE workflows.

Hertzian contact theory is used to calculate the deformation and pressure distribution between two contacting non-congruent, elastic surfaces (Johnson 1985). While this approach can be used to approximate knee contact mechanics, it is ideally suited for quasistatic normal loads, frictionless surfaces and small deformations – assumptions which are not always true of real joints (Zdero et al. 2023). However, Hertzian contact has been used to model TKR joint contact forces (Dao and Pouletaut 2015) as implants have smoother, stiffer, and more congruent surfaces, making them better suited to this theory than the natural knee.

An elastic foundation model provides a better representation of articular cartilage properties and contact behaviour than Hertzian contact theory, as it can account for cartilage thickness variations and non-uniform pressure distributions. Elastic foundation models, also known as rigid body spring models or discrete element analysis, consider the contact of each element in a surface mesh independently of one another, calculating contact pressure based on local penetration depth (Johnson 1985). This can be used to model the articular cartilage in the knee as a “bed of springs” forming an elastic layer of known thickness to calculate contact pressure distribution across the joint surface (Li et al. 1997; Fregly et al. 2003; Segal et al. 2009; Henak et al. 2013).

Another approach to joint contact modelling in MSM pipelines is to use a surrogate contact model. These models employ machine learning from previous contact simulations to replicate more computationally expensive contact models (such as elastic foundation or FE models) (Eskinazi and Fregly 2016).

MSMs can also be integrated with FE models (Section 1.7) of specific joints to create a hybrid approach to perform contact analysis (Besier et al. 2005; Shu et al. 2018; Navacchia et al. 2019; Ali et al. 2020; Kainz et al. 2020; Esrafilian et al. 2022; Mohout et al. 2023). In this method, muscle forces and joint kinematics are first computed using an MSM pipeline. The resulting loads are then applied to a more detailed FE model, typically incorporating subject-specific geometries, to calculate cartilage deformation, stresses, and strains, as in a standard FE analysis. This approach has the benefit of capturing internal tissue mechanics (e.g. stress and strain) as well as allowing for subject specific accuracy. However, it requires a complex setup (typically with two separate models) which is computationally expensive.

1.6.2 OPENSIM-JAM

OpenSim-Joint Articular Mechanics (JAM) (https://github.com/clnsmith/opensim-jam/) is an open-source framework designed to estimate joint kinematics, muscle activations, and joint contact forces, including pressure distributions within the knee (Smith et al. 2016). It provides more detailed joint mechanics predictions by incorporating specialised articular contact representations (Lenhart et al. 2015) (Figure 1-6). A key concept in OpenSim-JAM is the distinction between measurable and unmeasurable kinematics from motion capture (Smith et al. 2016). Knee flexion is considered to be directly measurable from motion capture, whereas the secondary DOFs have greater uncertainty and are therefore constrained as functions of flexion using predefined splines.

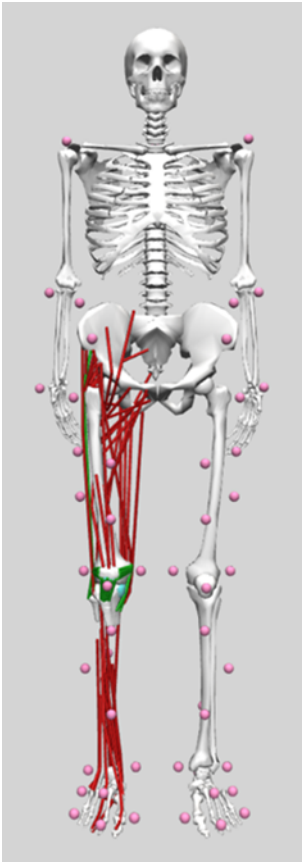

Figure 1-6 – Model developed by Lenhart et al. (2015) used in the standard OpenSim-JAM pipeline.

Like a conventional MSM pipeline, OpenSim-JAM begins by calculating inverse kinematics from experimental motion data. However, instead of allowing all kinematics to vary freely, it constrains secondary kinematics to be functions of knee flexion angle. The standard OpenSim-JAM workflow then uses the Concurrent Optimisation of Muscle Activations and Kinematics (COMAK) algorithm to refine these predictions. COMAK simultaneously optimises muscle activations and secondary kinematics while ensuring consistency with physics-based constraints. This approach aims to improve the accuracy of secondary kinematic predictions, which is particularly important given the strong dependence of joint contact mechanics on kinematic inputs (Anderson et al. 2008a; Henak et al. 2013; Bolcos et al. 2018). Once the kinematics have been optimised using COMAK, contact pressure distributions are computed using the specialised contact geometries (Lenhart et al. 2015) and an elastic foundation model (Bei and Fregly 2004; Smith et al. 2018) (Section 1.6.1).

Because of the ability of the OpenSim-JAM framework to estimate joint loading and contact pressure distributions, this approach has been utilised across a range of

applications. For example, it has been utilised in the study of knee joint contact force changes due to OA (Meireles et al. 2017; Di Raimondo et al. 2023), as well as linking cartilage strains to OA disease progression biomarkers (Mohout et al. 2023). It has also been used to investigate the effects of surgical interventions on knee joint loading, for example, pre- and post- high tibial osteotomy (Bowd et al. 2023) and the influence of TKR posterior tibial slope (Guo et al. 2024). Beyond applications to OA and its interventions, OpenSim-JAM has been used to investigate how articular contact geometry influences knee kinematics and contact mechanics (Clouthier et al. 2019) and how patella alta affects crouch gait in children (Brandon et al. 2017). It has also been used to contribute to future rehabilitation guidelines by investigating knee joint loading during a range of functional activities including squatting, lunging, hopping, stair climbing and gait (van Rossom et al. 2018). The variety of applications for the framework shown through these studies highlights the value of OpenSim-JAM's outputs, its estimations of muscle activations, joint kinematics and loading, for clinically-driven research.

1.6.3 VALIDATION OF MUSCULOSKELETAL MODEL ACCURACY

Validation of MSMs ensures computational model predictions are consistent with reality via comparison with experimental results (Henak et al. 2013). For joint contact analysis, there are three main validation checks: kinematics, contact patterns, and contact pressure and area magnitudes (Henak et al. 2013).

Joint contact mechanics have been investigated in-vitro using pressure sensitive films (Bachus et al. 2006; Kim et al. 2009; Chen et al. 2016a; Zdero et al. 2016; Imani Nejad et al. 2020). This is the most common in-vitro method for studying joint contact mechanics (Zdero et al. 2023). It produces outputs proportional to the mechanical loads applied which can be used to understand joint contact pressure magnitudes and distribution in a directly measurable way. However, the physical film inserted into the joint can disturb the joint's ordinary articulation (Zdero et al. 2023).

In-vitro comparisons of kinematics have also been performed to help validate MSM predictions (Farshidfar et al. 2023). This helps define how accurately the MSM recreates knee joint motion but is still not representative of true in-vivo movement as the knee motion is artificially generated.

In-vivo data can also be used to investigate MSM accuracy; this is often done by investigating output force distributions using instrumented implants (Chen et al. 2016b; Ding et al. 2016). For example, a common dataset used to validate models is from the “Grand challenge competition to predict in-vivo knee loads” (Fregly et al. 2012) which provides open-source knee kinematics and contact dynamics from instrumented implants. This dataset has been used to validate model kinematics (Shu et al. 2021), contact force predictions (Kinney et al. 2013), and compare accuracy between models (Curreli et al. 2021) as it provides in-vivo data with real loading conditions in the knee. However, the data is limited to TKR only and is, therefore, not representative of healthy joint mechanics. It also requires invasive surgery and is only appropriate where a TKR is already necessary.

Investigating the validity of results from an intact knee is more limited as joint contact pressures cannot be directly measured. Therefore, validation of measurable quantities is required to help ensure the model is physiologically reasonable. As BVR can be used to accurately determine knee joint kinematics (Section 1.4.1), model-predicted joint kinematics can be compared to these data to asses model accuracy (Ali et al. 2020).

By confirming the accuracy of these measurable parameters, i.e., joint kinematics, and checking joint contact output magnitudes are consistent with instrumented implant or in-vitro film measurements, the model outputs can be determined as representative of intact knee mechanics.

During their development of the standard model used in the OpenSim-JAM framework, Lenhart et al. (2015) used dynamic MRI to validate the secondary kinematics of the knee during passive flexion. The knee was cyclically flexed through a limited ROM of 36° (due to the MRI bore size) and the six DOF kinematics were compared to the model-predicted values during the passive flexion simulation. The secondary kinematics were generally found to be consistent between the two, with the MRI-measured results falling within the simulated uncertainty range (Lenhart et al. 2015).

Output contact load predictions from the OpenSim-JAM framework were compared to the knee “Grand challenge” results to assess the accuracy of the simulation (Smith 2017). A single model was created for one of the “Grand challenge”

participants with the generic contact geometries swapped for the implant geometries. During a standard gait trial, the OpenSim-JAM results were shown to have RMS errors of 0.33 BW, which is comparable to other proposed methods for calculating knee joint forces (Kinney et al. 2013; Thelen et al. 2014; Marra et al. 2015).

The output kinematics from the COMAK algorithm were also compared generally with in-vivo measurements (Smith 2017), showing a similar trend to bone pins of internal tibial rotation during stance phase (Lafortune et al. 1992a) and greater anterior tibial centre of pressure (COP) translation on the medial plateau compared to the lateral plateau which matched MRI-BVR kinematics (Kozanek et al. 2009; Liu et al. 2010). Although this confirms overall trends match in-vivo kinematics, further analysis is needed to validate the framework's predictions on an individual level. Smith (2017) acknowledged in his thesis that "*in the future, subject-specific model predictions should be compared against in-vivo subject-specific kinematics measured during functional movement to accurately quantify the true predictive capacity*."

1.6.4 PERSONALISED MUSCULOSKELETAL MODELS

To improve model prediction accuracy, MSMs are usually personalised to some degree to better represent in-vivo participant motion. This can range from a simple linear scaling of a generic model, to a highly personalised MSM using subject-specific data. This personalisation can include adding subject-specific bone and joint geometries (Zhang et al. 2014; Fernandez et al. 2016; Modenese and Renault 2021; Davico et al. 2022), as well as personalising contact surfaces and joint mechanisms (Marra 2019; Davico et al. 2022; Killen et al. 2024) to better represent an individual's kinematics and kinetics. It could also involve adjusting muscle attachment sites, muscle pathways or wrapping surfaces to better reflect an individual's anatomy (Killen et al. 2020; Davico et al. 2022). EMG data can also be used to tailor muscle activation patterns for personalised movement patterns (Lloyd and Besier 2003; Davico et al. 2022; Esrafilian et al. 2022); this is particularly useful in pathological populations with altered neuromuscular control.

Generic models, while convenient, often fail to capture anatomical variability, especially in pathological or atypical populations (Fernandez et al. 2023). The addition of personalised joint geometries (including bone and cartilage), can lead to

notable differences in kinematics, kinetics and muscle forces (Marra 2019; Kainz et al. 2021; Davico et al. 2022; Fernandez et al. 2023; Killen et al. 2024) due to the models being highly sensitive to joint geometries (Cleather and Bull 2012). Generic models may also underestimate or misrepresent joint loading patterns, potentially leading to inaccurate predictions, thus inclusion of subject-specific geometries allows for more reliable results for clinical assessments and intervention planning (Fernandez et al. 2016).

Recent frameworks have been developed to allow for automation of personalised model creation to streamline the complicated process, reducing operator time and increasing reproducibility so they can be more widely utilised (Modenese and Renault 2021). One such pipeline, recently developed by Killen et al. (2024), allows for generation of a personalised model compatible with the OpenSim-JAM framework (Section 1.6.2) to model TF joint contact pressures. This involves swapping ‘generic’ bone and cartilage meshes for subject-specific segmentations, updating the muscle and ligament pathways, and calibrating soft tissue parameters to maintain physiological behaviour.

To evaluate the benefit of these personalisation pipelines, it is important to test them against high-quality in-vivo data. Such benchmark datasets are essential to assess whether personalised models provide meaningful improvements over generic alternatives (Lloyd et al. 2023). Ensuring that model outputs accurately reflect joint kinematics and mechanics is essential for producing meaningful results thus comparing the outputs to in-vivo gold-standard data is a key step in validating any new modelling approach.

1.7 FINITE ELEMENT MODELLING

Finite element modelling (FEM) offers an alternative technique for modelling joint contacts. As with MSM, it can be used to calculate unmeasurable parameters, such as joint contact forces and pressure distributions (Rullkoetter et al. 2017). However, unlike MSMs, where joint contact geometries are typically simplified into 2D surfaces, FEMs use meshes of 3D elements, allowing for calculation of internal tissue mechanics, e.g., stress and strain, as well as surface-level contact.

One platform specifically designed for finite element analysis of biomechanics is FEBio (Maas et al. 2012). This open-source platform specialises in representations of biological tissue interactions, providing a useful tool for modelling joint contact mechanics and has been used previously to model the knee joint for a wide variety of applications (Cooper et al. 2019; Mukherjee et al. 2020; Yan et al. 2024).

1.7.1 FINITE ELEMENT MODELLING OF KNEE OSTEOARTHRITIS

Publications on knee modelling have become increasingly prevalent in the last decade (2015 to 2025), with the number of papers focusing on knee modelling or simulation reaching up to 1000 per year (Erdemir et al. 2019). This reflects the usefulness of these techniques to investigate a range of biomechanical applications in the knee. However, the large number of studies also highlights the need for tailored models to suit specific applications application.

FEMs have been developed to understand joint loading and contact mechanics in articular cartilage (Fernandez et al. 2008; Meng et al. 2014; Gu and Pandy 2020), investigate ligament internal mechanics and repairs (Mootanah et al. 2014; Ali et al. 2017; Yanez et al. 2024), influence pre-operative planning or implant designs (Kwon et al. 2014; Rullkoetter et al. 2017; Shu et al. 2021), study disease progression (Bolcos et al. 2020; Mukherjee et al. 2020; Lampen et al. 2023), and analyse injury mechanisms (Mo et al. 2012; Kiapour et al. 2014a).

As discussed in the introduction (Section 1.1), OA is a disease of the whole joint and it is associated with altered joint loading (Griffin and Guilak 2005; Kumar et al. 2013; van Tunen et al. 2018). FEM is a useful tool for understanding the internal tissue mechanical changes, i.e., excessive tissue stresses and strains, that have been suggested as being a key driver for the onset and progression of OA (Mukherjee et al. 2020).

Articular cartilage is one of the primary load-bearing structures within the knee that becomes damaged through the excessive mechanical loading, which can lead to OA (Mukherjee et al. 2020). Weakening of the mechanical properties of articular cartilage is a common indicator of OA and is a significant factor in the loss of joint function (Sinusas 2012; Katz et al. 2021; Mohout et al. 2023). For this reason, it is important to understand the internal tissue mechanics of the articular cartilage under typical joint loading in both healthy and diseased knees.

Knee FEMs have investigated various mechanical changes in the knee resulting from OA, including how altered joint loading affects the articular cartilage and meniscus (Tarniţă et al. 2014; Thienkarochanakul et al. 2020; Daszkiewicz and Luczkiewicz 2021) as well as understanding OA disease indicators and progression (Arjmand et al. 2018; Mohout et al. 2023).

The most commonly analysed parameters for quantifying altered knee mechanics due to OA included stress (Bolcos et al. 2020; Lampen et al. 2023; Mononen et al. 2023), most commonly von Mises stress (Tarniţă et al. 2014; Trad et al. 2017; Arjmand et al. 2018; Peters et al. 2018), strain (Arjmand et al. 2018; Peters et al. 2018; Bolcos et al. 2020; Lampen et al. 2023), load distribution between the medial and lateral compartments (Trad et al. 2017; Arjmand et al. 2018; Mononen et al. 2023), and contact pressures (Trad et al. 2017; Mononen et al. 2023).

Overall, these results showed that knee OA is associated with increased medial compartment loading (Trad et al. 2017; Arjmand et al. 2018; Mononen et al. 2023) resulting in an increase in both joint stress and strain (Tarniţă et al. 2014; Arjmand et al. 2018; Bolcos et al. 2022; Lampen et al. 2023).

The outputs from any new model should be compared with previously reported output magnitudes to assess consistency and reliability of any results. Stress, strain and contact pressure articular cartilage outputs from FEMs of healthy knees in literature are presented in Table 1-2, Table 1-3 and Table 1-4, respectively.

*Table 1-2 – Articular cartilage **stress** findings from FEMs of healthy knees in literature.*

Reference	Model setup/loading	Main stress findings
Yang et al. (2010)	In-vivo gait data (motion capture) and GRFs.	Max normal stress: 17 MPa (FC),16 MPa (lat TC),13 MPa (med TC)
Halonen et al. (2013)	Simulated gait cycle driven using force/kinematics combination	Max principal stress: 30-40 MPa (at 25% stance) Max von Mises stress: 10 MPa (at 20% stance)
Tarniţă et al. (2014)	Loading of 800 N &1500 N (compression force applied to femoral head)	Max von Mises Stress: 2.17 MPa (TC 800N), 3.22 MPa (TC 1500N), 2.41 MPa (FC 800N) and 4.53 MPa (FC 1500N)
Mononen et al. (2015)	Treadmill walking data (motion capture) and GRFs.	Max principal stress: 35.2 MPa (med at 20% stance), 16.1 MPa (lat at 80% stance)

Table abbreviations: max = maximum, FC = femoral cartilage, TC = tibial cartilage, med = medial, lat = lateral, GRFs = ground reaction forces

As summarised from Table 1-2, studies generally report higher maximum stresses in the femoral cartilage compared to the tibial cartilage (Yang et al. 2010; Tarniţă et al. 2014). Within the tibial cartilage, the medial compartment was shown to experience greater stress magnitudes than the lateral compartment (Mononen et al. 2015). Peak stresses were shown to occur at around 20-25% stance, consistent with a peak in joint loading (Halonen et al. 2013; Mononen et al. 2015).

*Table 1-3 – Articular cartilage **strain** findings from FE models of healthy knees in literature.*

Reference	Model setup/loading	Main strain findings
Yang et al. (2010)	In-vivo gait data (motion capture) and GRFs.	Max axial strain: 17.01% (med TC) and 20.67% (FC)
Adouni et al. (2012)	Mean reported in-vivo gait data (motion capture) and GRFs.	Max principal strain: 20% (lat TC at 25% stance)
Halonen et al. (2013)	Simulated gait cycle driven using force/kinematics combination	Max principal strain: 7.5-8.5% (at 25% stance) Max axial strain: 6% (at 25% stance)
Mononen et al. (2015)	Treadmill walking data (motion capture) and GRFs.	Max principal strain: 8% (med TC at 25% stance), 5% (lat TC at 75% stance) Max axial strain: 20% (med TC), 10% (lat TC)
Fu et al. (2022)	Stance phase of gait.	Max principal strain: 21.20% (med TC at 25% stance), 24.35% (lat TC at 75% stance), 29.68% (FC at 25% stance)
Mohout et al. (2023)	In-vivo gait data (motion capture) and GRFs.	Max shear strain: <25% (throughout gait cycle)

Table abbreviations: max = maximum, FC = femoral cartilage, TC = tibial cartilage, med = medial, lat = lateral, GRFs = ground reaction forces

As with stress, the peak strains (Table 1-3) in the medial compartment of the tibial cartilage were typically found at 20-25% stance, consistent with peak joint loading (Adouni et al. 2012; Halonen et al. 2013; Mononen et al. 2015; Fu et al. 2022). Maximum lateral compartment strains were typically found later (at 75% stance) corresponding with the second joint loading peak (Mononen et al. 2015; Fu et al. 2022). Studies disagreed on which half of the tibial cartilage the maximum strain occurred, with some finding the medial tibial cartilage to experience higher strains (Yang et al. 2010; Mononen et al. 2015), whereas others found the lateral to present

higher values (Adouni et al. 2012; Fu et al. 2022). The femoral cartilage was found to experience higher strains than the tibial cartilage (Yang et al. 2010; Fu et al. 2022)

*Table 1-4 - Articular cartilage **contact pressure** findings from FE models of healthy knees in literature.*

Reference	Model setup/loading	Main contact pressure findings
Haut Donahue et al. (2003)	1200N and 0° flexion	Peak contact pressure: 3.69 MPa (lat), 3.44 MPa (med)
Adouni et al. (2012)	Mean reported in-vivo gait data (motion capture) and GRFs.	Peak contact pressure: 8.1 MPa (med TC at 25% stance)
Halonen et al. (2013)	Simulated gait cycle driven using force/kinematics combination	Peak contact pressure: 14-17 MPa (med at 25% stance)
Mononen et al. (2015)	Treadmill walking data (motion capture) and GRFs.	Peak contact pressure: 14 MPa (med at 25% stance), 12 MPa (lat at 80% stance)
Daszkiewicz and Luczkiewicz (2021)	Stance phase of gait (focussed on meniscus)	Peak contact pressure: 8.0 MPa (med TC at 75% stance), 5.5 MPa (lat TC at 25% stance)
Fu et al. (2022)	Stance phase of gait.	Peak contact pressure: 17.07 MPa (med TC at 75% stance), 14.7 MPa (lat TC at 75% stance), 15.58 MPa (FC at 25% stance)

Table abbreviations: max = maximum, FC = femoral cartilage, TC = tibial cartilage, med = medial, lat = lateral, GRFs = ground reaction forces

Peak contact pressure (Table 1-4) was found to be associated with the two peaks of force during stance phase of gait (25% and 75% stance) (Adouni et al. 2012; Halonen et al. 2013; Mononen et al. 2015; Daszkiewicz and Luczkiewicz 2021; Fu et al. 2022). Peak medial tibial cartilage contact pressure was consistently found to be higher than the peak in the lateral compartment (Haut Donahue et al. 2003; Adouni et al. 2012; Halonen et al. 2013; Mononen et al. 2015; Daszkiewicz and Luczkiewicz 2021; Fu et al. 2022).

1.7.2 REPRESENTATION OF KEY STRUCTURES OF THE KNEE

Choosing how to represent key knee structures (Figure 1-7) in an FEM requires balancing the model complexity, computational efficiency and numerical stability with the model requirements and application. More complex material models can capture important tissue behaviours (such as nonlinearity, anisotropy, or viscoelasticity) but they are often more complex and less stable, making them less suitable for large-scale or population-based simulations (Weiss and Gardiner 2001; Peña et al. 2006). However, simpler models, although more efficient, may not capture important tissue mechanical behaviours. All material models are based on specific assumptions which affect their behaviour, so it is important to understand the benefits and limitations of each model in relation to specific study aims.

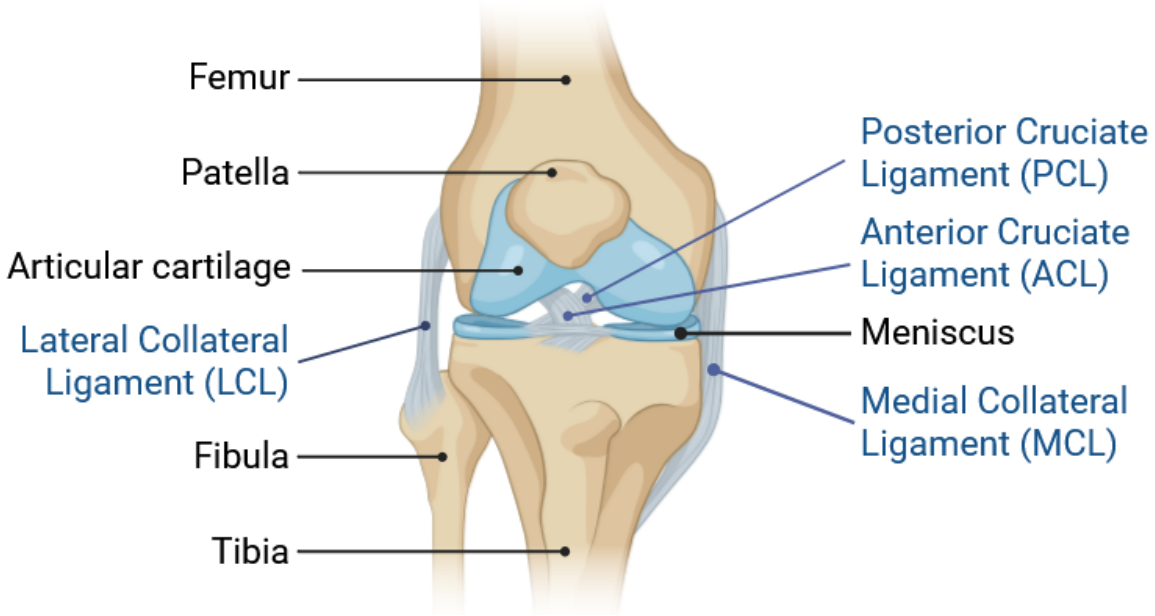

Figure 1-7 – Key structures of the knee. The four main ligaments of the knee are labelled in blue. Created with Biorender.com.

In this section, the key mechanical characteristics of the major tissues in the knee are discussed, focussing on which aspects of their function have been modelled in literature, rather than an exhaustive review of all mathematical models used. The material models described in more detail in the following sections were used in the development of the FEM for this study (Chapter 4). The chosen material models and parameter values were taken from literature due to the time constraints and difficulties associated with generating personalised material parameters from in-vivo data (Cooper et al. 2019).

Bones

In knee FEMs, on a joint level scale, the bones are most often modelled using rigid bodies, due to the much greater Young's modulus and density when compared to the surrounding soft tissues (Donahue et al. 2002; Adouni et al. 2012; Liu et al. 2022; Steineman et al. 2022; Uzuner et al. 2022; Yan et al. 2024). This approach has the advantage of being less computationally expensive as each element in the body is treated as mathematically identical. For kinematically-driven models, modelling the bones as rigid bodies also allows for kinematics to be applied directly, using them to drive the model.

In some cases, a linear elastic material may be used to study internal bone mechanics (Shirazi and Shirazi-Adl 2009; Guess et al. 2010; Mootanah et al. 2014; Benos et al. 2020). A deformable model is typically used when the model is investigating internal bone mechanics (e.g. in the subchondral bone) or for studies involving complex loads (Yan et al. 2024).

Articular cartilage

Articular cartilage is an inhomogeneous, anisotropic soft tissue that exhibits strong creep and stress relaxation behaviour (Mow et al. 1989). Although models have been developed to capture the poroelasticity (Donahue et al. 2002; Wilson et al. 2003; Vaziri et al. 2008), hyperelasticity (Anderson et al. 2008b) and anisotropy (Wilson et al. 2003; Vaziri et al. 2008), cartilage is often simplified to a homogeneous, isotropic, linearly elastic material (Peña et al. 2007; Klets et al. 2016). This simplification reduces the complexity of the model, reducing the computational demand, whilst capturing the general behaviour of articular cartilage under loading in a manner suitable for joint-level modelling (Chokhandre et al. 2023a).

The articular cartilage was modelled as an isotropic, linear elastic, nearly incompressible material (Donahue et al. 2002; Chokhandre et al. 2023a) represented using a Neo-Hookean model. The Neo-Hookean model (Treloar 1943a,b) provides a mathematically simplistic representation of the non-linear deformation of a rubber-like material (Holzapfel 2000), making it suitable for a simplified cartilage model.

To achieve the Neo-Hookean representation, a Mooney-Rivlin material model (Equation 1-1) (Mooney 1940; Rivlin 1948,1949b,a) was used with the constant c_2

set to 0 to avoid element locking associated with incompressible elements (FEBio 2022c).

$$\Psi = c_1(I_1 - 3) + c_2(I_2 - 3) \quad \textit{(Eq. 1-1)}$$

Where Ψ = strain energy function, I_1/I_2 = strain invariants and c_1/ c_2 = constants defined as:

$$c_1 = \frac{\mu_1}{2} \textit{ and } c_2 = \frac{\mu_2}{2} \quad \textit{(Eq. 1-2)}$$

Where the shear modulus μ = μ_1 - μ_2.

This Mooney-Rivlin model was reduced to an uncoupled Neo-Hookean model by setting the constant c_2 to 0 (FEBio 2022a), giving the following equation:

$$\Psi = c_1(I_1 - 3) \quad \textit{(Eq. 1-3)}$$

Where Ψ = strain energy function, I_1 = strain invariant and c_1 = a constant based on the shear modulus (Equation 1-2).

In a review of tissue material properties of the TF joint by Peters et al. (2018), the range of elastic modulus used to model the articular cartilage varied from 5 MPa (Peña et al. 2006) to 67.6 MPa (Potocnik et al. 2008) where only a single value was used, with 12 MPa being the most common; the Poisson's ratios presented ranged from 0.3 (Potocnik et al. 2008) to 0.46 (Peña et al. 2006), with the majority of models using a value of 0.45.

Articular cartilage in the knee has also been previously modelled as a Neo-Hookean material with an elastic modulus of 15 MPa and Poisson's ratio of 0.475 (Donahue et al. 2002; Zielinska and Donahue 2006; Guess et al. 2010; Kiapour et al. 2014b); the corresponding Mooney-Rivlin model parameters for these material properties are given in Table 1-5 (Chokhandre et al. 2023b).

Table 1-5 – Articular cartilage Mooney-Rivlin material parameters to achieve a Neo-Hookean response (Chokhandre et al. 2023b).

Parameter	Definition	Value
C1	Coefficient of the first invariant term (associated with shear stress)	2.54 MPa
C2	Coefficient of the second invariant term (reduces the model to Neo-Hookean when set to 0).	0 MPa
K	Bulk modulus (resistance to volume change).	100 MPa

Meniscus and meniscal horns

As the meniscus plays a key role in stabilisation, load bearing and stress distribution within the knee (Walker and Erkiuan 1975; Messner and Gao 1998; Peña et al. 2006; Athanasiou and Sanchez-Adams 2009; Imeni et al. 2020), it is an important structure often included in FE knee models.

The meniscus has a complicated architecture, including a circumferential arrangement of collagen fibres in the main body of the meniscus (Petersen and Tillmann 1998; Mow and Huiskes 2005) which provides greater stiffness and strength to resist hoop stresses (LeRoux and Setton 2002; Li et al. 2005; Peloquin et al. 2016; Morejon et al. 2023). To capture this structure, the meniscus is often modelled using transversely isotropic (Donahue et al. 2002; Yao et al. 2006; Zielinska and Donahue 2006; Yang et al. 2010; Klets et al. 2016) or fibril-reinforced materials (Bendjaballah et al. 1995; Jilani et al. 1997; Moglo and Shirazi-Adl 2003; Mononen et al. 2011), although isotropic linear elastic materials (Périé and Hobatho 1998; Beillas et al. 2004; Peña et al. 2008; Beidokhti et al. 2016; Li et al. 2020) and spring-elements (Li et al. 1999) have been used as simpler, less computationally expensive alternatives.

Along with its anisotropic behaviour, the meniscus also exhibits hyperelasticity due to its complex structure. Various hyperelastic materials have been used to capture this aspect of meniscal behaviour (Haemer et al. 2012; Kazemi and Li 2014; Khoshgoftar et al. 2015; Shriram et al. 2017), adding realism but further complexity to the model.

The time dependent mechanical response of the meniscus – resulting from fluid flow and the intrinsic viscoelasticity of the collagen fibres (Imeni et al. 2020) – has also been captured using more complex material models (Kazemi et al. 2011; Mononen et al. 2011; Haemer et al. 2012; Kazemi and Li 2014; Halonen et al. 2017). This poroelastic behaviour is typically neglected in full knee models as the length of a typical functional activity modelled (e.g. stance phase of level gait) is significantly smaller than the viscoelastic time of the meniscus (Imeni et al. 2020).

Various combinations of the anisotropic, hyper-poro-elastic properties of the meniscus have been used in different models depending on the application and resources available. Despite the variation in complexity of meniscus material models, it has been shown that geometry has a greater effect on meniscal kinematics and

knee contact mechanics than the material parameters chosen (Yao et al. 2024). This suggests that for a subject-specific model, an emphasis should be placed on using personalised geometries to increase accuracy, whereas generic material properties may be sufficient (Yao et al. 2024).

In the review of knee material parameters for FEM by Peters et al. (2018), the elastic modulus of the meniscus was shown to vary greatly with magnitudes varying from 8 MPa (Bendjaballah et al. 1995) to 250 MPa (Beillas et al. 2004), with some models even using a modulus of 0 MPa (Kazemi and Li 2014). The Poisson's ratio was also shown to vary from 0.2 (Yang et al. 2010; Mootanah et al. 2014) to 0.49 (Peña et al. 2006). Another review of meniscus modelling by Imeni et al. (2020) found that for transversely isotropic material, the Young's modulus was found to be 120-150 MPa and 20 MPa in the circumferential and radial directions, respectively.

In the most recent OpenKnee(s) model cohort (Chokhandre et al. 2023b), the meniscus was represented by a nearly incompressible, transversely isotropic hyperelastic material using the parameters given in Table 1-6.

These values correspond to a Young's modulus of around ~45 MPa in the circumferential direction and ~27 MPa in the radial direction, as well as a Poisson's ratio of ~0.45 in both directions. This was achieved using the in-built *fibre generator* tool in FEBio (FEBio 2021b) to generate circumferential fibres (described in more detail in Chapter 4, Section 0) to capture the anisotropic stiffness that largely dictates meniscus behaviour and its capacity for sustaining compressive loading (Chokhandre et al. 2023a).

Like with the articular cartilage model, the meniscus model utilised a Mooney-Rivlin (Equation 1-1) ground substance, converted to a Neo-Hookean material by setting the constant c_2 to 0 (Equation 1-3), again to avoid element locking of nearly incompressible elements (FEBio 2022c).

Table 1-6 – Meniscus transversely isotropic Mooney-Rivlin material parameters taken from Chokhandre et al. (2023a)

Parameter	Definition	Value
C1	Coefficient of the first invariant term (associated with shear stress)	4.61 MPa
C2	Coefficient of the second invariant term (reduces the model to Neo-Hookean when set to 0).	0 MPa
K	Bulk modulus (resistance to volume change).	92.16 MPa
C3	Exponential stress coefficient	0.1197 MPa
C4	Fibre uncrimping coefficient	150
C5	Modulus of straightened fibres	400 MPa
λ_m	Fibre stretch for straightened fibres	1.019

The meniscal horn attachments, ligamentous structures connecting the meniscal bodies to the tibial subchondral bone (Messner and Gao 1998), can either be represented by linear elastic solids (Donahue et al. 2002; Dhaher et al. 2010) or spring elements (Donahue et al. 2002; Yao et al. 2006; Gu and Pandy 2020). Spring elements are more commonly used (Imeni et al. 2020) as this reduces model complexity compared to adding more 3D structures as they require more elements as well as additional contacts with the surrounding structures.

The review by Imeni et al. (2020) found the most commonly used material properties for modelling the meniscal horns to be linear elastic, with Young's moduli typically ranging from about 90 to 600 MPa, and stiffness values between roughly 200 and 2000 N/mm depending on the horn and study.

Knee ligaments

The ligaments in the knee also exhibit a complex material behaviour due to the water-rich ground substance reinforced with crimped collagen fibres (Diamant et al. 1972; Comninou and Yannas 1976; Daniel et al. 1990). This results in a force-strain relationship with two distinct regions: the non-linear toe-region as the crimping progressively disappears and the fibrils become aligned with the loading direction, then an almost-linear, higher stiffness region corresponding with the stretching of the fibrils (Trent et al. 1976; Weiss and Gardiner 2001; Galbusera et al. 2014). This

tissue structure also causes the ligaments to be anisotropic, incompressible, hyperelastic and viscoelastic (Yan et al. 2024).

Another complex element of ligament behaviour is reference strain (ε_r), also known as pre-strain. This is the strain within the ligament in full knee extension (the reference position) as, in-vivo, the ligament will always be sustaining a tensile load (Daniel et al. 1990; Galbusera et al. 2014). When modelling, consideration of this initial reference strain before dynamic motion can be implemented to better represent true material behaviour.

One-dimensional (1D) line elements are the most common representation of ligaments in FE models of the knee joint (Blankevoort et al. 1991; Li et al. 1999; Donahue et al. 2002; Beillas et al. 2004; Mesfar and Shirazi-Adl 2006; Checa et al. 2008; Amiri and Wilson 2012; Bloemker et al. 2012; Guess and Stylianou 2012; Mohout et al. 2023). Although single elements have been used (Yu et al. 2001), more frequently they are represented by bundles of multiple springs covering the insertion sites (Galbusera et al. 2014). Using non-linear 1D springs allows for easy implementation and replication of the force-strain curves from experimental tests, along with the pre-strain, at a low computational cost. However, it only provides information in the fibre direction and requires special techniques for incorporating ligament wrapping. Despite these limitations, 1D spring models are still recommended for simulation of global knee behaviour where the ligament itself is not the focus of the model (Galbusera et al. 2014).

Alternatively, ligaments can also be modelled as 3D structures (Peña et al. 2006; Kazemi and Li 2014; Uzuner et al. 2022; Chokhandre et al. 2023b), segmented from MRI, which inherently accounts for ligament wrapping and provides a more accurate anatomical, personalised structure representation. Recommended for when the ligament or its interaction with surrounding tissues is the focus (Galbusera et al. 2014), it provides information about internal tissues mechanics (such as ligament strain) that cannot be determined from a 1D model. The disadvantages of the high computational cost and difficulty in validation associated with the more complex 3D models make 3D structures unsuitable for all applications. As ligaments are strongly anisotropic and not able to sustain compression, they are difficult to model using 3D

materials, and this can result in oversimplified constitutive models being used instead (Galbusera et al. 2014).

As a compromise, ligaments have also been modelled using 2D shells or membranes reinforced with line elements to capture both the anisotropy and pre-strain material behaviours (Halloran et al. 2005; Baldwin et al. 2009; Clary et al. 2013a; Zelle et al. 2014).

When looking at the material properties used to model ligaments in literature, a review by Galbusera et al. (2014) found their values exhibited considerable variability across studies, particularly for reference strain. For example, the reference strain was shown to vary from 0 to 0.16 for the ACL and -0.169 to 0.24 for the PCL (Galbusera et al. 2014).

One of the most common 1D spring ligament models is the Blankevoort model. The force-strain relationship is split into three distinct regions (Equation 1-4), including no force below 0 strain, a quadratic toe-region up to the linear strain limit (ε_l) of 0.03 (Butler et al. 1986), and a linear relationship above that threshold (Blankevoort and Huiskes 1991). A visualisation of this force-strain relationship is given in Figure 1-8.

$$f = \begin{cases} 0 & \varepsilon < 0 \\ \frac{1}{4} k_l \varepsilon^2 / \varepsilon_l & 0 \leq \varepsilon \leq 2\varepsilon_l \\ k_l(\varepsilon - \varepsilon_l) & \varepsilon > 2\varepsilon_l \end{cases} \qquad \textit{(Eq. 1-4)}$$

Where f = tensile force in each ligament element, k_l = ligament stiffness, ε_l = linear strain limit, ε = current ligament strain.

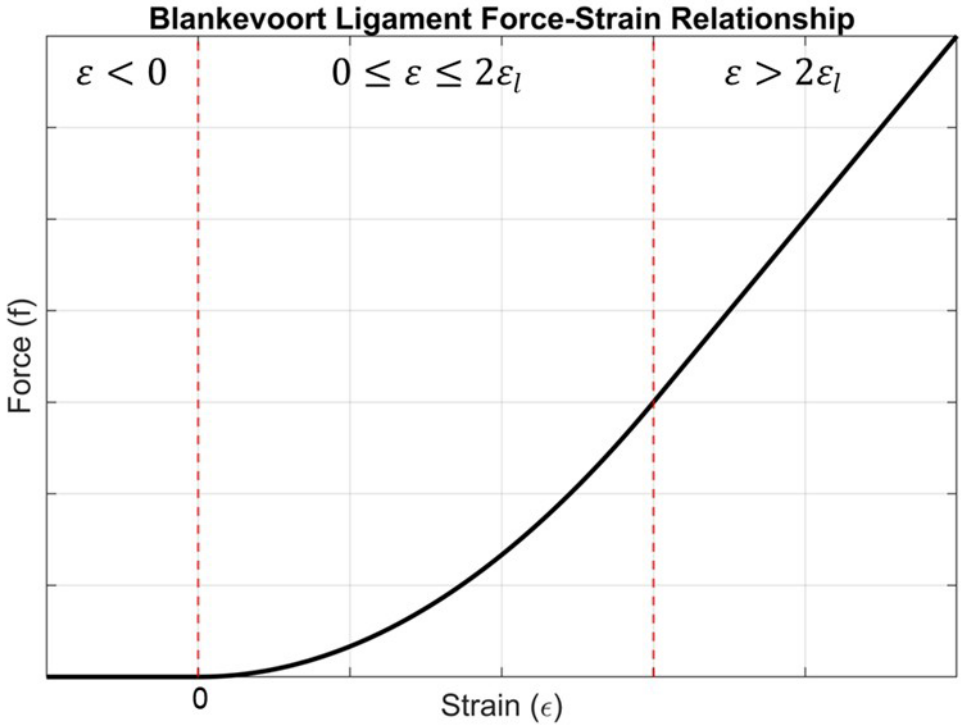

Figure 1-8 – Blankevoort Ligament model force-strain relationship.

The strain is then calculated at any time point using Equation 1-5 and the corresponding force determined from the Blankevoort relationship (Equation 1-4, Figure 1-8) with the parameters given in Table 1-7.

$$\varepsilon = \frac{(L - L_0)}{L_0} \qquad \textit{(Eq. 1-5)}$$

Where ε = current ligament strain, L = current ligament length and L_0 = ligament zero load length.

Table 1-7 – Material parameters for the force-strain relationship of each ligament taken from Blankevoort et al. (1991).

Ligament	Total stiffness/k_l [kN]	Reference strain/ε_r [%]
ACL	10	8
PCL	18	-13.5
LCL	6	-7.33
MCL	8.25	3.66

For each ligament, an individual zero-load length (L_0) is needed to calculate the strain. This represents the length of the ligament in a completely unloaded state (with

no pre-strain). However, as this parameter is un-measurable in-vivo, it is calculated using the reference length (L_r) and reference strain (ε_r) parameters determined when the knee is in its 'reference position' in full extension (Equation 1-6) (Blankevoort et al. 1991).

$$L_0 = L_r \,/\, (\varepsilon_r + 1) \qquad \textit{(Eq. 1-6)}$$

Where L_0 = ligament zero-load length, L_r = the ligament reference length, and ε_r = the reference strain.

1.7.3 KINEMATIC DRIVEN FINITE ELEMENT MODELLING OF THE KNEE

Models are typically force-driven due to the sensitivity of FEMs to kinematics (Fregly et al. 2008) and the lack of accurate input kinematics.

A few studies (summarised in Table 1-8) have created models of the knee that are fully or partially driven by kinematics. Typically these models have utilised more accurate inputs kinematics derived from X-ray imaging, with bead-based imaging (such as RSA, Section 1.2.4) (Beillas et al. 2004; Gu and Pandy 2020) or BVR (Fernandez et al. 2008; Halonen et al. 2013; Carey et al. 2014; Xiao et al. 2021) being commonly used. However, some models did use motion-capture or MSM to derive the input kinematics instead (Halonen et al. 2016; Bolcos et al. 2018).

Despite more accurate inputs, a hybrid force-kinematic approach was often used to drive the FEM to account for potential errors in the input kinematics. One approach taken was to prescribe up to five TF DOFs, leaving a translation (typically CD/SI) free to settle based off external forces (Halonen et al. 2013; Carey et al. 2014; Gu and Pandy 2020). Other models only prescribed one or two kinematic DOFs (Kwon et al. 2014; Bolcos et al. 2018), whereas others prescribed the TF kinematics to model PF movement.

Table 1-8 – Kinematically-driven FE knee models from literature.

Study	Kinematics		Application for model
	Prescribed DOFs	**Activity modelled**	
Beillas et al. (2004)	Femur kinematics prescribed, tibia motion driven by the knee and ankle joints and muscle actions (EMG).	One participant performed a single-leg hop and was imaged using RSA.	Development of a framework to apply subject-specific kinematics to a generic low limb model.
Fernandez et al. (2008)	TF six DOF kinematics prescribed (patella motion predicted by the model).	One healthy participant was imaged during a step-up activity using BVR.	Investigating PF joint function – including joint contact stresses.
Halonen et al. (2013)	TF FE, IE, AP and ML prescribed (AA and CD assumed to be left free).	One healthy participant with simulated gait and loaded standing (using BVR as input data).	Used to investigate the importance of cartilage proteoglycan and collagen distributions on stresses and strains.
Carey et al. (2014)	Five DOFs constrained, SI translation left free.	One participant intact vs menisectomised knee. BVR collected during standing.	Comparison of MRI (supine) and BVR (standing) kinematically constrained models.
Kwon et al. (2014)	FE and IE rotations prescribed.	One healthy participant with a virtual UKA performed. Simulated gait cycle.	Compared the contact pressures and stresses in two UKA designs.

Halonen et al. (2016)	TF six DOFs constrained but AA and IE implemented as moments not rotations.	One participant's gait kinematics derived from motion capture and MSM.	Comparison of FE modelling with and without the patella and quadriceps to investigate their importance.
Bolcos et al. (2018)	FE and IE rotations prescribed in some models. (All other DOFs force-driven or left free).	One participant had three gait trials averaged. Kinematics during the stance phase of level gait were calculated using MSM.	Comparison of four models with varying complexity, implementing kinematics to simplify the model.
Gu and Pandy (2020)	Five DOFs constrained, SI translation left free.	Three cadaveric knees simulated flexion (15-60°) with a load applied. Kinematics derived using BVR and implanted beads.	Validate model predictions of contact pressure, contact area and contact force.
Xiao et al. (2021)	All six DOFs.	One healthy participant performed a lunge. Kinematics from in-vivo BVR.	Estimate forces and strains in a single-bundle ACL reconstruction

Out of all the models in Table 1-8, only Xiao et al. (2021) and Fernandez et al. (2008) prescribed all six DOFs of the TF joint, both using BVR-derived kinematics. Fernandez et al. (2008) used their model to investigate PF kinematics and Xiao et al. (2021) used their model to investigate forces and stresses on ACL reconstruction grafts, so the only soft tissue structure included was the ACL. These models provide examples of a fully kinematic-driven simulations that utilise accurate BVR kinematics to investigate clinically relevant questions. However, neither model investigated the internal mechanics of the articular cartilage in the TF joint and so there is scope to developing a new model, expanding the soft tissues included.

1.8 RESEARCH AIMS

As discussed in the introduction (Section 1.1), a clear understanding of knee joint biomechanics is fundamental to identifying and explaining changes associated with diseases such as OA. OA is strongly linked to altered joint loading and kinematics (Mills et al. 2013; Farrokhi et al. 2014; Yamagata et al. 2021), which disrupt the normal distribution of mechanical stresses across the knee. Mechanical factors, including malalignment, injury, and changes in neuromuscular control, are primary drivers of cartilage degeneration and disease progression (Griffin and Guilak 2005; Felson 2013). Accurate quantification of these biomechanical changes is therefore essential. Longitudinal studies have shown that elevated medial knee loading, reflected by increased knee adduction moments during gait, predicts both the onset and progression of medial TF OA (Baliunas et al. 2002; Miyazaki et al. 2002; Andriacchi and Mündermann 2006). Imaging and alignment analyses further demonstrate that abnormal load distribution accelerates structural deterioration of the joint (Sharma et al. 2001). The combination of high precision in-vivo imaging techniques, such as BVR, with personalised modelling pipelines provides a robust and detailed characterisation of individual knee loading during dynamic functional activities, enabling a mechanistic understanding of OA development and progression (Andriacchi et al. 2009; Gustafson et al. 2021; Mononen et al. 2023).

The primary aim of this research thesis was to develop a framework that integrates accurate six DOF TF kinematics, obtained from the BVR system at Cardiff University, into MSM and FEM pipelines. Access to the BVR system provided the opportunity to generate and leverage a high-quality dataset of precise in-vivo measurements of knee bone motion, enabling a more detailed understanding of joint mechanics. By integrating these measurements into MSM and FEM pipelines, the research aimed to establish a robust methodology for quantifying and predicting knee joint behaviour under physiologically relevant conditions.

BVR (Chapter 2)**:** As this was the first study of the knee using the new BVR system at Cardiff, the initial focus of the work was to establish a robust protocol for the simultaneous acquisition of BVR and marker-based motion capture data during multiple dynamic knee activities. The study also developed a dedicated processing pipeline to compute six DOF TF joint kinematics from BVR data, using MRI-

segmented bone models and image registration techniques. The complete data acquisition and processing framework was then implemented and evaluated for the first time in a cohort of healthy participants.

MSM (Chapter 3): Following this, the marker-based motion capture data were processed through a musculoskeletal modelling (MSM) pipeline (OpenSim-JAM) to estimate TF kinematics and contact pressures during the imaged movements. This stage included the first comparison between MSM-derived outputs and BVR-measured kinematics to evaluate the general accuracy of the MSM in typical applications, providing valuable insight for other users of the pipeline.

In particular, the work investigated the potential benefits of model personalisation by addressing the question: does incorporating personalised contact geometries improve MSM predictions of TF kinematics and loading? Using a new framework for generating MSMs with subject-specific knee joint geometries (Killen et al. 2024), the study examined potential improvements in model predictions to better understand the advantages of personalised modelling approaches.

FEM (Chapter 4): The final stage of the framework development aimed to generate the first fully kinematically driven FEM of the knee for investigating articular cartilage mechanics. In this work, the BVR-derived kinematics were utilised in a novel way by driving the model using TF bone poses. To demonstrate the potential of this modelling approach, variations in cartilage contact pressures, stresses, and strains were examined during the stance phase of level gait.

Each component of the framework provided distinct yet complementary outputs: kinematics from the BVR, contact pressures and muscle forces from the MSM, and internal tissue mechanics from the FEM. By integrating these techniques and capitalising on the strengths of each, the framework combines BVR, MSM, and FEM approaches to deliver a more comprehensive understanding of knee biomechanics during functional joint loading using highly personalised models. This integration aims to not only demonstrate the potential modelling applications of accurate BVR-derived kinematics but also provide valuable insights for researchers without access to such data, highlighting the respective benefits and limitations of the different methods employed. Although highly personalised models and precise kinematic data are not always feasible or available, they can inform broader modelling strategies;

therefore, the development of detailed pipelines remains essential for advancing understanding of knee joint health.

This thesis aims to demonstrate the feasibility of developing tools capable of enhancing the accuracy, personalisation, and clinical relevance of computational models of the knee. Whether applied as individual components or as an integrated system, the framework can be extended to include pathological knees to address clinically relevant questions and to deepen understanding of the relationships between knee biomechanics, pathology, and pain. Ultimately, the tools and framework developed in this research are designed to be applied in translational settings, supporting clinicians and researchers in developing personalised, data-driven approaches to diagnosing, monitoring, and treating knee joint pathologies such as OA.

CHAPTER 2: QUANTIFYING TIBIOFEMORAL KINEMATICS USING BIPLANE VIDEORADIOGRAPHY

2.1 INTRODUCTION

2.1.1 BACKGROUND

Accurately determining in-vivo tibiofemoral (TF) kinematics in all six degrees of freedom (DOF) is necessary to understand joint movement in both healthy and pathological cohorts (Giphart et al. 2012). It allows for better quantification of altered biomechanics due to diseases such as osteoarthritis, injury, and various interventions (Postolka et al. 2020; Ulbricht et al. 2020).

Marker-based motion capture is the current research gold-standard technique for measuring three-dimensional (3D) in-vivo kinematics and provides high repeatability in the sagittal plane for the knee (Mackey et al. 2005), but insufficient accuracy in the other planes (Ramsey and Wretenberg 1999). This technique can provide whole body kinematics, however, it suffers from errors caused by inaccurate marker placement on anatomical landmarks (Tranberg et al. 2011), as well as soft tissue artefact (Ramsey and Wretenberg 1999; Akbarshahi et al. 2010; Miranda et al. 2013).

Biplane Videoradiography (BVR) is currently the most accurate technique for measuring in-vivo skeletal kinematics noninvasively (Gray et al. 2017; Gray et al. 2018), and has emerged as the new gold standard for in-vivo kinematics during physiological loading (Setliff and Anderst 2024). For BVR, two X-ray source-detector pairs fire from different perspectives to produce image pairs that can be used to determine 3D information about the bones within the knee (Gray et al. 2018). Unlike traditional motion capture, BVR has been shown to produce highly accurate 3D arthrokinematics of the knee joint in all planes (Li et al. 2008; Anderst et al. 2009; Miranda et al. 2011; Guan et al. 2016) and is not affected by soft tissue artefact or marker misplacement. However, BVR does suffer from a limited imaging volume and occlusion by the contralateral limb (Gray et al. 2018). Different X-ray source-detector pairs configurations are required for different activities to minimise these limitations (Gray et al. 2017; Gray et al. 2018). BVR has typically only been used on studies with small cohorts (with a mean of 11 participants per study) due to the high costs

and significant amount of time required to process the results (Setliff and Anderst 2024).

Although BVR is the more accurate technique, marker-based motion capture remains widely used due to its accessibility and lack of ionising radiation. Comparing joint kinematics from marker-based motion capture to those obtained using BVR leads to better understanding of its inaccuracies and limitations. This understanding enables motion capture users to interpret their data with greater nuance and additionally highlights potential areas for improvement in the data collection and processing methods.

Simultaneous capture of accurate joint-specific kinematics using BVR alongside whole body marker-based motion capture, not only facilitates direct comparison between the two methods, but also enables further analysis of the links between whole body and joint specific biomechanics. As BVR is limited by capture volume and duration (to minimise ionising radiation exposure), there is a need for an integrated approach to investigate whole body responses alongside detailed joint-level mechanics (Li et al. 2012). Developing successfully integrated approaches for data collection is important for understanding altered joint mechanics due to pathologies and their broader effects on other joints in the body.

2.1.2 AIM & OBJECTIVES

As explained in Section 1.8, the overall aim of this chapter was to develop and define a robust protocol for collecting and processing simultaneous BVR and marker-based motion capture data, along with 3D magnetic resonance imaging (MRI) sequences. This protocol was designed to investigate TF joint kinematics across multiple dynamic functional movements and was to be applied for the first time to a cohort of healthy participants.

This was further broken down into the following objectives:

- To use the defined X-ray data collection and processing pipeline to calculate healthy TF kinematics for multiple participants during multiple activities to demonstrate its potential for use in future studies.

- To compare the resulting X-ray derived kinematics to those found in literature to assess the validity of the pipeline outputs by assessing their similarity and consistency with previous studies.
- To compare equivalent marker-based motion capture rotations – derived using Visual3D (V3D, HAS-Motion, Canada) – to those calculated from the 'gold standard' BVR data, to better understand the accuracy and limitations of this more commonly used technique.

2.2 DATA COLLECTION: MAGNETIC RESONANCE IMAGING

Each healthy volunteer took part in two separate data collection sessions. The first involved a series of MRI scans to obtain 3D joint geometry, and the second captured simultaneous BVR, marker-based motion capture and electromyography (EMG) during dynamic movements.

Ethical approval was granted by the Wales Research Ethics Committee 3 (Ref: 10/MRE09/28) and written informed consent was obtained before each data collection session.

For the first session, the MRI scans were carried out at the Cardiff University Brain Research Imaging Centre (CUBRIC, Cardiff University) in a 3T Magnetom Prisma MRI scanner (Siemens Healthcare GmbH, Germany). Sequences were based off previously defined imaging protocols (Williams 2018), with key details and associated parameters recorded in Table 2-1.

.

Table 2-1 – MRI sequence parameters

Sequence	**MPRAGE (Long leg)**	**CISS-3D**	**DESS-3D**	**T1-VIBE**
Repetition Time (TR, ms)	2200	5.84	14.84	11.7
Echo Time (TE, ms)	2.18	2.92	5.04	5.46
Flip Angle (°)	8	50	25	10
Echo train length	1	1	2	1
Pixel Spacing (mm)	0.78125 x 0.78125	0.6445 x 0.6445	0.6328 x 0.6328	0.59 x 0.59
Slice Thickness (mm)	5	0.64	0.63	0.60
Field of View (FOV, mm)	328 x 500	165 x 165	162 x 162	150 x 150
Matrix	320 x 210	256 x 256	256 x 256	256 x 256
Total Acquisition Time (minutes:seconds)	4:37 per section	7:10	5:28	6:26
Orientation	Transverse	Sagittal	Sagittal	Sagittal

Before scanning, informed consent was given by each participant and a safety screening form was completed. The participants were then asked to change into appropriate clothing and remove all metallic items.

Participants were positioned in the scanner feet-first supine with their legs in a neutral position and the scanner bed was roughly aligned to the palpated location of the greater trochanter.

Firstly, a whole-leg scan was obtained using the body radio frequency (RF) coil. A ’FastView’ scan was performed to ensure the whole leg was visible (from hip to ankle) in the imaging volume, and to determine which sections of the body RF coil were required. Then the leg was scanned in sections using a series of Magnetisation-Prepared Rapid Acquisition Gradient Echo (MPRAGE) scan sequences. The number of scans required to image the whole leg depended on the height of the participant but was typically around 3-4 scans.

A series of higher resolution scans were then captured using a Tx/Rx Knee 15 Flare Coil. A short 10-15 second localiser scan sequence was used to align the imaging volume around the centre of the TF joint. This ensured all structures of interest were captured in subsequent scan sequences.

A 3D Constructive Interference in Steady State (CISS-3D) scan sequence was obtained as it provides high contrast between cortical and cancellous bone (Figure 2-1). The CISS-3D scan sequence was used as an equivalent to the FIESTA-C sequence in the original protocol (Hingwala et al. 2011; Williams 2018).

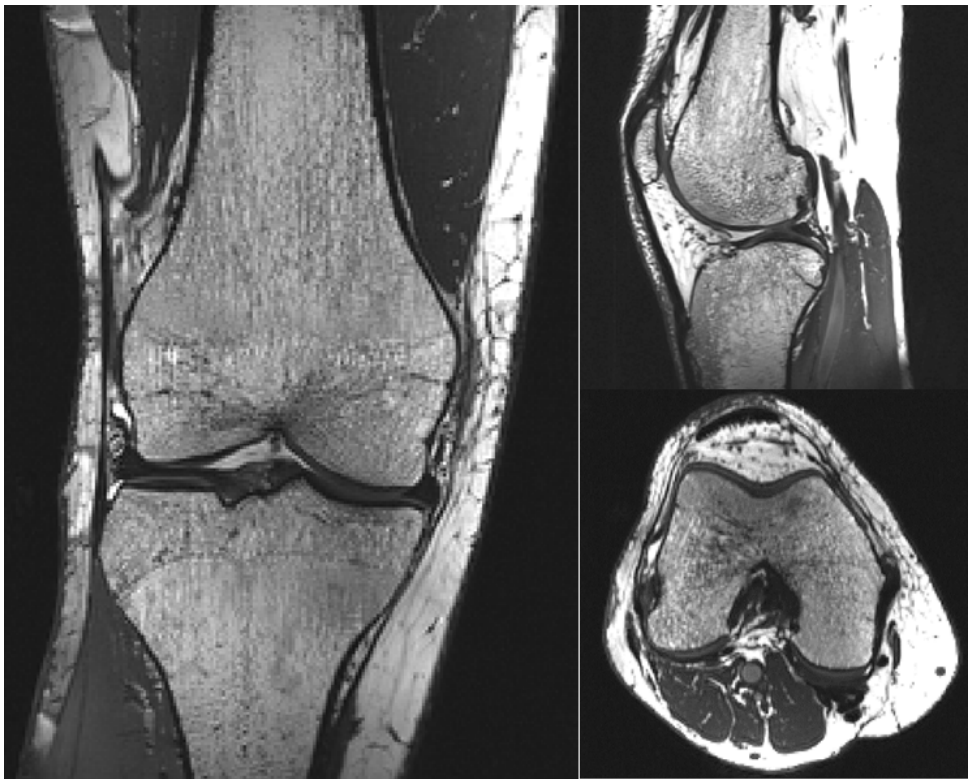

Figure 2-1 – CISS-3D scan of the TF joint visualised in all 3 planes.

A 3D Dual Echo Steady State (DESS-3D) scan sequence was also performed as it provided high contrast between the articular cartilage and its surrounding tissue (including the subchondral bone interface) (Thakkar et al. 2011). As the cartilage was well defined in the DESS-3D scan, this sequence was used to segment the articular cartilage and meniscus (Section 2.4.1).

For the last two participants, a T1-weighted Volume-Interpolated Breath hold Examination (VIBE) was added to the MRI collection protocol. This sequence has been shown to provide similar results to the DESS-3D sequence when imaging cartilage (Zink et al. 2015). The higher visual contrast between bone and the soft tissues in the T1-VIBE scan made it easier to utilise segmentation tools (such as thresholding tools) and see the boundary between certain tissues (e.g. femoral and tibial cartilage) reducing the time required for each segmentation (Figure 2-2). Therefore, for these two participants, the T1-VIBE scan was used to segment the articular cartilage and meniscus instead of the DESS-3D scan (Section 2.4.1).

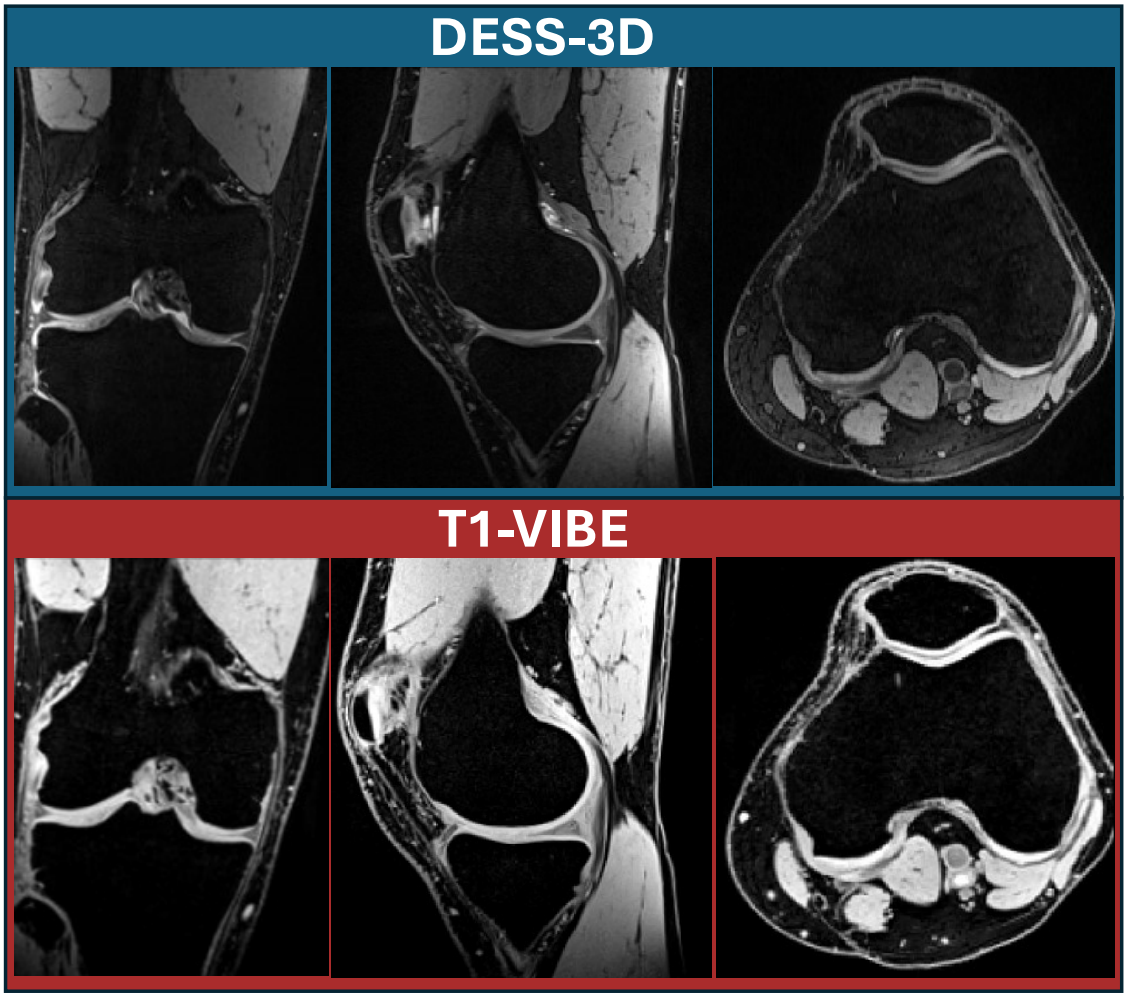

Figure 2-2 – A DESS-3D compared to a T1-VIBE scan sequence in all three planes.

2.3 DATA COLLECTION: COMBINED BIPLANE VIDEORADIOGRAPHY, MARKER-BASED MOTION CAPTURE AND ELECTROMYOGRAPHY PROTOCOL

The second data collection session took place at the Musculoskeletal Biomechanics Research Facility (MSKBRF, School of Engineering, Cardiff University), and involved capturing BVR, marker-based motion capture data, force plate data, EMG, and video footage. An existing pilot study protocol, established in Cardiff as part of the initial development of the BVR system, was used for this study. It involved imaging the knee during three functional activities: level overground gait, a stair ascent, and a dynamic, weightbearing lunge. As part of this work, some modifications were made to the protocol to improve the quality of data collected; for example, camera positions were well-defined to allow for repeatability in the setup (Section 2.3.2).

2.3.1 BIPLANE VIDEORADIOGRAPHY EQUIPMENT POSITIONING AND CALIBRATION IMAGES

Custom-built BVR equipment (Williams 2018) was used to collect BVR imaging for this study. The BVR system has 16 adjustable axes to allow for flexible positioning of the machine (Figure 2-3). Using these axes, the equipment can be manipulated into many orientations, including its location within the room, the position of each individual source and detector on their respective arms, and the angle of the source-detector pairs within the room and in relation to each other (Figure 2-4). As ten of the axes are computer-controlled, re-positioning of the machine was quick and consistent. This allowed for easy changeover of equipment setup during the data collection session, where a new configuration was needed for each activity. Key parameters for the three X-ray equipment configurations for each activity can be found in Table 2-2 – with additional information in Appendix A.

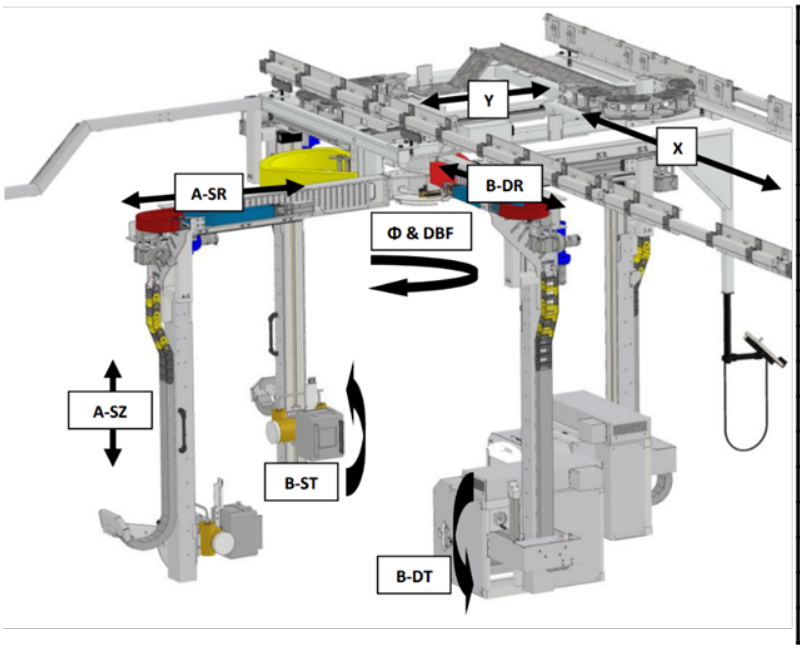

Axis ID	Description
X*	Longitudinal axis along direction of walking
Y *	Lateral axis perpendicular to X
Φ	**Rotate Axis – set A**
A-DT	Tilt Axis – set A detector
A-S T	Tilt Axis – set A x-ray source
A-DR*	Radial Axis - set A detector
A-SR*	Radial Axis - set A x-ray source
A-DZ*	Vertical Axis – set A detector
A-SZ*	Vertical Axis – set A x-ray source
DBF	**Rotate Axis – set B**
B-DT	Tilt Axis – set B detector
B-ST	Tilt Axis – set B x-ray source
B-DR*	Radial Axis - set B detector
B-SR*	Radial Axis - set B x-ray source
B-DZ*	Vertical Axis – set B detector
B-SZ*	Vertical Axis – set B x-ray source

Figure 2-3- Diagram detailing the 16 controllable axes of the BVR equipment. '' denotes computer-controlled axes; the remaining axes require manual manipulation by aligning the angles with permanently attached protractors.*

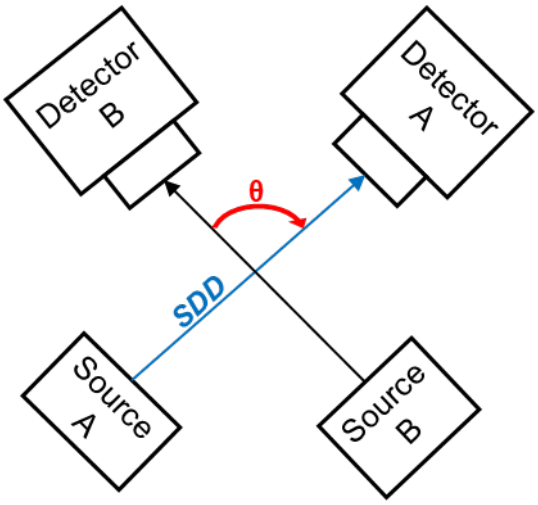

Figure 2-4 – Birdseye view of the two source-detector pairs showing θ, the angle between the two systems, and SDD, source-to-detector distance

Table 2-2 – Key BVR equipment setup parameters for each of the three activities, as depicted in the diagram in Figure 2-4

Parameter *	Level Gait	Lunge	Stair Ascent
Voltage (kV)	80	70	80
Current (mA)	160	125	160
Source-to-Detector Distance (SDD) (mm)	1785	1350	1700
Source-tilt (°)	0	0	0
Detector-tilt (°)	0	0	0
Angle θ (°)	61	150	130

**All parameters are the same for both System A and System B, except Angle θ which is the angle between the two systems.*

The only difference in X-ray equipment positioning between participants was the height of the source-detector pairs from the ground. For each activity, the participant placed their foot on the location of the central laser point (projecting downwards from where the two arms meet at the centre of the ceiling mount), and the source-detector pairs were adjusted vertically until the lasers from each source were aligned with the participant's knee joint. This ensured the knee was centred in the X-ray volume during the trials.

For each configuration, four pairs of BVR calibration images were collected (Figure 2-5). A 'white' image – with nothing in the X-ray volume – was captured for non-uniformity correction (Figure 2-5a). To correct for image distortion, uniform grids with circular holes of known dimension and spacing were X-rayed (Figure 2-5b). A cube constructed of LEGO® bricks containing a grid of 64 radio-opaque beads was imaged to allow for calculation of the 3D configuration of the X-ray hardware (Knörlein et al. 2016). The cube was carefully placed in the X-ray volume to ensure the beads filled the majority of both 2D X-ray images, with minimal overlap of beads, to provide the largest number of visible beads for the calculation (Figure 2-5c).

Finally, a cone with six radio-opaque beads, each covered with a retroreflective surface, was imaged simultaneously with the BVR and marker-based motion capture systems to allow the two to be registered together by calculating the positions of the beads in both coordinate systems, allowing for the calculation of the transformation between the two global coordinate systems (GCSs) (Figure 2-5d). The results from

one system can then be expressed in the coordinate system of the other, facilitating direct comparison of the collected data, which is useful for visualising the BVR knee bone poses relative to the measured marker motion.

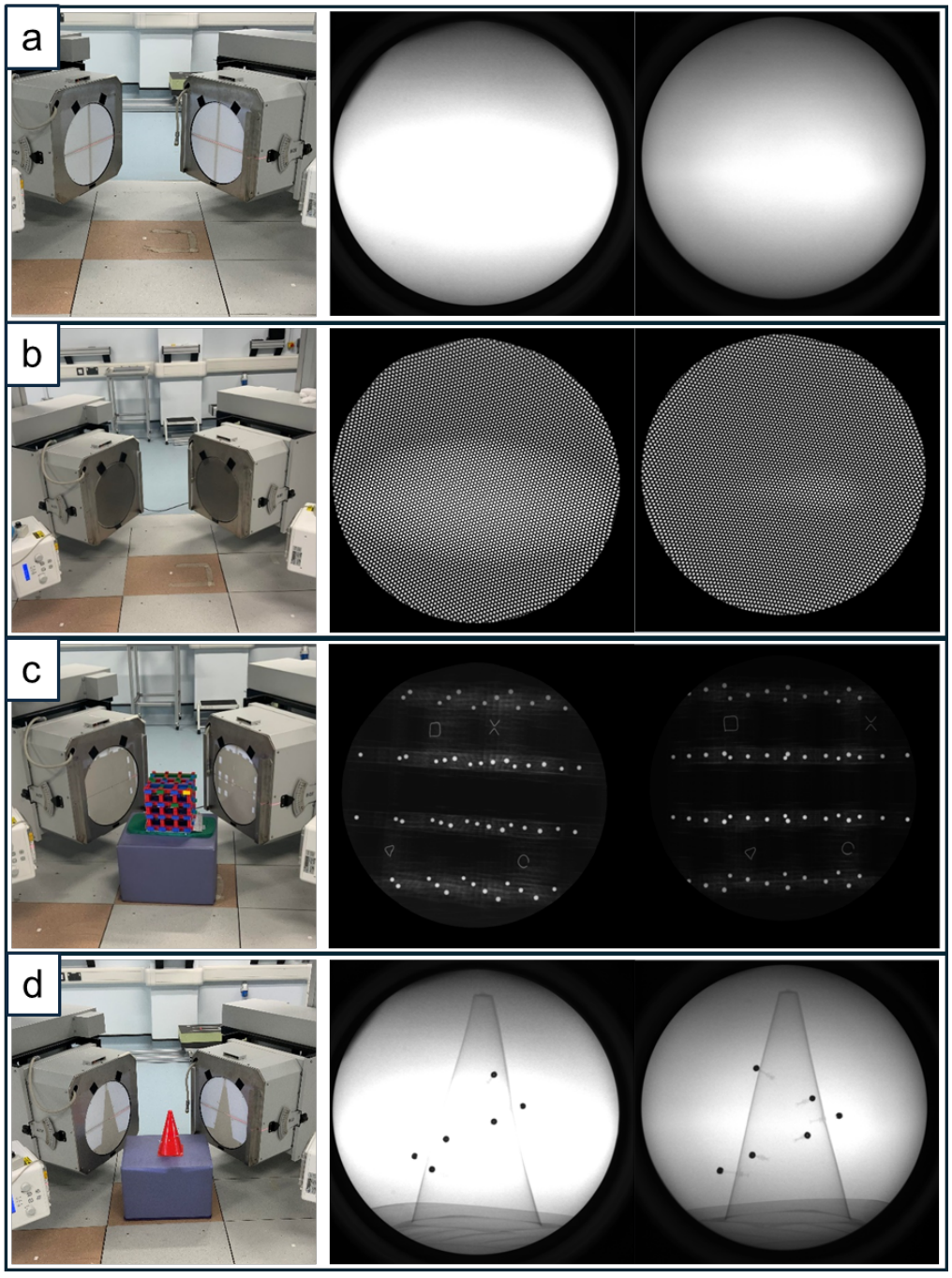

Figure 2-5 – Set of four X-ray calibration images taken at the beginning and end of every setup.

Section 2.4.3 contains more details on how these images were used to calibrate and process all collected X-ray images. Since they were critical to the processing pipeline, the four pairs of calibration images were collected at both the start and end of each activity, providing a spare set for redundancy.

All the other equipment used in this data collection session were time synchronised with the transistor-transistor logic (TTL) pulse from one of the BVR high-speed cameras (60 Hz) to allow for simultaneous data capture from multiple sources. This enabled direct comparison and integration of different datasets, offering a more complete representation of a participant's movement.

2.3.2 MARKER-BASED MOTION CAPTURE SETUP

A ring of 12 Oqus 700+ marker-based motion capture cameras (Qualysis, Sweden) and six Miqus Video Cameras (Qualysis, Sweden) were centred around five Bertec force plates (Bertec Corporation, Ohio, USA) embedded in the floor in the centre of the room (Figure 2-6).

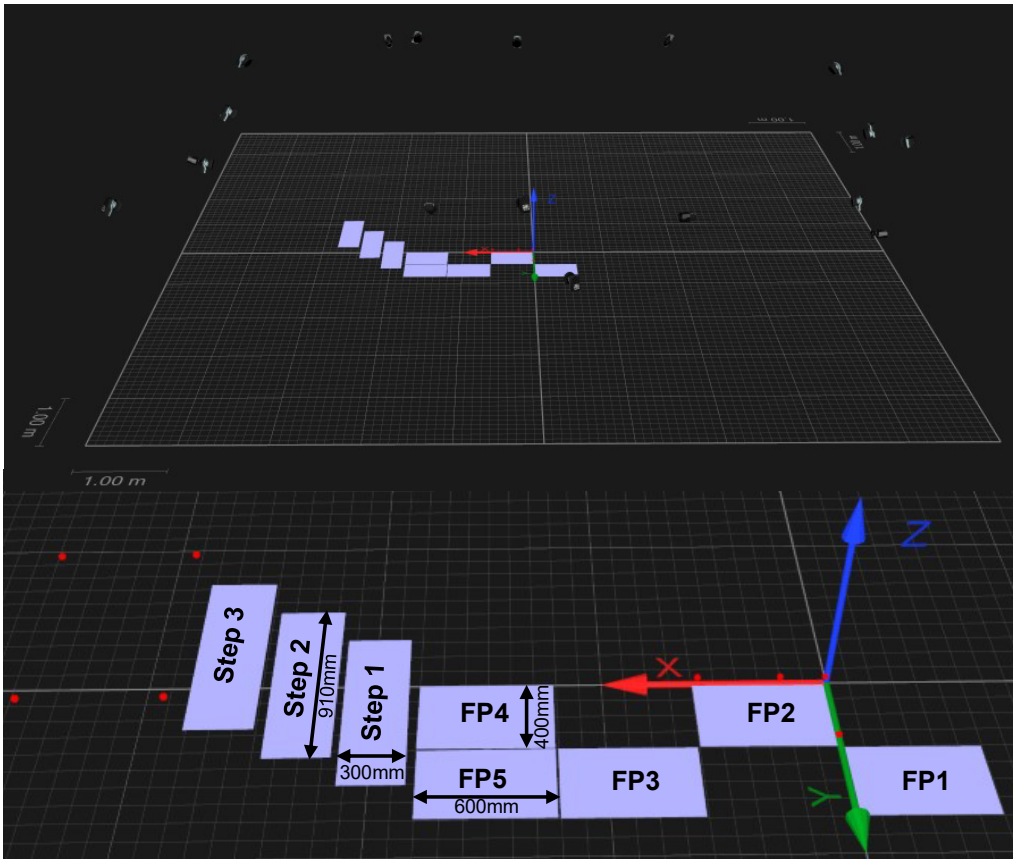

Figure 2-6 – Screen shots from Qualysis Track Manager (QTM, Qualysis, Sweden) of the laboratory camera configuration relative to the force plate and instrumented staircase placement (above), with an annotated, enlarged image of the force plates and stairs with the L-frame markers in position (below).

In the process of developing the data collection protocol, the positions of the cameras were trialled and optimised to reduce marker drop out during the dynamic trials, as this was identified as an issue with early participants.

To remove the need for recalibrating the motion capture cameras during the data collection session, a single camera configuration was used for all three activities. As the BVR equipment obscured the views of different cameras during different activities, it was important to trial all different activity X-ray and motion capture equipment configurations when deciding the final camera positions. Each camera was reviewed individually to check its view across the three configurations, as well as collectively, to check that marker coverage was sufficient for all activities.

Another aim of the final camera setup was to maximise the number of wall-mounted cameras. Wall-mounted cameras were quicker and easier to reposition than tripods, as they were attached to rails on the walls, requiring only their location on a fixed rail for positioning. This reduced the floor space occupied by tripods, minimising trip hazards, as well as allowing for ease of movement of equipment (such as the instrumented staircase and the BVR system) during the session. In the final camera configuration (Figure 2-6), nine cameras were wall-mounted and only three were on tripods.

Once the camera configuration was finalised, the camera angle on its mount and its settings in Qualisys Track Manager (QTM, Qualisys, Sweden) were recorded. For each wall-mounted camera, the rail it was attached to and its distance from a specified end of the rail were noted. For tripod-mounted cameras, detailed information about the tripod and its position in the laboratory was recorded, including the tripod's centre position, the location of each leg relative to a fixed point on the laboratory floor, the height of each tripod section, and the length of each leg.

The camera positions used in this study were documented in the data collection protocol (Appendix A). Recording this information ensured a repeatable camera setup for each data collection session, maintaining consistency in camera coverage and, therefore, reliable marker trajectory identification across participants.

Before each data collection session, the motion capture cameras were calibrated to account for any shifts in position and to establish the laboratory's GCS. This process determined the relative positions of each camera and force plate within the GCS.

Calibration involved placing an L-frame, consisting of a long and short arm with different numbers of markers, around the selected force plate (FP2 in Figure 2-6), with the long arm aligned to the direction of travel. The L-frame's corner was placed

on the force plate's corner, aligning its arms with the plate's edges. The marker at the join of the arms defined the global origin (0,0,0), with the long arm defining the x-axis, the short arm the y-axis, and the z-axis calculated as their cross product, pointing vertically upwards. All 3D marker locations throughout the session were recorded as X, Y, and Z distances from this GCS.

The cameras positions were then calibrated relative to the GCS using a calibration wand. This consisted of two markers at either end of a T-shaped wand which were a known distance apart. This wand was passed through the volume to be calibrated which covered the area the dynamic activities would be performed in. This included above each step of the staircase and directly above the five force plates embedded in the floor. For calibration, the laboratory was set up for the stair ascent activity (the first activity). With the X-ray equipment positioned for the stair ascent activity, the volume it occupied could not be calibrated. However, since the participant never moved through this area during any activity (even after the equipment was repositioned), it remained a suitable and repeatable location for the initial calibration.

From the 2D marker positions of the wand markers and L-frame markers seen by each camera, the relative 3D positions of each camera to each other and the GCS were calculated and reconstructed in QTM (Qualisys, Sweden) (Figure 2-6). The average residual error between the detected and expected marker positions across all cameras and calibration points was calculated for each motion capture camera. The calibration was repeated if the average residual error was >1 mm for any camera to ensure marker tracking quality.

After camera calibration, every force plate was located by placing a single marker on its each of its four corners. A marker-mounted plate, designed to slot down the sides of the force plate (Figure 2-7), ensured consistent marker placement. Similarly, the location of each step of the staircase was also found by placing a single marker on each of the corners.

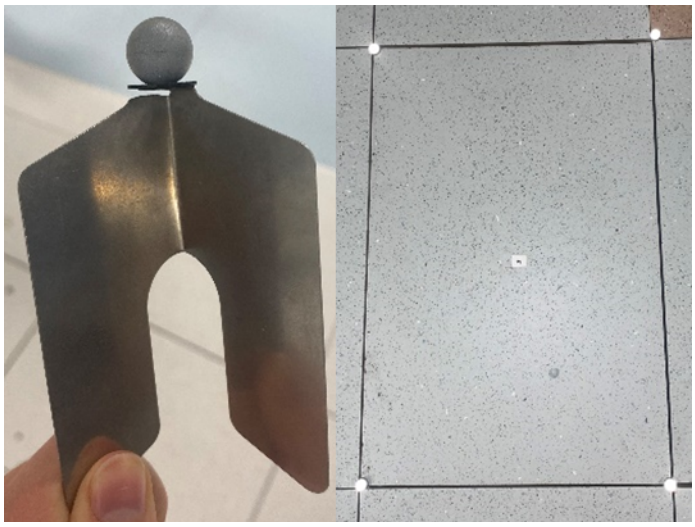

Figure 2-7 – Force plate corner marker mount (left), and in-situ on the 4 corners (right)

A modified Cleveland Clinic marker set involving 54 individual retroreflective markers was used (Kinney et al. 2013; Whatling et al. 2020) (Figure 2-8). Anatomical markers, used to calculate body reference frames, were located by palpating bony landmarks. Four individual tracking markers were used for each segment, as at least three are required to calculate 3D segment motion, with the fourth marker allowing for possible marker dropout due to obstruction (e.g. by equipment or clothing).This marker set was chosen as it had been used for previous studies at Cardiff (Whatling et al. 2020; Bowd et al. 2023), so this new data collected could extend the existing dataset as it would be directly comparable.

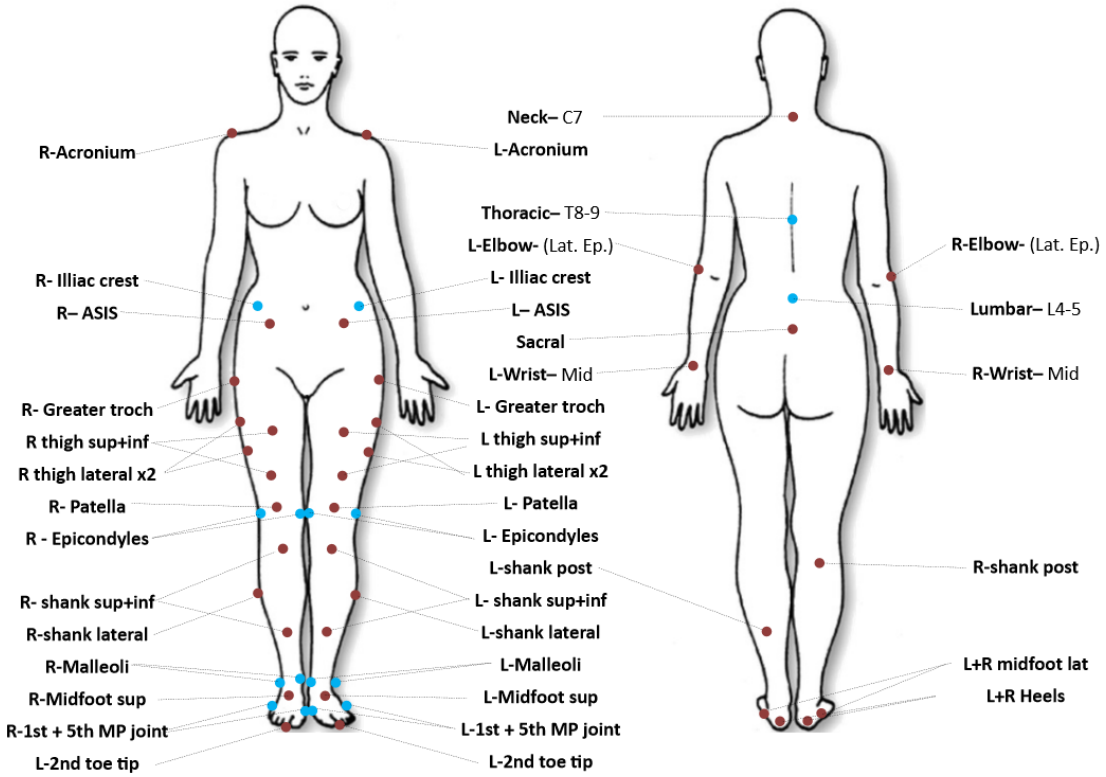

Figure 2-8 – Modified Cleveland Clinic marker set.

Marker trajectories were captured at 120 Hz as the motion capture cameras were synchronised to the TTL signal from one of the BVR high-speed cameras (60 Hz) with a two-times frequency multiplier applied. The trajectories were recorded alongside the EMG and force plate data using QTM (Qualisys, Sweden).

2.3.3 ELECTROMYOGRAPHY

A total of 14 EMG sensors (Delsys Inc, Massachusetts, USA) were used to record the electrical activity of 7 muscle targets per leg (Figure 2-9). This configuration of EMG sensors was chosen similarly to the motion capture marker set, due to its prior use in studies within the research group at Cardiff (Khatib 2018). The sensor placements were based on a modified version of the Surface Electromyography for the Non-invasive Assessment of Muscle (SENIAM) Guidelines (Hermens and Freriks 1997) with the specific targets selected based on previous recommendations to minimise crosstalk between lower limb surface signals during gait (Hermens et al. 2000).

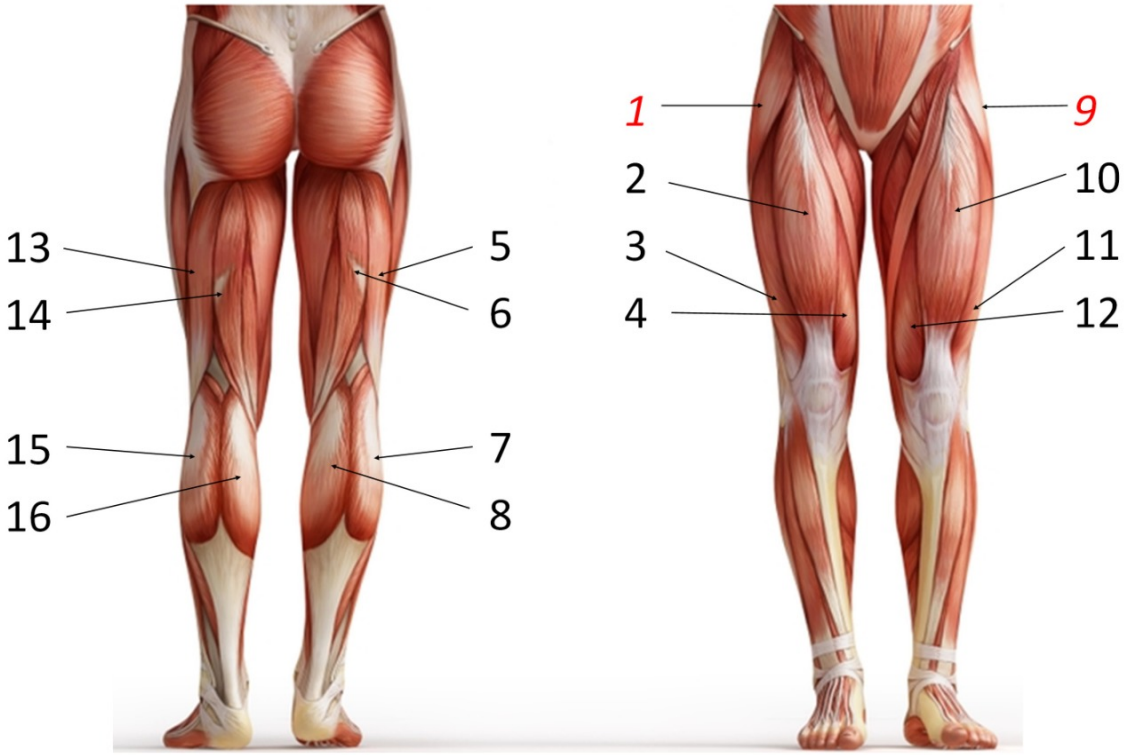

Figure 2-9 - Electromyography electrode placement protocol. Numbers represent electrode labels. Rectus femoris (2, 10); Vastus lateralis (3, 11); Vastus medialis (4, 12); Biceps femoris (5, 13); Semitendinosus (6, 14); Gastrocnemius lateral (7, 15); Gastrocnemius medial (8, 16).

The muscle bellies were located by asking the participant to tense specific muscle groups via a series of activities (e.g. standing on tiptoes) allowing for visual inspection and palpation of the muscle region by the researcher to locate the largest part of the muscles. The muscle belly sensor locations were then marked using an eye liner pencil to indicate the areas that required skin preparation. The placement areas were shaved to remove hair and exfoliated to remove dry skin, improving the contact between the skin and EMG sensors. An electro-gel was applied to the electrodes on the back of each sensor to improve the conductivity of muscle signals. The EMG sensors were attached to the participant using double-sided stickers and further secured using an elastin tubing (Tubigrip, Mölnlycke Health Care, Sweden).

EMG was collected as part of this protocol to allow for future analysis of muscle activity patterns, although it was outside the scope of this research to process the EMG signals due to time constraints.

2.3.4 DEMOGRAPHIC DATA, ANTHROPOMETRIC DATA, AND QUESTIONNAIRES

Basic demographic data was collected at the start of each session, including date of birth, height and weight. The demographics for each participant are given in Table 2-3.

Table 2-3 – Participant demographics

Participant ID	Sex	Age (years)	Height (cm)	Weight (kg)
HV001	M	28	185.0	85.0
HV002	F	57	169.5	62.4
HV003	M	54	182.0	87.5
HV004	M	52	176.5	67.1
HV005	F	47	158.5	51.0

Each participant was asked to fill out a series of questionnaires during the BVR data collection session to ascertain details about their perceived general knee health. These were the Knee Outcome Survey (KOS) (Irrgang et al. 1998), the Knee injury and Osteoarthritis Outcome Score (KOOS) (Roos et al. 1998), the Oxford Knee Score (OKS) (Dawson et al. 1998), the Pain Audit Collection System (PACS) proforma assessment form, and the Western Ontario and McMaster Universities Osteoarthritis Index (WOMAC) (Bellamy et al. 1988). The mean cohort questionnaire results, along with the score that deviated the most from the healthy reference score, are presented in Table 2-4.

Table 2-4 – Cohort questionnaire results

Questionnaire	***Healthy reference score***	Mean	Worst observed score*
KOS	*85*	84.5	83
KOOS	*100%*	99.0%	97.6%
OKS	*48*	47.3	46
PACS	*0*	0	0
WOMAC	*0%*	0.260%	1.04%

**The participant score that deviated the most from the healthy reference score*

The small amount of cohort deviation from the healthy reference score for each questionnaire was reflective of the average age of the participants, with slight deviations being expected with aging and not necessarily indicative of disease.

A copy of the questionnaires can be found in Appendix B. These specific questionnaires were chosen as they were part of previous studies completed at Cardiff (Williams 2018; Bowd 2022) so this would allow for possible future comparison amongst a wider cohort.

2.3.5 STATIC TRIALS

Static trials were obtained at the start of each activity with the participant standing in a neutral position, arms by their sides. The first static trial captured was motion capture only, and the resulting trajectories were checked carefully to ensure all markers were visible in the calibrated motion-capture volume. A static trial with all markers visible was required for scaling both the V3D models and musculoskeletal models (MSMs), so this static trial was repeated until all markers were visible.

Static trials, including BVR, were then performed to determine bone poses in a neutral knee position. BVR static recordings were performed for the gait and lunge configurations, with participants standing perpendicular to the normal direction of travel. This ensured their imaged (right) knee remained within the X-ray volume while the contralateral knee was out of both views. Initially, static trials were collected for all three activities, but the stair ascent static trial was later removed as, in this setup, participants stood with one leg on the ground and the other on the first step with a bent knee, meaning the position was not neutral.

2.3.6 DYNAMIC TRIALS

Each participant performed multiple repeats of the following three dynamic activities: stair ascent, level gait, and lunge. Before collecting X-ray trials, several practice repeats were conducted using only motion capture, EMG, force plates, and video cameras (without BVR). The number of practice trial repeats varied by participant and activity, depending on participant and researcher confidence in performing the movement correctly under X-ray conditions.

Once confident with the practice trials, up to five repeats of each activity were captured with X-rays firing. The number of X-ray trials collected was carefully

controlled to ensure the radiation exposure remained within the 0.154 mSV limit (per session) defined under the study ethics.

The first activity consisted of a stair ascent starting with both feet on the floor, ascending three instrumented steps, and finishing with both feet on the platform at the top of the staircase. For this activity, the BVR equipment was located around the first step of the stairs (Figure 2-10).

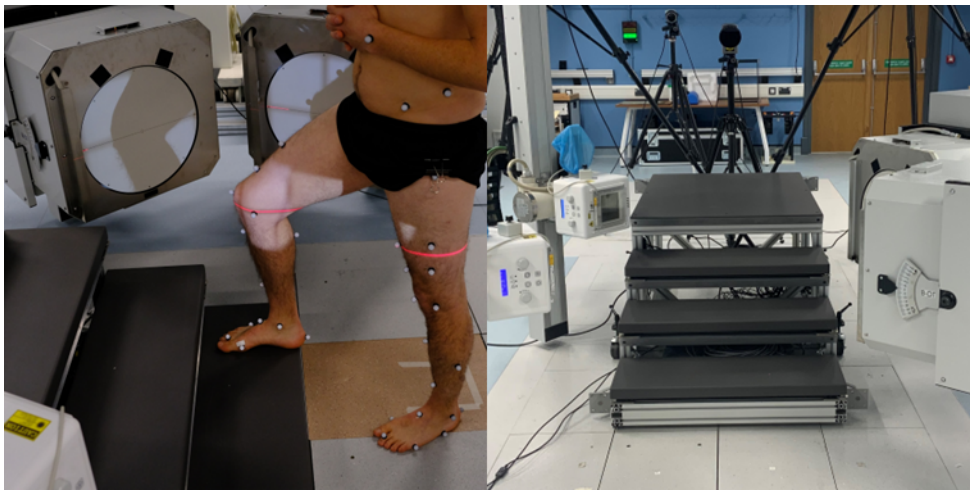

Figure 2-10 – Collection setup for the stair ascent activity.

The next activity was level overground gait performed at a self-selected speed across a 7 m walkway. Force plates were located in the central portion of the walkway, with the BVR equipment centred around FP2 (Figure 2-11) (for context with motion capture setup see Figure 2-6). To allow the participant to walk with their natural gait pattern, avoiding force plate targeting, the participants were unaware of the locations of the force plates. The participant's starting location was adjusted until they achieved clean force plate hits (defined as all of the foot stepping within the boundary of the force plate).

Figure 2-11 – Level gait equipment configuration with target area marked using masking tape.

For the earlier participants in the study, blinding to the force plate locations was maintained throughout the whole activity. However, when carrying out the X-ray trials, participants were often inconsistent with their heel-strike placement on the X-ray force plate (FP2, Figure 2-6) which meant that their knee was not always central in the X-ray imaging volume. Due to the amount of joint movement through the imaging volume during gait, this activity only captured a small number of frames of motion, which was decreased further by inaccurate foot placement on the force plate.

The area of the heel-strike location to ensure good knee placement in the imaging volume (approximately 0.06 m^2) was significantly smaller than the size of the force plate (0.24 m^2) (Figure 2-12). This made it harder to ensure correct foot placement solely through adjustments to the participant's starting location. For this reason, once they had completed their trial repeats with no X-rays (blinded), the later participants in the study were asked to aim for a marker area on the second force plate for the X-ray trials (Figure 2-11). This improved consistency of the portion of stance phase collected during the X-ray trials.

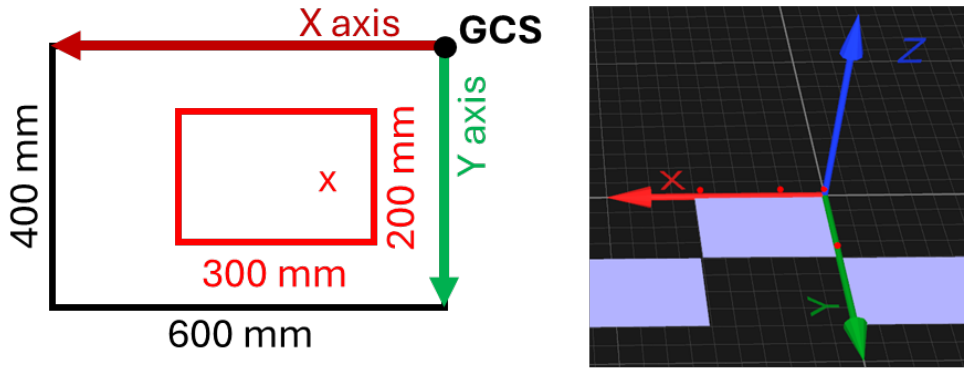

Figure 2-12 – Diagram of target region (outlined in red) on FP2 for foot placement during level gait (left) relative to the global coordinate system (GCS) of the motion-capture laboratory (right). The 'x' denotes the centre of the X-ray volume relative to the FP.

The third activity was a weightbearing, dynamic lunge onto a single force plate where the participant performed a single continuous movement from an upright standing position, to a self-selected lunge length and flexion angle, then back to standing (Figure 2-13).

Figure 2-13 – Participant carrying out a dynamic, weightbearing lunge

2.4 DATA PROCESSING

2.4.1 IMAGE SEGMENTATION

The MRI images (Section 2.2) were segmented using Simpleware Scan IP (Synopsis, United States) to produce 3D models of the structures within the joint. For the process of model-based image registration (Section 0), models of the cortical and cancellous bone of the distal femur and proximal tibia were required as part of the BVR kinematics calculation pipeline.

Firstly, cortical bone masks were created by manually segmenting the desired region from the high-resolution CISS-3D scan (Figure 2-14). The initial segmented models were then dilated isotropically by one pixel, smoothed using a recursive Gaussian filter, and eroded by one pixel to preserve their overall shape.

The recursive Gaussian filter achieved smoothing by modifying each voxel based on surrounding voxels, with weightings defined by a Gaussian distribution and a specified standard deviation (σ) (Synopsys 2024). An isotropic Gaussian σ value of 1.5 was chosen as it reduced the surface noise whilst preserving bony details needed for image registration.

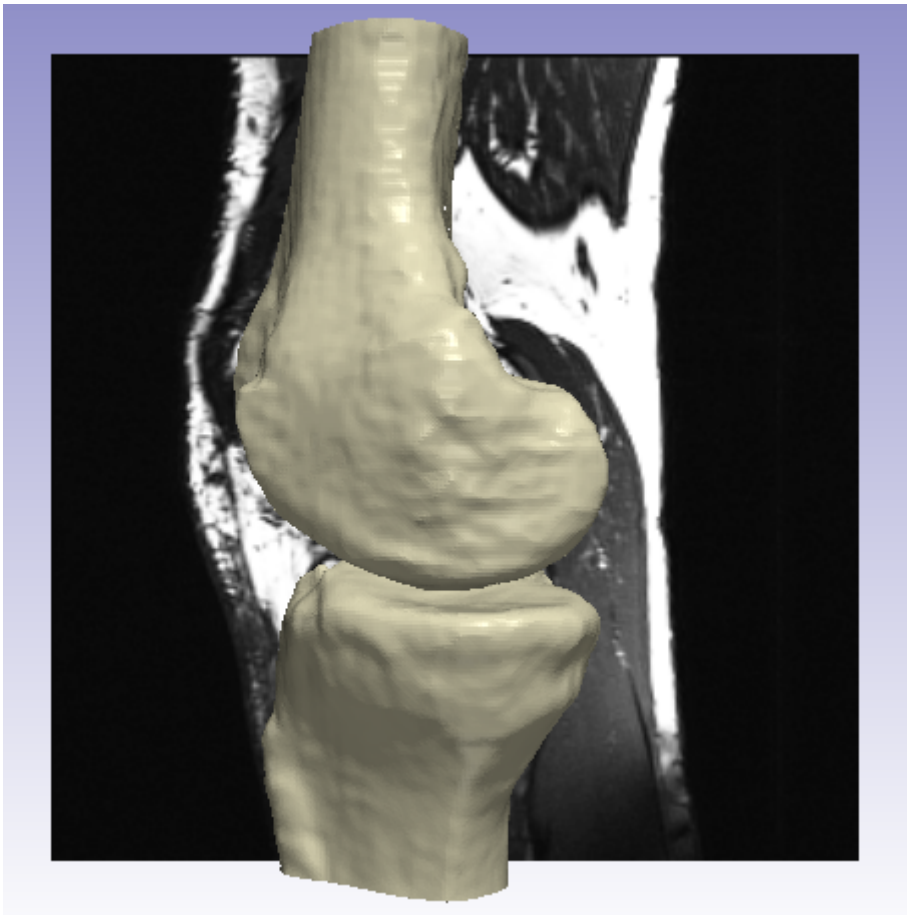

Figure 2-14 – 3D femur and tibia models (with recursive Gaussian smoothing applied) segmented from a CISS-3D scan.

To generate the cancellous bone models, a mask was created using the threshold tool to select all pixels in the image that were above a defined value, removing pixels representing cortical bone (Figure 2-15). The cortical bone shows up as darker pixels than the cancellous bone in the CISS-3D scan due to its lower water content, allowing for thresholding.

A Boolean operation was then performed to produce a mask only containing pixels from the thresholding result that intersected with the cortical bone mask. Finally, a visual inspection was performed of the result of the Boolean operation to ensure that the cancellous bone mask was fully encased by the cortical mask as a watertight model was needed to generate the DRR (Section 2.4.2) for image registration (Section 0). If any of the cancellous pixels were visible through the cortical mask, the cancellous mask was eroded by the minimum amount required to fully conceal it.

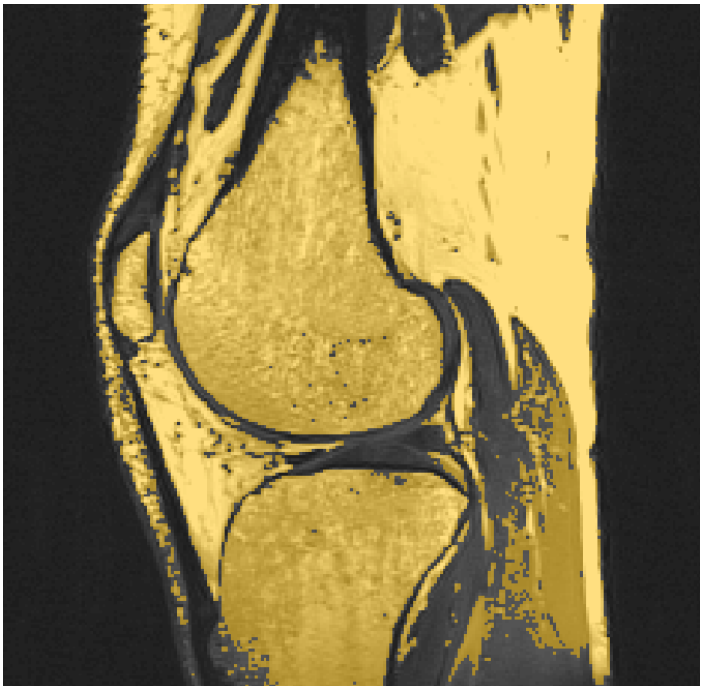

Figure 2-15 – Threshold applied to CISS-3D pixels to select only those above a given value.

The bone meshes were exported from Simpleware as .stl files, then converted into .obj files using MeshLab (Cignoni et al. 2008) for import into the DSX Suite (HAS-motion, Canada).

Additionally, full bone models for both the femur and tibia were segmented from the long leg scan for each participant. These were used to define the anatomical coordinate systems (ACSs) for each bone (Section 2.4.3).

The DESS-3D (or T1-VIBE scan for later participants) was used to segment soft tissue structures, such as the articular cartilage, to be used for subject-specific musculoskeletal and finite element modelling in subsequent chapters. More details of how these structures were segmented and utilised can be found in Chapter 3 and Chapter 4.

2.4.2 'SIMULATED CT' GENERATION

Model-based image registration (Section 0) requires a Digitally Reconstructed Radiograph (DRR) created from a 3D imaging scan, typically computed tomography (CT), which is then matched to each X-ray image pair (Gray et al. 2018). DRRs are synthetic X-ray images generated by tracing rays from each X-ray source to its corresponding imaging plane through a floating 3D bone model, casting a 2D radiographic projection. Each pixel in the 2D DRR represents the total accumulated

CT values along the ray's path from the X-ray source to the imaging plane (Russakoff et al. 2005).

When using a CT scan for model based image registration, the segmented models are exported as partial volumes with voxel radiographic properties that inherently differ between cortical and cancellous bone (Welte et al. 2022). However, since this dataset was acquired using MRI, 'simulated CT' data were generated using the 'Image Data Generator' tool (Orient3D, DSX Suite, HAS-Motion, Canada). This tool constructs an artificial partial CT volume from user-defined voxel size, generic cortical and cancellous bone density properties, and input masks representing the inner and outer cortical bone surfaces (Section 2.4.1). This simulated CT was then used to generate DRR projections during image registration (Section 0).

2.4.3 ANATOMICAL COORDINATE SYSTEM DEFINITION

As well as generating the 'simulated CT', Orient3D was also used to apply ACSs to the segmented bone models using automated algorithms (Miranda et al. 2010) (Figure 2-16).

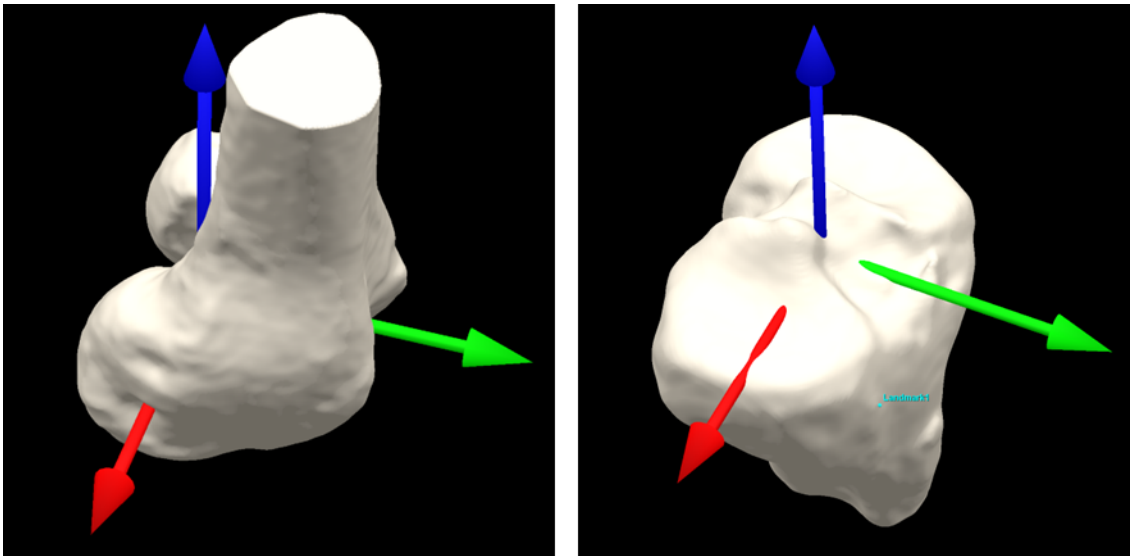

Figure 2-16 – Anatomical Coordinate Systems (ACSs) applied to the femur (left) and tibia (right).

Manually defined landmarks (including an anterior point, as well as proximal and distal points on the bone shaft) were used to assist the algorithm in determining bone orientation and isolating specific regions of the bone model.

The algorithm developed by Miranda et al. (2010) generates an ACS for the femur by first fitting a cylinder to the femoral condyles, with the cylinder's central vector

defining the medial-lateral (ML) axis. The inertial axis is then calculated through the femoral diaphysis, and the anterior-posterior (AP) axis was defined as the cross product of the inertial and ML axes. Finally, the long axis (compression-distraction, CD) is determined by recrossing the AP and ML axes. For the tibia, the ACS is established by isolating the tibial plateau using the inertial axes and positioning a plane at the largest cross-sectional area (Miranda et al. 2010). In both cases, defining the ACS relied on correctly calculating the inertial axis.

The automated approach was chosen to ensure consistency across participants, reducing human error and processing time. However, when applied to partial bone models, despite the use of additional manual landmarks, the algorithm often struggled to correctly determine the inertial axes. This led to errors in ACS orientation, as inaccuracies in isolating the femoral diaphysis or tibial plateau interfered with the calculation of the axes. These orientation errors affected the subsequent six DOF kinematics calculations due to crosstalk between axes.

Although Miranda et al. (2010) developed their algorithm for partial distal femur and proximal tibia 3D geometries, without the traditional use of hip and ankle joint centres, it was found to perform better and more consistently when these landmarks could be identified by inputting the full bone geometry into the algorithm (Figure 2-17). This was likely due to the automated algorithm requiring the femoral diaphysis length to be at least 55 mm (Miranda et al. 2010), with some bone models being close to that threshold.

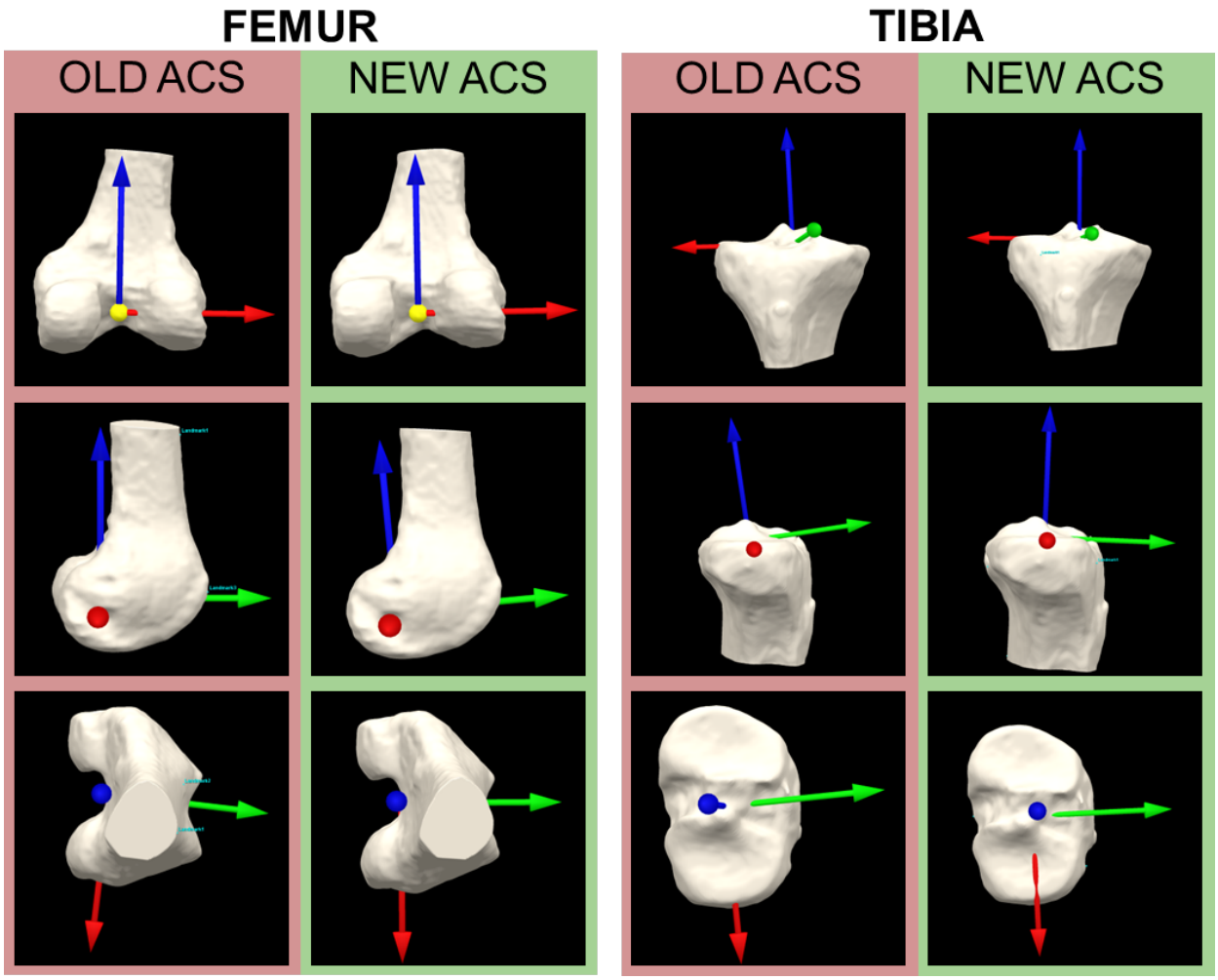

Figure 2-17 – Anatomical Coordinate Systems (ACSs) generated using the automated algorithms (Miranda et al. 2010) for the femur and tibia. The 'old' ACSs were generated using the partial bone models only and the 'new' ACSs were generated using the full bone models.

Therefore, to ensure physiologically meaningful axes were generated, the full femur and tibia models, segmented from the long leg scan (Section 2.4.1), were aligned with the high-resolution partial bone models (MeshMixer, Autodesk, USA), and the ACSs were recalculated using the full bone geometries. In most cases, the algorithm successfully identified the inertial axes using only the full bone models. However, for some femurs, an additional hip joint centre landmark was needed to accurately define the ACS. For these cases, the centre of the femoral head was identified by fitting a sphere to the full bone model (Rhino, Robert McNeel & Associates, USA). This process is summarised in Figure 2-18.

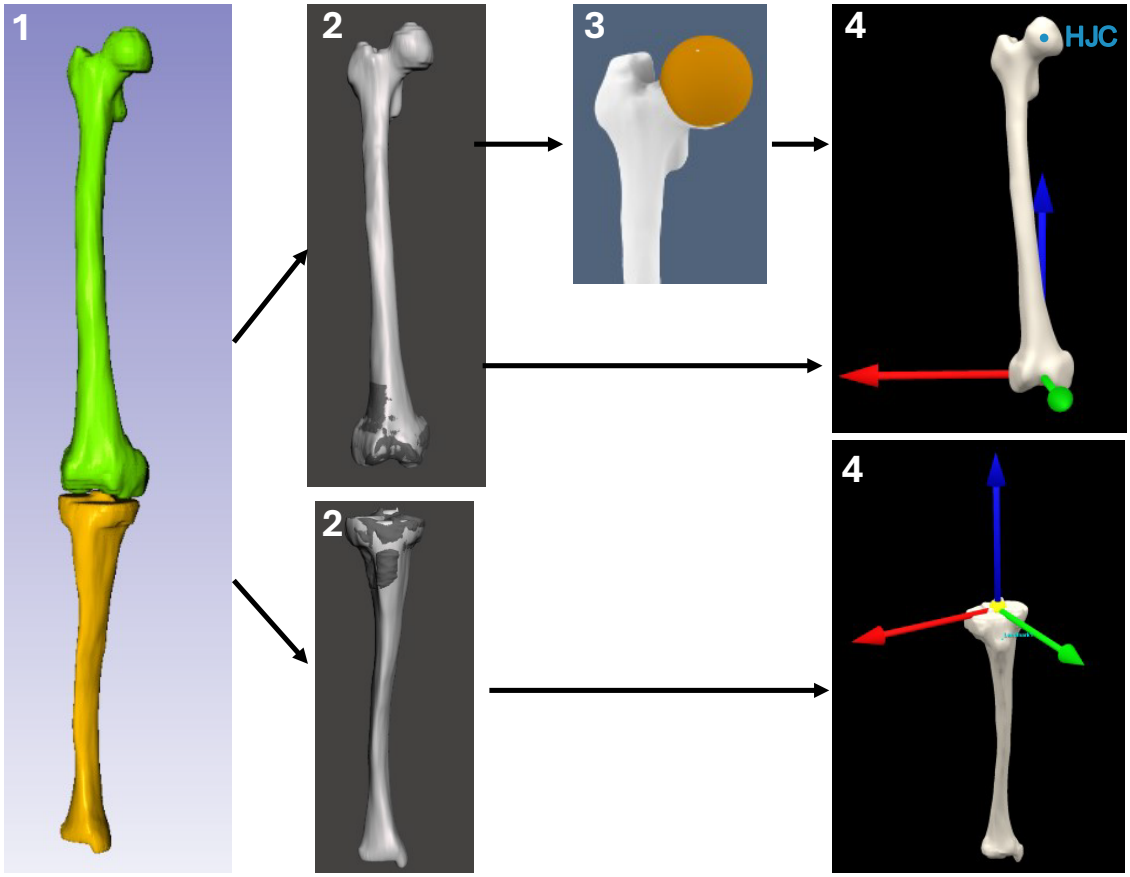

Figure 2-18 – Showing the process of generating full bone models to calculate bone ACSs. (1) Full bone models segmented from the long leg scan in Simpleware Scan IP (Synopsis, United States). (2) Full bone models were aligned with the partial bone models and exported in their new positions. (3) Hip joint centre (HJC) landmark was identified by fitting a sphere to the femoral head when the algorithm did not apply correctly to just the full femur model (Rhino, Robert McNeel & Associates, USA). (4) ACSs applied to the full bone models ready to be applied to the partial bone models.

2.4.4 X-RAY CALIBRATION

Before image registration, all X-ray images were calibrated using the corresponding set of calibration images for each configuration (Section 2.3).

The X-ray images were captured using Photron FASTCAM Mini WX100 high-speed cameras (Tech Imaging Services, Massachusetts, USA) controlled through Photron FASTCAM Viewer 4 (PFV4, Tech Imaging Services, Massachusetts, USA). The images were originally saved in the 'MRAW' format when collected and then were converted into multipage '.TIFF' files for image registration. Each X-ray also had to be rotated 90 degrees because the cameras were mounted sideways in the detector units. They were also down sampled from 2048 x 2024 pixels to 1024 x 1024 pixels to reduce image noise and produce stronger edge contrast (Williams et al. 2026) to

improve the clarity of the edge detection algorithm results (Section 0), making image registration easier as the bone edges were clearer.

Once converted, the intensity (or ‘white’) image for each detector was used to correct for inherent discrepancies in the pixel intensities recorded across the detector. The ‘white threshold’ parameter value for each view was adjusted to remove any pixels outside the view of the image detector (Figure 2-19). The pixel values of each X-ray were taken away from the remaining ‘white’ image pixels of the relevant detector (inverting the image) to perform uniformity correction for all X-ray trials (HAS-Motion 2024a).

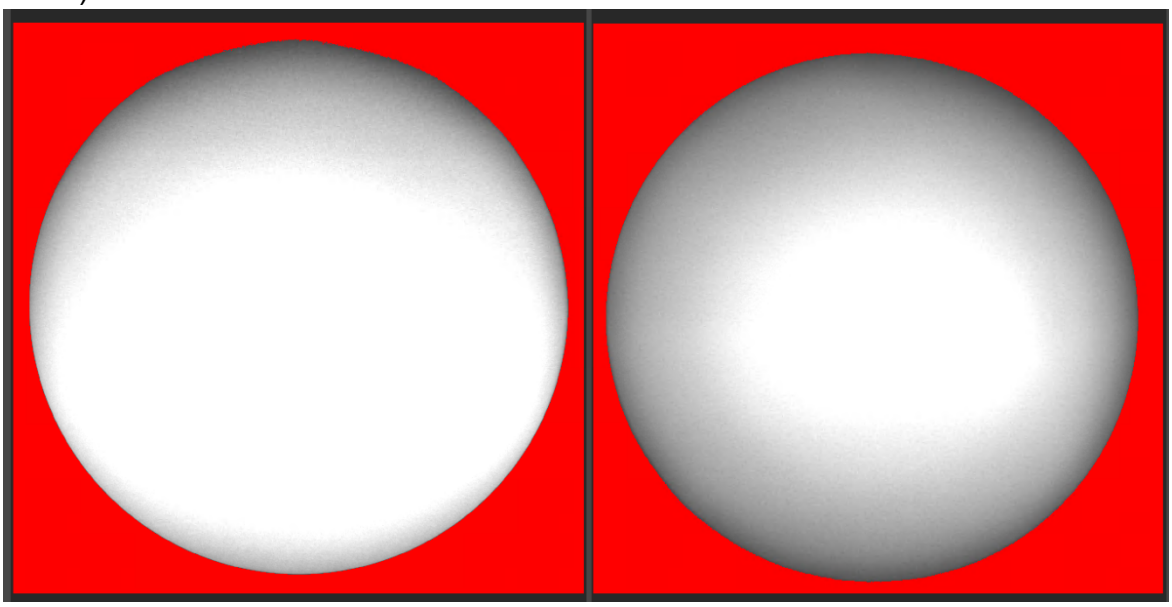

Figure 2-19 – Uniformity correction ‘white’ image, with red exclusion zone defining the circular capture region of the X-ray detector.

Subsequently, the X-rays were corrected for image distortion using the ‘grid’ images (Figure 2-20). Two main types of distortion need to be corrected: ‘pincushion’ distortion, which occurs due to the curved X-ray photocathode projecting onto a flat image intensifier, and ‘S-curve’ distortion due to the Earth’s magnetic field affecting the emitted electrons (Rudin et al. 1991; Cowen et al. 2008). The grids each contained a uniform pattern of holes so the distortion of each region of this pattern could be calculated and corrected for. Partial grid holes, which were too small to give an accurate representation of where the centre of the hole was, were removed by adjusting the ‘grid centroid size range’ until only the complete grid holes were selected as valid. Using the centroid locations of all valid grid holes, a displacement map was calculated and used to move each pixel to its proper location (HAS-Motion 2024a).

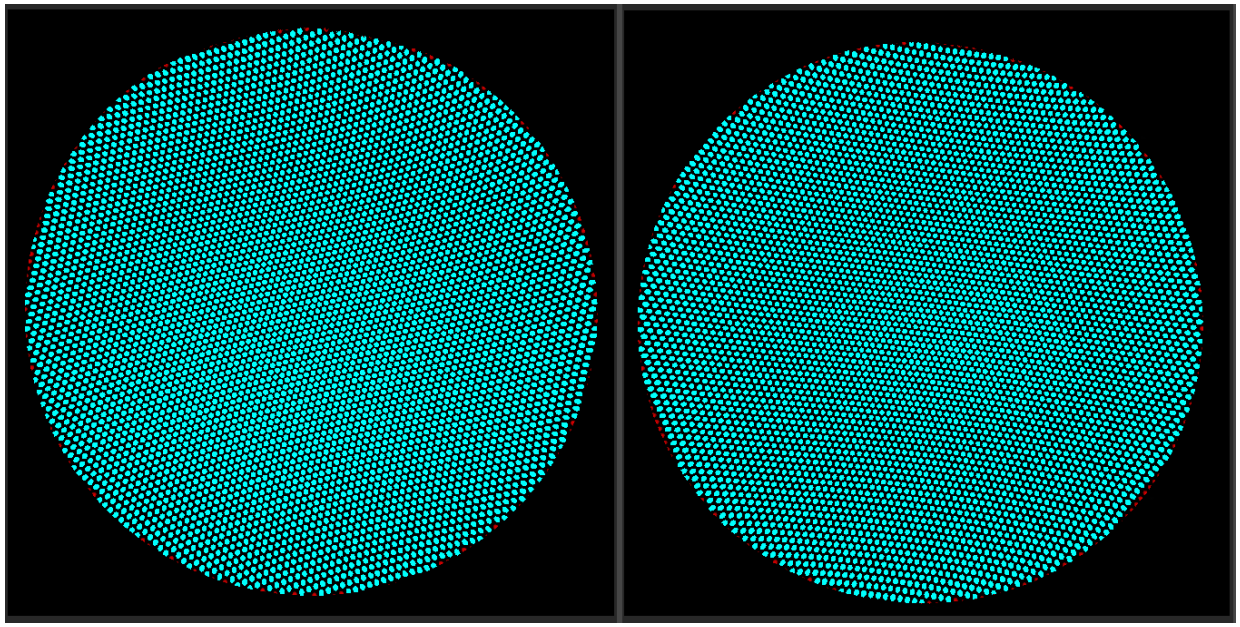

Figure 2-20 – Image distortion correction example, with 'valid', full grid holes in blue and partial grid holes round the edges of the images in red.

The 3D configuration of the X-ray source-detector pairs within the X-ray GCS was determined using images of the LEGO® cube (Knörlein et al. 2016). As well as an equally spaced array of 64 radio-opaque beads, the cube also contained four wire shapes (square, circle, triangle, cross) whose centres were identified by the user (Figure 2-21). The shape centre landmarks helped the software to identify the centroid location of each bead (numbered 1 to 64). However, as the shape centres may not have been accurately positioned, they were removed before calculating the 3D configuration of the system from the digitised bead positions.

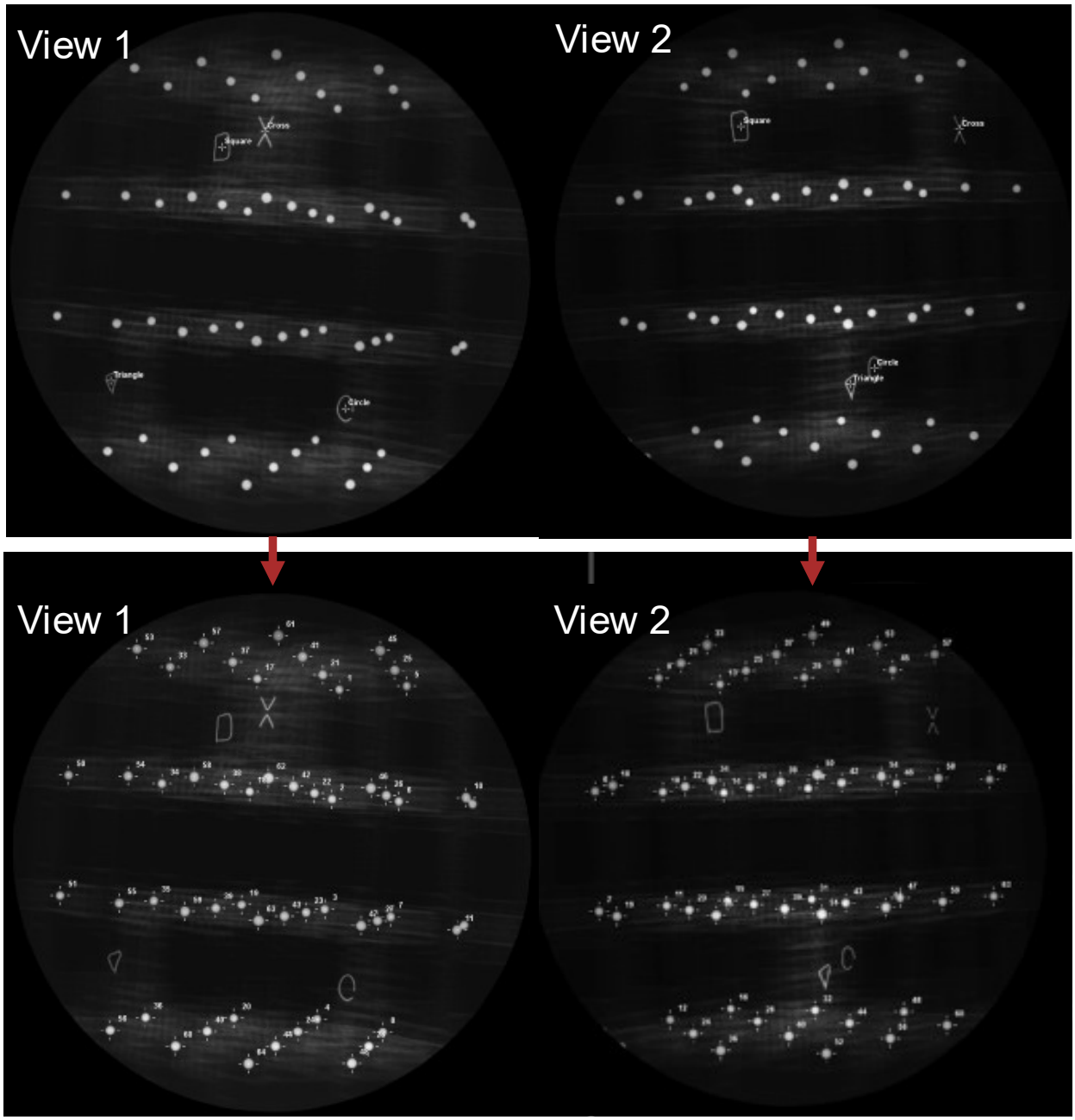

Figure 2-21 - X-ray images of the LEGO® cube containing a 3D grid of radio-opaque beads in the DSX Suite (HAS-motion, USA). The four wire shapes were manually identified (above) and the beads were automatically numbered using those shape locations (below).

The residual error between the predicted and identified centroid location of each bead was then calculated, along with the total residual error across all beads. High residual errors were seen when centroid locations were difficult to predict, such as when beads overlapped in one or both X-ray views. These bead centroids were removed, and the 3D configuration was recalculated. This was repeated iteratively until only beads with low residuals (<0.4 mm) remained.

The X-ray images of the pylon and its corresponding motion capture were used to register the BVR and motion-capture systems together to allow their data to be viewed in the same coordinate space (Figure 2-22). The beads were identified in the same order from the same trial image in both QTM (Qualisys, Sweden) and SlicerAutoscoperM (Akhbari et al. 2019). The positions of the beads were then co-registered using MATLAB code provided by Dr Michael Rainbow from Queens University and the transform between the motion-capture GCS and the BVR GCS was calculated to allow for conversion between the two. This works by calculating the optimal rotation matrix between the centroid of the six beads in the BVR coordinate system and the motion capture coordinate system using singular value decomposition (Söderkvist and Wedin 1993; Challis 1995), then calculating the translation between the centroid locations after rotating (Jacobs and van de Bogert [no date]).

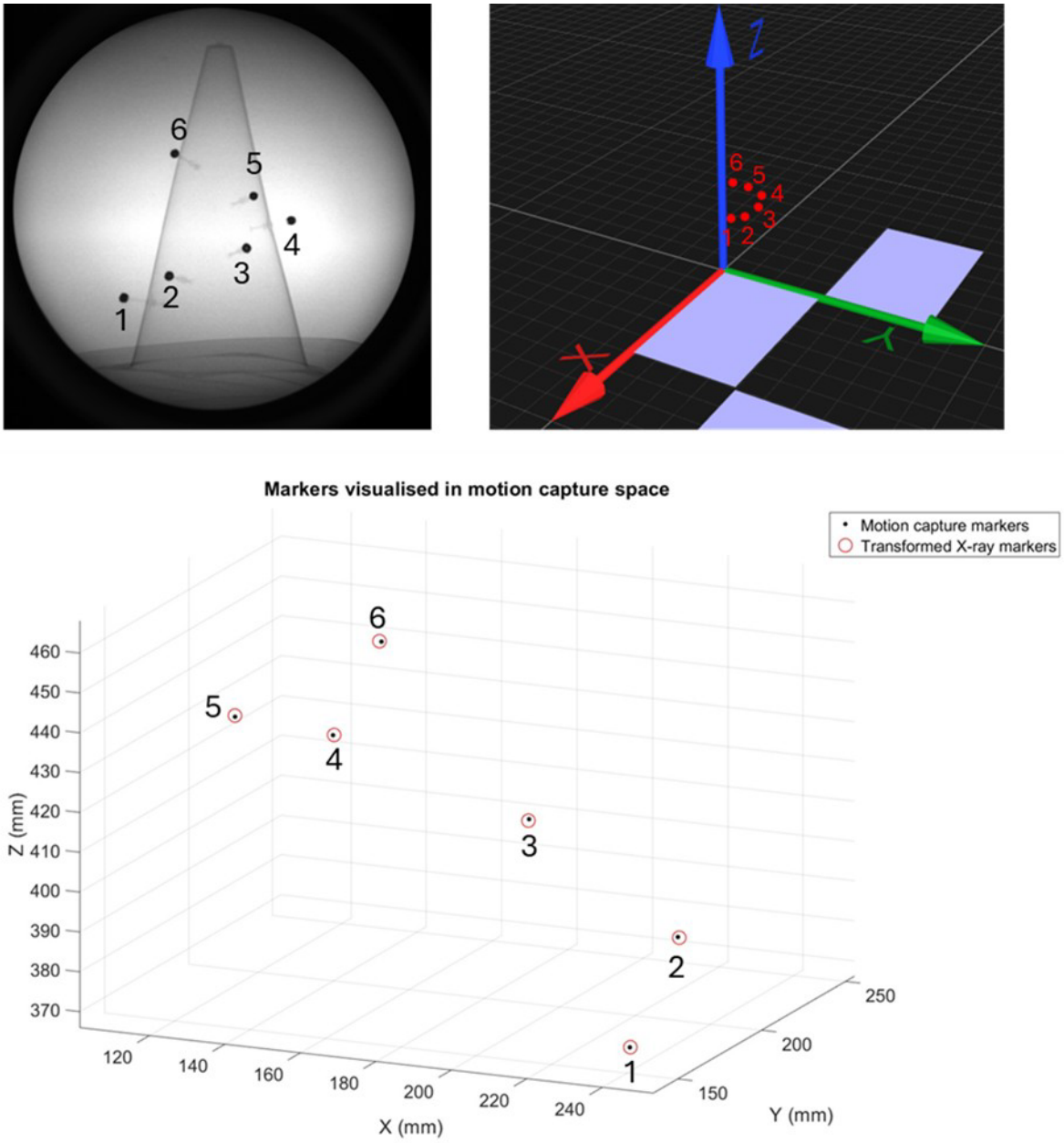

Figure 2-22 – Labelled pylon marker positions from motion capture and BVR co-registered to calculate the transformation matrix between the two systems.

2.4.5 MODEL-BASED IMAGE REGISTRATION

Model-based image registration generated pose maps containing the XYZ rotations and translations required to fully describe the 3D position and orientation of each bone within the X-ray GCS at each frame. The model-based image registration processing pipeline was carried out using the DSX Suite (HAS-Motion, USA) on Windows 10 with an Intel® Core i7 processor, 32.0 GB RAM, and a Nvidia RTX 2080 graphics card.

The DRR from the 'simulated CT' (Section 2.4.2) was projected onto each X-ray view and matched to both views at once for every frame of motion (Figure 2-23). For the first frame of each new trial, image registration was performed by manually manipulating the six DOFs of the floating bone model in the 3D view to roughly position and orientate the DRR, before using finer keyboard controls to precisely match the bone outlines to both views simultaneously (Figure 2-24).

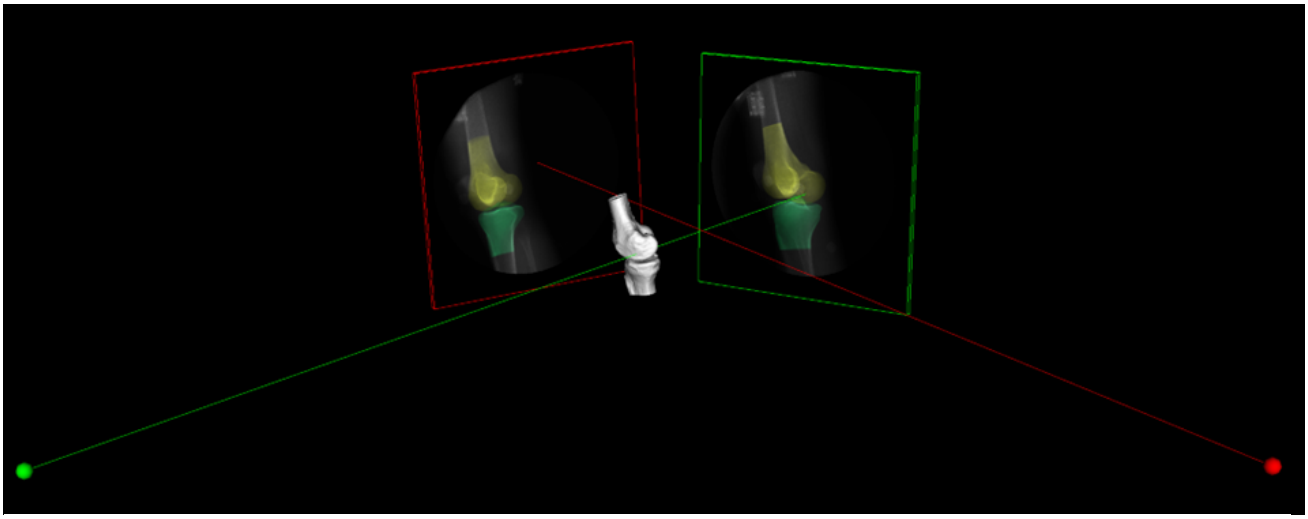

Figure 2-23 – Screenshot of the 3D view (DSX suite, HAS-motion, Canada) showing the matched DRRs projected onto a pair of images from a single frame of a level gait trial. The green and red dots in the foreground represent the location of each X-ray source with a ray traced to the centre of the detector image to show the configuration of the BVR equipment.

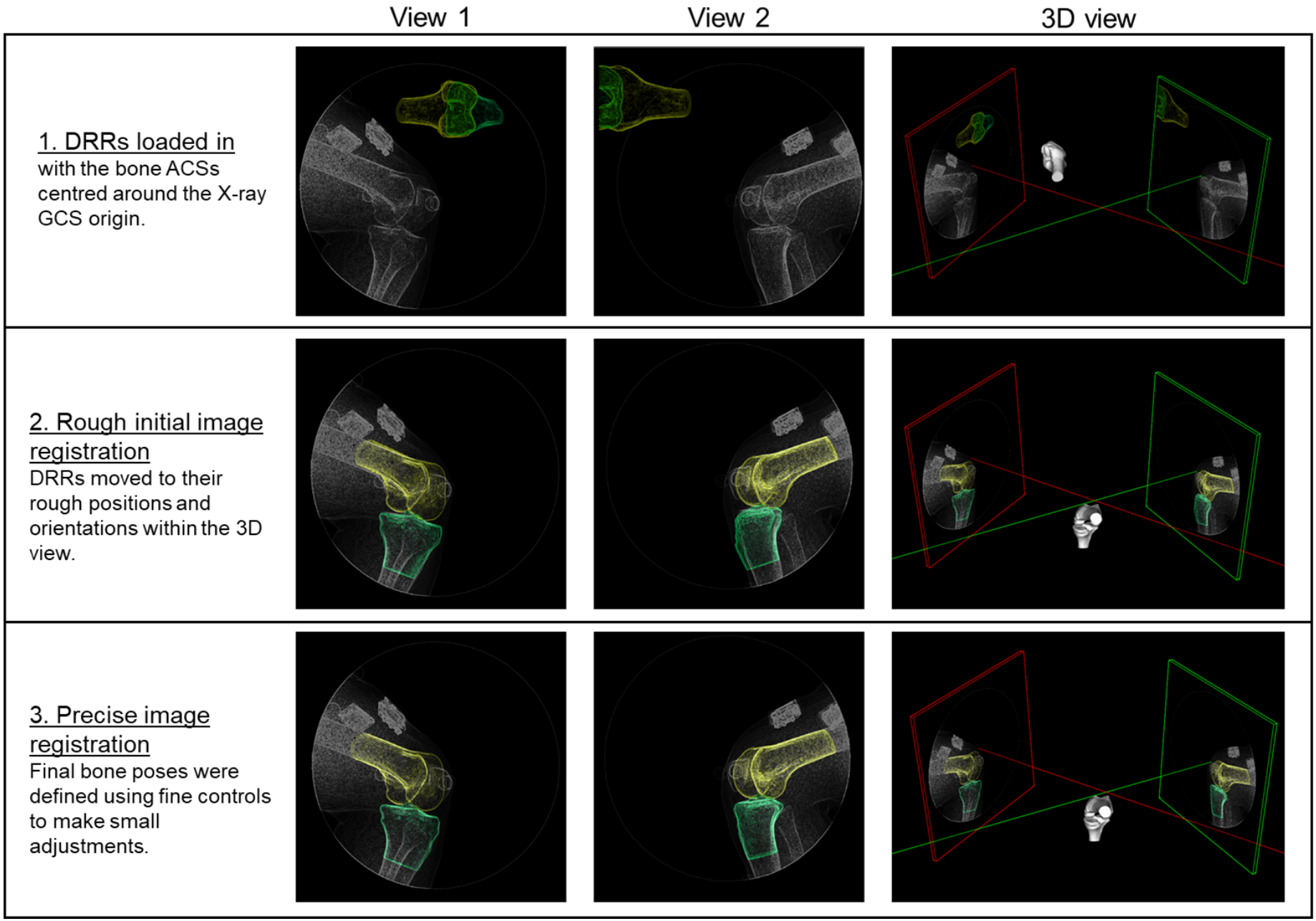

Figure 2-24 – Image registration process for the first frame of a new trial. A single frame from a lunge is given here as an example.

To make image registration of the DRR easier, a Sobel edge detection algorithm (built into the DSX Suite) was applied to both the X-ray images and the projected DRR to enhance the edges of the bones (HAS-Motion 2024c) (Figure 2-25). The 3D bone pose was then added to the pose map defining the XYZ translations and XYZ Euler angles from the X-ray GCS to the bone's ACS. This was repeated for every frame where both the femur and tibia were visible in the trial.

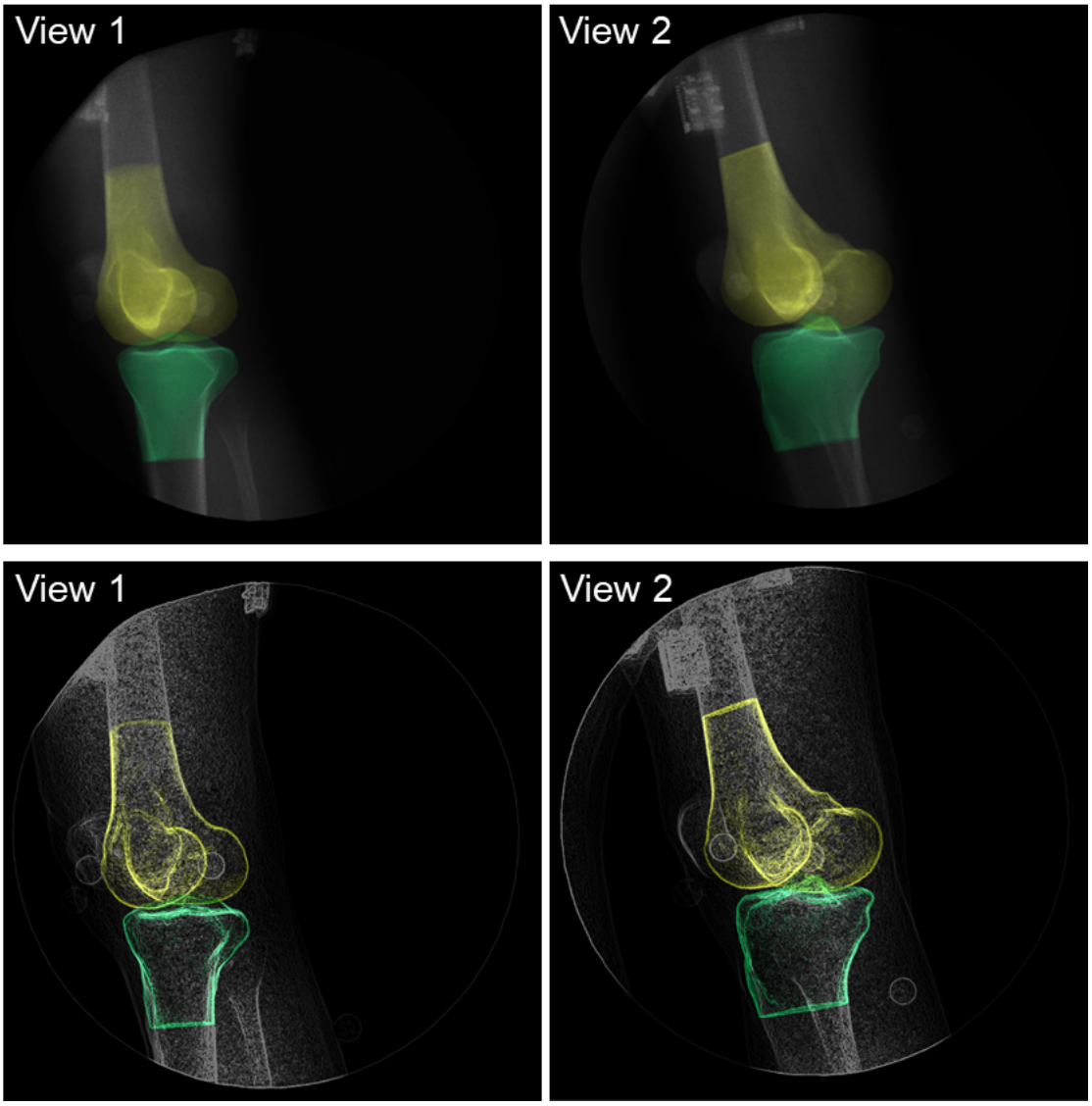

Figure 2-25 – X-ray images with (below) and without (above) the Sobel edge detection algorithm applied.

For each trial, initially bone poses were generated at approximately every five frames through the motion by manually adjusting the bone's position and orientation. Then, using spline generated poses as an initial starting point for manual matching, the remaining frames were added to the pose map. When all poses were recorded, each DOF was adjusted using the graph widget to smooth the unrealistic changes in DOFs values between frames.

For the activities where both knees passed through the imaging volume, the contralateral limb occluded part, or all, of the target limb during some stages of the activity. When this occurred, the bone outlines became obscured, and the edge detection algorithm made the image noisier (Figure 2-26). This made image registration more difficult during those frames. To minimise these effects, the frames either side of the occlusion were manually matched, and the resulting splines were used to help inform the poses for the remaining frames affected by occlusion.

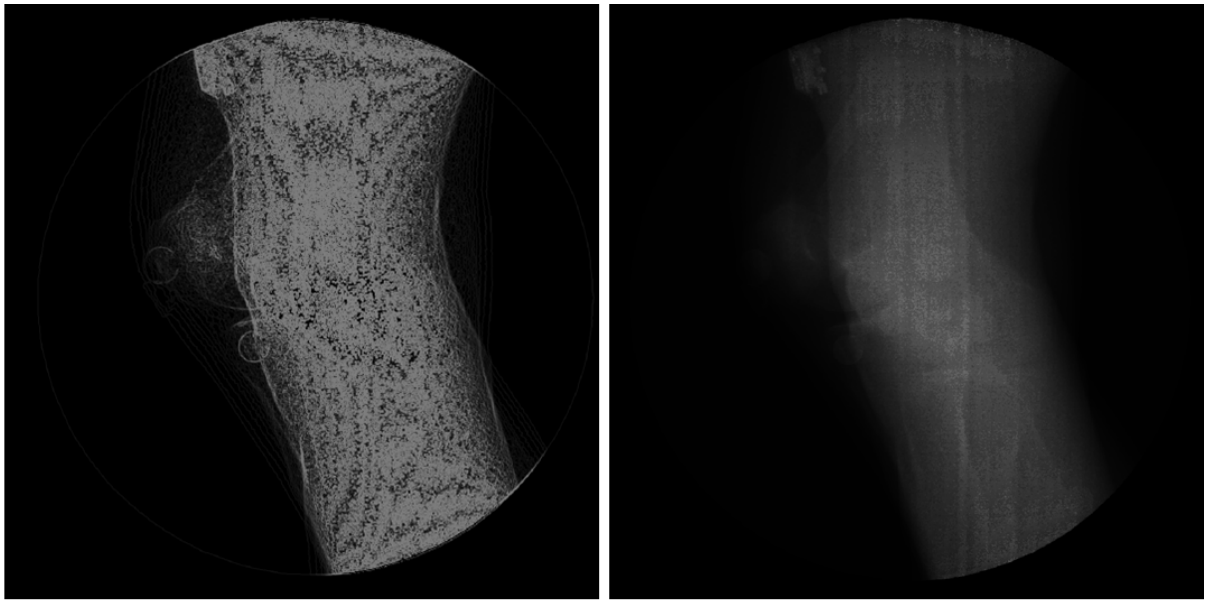

Edge detection algorithm applied when the contralateral limb is obscuring the imaged knee

Same image but with no filter applied.

Figure 2-26 – Extreme example of occlusion by the contralateral limb.

The final matched bone poses were visualised as a continuous motion using FEBio's 'Kinemat' tool (Maas et al. 2012) to see if the movements produced looked physiologically reasonable. This was particularly valuable during sections of motion where the contralateral limb obscured the bone being matched in one or both X-ray views, as this was where it was hardest to perform image registration.

2.4.6 TRIAL SELECTION CRITERIA

Due to the substantial amount of time required to complete image registration for a single trial, only one trial per activity was processed for each participant. To qualitatively assess the X-ray trials to pick the "best" trial repeat for image registration, the following set of criteria were defined:

- Discount any trials where the activity was not performed correctly (e.g. the participant did not follow the instructions correctly/there was no clean hit of the 'X-ray' force plate).
- Discount trials where the X-ray images didn't fully capture the participant moving through the volume.
- Select the trial with the greatest number of "trackable frames" (frames where a substantial proportion of the outline of all bones to be tracked are clearly visible). The number of trackable frames can be calculated by total frames of movement (count from first trackable frame to the last trackable frame) minus the number of frames with contralateral limb obscuring one/both bones, or the bones going out of shot (e.g. at peak lunge).
- If two or more trials for a particular activity have a similar number of "trackable frames" consider which has the better additional data (motion capture/EMG/etc.) and if image registration has already been started on any of them.

All X-ray trials were examined using the above criteria, and one trial was selected for each activity resulting in a set of three processed X-ray trials for each participant.

2.4.7 CALCULATING BIPLANE VIDEORADIOGRAPHY TIBIOFEMORAL KINEMATICS

Once image registration was completed for each trial, the bone pose at each frame of motion was converted into a 4x4 transformation matrix within the software (X4D, DSX Suite, C-Motion). A text file was exported for each bone per trial, where a line of text contained the transformation matrix between the X-ray laboratory GCS and the bone's ACS at each frame.

Custom MATLAB code was written to calculate the 6 DOF kinematics of the TF joint of the tibia relative to the femur at each frame (Grood and Suntay 1983). This code was also used to filter the resulting kinematics. An adaptive low-pass Butterworth filter (cut-off frequency range 5-10 Hz) was applied (Erer 2007).

6 DOF kinematics were also calculated after redefining the tibial ACS to be aligned the femoral ACS in the MRI scan position. This normalised differences in bone origin locations between participants, particularly seen in the translations.

The largest offsets were seen in CD as this was the most affected by knee size (due to the SI offset in the ACSs). By accounting for these offsets, compression was standardised, enabling direct comparison across participants. This approached was also commonly used to define joint distraction in literature (Gray et al. 2019; Thomeer et al. 2020; Thomeer et al. 2021).

2.4.8 MARKER-BASED MOTION CAPTURE KINEMATICS

An overview of marker-based motion capture data processing is shown in Figure 2-27 and explained in more detail below.

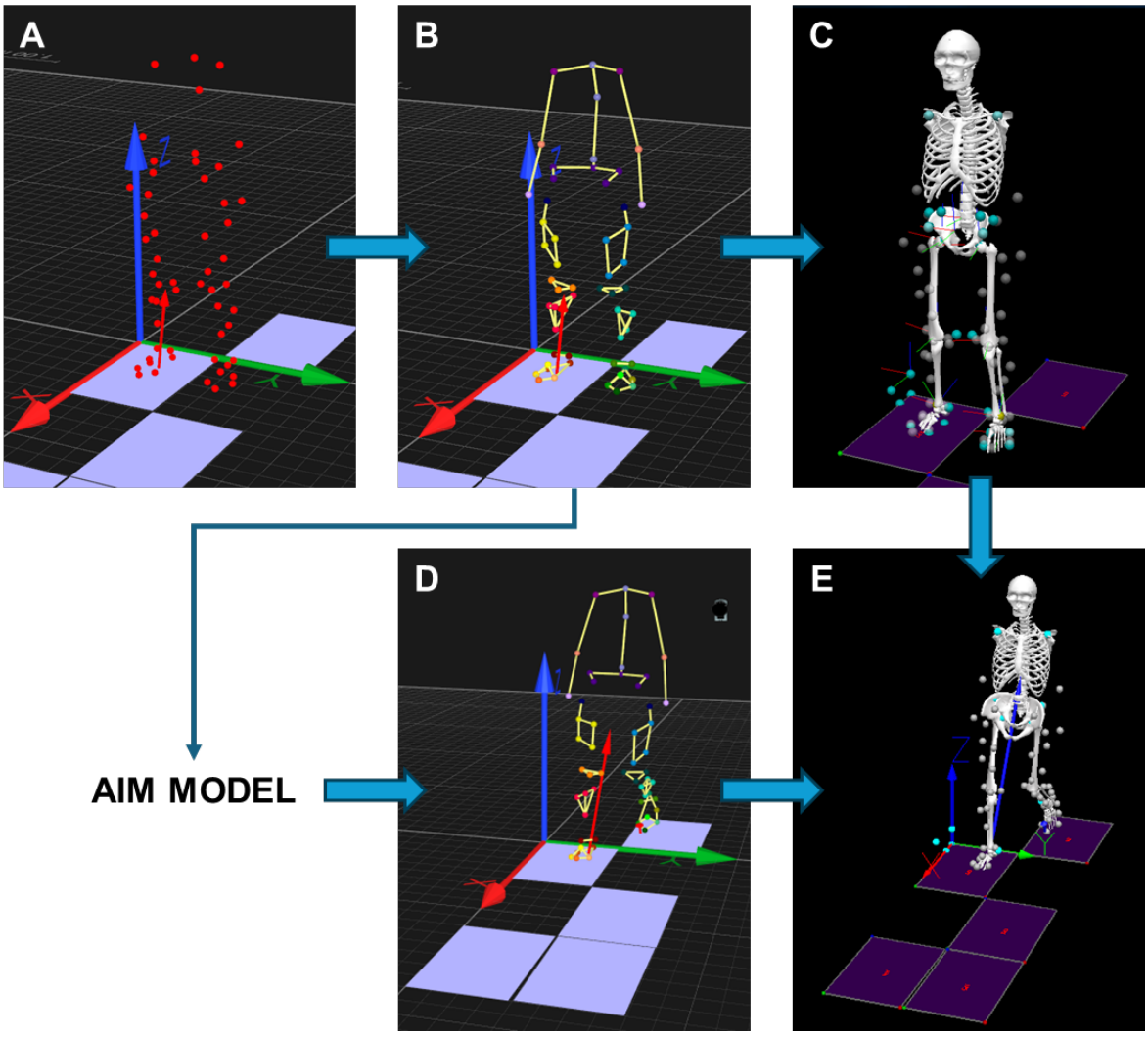

*Figure 2-27 – **A)** Static trial marker data captured in QTM (Qualysis, Sweden) **B)** Marker trajectories manually identified and labelled. One static and one dynamic trial were manually labelled to generate the Automatic Identification of Markers (AIM) model. **C)** A model was created in Visual3D (V3D, HAS-Motion, Canada) by scaling virtual body segments using the static trial marker positions. **D)** The AIM model was applied to all remaining trials, including dynamic motions. **E)** Joint kinematics and kinetics data was calculated by applying the V3D model to the dynamic trials. Gait event markers, such as heel-strike (HS) and toe-off (TO) were also calculated during this step.*

Marker trajectory identification was performed using QTM (Qualisys, Sweden). Trajectories were labelled manually for the first static and dynamic trial; these two trials were then used to generate an Automatic Identification of Markers (AIM) model which was applied to subsequent dynamic and static trials.

As discussed in Section 2.2.1, the arms of the BVR equipment occasionally obscured the marker trajectories during dynamic trials. Marker trajectories gaps of fewer than 15 frames were filled using a polynomial algorithm, while larger gaps – or those at the start or end of a movement – were reconstructed using a relational fill, which used three tracked marker trajectories to estimate the position of a fourth.

When tracking the marker trajectories from the first participant's data collection session, a lot of marker dropout was discovered. This increased the processing time, as more manual intervention was required to piece together short trajectory segments and perform additional gap-filling. To improve data quality and reduce these issues in subsequent sessions, camera positions were optimised (Figure 2-28) (Section 2.3.2). The full location map of the final camera positions, including the camera heights and location of the X-ray equipment relative to the GCS can be found in the data collection protocol in Appendix B.

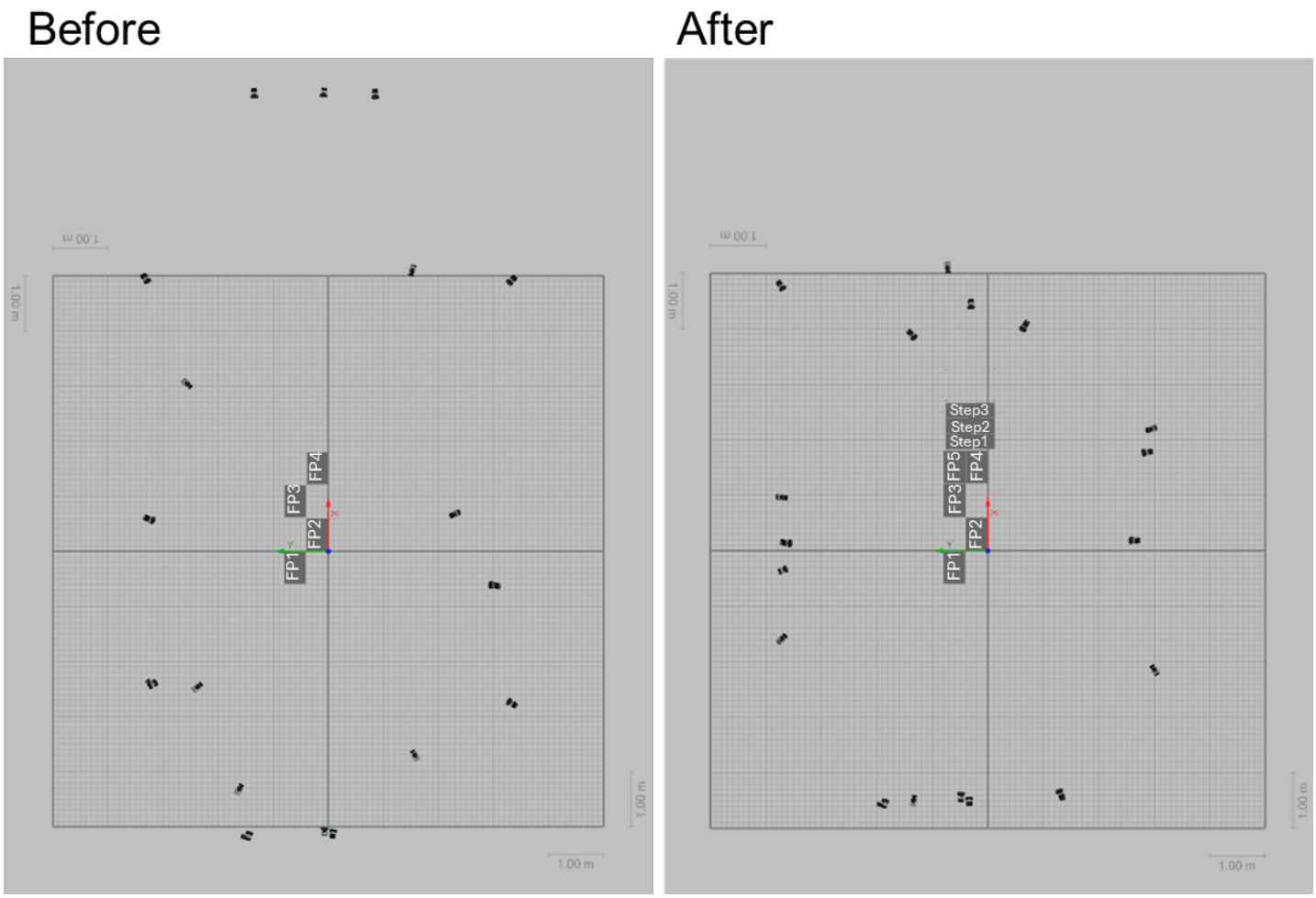

Figure 2-28 – Camera positions before (left) and after (right) optimising their positions in the room. 'FP' indicates a force plate. The final laboratory setup (right) shows the additional force plate added, as well as the position of the instrumented stairs within the room.

Once the camera positions had been optimised, there was little-to-no marker dropout for the gait and lunge activities. However, the stair ascent activity still had some marker dropout in all trials (particularly the foot and ankle markers) due to the participant having to position their foot close to the X-ray detector and the higher stairs blocking the lower ones.

Complete marker trajectories were exported as C3D files and imported into Visual3D (HAS-Motion, Canada). A previously defined Visual3D pipeline was used to calculate the TF joint rotations throughout each trial (Bowd 2022). During this pipeline, virtual segments were created, and a generic model scaled using the relative marker positions and the participant's body weight.

The CODA pelvis (Codamotion Ltd., United Kingdom) was chosen as it was equivalent to the MSM pelvis ACS definition in the MSM used in a later chapter (Chapter 3) (Arnold et al. 2010; Lenhart et al. 2015). The pelvis coordinate system was defined using the anterior superior iliac spine (ASIS) and sacral markers, with the origin at the midpoint of the two ASIS markers (HAS-Motion 2024b) (Figure 2-29).

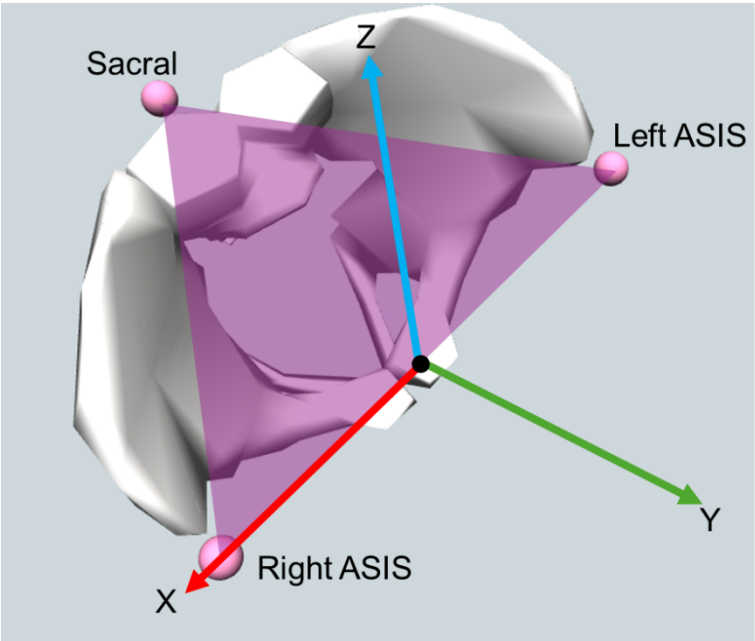

Figure 2-29 – CODA pelvis axes definition.
Figure adapted from HAS-Motion (2024b).

Time-stamped event markers were used to define the start and end of the stance phase, or the weightbearing portion of the lunge, defined as the foot making contact with or leaving the force plate, using a 20 N threshold (Bowd 2022). The pipeline was adapted to export these event markers, as well as the calculated TF rotations.

2.4.9 RESEARCH QUESTIONS

With the methodology fully defined, fulfilling the overall objective set out at the start of the Chapter (Section 2.1.2), a series of research questions was developed to evaluate the robustness of the pipeline. These questions were chosen to demonstrate how the data collection and processing methods achieve the research aims (Section 2.1.2), and their rationale is outlined below.

Q1: How well do the different BVR X-ray and motion capture equipment configurations capture their respective activities?

As this was a pilot study, this was the first protocol developed to capture in-vivo

kinematics for this specific BVR equipment. Therefore, it is important to assess how effectively the proposed X-ray equipment configurations were able to image the knee during all three pilot activities to inform future studies. Capturing full knee motion with BVR is challenging due to the joint's large range of motion relative to the small imaging volume, therefore only a specific portion of the activity, such as stance phase, can typically be targeted. Understanding which sections of the activities were captured successfully in this pilot cohort will provide future protocol refinements to improve consistency, as well as a more comprehensive understanding of the potential limitations of these specific configurations.

Q2: Are the six DOF TF kinematic trends and magnitudes for this cohort consistent with results presented in literature?

This question addresses the validity of the pipeline by comparing the calculated TF kinematics to published values. Demonstrating consistency with established trends and magnitudes from other studies will confirm if the methodology is suitable for the proposed application. As this is a novel dataset acquired with a newly developed protocol, benchmarking against the literature also helps identify any unexpected differences and builds confidence in the reliability and physiological relevance of the outputs.

Q3: How does changing the ACS representations alter the kinematic outputs?

TF kinematics in literature are often presented using different bone ACS definitions, which can substantially affect the resulting kinematic outputs (Section 1.3.3). The most widely used method for defining TF kinematics is using the Joint Coordinate System (JCS) set out by Grood and Suntay (1983) recommended by the ISB for defining femoral and tibial ACSs (Wu et al. 2002). The JCS uses separate ACSs for the femur and tibia based off bone morphology and defines the rotations and translations around each respective axes to conform to clinically relevant definitions, allowing for meaningful application of the output kinematics.

These separate ACS definitions were applied using the automated algorithm by Miranda et al. (2010) (Section 2.4.3) to compare with BVR results in literature as this was the most common way TF kinematics were presented (Kozanek et al. 2009; Gray et al. 2019; Gale and Anderst 2020; Thomeer et al. 2021; Thomeer et al. 2022).

Using two separate bone ACS definitions and the JCS provides clinically relevant kinematics. However, this may not be suitable in all contexts. For example, CD of the knee can be influenced by knee size – larger bones increase the distance between the femoral and tibial ACSs, which introduces an offset in the CD values. This makes it harder to compare overall compression patterns across a cohort as the results will be offset due to knee size variation.

To address this, some studies modify ACS definitions. For example, Gray et al. (2019) adjusted the tibial origin to align with the femoral origin in an unloaded extended pose, setting CD to start from zero. Similarly, rigid body modelling approaches (e.g. Visual3D, OpenSim) often use coincident ACSs in the neutral pose for simplicity and consistency across participants.

In this study, both approaches were used: one with separate ACSs, as per the JCS, for comparison with literature, and another with coincident ACSs to reflect the definitions used in the V3D model (Section 2.4.8) as well as the OpenSim Model used in the MSM pipeline in the following Chapter. Comparing these outputs helps highlight how ACS definitions influence interpretation and comparability of TF kinematic results.

Q4: Do the secondary TF kinematics (all DOFs except flexion) couple with flexion?

Understanding potential coupling between knee flexion and the secondary TF DOFs is important for correctly modelling the relationship between anatomy and function of the TF joint (Koo and Koo 2019; Thomeer et al. 2021). Such coupling of the secondary DOFs to flexion in the knee has previously been reported in literature (Kozanek et al. 2009; Gray et al. 2019; Koo and Koo 2019; Thomeer et al. 2021). Identifying these coupled motions is also relevant for a range of biomechanical applications, from computational modelling to TKR design (Thomeer et al. 2021).

It has been suggested that if all five secondary TF DOFs are found to be coupled with flexion, the relative bone movements are guided primarily by ligament geometry and articular contact (Thomeer et al. 2021). This assumption has led to coupling being incorporated into the design of MSMs by setting the secondary DOFs as functions of knee flexion to provide better estimates of six DOF TF motion than can be calculated using motion capture (Smith 2017; Hume et al. 2018). This is true of

the MSM used to calculate knee joint contact in a later chapter of this thesis (Chapter 3), therefore, it is important to investigate these relationships within this cohort to understand potential errors in the model's assumptions.

Q5: How accurately does marker-based motion capture calculate TF rotations compared to the gold-standard in-vivo BVR results?

Finally, comparing simultaneous motion capture and BVR knee kinematics enables the quantification of motion-capture errors on a subject-specific basis. This can help demonstrate the strengths and weaknesses of the technique in calculating kinematics, as well as highlighting potential areas for improvement. Despite the accuracy of motion capture being previously well documented (Sati et al. 1996; Reinschmidt et al. 1997a; Stagni et al. 2005; Akbarshahi et al. 2010; Tranberg et al. 2011; Tsai et al. 2011; Miranda et al. 2013; Hume et al. 2018), it was included in this study to serve as a baseline comparison for the dataset used in Chapter 3, where an algorithm aimed to optimise and improve the secondary kinematic predictions within a MSM pipeline.

2.4.10 STATISTICAL ANALYSES

The following analyses were performed to help answer the research questions set out above (Section 2.4.9).

The mean and standard deviation (std) of the results of the five participants were calculated for each activity for all frames where data were available for all five participants. This provided a mean overall kinematic profile for each DOF, as well as showing the variation across the cohort.

To investigate coupling between flexion and the other DOFs (research question 4, Section 2.4.9), Pearson's coefficient (r) was calculated for the relationship between flexion and each DOF in turn, then squared to calculate the coefficient of determination (r^2) – which can range between 0 (no correlation) and 1 (perfect coupling). The r^2 threshold values in Table 2-5 were used to define the levels of correlation between each DOF and flexion. These values were chosen due to their use in literature (Moore et al. 2015; Thomeer et al. 2021).

Table 2-5 – r^2 thresholds for defining correlation with flexion

Threshold	**Correlation of the DOF with flexion**
$r^2 \geq 0.7$	Coupled
$0.5 \leq r^2 < 0.7$	Moderately correlated
$r^2 < 0.5$	Weakly correlated

To investigate research question 5 (Section 2.4.9), the rotation angles output from the marker-based motion capture data using the V3D pipeline (Section 2.4.8) were compared with the gold-standard rotations from the simultaneous BVR data (Section 2.4.7) using a Bland-Altman analysis (Altman and Bland 1983). This plotted the difference between the rotations (V3D value minus BVR value) at each frame against the 'ground truth' BVR-calculated rotation for that same frame (Figure 2-30). It was chosen to plot against BVR on the x-axis as the BVR was the gold-standard for comparison in this instance. This allowed the distributions of the differences in V3D-calculated rotations to be visualised, including underestimation and overestimation. The median and limits of agreement – ±1.45 times the interquartile range (IQR) – were calculated as part of the Bland-Altman analysis. The differences for all participants were collated and also plotted as violin plots to help visualise the range of differences (Figure 2-30).

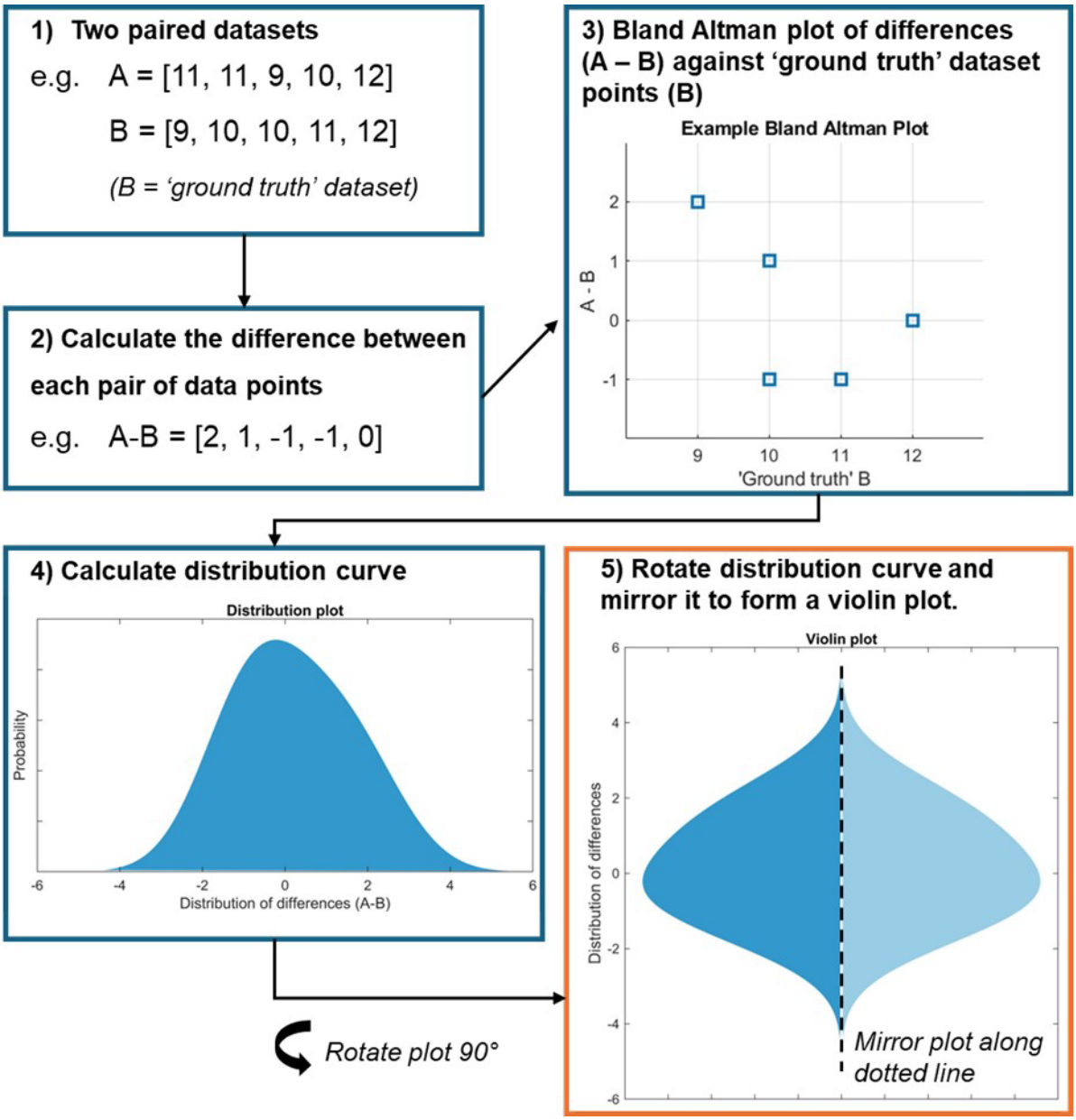

Figure 2-30 – How the Bland Altman and Violin distribution plots are generated.

2.4.11 VISUALISING MOTION CAPTURE MARKERS IN THE BVR COORDINATE SPACE

To help answer research question 5 (from Section 2.4.9) and explore the relationship between BVR and motion-capture kinematics, it was useful to visualise the motion capture marker positions relative to the underlying bone poses defined from image registration. As errors in anatomical landmark placement can propagate to the bone ACS definitions, resulting in constant errors in the subsequent kinematics (Della

Croce et al. 1999), visual inspection of marker positioning provided insight into how these placement errors may have influenced the kinematic outputs in this study.

The marker locations were visualised along with the BVR bone positions (Figure 2-31) in the same coordinate space (Section 2.4.3) within the DSX suite (HAS-Motion, Canada). This was initially done for a static trial to visualise the positions of the condyle markers relative to the underlying femur position, as these marker positions were used for scaling of the model in relation to the ACS of the knee bone segments. The marker positions were then also visualised during dynamic trials to investigate their relative locations throughout dynamic movement.

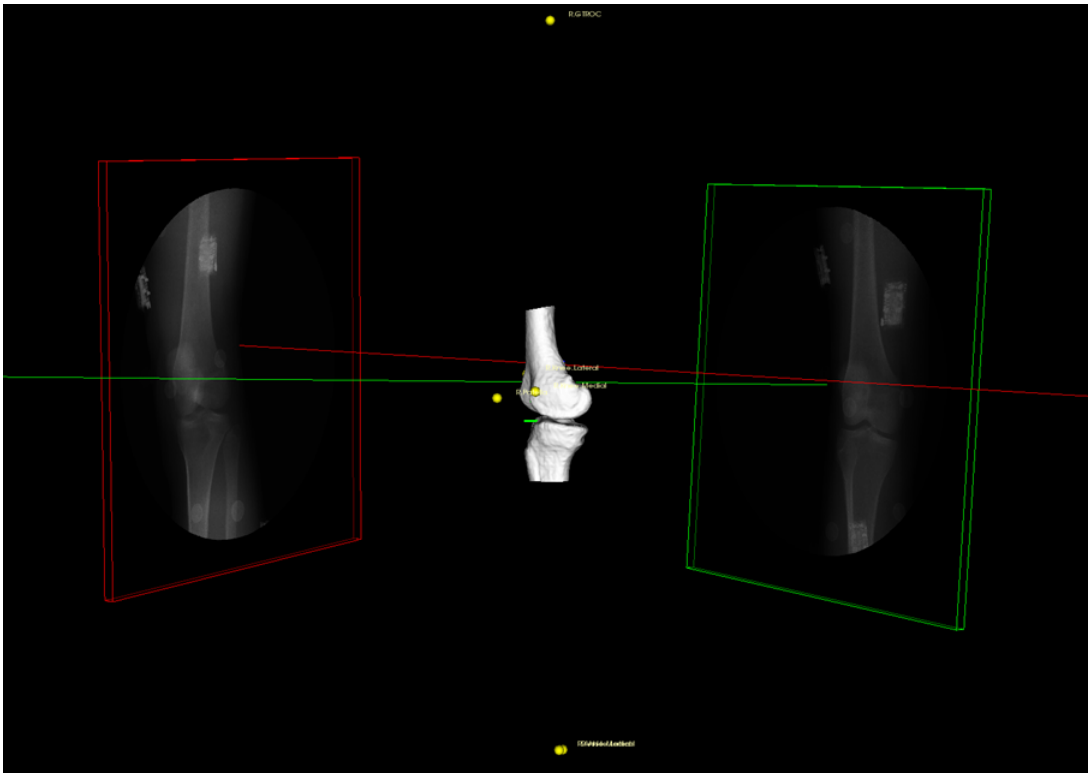

Figure 2-31 – Marker locations (yellow dots) visualised relative to the BVR bone positions in DSX (HAS-Motion, Canada).

2.5 RESULTS AND DISCUSSION

The results from five healthy volunteers (3 male/2 female, mean age 47.8 years, mean BMI 23 kg/m^2) were used to demonstrate the pipeline. For each participant, one repeat of each activity was processed (chosen using the criteria in Section 2.4.6).

2.5.1 RESEARCH QUESTION 1: HOW WELL DO THE DIFFERENT BVR X-RAY AND MOTION CAPTURE EQUIPMENT CONFIGURATIONS CAPTURE THEIR RESPECTIVE ACTIVITIES?

Due to a small X-ray capture volume compared to the amount of knee motion during typical dynamic activities, it is difficult to capture the entirety of a movement using BVR. Hence why portions of a motion are typically targeted (e.g. stance phase of gait) using unique setups to optimise capture of each specific activity. For this reason it is important to investigate the performance of individual equipment configurations and activity combinations (Research Question 1 - Section 2.4.9), as capture quality will differ due to the path of the knee through the X-ray capture volume, influenced by individual variation in movement.

The percentage coverage of the targeted portion of each pilot activity was investigated to demonstrate the effectiveness of the X-ray configurations for capturing their respective activities. For gait and stair ascent, this was % stance phase, and for lunge it was % lunge (with 0-100% representing HS-TO). The percentage where image registration was possible for each of the five participants was calculated, along with the mean percentage coverage of the cohort and the percentage coverage where data was available for all five participants (Table 2-6).

Table 2-6 – Percentage of total stance phase (or lunge) captured by BVR for each participant and the mean of the five participants for each activity. (Frames captured outside of stance phase - HS to TO - ignored in these calculations)

	Gait (%)	Stair ascent (%)	Lunge (%)
HV001	62	92	87
HV002	42	100	82
HV003	55	62	63
HV004	59	100	80
HV005	53	88	78
Mean	**54**	**88**	**78**
% coverage of frames with data for all five participants	**23**	**49**	**62**

Table 2-6 shows variation in percentage coverage across the activities with level gait presenting the lowest mean coverage of all three activities (mean = 54%), as well as the lowest absolute percentage stance captured (42%). This low percentage coverage was due to the higher amount of horizontal movement through the imaging volume compared to the other activities. The part of stance phase captured during level gait was also not consistent across the different participants (as seen in Figure 2-33 in Section 2.5.2) resulting only 23% of the total stance phase where data were available for all five participants simultaneously (occurring at approximately 40-60% stance). This was due to variations in foot placement on the force plate below the X-ray equipment, affecting the path of the knee through the X-ray volume changing which portion of stance was captured, highlighting the difficulty in repeatability when using BVR to capture level gait in this configuration.

Aiming to reduce this error and increase the consistency of percentage stance captured, later participants were unblinded to the desired foot placement location (Section 2.3.6). Although this is not ideal as it may alter natural walking, the kinematic results from HV003, HV004 and HV005 cover a more consistent region of stance phase (Figure 2-33) suggesting that this unblinding had the desired effect of creating greater consistency of data collected between participants.

Another limitation of the level gait setup was occlusion, with the contralateral limb at least partially obstructing the imaged knee in one X-ray view in about half of all collected frames. However, the BVR system configuration was optimised to prevent complete occlusion in both views at once, ensuring at least one clear image for registration throughout (Figure 2-32). Despite this, the occlusion likely reduced image registration accuracy, as both views are needed for precise 3D bone positioning.

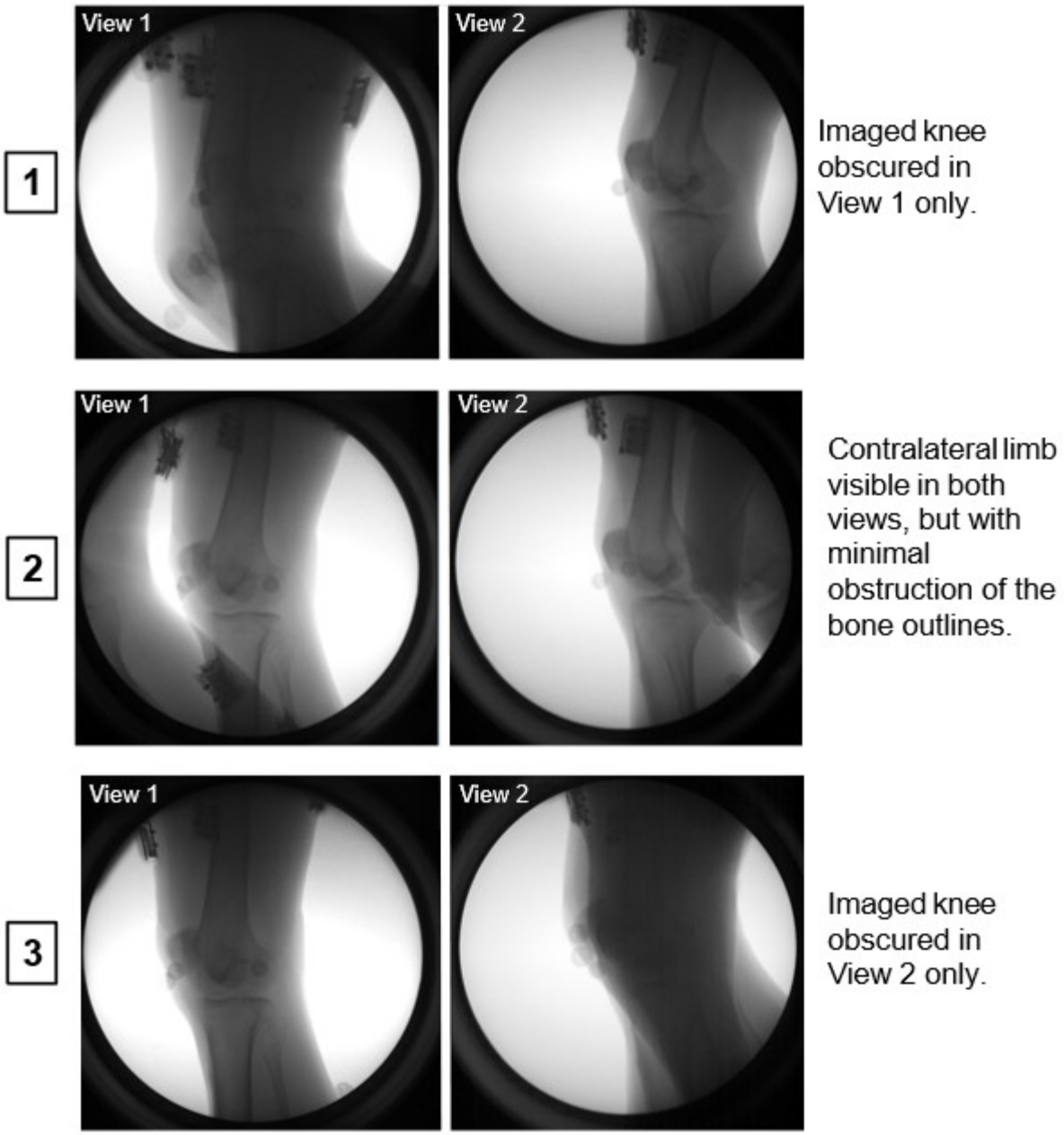

Figure 2-32 – Three phases of occlusion of the image knee by the contralateral limb during the stance phase of gait. All images have a level 3 high dynamic range filter applied for image clarity.

Like level gait, the stair ascent activity also suffered from occlusion of the contralateral limb. A similar pattern of occlusion occurred, with the target limb being obscured in one X-ray view, then in the other X-ray view (Figure 2-32), again aiming for minimal frames where the target knee was occluded in both images at once.

Again, like level gait data capture, the entirety of the stance phase was not captured for all five participants during stair ascent. However, there was a larger proportion where data were available for all participants (49% compared to 23% for level gait, Table 2-6) and a larger percentage of stance phase was covered by each of the

participants individually (mean coverage = 88%). During stair ascent, the knee initially moved horizontally (similar to gait), but in the second half of stance phase, the knee shifted back towards the centre of the imaging volume as the participant's centre of mass moved vertically. This vertical motion, combined with the shorter horizontal step distance on the staircase, resulted in a reduced stride length compared to level gait. As a result, the knee remained within the X-ray capture volume for longer, enabling a greater proportion of the stance phase to be recorded.

Stair ascent was the only activity to capture the full stance phase for any participant (HV002 & HV004). This shows potential to capture a consistent portion of this activity across more participants, if repeated in the future.

Although stair ascent had the highest mean percentage coverage of stance phase, it did not have the highest coverage of where data were available for all participants. This was due to one participant having data captured prior to stance phase but missing the last ~40% (HV003), and another participant not having the first ~10% of stance phase captured. This left an overlapping region of 50% of stance phase collected for all participants.

The lunge activity had the largest overlap where data were available for all participants (62%, Table 2-6). The participant practiced their lunge to align the anterior edge of the knee during peak lunge with the extent of the X-ray volume. Therefore, once the knee came into the volume, it remained in the volume throughout the lunge until the person began to stand up again, resulting in a consistent central portion of the activity captured across the cohort. This also meant that this activity did not suffer from any occlusion as the contralateral limb was not moved during the lunge.

The mean percentage covered by all participants for lunge (78%) was lower than stair ascent (88%) because the beginning and end of the lunge was cutoff when the knee left the X-ray field of view. However, as this activity was intended to look at larger knee flexion angles, missing the beginning and end of the activity at the lower flexion angles does not affect the intended purpose of the chosen movement.

Understanding how much of the activity is captured, and which portions are captured, with a given setup is important for targeting specific phases of motion. For example, to ensure consistent capture of HS during level gait, the position of the

BVR equipment relative to the foot position could be adjusted so the frames captured are centred around HS instead of mid-stance as they are currently.

Overall, the effectiveness of the BVR equipment setup to capture dynamic motion varied depending on the activity, with level gait being captured poorly but stair ascent and lunge having a larger proportion of the activity covered.

2.5.2 RESEARCH QUESTION 2A: ARE THE **LEVEL GAIT** SIX DOF TF KINEMATIC TRENDS AND MAGNITUDES FOR THIS COHORT CONSISTENT WITH RESULTS PRESENTED IN LITERATURE?

The six DOF kinematics of the TF joint during stance phase of level gait for the five healthy volunteers are shown in Figure 2-33. For each DOF, the mean and ±1 standard deviation (std) were plotted for all points where data was available for all participants.

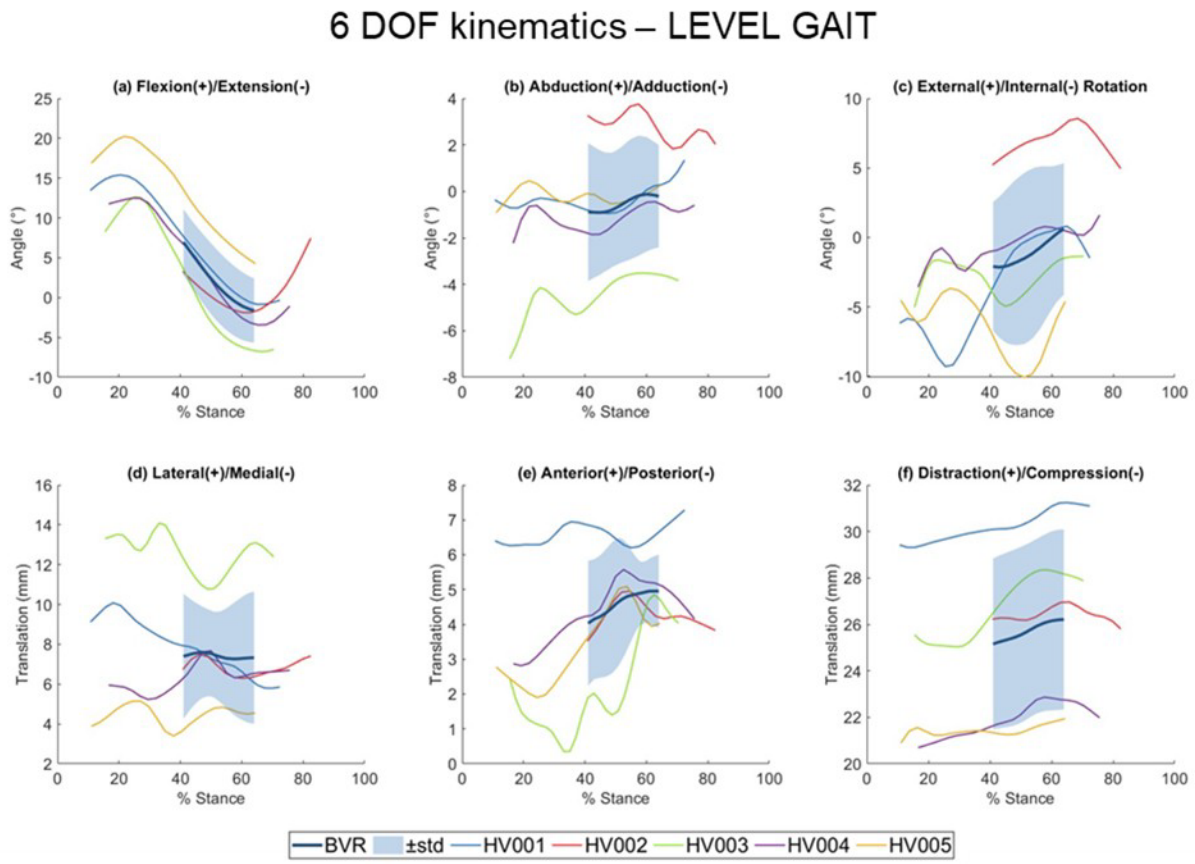

Figure 2-33 – Six DOF kinematics of the TF joint calculated for five participants during level gait. Mean and ±1 std calculated for all frames where data were available for all participants.

The TF joint was found to have a peak of flexion at ~20% stance, before extending through to ~60% stance where the knee began to flex again (Figure 2-33a). Flexion values ranged from a maximum ~20° to ~-6° (extension). These results were consistent with the general patterns reported in literature (Section 1.5.1) where a flexion peak of ~15° occurs during early stance, followed by knee extension towards neutral (0° flexion), as reported in other studies using BVR to obtain TF kinematics. (Kozanek et al. 2009; Gray et al. 2019; Gale and Anderst 2020; Thomeer et al. 2020; Thomeer et al. 2021). Similar variation of some participants' knees remaining flexed throughout stance phase, whereas other individuals displayed some joint extension

towards the end of stance, was also found in studies with larger cohorts (Gale and Anderst 2020), suggesting this is representative of natural population variation.

AA (Figure 2-33b) was found to have the smallest rotational ROM out of the three planes; for example, the peak-to-peak ROM (mean ± std) for the cohort during 40-60% stance was 1.1 ± 0.4° for AA, compared to 8.4 ± 1.9° for FE and 3.3 ± 1.2° for IE. This is consistent with literature reporting mid-stance AA ROM of approximately 1-2 ± 2° (Kozanek et al. 2009; Myers et al. 2012; Kefala et al. 2017; Gale and Anderst 2020; Hamilton et al. 2023). Adduction was described as having a non-descript profile throughout stance phase (Kozanek et al. 2009; Gray et al. 2019; Gale and Anderst 2020; Thomeer et al. 2020; Thomeer et al. 2021) which was also seen in this cohort. On average, the knee was found to be slightly adducted throughout stance, however one participant displayed greater adduction throughout (HV003) and one participant (HV002) displayed abduction throughout.

The tibia was generally found to be internally rotated relative to the femur in most of the participants, but one participant (HV002) displayed external rotation instead (Figure 2-33c). This variation was also seen by Gale and Anderst (2020) who reported individual differences ranging from only internal rotation throughout stance to only external rotation. This DOF displayed the second largest rotational ROM, after flexion. Cohort mean internal rotation during 40–60% stance was 0–2°, similar to the ranges reported in the literature which generally found the knee to be internally rotated on average (~0–5°) during stance (Kozanek et al. 2009; Kefala et al. 2017; Thomeer et al. 2021), or found the mean IE rotation to fluctuate around 0° for the majority of stance (Gray et al. 2019; Thomeer et al. 2020). However, one study found the mean of their cohort to be externally rotated (by ~1-5°) for the majority of stance phase, with mean internal rotation (by ~2°) only occurring at terminal stance (Gale and Anderst 2020).

Figure 2-33e shows that the tibia was found to be translated anteriorly relative to the femur throughout stance phase of gait, with the mean translation around 4-5 mm during 40-60% stance. This was within the mean anterior translation range presented in literature of ~1-7 mm during mid-stance (Kozanek et al. 2009; Gray et al. 2019; Gale and Anderst 2020; Thomeer et al. 2020; Thomeer et al. 2021). The overall trend of this cohort was a slightly increasing anterior translation through

stance phase. Other BVR studies also found anterior translation during stance phase, but found the opposite trend of a slight decrease in anterior translation instead of a slight increase (Gray et al. 2019; Gale and Anderst 2020; Thomeer et al. 2020; Thomeer et al. 2021). Although the overall trends found were different, as the magnitudes of AP translation ROM found were small (~5 mm), the impact of these differences on overall knee motion is likely minimal. Further investigation with a larger cohort would be needed to see if this difference in trend is seen consistently with this methodology.

The tibia was found to be laterally translated during stance phase for all participants (Figure 2-33d). The absolute value of lateral translation during stance phase was large compared with the relative changes seen.

CD was seen to have only a small ROM in each participant, but with variation in the absolute values seen between participants (Figure 2-33f).

The six DOF TF kinematics were also compared as changes from the relative bone position from the MRI by making the femoral and tibial ACSs coincident (Section 2.4.10) as this was how some BVR studies have presented their results (Gray et al. 2019; Thomeer et al. 2020; Thomeer et al. 2021). The coincident ACS kinematics were also plotted against % stance phase (Figure 2-34). Further discussion of how the kinematics differ when calculated using separate and coincident ACS definitions can be found in Section 2.5.5.

When comparing the results from the coincident axes, the magnitude of lateral translation seen, -1 mm to 2.5 mm (Figure 2-34j), is consistent with the range of -1 mm to 3 mm found in other studies during the stance phase of gait (Gray et al. 2019; Thomeer et al. 2020; Thomeer et al. 2021).

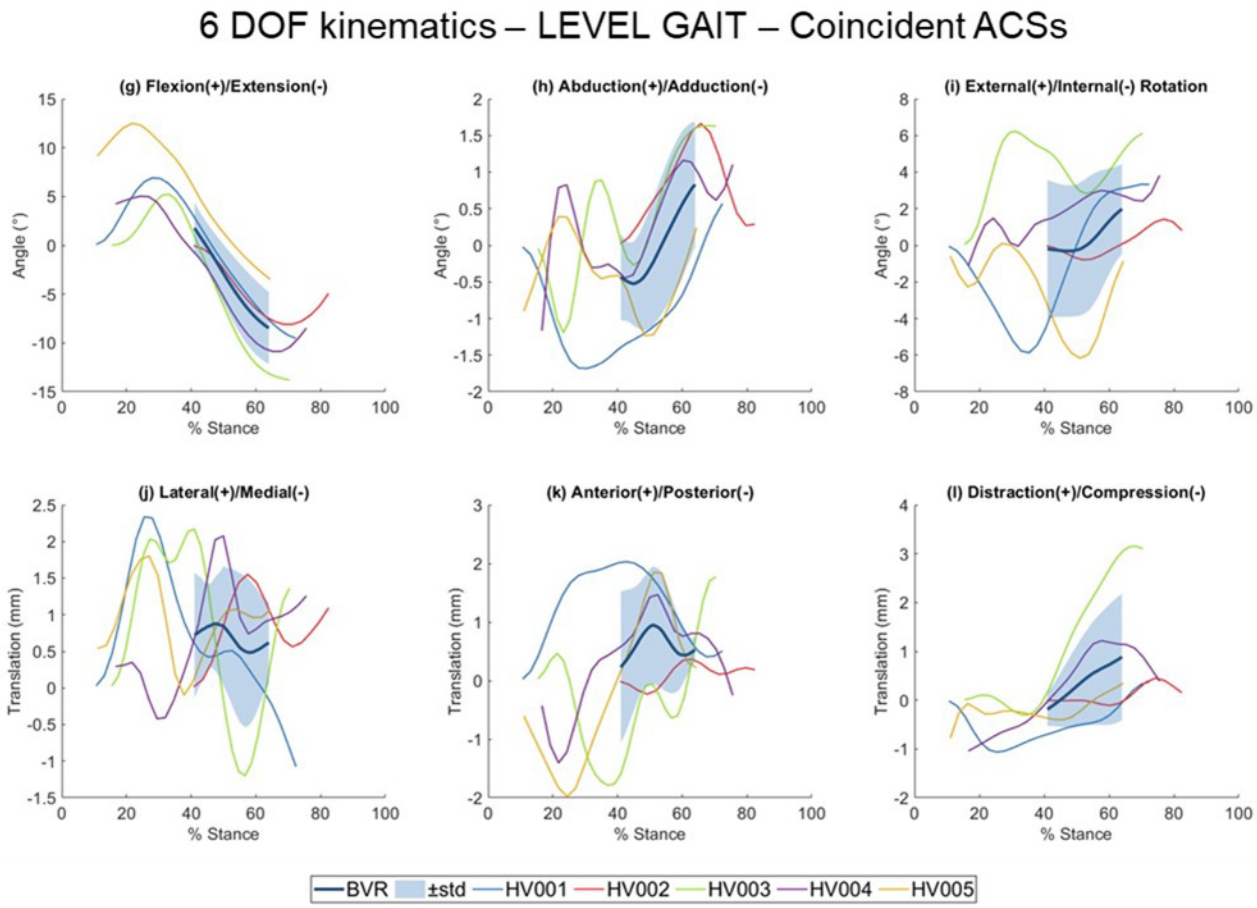

Figure 2-34 – Six DOF TF kinematics calculated using coincident ACSs for the femur and tibia.

For CD there was a slight trend of compression, transitioning to slight joint distraction throughout the stance phase (Figure 2-34l). This was not seen in literature where mean compression of ~1-2 mm was found throughout the whole of stance phase (Gray et al. 2019; Thomeer et al. 2020; Thomeer et al. 2021). When defined from coincident axes, CD translation was found to have the smallest peak-to-peak translational ROM of 1.1 ± 0.6 mm (mean ± std), compared to 1.5 ± 0.5 mm for ML and 1.6 ± 0.7 mm for AP, which was consistent with literature findings (Kozanek et al. 2009; Thomeer et al. 2020; Thomeer et al. 2021; Hamilton et al. 2023).

Overall, the six DOF kinematics observed during level gait were generally consistent with the patterns and magnitudes described in literature, although due to the variation seen within this cohort a larger number of participants would be needed to confirm the similarity of the mean profiles with those presented in literature.

2.5.3 RESEARCH QUESTION 2B: ARE THE **STAIR ASCENT** SIX DOF TF KINEMATIC TRENDS AND MAGNITUDES FOR THIS COHORT CONSISTENT WITH RESULTS PRESENTED IN LITERATURE?

The six DOF kinematics of the TF joint during stance phase of a stair ascent for the five participants are shown in Figure 2-35.

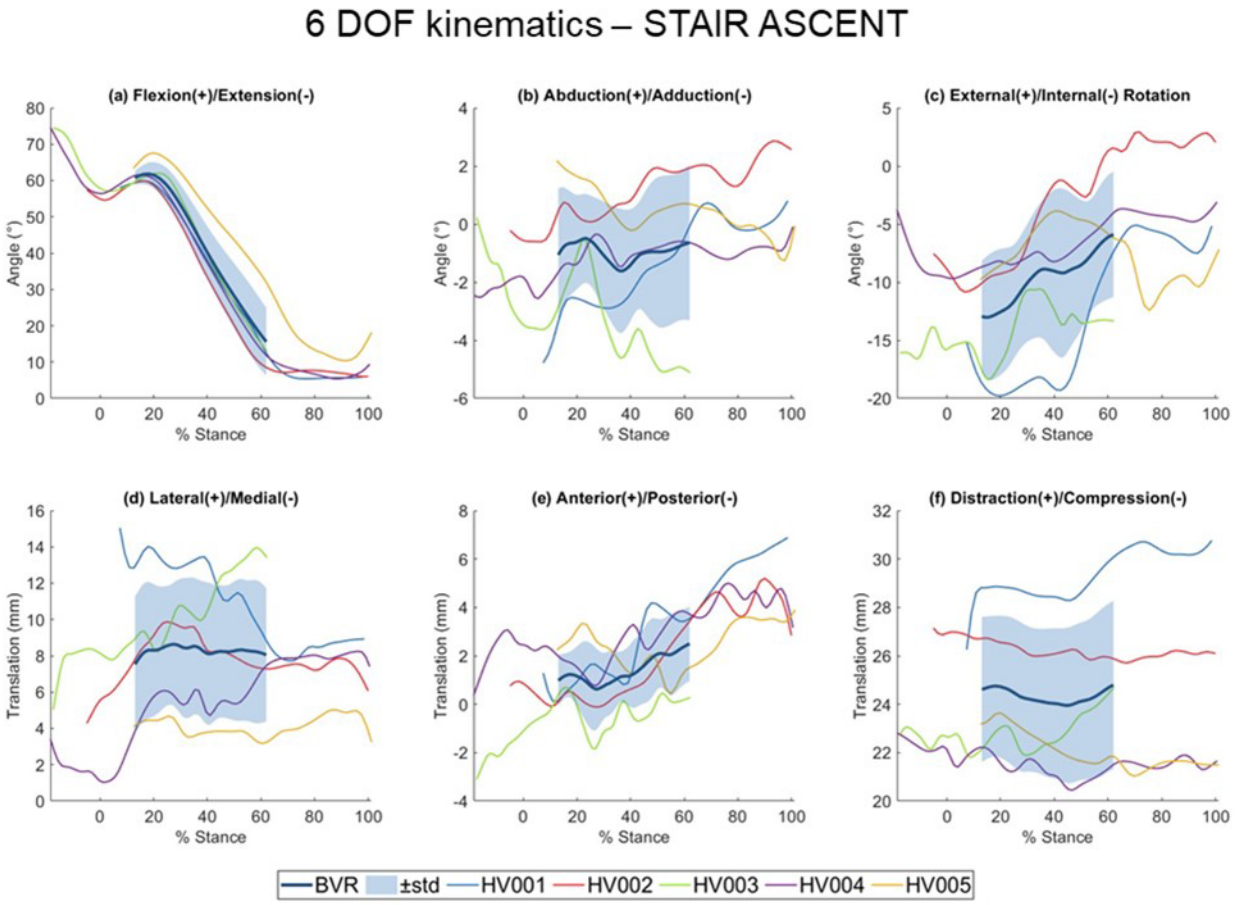

Figure 2-35 – Six DOF TF kinematics calculated for five participants during stair ascent. Mean and ±1 std calculated for all frames where data were available for all participants.

Flexion across all five participants displayed a similar profile (Figure 2-35a), with the knee being flexed (~50°) at HS, increasing to peak flexion (mean peak = 61.8°) at around 20% stance phase, before the knee began extending until about 75% stance where flexion remained relatively constant until just before TO. At the lowest point of flexion, during the final 25% of stance phase, of the four participants that had BVR collected during that section of stance, two participants remained slightly flexed, whilst the other two had slight extension of the knee. These flexion profiles were generally consistent with those presented in literature (Tsai et al. 2011; Li et al. 2012; Suzuki et al. 2012; Li et al. 2013; Thomeer et al. 2021), with the peak flexion

occurring within the range of percentage stance seen in literature and with a mean peak flexion magnitude of 61.8° sitting in the middle of the range presented in literature (50-70°). The steady decrease in flexion angle, followed by a steady period at around ~10° and a slight increase seen in some participants just before TO was also consistent with the patterns seen by other studies (Tsai et al. 2011; Thomeer et al. 2021).

As observed for level gait, AA had a non-descript profile. The mean angle was adducted throughout by ~0.5-1.5° (Figure 2-35b) which was slightly lower than the 1-5° mean adduction range presented in literature (Li et al. 2012; Thomeer et al. 2021). AA also had the smallest ROM of the three rotational DOFs, with the mean peak-to-peak ROM ± std (where data were available for all participants) being 2.4 ± 1.3° (compared to 44.0 ± 6.8° for FE and 7.8 ± 3.3° for IE).

The mean IE rotation of the knee from this dataset (Figure 2-35c) presented internal rotation throughout the whole of stance phase, with the mean internal rotation decreasing throughout from 12.9° to 5.9°, matching the ranges of ~4-18° of internal rotation seen in literature that followed the same pattern of decreasing internal rotation (Tsai et al. 2011; Li et al. 2012; Thomeer et al. 2021). Although the mean rotation angle was consistent with literature, a wide ROM was seen across the cohort. All participants remained internally rotated throughout stance phase, except HV002 who externally rotated their knee during the last 40% of stance.

Again, as observed for level gait, all participants presented lateral translation throughout stance phase of stair ascent (Figure 2-35d). Most participants displayed slight anterior translation (Figure 2-35e), however this was not exclusively seen, as seen in level gait. Figure 2-35e shows an overall trend of increasing anterior translation across stance phase of stair ascent.

When compared to the other studies that have presented the translations as changes of the position of the bone origins relative to one another, the mean translation was anterior in both this cohort and the literature. However, this cohort had a lower mean anterior translation (~-0.5 to -2 mm) compared to literature, where an initial peak (~5 mm) was followed by a decrease toward ~0 mm (Tsai et al. 2011; Thomeer et al. 2021). In contrast to that trend, the mean translation in this cohort increased anteriorly.

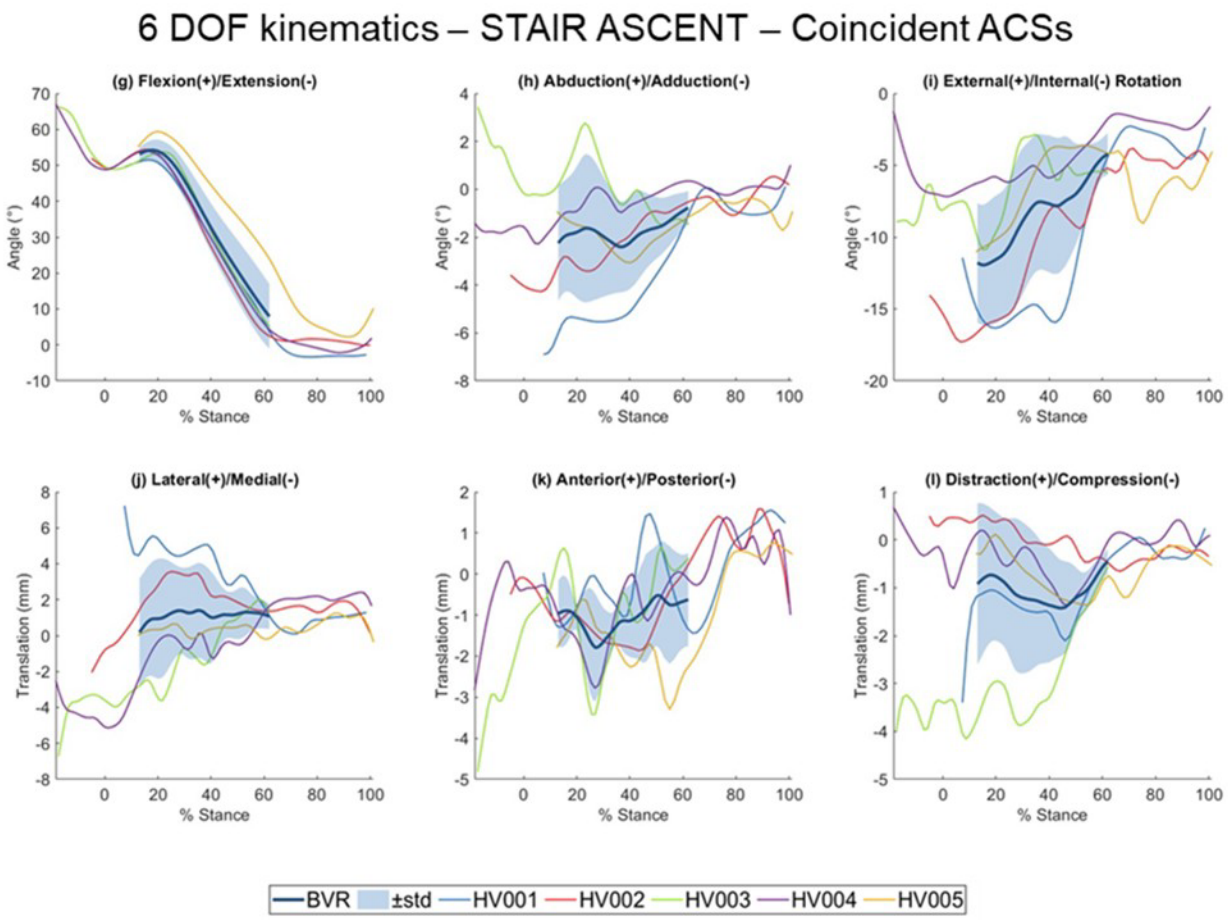

Figure 2-36 – Six DOF TF kinematics calculated using coincident ACSs during stair ascent.

The mean ML translation was found to be non-descript with little variation due to the diverging profiles between participants at the start of the activity. This mean remained slightly laterally translated throughout, remaining around 1mm, which was similar to the results presented by Li et al. (2012).

Like with ML translation, the mean CD value remained fairly consistent (around 1 mm compression) due to the variation seen between participants at the start of the activity. The mean sat between the profiles presented in literature (Tsai et al. 2011; Thomeer et al. 2021).

Generally, the mean kinematic profiles seen across the six DOFs were consistent with results in literature (Tsai et al. 2011; Li et al. 2012; Suzuki et al. 2012; Li et al. 2013; Thomeer et al. 2021). However, with only a few studies presenting in-vivo kinematics of stair ascent using BVR, it is challenging to define the expected variation across participants. Particularly, for the translations where diverging kinematic profiles are seen during the higher flexion angles (Figure 2-36), it is hard to

get a true mean and know if these profiles are representative of a typical healthy population or not.

2.5.4 RESEARCH QUESTION 2C: ARE THE **WEIGHTBEARING LUNGE** SIX DOF TF KINEMATIC TRENDS AND MAGNITUDES FOR THIS COHORT CONSISTENT WITH RESULTS PRESENTED IN LITERATURE?

A dynamic, weightbearing lunge was chosen as an activity as part of this pilot protocol as it provided an unobscured view of the bones in the knee throughout the whole activity (unlike gait and stair ascent where the contralateral limb crosses the target limb for a portion of stance phase). It also enabled investigation of the secondary DOFs during higher values of flexion, which is important as deep flexion activities have been highlighted as a key outcome for TKR patients (Weiss et al. 2002; Huddleston et al. 2009; Galvin et al. 2018).

The six DOF kinematics of the TF joint during a weightbearing, dynamic lunge are shown in Figure 2-37. The % lunge displayed on the x-axis was defined as the period where the participant was weightbearing and making contact with the force plate – similarly to how stance phase was defined for the other two activities (Section 2.4.8).

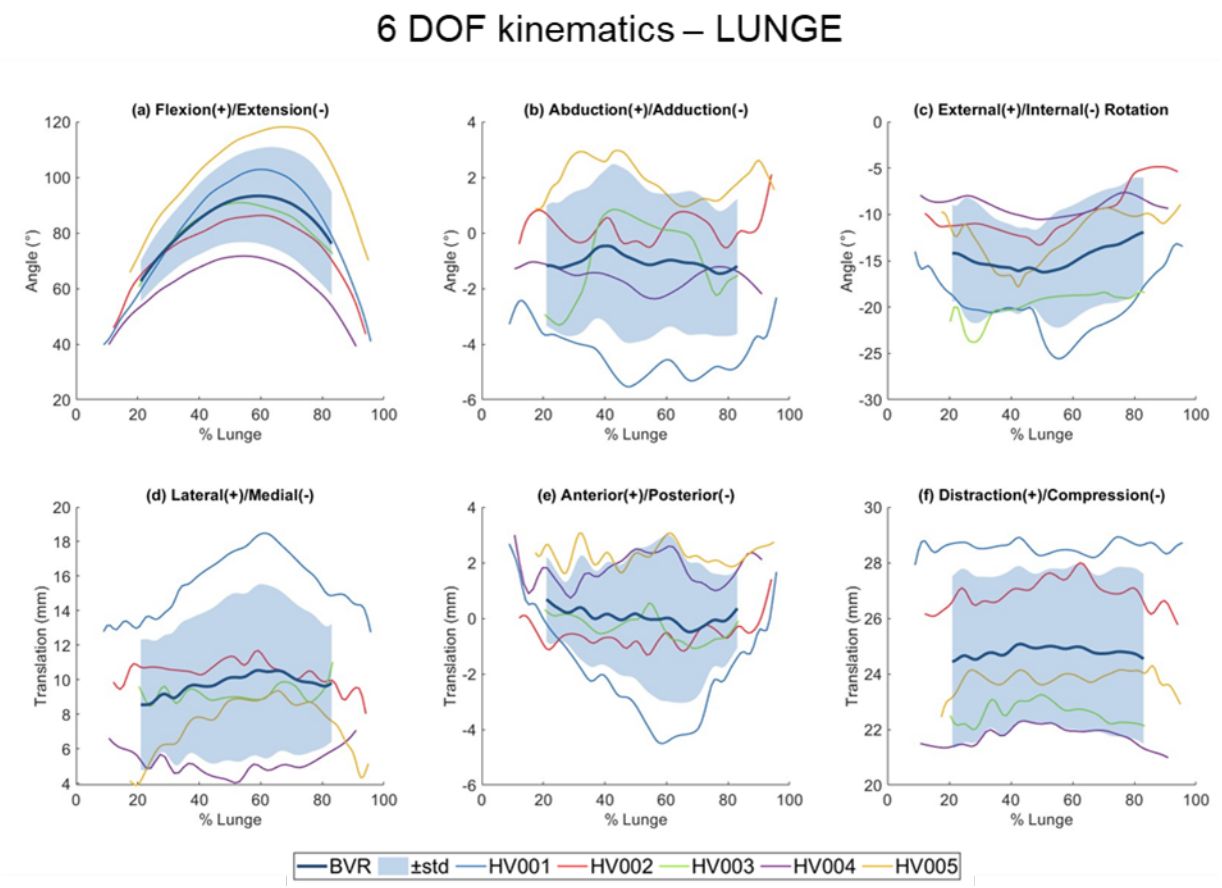

Figure 2-37 - Six DOF TF kinematics calculated for five participants during a weightbearing lunge. Mean and ±1 std calculated for all frames where data were available for all participants.

Figure 2-37a shows that there was a large range in the maximum TF flexion that each participant reached during their lunge (64 - 110°). As each participant was instructed to lunge as deeply as they felt comfortable with, the maximum flexion angle achieved varied greatly between participants. To investigate larger or a more specific range of flexion angles, it may be better to utilise an open-chain flexion activity, as this may allow less-confident participants to achieve higher flexion angles. However, this does neglect the effects of weightbearing on joint kinematics so may not be suitable depending on the research question. Alternatively, squatting and kneeling have been shown to present similar kinematic motions (Galvin et al. 2018) which would allow analysis of the same range of deep flexion but may present similar obstacles to a weightbearing lunge of difficulty performing the full movement and balancing for OA sufferers and TKR patients.

This inconsistency in maximum flexion angle reached was also seen across the studies in literature, with some reaching much higher values of flexion than others as

some studies modified a typical lunge to reach deeper flexion (Leszko et al. 2011; Hamai et al. 2013), whereas others only measured to 90° flexion (Myers et al. 2012). The lack of consistency between studies and participants makes comparisons difficult, so only general overall trends should be evaluated.

The other 5 DOFs showed variation between participants. The mean profile for AA, AP, and CD displayed relatively little change during the lunge, each displaying a non-descript profile. IE rotation had a slight increase in internal rotation towards the peak of the lunge (Figure 2-37c); a similar profile was seen in an increase in lateral translation towards the maximum flexion value, but this was not consistent across all participants (Figure 2-37f).

The large variation was still seen when the kinematics were calculated using the coincident axes, with only AP displaying a particular reduction in ROM (Figure 2-38).

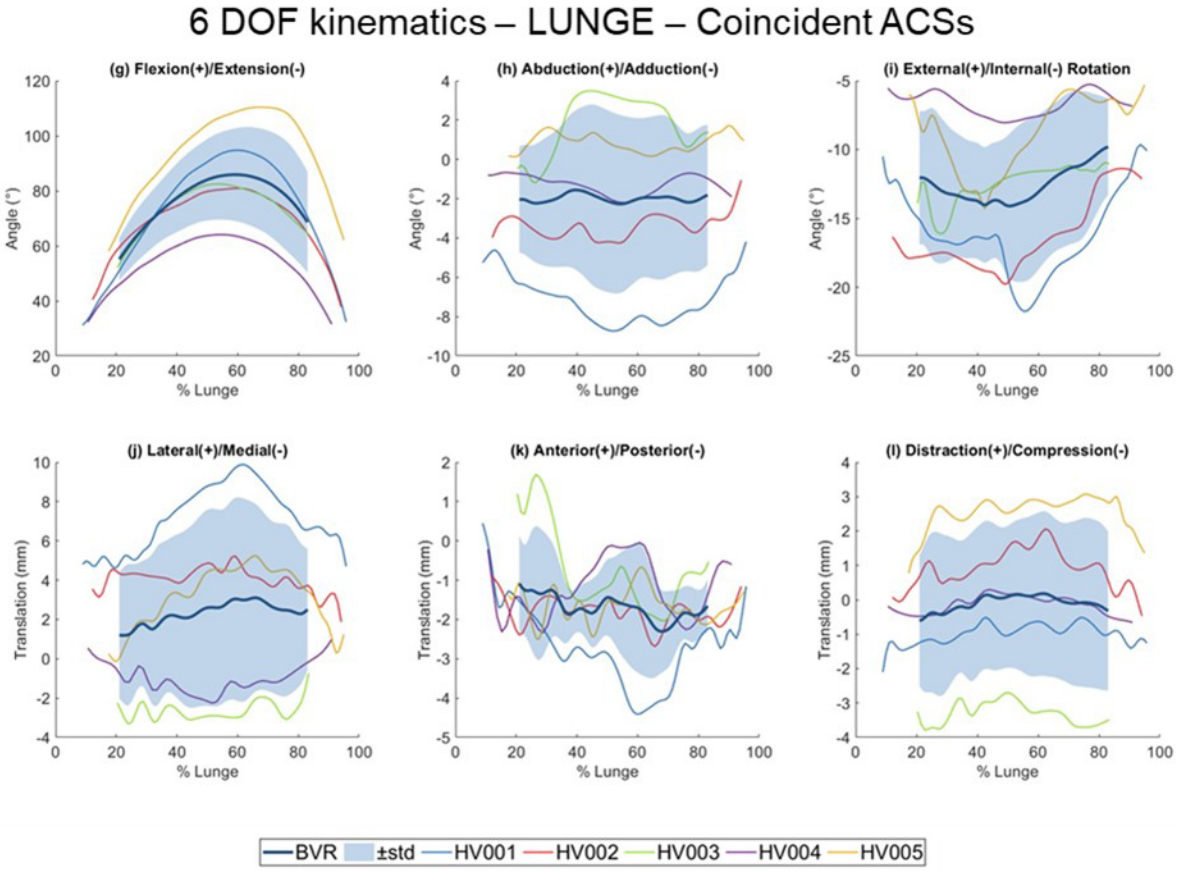

Figure 2-38 – Six DOF TF kinematics calculated using coincident ACSs during a lunge.

Activities involving smooth flexion-extension cycles, such as lunging or open-chain flexion, are often used to investigate the relationship between flexion and the other five DOFs in the knee (Leszko et al. 2011; Hamai et al. 2013; Kefala et al. 2017; Hamilton et al. 2022). To compare with the trends seen in literature, each DOF was

plotted against flexion (Figure 2-39); this figure is repeated in Section 2.5.6 where coupling of flexion with the secondary DOFs is discussed further.

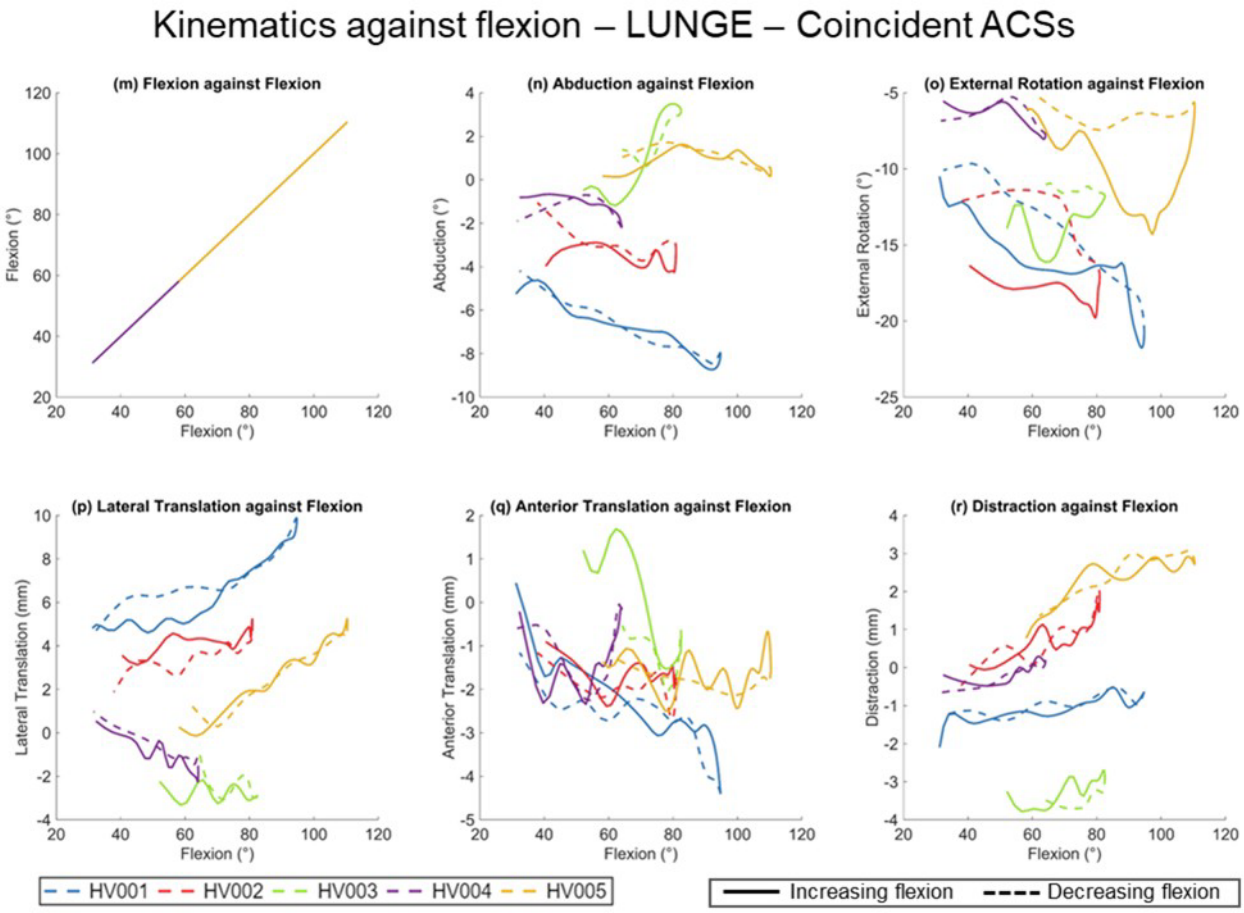

Figure 2-39 - Six DOF TF kinematics of a lunge (calculated using coincident ACSs) plotted against flexion angle.

Three participants (HV001, HV002 & HV004) displayed knee adduction throughout the lunge, consistent with literature (Leszko et al. 2011; Qi et al. 2013; Kefala et al. 2017; Thomeer et al. 2021; Hamilton et al. 2022). These same three participants also showed an overall trend of increasing adduction as flexion increased (Figure 2-39), also seen by some studies in literature (Leszko et al. 2011; Hamai et al. 2013; Qi et al. 2013). However, the remaining two participants showed abduction instead, with HV003 in particular demonstrating an opposite trend of increasing abduction with increased flexion.

TF internal rotation was seen throughout the lunge in all the participants, which was consistent with literature for the same range of flexion (Leszko et al. 2011; Hamai et al. 2013; Qi et al. 2013; Kefala et al. 2017; Thomeer et al. 2021; Hamilton et al. 2022).

On average, the tibia was translated posteriorly throughout which is the opposite of the results presented in literature which showed increasing anterior translation with increased flexion (Qi et al. 2013; Kefala et al. 2017; Thomeer et al. 2021; Hamilton et al. 2022). As the magnitude of the mean posterior translation was small (approximately 1-2 mm throughout) and the expected correlation with increasing flexion was not observed, it is assumed that a larger dataset is required to confirm consistency with literature.

The ML translation seemed to be split into two profiles in this cohort (Figure 2-39), with one group (HV001, HV002 & HV005) showing lateral translation of the tibia which increased with flexion, and another group (HV003 & HV004) showing medial translation. The latter is more consistent with literature, with a slight trend of increasing medial translation with flexion (Qi et al. 2013; Thomeer et al. 2021; Hamilton et al. 2022). Kefala et al. (2017) found variation between participants, with a mixture of TF medial and lateral translation during seated knee FE, thus it is possible that variation seen in this cohort is representative of the wider population.

CD was inconsistent between the participants, with some participants showing non-descript joint compression profiles and others displaying distraction proportional increasing flexion which is contrary to other recent findings (Hamilton et al. 2022).

The high variability of results in the six DOFs of this cohort may indicate usage of different coordination strategies, possibly arising from the inconsistent performance of the activity due to the lack of specific instructions. The lunge length, maximum flexion angle achieved and speed of their lunge may all have affected participant movement and balance during their lunge, increasing the observed differences. A more consistent way of carrying out this activity to remove extraneous variables would allow for easier comparison and interpretation of the data.

In conclusion, the kinematics calculated during lunging for these five participants had varied similarity with literature. For example, the consistent internal rotation observed matched literature (Leszko et al. 2011; Hamai et al. 2013; Qi et al. 2013; Kefala et al. 2017; Thomeer et al. 2021; Hamilton et al. 2022), however the posterior translation calculated contradicted reported trends (Qi et al. 2013; Kefala et al. 2017; Thomeer et al. 2021; Hamilton et al. 2022). The inconsistency of the execution of the lunge

between participants may have contributed to the differences seen across the cohort.

2.5.5 RESEARCH QUESTION 3: HOW DOES CHANGING THE ACS REPRESENTATIONS ALTER THE KINEMATIC OUTPUTS?

As discussed in Chapter 1.3.3, translations of the TF joint are not always presented in literature using the standard Grood and Suntay (1983) conventions, and can be presented as changes relative to an original coincident point instead. By presenting the kinematics calculated using both separate and coincident ACSs, the effect of altered coordinate system definition can be investigated.

To investigate the variation in the kinematics calculated using separate and coincident ACSs (research question 3, Section 2.4.9), the overall cohort ROM was calculated by subtracting the minimum value of any participant from the maximum value of any participant for each DOF, for each activity (Table 2-7).

Table 2-7 – Overall Cohort ROM (overall maximum – overall minimum value) for the three activities comparing the two ACS definitions. A positive difference indicates the separate ACSs resulted in a larger kinematic ROM; a negative difference indicates the coincident ACSs resulted in a larger ROM.

	LEVEL GAIT			STAIR ASCENT			LUNGE		
	Separate ACSs	Coincident ACSs	Difference	Separate ACSs	Coincident ACSs	Difference	Separate ACSs	Coincident ACSs	Difference
Flex (°)	26.98	26.37	0.61	62.18	62.73	-0.55	78.32	79.16	-0.84
Abd (°)	10.80	4.08	6.72	7.95	9.64	-1.69	8.50	12.21	-3.72
Ext (°)	18.59	12.43	6.15	22.67	15.94	6.73	20.69	16.47	4.22
Lat (mm)	10.64	4.06	6.58	13.50	11.73	1.77	14.58	13.20	1.39
Ant (mm)	6.90	4.05	2.85	8.66	5.00	3.66	7.56	6.06	1.49
Dist (mm)	10.53	4.27	6.27	10.25	4.65	5.60	7.89	6.85	1.04

Table 2-7 shows there was little difference in the flexion ROM between the two methods calculated during any of the activities (all differences were within 1°). This would suggest that the separate tibia ACS had a similar alignment to the femoral

ACS in the sagittal plane leading to minimal observed flexion differences when they were made coincident. This was likely due to the placement of the leg within the Tx/Rx Knee 15 Flare MRI Coil, resulting in a neutral knee flexion angle (0°) for the CISS-3D scan (Section 2.2), from which the coincident axes were defined.

Although the ROMs showed minimal differences during level gait, the flexion magnitudes from the coincident ACSs (Figure 2-34g) were lower than when calculated using separate ACSs (Figure 2-33a), although they still displayed a similar overall profile.

For level gait, the ROM when the changes are defined using coincident axes were all Found to be smaller than when using separately defined axes in all six DOF (Table 2-7). However, this was not true for the other two activities. For both stair ascent and lunge, the abduction ROM was greater when calculated using the coincident axes. Abduction had the smallest rotational ROM during all the activities, demonstrating that even small differences in axis definition can substantially affect the calculated range for lower-magnitude motions. This highlights the sensitivity of certain DOFs, particularly abduction, to ACS setup and reinforces the need for consistency in axis definitions when comparing results across studies or applications.

When analysing the three translational DOFs calculated using the Grood and Suntay (1983) approach (Figure 2-33), the translational ROMs were comparable to those found in the literature (Gale and Anderst 2020). They display large magnitude, and ranges of magnitude, relative to the ROMs in all three planes. This is representative of the variation in knee size across participants, resulting in variation in absolute translational values seen as the bone size differences, will cause offsets in the relative positions and rotations of the femur and tibia ACSs. This is seen most clearly in CD (Figure 2-33f) where the translations of 20-30 mm were a result of defining the femoral ACS between the condyles and the tibial ACS on the tibial plateau.

By making the femoral and tibial ACSs coincident (as described in Section 2.4.7), the kinematics could be described as changes from a coincident (neutral) position, as defined from the MRI scan knee alignment, thus reducing inter-participant variation caused by differences in bone sizes. This resulted in smaller translational ROM during all activities (Table 2-7) because, when calculated from the coincident starting point, the translations only represent the relative motion of the bones, removing any

influence of initial ACS offset on translation magnitudes. This is the reason why translational DOFs are often presented as changes from a coincident set of axes in the literature (Gray et al. 2019; Thomeer et al. 2020; Thomeer et al. 2021). It is also why the coincident ACS definition here resulted in secondary kinematics being closer to neutral (0°/mm) in all five secondary DOFs.

As the ROMs for the translational DOFs were small across all three activities, identifying trends from this dataset should be done cautiously, as the results are of a similar magnitude to the accuracy of BVR.

In addition to affecting the ROM, altering the ACS definitions also influences the kinematic patterns seen in the secondary DOFs. For example, during stair ascent, using separate ACSs resulted in generally consistent variation across the entire activity in the secondary DOFs (Figure 2-35). Whereas, when using the coincident ACS definitions, AA, ML, and CD demonstrated greater variability between participants at the beginning of stance phase when flexion was high, before converging more towards the end of stance phase where the flexion angle was lower and was changing less (Figure 2-36).

The differences seen between the kinematics when calculated using these two different ACSs definitions demonstrates the importance of consistency in ACS choice when comparing kinematics between methods. Different ACS definitions may be more appropriate for certain applications, for example, if using marker-based motion capture data, it may be more appropriate to define the joint from a single coincident set of axes rather than two separate axes.

2.5.6 RESEARCH QUESTION 4: DO THE SECONDARY TF KINEMATICS (ALL DOFS EXCEPT FLEXION) COUPLE WITH FLEXION?

To investigate the coupling between flexion and the other DOFs (Question 4, Section 2.4.9), each of the kinematics calculated using the coincident ACSs were plotted against their flexion values at each frame (Figure 2-40, Figure 2-41 & Figure 2-42) and coefficient of determination (r^2) was calculated (Section 2.4.10) for each activity (Table 2-8).

Figure 2-40 shows each DOF plotted against flexion for all frames of level gait for each participant. These results highlight the variation in how secondary kinematics are related to flexion angle in different participants. Some DOFs, such as abduction, external rotation and distraction, display an overall decreasing trend with increasing flexion, however, on examination of individual results, this pattern is less clear.

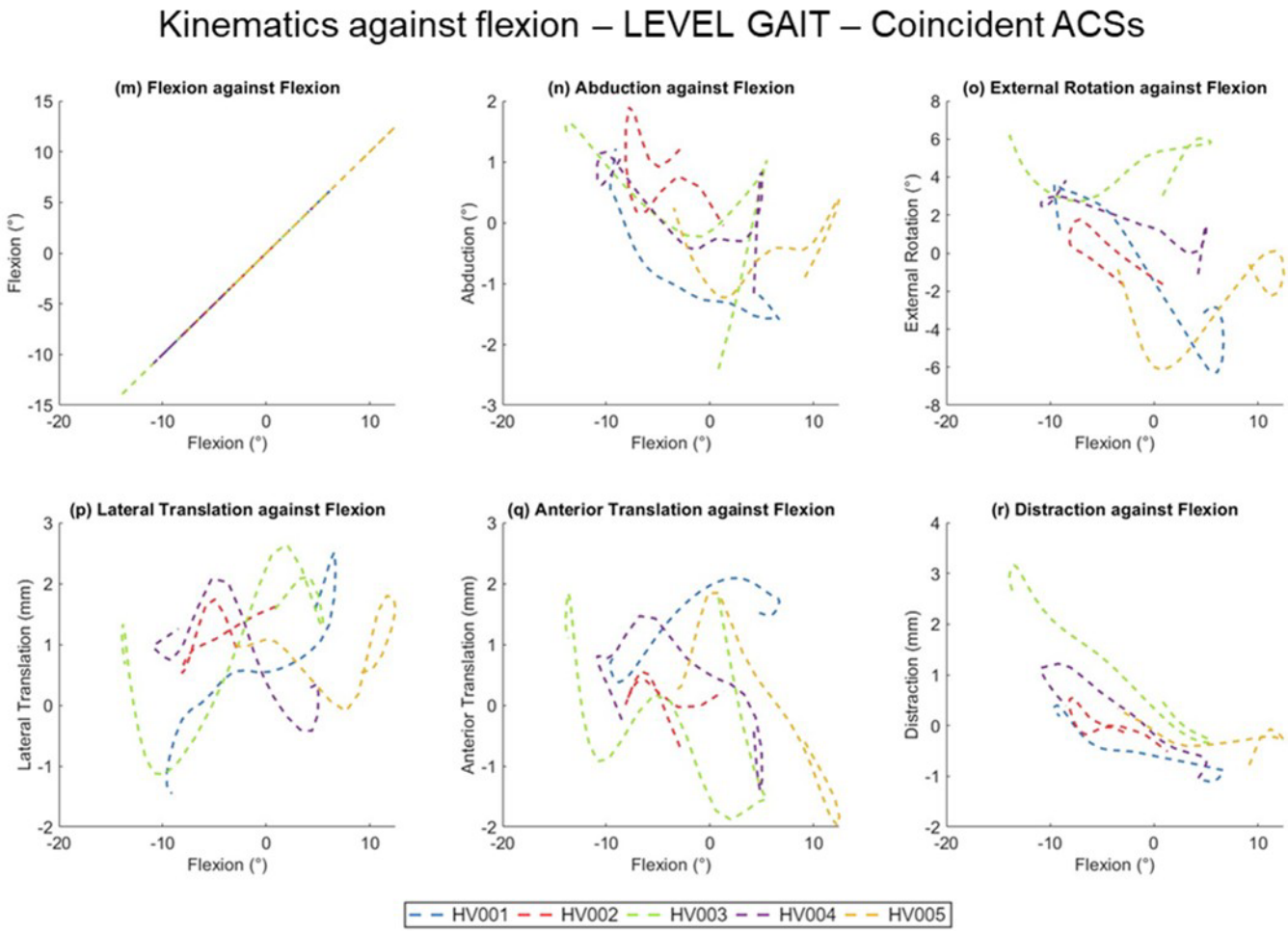

Figure 2-40 – Six DOF TF kinematics of level gait (calculated using coincident ACSs) plotted against flexion angle.

The overall trends observed for the level gait activity were not observed across the other activities. When looking at the secondary DOFs for stair ascent (Figure 2-41), the variation in secondary kinematics between participants increases as flexion increases. This is seen particularly in abduction and lateral translation where the results are converged (at around 0° flexion) then diverge as flexion reaches its peak for this activity.

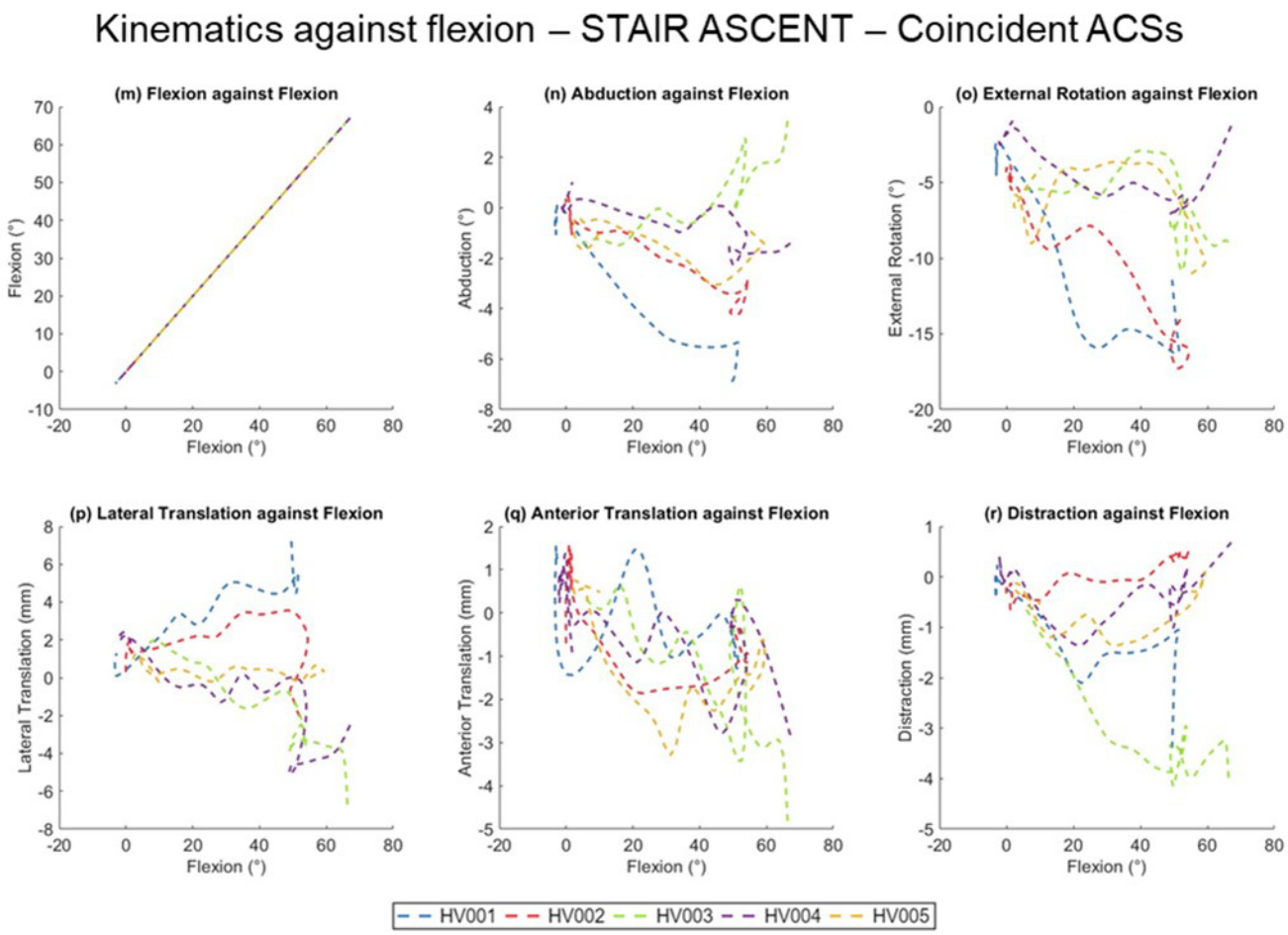

Figure 2-41 - Six DOF TF kinematics of stair ascent (calculated using coincident ACSs) plotted against flexion angle.

Looking at the individual profiles, there is some apparent correlation between the diverging kinematics. For example, HV001 displays an overall decrease in abduction with increasing flexion during stair ascent, with the largest adduction value of the five participants at peak flexion; HV001 also had the highest lateral translation which increased with increasing flexion. HV003, however, presented the opposite of both these trends, with increasing adduction and medial translation (reaching the highest values of the cohort for both of these). These results suggest potential relationships between some of the secondary DOFs and further investigation is required to fully describe knee motion.

As with stair ascent, greater variation was seen between participants when plotting the secondary kinematics against flexion during lunge (Figure 2-42), than during level gait. The trends seen for abduction, lateral translation and distraction for each individual follow a fairly consistent path for the increase (solid line) and subsequent decrease (dashed line) in flexion, even if each participant's kinematic profile is

different. However, this consistency is not seen in external rotation where there is a difference in the profile between the increase (solid line) and the decrease (dashed line) in flexion, with all participants displaying larger internal rotation when lunging forward than when they were returning to an upright position. This increased internal rotation during the flexion increase may be to stabilise the knee during weight acceptance.

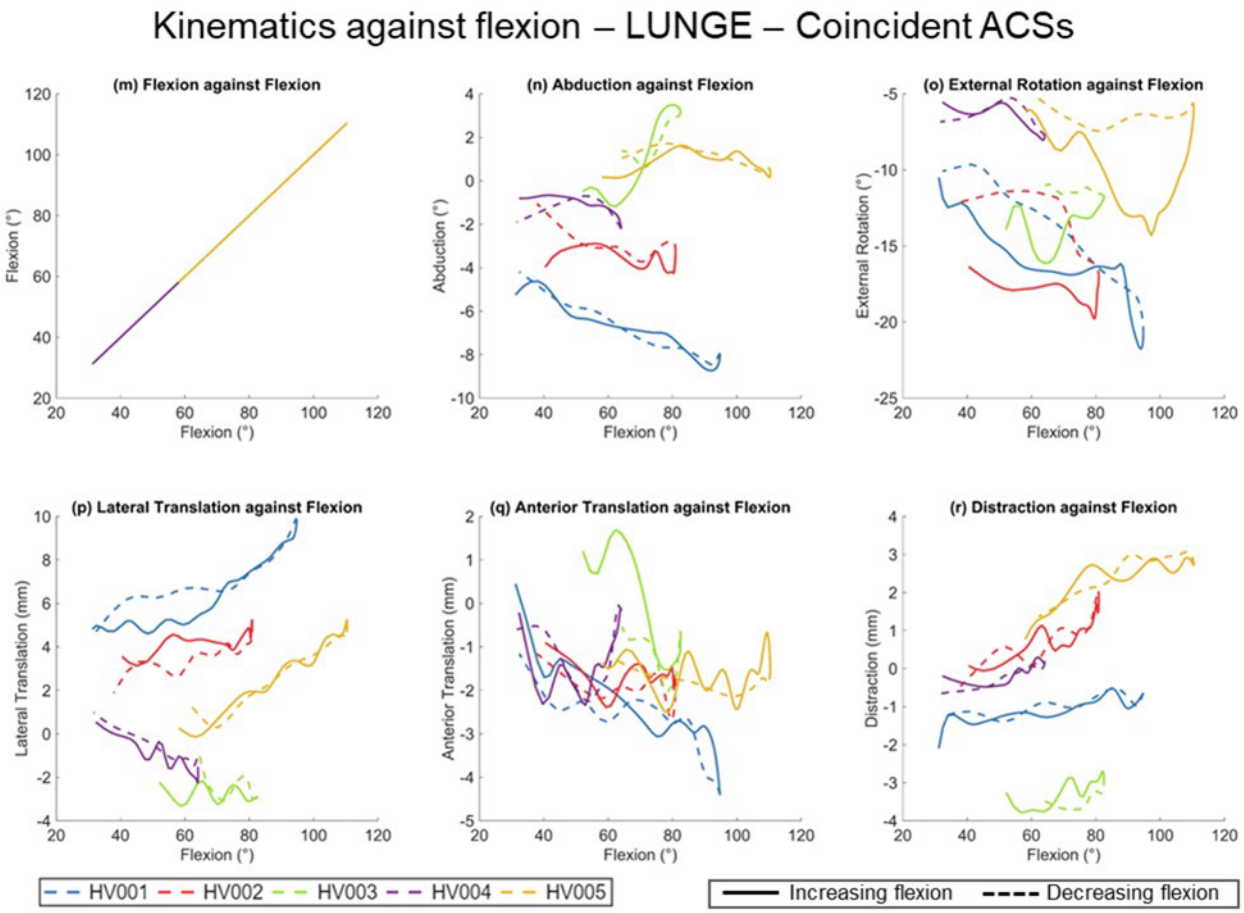

Figure 2-42 - Six DOF TF kinematics of a lunge (calculated using coincident ACSs) plotted against flexion angle. (This figure is the same as Figure 2-39 in Section 2.5.4)

From literature, clear trends were shown for several of the secondary DOFs when plotted against knee flexion angle during weight bearing or open-chain flexion activities. This included increasing internal rotation of the tibia relative to the femur with increasing flexion (Leszko et al. 2011; Hamai et al. 2013; Kefala et al. 2017; Hamilton et al. 2022). Although this was not seen in the whole cohort, some of the individual kinematic profiles (for example, HV001) displayed this trend (Figure 2-42).

The r^2 values of each DOF for each activity are presented in Table 2-8. These were evaluated against the threshold values of ≥0.7 to define coupling (highlighted in green), $0.5 \leq r^2 < 0.7$ for moderate correlation (highlighted in yellow) and < 0.5 for

weak correlation between a secondary DOF and flexion (Section 2.4.10). R^2 is presented per activity for each participant, then the mean of the five individual r^2 values for the activity, followed by the r^2 of all data from all participants pooled (combined), and finally the r^2 of the mean kinematic profile (where data were available for all five participants).

Table 2-8 - Coefficient of determination (r^2) between flexion and each DOF for the three different activities.

r^2	**Gait**					
	FE	AA	IE	ML	AP	CD
HV001	1.000	0.798	0.896	0.874	0.697	0.903
HV002	1.000	0.234	0.586	0.493	0.112	0.593
HV003	1.000	0.403	0.015	0.397	0.470	0.988
HV004	1.000	0.379	0.759	0.430	0.475	0.932
HV005	1.000	0.199	0.384	0.025	0.743	0.333
Average (mean)	*1.000*	*0.403*	*0.528*	*0.444*	*0.499*	*0.750*
Combined	1.000	0.399	0.116	0.093	0.065	0.037
Mean kinematics	1.000	0.915	0.851	0.401	0.392	0.965
r^2	**Stair Ascent**					
	FE	AA	IE	ML	AP	CD
HV001	1.000	0.933	0.861	0.908	0.206	0.555
HV002	1.000	0.911	0.954	0.002	0.432	0.850
HV003	1.000	0.689	0.303	0.879	0.445	0.743
HV004	1.000	0.683	0.655	0.747	0.468	0.007
HV005	1.000	0.426	0.091	0.212	0.357	0.003
Average (mean)	*1.000*	*0.728*	*0.573*	*0.549*	*0.382*	*0.432*
Combined	1.000	0.259	0.106	0.069	0.049	0.039
Mean kinematics	1.000	0.390	0.914	0.144	0.466	0.003
r^2	**Lunge**					
	FE	AA	IE	ML	AP	CD
HV001	1.000	0.947	0.756	0.857	0.790	0.670
HV002	1.000	0.257	0.215	0.489	0.097	0.738
HV003	1.000	0.816	0.219	0.031	0.631	0.421
HV004	1.000	0.303	0.366	0.848	0.086	0.744
HV005	1.000	0.125	0.003	0.968	0.003	0.731
Average (mean)	*1.000*	*0.490*	*0.312*	*0.639*	*0.321*	*0.661*
Combined	1.000	0.061	0.027	0.021	0.016	0.014
Mean kinematics	1.000	0.011	0.052	0.821	0.408	0.894

Coupled | Moderately correlated | Weakly correlated

'Average (mean)' *is the mean of the five r^2 values of each participant for the given activity (the five values above in the column).* ***'Combined'*** *is the r^2 of the pooled kinematic data points of the whole cohort.* ***'Mean kinematics'*** *is the r^2 of the mean kinematic profile of the cohort (where data were available for all five participants).*

The results in Table 2-8 show that the degree of coupling varied between participants, activities, and DOFs with no consistent pattern. Some participants, like HV001, show high r^2 values between flexion and the secondary DOFs during all three activities. For HV001, only AP translation during stair ascent was found to be weakly correlated to flexion, with all other DOFs moderately correlated or coupled across the three activities. However, other participants display weaker correlations in general between flexion and the secondary DOFs; for example, HV005 found weak correlations of r^2= 0.03 for both IE rotation and AP translation during the lunge. This suggests that coupling of the secondary coordinates to flexion may be dependent on the movement patterns of an individual.

To investigate coupling with flexion across the cohort, three different metrics were calculated. Firstly, the mean of the five individual r^2 values was calculated. Next, the r^2 of all pooled data point values across all participants was calculated. Finally, r^2 was calculated by inputting mean kinematic profiles of the cohort (including all frames where data were available for all participants). Out of these three metrics, the combined dataset found the lowest r^2 values, with all secondary DOFs weakly correlated to flexion during all three activities. This is due to the different trends seen between the participants, so although there may be correlations between flexion and the secondary DOFs on an individual level, this is not seen when the data are pooled.

When taking the average of the five r^2 values, there was some coupling and moderate correlations seen between flexion and the secondary DOFs, but it was not consistent across the three activities. This was reflective of the inter- and intra-participant variability in the r^2 values calculated across the activities.

The r^2 value of the mean input kinematic profile have the highest levels of correlation during level gait of the three metrics. This is likely due to the small number of frames of input data where the mean could be calculated from all five participants not capturing the variation seen throughout the whole of stance phase. This is the method used to calculate coupling between flexion and the other DOFs in literature (Kozanek et al. 2009; Gray et al. 2019; Thomeer et al. 2021). Whereas in this study adduction was found to be coupled with flexion during stance phase of level gait, it was only found to be moderately (Kozanek et al. 2009; Thomeer et al. 2021) or

weakly (Gray et al. 2019) correlated with flexion in literature. External rotation was only found to be coupled with flexion by one other study (Gray et al. 2019), with the others reporting moderate correlation (Kozanek et al. 2009; Thomeer et al. 2021).

In literature, all the translational DOFs were found to be coupled with flexion during level gait (Kozanek et al. 2009; Gray et al. 2019; Thomeer et al. 2021), however in this cohort, only compression was found to be correlated with flexion; anterior and medial translation were both found to be weakly correlated with flexion.

For stair ascent, the only secondary DOF coupled with flexion was external rotation, with all other DOFs weakly correlated. This disagreed with the results presented by one other study (Thomeer et al. 2021) which found all secondary DOFs to be at least moderately coupled with flexion during stair ascent.

During lunging, the mean kinematic profile was found to be coupled with flexion for medial translation and compression but weakly correlated for the other secondary DOFs. Both rotational DOFs were found to have very weak correlations (r^2 <0.1). In contrast, Thomeer et al. (2021) found coupling between flexion and all five secondary DOFs during a different high flexion activity (open-chain flexion reaching around 100°) with r^2 values >0.8. This suggests that although the lunge provides a high flexion ROM to calculate coupling with, it may not be suitable as weightbearing changes the kinematic profile during the increase and decrease of flexion (as seen with external rotation in Figure 2-42).

Despite r^2 being calculated from the mean kinematic profile in literature, the results in Table 2-8 suggest it may not be the most suitable method for assessing coupling between flexion and the secondary DOFs for a cohort due to the variation seen in levels of correlation between individuals. When the mean profile of all kinematics is used for this calculation, the opposing trends within the dataset cancel each other out and remove some of the variation seen. Calculating the cohort mean after the r^2 values have been calculated individually may give a better representation of the coupling for the cohort as this will reflect the participants with strong and weak correlations. Particularly for this study where the number of participants was small and the mean could only be calculated over part of stance phase, the r^2 of the mean kinematic profile is not a good representation of relationship between flexion and the other DOFs.

Another factor affecting the strength of correlation would be the filtering applied to the output kinematics. Heavier filtering would smooth the data more, increasing the chance of the r^2 value exceeding the threshold for coupling. As the data in this study was lightly filtered to preserve kinematic features, residual noise may be contributing to lower r^2 values.

Understanding the coupling between flexion and the secondary DOFs facilitates correct modelling of knee function and its relation to anatomy (Koo and Koo 2019; Thomeer et al. 2021), particularly when using the assumption of coupling to drive MSMs. If the coupling relied on to improve MSM estimates of TF motion compared with marker-based motion capture (Smith 2017; Hume et al. 2018) does not exist, then the resulting kinematics generated will not be representative of in-vivo motion. For example, in this study, anterior translation was only weakly correlated with flexion across all three activities for the three average cohort metrics, as well as for all five participants during stair ascent. This suggests that anterior translation may not be accurately predicted by a function of flexion.

While weakly correlated DOFs may not be well captured by generic functions of flexion, the variation observed between participants in the relationships between flexion and each secondary DOF (Figure 2-40, Figure 2-41 & Figure 2-42) suggests that personalisation within MSM pipelines could still be valuable. Pipelines that use scaled models or incorporate personalised geometries to create individualised functions of flexion (such as the ones described in Chapter 3) may better represent participant-specific coupling patterns and, therefore, capture the individual kinematic variations.

2.5.7 RESEARCH QUESTION 5: HOW DO MARKER-BASED MOTION CAPTURE TF ROTATIONS COMPARE TO THE GOLD-STANDARD IN-VIVO BVR RESULTS?

To investigate the accuracy of the marker-based motion capture rotations, the results from the V3D pipeline (Section 2.4.8) were compared with the BVR kinematics, defined as a ‘gold-standard’. This is because the BVR approach is expected to produce higher fidelity data (Sati et al. 1996; Stagni et al. 2005; Akbarshahi et al. 2010; Tsai et al. 2011). Although the accuracy of marker-based motion capture for the knee has been well documented (Sati et al. 1996; Reinschmidt et al. 1997a;

Stagni et al. 2005; Akbarshahi et al. 2010; Tranberg et al. 2011; Tsai et al. 2011; Miranda et al. 2013; Hume et al. 2018), it was included as part of this study because it provides a comparator for potentially improved secondary kinematic predictions (from the same data collection sessions) for use in the MSM pipeline utilised in a later chapter (Chapter 3).

For this comparison, the V3D rotations were compared with the BVR kinematics calculated using the coincident ACSs as this relates to how the knee joint is defined in the V3D model (Section 2.5.5).

The mean rotations ±1 std from the V3D and BVR pipelines were plotted for each activity (Figure 2-43, Figure 2-44, Figure 2-45). For clarity, the individual kinematics were plotted along with the mean ±1 std for BVR in the first column and V3D in the second column, with the mean ±1 std for both plotted in the third column for each of the three activities in turn. The results of the Bland-Altman analysis (Section 2.4.10) for each rotational DOF were included as a fourth column. The Bland-Altman analysis presents the difference between the V3D rotation and the BVR rotation at each frame (where both were calculated), plotted against the gold-standard BVR 'ground-truth' value. The median difference and ±1.45 interquartile range (IQR) of the whole dataset are also indicated on each Bland-Altman plot.

Only the TF rotations were included in this analysis as translations are not typically reported from marker-based motion capture due to the known inaccuracies associated with the technique. Previously reported translational errors between marker-based and BVR calculations are around 20 mm (Miranda et al. 2013; Hume et al. 2018), thus significantly larger than the expected ROM in these DOFs, Marker-based motion capture is therefore unsuitable for measuring translations.

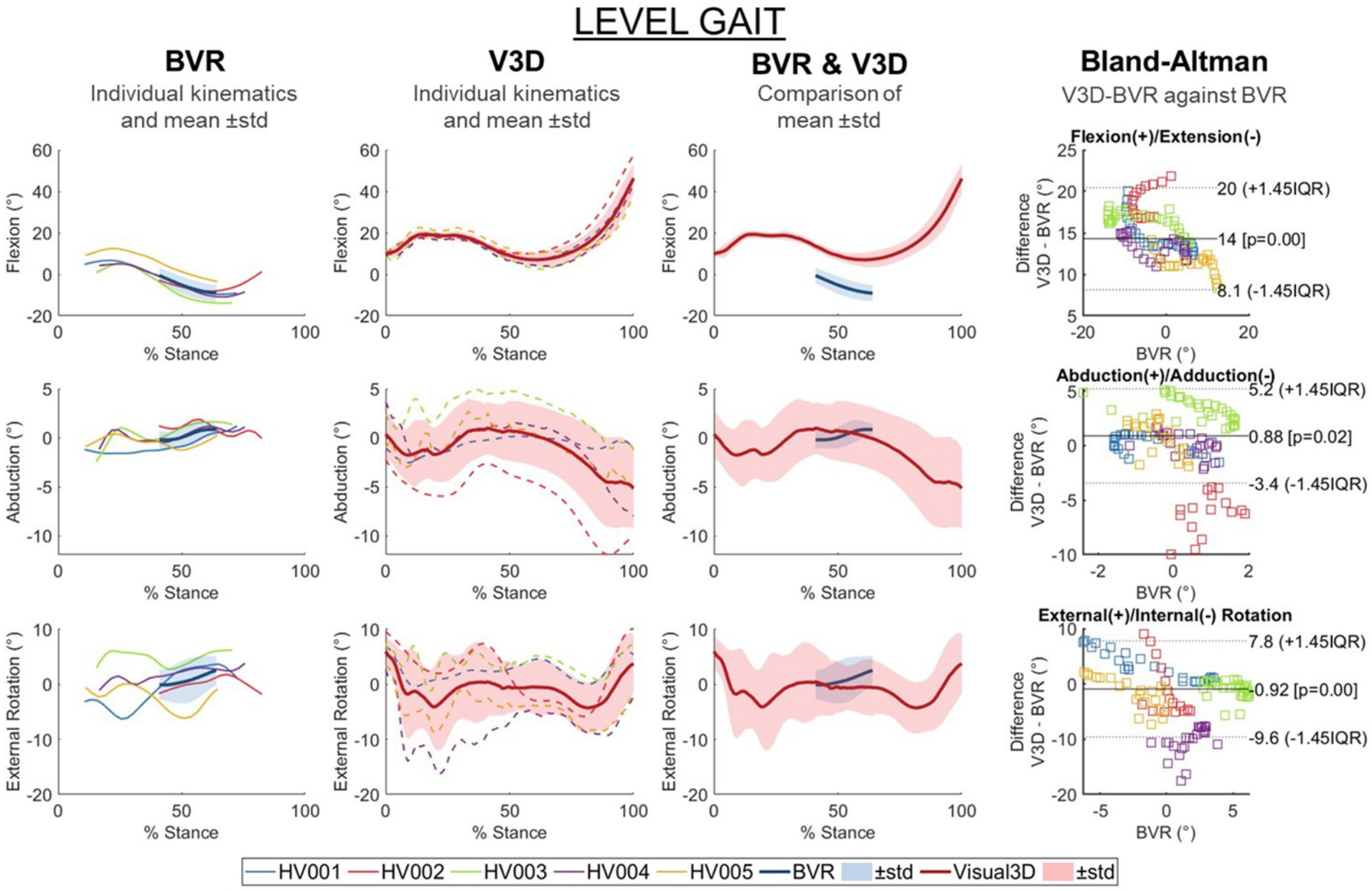

Figure 2-43 – TF rotations during gait calculated Visual3D compared with BVR, with individual results as well as mean ±1 std plotted for comparison. Bland-Altman analysis results are also included in the fourth column.

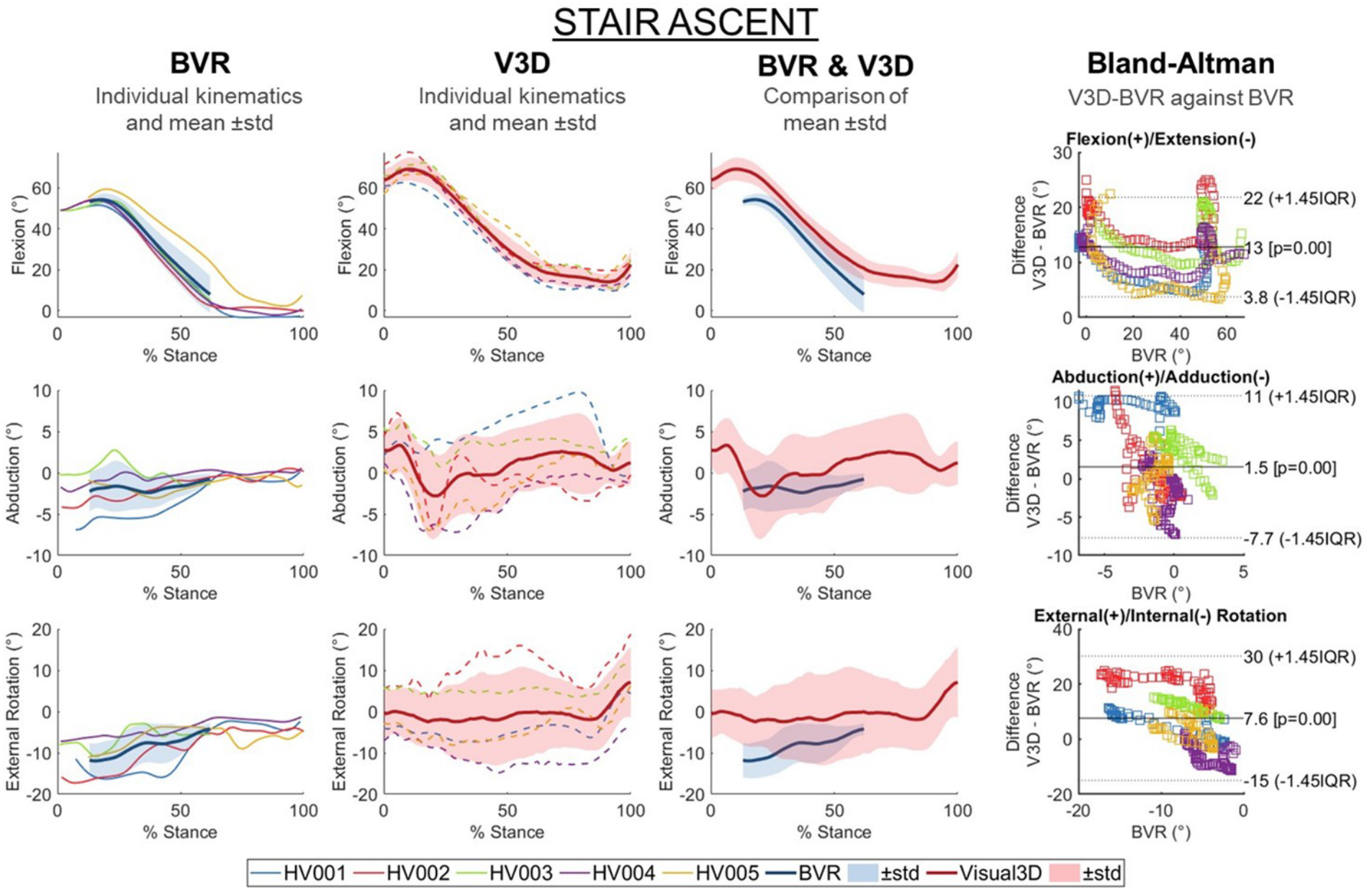

Figure 2-44 - TF rotations during stair ascent calculated Visual3D compared with BVR, with individual results as well as mean ±1 std plotted for comparison. Bland-Altman analysis results are also included in the fourth column.

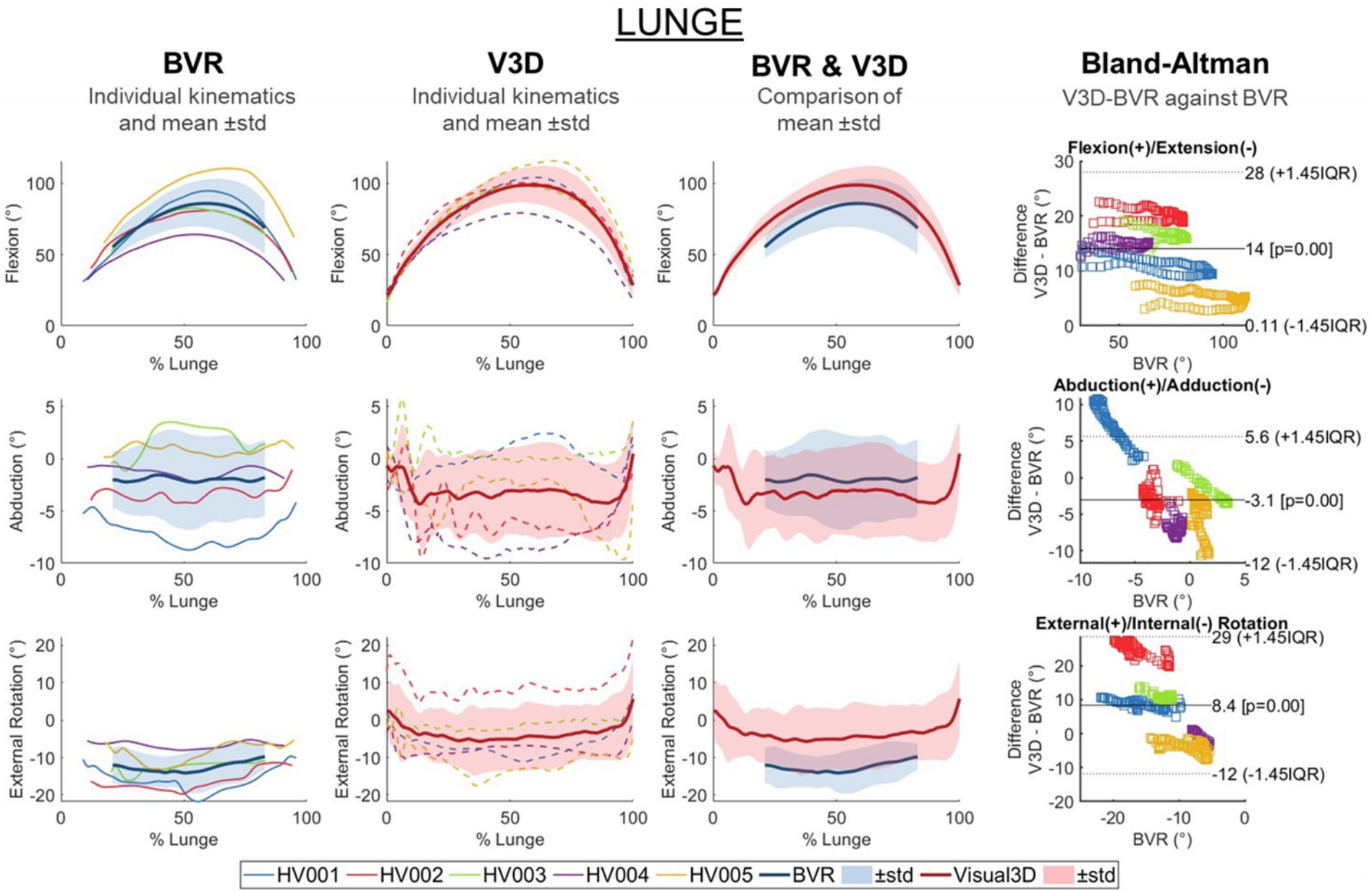

Figure 2-45 - TF rotations during lunge calculated Visual3D compared with BVR, with individual results as well as mean ±1 std plotted for comparison. Bland-Altman analysis results are also included in the fourth column.

As seen in the graphs presented in Figure 2-43, the V3D calculated flexion angle during level gait is higher than BVR by a median of 14°. The Bland-Altman plot also shows that as the BVR calculated flexion increases, the difference between V3D and BVR decreases. The flexion profiles between the recorded section of BVR and the V3D angles are generally similar, with a consistent offset.

For both AA and IE during gait, the ranges calculated by V3D are much higher than BVR, reflected in the magnitude of the standard deviations. Despite this, the mean values calculated are similar between the two methods, with an absolute median difference of less than a degree for both angles.

For both BVR and V3D, the mean abduction angle remains around 0° for the central portion of stance phase of gait (where BVR kinematics were available) with a non-descript profile in that section. For three of the participants, absolute values of abduction are within a couple of degrees of the BVR calculated values, but HV003 has higher abduction and HV002 has higher adduction causing the standard deviation to be larger in the V3D than BVR results.

External rotation during gait shows the greatest difference out of the three rotational DOFs due to the large variation calculated from the marker data. For example, in Figure 2-43, the maximum difference found was 17.5° for HV004.

As with level gait, the V3D results for stair ascent show a similar offset from the BVR results, with a median difference of 13° (Figure 2-44). The Bland-Altman plot indicated greater differences at the lowest and highest degrees of BVR flexion, while mid-range flexion values (10-45°) showed more consistent differences. This pattern was also evident in the kinematics graphs, where between ~30-50% of stance phase, both V3D and BVR have a similar rate of decrease in flexion angle, though with a magnitude that is offset.

The largest differences occurred at the start and end of each set of collected BVR results, corresponding to the region of maximum and minimum flexion angles. V3D found the peak of stance during stair ascent to be not only higher in magnitude than BVR but also occurring earlier in the stance phase, increasing the differences observed at peak flexion. Aside from this difference in occurrence of peak flexion, the flexion profiles for each individual were similar between V3D and BVR, just with an offset. Despite HV005 exhibiting a higher flexion angle and a more variable rate

of change during flexion decrease, both V3D and BVR captured the same variation in gradient.

V3D abduction ROM was larger than the BVR ROM, reflected in the Bland-Altman plot where there is a large spread of differences across a small range of BVR abduction values.

Both BVR and V3D mean curves show internal rotation throughout 20-60% stance phase of stair ascent, however BVR calculated greater internal rotation compared to V3D. For the participants where the final 20% of stance phase was captured by BVR, the data shows no further change of internal rotation, whereas the V3D calculated an increase into external rotation in the same period.

Similarly to the other two activities, V3D overestimated flexion during the lunge, with the same median difference as observed for level gait (14°) (Figure 2-45). The flexion profiles were also similar between the two datasets, with peak flexion occurring at a similar percentage of the stance phase for each individual. For example, HV005 reached peak flexion later, as they took longer to lunge than to return upright. This pattern was reflected in both V3D and BVR flexion profiles. HV005 also exhibited the highest flexion of all participants in both datasets, while HV004 had the lowest peak flexion in both. The order of participants by peak flexion magnitude was the same across both methods, supporting the possibility of a consistent offset.

Both V3D and BVR methods found the knee to be adducted on average during the lunge, with both methods showing relatively large standard deviations. V3D generally overestimated adduction during lunge. The adduction of one participant in particular (HV001) was poorly estimated with the BVR approach calculating the greatest adduction out of the cohort, whereas V3D found the same participant to have one of the lowest adduction values, with some abduction for a portion of the lunge.

The knee was found to be externally rotated on average during the lunge, with the V3D pipeline displaying a similar profile to the BVR, however the BVR found greater internal rotation (by a median of 8.4°) with a lower standard deviation. As with other rotations, the accuracy of the V3D-calculated rotation varied between participants. For instance, HV002 had one of the highest BVR internal rotations, but V3D

calculated it to be externally rotated throughout, significantly affecting the overall accuracy of external rotation for this activity.

The distribution of the differences for each rotation during each activity from the Bland-Altman analyses is shown in Figure 2-46, presented as violin plots with overlaid box plots to indicate the median difference and ±IQR, along with any outliers.

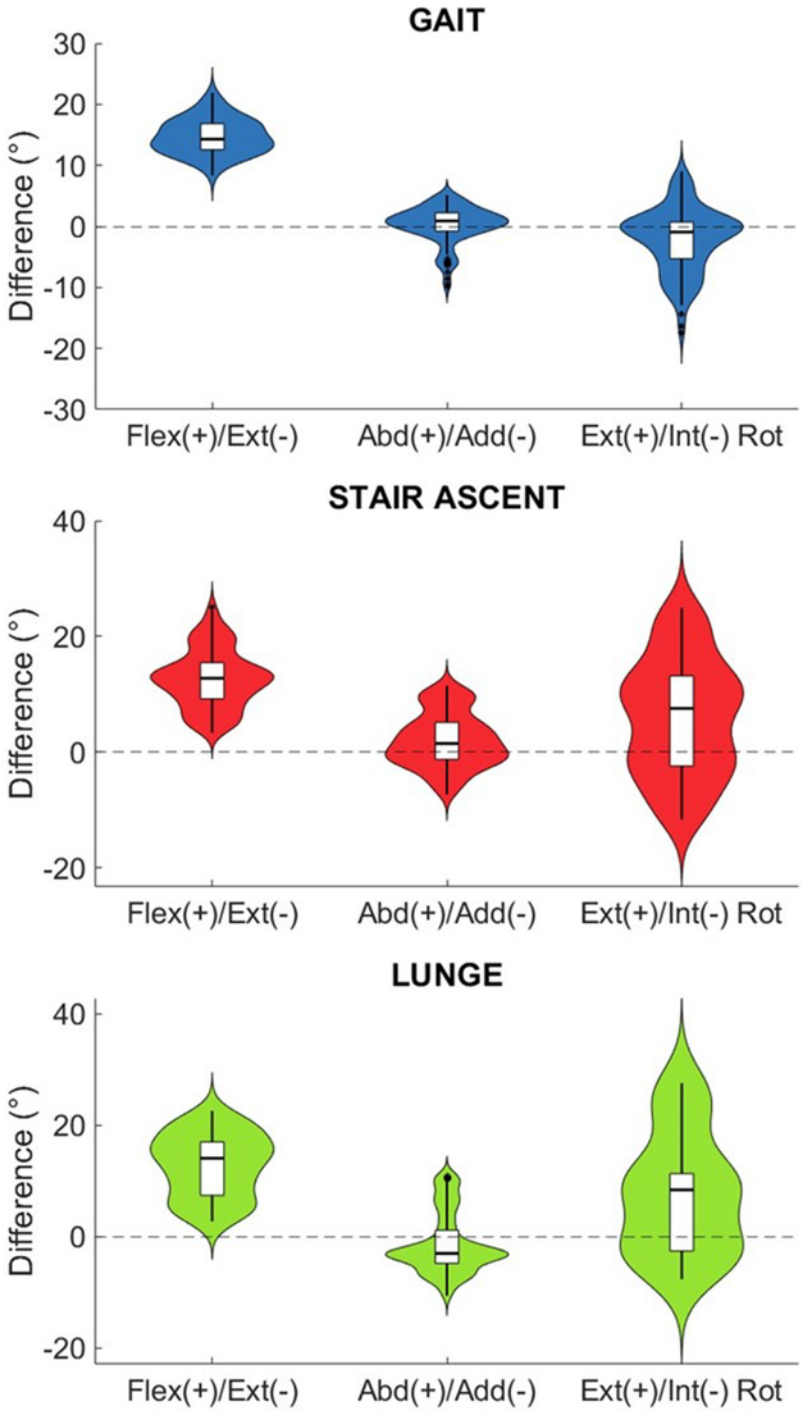

Figure 2-46 - Violin plots with overlayed boxplots showing the distribution of the differences between V3D and BVR rotations during the three activities.(Flex/Ext = flexion/extension, Abd/Add = abduction/adduction, Ext/Int Rot = external/internal rotation)

For all three activities, external rotation exhibited the largest range of differences. While the median difference for external rotation in level gait was within 1°, for the other two activities involving higher flexion, the median difference was overestimated, with a wider distribution. Adduction was the most accurate of the three rotations with the smallest median difference in all three activities. The consistent offset in flexion across the activities is also highlighted in Figure 2-46 by the position of the violin plots relative to the 0° difference.

The limits of agreement (±1.45IQR) in flexion were relatively small compared to the ROM in the sagittal plane, whereas the limits of agreement for abduction and external rotation were much larger relative to their ROM. External rotation, in particular, had a large IQR, highlighting the challenge of estimating this rotation from marker-based motion capture data.

A similar median difference in flexion angle between V3D and BVR derived rotations was seen across all activities (Figure 2-43, Figure 2-44 & Figure 2-45), indicating a consistent offset in calculation of the V3D flexion angles compared to the gold-standard BVR flexion. Although other studies have shown overestimation of flexion from marker-based motion capture data, with maximum errors of 9° (Miranda et al. 2013), the differences found in this study were higher than expected, displaying a constant offset.

To investigate if the offset was due to the marker positioning relative to the bone, as this is a known cause of a constant offset in marker-based motion capture kinematics (Della Croce et al. 1999), the markers were visualised in DSX (HAS-Motion, Canada) as described in Section 2.4.11 (Figure 2-47).

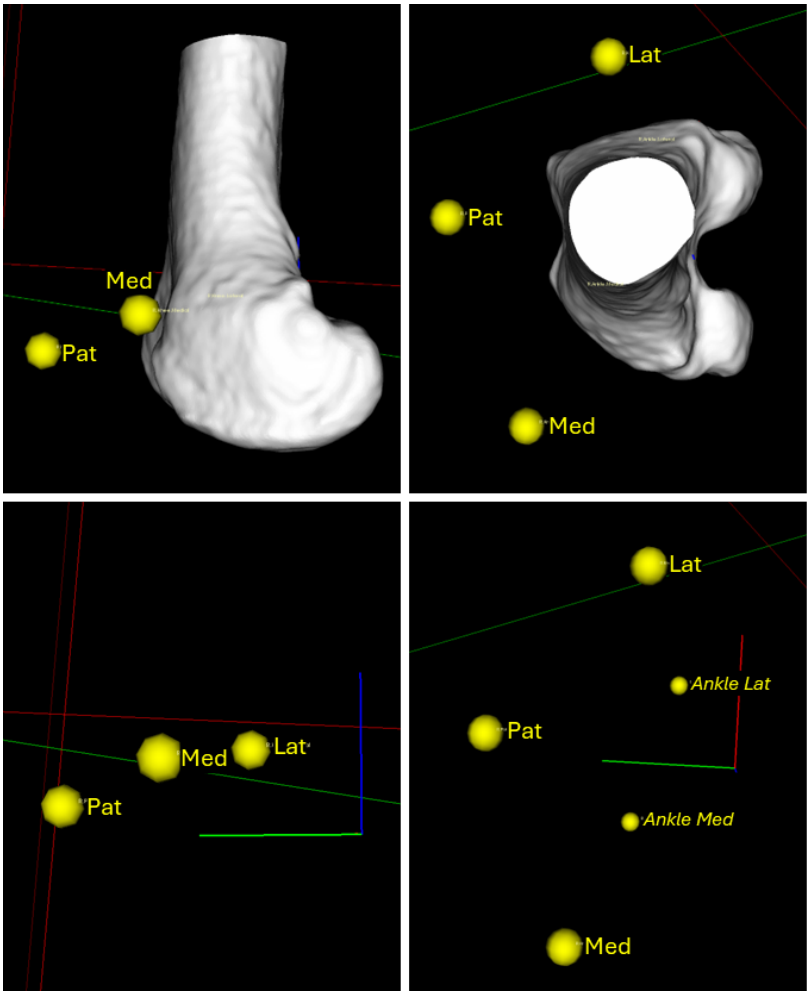

Figure 2-47 – Markers (yellow) visualised in X4D (DSX Suite, HAS-Motion, Canada) relative the BVR femur pose from a single frame of a static trial. The markers are shown with the bone model (above) and the femur ACS (below) from two views (a sagittal view on the left and a transverse view on the right). Marker definitions: Med = medial femoral condyle, Lat = lateral femoral condyle, Pat = patella, Ankle Med/Lat = medial/lateral malleolus.

The anterior offset of the femoral condyle markers relative to the underlying bone, seen in the static trial (Figure 2-47), was also seen during the dynamic trials. This was consistent with the overestimation of flexion seen in the kinematic results from all three activities (Figure 2-43, Figure 2-44 & Figure 2-45). This marker offset creates a more anterior ML axis in the V3D model as compared to the BVR bone model which could explain the consistent overestimation of median flexion observed across all activities.

The V3D outputs are not only showing a systematic error due incorrect marker placement; they are also subject to unpredictable errors in relation to soft tissue artefact. The consequences of these combined errors can lead to incorrect interpretation of joint ROM, a parameter often used as an indicator of joint health and

recovery (Minns 2005; McCarthy et al. 2013; Oka et al. 2020). Furthermore, a higher joint flexion angle, calculated by computational models using this data, would lead to an anterior shift in the joint contact location on the tibial plateau and increased calculated contact forces.

The impact of the femoral condyle marker misplacement was particularly evident in stair ascent at the peak flexion and extension values (Figure 2-44). When markers are placed anteriorly on the skin, their movement differs from the underlying bone, leading to greater soft tissue artefact, particularly as the skin stretches at peak flexion. This explains why the V3D-calculated peak flexion occurred earlier in stance phase, as the anteriorly placed skin markers reach their ‘peak flexion’ location earlier than the actual underlying bone anatomical markers.

The findings of this study are consistent with previous research that has reported the tendency for overestimation of joint angles when using skin markers (Reinschmidt et al. 1997a), particularly for external rotation, which exhibited a large range of V3D-calculated values compared to BVR-calculated rotations (Figure 2-46). Although AA and IE rotations showed good agreement in terms of median differences during gait (Figure 2-43), the ROM in each DOF from the V3D results highlights variable accuracy. In some participants, differences between V3D and BVR calculated joint angles were larger than the magnitude of the rotation calculated from BVR, demonstrating the limitation of marker-based motion capture in estimating secondary knee rotations.

Adduction was the most accurate of the three rotations, with the smallest median difference across all activities. However, the accuracy of AA varied between participants and activities, showing inconsistency in motion capture results. For level gait, AA was generally accurate (median = 0.88°), but the results were skewed by two participants (Figure 2-43); HV002 had the largest adduction angle calculated by V3D, leading to consistently lower differences, below the lower IQR boundary of -3.4°, whereas HV003 exhibited greater abduction in the V3D results but remained within the upper IQR boundary. However, these extremes were not consistent across other activities. For example, during stair ascent and lunge, HV001 had the largest absolute differences in abduction (Figure 2-44 & Figure 2-45), further demonstrating variability in AA calculation.

IE had particularly poor accuracy for stair ascent and lunge (Figure 2-46), with a greater IQR than flexion despite having a much smaller ROM. This suggests that higher flexion activities introduce greater errors in IE, likely due to increased skin motion as the knee flexes. Larger IQRs during stair ascent and lunge were also seen in AA and FE, supporting the suggestion that increased skin-motion during deeper flexion increases marker-based rotation calculation errors. As with other studies, better agreement was found between marker- and X-ray- derived kinematics at lower flexion angles (Tranberg et al. 2011; Hume et al. 2018), demonstrated by the higher median difference and IQR during the stair ascent and lunge activities than during level gait.

The large variation in the differences for the secondary DOFs are mostly due to STA. Skin-marker motion has been shown to vary greatly in relation to the underlying bone motion (Sati et al. 1996; Reinschmidt et al. 1997a; Stagni et al. 2005; Akbarshahi et al. 2010; Tsai et al. 2011), as well as being subject and task dependent (Akbarshahi et al. 2010). These STA errors propagate into the subsequent kinematic results and are evident in the results from the variability and range of differences seen across the participants and activities, showing one of the key challenges associated with skin-mounted markers. As STA errors are not constant, it cannot be accounted for when calculating the kinematics, therefore it remains a known limitation of marker-based motion capture.

The limits of agreement (±1.45 IQR) are low compared to the overall sagittal plane ROM. This is not the same for AA or IE. These findings align with previous research investigating the accuracy of marker-derived TF kinematics, which has also concluded that while marker-based motion capture provides suitable accuracy for measuring flexion, it is not as reliable for the secondary DOFs (Reinschmidt et al. 1997a; Stagni et al. 2005; Tranberg et al. 2011; Miranda et al. 2013; Hume et al. 2018).

Small changes in TF kinematics are often examined when interpreting the impact of injury (Moglo and Shirazi-Adl 2005; Ali et al. 2017) or interventions (Schwechter and Fitz 2012; Clary et al. 2013b; Heyse et al. 2017). However, large percentage errors may limit the usefulness of the secondary rotations for clinical interpretations of gait and dynamic movement analysis (Stagni et al. 2005). This highlights the need for

alternative methods, such as BVR, to measure knee kinematics accurately and thus fully understand bone motion.

From literature, motion capture has been shown to exhibit rotational errors of up to 25°(Akbarshahi et al. 2010) and translational errors of up to 30 mm (Miranda et al. 2013) (Section 1.4.2). In contrast, BVR has demonstrated substantially higher accuracy, with reported errors of approximately 1-2° or less for rotational DOFs and 0.5-1.0 mm or less for translational DOFs (Bey et al. 2006; Anderst et al. 2009; Anderst et al. 2011; Pitcairn et al. 2018; Akhbari et al. 2019; Pitcairn et al. 2020). These differences in accuracy are particularly relevant in the context of clinical decision-making, where surgical tolerances are often small. For example, in total knee replacement, post-operative alignment is typically targeted to within ±3° of neutral mechanical alignment (Abdel et al. 2014). Accuracy differences are also critical in computational modelling, where sensitivity to kinematic inputs has been shown to result in changes in contact force, pressure and contact area of 100-200% with variations as small as ±0.1° or ±0.1 mm (Fregly et al. 2008). Therefore, accurate measurement of in-vivo joint kinematics is essential, along with an understanding of how measurement uncertainty may influence both clinical interpretation and model-based outcomes.

2.5.8 CHALLENGES AND RECOMMENDATIONS

BVR based research involves a number of associated challenges, particularly when developing new protocols to collect high quality data. From this study, the following specific challenges have been identified related to the BVR data collection protocol, including collecting marker-based motion capture in a BVR environment, and the processing of these data. Alongside these challenges are recommendations are suggested to address them.

BVR data capture and processing challenges

The main challenges of developing a BVR protocol are associated with the ability to consistently capture the same portion of the chosen dynamic motions, with the knee clearly visible in both X-ray views for as many frames of motion as possible. This can be broken down further into the following challenges:

Challenge: Only a limited number of frames were obtained during level gait using the current X-ray equipment configuration and the section of stance captured was not consistent.

Level gait is commonly studied using BVR (Kozanek et al. 2009; Gray et al. 2019; Gale and Anderst 2020; Thomeer et al. 2020; Thomeer et al. 2021). Locomotion is a key activity of daily living and it is therefore important to understand the effect of clinical interventions on patient movement including level gait. However, collecting level gait data using a typical BVR setup is challenging due to the large level of knee motion relative to the X-ray volume. Thus a limited portion of the stance phase can be recorded using the current X-ray/camera configuration (mean coverage = 54%, Table 2-6).

In an attempt to address this issue during X-ray capture of level gait in the current study, the final three participants were unblinded to the desired location of their foot placement on the ground reaction force plate, directly beneath the BVR capture volume. A smaller targeted foot placement area on the force plate ensured that the knee was maintained centrally in the X-ray images, (Figure 2-12), and unblinding the participants to target this area improved the consistency of the stance phase coverage.

This study was the first to attempt to collect and quantify knee kinematics data using the new BVR laboratory in Cardiff for comparison with synchronously recorded marker-based motion capture and explore the subsequent impact on outputs and musculoskeletal models. Therefore, although unblinding participants could potentially alter their natural gait; by encouraging targeted foot placement, the benefit of increased data collection outweighed this potential limitation. However, despite this unblinding, a large portion of the stance phase of gait was still not captured, suggesting this could still be improved for future protocols.

Recommendation: Use of a treadmill to capture walking.

Although treadmills have been shown to alter walking patterns compared to level overground gait (Hollman et al. 2016), they have frequently been used to investigate TF kinematics during walking in previous BVR studies (Kozanek et al. 2009; Liu et al. 2010; Barre et al. 2013; Guan et al. 2016; Guan et al. 2017; Yang et al. 2018; Gale

and Anderst 2019; Koo and Koo 2019; Nagai et al. 2019; Gale and Anderst 2020; Byrapogu et al. 2022) as they allow for capture of a larger portion of the gait cycle.

One benefit of the using a treadmill for BVR is the reduced occlusion by the contralateral limb as the source-detector pairs can be oriented around the target limb as the participant will remain in a consistent, central position relative to the equipment. Using a treadmill also reduces the variation in knee location and motion relative to the X-ray capture volume, resulting more frames of gait being captured.

Capturing a greater portion of the activity than is possible with the current overground setup would enable better comparisons between participant cohorts (e.g. healthy vs pathological volunteers). A treadmill offers a compromise between maintaining a natural walking motion and recording a sufficient part of the gait cycle. Therefore, it is recommended for future data collection protocol development and adoption, that an instrumented treadmill is integrated into the activities.

Challenge: Image registration issues caused by occlusion of the target bones by the contralateral limb or the imaged knee partially leaving the X-ray view during dynamic activities.

In adopting BVR for any desired activity, minimising occlusion by the contralateral limb should be integral to the design of BVR configurations to optimise output image quality. When both knees overlap in the imaging volume, the bone outlines become obscured and the edge detection is unusable, making image registration much harder during those frames. BVR configurations should not allow any occlusion of the target limb for accurate definition of bone poses throughout the whole activity, however this is an ideal and, in reality, would not be practical for all activities.

Even in activities that do not involve contralateral limb occlusion, like the lunge, image registration issues may still arise. For example, despite conducting practice trials to ensure appropriate positioning of the knee within the X-ray volume, for some participants, the knee moved partially out of frame during the peak of their lunge. This affected each trial differently, as the difficulty of image registration varied based on how much of the femur and tibia remained in the frame to be matched.

Recommendation: Choosing X-ray equipment configurations to minimise these issues.

Where possible, X-ray configurations should be chosen to avoid occlusion of the contralateral limb by placing the source-detector pairs so the contralateral limb does not cross their path. This is easier to do for activities where the participant does not have to move through the volume perpendicular to the X-rays. For example, performing level gait on a treadmill allows for one X-ray to image the knee from a direct anterior view, which is not possible with overground gait due to the travel required. When this is not achievable, consideration of foot placement and knee location within the volume may help to minimise the occlusion during certain portions of the movement but is not the best option.

To mitigate image registration challenges due to the knee leaving the X-ray view, multiple trial repeats were recorded, and positional adjustments were made between recordings to keep the knee in shot as much as possible. However, there is a tricky balance between ensuing the knee is fully in frame at all times and moving it too far back, which results in capturing less of the activity when the knee is moving from lower to higher flexion angles and only recording the peak lunge as the bones come into shot later in the movement. Therefore, for future protocols it is recommended to practice the movement before X-ray capture, so the participant is confident with the activity, and to capture multiple trials to account for variation in human movement.

Challenge: Inconsistent execution of the lunge activity makes comparison between participants difficult.

By not providing the participant with specific instructions about the length, depth and timing of the lunge, the weightbearing lunge was carried out in an inconsistent manner by participants during this study. Although these individual parameters could be used to differentiate between healthy and pathological cohorts, for example, maximum flexion angle has been shown to be lower in OA patients (Wang et al. 2024), asking participants to aim for their maximum possible lunge may result in overbalancing or falling if they have no additional support. However, if the participant is only asked to lunge as low as they feel confident to, they may not reach the same maximum flexion angle.

Recommendation: Provide more prescriptive instructions or choose an alternative high-flexion activity depending on the research context.

Defining of the purpose of the activity within the protocol relative to the research question being posed will determine what is asked of the participant. If the primary goal of the activity is to understand knee kinematics during a weightbearing functional task that mimics daily life, a lunge still may be suitable choice, particularly if the instructions are given with more specificity – e.g. a specific lunge length or target angle. This should remove some variability from the activity performance and make the results more comparable.

However, when investigating coupling between flexion and the other five DOFs in the TF joint, a more controlled, consistent activity, such as a seated knee extension or open chain flexion, may be more appropriate. For example, a non-weightbearing flexion ROM activity would be more suitable for defining the relationship between flexion and the secondary DOFs.

Challenge: Collection and processing of X-ray static trials.

A further consideration regarding the X-ray data capture is the positioning of the participant's knee relative to the X-ray detectors during the X-ray static trials. For the neutral static data recordings, the static trials proved more difficult to match compared to the dynamic trials captured using the same configurations due to the orientation of the leg.

For the level gait and lunge setups, in order to position the leg within the X-ray field of view and also prevent occlusion by the contralateral limb while maintaining a neutral stance, the leg had to be shifted from a position that would be adopted naturally for each particular dynamic activity. As a result, the camera/X-ray configuration was not optimised for image registration with the knee in a 'static' data capture orientation, leading to inconsistencies with subsequent manual matching of the bone models to the X-ray video frames.

This was not relevant for the stair ascent setup as, initially, a static X-ray capture was taken with the foot on the first step of the staircase with the knee bent. It was later removed from the protocol (for the last three participants) as it was deemed to have limited value because the knee was not maintained in a consistent neutral position (standing extension) or at a consistent angle of flexion. Given its limited benefit with the exposure to ionising radiation, the stair ascent X-ray static was excluded from the protocol.

Recommendation: Capture X-ray static poses with the leg in a similar orientation to its counterpart dynamic movement for a given equipment configuration.

To make image registration between the dynamic and static trials more consistent, where possible, the knee should be positioned in the same orientation as it would be in for a dynamic trial in a given setup. This is only possible for certain X-ray configurations where the contralateral limb will not occlude the target limb in a neutral standing position and is not possible with any of the setups used in this study. For this reason, when designing future BVR protocols, alternative activity setups should be considered for capturing X-ray static trials.

Challenge: Consistent definition of ACSs to describe knee kinematics.

As shown in Section 2.5.5, changing the ACS definition alters the kinematics output from the pipeline. Therefore, it is important to have a consistent approach for describing and defining ACSs and the resulting kinematics. Inclusion of the automated algorithm in this study helped achieve this by removing human inconsistency in ACS application whilst also speeding up this part of the process. However, the algorithm was not consistent when identifying the ACS axes for the initially input partial bone models (Section 2.4.3).

Recommendation: Use automatic algorithms with full bone models (or anatomical landmarks) to generate consistent ACSs between participants.

Using full bone models, or alternatively hip joint centre or medial malleolus ankle landmarks, improved the consistency of the ACS generation by the algorithm. This removed the crosstalk errors between the planes in the subsequent six DOF kinematics calculated.

For this reason, it is recommended that a long leg scan is included for future research to allow for segmentation of the full bone models. If full bone models are not available, inclusion of as much of the bone shaft as possible is recommended, as well as ensuring that the shaft cut is parallel to the femoral condyles or tibial plateau to help the automated algorithm correctly orient the plane used to calculate the axes.

Marker-based motion capture challenges

Challenge: Marker dropout due to BVR equipment blocking camera views.

As this was a pilot study, there were several iterative updates to the data collection protocol with the aim to improve the quality of the output data. For example, the data collection session for the first participant suffered from a large amount of marker dropout due to sub-optimal camera placement. This was associated with occlusion of markers by the BVR equipment.

Recommendation: Optimise camera placement relative to all X-ray equipment configurations.

For subsequent participants, a fully documented, repeatable camera configuration was designed and adopted to ensure markers were clearly visible for as much of the activity as possible, across all activities (Section 2.3.2).

Challenge: Marker placement errors – specifically the femoral condyle markers.

Marker-based motion capture data are always subject to the inherent errors associated with STA and marker placement. However, in particular for this study, the anterior placement of the femoral condyle markers relative to the underlying bony condyles, resulted in large overestimates of TF flexion in all activities (Section 2.5.7). This highlights the importance of careful marker placement to minimise these errors. To locate the femoral condyles, participants were asked to perform a seated knee flexion-extension whilst the researcher palpated to locate the anatomical, bony landmarks, and then then the markers were placed on the flexed knee. However, the palpated marker locations could shift anteriorly when the participant stood upright, thus relocating the markers relative to the underlying bony condyles.

Recommendation: Palpate femoral condyle markers whilst the participant is standing.

To minimise the error associated with the overestimation of flexion, it is therefore recommended for future data collection protocol development and adoption, that the femoral condyles are palpated and located on the standing subject with markers placed on the extended knee.

Other study limitations

As well as the challenges associated with the BVR and motion capture data collection and processing, there were also some limitations to the current study.

Limitation: The accuracy of the new BVR system at Cardiff is currently unknown.

Although BVR accuracy has been shown to be within two degrees and millimetres for calculating TF kinematics (Li et al. 2008; Anderst et al. 2009; Guan et al. 2016), the accuracy of each specific system can vary (Section 1.4.1). Because the BVR system at Cardiff was custom built, the accuracy of this system for calculating TF kinematics for the configurations and activities used in this study is not yet known. To better understand the true fidelity of the 'gold-standard' data used in comparisons with motion capture, future studies should analyse the accuracy of this equipment and its configurations, potentially through comparison with implanted beads or roentgen stereophotogrammetric analysis (RSA) (Section 1.2.4). RSA is a commonly used technique for determining model-based image registration accuracy (Setliff and Anderst 2024) as it involves comparing bone poses from the standard pipeline to bone positions calculated by tracking radiopaque implanted beads. The bead positions can be determined with greater accuracy as they do not suffer from errors in the model geometry or bone edge definition in the images. RSA could also be used to quantify the impact of occlusion on image registration, as well as quantifying the accuracy of the setup for calculating the kinematics more generally.

Limitation: Small dataset.

One of the main limitations of this study is the small dataset of only five participants. BVR studies typically involve small cohorts, with 77% of BVR studies between 2004 and 2022 including 20 or less, due to the high cost and long time required for processing – estimated to be between 40 and 80 hours per BVR data collection session (Setliff and Anderst 2024). However, as the overall aim for this thesis was development of the methods and pipelines to more fully utilise the outputs from the new BVR system, only a small pilot dataset was required to establish these protocols.

Future studies utilising these protocols to answer clinically relevant questions should try to include a greater number of participants to be able to draw statistically significant conclusions. With a variety of emerging automated approaches for image segmentation (Ridhma et al. 2020) and image registration (Miranda et al. 2011; Lin et al. 2018; Burton et al. 2024), automatic methods with sufficient accuracy could be integrated into the pipeline to enable these larger datasets by reducing the number of hours of manual intervention required.

Limitation: Patellofemoral kinematics ignored in this study.

Due to time restrictions, this study was limited to investigating TF motion only. However, these techniques could be extended to include patellofemoral (PF) joint kinematics investigations. Image registration of the patella could be performed on the existing data set to investigate the relationship between TF and PF kinematics during dynamic movements.

Since the pilot protocol was originally designed for the TF joint, it is not optimised for patella matching, making image registration more challenging. Additionally, because the patella is a sesamoid bone, accurately determining rotations is more complex compared to the femur or tibia which have more distinct shapes and edges. For focused PF kinematics investigation, alternative X-ray and motion capture equipment configurations should be considered to obtain clearer images of the patella and minimise overlap with the femur.

2.6 CONCLUSION

A protocol for collecting and processing simultaneous BVR and marker-based motion capture data, along with generating 3D bone models from MRI, has been developed and defined, for three functional activities, as demonstrated by the successful calculation of six DOF TF kinematics. The protocol was successfully applied to multiple participants, highlighting its potential for future research. By incorporating three different dynamic activities, the protocol proved capable of imaging the knee across a range of flexion angles, with the potential for expansion to include other activities, such as treadmill walking or step-down, to further investigate typical knee kinematics. It also has the potential to be utilised with pathological

cohorts to assess how injury or disease affects the joint, as well as the effects of potential interventions.

The BVR-derived kinematics from this study were compared with existing literature and generally agreed with previous findings. For example, flexion angles during both level gait (Figure 2-33) and stair ascent (Figure 2-35) were consistent with both the magnitude and profile reported in prior studies, with AA displaying the smallest ROM in these activities (Kozanek et al. 2009; Tsai et al. 2011; Li et al. 2012; Myers et al. 2012; Suzuki et al. 2012; Li et al. 2013; Kefala et al. 2017; Gale and Anderst 2020; Thomeer et al. 2021; Hamilton et al. 2023). The mean internal rotation was shown to increase with flexion during all three activities, also agreeing with previous studies (Leszko et al. 2011; Tsai et al. 2011; Li et al. 2012; Hamai et al. 2013; Kefala et al. 2017; Thomeer et al. 2021; Hamilton et al. 2022).

TF translations were found to have similar magnitudes to those in literature (Kozanek et al. 2009; Qi et al. 2013; Kefala et al. 2017; Gray et al. 2019; Thomeer et al. 2020; Thomeer et al. 2021; Hamilton et al. 2022; Hamilton et al. 2023). However, substantial variation was observed across participants and activities; also commonly seen in the literature. This variation is likely due to differences in individual coordination strategies, as well as the small magnitudes of the translations, which can cause potentially larger proportional inaccuracies in the results.

The BVR-derived TF rotations were also compared with the marker-based motion capture rotations, calculated using V3D (HAS-Motion, Canada). These results (Figure 2-43, Figure 2-44, Figure 2-45) showed a systematic offset of the flexion angle calculated between the two methods which was due to consistent anterior marker misplacement relative to the underlying femoral condyles. This highlights the difficulty of correctly locating and placing the markers relative to the anatomical landmarks. AA and IE displayed greater variability in their results compared to flexion, with large percentage errors relative to their planar ROM, particularly at higher flexion angles. This illustrates the influence of STA on marker-derived kinematics, along with variation across different participants and activities, making it challenging to correct for.

The errors in marker-based motion capture rotations, caused by marker misplacement and STA, have potential implications for use in clinical decision-

making, as well as for models derived from this data, such as joint contact models. This highlights the need for alternative methods to calculate joint kinematics from motion-capture data, especially where an alternative such as BVR is not viable, as well as careful consideration of the possible errors when interpreting such data.

Overall, the aims for this chapter, which were set out in Section 1.8, were achieved. Simultaneous BVR and marker-based motion capture were successfully captured during multiple dynamic activities. These data were processed using the developed pipeline, which combined model-based image registration with MRI-derived bone geometries to calculate six DOF TF kinematics. The data collection and processing workflow was implemented for the first time in a cohort of healthy participants, demonstrating its potential for future studies investigating knee pathology and intervention outcomes. Together, the imaging datasets and BVR kinematics produced in this chapter provide the foundation for the subsequent modelling components of the framework, bridging the experimental and computational aspects of this work.

CHAPTER 3: DO PERSONALISED GEOMETRIES IMPROVE KNEE KINEMATIC AND JOINT CONTACT PREDICTIONS IN MUSCULOSKELETAL MODELS?

3.1 INTRODUCTION

3.1.1 BACKGROUND

Musculoskeletal modelling (MSM) enables estimation of dynamic in-vivo muscle activations, joint kinematics and forces, making it a valuable tool in both clinical and research settings (Cardona and Garcia Cena 2019; Luis et al. 2022). Such models enable quantification of internal mechanics that are otherwise difficult or impossible to measure directly using in-vivo methods, such as muscle forces, joint torques, and joint contact forces during movement (Erdemir et al. 2007; Pandy and Andriacchi 2010; Cheze et al. 2015; Moissenet et al. 2017).

MSMs have been widely applied to explore conditions such as stroke and osteoarthritis (OA), providing insights into altered neuromuscular control and joint loading patterns (Lin and Yan 2011; Kumar et al. 2013; Dzialo et al. 2019; Price et al. 2020; Ghazwan et al. 2022; Giarmatzis et al. 2022; Wang et al. 2022; Bowd et al. 2023). In particular, altered joint contact loading has been associated with OA progression (Richards et al. 2018; Dumas et al. 2020; Yamagata et al. 2021), reinforcing the importance of accurate joint-level estimations.

Typically, MSMs rely on motion capture data to provide external kinematic inputs, but as discussed previously (Section 1.4.2 and Section 2.5.7), marker-based motion capture cannot accurately measure the smaller rotational and translational degrees of freedom (DOFs) of knee motion. Motion capture data alone cannot measure noninvasively more complex biomechanical data, such as these secondary joint kinematics, as well as resulting joint tissue forces stresses and strains (Lloyd et al. 2023).

One approach aiming to overcome these limitations is the OpenSim-Joint Articular Mechanics (JAM) (https://github.com/clnsmith/opensim-jam/) framework (Chapter 1, Section 1.6.2) which utilises specialised articular contact representations (Lenhart et al. 2015) to estimate joint kinematics (which cannot be reliably measured form

motion capture), muscle activations, joint contact forces, and pressure distributions within the knee (Smith et al. 2016). To have confidence in predictions from such models, it is important to use benchmark data to ensure the quality of model outputs (Lloyd et al. 2023).

Since direct in-vivo measurement of joint contact pressure, joint contact forces and muscle forces are not possible in intact human knees, model outputs must be validated using alternative measurable parameters – such as kinematics. Biplane videoradiography (BVR) provides gold-standard, highly accurate six DOF kinematics (Li et al. 2008; Anderst et al. 2009; Miranda et al. 2011; Guan et al. 2016; Gray et al. 2017; Gray et al. 2018; Setliff and Anderst 2024), providing a suitable benchmark for MSM validation. As joint mechanics are highly sensitive to bone positioning (Yao et al. 2008), such validation is important when using previously benchmarked models to observe generalised trends. But it is even more important when considering personalised models to investigate subject-specific predictions against subject-specific data to understand the true predictive capabilities of the model on an individual level (Smith 2017).

As well as providing a direct measure of individual bone motions, BVR also enables investigation of joint contact in the knee, utilising bone poses to directly calculate contact mechanics (Anderst and Tashman 2010; Hoshino and Tashman 2012; Li et al. 2013; Thorhauer and Tashman 2015). Again, these BVR outputs can be used as a comparator to assess MSM pipelines to understand knee joint contact mechanics.

A key question in improving model fidelity is whether including subject-specific anatomical detail, particularly bone and cartilage geometry, enhances the accuracy of predicted joint mechanics. While personalisation may improve estimates of joint kinematics and contact, it requires additional imaging, segmentation, and processing, making it more time-consuming and technically demanding than using generic geometries. Recent developments to the Opensim-JAM modelling pipeline have included creating personalised MSMs with personalised contact geometries (Killen et al. 2024), aiming to further improve the accuracy of the model's predictions. It is therefore important to investigate whether the added complexity of incorporating personalised joint geometry leads to meaningful improvements in joint contact predictions, and if these gains are significant enough to justify the increased effort.

3.1.2 AIM & OBJECTIVES

The main aim of this research was to test the hypothesis: does including personalised contact geometries improve MSM estimates of TF kinematics and contact pressures?

To answer this question fully, the following key research questions were proposed:

1. Does adding personalised TF geometries improve model estimates of TF kinematics during level gait compared to a model with generic contact geometries, when validated against gold-standard BVR kinematics?
2. Are MSM contact pressure maps more similar to BVR maps when using personalised or generic contact geometries in the model?
3. Do the observed differences between the personalised and generic model outputs reported during gait carry over to activities involving higher TF flexion angles?

To answer these questions, the following objectives were defined:

- To generate MSMs incorporating personalised TF contact geometries.
- To apply the OpenSim-JAM MSM pipeline to multiple activities for both the standard ‘generic’ model and the model with the personalised geometries incorporated.
- To generate equivalent joint contact maps using bone poses from BVR.
- To compare the kinematic and contact pressure outputs from the generic and personalised versions of the MSM to assess the accuracy and benefit of model personalisation.

3.2 METHODOLOGY

The data collection protocol used to generate inputs for the following pipeline was described in Chapter 2.

The participant data used in this chapter was the same as described previously (Chapter 2), with the exception that HV001 was replaced by a new participant, HV006. HV001's motion capture data had known issues (Section 2.3.2), so a new participant with improved data quality was used to ensure a fair comparison across all datasets.

The demographics for the participants used in this chapter (including the new participant) can be found in Table 3-1.

Table 3-1 – Participant demographics

Participant ID	Sex	Age (years)	Height (cm)	Weight (kg)
HV002	F	57	169.5	62.4
HV003	M	54	182.0	87.5
HV004	M	52	176.5	67.1
HV005	F	47	158.5	51.0
HV006	M	54	174.0	84.7

3.2.1 THE GENERIC MODEL

The MSM used for this study was the generic OpenSim-JAM model (Lenhart et al. 2015). Figure 3-1 shows the full body model which was based on a lower limb model containing a six DOF TF joint, a six DOF patellofemoral joint, a six DOF pelvis, a three DOF ball-and-socket hip joint and a one DOF hinge joint representing the ankle (Arnold et al. 2010).

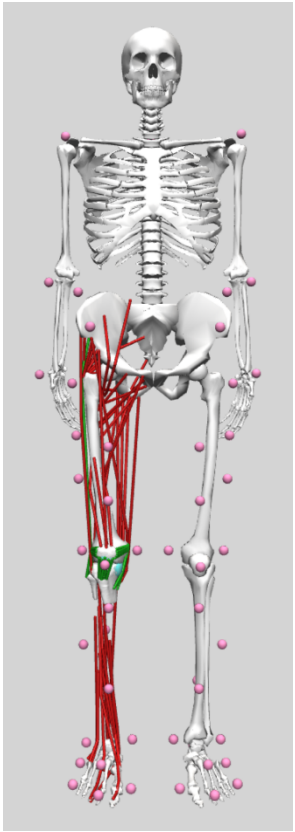

Figure 3-1 – The generic model used for this study (Lenhart et al. 2015)

The model represented muscles acting about the right hip, knee and ankle joints using 44 damped equilibrium musculotendon units (Millard et al. 2013; Lenhart et al. 2015). The equilibrium musculotendon model is a variation of the Hill-type model (Section 1.6) commonly used in MSM simulations of human movement (Millard et al. 2013). Whereas in the standard Hill-type model the force generated by a muscle is dependent only on the current muscle length, velocity and activation (Zajac 1989), the equilibrium model expands on the model by adding a nonlinear elastic tendon component, alongside the active contractile element and passive elastic elements contained in a standard Hill-type model. Muscle force was calculated based on the force-length-velocity relationship, varying nonlinearly with muscle stretching. Each muscle force was assumed to be a scaled version of its representative fibres (Millard et al. 2013). A damping coefficient of 0.1 was applied to the normalised muscle velocity component of the equation to stop numerical singularities being reached, reducing the simulation time (Millard et al. 2013).

Specialised contact geometries were incorporated into the right knee of the model, including the bone and cartilage geometries of the distal femur, proximal tibia and patella segmented from MRI scans of a 23-year-old female (Lenhart et al. 2015). The femoral skeletal and cartilage geometries were aligned with the femoral geometry of the base model (Arnold et al. 2010), and tibial and patellar geometries were placed just [contacting] the femoral surfaces in an upright position (Lenhart et al. 2015). These meshes were used to calculate contact pressures using an elastic foundation model described in more detail below (Section 3.2.3).

Also segmented from MRI, the major ligaments in the right knee were represented in the model by 14 bundles – including the superficial and deep medial collateral ligament (MCL), lateral collateral ligament (LCL), anteriomedial and posteriolateral anterior cruciate ligament (ACL), anteriolateral and posteriomedial posterior cruciate ligament (PCL), and patella tendon. Each bundle contained between 5-8 elements, apart from the iliotibial band which was represented by a single element (Lenhart 2015). The ligaments were modelled using the Blankevoort model (Section 0) which assumes a nonlinear relationship at low strains and a linear region above a linear strain limit of 0.03 (Butler et al. 1986; Blankevoort and Huiskes 1991).

For the purpose of this study, this model was considered as the ‘generic’ model as the geometries remained consistent across all participants, although the model was tailored to each participant via a standard scaling procedure.

3.2.2 ADDITION OF PERSONALISED GEOMETRY

After scaling the ‘generic’ model, a ‘personalised’ version of the model was created for each participant by swapping the generic contact geometries with a personalised representation of the bones and cartilage surfaces of the knee (Killen et al. 2024).

Bone and cartilage geometries of the distal femur, proximal tibia and patella were segmented from a high-resolution MRI scan with clear delineation between bone and cartilage (Section 2.2). Geometries were segmented using a semi-automatic thresholding approach, followed by manual refinement where necessary. For earlier participants, these geometries were segmented from a DESS-3D scan, but this was later replaced with a T1-VIBE scan as it produced a clearer boundary between articular cartilage structures (Section 2.4.1).

Once segmented, bone and cartilage geometry models were smoothed using a recursive Gaussian filter with a standard deviation of 2.0. The geometries were meshed within Simpleware Scan IP (Synopsis, United States) using a standard in-built meshing procedure. All models were then exported as surfaces (.stl files) to match the format required for the MSM.

In the OpenSim-JAM MSM (Section 3.2.1), the contact cartilage geometries were represented by single-surface geometries of only the contacting region where all triangle normals were pointing toward the direction of contact. Therefore, articular cartilage surface meshes were reduced to only this surface by manually selecting the desired region and smoothing the newly created edge (MeshMixer, Autodesk Inc., USA) (Figure 3-3).

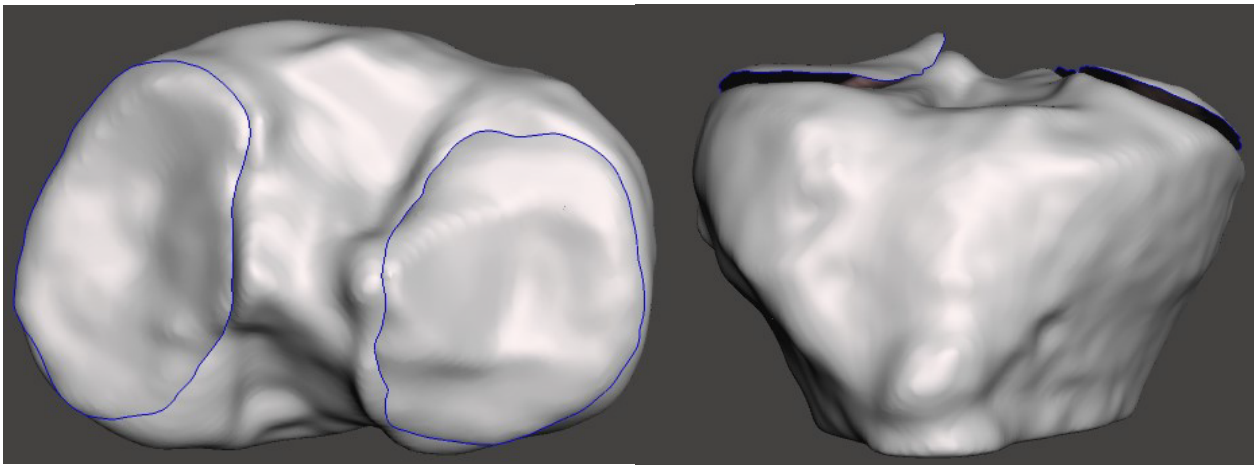

Figure 3-3 – Example of the tibial plateau cartilage contact surface isolated with the boundary (blue) smoothed.

Normals of the tibia and patella cartilage surfaces were then visually checked in MeshLab (Cignoni et al. 2008) (Figure 3-2) as any that were not aligned with the contact direction would cause erroneous forces resulting in the model being unable to solve. Any elements with unsatisfactory normal directions were manually removed. As they only occurred around the mesh boundary (i.e., in non-contacting regions), they could be removed without affecting the rest of the geometry.

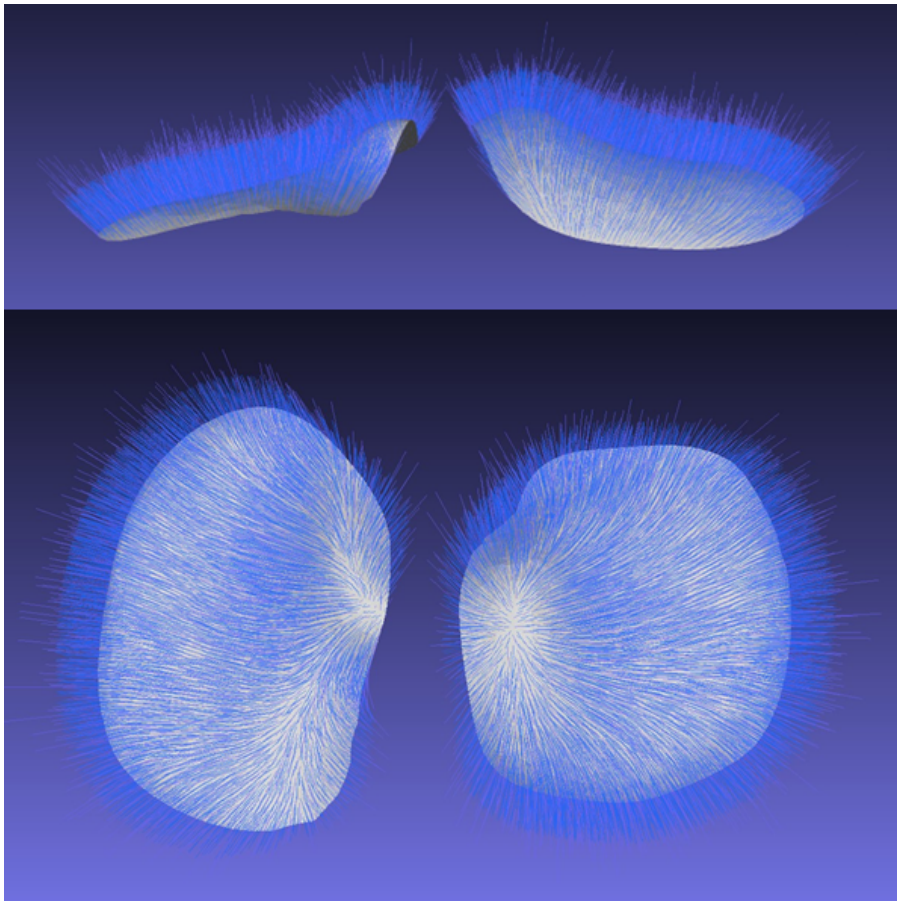

Figure 3-2 – Visualisation of the triangle normal directions in MeshLab.

The number of elements in the final meshes were then reduced using a quadratic edge simplification algorithm (MeshLab) to assist with computational time when calculating element-wise contact. All three cartilage meshes were reduced so they contained a similar number of elements to the original ‘generic’ geometries (i.e. around 30k, 8.5k, and 6k elements for the femoral, tibial and patellar cartilage respectively).

Once the surfaces were prepared, an open-source framework was used to implement the personalised model geometries (Killen et al. 2024). This framework involved three main steps: registration and positioning of the personalised geometries, morphing and optimisation of the muscle and ligament pathways, and calibration of the new muscle and ligament parameters (including resting, optimal fibre and tendon slack lengths).

For the first step, the MRI femur bone model was transformed to match the OpenSim axes convention by defining manually selecting points on a 3D visualisation of the bone to define the medial-lateral (ML), anterior-posterior (AP) and superior-inferior (SI) directions which were mapped to the OpenSim convention (i.e. X = AP, Y= SI, Z = ML). The rotated segmentation was smoothed and remeshed to 500 faces to allow for alignment with the full femur bone geometry from the generic model. This alignment was achieved by firstly translating the bone to an arbitrary centre point (based off the average position of all vertices) which was placed at the origin (0,0,0) point of the full femur geometry (the femoral head), then the partial femur segmentation was coarsely aligned with the distal part of the full femur model using the midpoint of the model’s femoral condyle markers, before finally, an iterative point algorithm was used to more accurately align the models (Figure 3-4) (Killen et al. 2024). The same transformations were then also applied to the tibia and patella bone models, and all cartilage geometries, as well as selected manually defined landmarks on the original MRI segmentation, so the geometries remained positioned relative to one another (Figure 3-4).

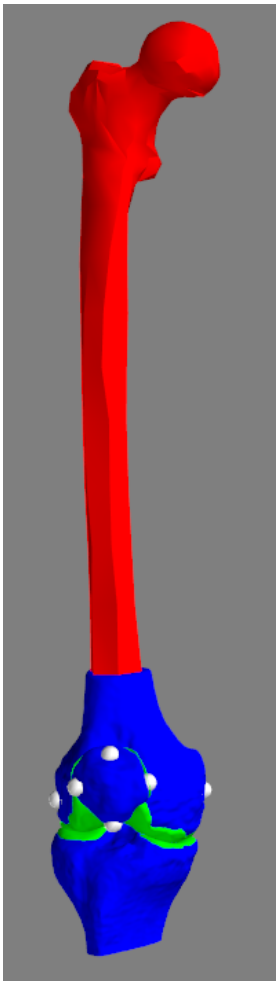

Figure 3-4 – Alignment of the personalised distal femur (blue) and the generic full femur (red) with the other personalised geometries placed relative to the femur. The defined landmarks are shown in white.

The following landmarks were defined for each participant: medial and lateral femoral condyles, as well as superior, inferior, medial and lateral points on the patella (Figure 3-4). To maintain consistency between participants, the femoral condyle landmarks were defined as the points on the ML axis, as defined by the automated ACS code (Miranda et al. 2010), where the bone geometry intersected on either side. Patella landmarks were defined by calculating an ACS based on the segmented bone geometry using another automated algorithm (Rainbow et al. 2013), then selecting the bone intersections between the SI axis and ML axes to define the four points. These landmarks were then used to define the femoral and patellar ACSs in the model; as is the case in the generic model, the tibial ACS was set as coincident with the femoral ACS.

Muscle, ligament, and wrapping points were embedded as passive points within this host-mesh and morphed, together with the bone geometry, using an atlas-based

fitting approach (Zhang et al. 2014). Muscle and ligament attachment points were then projected onto the closest points on the personalised bone mesh.

Muscle and ligament path wrapping surfaces were also optimised to address muscle and ligament path discontinuities by altering their position and orientation to best match the muscle and ligament length changes of the reference ('generic' scaled) model (Killen et al. 2020).

Finally, the muscle and ligament parameters were calibrated to ensure both the passive and dynamic behaviour of the knee were physiological and comparable to the reference ('generic' scaled) model. The ligament resting lengths and tendon slack lengths were optimised to best match the strains between the personalised and reference models, and the optimal muscle fibre lengths were calibrated to match between the models (Modenese et al. 2016; Killen et al. 2024).

3.2.3 MUSCULOSKELETAL MODELLING PIPELINE

The pipeline was implemented in OpenSim version 4.1 (Delp et al. 2007; Seth et al. 2018) and was applied to all five participants (for the same repeat of the three activities presented in Chapter 2 for HV002-HV005), firstly with the 'generic' model (Section 3.2.1) and then again using the 'personalised' model (Section 3.2.2). Both versions of the model had the rigid-body segments scaled based off the distance between markers from the same standing static motion capture (Section 2.3).

The marker trajectories for the static and dynamic trials were tracked and exported along with the ground reaction forces (Qualisys Track Manager, Qualisys, Sweden, & Visual3D, C-motion Inc., Maryland, USA) as described in Chapter 2 (Section 2.4.8).

An overview of the OpenSim-JAM (https://github.com/clnsmith/opensim-jam/) MSM pipeline that was used in this study is presented in Figure 3-5. This pipeline is centred around the Concurrent Optimisation of Muscle Activations and Kinematics (COMAK) algorithm and relies on the concept of measurable (primary) and unmeasurable (secondary) DOFs from marker-based motion capture data (Smith 2017).

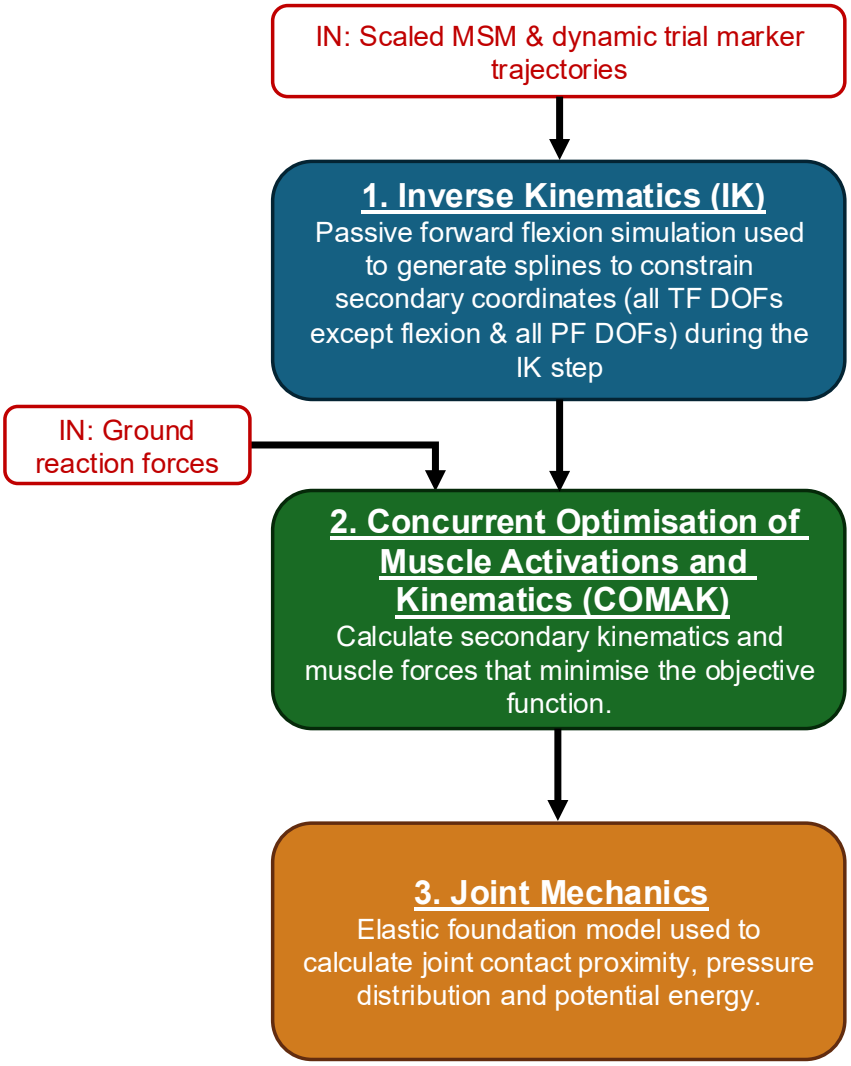

Figure 3-5 – Overview showing the three main steps of the OpenSim-JAM MSM pipeline used to calculate joint kinematics and contact pressure maps. In-vivo data inputs are shown in the red boxes. More detailed diagrams for each of the three steps can be found in Figure 3-6, Figure 3-7, and Figure 3-8.

The aim of the COMAK algorithm is to generate secondary kinematics, muscle forces and ligament and contact moments that allow for the primary DOFs to be prescribed as observed from the motion capture-derived kinematics, with the primary DOF joint moments balanced by the muscle forces. As discussed in Section 1.4.2, standard calculation of marker based motion capture knee kinematics have been shown to be reliable for calculating flexion-extension (FE), but less accurate for internal-external rotation (IE), abduction-adduction (AA) and all three translational DOFs due to the size of the errors relative to the magnitude of the DOF ranges of motion (ROMs) (Reinschmidt et al. 1997a; Akbarshahi et al. 2010; Tranberg et al. 2011; Miranda et al. 2013; Hume et al. 2018). COMAK utilises this concept, defining TF flexion as a 'primary' DOF (as well as the three rotations at the hip and ankle

dorsiflexion) and all the other five TF DOFs, along with all six patella DOFs, as ‘secondary’ DOFs. A third model DOF definition, ‘prescribed’, was used to define all other joint DOFs. Like primary DOFs, prescribed DOFs were set to their observed values from motion capture, however, they were not used to inform the secondary kinematics.

When running the pipeline on the dynamic trial data, an issue was encountered with the lunge activity from one individual (HV005) where the model became unstable near the peak of the lunge due to the patella dislocating. To enable the model to produce physiologically realistic results, all six DOFs of the patella were changed from secondary coordinates to prescribed coordinates. This issue may have arisen because this participant exhibited the highest flexion angle during the activity, potentially exceeding the model’s functional limits as, when developed, the model was assessed against cadaveric data up to 90° and in-vivo data up to 50° (Lenhart et al. 2015). As the focus of this study was TF contact rather than patellofemoral (PF) mechanics, this solution was considered an acceptable compromise. However, future investigations involving high knee flexion may require modifications to the model to ensure stability in such cases.

Inverse Kinematics

The first step of the MSM pipeline is shown in more detail in Figure 3-6. Before performing the inverse kinematics routine, a passive forward flexion simulation generated splines defining the relationship between the secondary kinematics relative to TF flexion angle. For this forward flexion simulation, the model was first stabilised into an initial neutral position, then the knee was moved steadily from 0° to 120° flexion whilst the muscles were set to produce 1% of their maximum isometric force. Muscle activations were set to 1% to simulate passive flexion as this is minimum activation value used with the muscle model to stop the singularities in the equations from being approached as this would significantly slow down the numerical integration (Millard et al. 2013). During at each flexion angle dynamic equilibrium was achieved by adjusting secondary TF and PF coordinates to balance the calculated ligament and cartilage contact forces and moments at each step.

A global optimisation inverse kinematics routine was then used to generate the primary and prescribed coordinates (q), velocities ($\dot{q}$), and accelerations ($\ddot{q}$) by minimising the difference between the model and measured marker positions at each time step.

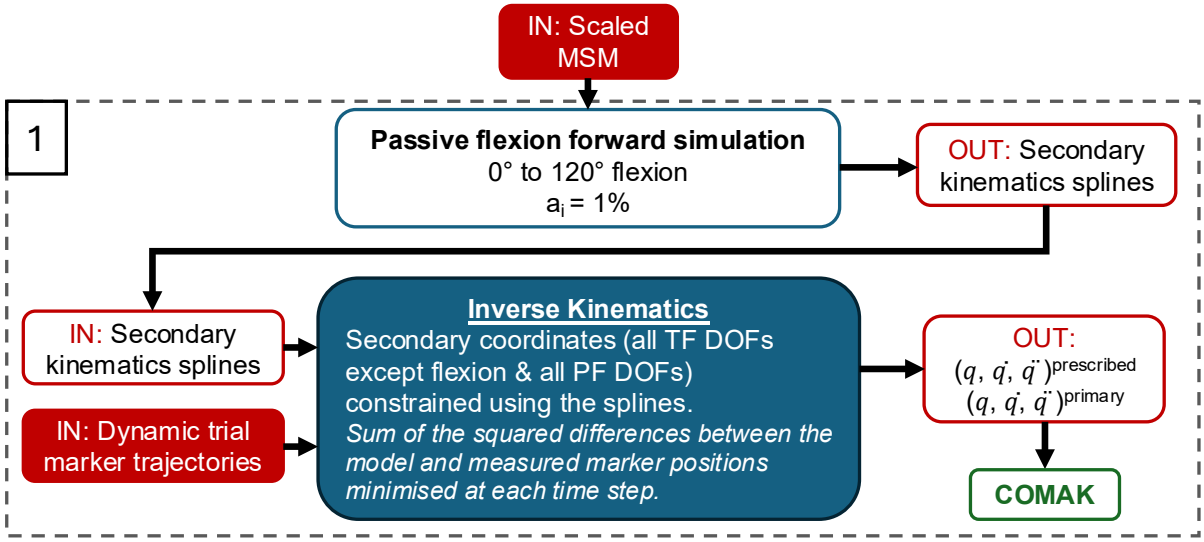

Figure 3-6 – Overview of the main inputs and outputs of the inverse kinematics step from Figure 3-5, including the prior passive flexion simulation.
a_i = muscle activations, and q, $\dot{q}$, $\ddot{q}$ = coordinate, velocity and acceleration, respectively.

Concurrent Optimisation of Muscle Activations and Kinematics (COMAK) Algorithm

The inverse kinematics results were then used as an input into the COMAK algorithm (Figure 3-7). Firstly, primary and prescribed coordinates and velocities, as well as the prescribed accelerations, were used in a forward settling simulation to generate a stable initial model position, including secondary coordinates values, for the first frame of the dynamic motion.

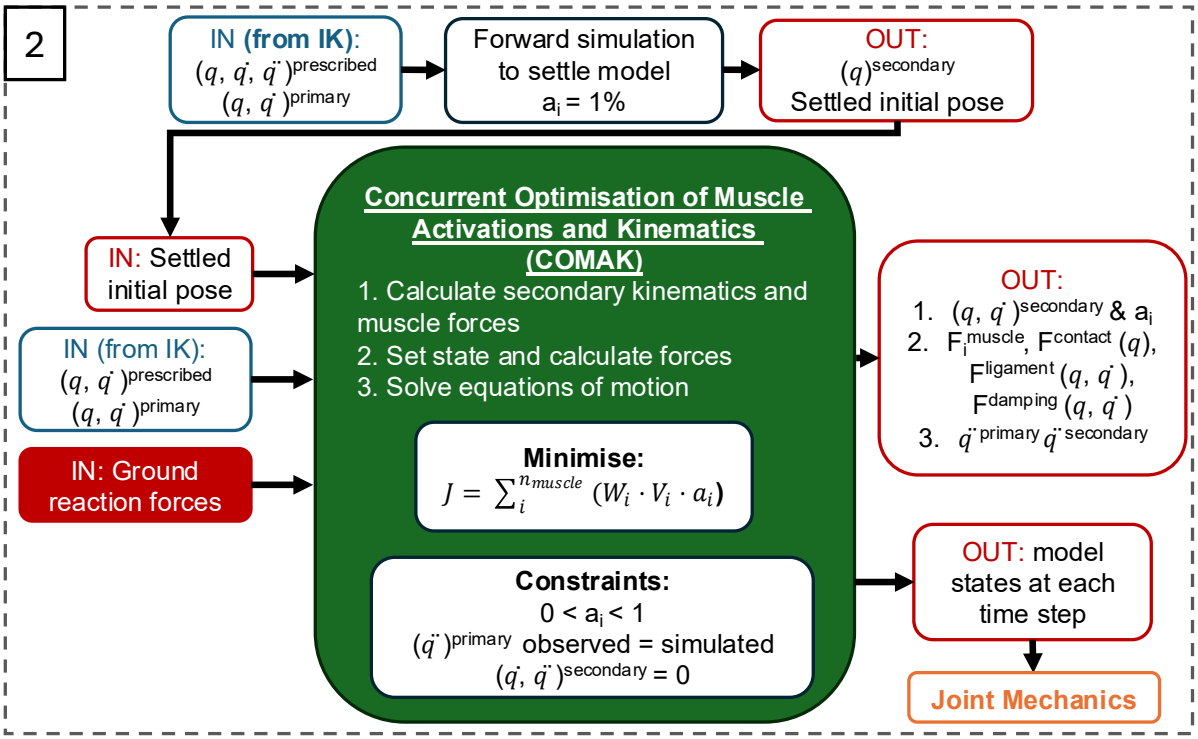

Figure 3-7 - Overview of the main inputs and outputs of the COMAK step from Figure 3-5.
a_i = muscle activations, J = objective function, W_i = muscle weightings, V_i = muscle volumes, F = force, q, $\dot{q}$, $\ddot{q}$ = coordinate, velocity and acceleration, respectively

For all subsequent frames of motion, the prescribed and primary coordinates and speeds were set to their observed values (from the inverse kinematics solution). The algorithm then iteratively solved to find values for the secondary coordinates and muscle activations that minimise the objective function (Equation 3-1) at each frame, whilst adhering to specific constraints.

$$J = \sum_{i}^{n_{muscle}} (W_i \cdot V_i \cdot a_i^2) \qquad \textit{(Eq. 3-1)}$$

Where W_i = muscle weightings, V_i = muscle volumes, a_i = muscle activations

All model states were required to satisfy the following constraints to ensure they were physiologically reasonable:

1. Muscle activations must be between 0 and 1 ($0 < a_i < 1$) to maintain physiological realism.

2. Primary accelerations must match their values from the inverse kinematics results to replicate the dynamic movement.

3. Secondary kinematic velocities and accelerations were set to 0 to stop unrealistic accelerations and keep the motions smooth.

During each iteration of the COMAK algorithm, once the secondary coordinates and muscle activations were determined, and the model state was set, the generalised forces were calculated and applied; this included the contact, ligament, damping, muscle, and external forces. The equations of motion were then solved for the primary and secondary accelerations, whilst the prescribed accelerations were constrained to their measured values.

Joint Mechanics

The output model states at each frame were then used to provide a more detailed analysis of element-level joint mechanics of the contact meshes of the knee (Figure 3-8). This was done using a hierarchical bounding boxes and ray tracing method (Thelen et al. 2014) to implement a nonlinear elastic foundation formulation (Bei and Fregly 2004) to calculate the pressure on each face in the mesh (Smith et al. 2018).

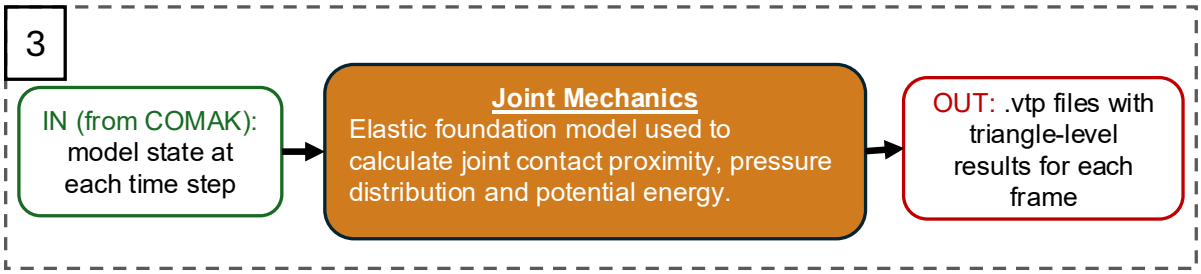

Figure 3-8 - Overview of the main inputs and outputs of the Joint Mechanics step from Figure 3-5.

For the bounding box and ray tracing method, rays were traced from each element of the ‘casting’ mesh (the mesh with fewer elements, in this case tibial cartilage) towards the other mesh to determine overlap.

The other mesh (the femoral cartilage) is broken down into an oriented bounding box (OBB) tree containing a hierarchy of boxes each representing different sections of the mesh. Firstly, a box was created that tightly surrounded the whole femoral cartilage mesh, then the mesh was iteratively bisected into smaller regions (with roughly half the elements in each section), until the leaf nodes (individual faces) were reached (Figure 3-9).

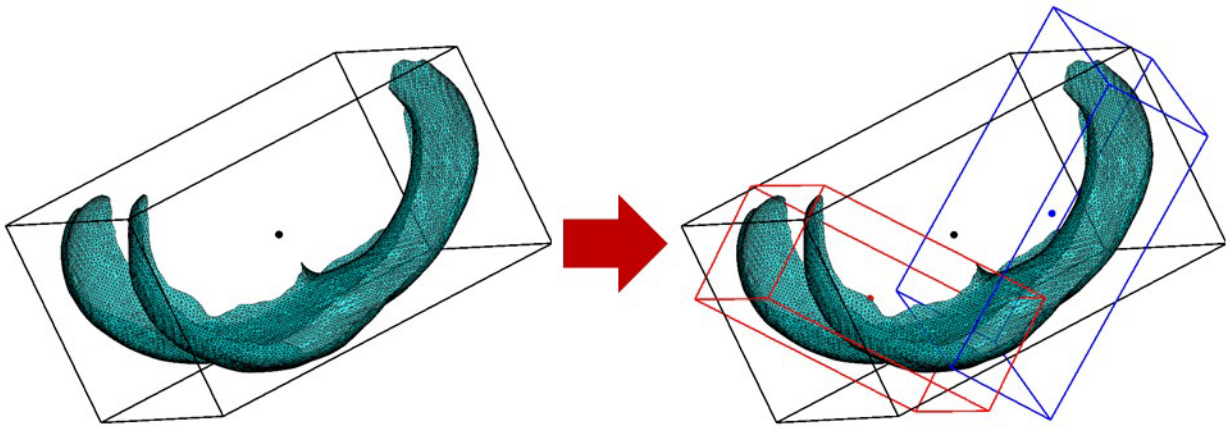

Figure 3-9 – An oriented bounding box generation example where the black box containing the whole mesh was bisected into two new regions (blue and red). Each of these regions would subsequently be split in a similar manner.

Then, for each triangle on the tibial cartilage mesh, a ray was traced from the normal of that triangle downwards towards the tibia bone surface (Figure 3-10) to determine if that triangle has overlapped with the femoral cartilage mesh and, therefore, is in contact at that frame. If the ray intersected with the box bounding the entire femoral cartilage mesh, that tibial mesh triangle is determined as "in contact" at that frame.

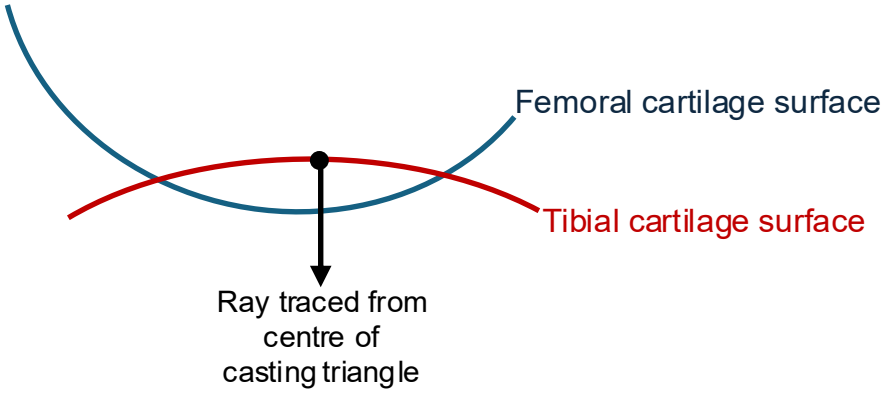

Figure 3-10 – Diagram of ray tracing direction from casting mesh (tibial cartilage) to the target mesh (femoral cartilage).

Once contact was established, the corresponding contacting triangle on the femoral cartilage was determined by iteratively working through the OBB tree, checking at each level if the ray intersects with each bounding box, until reaching a leaf node. The 'contact distance' – i.e. the amount of overlap between the two triangles – was then calculated between the selected tibial cartilage face and the femoral cartilage face specified in the contacting leaf node.

Once the contacting pair of triangles were identified, the depth of penetration (d) between them was computed using Equation 3-2.

$$d = \frac{(\vec{P}_f - \vec{C}_t) \cdot \hat{n}_f}{\hat{n}_t \cdot \hat{n}_f} \quad \textit{(Eq. 3-2)}$$

$\vec{P}_f$ = the intersection point on the femoral cartilage triangle, $\vec{C}_t$ = the centre of the ray casting triangle on the tibial cartilage, $\hat{n}_f$ = the unit normal vector of the femoral cartilage triangle, and $\hat{n}_t$ = the unit normal vector of the tibial cartilage triangle.

This allowed for the cartilage contact pressure for each contacting triangle to be calculated using an elastic foundation model developed for articular cartilage (Bei and Fregly 2004). The contact pressure (p) calculated was dependent on the contact overlap depth (d), combined cartilage thickness (h = 6 mm), and material properties (Young's modulus, E = 5 MPa and Poisson's ratio, v = 0.45) (Equation 3-3).

$$p = -\frac{(1-v)E}{(1+v)(1-2v)} ln\left(1 - \frac{d}{h}\right) \quad \textit{(Eq. 3-3)}$$

The resulting contact map at each frame was then output as a .vtp file containing both the geometric mesh information (vertices and connectivity) as well as the overlap depth and contact pressure of each triangle of the mesh.

3.2.4 BVR CONTACT MAP GENERATION

To calculate the TF joint contact pressure maps from the subject-specific BVR kinematics and MRI geometries, the same approach from the OpenSim-JAM workflow (described above in Section 3.2.3) was adapted and implemented in MATLAB (MathWorks, USA). The code iteratively divided the femoral cartilage mesh into an OBB tree and then a ray-intersection test was performed for each element on the tibial cartilage mesh. If an intersection was found, the overlap depth and resulting contact pressure were calculated.

At each frame of motion, the femoral and tibial cartilage meshes were positioned based on the relative bone poses given by the 4×4 object transforms (OTs) from the BVR data processing pipeline (Section 2.4) (Figure 3-11). First, the femoral cartilage mesh was aligned with the global coordinate system (GCS) using the femur's anatomical coordinate system (ACS). The corresponding OT was then applied to transform the cartilage to its correct position based on the femur's motion. The same process was applied to the tibial cartilage, ensuring both meshes were positioned according to their respective bone motions for contact analysis.

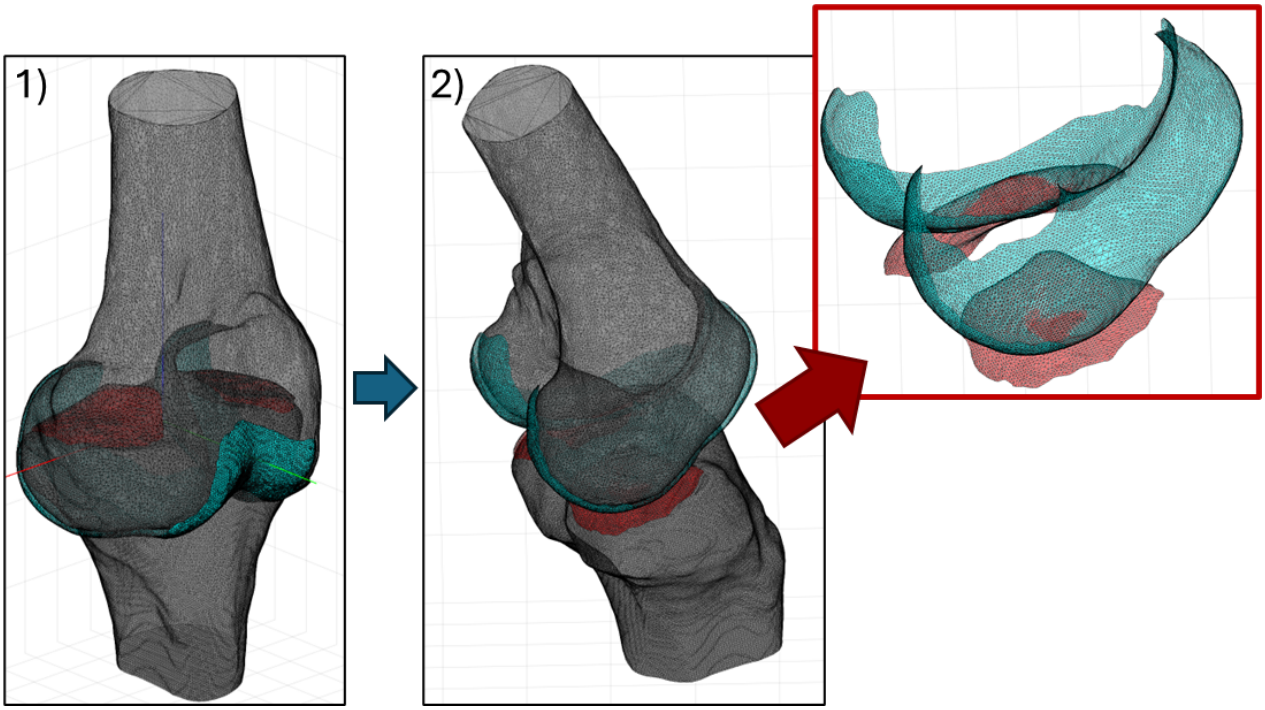

Figure 3-11 – (1) Geometries aligned with the global origin (2) Geometries moved into their relative positions for a single frame. The red box shows the overlap of the cartilage meshes where contact pressures will be calculated.

The BVR contact map generation code was tested to ensure consistency with the OpenSim-JAM approach; the test process and results are presented in Section 3.3.1.

By using the same mathematical approach as the OpenSim-JAM code, this enabled consistent comparison between the MSM output contact maps and the resulting BVR contact maps. The same personalised geometries used to create the personalised MSM (Section 3.2.2) were used to calculate the BVR contact maps, again for consistency.

3.2.5 REMAPPING PRESSURES TO GENERIC GEOMETRY

To standardise across the multiple geometries used to create the personalised and BVR contact maps, all the personalised pressure results were remapped onto the generic geometry. This not only allowed for comparison across the cohort, but it also allowed for element-wise comparisons between the three versions of the contact maps for the same individual – generic, personalised and BVR. While contact surface morphology influenced the results during processing, remapping all data onto the generic geometry removed its effect from the subsequent analysis. This

ensured that any observed similarity between the personalised and BVR maps was not simply due to shared geometry.

Remapping was performed to transfer the contact pressure distributions from the personalised tibial cartilage meshes (output as .vtp files during the joint mechanics step) onto the generic geometry using code provided by Dr Bryce Killen (KU Leuven). To reassign the pressure distribution at each frame from the personalised geometry to the generic mesh, the points from the personalised tibial cartilage mesh were morphed to match the generic geometry using a host-mesh fitting algorithm. Then, for each triangle in the generic mesh, the pressure value was assigned based on the closest element in the morphed mesh.

The code was then also adapted to remap the BVR contact pressures to the generic geometry in the same way. This resulted in all contact pressures being defined on a common mesh, allowing for element-wise comparison.

3.2.1 WEIGHTED CENTRE OF PRESSURE

To compare the position of the contact pressure region between the three methods, weighted centre of pressure (COP) was calculated for each half of the tibial plateau separately. This allowed for identification of the movement of the pressure region on both the medial and lateral side of the tibial cartilage. By weighting the COP based on pressure magnitude, the whole pressure region location and value could be condensed into a single point for ease of comparison.

To remove any differences due to the size and geometry of the personalised mesh morphology, the weighted COP was calculated using the pressures remapped to the generic geometry (Section 3.2.5).

Firstly, the tibial cartilage was split into its medial and lateral components by splitting the mesh aligned with the global origin (Figure 3-12). Therefore, the cartilage was split by its positive (lateral) and negative (medial) X coordinate values.

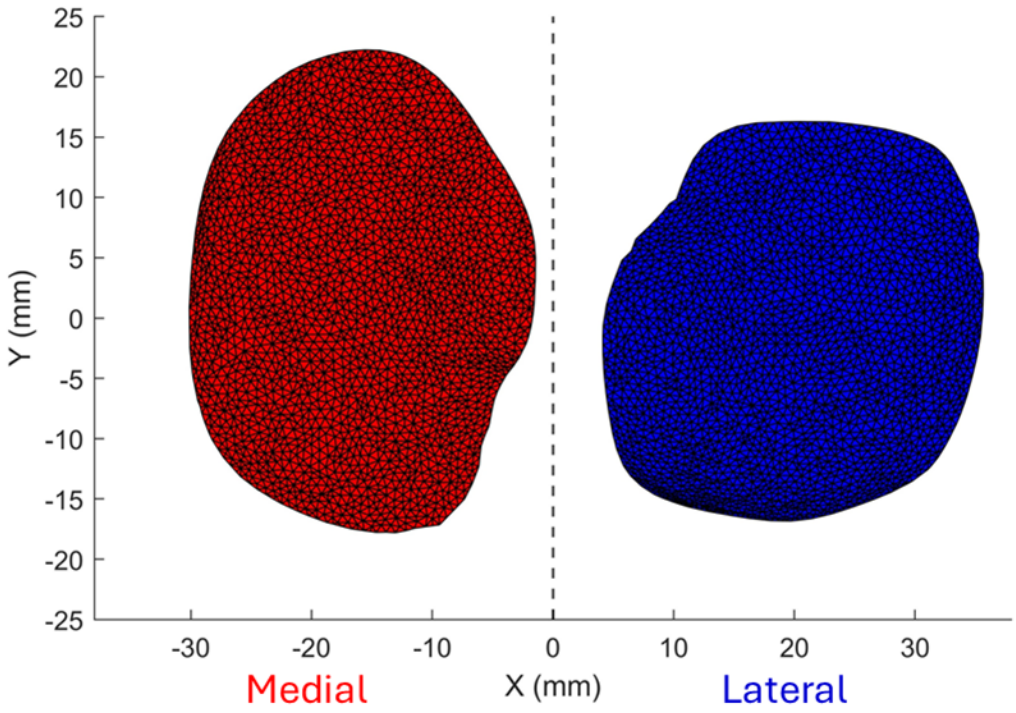

Figure 3-12 – Tibial cartilage split into the medial and lateral sides based on the X coordinate value.

For each half of the tibial plateau, the centroid location of each element was calculated, then weighted by multiplying it by the pressure of that element. The sum of all weighted centroids in each axis direction was divided by the total pressure of that plateau half to determine the coordinates of the COP.

The weighted COP results were calculated for each of the three methods for each participant and plotted back onto the generic tibial cartilage mesh to visualise the COP displacement during the activity.

The range of displacement of the COP on the medial and lateral sides of the tibial cartilage were calculated for each of the three methods to compare the amount of COP motion in both the ML and AP directions.

The mean error between the MSM and BVR COP locations in the X and Y directions across all available frames were also calculated for the generic and personalised model for both plateaus. The overall mean error for the cohort was also calculated.

3.2.2 STATISTICAL METHODS

Methods for comparing TF kinematics

For all six DOFs the mean and standard deviation (std) of the cohort were calculated for the generic MSM, personalised MSM and BVR results. It was calculated for the whole of stance phase for the MSM outputs, and only where data were available for all five participants for the BVR kinematics.

Similarly to the comparison of the Visual3D pipeline outputs in Chapter 2 (Section 2.5.7), both sets of kinematics from the generic and personalised model versions of the MSM pipeline were compared to the 'ground truth' BVR kinematics using a Bland-Altman analysis (Altman and Bland 1983). As well as plotting the difference at each frame against its corresponding BVR kinematic value, the median and interquartile range (IQR) of the differences for the cohort were also calculated for each DOF. Again, the results were simplified into violin plots to show the distribution of these differences. See Figure 2-30 in Section 2.4.10 for more a more detailed explanation of the generation of the Bland-Altman and violin plots.

To visualise the differences in the distribution between the generic model and personalised model results compared to the 'ground truth' BVR results, a split violin plot was used to show the distributions side by side (Figure 3-13).

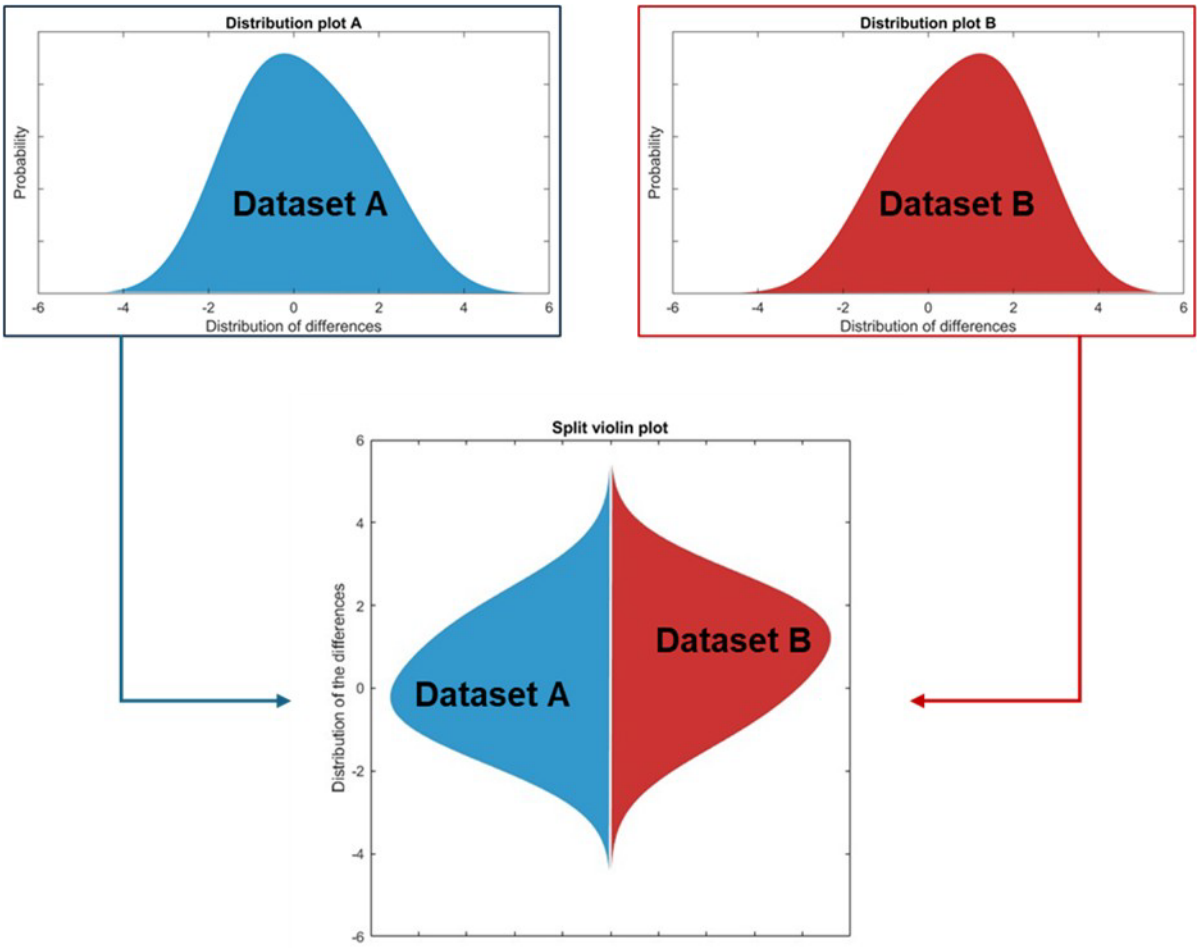

Figure 3-13 – Generation of a split violin plot comparing the distributions of two datasets (A & B).

Dice Scores

The tibial cartilage contact pressure maps were compared by calculating the Sørensen-Dice coefficient, also known as a Dice score, between pairs of images of MSM and BVR contact pressure maps at each frame, allowing for quantification of agreement between contact region shape between the two sets of results (Willing et al. 2013; Thorhauer and Tashman 2015). The Dice score reduces the difference between two binary 2D images to a single value by comparing “common” pixels between the images. This value is calculated by doubling the total common pixels then dividing by the total number of pixels in both images (Equation 3-4).

$$D(A,B) = \frac{2|A \cap B|}{|A| + |B|} \qquad \textit{(Eq. 3-7)}$$

Where $|A \cap B|$ is the count of the common pixels between image A and image B, $|A|$ and $|B|$ are the total number of pixels in image A and image B, respectively.

For each participant, the subject-specific tibia bone and cartilage models were viewed superiorly in the transverse plane with the tibial ACS origin aligned with the centre of the figure, so the tibial plateau was visible as a 2D image (Figure 3-14). This was also repeated with the 'generic' MSM geometries. Each triangle on the cartilage was then defined as in contact (value = 1, black) or not in contact (value = 0, white) based on the pressure results at the given frame.

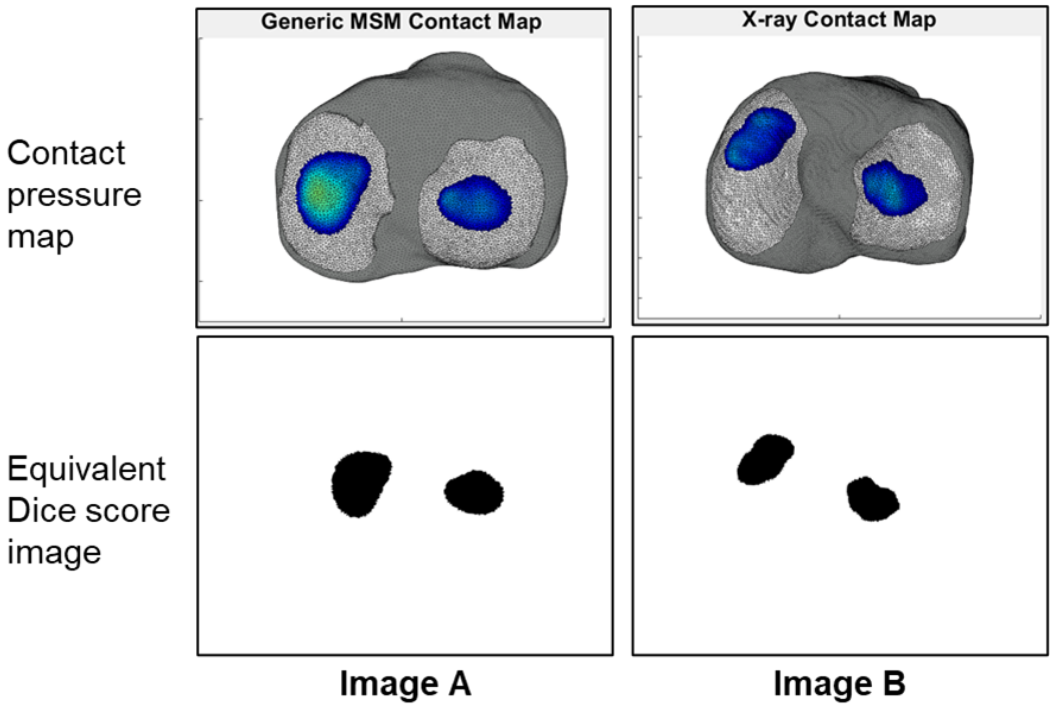

Figure 3-14 – Example of the image generation for calculating the Dice score between the generic MSM (Image A) and the BVR contact map (Image B) at a single frame.

The resultant binary images of the contact regions were then compared in pairs; firstly, the Dice score between the generic MSM and BVR contact maps were calculated for all frames, then the personalised MSM and BVR contact map Dice scores were calculated.

Wilcoxon signed-rank test

To determine if the differences in the calculated Dice scores were statistically significant between the generic and personalised MSM contact maps when compared to the BVR contact maps, a paired Wilcoxon signed-rank test was performed (MATLAB, MathWorks, USA). This non-parametric test was chosen as it does not assume normality of the differences and is suitable for paired data (Hollander et al. 2014).

The frame-by-frame Dice scores for the generic and personalised model contact map images compared to their corresponding BVR-equivalents were pooled across all participants. For this test, the differences between the personalised and generic Dice scores were calculated, ranked by absolute difference, and then the signs of the ranks were reintroduced. The sum of the positive and negative signed ranks were computed, and the test returned the smaller of these two values as the W statistic. The p-value was then calculated by comparing the W statistic to the distribution of W under the null hypothesis. The null hypothesis – that there is no statistically significant difference between the Dice scores of the two methods – was rejected if the p-value was found to be below 0.05.

Statistical Parametric Mapping

For element-wise comparison between the pressure distributions generated using the personalised and generic tibial cartilage geometries, all pressure maps were first remapped onto the generic geometry (Section 3.2.5). Statistical Parametric Mapping (SPM) was then performed on these remapped pressure maps to identify regions where the error (the difference between the MSM and BVR pressures) differed significantly between the personalised and generic MSM predictions.

For each participant, a paired t-test was conducted in MATLAB (MathWorks, USA) using the SPM1D Toolbox (Pataky 2012). The test compared the absolute error (MSM – BVR) between the personalised and generic predictions at each element across the generic tibial cartilage surface, averaged across all available frames of data which fell within stance phase for each participant. For each element, the resulting t-statistic was normalised to a z-statistic value. Each element's z-statistic was then compared to the critical threshold (z*) to determine statistical significance. The z* threshold was calculated separately for each participant based on random

field theory (Adler 2010), which adjusts for multiple comparisons by considering the number of elements tested and the smoothness of the data. Although each participant had a different z* value depending on their data characteristics, a consistent significance level of $\alpha = 0.05$ was applied throughout.

After calculating individual results, a single overall mean map for the cohort was generated by averaging the participant-specific t-maps. The mean z* value across all participants was used as the threshold to visually indicate regions of significance on the cohort-level map.

Comparing the contact maps like this allowed for areas of significantly better or worse prediction to be highlighted, indicating where contact prediction differences were occurring between the two sets of MSM maps. A larger number of elements with a significantly higher error from the generic model results would indicate that the personalised geometry improves contact pressure predictions.

Elements where the z-statistic exceeded the positive or negative z* threshold were highlighted to show statistically significant differences in error between the generic and personalised MSM predictions compared to the BVR results.

SPM was also applied to the mean error value (personalised – generic) across all elements to investigate the differences in prediction accuracy through stance phase. The same significance level of $p < 0.05$ was also applied for this comparison. By investigating the differences over time, periods of stance phase where the model accuracies diverged could be identified to investigate if there were certain points in the activity where personalisation made a greater difference.

3.3 METHOD EXPLORATION

To expand on the method development, further exploration was performed on three specific aspects of the pipeline to understand the suitability of these methods for this application, as well as understanding of some of the potential limitations.

3.3.1 TESTING THE BVR CONTACT MAP GENERATION CODE

The BVR contact map calculation code (Section 3.2.4) was tested to ensure it accurately replicated the OpenSim-JAM equivalent ray tracing and bounding box method (Section 3.2.3).

Firstly, a simple test was conducted to compare the outputs from the two methods. Contact maps were generated using the generic MSM pipeline geometry (from the Lenhart et al. (2015) model – Section 3.2.1) with the knee at 0°, 30°, 45°, 60°, and 90° flexion, with the other five TF DOFs set to 0°/mm.

For the MATLAB joint contact code, five OTs were created to represent these flexion angles. Since the femur and tibia meshes from the MSM model were already aligned with the origin (at 0,0,0), the OTs were directly applied to the tibia to achieve the desired poses.

For the OpenSim-JAM comparison, a passive flexion simulation was run using the ‘forsim’ tool on the generic model. The five closest model states to the target flexion angles were extracted, and the knee flexion was adjusted to match the exact values, with the other five knee DOFs set to 0°/mm. These five frames were then processed using the Joint Mechanics tool to generate contact maps.

The resulting five pairs of contact maps were visually compared to ensure no discrepancies between the two sets of code (Figure 3-15).

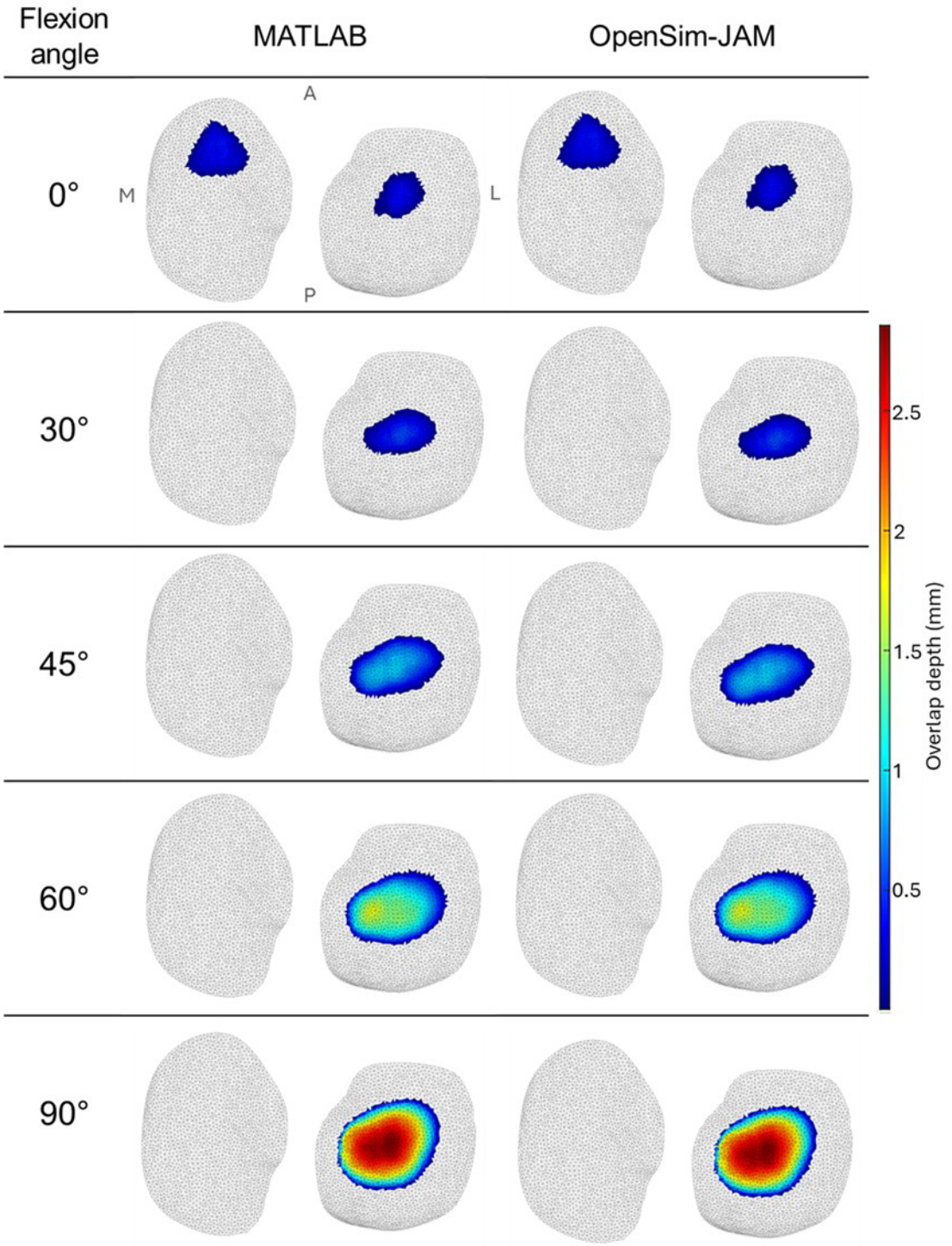

Figure 3-15 – Contact map outputs from the MATLAB (left) and OpenSim-JAM (right) pipelines of the generic geometry at the 5 tested flexion angles.

As well as visually checking the similarity, the following numerical parameters were also compared to ensure consistency: the number of triangles in contact, the maximum contact distance and the number of the triangle where that maximum

distance occurred. These results are presented in Table 3-2 and confirm the consistency of the outputs from the two methods as the results were identical.

Table 3-2 – Numerical results comparing the MATLAB (MAT) and OpenSim-JAM (JAM) codes for calculating joint contact using the generic geometries at five flexion angles.

Flexion angle (°)	Count of triangles in contact			Maximum overlap depth (mm)			Index of triangle with maximum overlap depth	
	MAT	JAM	Difference	MAT	JAM	Difference	MAT	JAM
0	681	681	0	0.404	0.404	0.000	6494	6494
30	424	424	0	0.552	0.552	0.000	5376	5376
45	731	731	0	0.945	0.945	0.000	5359	5359
60	984	984	0	1.730	1.730	0.000	1494	1494
90	1276	1276	0	2.857	2.857	0.000	5369	5369

A subsequent test was conducted using a randomly selected dynamic trial from one participant. TF kinematics were extracted from the MSM pipeline's IK results (Section 3.2.3) and converted to OTs using a custom MATLAB script. The MATLAB contact code was then run with these OTs and the generic model's femoral and tibial cartilage geometries. The results were compared with those from the standard Joint Mechanics pipeline to assess consistency. Again, the differences between the number of triangles in contact and the maximum overlap depth between the MATLAB and OpenSim-JAM results were 0 across all 120 frames of dynamic movement. The pressure values at each frame were also compared and no differences were found (Figure 3-16).

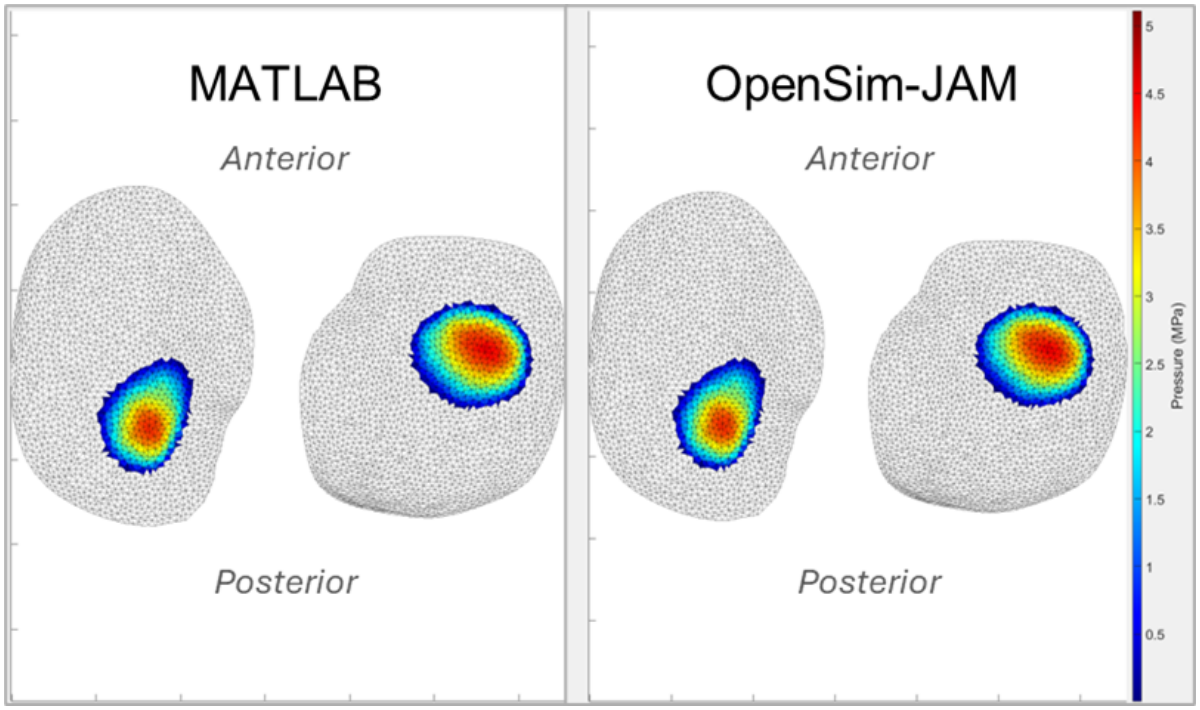

Figure 3-16 – Comparison of the contact maps from the two methods for an example frame of dynamic motion.

During both tests, the two methods produced identical results, confirming that they perform in the same way and, therefore, the MATLAB code could be used to calculate contact maps from the BVR input data comparable to the results from the OpenSim-JAM pipeline.

3.3.2 BVR CONTACT MAP SENSITIVITY TO OVERLAP DEPTH

When visualising the resulting BVR contact maps calculated for the three dynamic activities using the MATLAB version of the bounding box and ray tracing method (Section 3.2.4), some contact maps were found to have little or no triangles in contact on either the medial or lateral plateau or both (Figure 3-17).

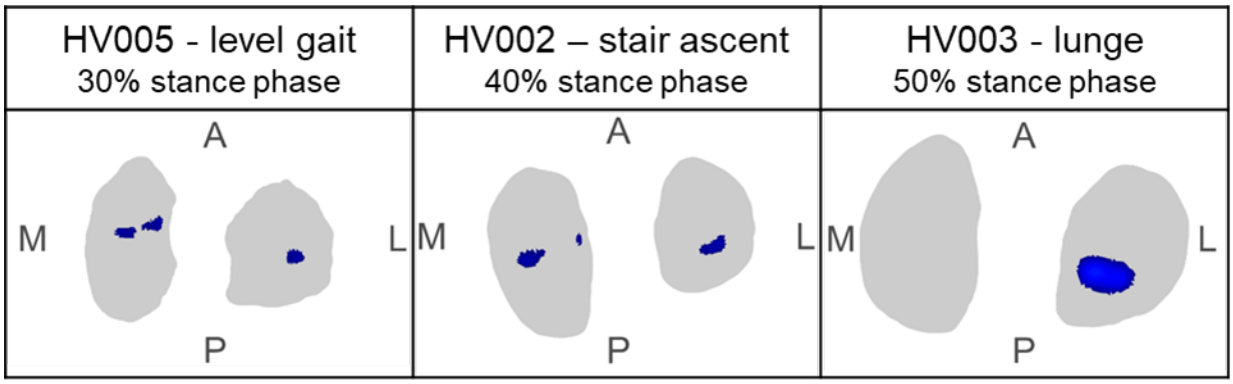

Figure 3-17 – Examples of small or one-sided contact regions from three different participants, one from each activity.

This minimal BVR contact was due to the lack of overlap between the femoral and tibial cartilage meshes resulting from a combination of the cartilage geometries and their relative positions due to the bone poses at each frame. Small errors in the cartilage segmentation or bone poses generated from image registration potentially contribute to the lack of contact seen between the two meshes.

For this reason, it was decided to investigate the sensitivity of the BVR pressure map results to contact (overlap) depth. The threshold for a triangle to be considered “in contact” in the MATLAB version of OpenSim-JAM was adjusted to reflect potential errors. Three different minimum proximity thresholds were applied to the same gait trial from one participant: the standard 0 mm threshold (i.e. the meshes physically contact), -0.5 mm and -1 mm, so triangles within close proximity were also considered “in contact”. By making the threshold negative, the ray was also traced in the opposite direction to the usual ray direction (Figure 3-10) to find any triangles closer than the specified threshold value. Altering the threshold like this aimed to represent potential cumulative errors resulting in triangles not overlapping.

An example frame at 40% stance phase of level gait from HV003 was chosen for this investigation as this participant displayed no contacting triangles on the lateral tibial plateau at this frame (Figure 3-18). As well as visualising the contact area on the mesh, the number of triangles in contact were counted and the contact area calculated for each of the three threshold iterations.

The example in Figure 3-18 shows that as the threshold was reduced, the number of triangles and total area in contact on the tibial plateau increased. When the threshold was decreased by 0.5 mm, the contact area approximately doubled. Again, when the threshold was decreased from 0.5 mm to 1 mm, the contact area increased, although by a smaller proportion (increase of around 1.7 times).

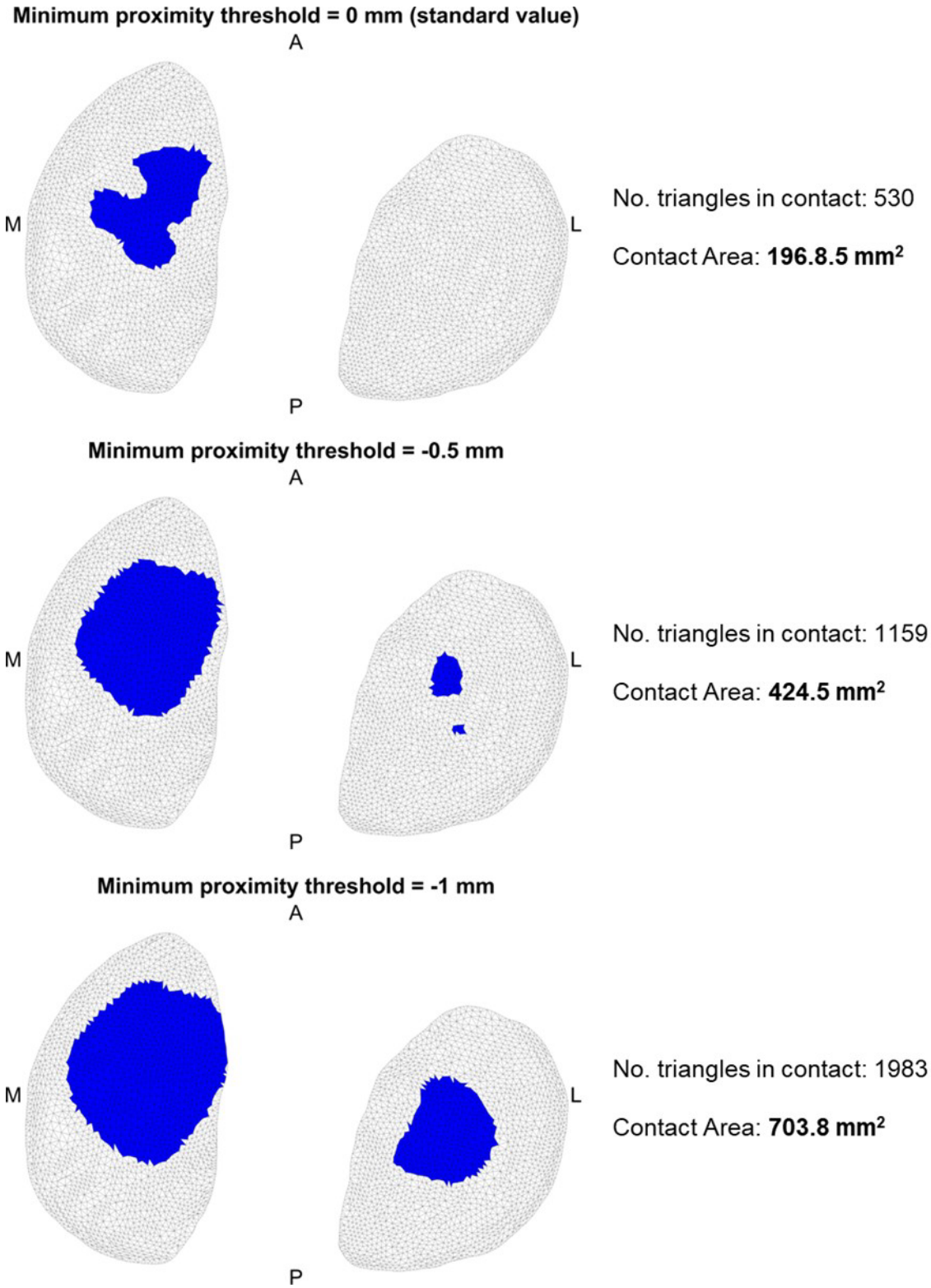

Figure 3-18 – Example of HV003 at 40% stance phase of level gait with three different minimum proximity threshold values.

These results show that predicted contact regions using the ray tracing and bounding box method were sensitive to the threshold value used. This confirms the sensitivity of this method to potential small errors in mesh segmentation or bone poses.

However, when considering TF joint contact in this context, it is also important to recognise that “no” contact seen between the cartilage meshes does not mean there was no contact in the knee, as contact between the cartilage and the meniscus was inherently included in the bone poses generated from BVR but not visualised. In this context, “no” visible cartilage contact means the bones of the knee moved further apart from each other relative to their positions in the MRI scanner (so no mesh overlap occurred), not necessarily that the joint was out of contact.

3.3.3 KNEE MARKER POSITIONING ON MODEL

As discussed in the previous chapter (Section 2.5.7), during data collection, the femoral condyle motion capture markers were placed too anteriorly compared to the underlying bony landmarks when the participants stood in their static, neutral standing positions. This affected the flexion accuracy of the motion-capture based kinematic results as the flexion value was consistently overestimated.

As TF flexion angle is set as a primary coordinate in the COMAK algorithm, its value is directly taken from the IK results and used to calculate all other secondary DOFs. Hence, it is important to understand the effects of incorrect marker placement on the flexion angle predicted during IK as this will have a direct influence on all the other results – including the secondary kinematics and contact map predictions.

Errors in the femoral condyle marker placement would affect the MSMs calculation of the femur’s location, altering the predicted hip joint positioning. The hip, and subsequent global alterations, associated with the IK routine would likely result in an overestimation of knee flexion.

To investigate how potential errors in marker position would affect IK knee flexion outputs, the femoral condyle markers on the generic model were manipulated to represent different marker placements during in-vivo data collection. A standing static trial from a single participant (HV005 - chosen at random) was run through the IK routine with variations of the generic model with the virtual model markers moved anteriorly from their default position by 1 mm, 2 mm, 3 mm and 10 mm (for an extreme change). The output TF flexion for each model variation was then compared with the BVR flexion angle (from image registration at the same frame) to see if manipulating the marker reduced the difference between the results. The virtual markers were also then manually manipulated to visually matched the experimental

marker positions relative to the femur geometry using the visualisation of the markers in the BVR coordinate space (as described in Chapter 2, Section 2.4.11) (Figure 3-19).

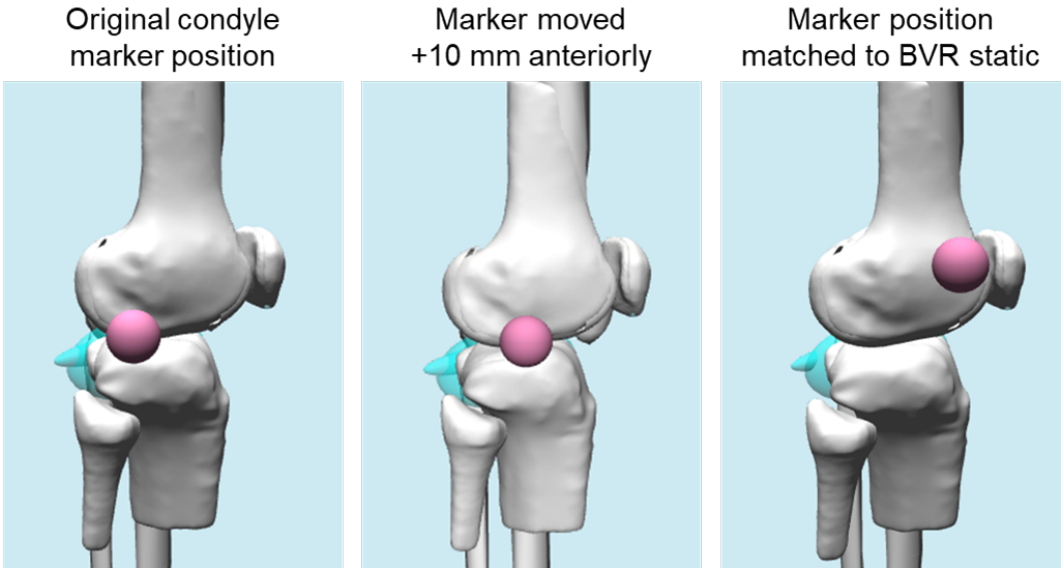

Figure 3-19 – Femoral condyle marker manipulation on the generic MSM.

The resulting flexion angles are presented in Table 3-3. These results show that as the position of the markers increased anteriorly, the flexion angle also decreased, resulting in a value closer to the BVR measured position.

Table 3-3 – Knee flexion angles during standing static for one individual where the condyle marker positions have been manipulated to better match their true positions relative to the underlying bone.

HV005 - Static	**Knee flexion angle (°)**
BVR	-15.96
Gen. MSM - original	0.31
Gen. MSM - condyle makers moved anteriorly +1mm	0.03
Gen. MSM - condyle makers moved anteriorly +2mm	-0.27
Gen. MSM - condyle makers moved anteriorly +3mm	-0.56
Gen. MSM - condyle makers moved anteriorly +10mm	-2.46
Manual manipulation of condyle markers to visually (approximately) match BVR static	-4.20

These results also show that even when the virtual condyle markers were manually manipulated to visually match their true positions, the knee flexion angle was still overestimated by over 10°. This suggests that the differences in flexion angle calculate were not solely due to marker misplacement but may also have been influenced by other factors, such as differences in ACS definition between the MSM and the BVR pipelines. Further investigation would be needed to understand the effects of this offset, including by calculating the exact relative positions of the markers to the bony landmarks and moving them to their precise positions accordingly.

When looking at the manually moved marker position compared to its original position on the model, the marker was not only translated anteriorly but also superiorly. Again, further investigation would help determine how this superior movement also affects the calculated flexion angle by performing a similar test with superior manipulation of the virtual marker.

As well as using a static trial, the flexion angle of the same participant was also tested using a level gait trial to investigate the effects of marker positioning on dynamic trial results. The model with the markers manually manipulated into visual alignment was run through the IK routine; the resulting TF flexion angle was plotted alongside the original MSM COMAK flexion result and the BVR calculated flexion (Figure 3-20).

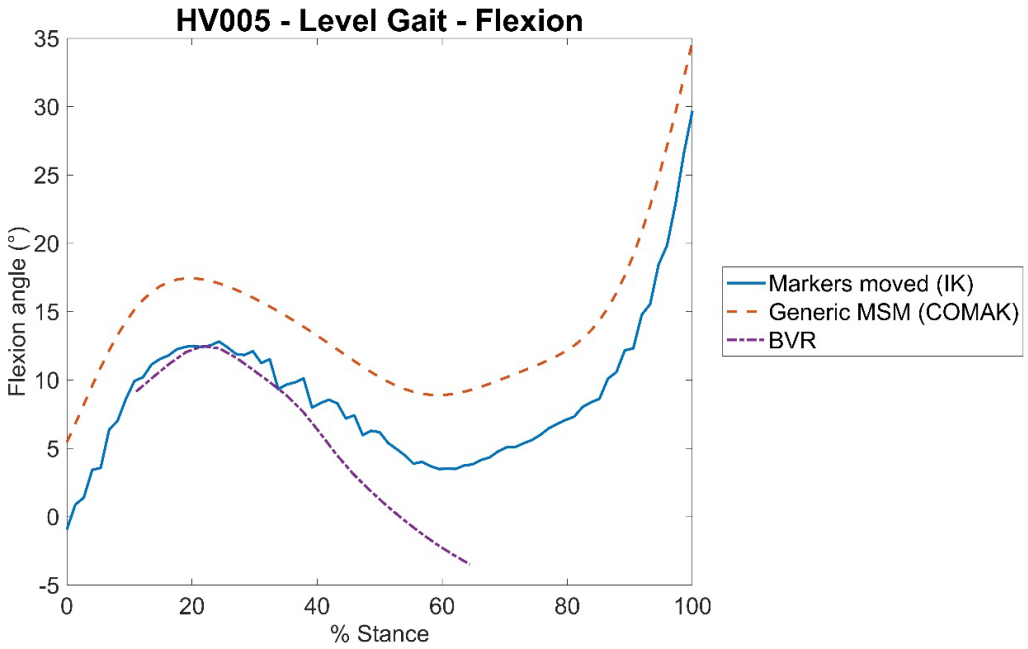

Figure 3-20 – Graph showing flexion angle during stance phase of level gait to compare the original generic MSM COMAK flexion result and the new manipulated marker position IK flexion to the BVR calculated flexion during a dynamic trial.

These results show that when the marker position was moved to visually match its true position, the resulting flexion angle calculated was closer to the gold-standard BVR angle. This highlights the need for accurate marker placement during data collection, so the model's marker positions represent the data correctly, and accurately calculate the primary kinematics used to solve the optimisation algorithm.

3.4 RESULTS AND DISCUSSION

3.4.1 DO PERSONALISED GEOMETRIES IMPROVE KINEMATIC PREDICTIONS DURING GAIT?

To answer research question 1 (Section 3.1.2):

> *Does adding personalised TF geometries improve model estimates of TF kinematics during level gait compared to a model with generic contact geometries, when validated against gold-standard BVR kinematics?*

The six DOF kinematics calculated for level gait from the MSM pipeline using the two versions of the model – one with generic contact geometries and one with personalised contact geometries – were compared to the gold-standard BVR kinematics (collected and calculated as described in Chapter 2).

It was decided to initially analyse the model predicted kinematics during level gait as this was the activity the OpenSim-JAM pipeline was developed for (Lenhart et al. 2015) (Section 1.6.2).

To match the joint definition in the MSM, the BVR kinematics were calculated with the femoral and tibial ACSs coincident when in their initial segmented position from the MRI scan. The kinematics of the five participants were plotted for the rotational (Figure 3-21) and translational (Figure 3-22) DOFs for the three different methods. For comparison, the methods were plotted in pairs in the first three columns: generic MSM with personalised MSM, generic MSM with BVR, and personalised MSM with BVR. The mean ±1 std for all methods were plotted in the last column for each DOF. Appendix C presents graphs comparing all three methods, split by individual participant, for analysis of MSM prediction accuracy on an individual level.

To quantify the difference between the generic and personalised MSM kinematics to the BVR results, a Bland-Altman analysis was performed for each DOF (Section 0), firstly for the generic results, then for the personalised. Figure 3-23 and Figure 3-24 show the Bland-Altman results for the rotational DOFs and translational DOFs, respectively, with each plot showing the difference between the MSM and BVR value against the gold-standard BVR value at each frame where X-ray data was collected. The median ±1.45 IQR were also calculated and marked on the plots for the whole dataset. The Bland-Altman plots were then simplified into split violin plots, with the generic MSM on the left half of the plot in red and the personalised MSM on the right half in green. The violin plots allow for comparison the distribution of the differences between the two methods, highlighting accuracy differences (see Figure 3-13).

As seen in Figure 3-21, the flexion angles calculated for the cohort using both the generic and personalised models were nearly identical. This was expected as the flexion angles for both the generic and personalised MSMs were calculated during the IK step, which was not influenced by the contact geometry. In the OpenSim-JAM approach, TF flexion is considered to be a primary DOF and, therefore, directly measurable from motion capture (Smith 2017). This means the flexion output was not optimised during the COMAK step and was the same for both models.

LEVEL GAIT - ROTATIONS

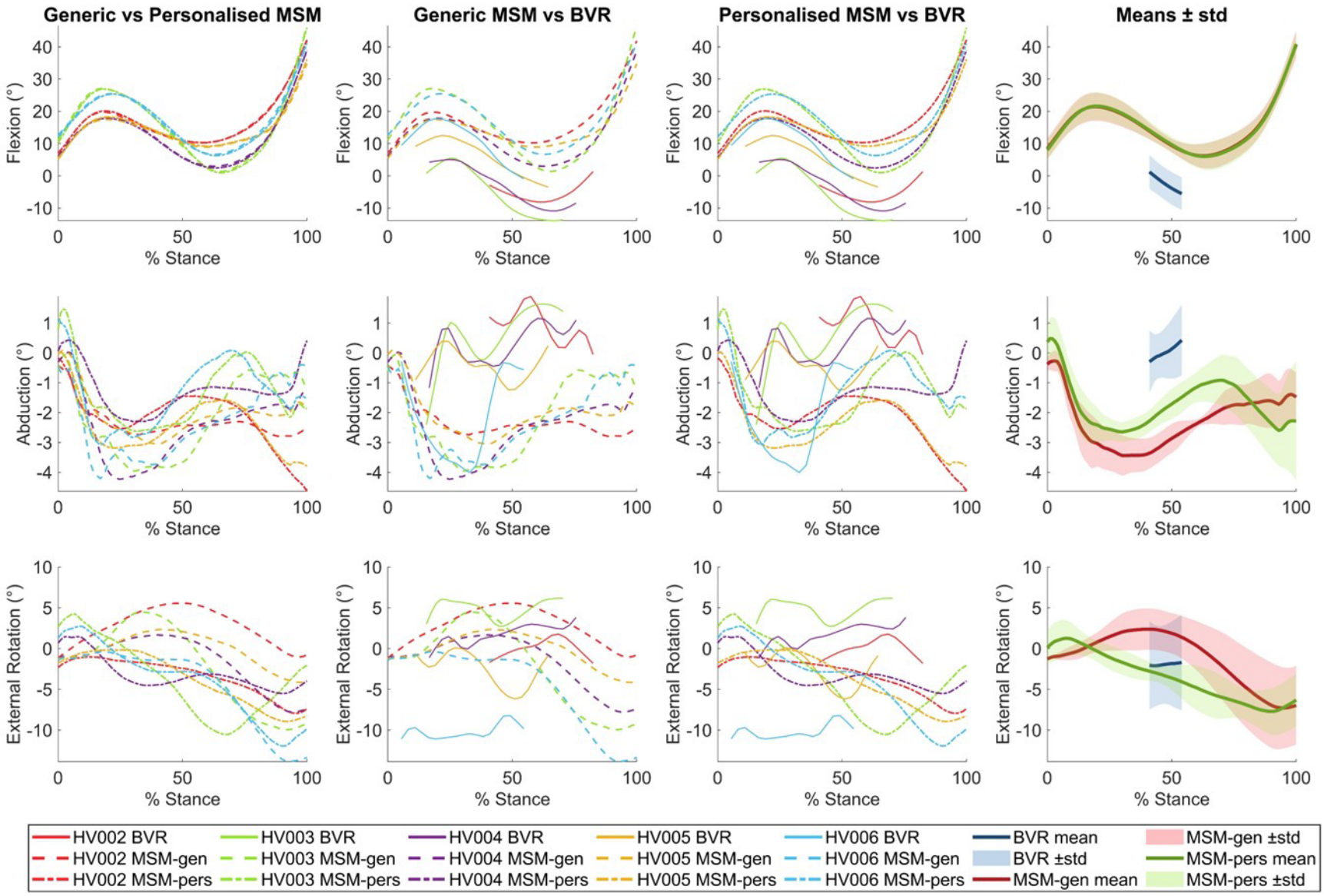

Figure 3-21 – Graphs showing the calculated rotations for the individual participants as well as the mean ±std of the cohort.

LEVEL GAIT - TRANSLATIONS

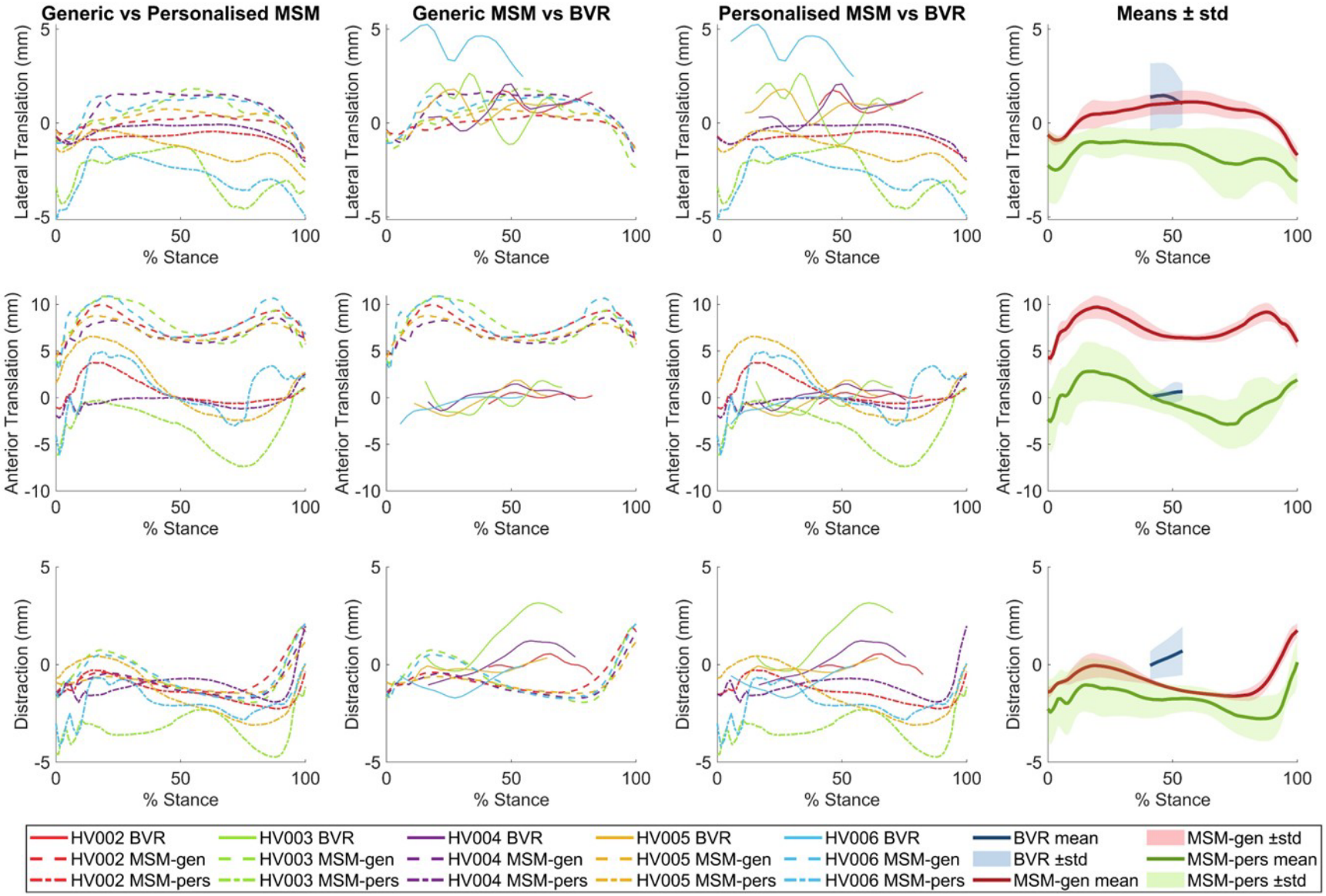

Figure 3-22 - Graphs showing the calculated translations for the individual participants as well as the mean ±std of the cohort.

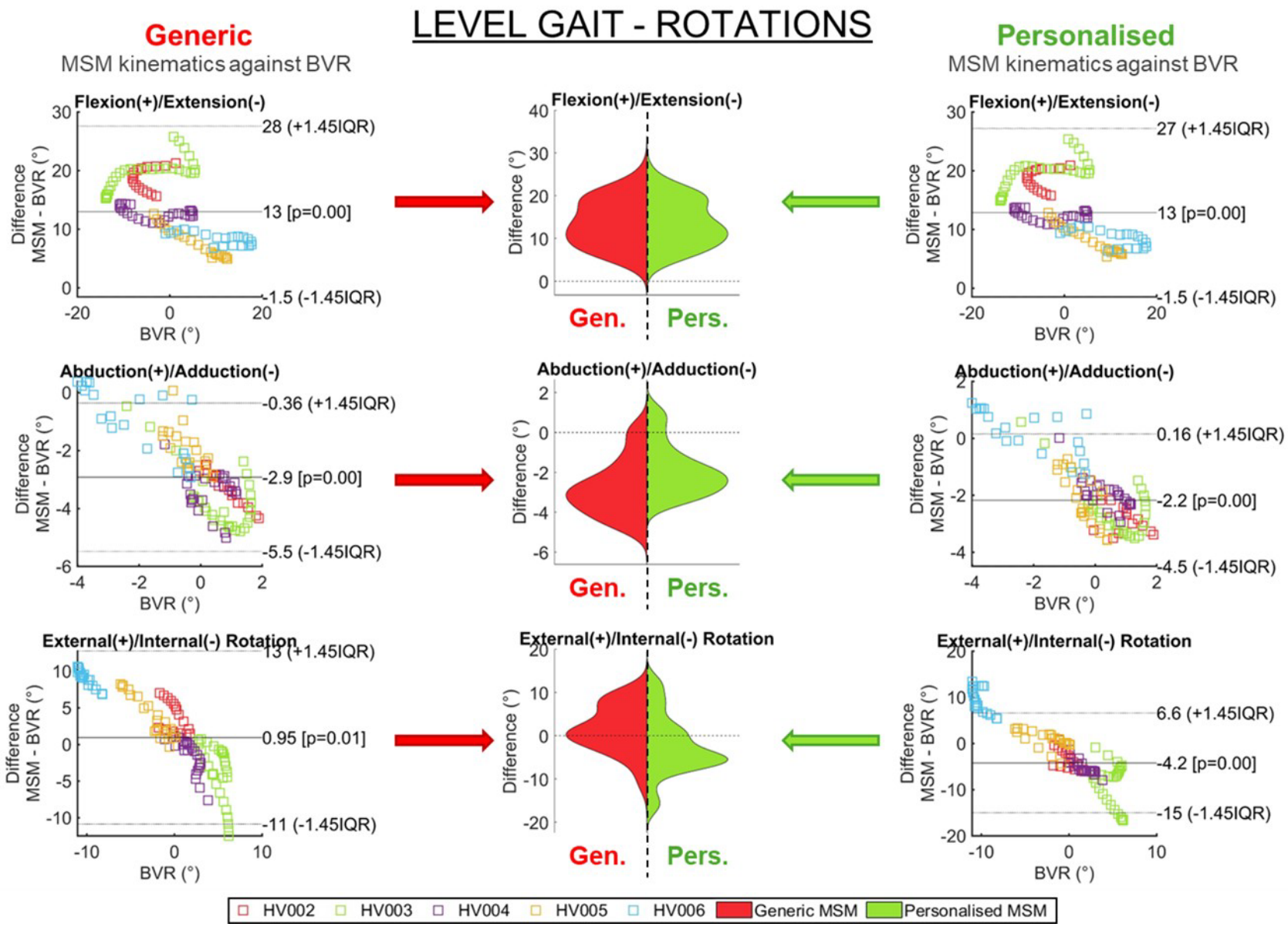

Figure 3-23 – Bland Altman analyses of the generic (left column, red) and personalised (right column, green) MSM rotations compared against gold-standard BVR rotations. These results were simplified into violin plots to show the distribution of the differences (middle column).

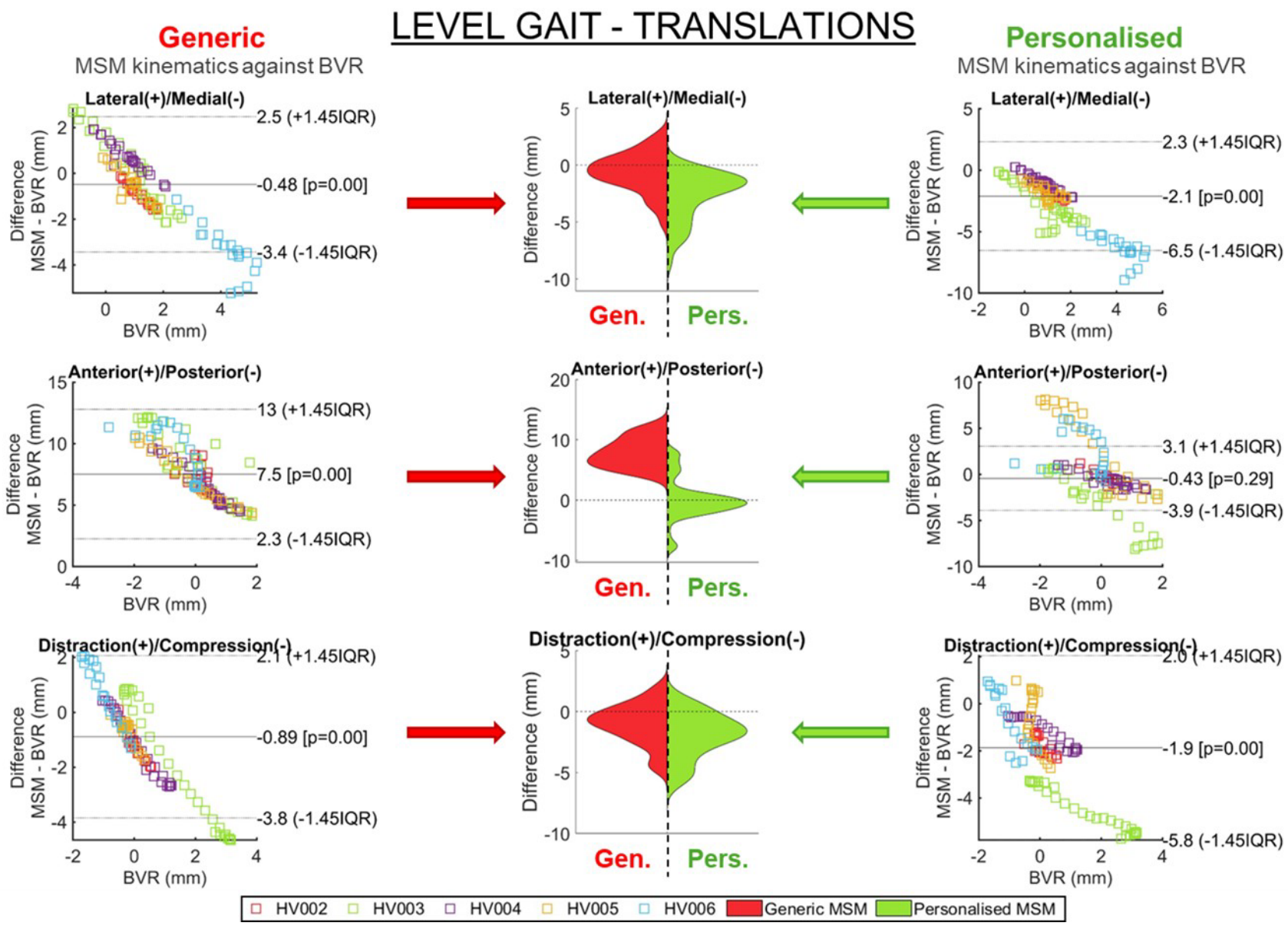

Figure 3-24 – Bland Altman analyses of the generic (left column, red) and personalised (right column, green) MSM translations compared against gold-standard BVR rotations. These results were simplified into violin plots to show the distribution of the differences (middle column).

The Bland-Altman plots for flexion angle (Figure 3-23) showed a median overestimation of 13° for both versions of the model, closely matching the 14° offset observed between Visual3D and BVR flexion angles (Figure 2-43 in Section 2.5.7). As discussed in Section 2.5.7, this offset was likely caused by anterior misplacement of the femoral condyle markers during data collection, leading to artificially elevated flexion angles. In the Visual3D pipeline, this primarily affects tibial positioning, while in the MSM pipeline it influences femur body positioning (including the hip). Despite this, both methods showed the same flexion offset. As flexion is a primary coordinate in the COMAK algorithm, secondary kinematics would also be affected by the overestimated knee flexion angles.

AA was shown to have a similar profile when calculated using the generic MSM and the personalised MSM, except towards the end of stance phase (80-100% stance) where the models with the personalised geometries showed more diverging results (Figure 3-21). As well as this, the mean predicted adduction angle was lower when using the personalised model compared to the generic model. This meant that the personalised model's mean adduction angle was closer to the BVR mean, although the median difference was only 0.7° closer overall (Figure 3-23).

External rotation showed greater variation in the generic model than the personalised, with the greatest profile difference between the two methods out of all the rotations (Figure 3-21). Although the median external rotation error for the generic model was better than the personalised (0.95° compared to -4.2°, Figure 3-23), it had a higher IQR. The large IQR seen in both sets of results shows the COMAK algorithm struggles to predict this rotation in general, even with personalised joint geometries. As IE rotation had a larger ROM than AA, it was likely more sensitive to the flexion overestimation error.

Both AA and IE rotation showed a negative correlation in their Bland-Altman plots between flexion angle and MSM-BVR difference with both model versions (Figure 3-23). This suggests the MSM may be over-constraining the model's secondary DOFs and not allowing for the full ROM seen in the BVR results.

All three translational DOFs presented similar kinematic profiles for the stance phase of gait between both models (Figure 3-22), although the offsets differed. For all three translations, the personalised model allowed for a greater ROM than the generic

model, suggesting that the TF translations were more sensitive to contact geometry than to the input kinematics.

The generic model predicted lateral translation on average during mid-stance, which was more consistent with the BVR results than the medial translation predicted by the personalised model (Figure 3-24). This resulted in a smaller median difference between the generic model and the BVR (-0.48 mm), than the personalised model (-2.1 mm). The personalised model also had a larger IQR than the generic, increased due to poor prediction of the ML translation of one participant (HV006).

AP translation showed the greatest median translational difference between the MSM and BVR results between the two models (Figure 3-24). The personalised model predicted this translation well (median difference with BVR = -0.43 mm), whereas the generic model consistently overestimated the anterior translation (median difference with BVR = 7.5 mm). The personalised model also had a narrower IQR (±1.45 IQR: 7 mm vs 10.7 mm) with most differences clustered around 0 mm (Figure 3-24).

Although both models predicted similar AP translation trends, the personalised model's predictions of AP translation fluctuating around neutral (0 mm) were not only more consistent with the BVR results, but were also more similar to literature values (0-5 mm) (Kozanek et al. 2009; Gray et al. 2019; Thomeer et al. 2020; Thomeer et al. 2021). When presenting the personalised model workflow, Killen et al. (2024) also found the generic model estimated greater anterior translation than the model with personalised geometries. This overestimation is likely due to the specific anatomy and alignment of the cartilage geometries of the individual used to define the generic model. However, this would need to be confirmed by testing the pipeline with a different 'generic' model (that uses a different set of contact geometries) with motion capture inputs from the same cohort to see if the anterior translation prediction improves.

Finally, CD translation presented a similar distribution of differences for both models (seen from the violin plot in Figure 3-24), although the generic model displayed a clearer correlation in the Bland-Altman plot, likely due to more consistent CD patterns predicted across participants. On average, the personalised model

predicted greater compression, which would likely lead to higher contact pressure outputs.

3.4.2 TIBIOFEMORAL JOINT CONTACT MAPS DURING LEVEL GAIT

As one of the main uses for the OpenSim-JAM pipeline (Section 3.2.3) is to generate contact pressure maps to understand loading distribution in the articular cartilage, it was important to understand the effects the kinematic differences (Section 3.4.1) had on the resulting maps.

The OpenSim-JAM contact pressure maps were compared with their BVR-equivalents (generated using the same OBB tree and ray tracing method, Section 3.2.4) at each frame of motion where BVR data were available. This comparison aimed to answer the second research question:

> *Are MSM contact pressure maps more similar to BVR maps when using personalised or generic contact geometries in the model?*

Figure 3-25 shows example contact maps from the BVR, personalised MSM, and generic MSM for each participant at 50% stance, chosen as it was the only time point with data available for all five participants. For a more comprehensive picture of the results of the cohort, Appendix D contains the contact maps calculated at 10% stance intervals of level gait for all participants individually. All the geometries in Figure 3-25 are shown at the same scale, so visual size differences reflect actual differences in model mesh sizes. Although the generic model rigid's bodies were scaled using marker landmarks, the specialised knee contact geometries were not scaled between participants (Section 3.2.3), which could affect contact predictions from the model.

Due to using identical contact geometries, the generic MSM contact maps showed more consistent contact region predictions across the cohort than the other two methods (Figure 3-25). This suggests that contact area predictions are sensitive to articular cartilage surface morphology, so the generic geometries struggle to capture inter-participant variation.

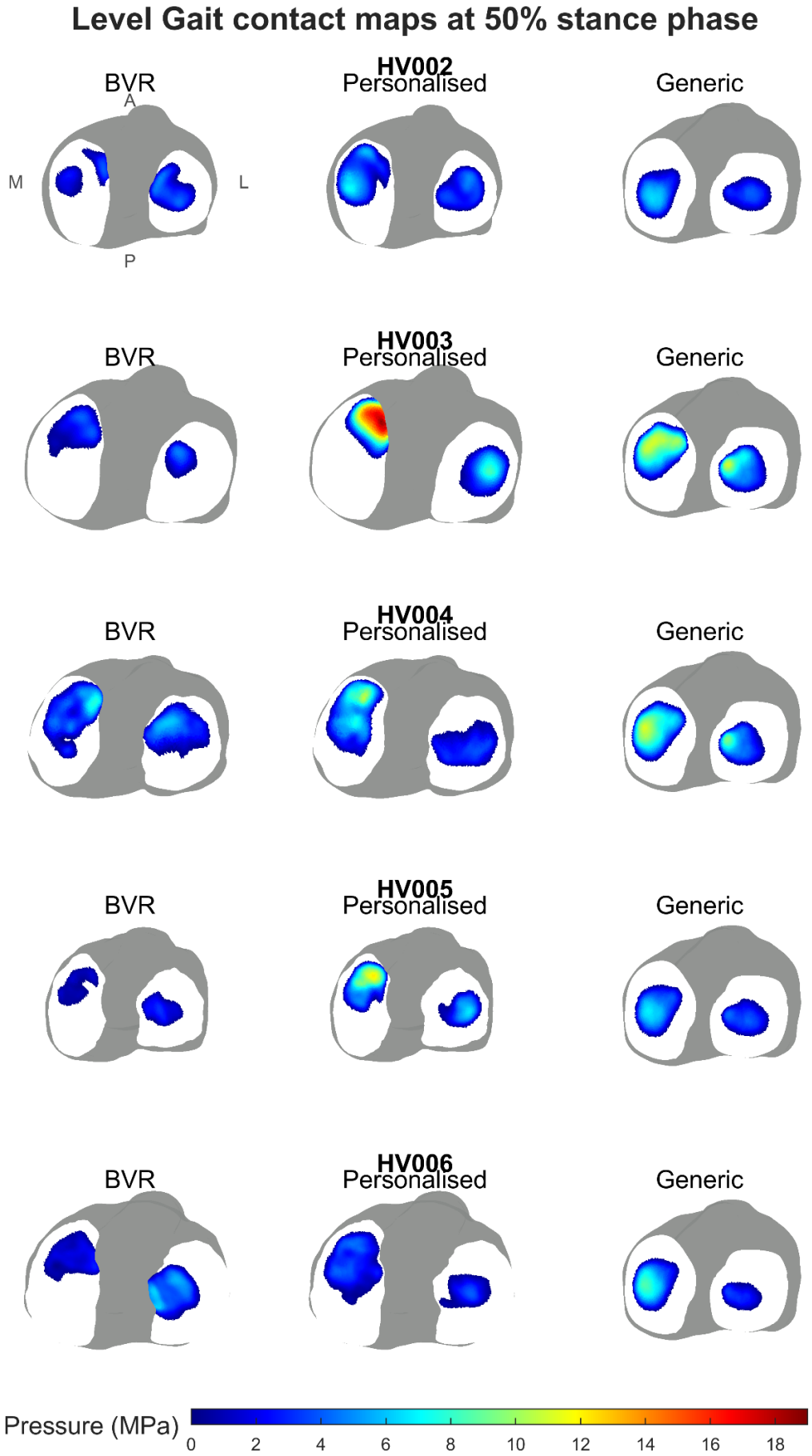

Figure 3-25 – Example contact maps for all participants at 50% stance phase during level gait. BVR contact map results in the first column, personalised MSM results in the second and the generic MSM contact map in the third.

Out of the three methods, the BVR contact maps showed the largest variation in contact area and location (first column of Figure 3-25), with some participants displaying small contact areas at various points during gait, particularly on the medial tibial plateau (three examples given in Figure 3-26). As joint contact area is sensitive to small changes in bone positions (as shown in Section 3.3.2), calculating contact pressure using this technique from BVR bone poses may not be suitable. Small errors in segmentation, model smoothing and image registration errors could have large effects on the predicted contact regions and pressure magnitudes from BVR. As the meniscus was excluded from the model, the MSMs generally predicted larger contact regions between the cartilage. In contrast, the BVR maps inherently include meniscus mechanics, reducing the visible cartilage-cartilage contact where the meniscus was situated.

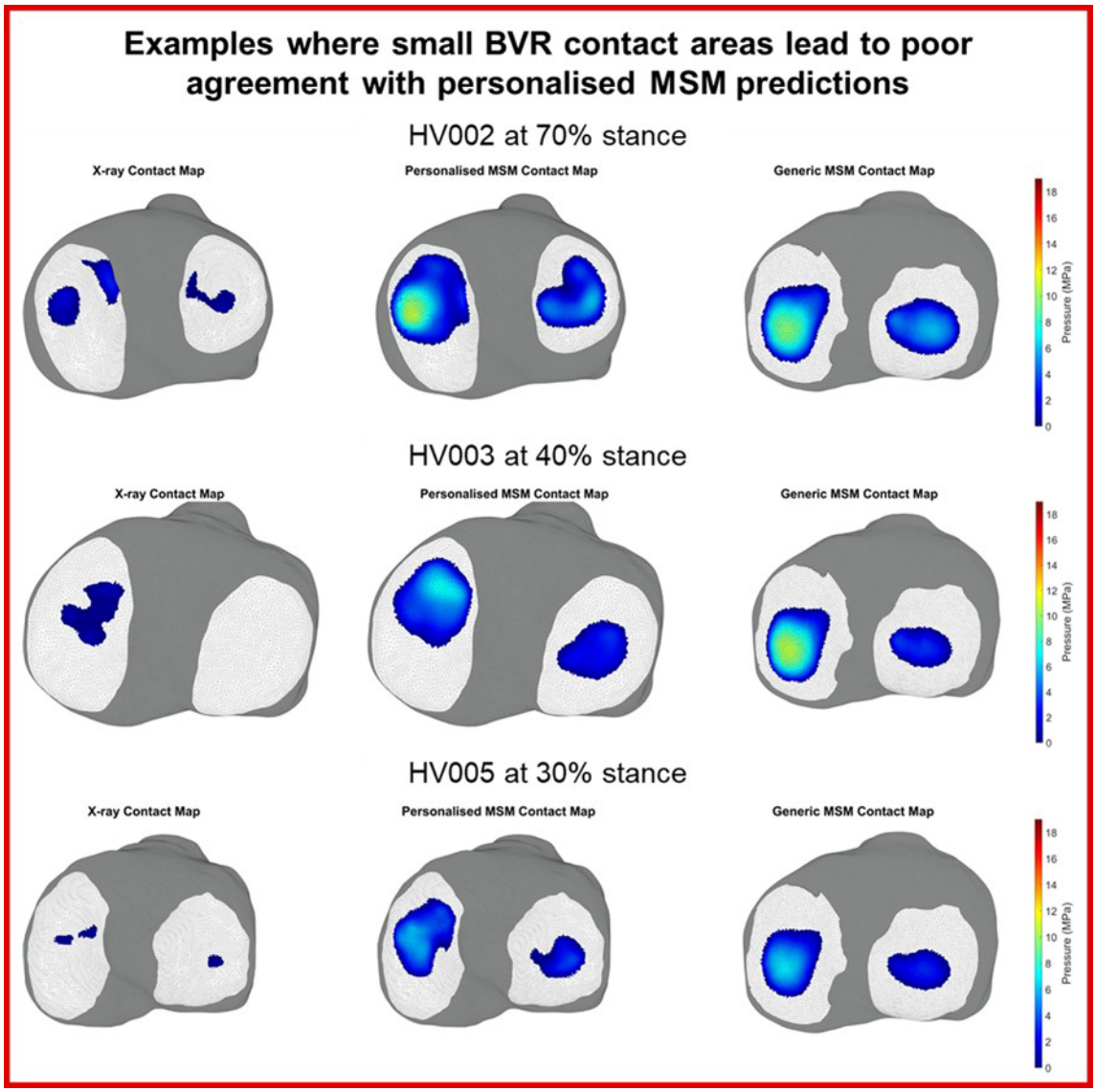

Figure 3-26 – Three example of small BVR contact areas calculated which affect comparisons with MSM contact maps.

Not all BVR contact maps showed such small contact regions. In some cases (like HV005 and HV006 at 50% stance, Figure 3-25), BVR predictions were visually similar to those from the personalised MSM. Three additional examples of good agreement during stance phase of level gait are shown in Figure 3-27, demonstrating how incorporating personalised geometries improves prediction of the size and shape of contact areas.

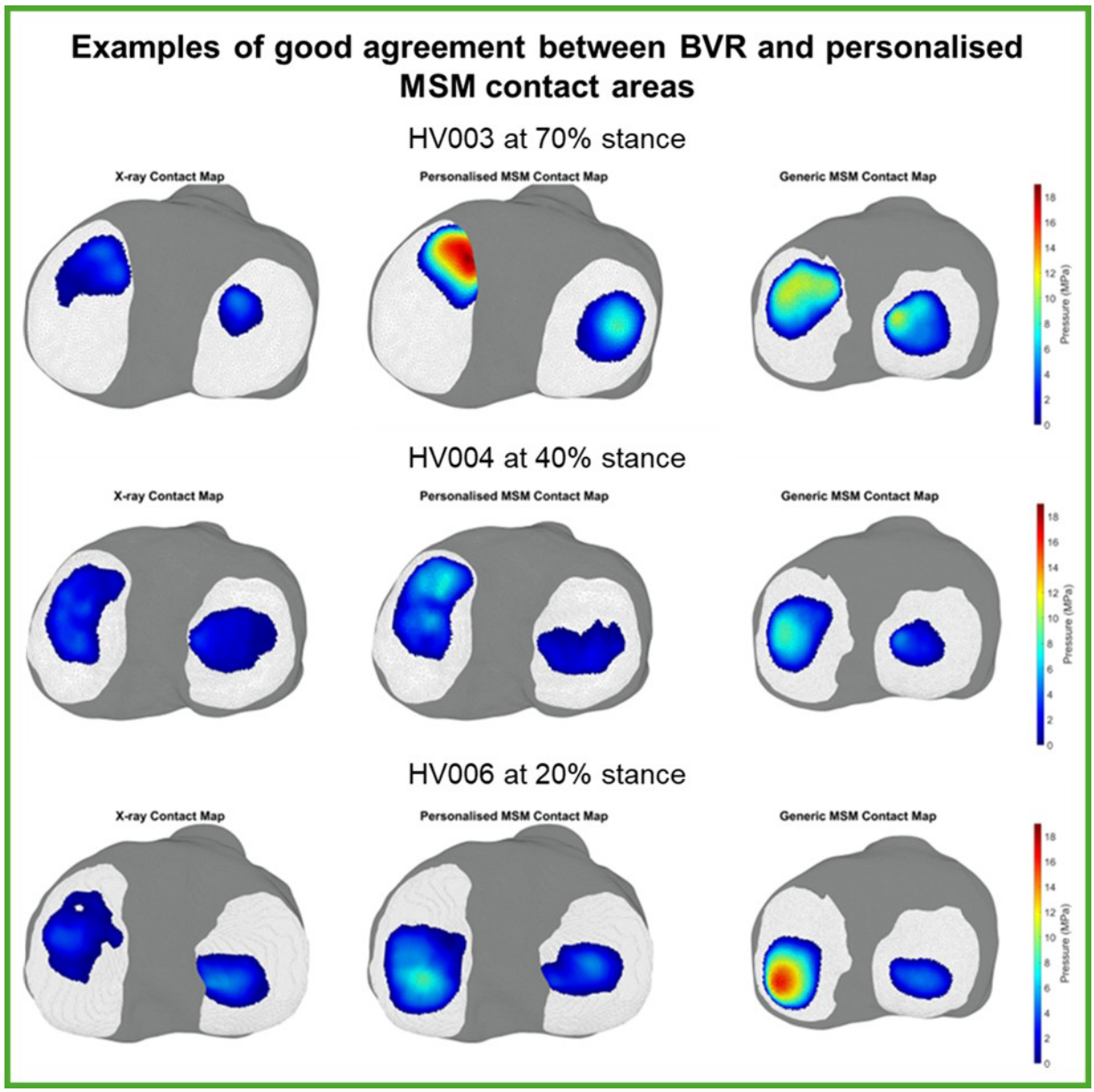

Figure 3-27 – Examples of contact predictions with good agreement in area between the personalised MSM and BVR results.

Figure 3-27 also highlights variation in the pressure magnitudes predicted across the different methods. In some cases (like HV003 at 70% stance, Figure 3-27) the personalised model predicted much higher pressures than the BVR and generic

MSM results, whereas in others (for example, HV006 at 20% stance, Figure 3-27), the generic model predicted the highest values. Although these are extreme examples, the BVR pressure magnitudes were generally lower than both MSMs. This was likely due to the MSM requiring constant cartilage contact to solve for joint forces, as well as the absence of the meniscus – which was inherently included in the BVR contact calculations.

Overall, visual inspection showed that the personalised model improved the contact region prediction compared to the generic model, when assessed against the BVR contact maps. This was seen in the examples at 50% stance in Figure 3-25, across the results in Appendix D, and in Figure 3-27.

Sørensen-Dice coefficient

To expand on the visual inspection, the Sørensen-Dice coefficient (Section 0) was calculated and used to compare each MSM map to its BVR equivalent at every frame. The mean Dice score across all frames for each participant was calculated, along with the overall mean Dice score for the cohort (Table 3-4).

Table 3-4 – Mean Dice scores for each participant during level gait

Participant ID	**Mean Dice score of level gait frames** *MSM compared against BVR contact map images.*		
	Generic MSM *(c.f. BVR)*	**Personalised MSM** *(c.f. BVR)*	**Difference** *(pers. – gen.)*
HV002	0.541	0.547	+0.006
HV003	0.334	0.377	+0.043
HV004	0.507	0.754	+0.248
HV005	0.336	0.427	+0.092
HV006	0.463	0.608	+0.145
Overall mean	***0.436***	***0.543***	***+0.107***

Table 3-4 shows that the personalised model increased the mean Dice score for all participants, with an overall mean improvement of 10.7%. Figure 3-28 visualises this, with the connecting lines highlighting that all participants had higher Dice scores with the personalised model, though the degree of improvement varied. The median Dice

scores for the cohort closely matched the overall means (Table 3-4) at 0.452 (IQR ±0.145) for the generic and 0.569 (IQR ±0.314) for the personalised model. These results support the hypothesis that including personalised contact geometries improves model predictions of joint contact area.

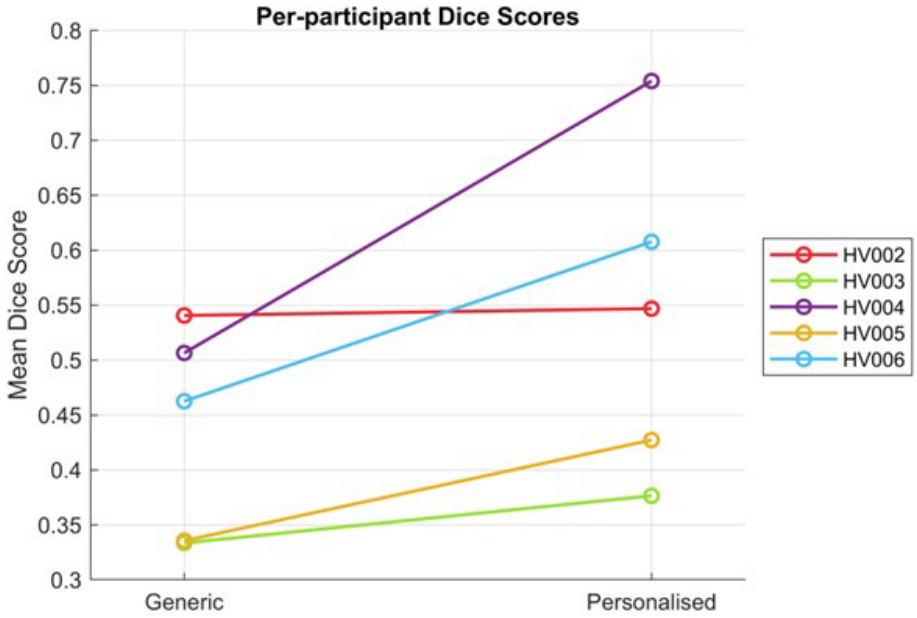

Figure 3-28 – Per-participant mean Dice scores plotted to visualise the improvements between the generic and personalised model contact predictions.

To confirm if the improvement in the Dice-scores was statistically significant, a Wilcoxon Signed-Rank test was performed, comparing the paired Dice scores for the five participants (Section 3.2.1). The test revealed a statistically significant improvement in the Dice scores for the personalised model compared to the generic model ($W = 5210$, $p < 0.0001$, $n = 109$ paired frames). This result confirmed that incorporating personalised geometries significantly improves the accuracy of contact map predictions during level gait, demonstrating the value of representing anatomical variation.

The Dice scores were also plotted against percentage stance to investigate how accuracy varied throughout the stance phase of level gait (Figure 3-29).

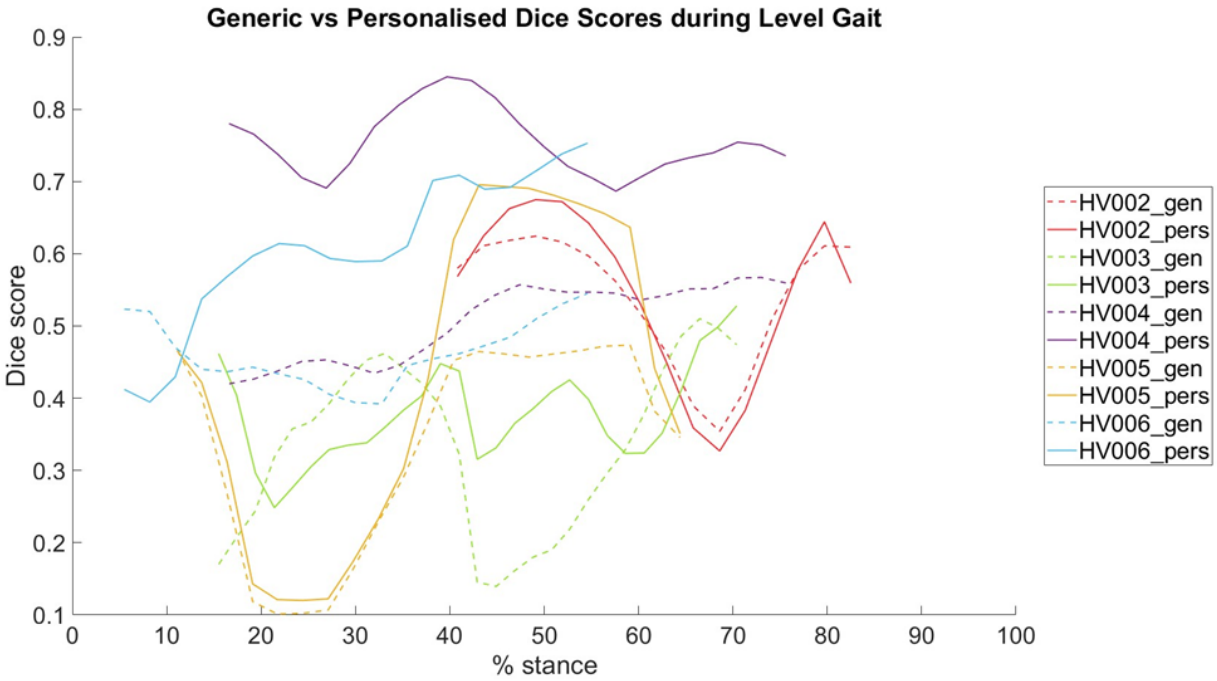

Figure 3-29 – The Dice scores between the MSM and BVR contact maps at each frame plotted against percentage stance of level gait for both the generic (dashed lines) and personalised (solid lines) versions of the model.

For all five participants, the personalised model had a higher Dice score than the generic model between 40-60%. However, outside of this range, the personalised model did not always have the higher Dice score. Only HV004 had a consistent, large improvement throughout all collected frames.

Some participants showed very similar Dice score profiles for both model versions. For example, HV002 had comparable magnitudes throughout, with slightly better predictions from 40-60% stance, but worse between 60-75% stance (Figure 3-29). This led to only a small mean Dice score improvement for that participant (0.06 higher, Table 3-4). This increased similarity in Dice score was likely due the split contact region on the medial tibial plateau (as a result of the contact morphology), as well as the close size match between this participant and the generic geometry.

Participants with small BVR contact areas (e.g. HV003 and HV005), presented low Dice scores with both model versions, as the limited BVR contact reduced overlap (with the MSM predicting contact where none was observed in BVR).

Statistical Parametric Mapping

As the generic and personalised contact maps were generated on different meshes, the personalised MSM and BVR results were remapped onto the generic model geometries (Section 3.2.5) to allow for element-wise comparison on both an individual and cohort level. This isolated discrepancies between the generic and personalised MSM predictions and their BVR counterparts to differences in pressure prediction, rather than mesh morphology.

SPM (Section 0) was used to compare the average errors of the (remapped) personalised and generic MSM pressures against to the (remapped) BVR pressures for each participant (Figure 3-30). For each element of the tibial cartilage, the z-value was calculated, and compared to that participant's z* value ($\alpha = 0.05$). These were coloured green if the personalised error was significantly lower (indicating better prediction) or red if higher. The average errors were computed across all available frames for each participant, which varied between individuals. A cohort mean map was also created by averaging the z-values across participants for each mesh element, with the mean z* of the five participants used as the threshold for statistical significance.

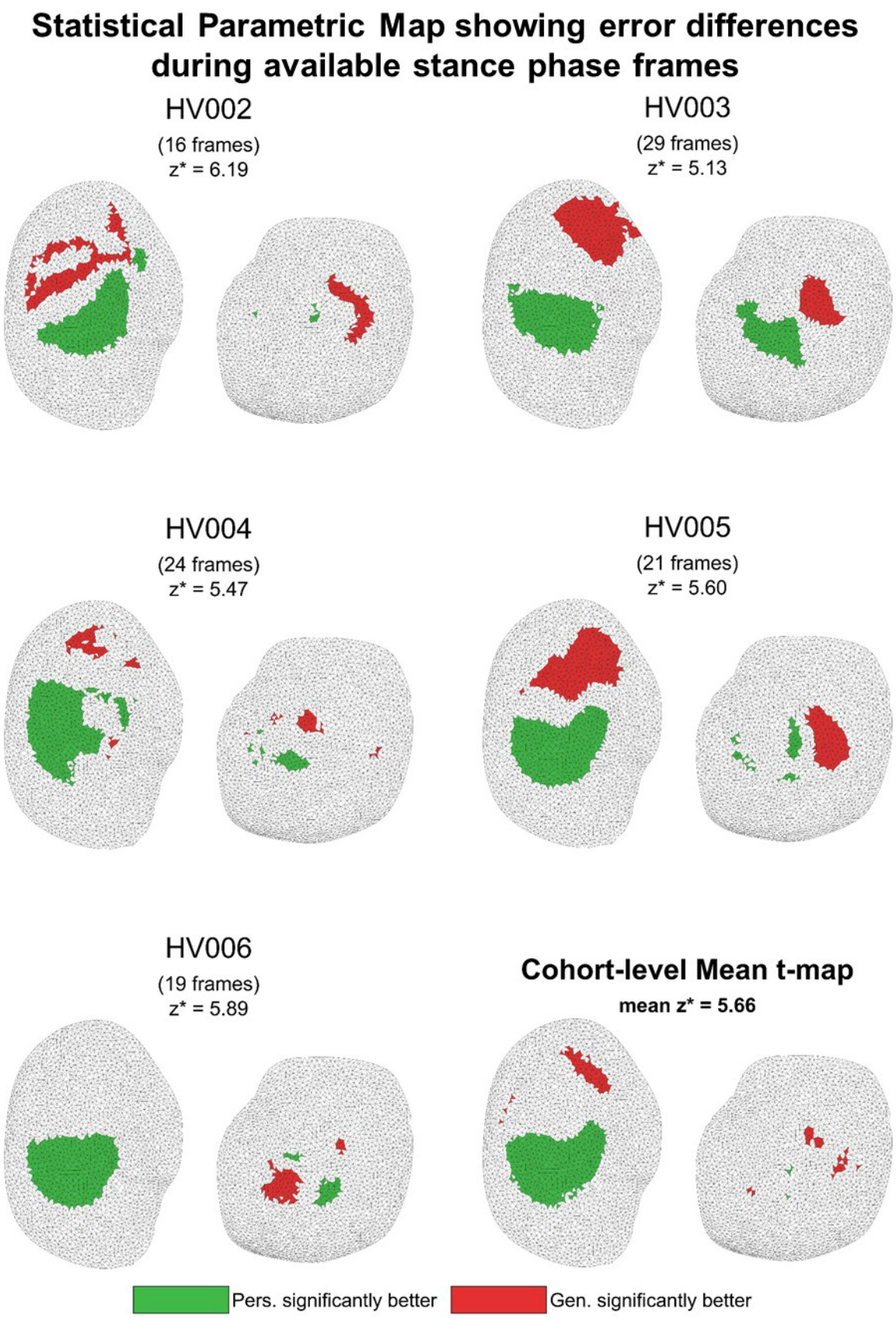

Figure 3-30 – Element-wise SPM comparing the mean error values (MSM – BVR) across the specified number of frames for each participant, with the final map showing the mean results across the whole cohort. Green = generic error was significantly higher (compared to that participant's z), and red = personalised error was significantly higher.*

Compared to the averaged results, individual SPM maps revealed more areas with significantly greater errors from the personalised model than the generic (red elements, Figure 3-30). This was largely due to the personalised model results having larger contact regions and higher pressures than the BVR data. The participants with the largest regions of significantly better generic predictions (HV003 & HV005) were the same participants with small BVR contact areas (Section 3.4.2) and low Dice scores (Figure 3-28, Section 0). These participants also showed large regions of green (significantly better personalised predictions) for the same reason.

However, when the errors were averaged across the cohort, a large region emerged on the medial tibial plateau where the generic model errors were significantly higher than the personalised model. This was due to the generic model predicting a more posterior contact region than the personalised MSM and BVR, resulting in significant errors where the generic model predicted contact, but it was not observed in the BVR results. This aligns with the greater anterior translation of the tibia relative to the femur predicted by the generic model compared to the BVR (Figure 3-22, Section 3.4.1), shifting the contact region posteriorly.

The z* threshold value varied slightly between participants due to differences in the number of frames included in the analysis. A higher z* threshold reflects a smaller dataset, where more random errors may be present and the data may be less smooth between frames. However, the z* values across participants were fairly similar, ranging from 5.13 to 6.19 (Figure 3-30).

As well as using SPM to investigate element-wise differences, it was also applied to per-frame analysis (Section 0). Figure 3-31 shows the total mean error difference (generic – personalised) of all mesh elements at each frame where data was collected per participant. The z* values for each participant are indicated on the graph as dotted red lines and any results that fall within this band are not statistically significant. Similarly to the element-wise comparison, green shaded regions indicate frames where the generic error was significantly higher than the personalised (personalised was better), whereas red shaded regions indicate significantly higher personalised errors.

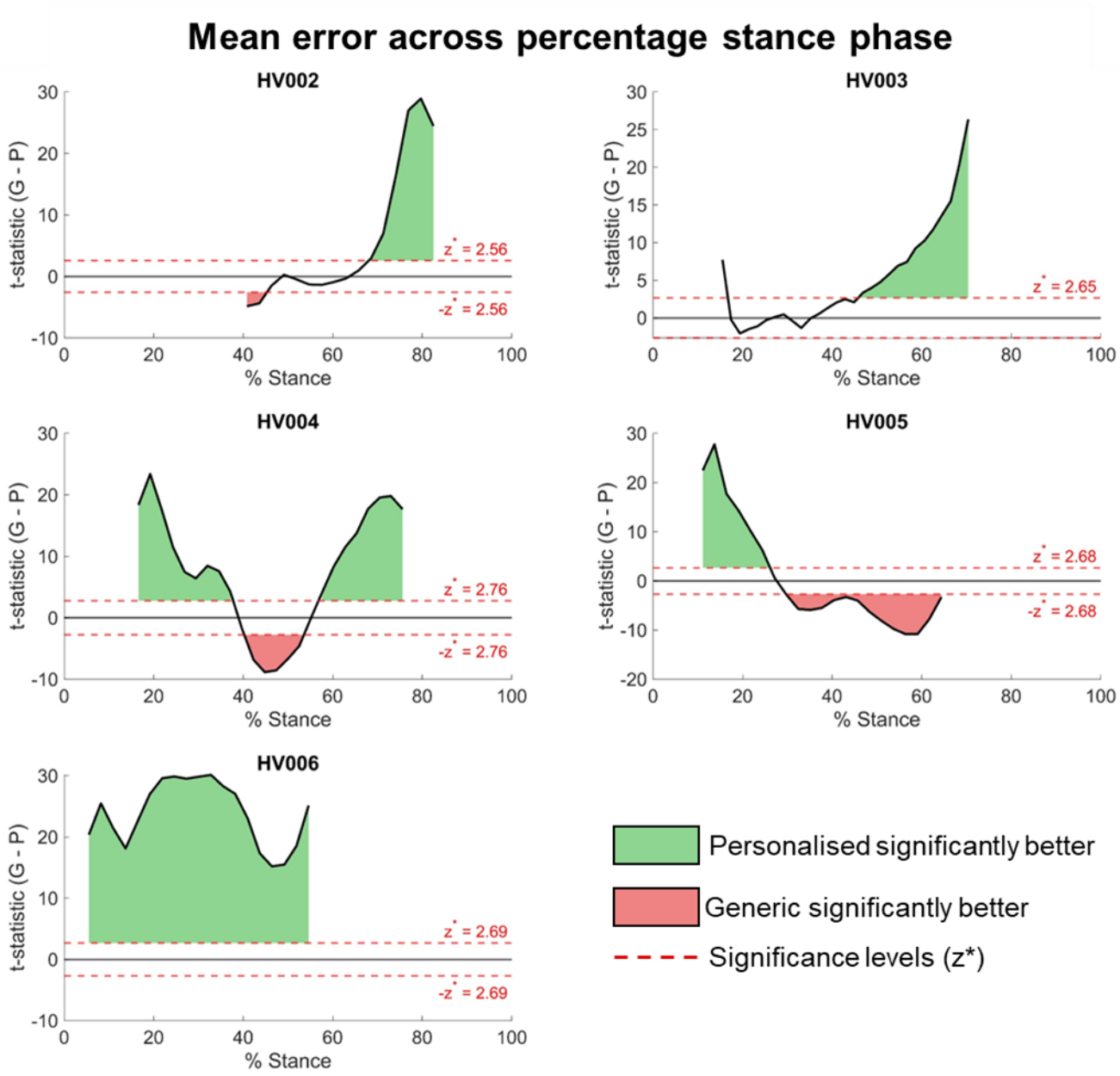

Figure 3-31 – SPM mean generic vs personalised results across percentage stance phase for each participant.

Although these results showed no consistent pattern of improved personalised model prediction for any specific part of stance phase, all participants had regions where the personalised MSM significantly outperformed the generic MSM (Figure 3-31). In contrast, only three participants showed any regions where the generic model was significantly better. For all participants, the maximum positive t-statistic (indicating better personalised model performance) was larger in absolute value than the minimum negative t-statistic, suggesting that improvements from the personalised model were more substantial than any areas where it underperformed.

Only HV006 showed a consistent, statistically significant improvement throughout all collected frames of gait using the personalised model. This was consistent with their high mean Dice score for the personalised model (Figure 3-28, Section 0), and low number of elements where the generic model errors were significantly smaller in the element-wise SPM results (Figure 3-30), supporting the visual improvement in contact map prediction seen in Appendix D. These results suggest that for HV006, the personalised model offered a particularly good match to the BVR-derived contact pressures, in part because its predicted magnitudes were closer to the lower BVR values, whereas the generic model pressures were particularly high for this participant.

Out of the five participants, HV005 presented with the largest percentage of stance phase where the personalised model was not significantly better than the generic model, with significant improvements only occurring during early stance. HV005 also had the highest number of elements where the generic model significantly outperformed the personalised model, and only a small number showing the opposite. These results are likely due to the more accurate lateral tibial plateau contact predictions by the generic model (as seen in the element-wise SPM in Figure 3-30), as well as the high pressure magnitudes calculated by the personalised model. Although this analysis shows the generic model outperformed the personalised from 30% stance onwards (Figure 3-31), this was not reflected in the Dice-scores for this participant, which showed a greater improvement in the personalised model from 40% stance onwards compared to earlier in the activity (Figure 3-29). This suggests that the contact area predicted by the personalised model was more consistent with the BVR results, while the generic model's pressure magnitudes were closer to the BVR values for this participant.

Weighted Centre of Pressure differences

Weighted COP (Section 3.2.1) changes were also investigated using the remapped contact pressure maps to allow for a fair comparison, not impacted by mesh size differences.

The medial and lateral plateau COP positions were calculated for the three different methods (personalised, generic and BVR), and their traces were plotted on the

generic tibial cartilage geometry to visualise the movement of the COP on the tibial plateau (Figure 3-32).

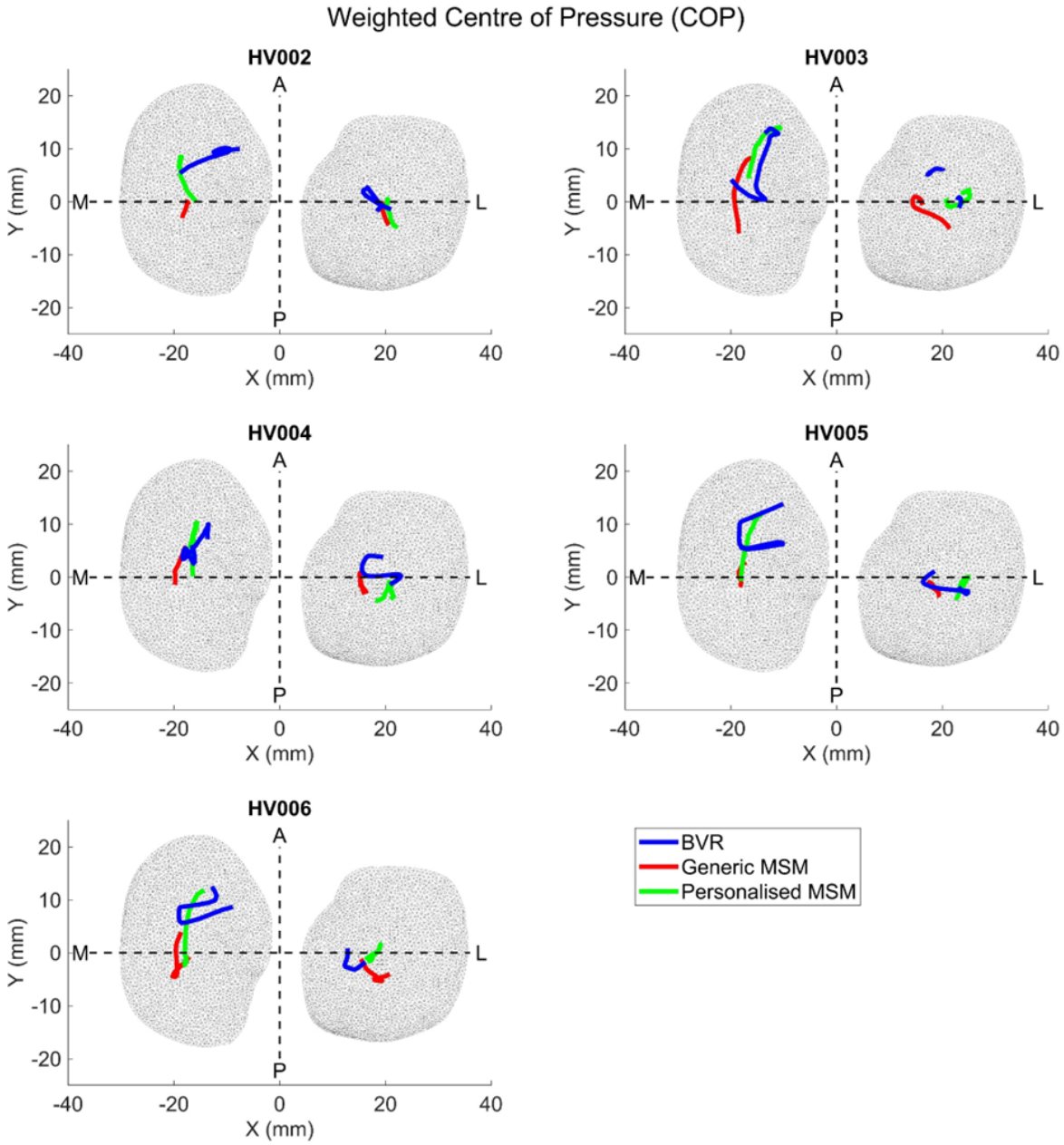

Figure 3-32 – Weighted COP trace on the tibial plateau plotted for each participant.

On the medial plateau, the personalised model COP traces were consistently more anterior (+y) than the generic model COP, consistent with the BVR results (Figure 3-32). The more posterior COP in the generic model was expected, given its greater anterior tibial translation relative to the femur (Figure 3-24).

The BVR COP was found to have a greater ROM in the ML (x) direction than either MSM when the mean range of COP displacements were calculated (Table 3-5). This

was true for both the medial and lateral half of the tibial plateau. This indicates the MSM may be over constraining the movement of the TF joint along the ML axis.

Table 3-5 – Mean range of COP displacement across all participants calculated for the three methods in both the ML and AP directions for the medial and lateral halves of the tibial plateau.

COP calculation method	Mean range of COP displacement			
	Medial tibial plateau		Lateral tibial plateau	
	ML (x) (mm)	AP (y) (mm)	ML (x) (mm)	AP (y) (mm)
BVR	8.75	8.22	6.31	5.14
Generic	2.14	7.31	3.50	4.23
Personalised	3.64	11.02	3.06	4.04

In the AP direction, the BVR had a slightly larger COP ROM than both models on the lateral plateau, but the personalised model displayed the largest ROM on the medial plateau (Table 3-5).

The error between the generic and personalised model COP predictions and the BVR COP were calculated for the two axes directions (ML and AP) at each frame. The mean error for each participant is presented in Table 3-6 along with the mean for the cohort.

Table 3-6 – Mean error across all frames between MSM and BVR COP positions in the ML and AP directions for the generic (gen.) and personalised (pers.) models. The difference in error (gen. – pers.) is colour-coded: red indicates lower error for the generic model, green indicates lower error for the personalised model.

Participant ID	Medial tibial plateau error (mm)					
	ML (x)			AP (y)		
	Gen.	Pers.	Diff.	Gen.	Pers.	Diff.
HV002	5.81	6.92	-1.11	9.84	2.53	7.32
HV003	4.68	1.17	3.51	6.85	3.77	3.08
HV004	2.74	1.77	0.97	3.13	3.89	-0.76
HV005	2.62	3.45	-0.83	7.35	2.80	4.54
HV006	3.50	2.23	1.27	9.40	4.48	4.92
Mean	**3.87**	**3.11**	**0.76**	**7.31**	**3.50**	**3.82**
Participant ID	Lateral tibial plateau error (mm)					
	ML (x)			AP (y)		
	Gen.	Pers.	Diff.	Gen.	Pers.	Diff.
HV002	2.02	3.09	-1.07	2.31	2.24	0.07
HV003	3.23	4.72	-1.49	4.74	2.85	1.89
HV004	2.92	3.70	-0.78	2.56	4.37	-1.81
HV005	3.34	3.93	-0.59	0.77	1.45	-0.68
HV006	4.31	4.62	-0.31	1.95	1.87	0.09
Mean	**3.16**	**4.01**	**-0.85**	**2.47**	**2.56**	**-0.09**

The largest difference in the mean cohort error (3.82 mm) between the two model versions was found in the AP direction on the medial plateau, with the personalised model showing a lower error (Table 3-6). In contrast, the AP translation on the lateral tibial plateau showed the smallest difference in mean cohort error (-0.09 mm). The mean cohort error in the ML direction was similar on both plateaus, with both below 1 mm. Although the personalised model had lower mean cohort errors on the medial plateau in both directions, it had higher errors on the lateral plateau. Despite this, errors were small in all directions except for AP translation on the medial plateau, indicating this is the main direction where the personalised model improves predictions.

3.4.3 MUSCULOSKELETAL MODEL PREDICTIONS DURING HIGHER FLEXION ACTIVITIES

As well as investigating the model accuracy differences during level gait, the comparison was expanded to two activities involving higher flexion angles: stair ascent and lunge(also collected as part of the pilot dataset from Chapter 2). These

activities challenged the model's capabilities at a range higher of flexion than it is typically used for aiming to answer the third research question:

> *Do the observed differences between the personalised and generic model outputs reported during gait carry over to activities involving higher TF flexion angles?*

Stair ascent

Like with the kinematic results for gait in Section 3.4.1, the six DOF TF kinematics were plotted against percentage stance for all three methods – BVR, generic MSM, and personalised MSM (rotations in Figure 3-33 and translations in Figure 3-34). The Bland-Altman results for these kinematics are presented in Figure 3-35 and Figure 3-36, along with violin plots summarising the distribution of differences across participants (Section 0).

The flexion angles predicted by both MSMs had a similar profile to the BVR mean result but with an earlier peak in flexion (Figure 3-33). They also showed a consistent offset from the BVR results, 10° for the generic and 11° for the personalised (Figure 3-35), which was similar to the offset observed during gait.

Although the mean adduction of the generic model was closer to the BVR mean (Figure 3-33), the median difference (MSM-BVR) was slightly smaller for the personalised model (Figure 3-35). Whereas the personalised model adduction values were more diverged at the beginning of stance, converging later in stance, the generic model predictions were the opposite. Neither of these trends was seen in the BVR results. The generic model tended to underestimate the adduction angle, whereas the personalised model slightly overestimated it (Figure 3-35). Both models poorly predicted the adduction for participant HV006, where they overestimated the value compared to BVR. This was attributed to the large adduction angle calculated for this participant by BVR, which was not replicated by either MSM.

IE rotation was poorly predicted by both versions of the model which both predicted external rotation, opposing the internal rotation calculated from the BVR data (Figure 3-33). The generic model predicted a wider range of differences than the personalised, but they had a similar mean profile with the same mean difference offset to the BVR results (16°, Figure 3-35).

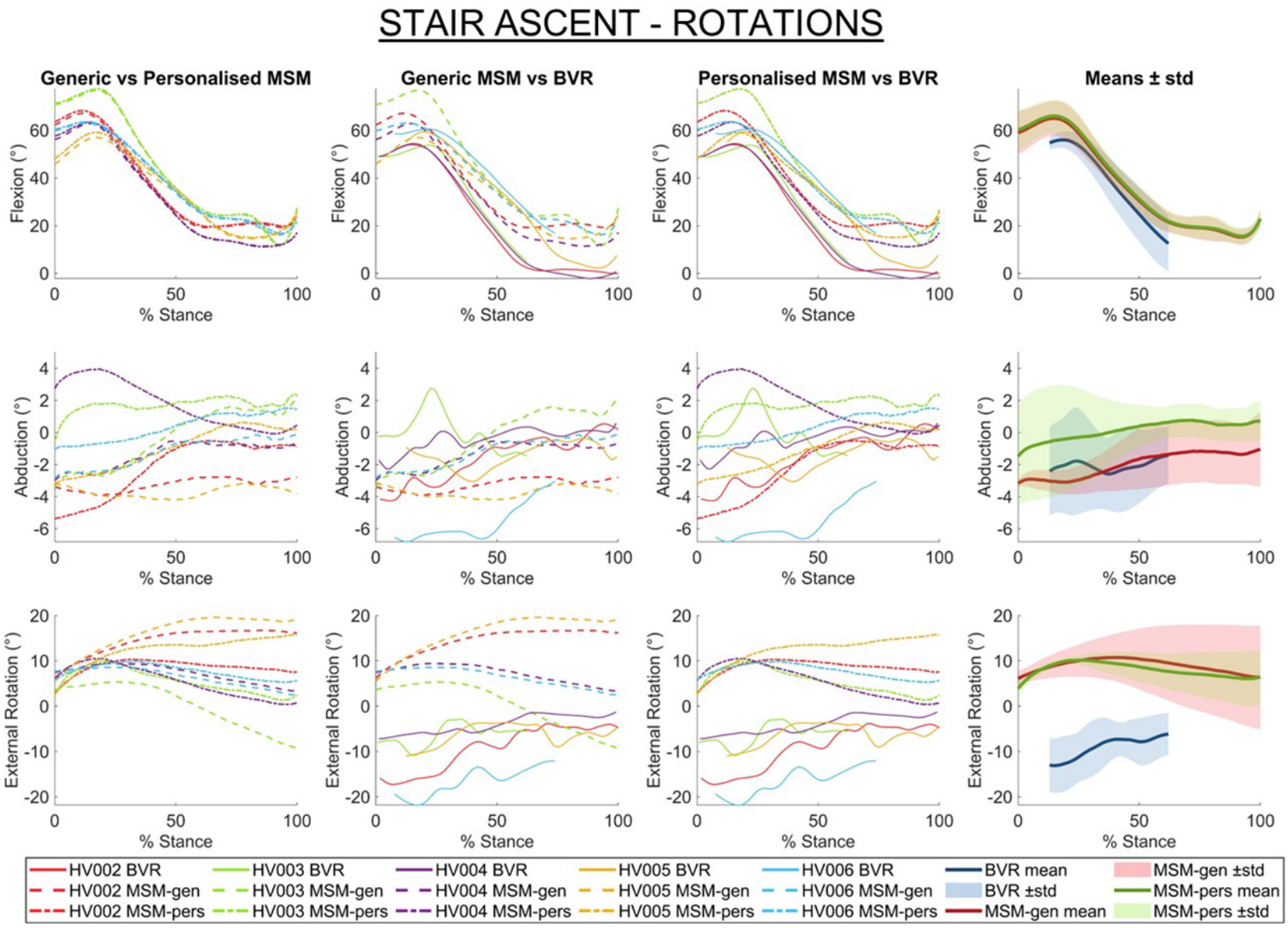

Figure 3-33 – Graphs showing the calculated rotations for the individual participants during stair ascent as well as the mean ±std of the cohort. The first column shows the BVR results, the second contains the generic MSM results, the third the personalised results and the fourth column contains the mean ±std of all three methods.

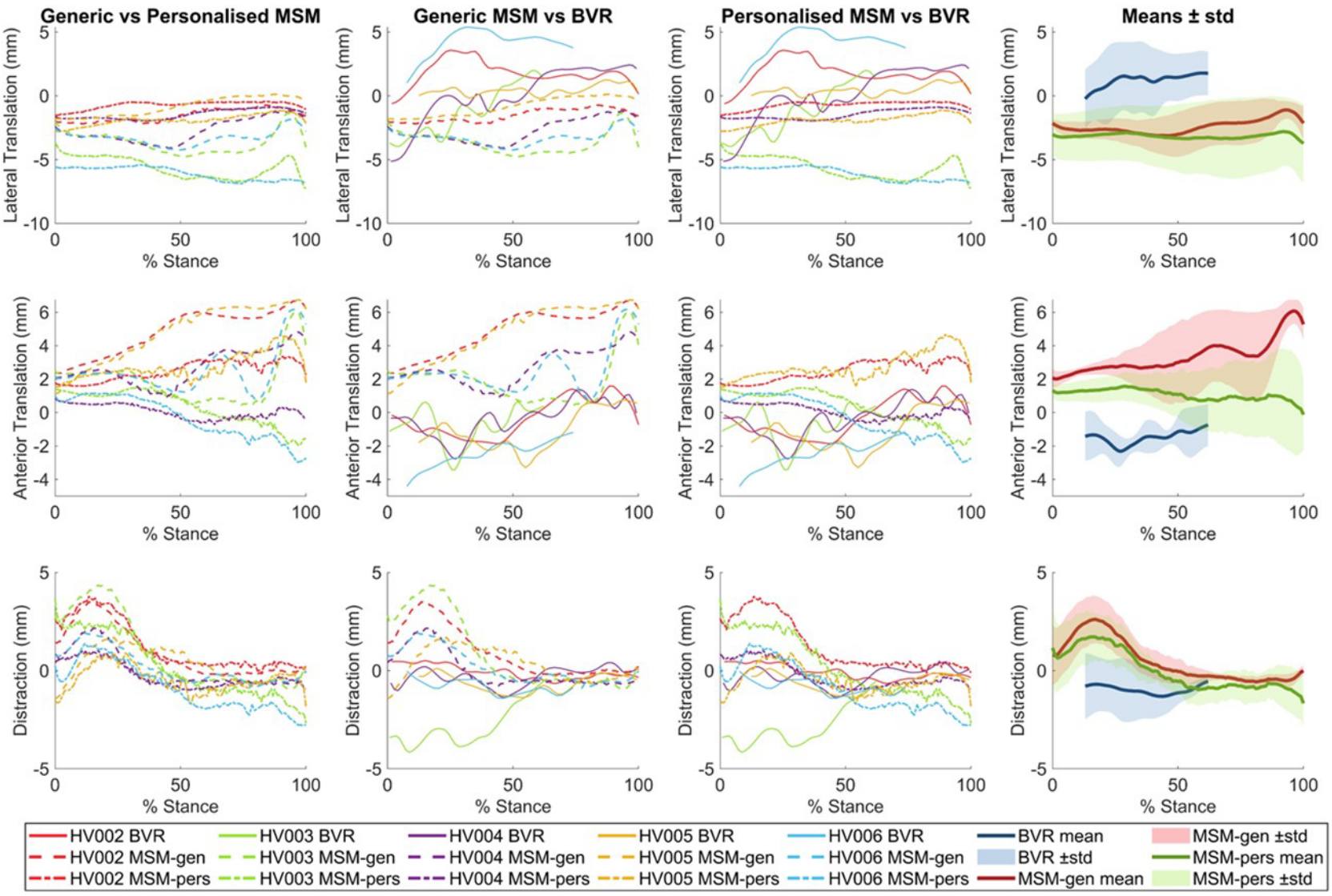

Figure 3-34 – Graphs showing the calculated translations for the individual participants during stair ascent as well as the mean ±std of the cohort. The first column shows the BVR results, the second contains the generic MSM results, the third the personalised results and the fourth column contains the mean ±std of all three methods.

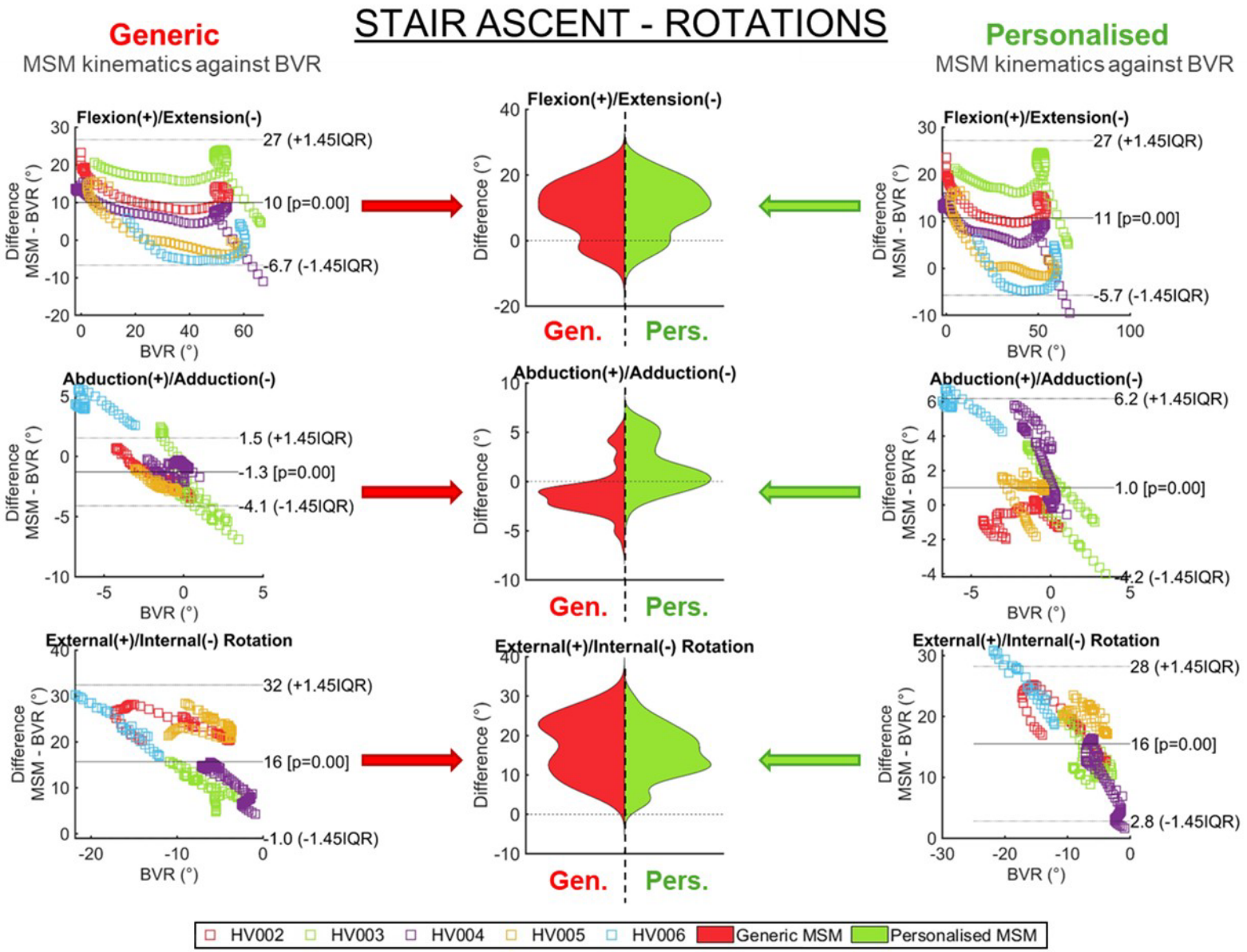

Figure 3-35 – Bland Altman analyses of the generic (left column, red) and personalised (right column, green) MSM rotations compared against gold-standard BVR rotations during stair ascent. These results were simplified into violin plots to show the distribution of the differences (middle column).

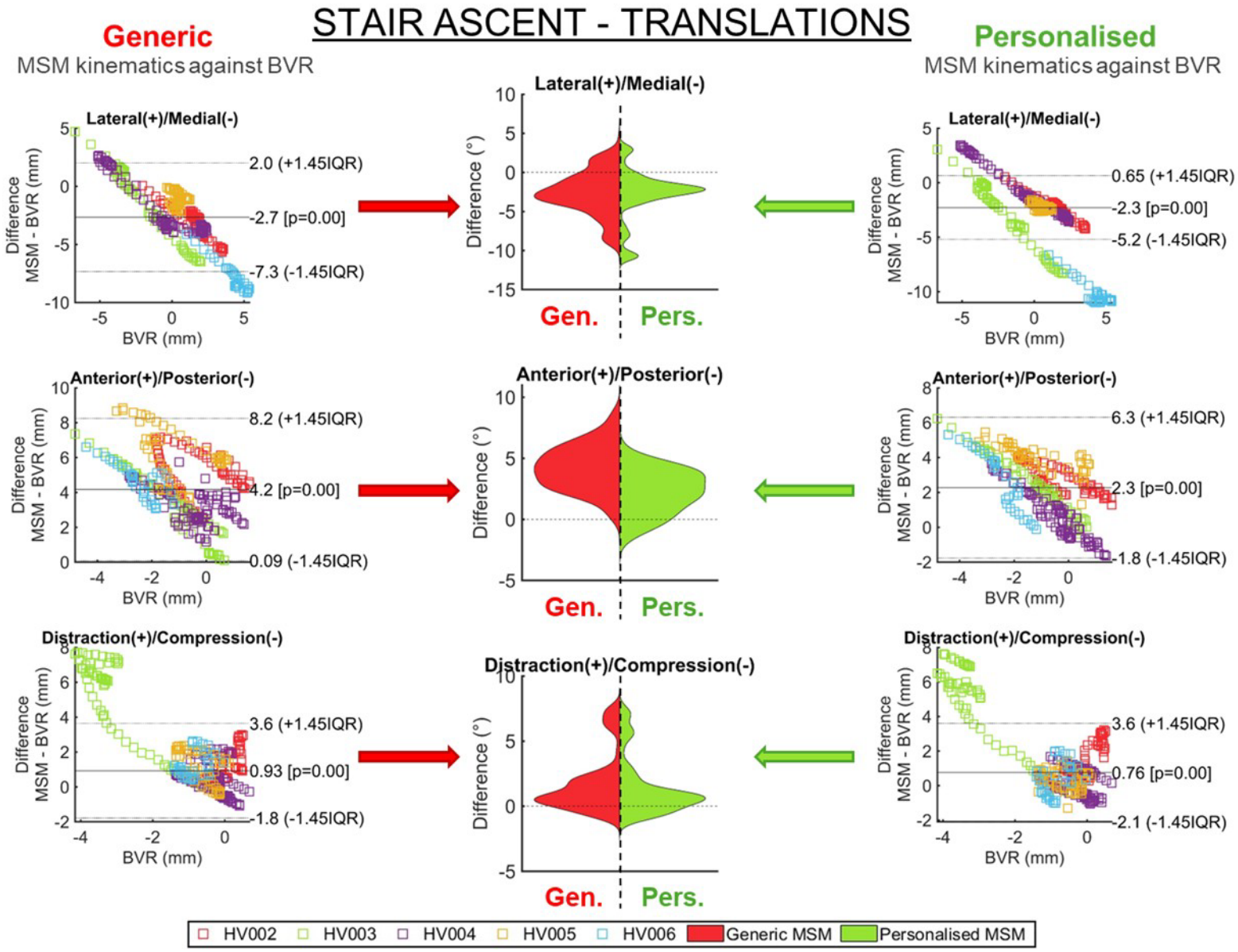

Figure 3-36 – Bland Altman analyses of the generic (left column) and personalised (right column) MSM translations compared against gold-standard BVR translations during stair ascent. These results were simplified into violin plots to show the distribution of the differences (middle column).

The personalised model improved the median translational difference between the MSM and the BVR results in all three DOFs (Figure 3-36), although there was little difference in the median value between ML and CD translations. AP translation accuracy was improved the most by the inclusion of personalised geometries, like with level gait. Although, this was much less pronounced for stair ascent with the personalised prediction being only 1.9 mm closer to the BVR translation value than the generic model (as compared to the improvement of 7.07 mm during gait).

Both models predicted similar mean lateral translation magnitudes (Figure 3-34). Like with external rotation, the models predicted the opposite magnitude of translation to the BVR results (which predicted a mean medial translation). There was also a negative correlation seen on the BA plots for both models (Figure 3-36), displaying the same over constraining of this DOF as seen with level gait (Section 3.4.1, Figure 3-24).

Both the personalised and generic model predicted a peak of distraction during early stance, coinciding with the peak in flexion during stair ascent (Figure 3-34). This was not seen in the BVR results due to HV003 presenting higher compression during early stance, skewing the mean.

To investigate the effects of the kinematic differences on the contact map results, the MSM (Section 3.2.3) and BVR (Section 3.2.4) contact map differences were visually analysed. See Appendix D for the contact maps at 10% intervals of stance phase during stair ascent for each participant.

Examples were taken at 20% stance (corresponding with peak flexion, Figure 3-37) and at 60% stance (the last 10% interval where data was available for all participants, Figure 3-38). These two intervals were chosen to investigate contact predictions at differing knee flexion magnitudes, as, compared to level gait, the peak flexion in early stance is much higher, but of a similar magnitude during late stance.

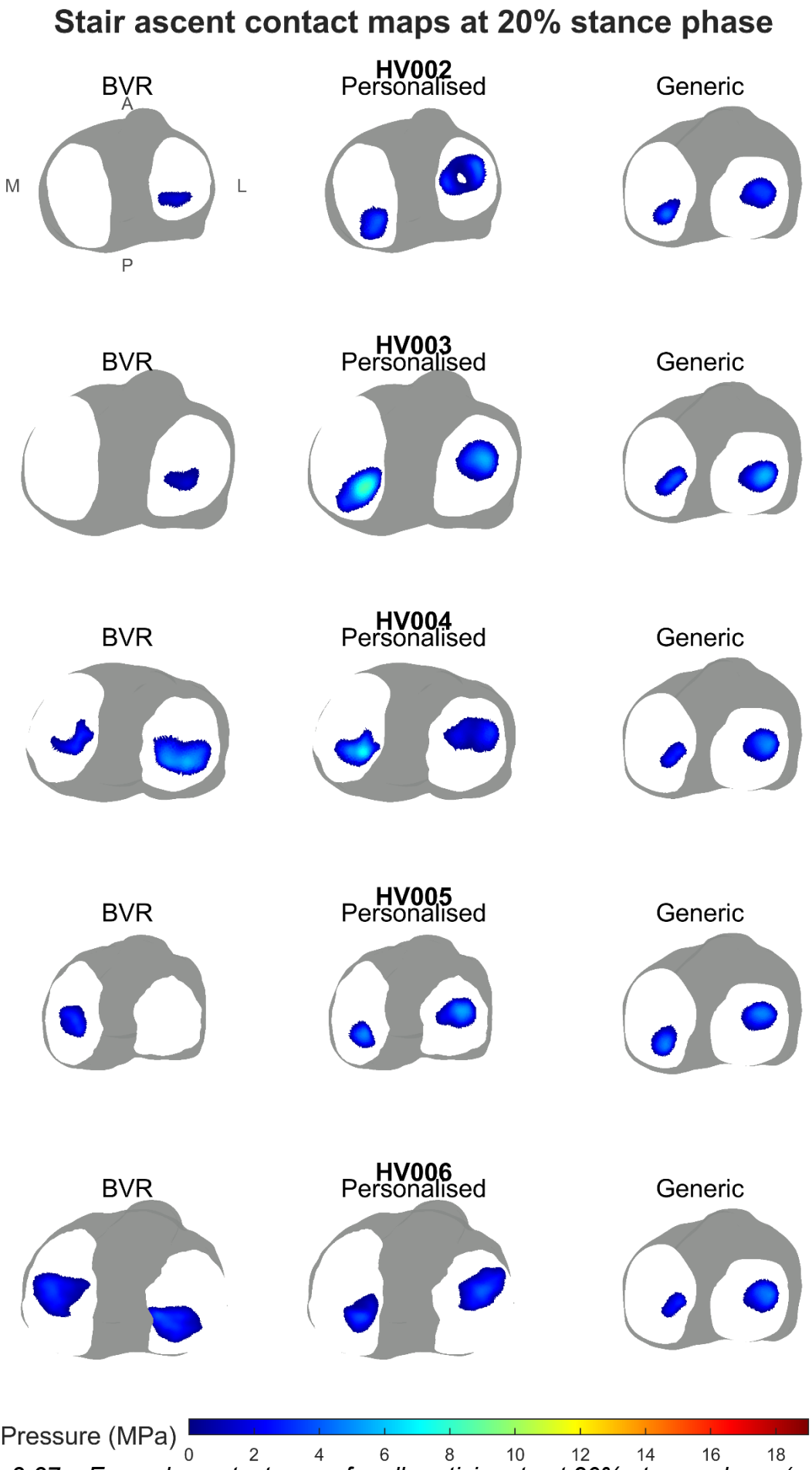

Figure 3-37 – Example contact maps for all participants at 20% stance phase (peak flexion) during stair ascent. BVR contact map results in the first column, personalised MSM results in the second and the generic MSM contact map in the third.

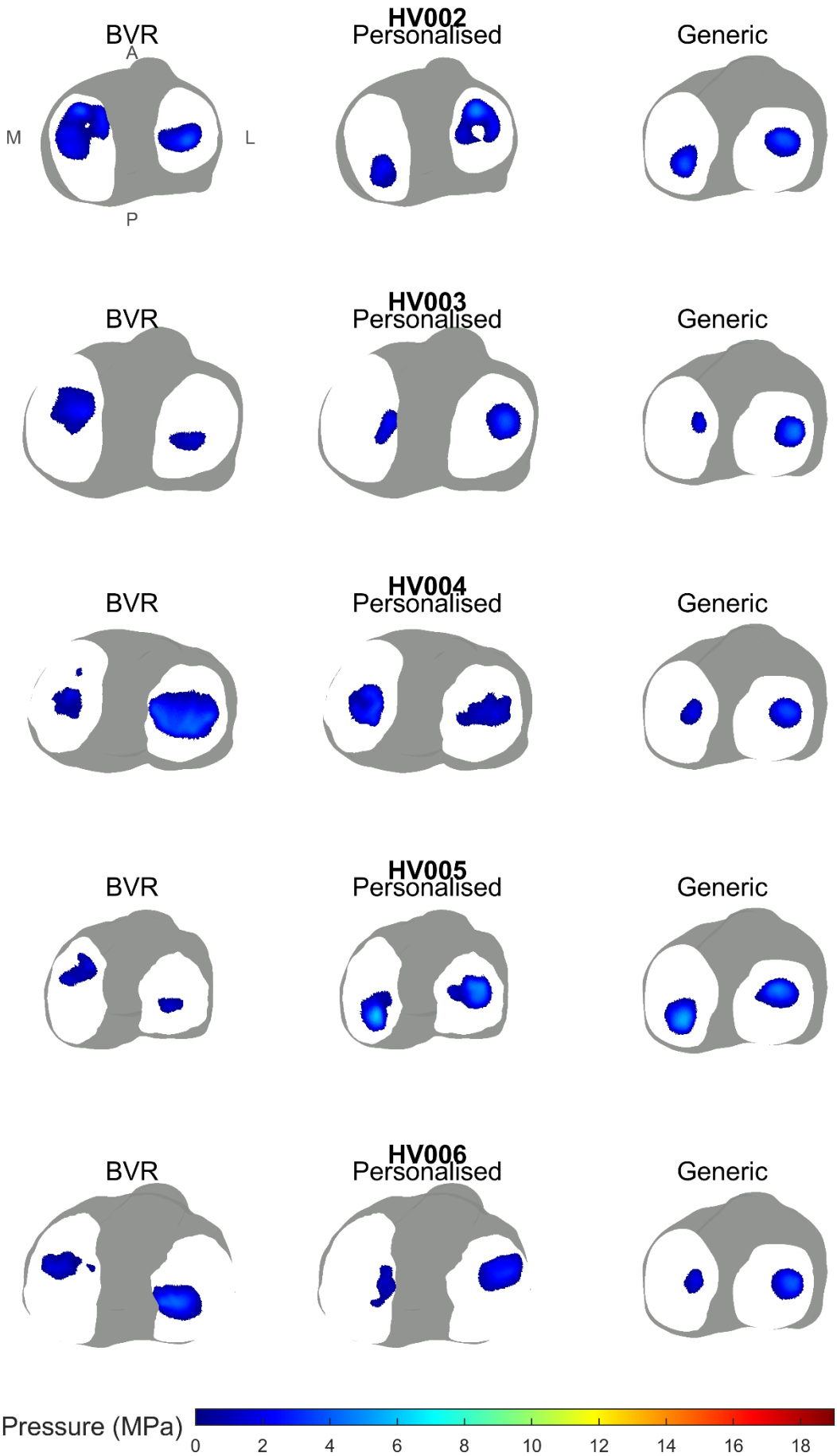

Figure 3-38 - Example contact maps for all participants at 60% stance phase (lower flexion) during stair ascent. BVR contact map results in the first column, personalised MSM results in the second and the generic MSM contact map in the third.

At 20% stance (Figure 3-37), contact was only found on one half of the tibial plateau for 3/5 participants using the BVR data. This highlights the limitations of calculating BVR contact using ray tracing and bounding boxes due to its sensitivity to mesh positioning. Where there is little or no contact calculated by the BVR data, differences in contact area between the MSM and BVR results are not easily comparable.

For this activity, instances of little or no contact on one or both plateaus were more commonly observed during the first half of stance phase when knee flexion was higher. Some participants displayed these small contact regions throughout (e.g. HV005), whereas some only displayed them in the first half of stance (e.g. HV004), and some displayed larger, more consistent contact areas all through the activity (e.g. HV006). This highlights the variable effects of personalised geometry and kinematics on predicted contact area through the BVR results.

The two sets of MSM results at 20% stance phase (Figure 3-37) displayed a similar pattern of contact region, with the medial tibial plateau contact sitting more posteriorly than the lateral plateau contact, reflecting the high external rotation of the tibia seen in both MSM results (Figure 3-33). This contrasted the contact pattern resulting from the internal rotation calculated by the BVR, seen in participants where contact was visible on both tibial plateau halves (Figure 3-39). The similarity between the generic and personalised contact regions became less pronounced at 60% stance phase (Figure 3-38) in some individuals (e.g. HV004), however was still clearly seen in other participants (e.g. HV002 & HV005).

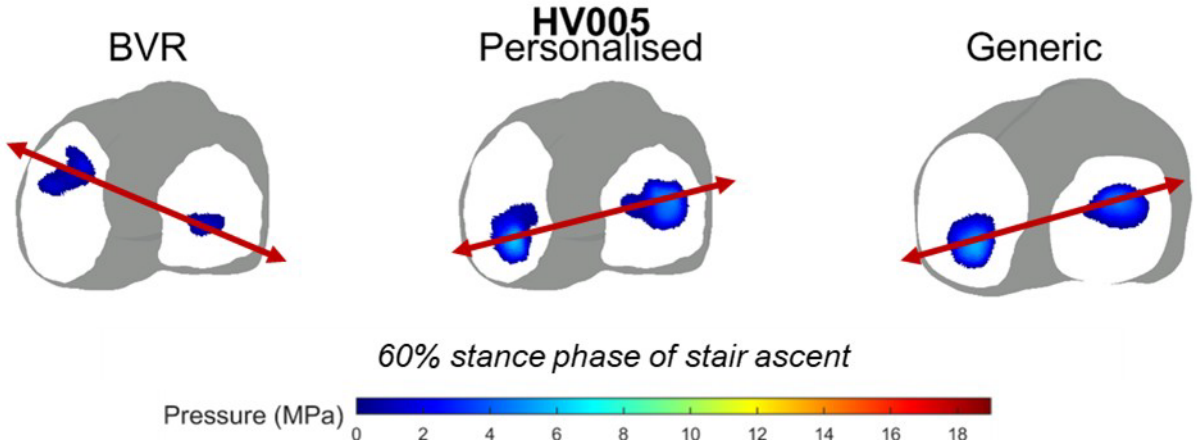

Figure 3-39 – Example highlighting the difference in contact slope on the tibial plateau caused by the variation in IE rotation.

The differences in contact area due to the difference in external rotation, along with the BVR results with little or no contact area predicted, resulted in low Dice scores between the MSM and BVR predictions for both the generic and personalised predictions during stair ascent (Table 3-7).

Table 3-7 – Mean Dice scores for each participant during stair ascent

Participant ID	**Mean Dice score of stair ascent frames** *MSM compared against BVR contact map images.*		
	Generic MSM *(c.f. BVR)*	**Personalised MSM** *(c.f. BVR)*	**Difference** *(pers. – gen.)*
HV002	0.188	0.162	-0.027
HV003	0.178	0.179	+0.001
HV004	0.181	0.457	+0.276
HV005	0.033	0.129	+0.096
HV006	0.002	0.070	+0.068
Overall mean	***0.117***	***0.199***	***+0.083***

All Dice scores were found to be below 0.2 for both models for all participants, except for the personalised model of HV004, which had a mean Dice score was 0.475. This participant was the exception due to a combination of having the smallest average BVR internal rotation of the cohort – resulting in a smaller offset in external rotation with the MSM – as well as having relatively large contact areas (particularly towards the end of stance phase). These factors led to a greater overlap between the BVR and personalised MSM contact maps, as the personalised model predicted a larger contact area than the generic model, increasing the number of shared contact pixels for the Dice score calculation.

For all participants, except for HV004, the difference in the mean between the personalised and generic Dice scores were found to be <0.1 due to the low Dice scores predicted. As well as low cohort mean Dice scores (generic = 0.117, personalised = 0.199), the cohort median Dice scores for stair ascent were also low, at 0.147 (IQR ±0.196) for the generic and 0.189 (IQR ±0.292) for the personalised model.

Despite these low averages and small differences, a Wilcoxon Signed-Rank test (Section 3.2.1) found the difference to be statistically significant ($W = 25947$, $p < 0.0001$). This suggests that the personalised geometry did improve the contact area prediction. However, as the Dices scores are low, caution must be taken when interpreting results from either model due to the lack of similarity with the BVR results.

Lunge

The six DOF kinematics during a dynamic weightbearing lunge are presented in Figure 3-40 and Figure 3-41 for the five participants from the generic MSM, personalised MSM and BVR results for comparison. The Bland-Altman results for these kinematics can be found in Figure 3-42 and Figure 3-43, along with the distribution of differences simplified into violin plots.

Like the other two activities, the flexion angle predicted by both MSMs was the same and the mean value was offset from the BVR results (Figure 3-40). The generic model had a median flexion offset from the BVR results of 9.4° and the personalised model had an offset of 10° (Figure 3-42). This was the smallest offset found for any of the activities and was also smaller than the 14° offset of the Visual3D motion-capture results for the lunge activity (Section 2.5.7).

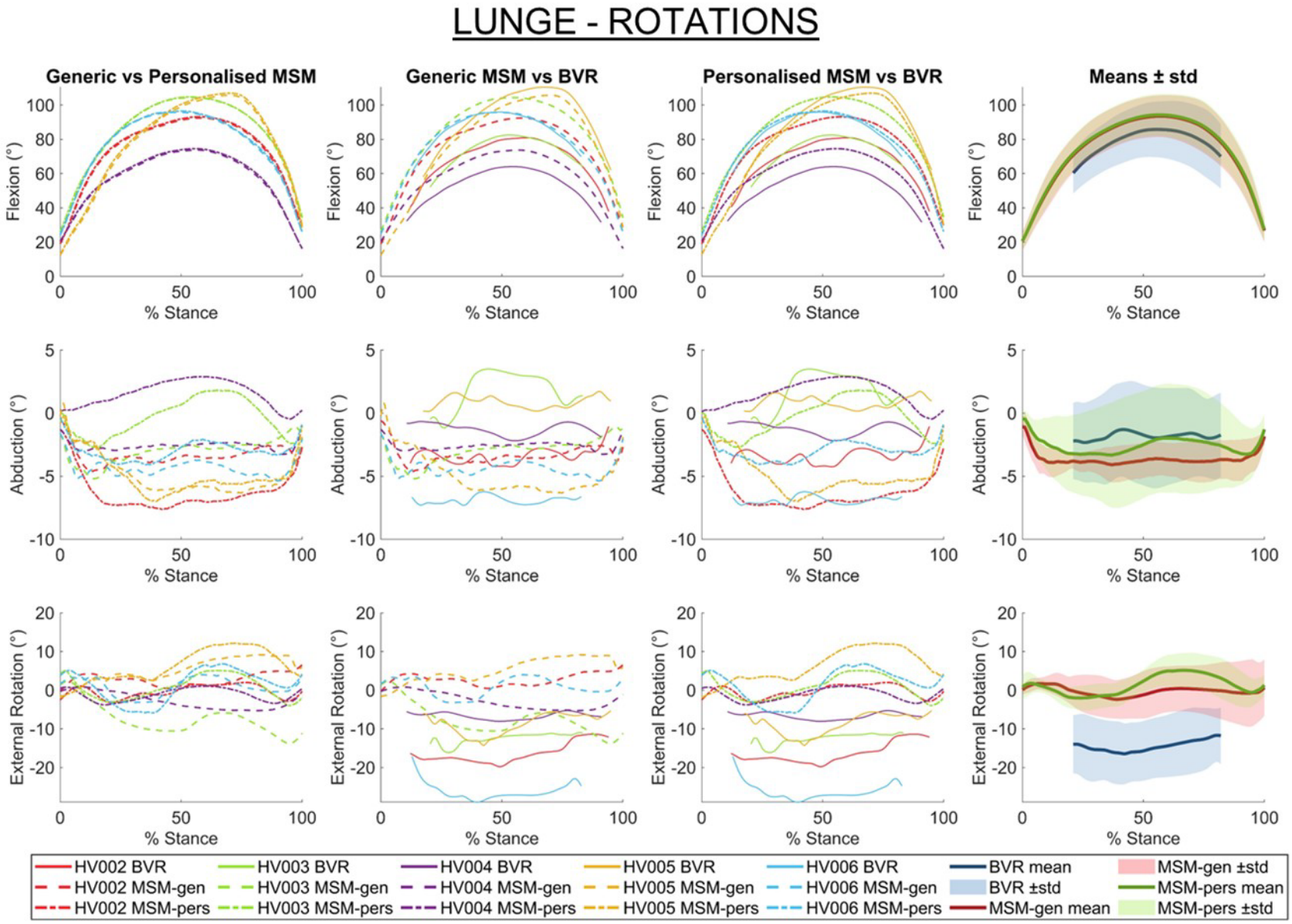

Figure 3-40 – Graphs showing the calculated rotations for the individual participants during lunging as well as the mean ±std of the cohort. The first column shows the BVR results, the second contains the generic MSM results, the third the personalised results and the fourth column contains the mean ±std of all three methods.

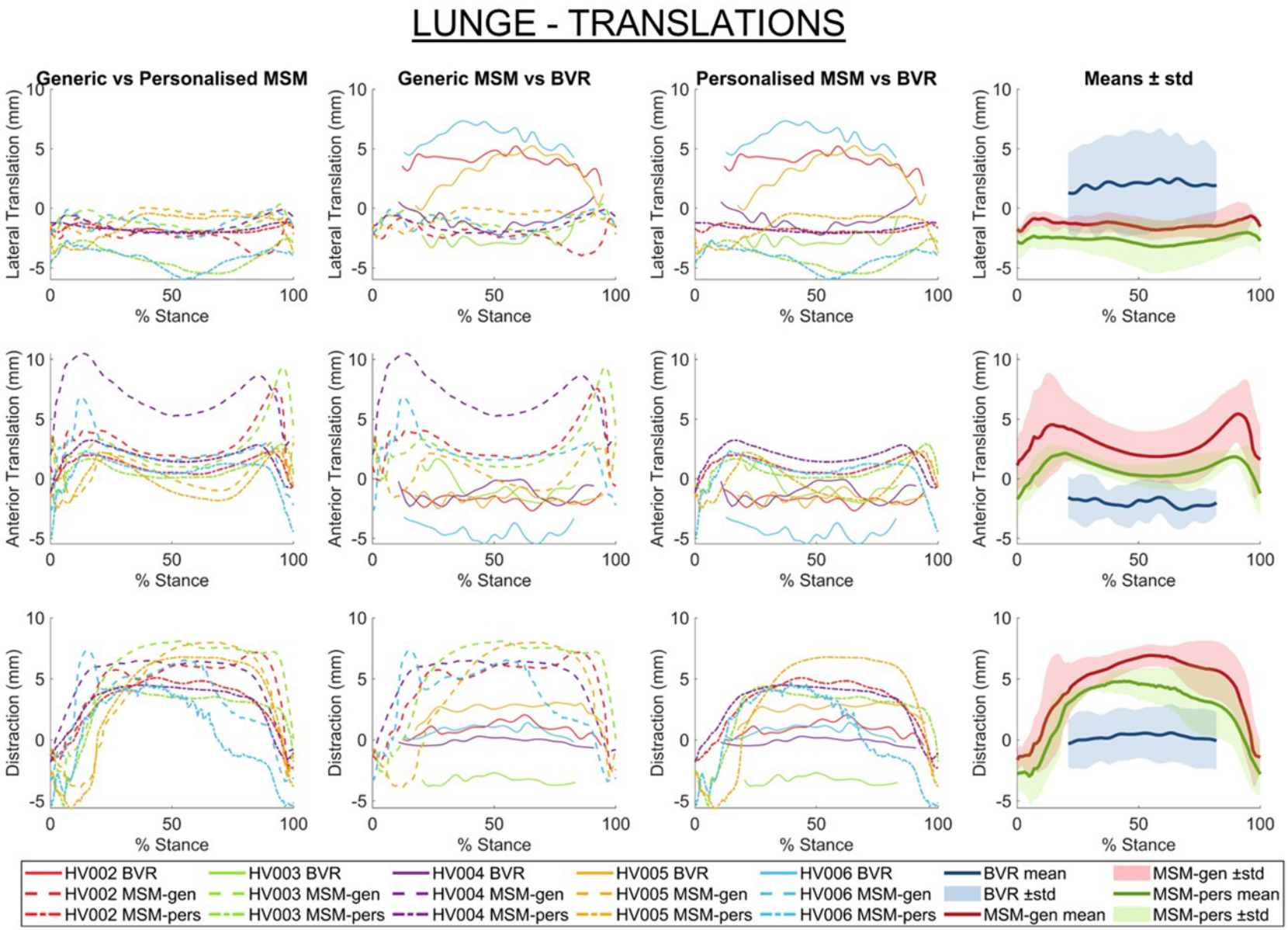

Figure 3-41 – Graphs showing the calculated translations for the individual participants during lunging as well as the mean ±std of the cohort. The first column shows the BVR results, the second contains the generic MSM results, the third the personalised results and the fourth column contains the mean ±std of all three methods.

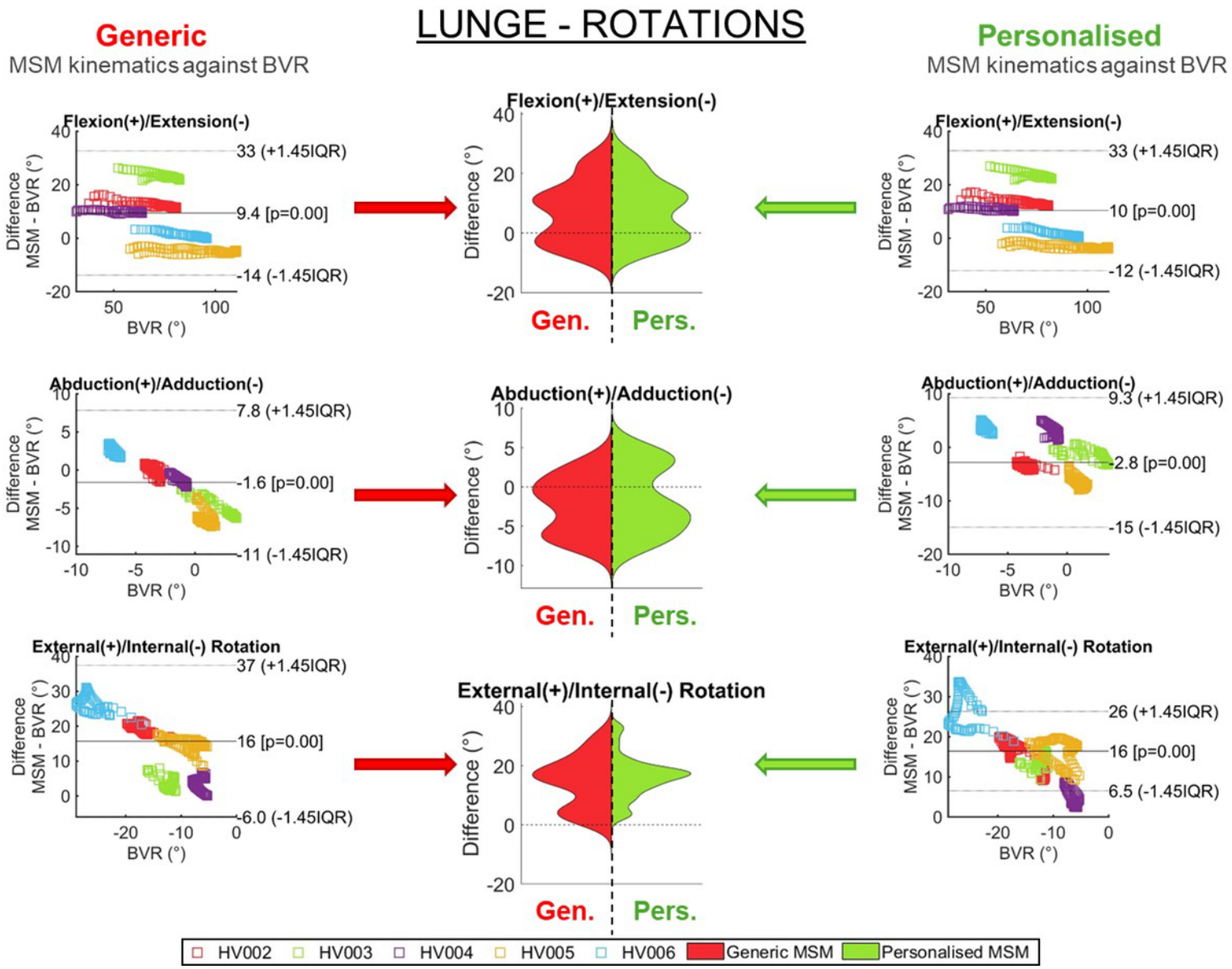

Figure 3-42 – Bland Altman analyses of the generic (left column) and personalised (right column) MSM translations compared against gold-standard BVR rotations during lunging. These results were simplified into violin plots to show the distribution of the differences (middle column).

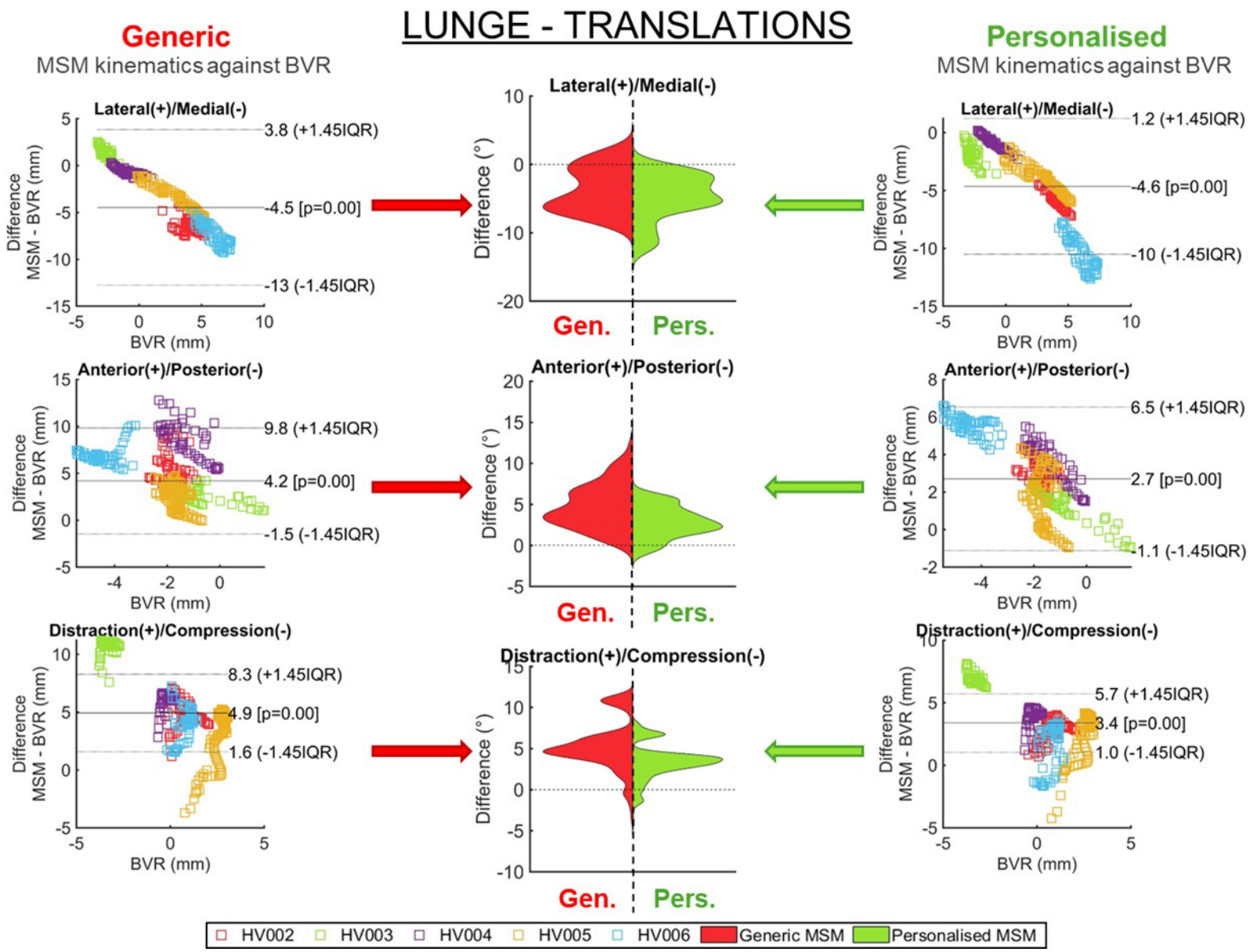

Figure 3-43 – Bland Altman analyses of the generic (left column) and personalised (right column) MSM translations compared against gold-standard BVR translations during lunging. These results were simplified into violin plots to show the distribution of the differences (middle column).

All three methods calculated the knee to be adducted on average during lunge, however, both the BVR and personalised MSM predicted a large range of magnitudes across the cohort, with some participants displaying abduction throughout (Figure 3-40). The adduction angle estimated by the generic model was more consistent between participants. Both models displayed a large range of differences between participants, but with a fairly consistent offset for each individual (Figure 3-43).

Like with stair ascent, both MSMs poorly predicted TF internal rotation displaying the same median rotation offset of 16° (Figure 3-42). The BVR results showed the knee to be constantly internally rotated throughout the lunge, whereas both MSMs found the average rotation fluctuated around 0° (Figure 3-40).

The personalised model presented a closer mean translation to the BVR results than the generic model in both the AP and CD directions, but not for ML translation (Figure 3-41). Both MSMs found medial translation overall, whereas the BVR presented mean lateral translation, although there was variation between participants, with some showing medial translation throughout. Again, like the other two activities, the trend of decreasing difference with increased BVR medial translation was present (Figure 3-43).

Similarly to the other two activities, the personalised model was found to improve the median AP translation difference, this time by 1.5 mm (Figure 3-43). Again, both models overestimated the translation, generally predicting anterior translation of the tibia relative to the femur, whereas BVR generally presented posterior translation.

Both models found the joint to be distracted during the central portion of the lunge, coinciding with the higher flexion angles, contrary to the BVR results where the median remained around neutral (Figure 3-41). Although both MSMs overestimated distraction, the personalised model did present a lower median difference and IQR than the generic model (Figure 3-43).

The lunge contact maps from the three methods were then compared visually for similarity. The results for each participant at intervals of 10% lunge can be found in Appendix D. Examples of the contact maps for the cohort at 50% lunge are shown in Figure 3-44; 50% lunge was chosen as this was a point of high flexion for all participants, roughly matching the mean peak flexion value of the cohort.

Like the other two activities, the BVR lunge contact maps had frames with little or no contact on half of the tibial plateau, particularly on the medial plateau. Again, some participants displayed more frames with small contact areas (e.g. HV002 & HV003) than others (e.g. HV006). There was no obvious kinematic pattern as to the participants that presented with smaller contact regions, suggesting this was more likely due to individual geometry, or segmentation and image registration errors than kinematic inputs.

Like with stair ascent, the MSM contact regions were located more posteriorly on the medial plateau compared to the lateral plateau (Figure 3-44), again due to the predicted external rotation of the tibia (Figure 3-40). This was more clearly seen in the personalised MSM lunge results than in the generic (e.g. HV002, HV003 & HV006 in Figure 3-44), likely due to the personalised MSM's external rotation being higher at 50% lunge. The BVR contact maps displayed the opposite pattern of the medial contact being more anterior than the lateral, reflecting the much higher internal rotation calculated using this method than the MSMs.

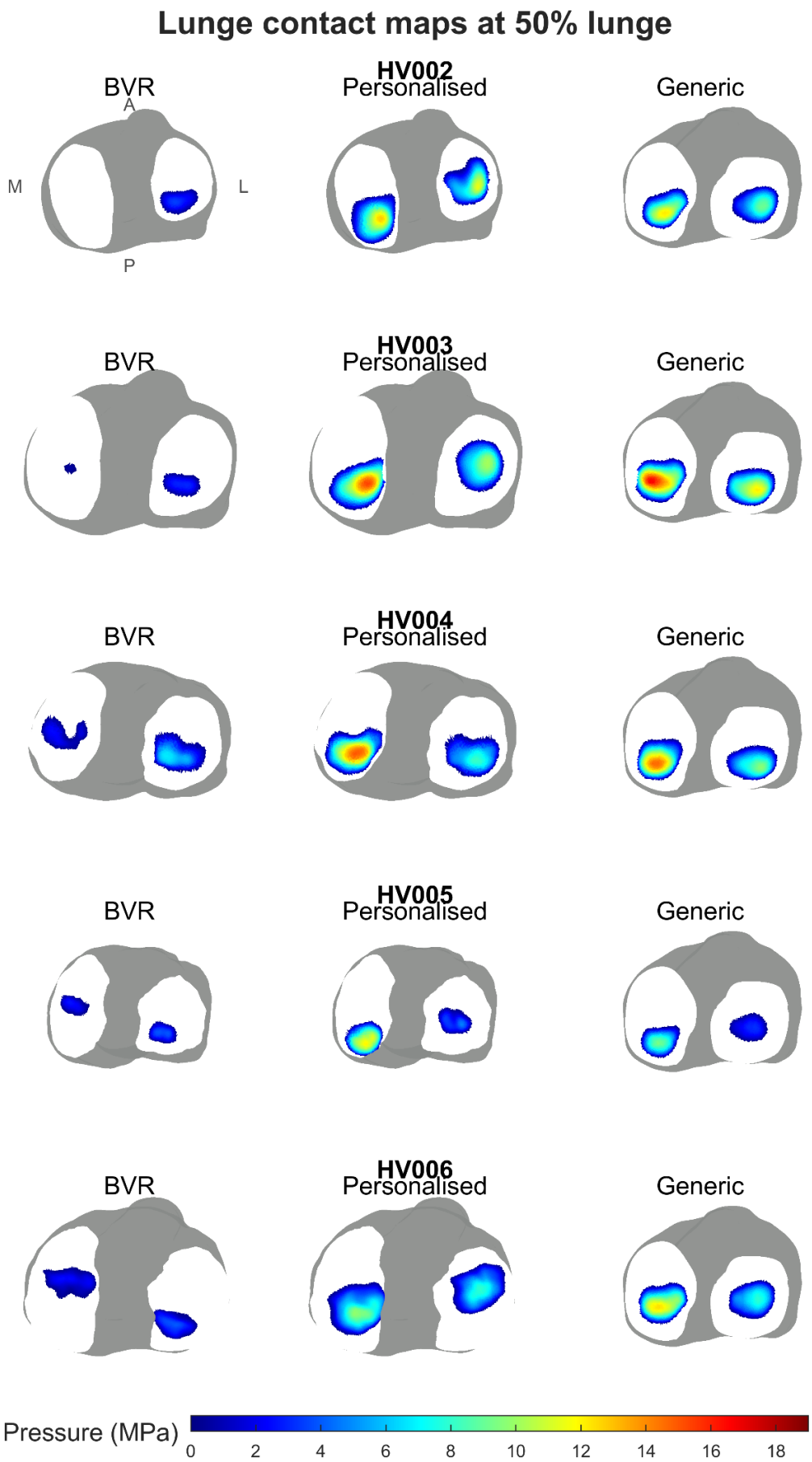

Figure 3-44 – Example contact maps for all participants at 50% lunge (high flexion). BVR contact map results in the first column, personalised MSM results in the second and the generic MSM contact map in the third.

The Dice scores for each participant between the generic and personalised MSMs and the BVR results were calculated for each frame for each participant; they are presented in Table 3-8 along with the cohort mean.

Table 3-8 - Mean Dice scores for each participant during lunging

Participant ID	**Mean Dice score of lunge frames** *MSM compared against BVR contact map images.*		
	Generic MSM *(c.f. BVR)*	**Personalised MSM** *(c.f. BVR)*	**Difference** *(pers. – gen.)*
HV002	0.245	0.171	-0.075
HV003	0.319	0.176	-0.143
HV004	0.569	0.628	+0.059
HV005	0.029	0.136	+0.108
HV006	0.166	0.283	+0.117
Overall mean	***0.265***	***0.279***	***+0.013***

The mean Dice scores for the cohort varied between participants with some having very low scores (e.g. HV005), but some presenting higher scores (HV004). Although, the overall mean difference (+0.013) for the cohort suggested that the personalised model improved the contact area prediction, it was only a very small difference, and the generic model had a higher mean Dice score for 2/5 participants. As well as this, the median difference was higher for the generic model at 0.217 (IQR = 0.283) than the personalised model at 0.180 (IQR = 0.205). When the Wilcoxon signed-rank test was performed on the paired lunge frames for the cohort, it found the generic model contact predictions to be statistically significantly better than the personalised (W = 33261, p = 0.0039). This again suggests that the model is not suitable for predicting TF contact during activities with high flexion, such as a lunge.

3.4.4 DISCUSSION OF RESULTS ACROSS THE THREE ACTIVITIES

As seen in Chapter 2 when the BVR kinematics were compared with Visual3D (V3D) (Section 2.5.7), an offset was seen between the marker-based calculation of the MSM flexion angle with the BVR measured flexion angle. To compare the offset across all three activities, the mean difference from the earlier Bland-Altman analyses (Figure 3-23, Figure 3-35 & Figure 3-42) are included in Table 3-9.

Table 3-9 – Median differences from the Bland-Altman analyses (Figure 3-23, Figure 3-35 & Figure 3-42) between the modelling pipelines and BVR flexion results.

Activity	Median flexion difference (method – BVR)		
	V3D (°)	Generic (°)	Personalised (°)
Gait	14	13	13
Stair ascent	13	10	11
Lunge	14	9.4	10

Whereas V3D found a similar flexion offset across the three activities, the MSMs both had a smaller offset for the activities with higher flexion than gait. This is likely because the marker misplacement would affect the femur body positioning in the model, rather than the direct joint kinematics (like in V3D) so their effect on the calculated flexion angle would be different. These significant flexion errors would have affected the secondary kinematics calculated by the MSM as they are defined as functions of flexion during the inverse kinematics step.

When looking at the secondary kinematics, external rotation differences most affected the contact area variation during the high flexion activities. During both stair ascent and lunge, the MSM predicted rotations were much higher than the internal rotations (considered negative) calculated from the BVR data (Figure 3-33, Figure 3-40). A median difference of 16° was found by both models during both activities, showing this rotation to be poorly predicted by the model for activities involving high flexion.

This difference between the model-predicted and BVR-calculated internal rotation of the tibia relative to the femur during activities with high flexion was likely due to the muscles, ligaments or wrapping surfaces in the model causing external rotation when the knee flexed. When visualising a stair ascent trial in OpenSim, the whole shank (including the foot) rotated despite the foot being planted on the floor during stance phase (Figure 3-45). This external rotation of the foot highlights the corresponding external rotation occurring at the knee, which was opposite to the internal rotation calculated by BVR during the same activity. As the experimental markers do not display the same external rotation as the virtual markers, this

suggests this rotation was not caused by the experimental data, but the behaviour of the model itself.

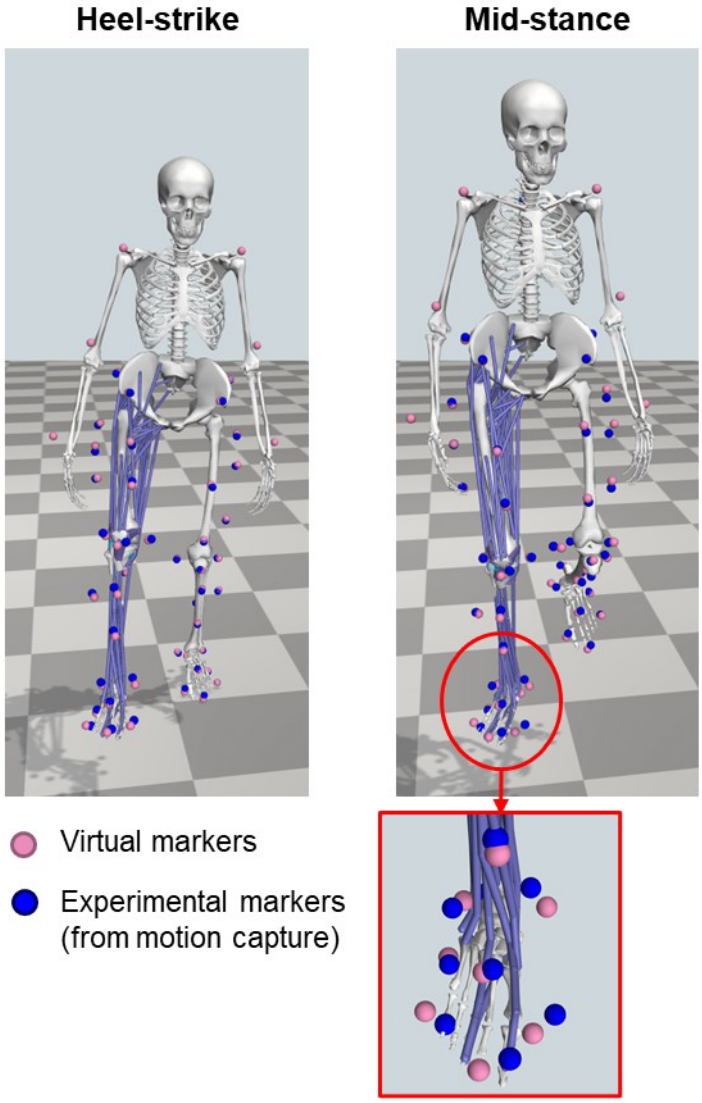

Figure 3-45 – Example of a personalised MSM (HV005) predicting internal rotation of the foot during a stair ascent. The pink markers are virtual markers showing the model's predicted marker locations (based off body segment positioning) and the blue show the marker locations as measured directly from motion capture.

When looking at the forward flexion simulation that generated the splines coupling the secondary coordinates to TF flexion angle (Section 3.2.3), the knee rotated externally as flexion increased (Figure 3-46). This trend opposes results found in literature, where TF flexion was shown to be coupled with internal rotation of the tibia in activities involving higher knee flexion angles (e.g. open-chain flexion) (Thomeer et al. 2021). As these forward flexion splines are used to set the initial secondary coordinate values during COMAK (before optimisation), the algorithm would be

solving for increasing external rotation values as knee flexion increases, getting further from the gold-standard BVR internal rotation measured. At the lower flexion angles involved in level gait (below 1 radian/~60°), the spline only allows for small degrees of external rotation, which is why the difference between model-predicted value and BVR-calculated rotation more evident during the activities with higher flexion.

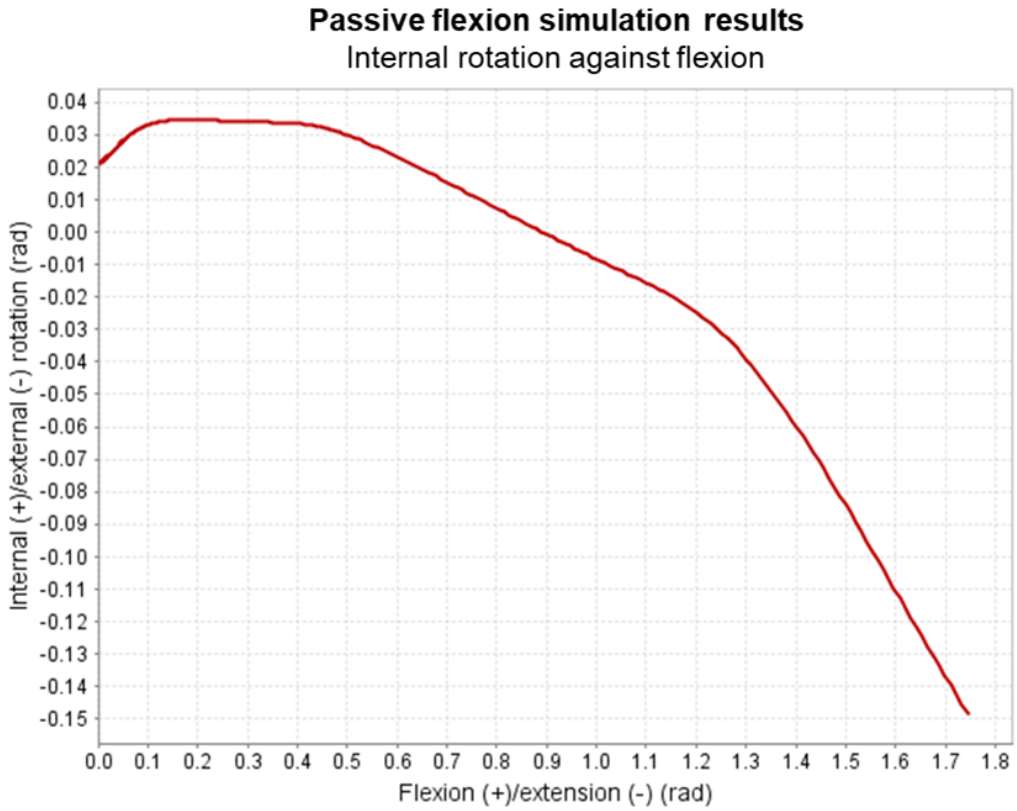

Figure 3-46 – Passive forward flexion simulation internal rotation plotted against TF flexion. This spine is used to generate the internal rotation (secondary coordinate) value used as an initial position for the COMAK algorithm.

For all three activities, the generic MSM had a larger external rotation standard deviation and IQR of the differences than the personalised model. Although greater variation in internal rotation may be expected from the personalised model results due to contact geometry variation, this was not the case. Further work is needed to investigate the reason for this reduced variability in this DOF from the personalised model, however it may be due to the repositioning of the soft tissue attachment points or wrapping surfaces, or calibration of the muscle and ligament parameters when creating the personalised versions of the models.

The adduction angle prediction showed mixed results across activities. The personalised MSM had a better median difference than the generic model during gait (Figure 3-23), a slight improvement during stair ascent (Figure 3-35), but a worse median difference during lunging (Figure 3-42). During the lunge, the personalised model produced a wider range of adduction angles across the cohort, more comparable to the BVR results, whereas the generic model gave more consistent values across participants. While the greater ROM meant the personalised model's mean adduction angle was closer to that of the BVR during stair ascent (Figure 3-40), the participants with the extreme values did not match between methods. As a result, the wider range did not translate to improved accuracy on an individual level, and personalisation did not improve adduction predictions during lunging.

Of the three translational DOFs, AP translation showed the greatest improvement in median difference (MSM-BVR) and smallest IQR when the model was personalised. The generic model consistently overestimated anterior translation across all activities studied (not seen in the personalised results), possibly due to the specific surface morphology or positioning of the generic contact meshes. These results support personalising the model geometry to improve prediction of AP translation across various activities and flexion ranges.

ML translation showed the same trend in the Bland-Altman results of both models across all the activities of negative correlation between the difference (MSM-BVR) and the measured BVR value (Figure 3-24, Figure 3-36 & Figure 3-43), suggesting the model over-constrained the joint translation in this direction. This was most clearly visible in the lunge results, where both MSMs had small standard deviations compared to the BVR results (Figure 3-41).

The MSMs predicted increased distraction with increased flexion, with the largest distraction values occurring during the middle of the lunge and beginning of the stair ascent, consistent with the high flexion angles during these periods. This was not seen in the BVR results. From the spline shown in Figure 3-47, there was a trend of greater distraction as flexion reached values above 0.5 rad (~30°), hence why the bones were more distracted during high flexion.

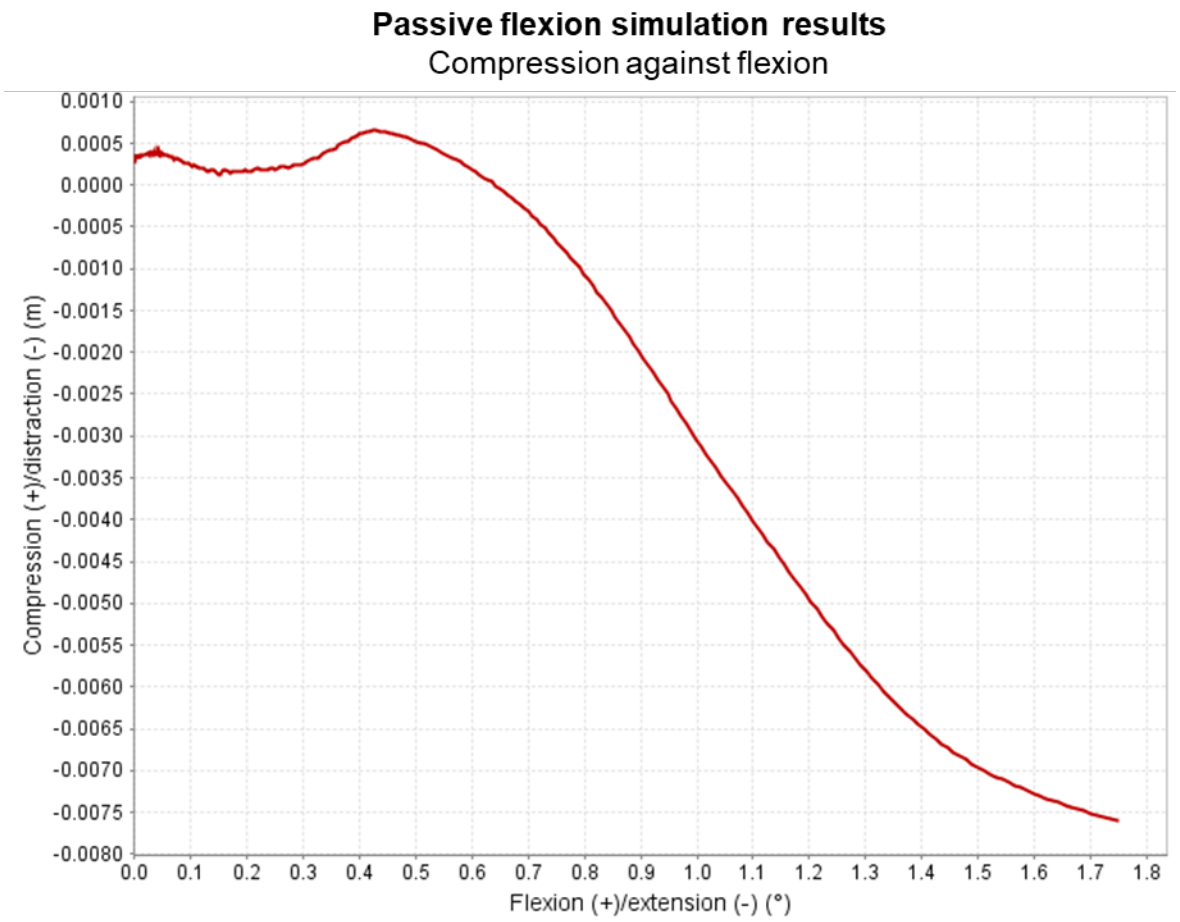

Figure 3-47 - Passive forward flexion simulation compression plotted against TF flexion.

The OpenSim-JAM framework relies on the assumption that the secondary DOFs are coupled with flexion angle to generate the initial secondary coordinate values before optimisation (Section 3.2.3). The weak correlation found between the secondary DOFs and flexion in the BVR results through all the activities (Chapter 2, Section 2.5.6) meant the model's secondary kinematics were not always accurate across the cohort. This would also contribute to the MSM kinematic predictions during higher flexion activities being worse than during level gait as the BVR correlations were weaker for these activities than gait.

The personalised model showed the greatest improvement in contact area prediction during activities involving lower flexion – i.e. during level gait and the second half of the stance phase of stair ascent. This was supported by the Dice scores, which found the largest mean difference between the personalised and generic models during gait, followed by stair ascent, then lunge (Table 3-10). Although only 3/5 participants had the greatest improvement (highest difference) between the

personalised and generic MSMs during gait, all participants had their highest mean Dice score (MSM c.f. BVR) for the personalised model during level gait.

Table 3-10 – Mean Dice scores for all activities showing the mean generic (gen.) and personalised (pers.) MSM scores (when compared to the BVR contact maps) across all frames, as well as the difference (personalised – generic) between the mean Dice scores for each individual and the cohort.
(Combination of Table 3-4, Table 3-7 & Table 3-8)

ID	Mean Dice score								
	Level gait			Stair Ascent			Lunge		
	Gen.	Pers.	Diff.	Gen.	Pers.	Diff.	Gen.	Pers.	Diff.
HV002	0.541	0.547	+0.006	0.188	0.162	-0.027	0.245	0.171	-0.075
HV003	0.334	0.377	+0.043	0.178	0.179	+0.001	0.319	0.176	-0.143
HV004	0.507	0.754	+0.248	0.181	0.457	+0.276	0.569	0.628	+0.059
HV005	0.336	0.427	+0.092	0.033	0.129	+0.096	0.029	0.136	+0.108
HV006	0.463	0.608	+0.145	0.002	0.070	+0.068	0.166	0.283	+0.117
Overall mean	***0.436***	***0.543***	***+0.107***	***0.117***	***0.199***	***+0.083***	***0.265***	***0.279***	***+0.013***

Overall, these results suggest that personalising contact geometries improves contact area predictions during lower-flexion activities where the kinematic differences between the MSMs and BVR values were lower. However, for higher flexion activities, alterations to the MSM would be required as the current model is not suitable for predicting kinematics when higher flexion angles are involved.

3.4.5 CHALLENGES AND RECOMMENDATIONS

One of the main drivers of personalisation of MSMs is the limitations of a generic model to represent individual variation in joint geometry and alignment, which standard linear scaling of model segments cannot achieve (Bakke and Besier 2020; Veerkamp et al. 2021; Davico et al. 2022). With associated errors increased in models that consider contact mechanics between articulating surfaces, such as in the OpenSim-JAM pipeline, accurately representing individual joint morphology is an important step in understanding contact pressures in, not only healthy, but diseased joints too (Killen et al. 2024). Hence it is important to understand if personalisation of

the contact geometries improves joint kinematics and contact predictions, as hypothesised.

As the generic model typically used with the OpenSim-JAM framework only used contact geometries from a single 23-year-old female subject (Lenhart et al. 2015), it is not representative of the population at large. As diseases, like OA, are more prevalent in an older population, younger ‘generic’ geometries may not provide the best representation of contact in an aged-matched population, even if they are considered ‘healthy’. Contact pattern differences are likely to increase with morphological changes due to disease progression, making personalisation even more important.

As well as age, the generic model geometries do not capture knee size variation; in the OpenSim-JAM framework, the specialised contact geometry meshes are not scaled with the rigid body segments, only translated to their new position (based on the leg length). In this study’s cohort, the ‘generic’ geometry was visually one of the smaller meshes (compared to the personalised geometries used) meaning that participants with larger knees may not have been accurately represented with the generic version of the model as the contact surface size was much smaller. Although no single ‘generic’ geometry can represent the variety of the whole population, a model with an average sized knee may be a better choice where personalisation is unfeasible and a generic model is required.

The current generic geometries used in this study may also be causing the consistent anterior translation overestimation seen in the kinematics results. Using an alternative participant as the ‘generic’ model basis would confirm if this offset was due to the specific geometries, as well as investigate how the generic geometry chosen affects the outputs contact patterns.

Another potential limitation of the generic model is the positioning of the contact geometries within the knee. In their paper setting out the model, Lenhart et al. (2015) state that the tibial cartilage surface was *“placed to just contact the femoral geometries in an upright position”*. This adds uncertainty to the comparisons with the generic model as it is unclear what manipulation was performed to alter the geometry positions and, therefore, how that alteration may influence the joint ACS definitions and the resulting kinematics.

To minimise the differences between the knee joint origin between the methods, the same algorithm (Miranda et al. 2010) was used to define the femoral ACSs in the generic model and the personalised bone models to facilitate direct comparison between results. As shown in the previous chapter, the ACS definition alters kinematic outputs (Chapter 2, Section 2.5.5), so it was important to use the same consistent ACS definition between the methods. Despite using the same algorithm to define bone ACSs, differences may still remain, and these would contribute to variation in the kinematics seen between methods.

Another challenge of comparing the MSM results with the BVR results was that the contact maps did not always show contact on both plateaus during stance phase of all three activities. This was likely due to the sensitivity of the method to small changes in mesh positioning (Section 3.3.2), as well as the BVR bone poses inherently including the meniscus and other soft tissues not included in the MSM, reducing the contact area. Segmentation or smoothing errors could also contribute to the small regions. For these reasons, it is recommended to explore alternative methods for calculating contact from BVR bone poses.

The contact region between the MSM and BVR results would also be affected by the assumption of the COMAK algorithm that the cartilage geometries must always be in contact, so it can solve for the constraint equations. This may artificially increase the predicted contact area as the meshes within the joint were being held together throughout, increasing the differences between MSM and BVR contact areas.

Due to project time constraints, this analysis focussed on the TF joint and the contact on the tibial cartilage. To expand the analysis in the future, the converse mapping of the TF contact onto the femoral cartilage mesh would allow for fuller understanding of the differences in contact location on both bones in the TF joint. Additionally, PF kinematics and joint contact could be examined, as the patella and its cartilage are also personalised in the model generation (Section 3.2.2). If using the same MSM to evaluate PF joint contact, it is important to test the benefits of personalisation separately to determine the accuracy for each individual joint.

Although the pipeline was only applied to a healthy population in this study, there is future scope to investigate the differences between generic and personalised MSM outputs in pathological cohorts. Diseased joints are like to show even greater

improvements in accuracy when the model is personalised, due to the altered kinematic strategies and contact morphologies being better captured by models that include personalised joint contact representations. Not all patients will present with the same differences from healthy joints, despite having the same disease, therefore, to successfully model an individual's biomechanics, personalisation of the joint morphology is recommended. Better model predictions can then be utilised in individualised care and interventions to improve patient outcomes.

3.5 CONCLUSION

All aims set out at the start of the chapter (Section 3.1.2) were successfully met, with the OpenSim-JAM pipeline being run for multiple dynamic activities, both with generic and personalised geometries, for five participants. The resulting MSM contact maps were then compared with BVR-equivalent maps for the first time to assess the benefit of incorporating personalised TF joint contact geometries.

The results showed that personalised TF geometries particularly improved model estimates of AP translation during the stance phase of level gait. When compared to the gold-standard BVR kinematics, model personalisation improved the absolute median difference between the MSM and BVR results by over 7 mm compared to the generic model (Figure 3-24). This resulted in a visual improvement in contact region prediction during gait when using the personalised geometries (Figure 3-25), supported by improved Dice scores (Table 3-4). Element-wise SPM analysis highlighted a significant region on the posterior medial plateau where the generic model overestimated contact (Figure 3-30), as the BVR contact maps found the medial contact to be located more anteriorly. The personalised model also found the contact to be located in a similar anterior position, demonstrating the benefits of the more accurate AP translation prediction. Weighted COP differences in the AP direction were also reduced when using the personalised model (Table 3-5), further supporting these findings.

As the medial side of the knee has been shown to be more susceptible to OA initiation and propagation (Vincent et al. 2012) associated with increased loading and COP shift on the medial tibial plateau during gait (Meireles et al. 2017), it is important to accurately model the contact on the medial side of the knee. Therefore, although the time and resource costs of personalising the contact geometries in the MSM are

high, model personalisation is recommended for assessing TF contact during gait trials as the generic model was less accurate at predicting the contact than the personalised model, particularly on the medial tibial plateau.

However, for the activities involving greater TF flexion, such as stair ascent and lunge, both models were less accurate. Errors in external rotation (Figure 3-35, Figure 3-42) led to shifts in contact location on the tibial plateau. As the model was originally developed for gait (Lenhart et al. 2015), further model optimisation would be required to ensure reliable contact predictions for activities outside of walking. It also highlights the benefit of testing model performance for each new activity, as accuracy may vary. Once the model has been optimised for higher flexion, the benefits of personalisation of contact geometries should be reevaluated as it would likely improve contact predictions.

In conclusion, adding personalised contact geometries overall improves TF kinematic and contact pressure region predictions during level gait, particularly in the AP direction, but not for activities involving higher flexion angles. Therefore, personalisation should be strongly considered when utilising the OpenSim-JAM pipeline to assess gait.

This chapter directly supports the overarching research aims described in Section 1.8 by benchmarking MSM predictions against accurate BVR-kinematics to evaluate the benefits of personalised modelling. Within the context of the wider framework, the MSM provides unique whole-body kinetic and kinematic data, complementing the joint-specific outputs from the BVR and FEM components. Importantly, as the MSM pipeline utilises different input data, the contact pressure maps it generates offer a valuable reference for comparison with both BVR-derived and FEM-based results. Together, these contributions strengthen the integrated framework developed in this thesis and enhance its capacity to capture and interpret the complex biomechanical behaviour of the knee during dynamic activity.

CHAPTER 4: KINEMATIC-DRIVEN, SUBJECT SPECIFIC FINITE ELEMENT MODELLING OF THE TIBIOFEMORAL JOINT

4.1 INTRODUCTION

As knee osteoarthritis (OA) onset and progression is linked to excessive mechanical loading of the tissues (Mukherjee et al. 2020), understanding of the stresses and strains within load-bearing structures, such as the articular cartilage, during typical in-vivo motion is important. Characterising the behaviour of healthy articular cartilage during functional activities (e.g. walking) is key to understanding how its mechanical properties weaken with OA (Sinusas 2012; Katz et al. 2021; Mohout et al. 2023).

Finite element modelling (FEM) is a technique used investigate internal mechanics of tissues that occur under different loading conditions. Unlike the musculoskeletal modelling (MSM) pipeline presented in Chapter 3, which calculated contact pressures using 2D representations of the articular cartilage surfaces, FEM uses 3D meshes to model element-wise deformations, allowing for the calculation of internal parameters, such as stress and strain, providing additional insight into soft tissue loading.

FEM has been widely used to investigate altered loading and disease progression within osteoarthritic knees (Tarniţă et al. 2014; Arjmand et al. 2018; Bolcos et al. 2020; Thienkarochanakul et al. 2020; Daszkiewicz and Luczkiewicz 2021; Lampen et al. 2023; Mohout et al. 2023; Mononen et al. 2023), using the popular approach of applying forces to drive the model. Determining the force inputs for a model requires assumptions, such as the magnitude, direction and the location the force originates from, as forces cannot be directly measured in-vivo in native joints. For a subject-specific in-vivo FEM of knee joint loading, forces are typically calculated using MSMs and motion capture data (Besier et al. 2008; Adouni and Shirazi-Adl 2014; Marouane et al. 2016; Richards et al. 2018; Shu et al. 2018), or by scaling mean gait patterns (Mononen et al. 2016; Paz et al. 2021). FEMs driven using these data will not accurately replicate underlying bone movement due to errors associated with motion capture (for example, soft tissue artefact and marker misplacement), as well as the assumptions within the MSM pipeline.

An alternative approach is to drive the model using in-vivo kinematics, however, this is less common due to the challenges associated with obtaining accurate input kinematics and the sensitivity of FEM to small kinematic changes (Fregly et al. 2008). Some kinematic-driven models of the knee have been created, but they often used a hybrid force-kinematic approach (prescribing up to five degrees of freedom, DOFs, and controlling the others based off force inputs) to account for potential errors in the input kinematics (Halonen et al. 2013; Carey et al. 2014; Kwon et al. 2014; Bolcos et al. 2018; Gu and Pandy 2020).

Despite the recent advancements in the collection and processing of accurate kinematics using biplane videoradiography (BVR) (Gray et al. 2018), exploration of using these inputs to drive six DOFs of a FEM to investigate joint contact in the knee has not been done to the author's knowledge. By combining BVR kinematics and geometries segmented from magnetic resonance imaging (MRI), a highly personalised model can be created to replicate measured in-vivo joint motion. It is important to understand the feasibility of this approach, as well as its potential limitations, as it may provide new, alternative insight into in-vivo soft tissue loading, complimenting discoveries from force-driven models.

4.1.1 AIM AND OBJECTIVES

Therefore, to investigate the potential of a fully kinematically-driven FEM of the tibiofemoral joint (TF) during in-vivo motion, the aim of this study was to create a subject-specific model of a healthy knee joint using geometries from MRI, where the six DOFs of the TF joint are prescribed using accurate kinematics from BVR to investigate contact pressure, stress and strain in the tibial cartilage during the stance phase of level gait.

To help achieve this aim, it was further broken down into the following objectives:

- Develop a subject-specific TF joint model, including the bones, articular cartilage and relevant soft tissues (segmented from MRI), that successfully runs through all frames of the kinematic input data.
- Compare the personalised contact pressure outputs to those generated from the ray tracing and bounding box method using the BVR and MSM pipelines (Chapter 3) to explore the differences between the methodologies.

- Use the FEM to calculate stresses and strains in the articular cartilage during stance phase of level gait and compare these results to typical force-driven models of healthy human knees in literature to assess the feasibility of equivalent kinematic-driven models.

These objectives were defined to understand the advantages, limitations and practicalities of using kinematics to drive an FEM and if there is potential for this technique to be applied in the future to investigate joint loading in diseased knees too.

4.2 METHODOLOGY

4.2.1 MODEL SUMMARY

To investigate the potential for a fully kinematically-driven FEM of the knee, a model was created in FEBio (Maas et al. 2012) of a single healthy participant (Figure 4-1). FEBio was chosen for developing this joint contact model as it is open source, specifically designed for biomechanical modelling, good for modelling soft tissue interactions, and is validated against other FEM software (Maas et al. 2012).

HV004 was chosen for the model from the cohort dataset (as described in Chapter 2) as a T1-VIBE MRI scan of their knee was collected (which was better for segmenting soft tissues compared to the DESS scan used for earlier participants – see Section 2.2) and a complete dataset (including segmented geometries and matched BVR image registration) was available at the time of initial model creation.

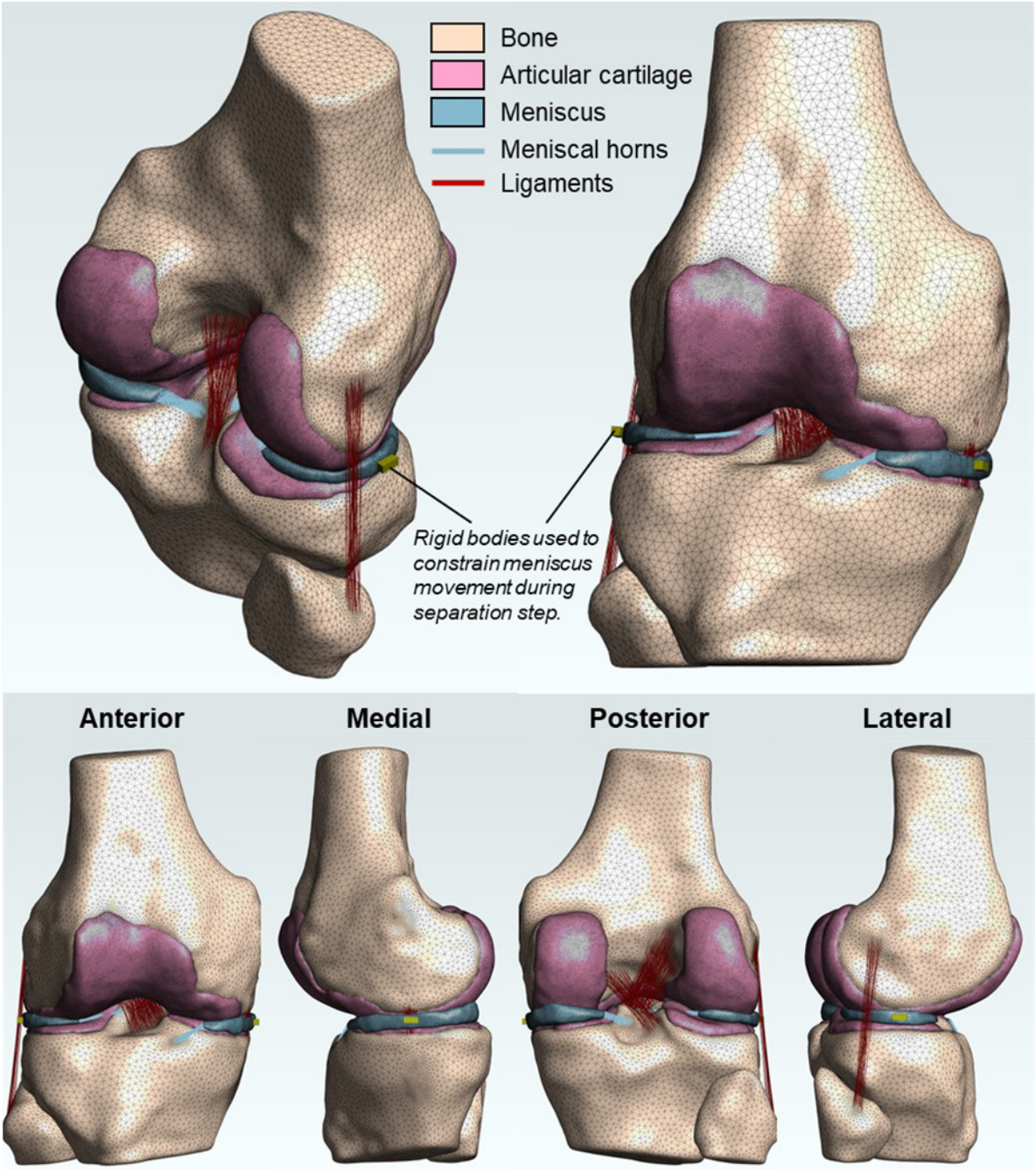

Figure 4-1 – FE knee model geometries.

An overview of the structures included in the model, along with their respective Material models and number of elements are given in Table 4-1. More details on the chosen material models – including the parameter values used, can be found in Section 4.2.2.

Table 4-1 – FE knee model structures included, their material models and number of elements/springs used to represent them.

Material	**Material Model**	**Structures**	**Number of elements/springs**
Bone	Rigid body	Distal femur	266,920
		Proximal tibia (& fibula)	131,182
Articular cartilage	Nearly incompressible Neo-Hookean *(modelled using Mooney-Rivlin)*	Femoral cartilage	312,696
		Tibial cartilage	103,383
Meniscus	Transversely isotropic Mooney-Rivlin	Medial meniscus	44678
		Lateral meniscus	23042
Meniscal horns	Linear spring bundles	Anterior medial horn	50
		Posterior medial horn	49
		Anterior lateral horn	37
		Posterior lateral horn	25
Ligaments	Non-linear Blankevoort springs	ACL	145
		PCL	70
		MCL	65
		LCL	25

The model was driven by prescribing the bones (rigid bodies) using the object transforms of the level gait trial for HV004 (Chapter 2, Section 0). It was chosen to model gait as this is a commonly used activity across FE knee models in literature (Yang et al. 2010; Adouni et al. 2012; Halonen et al. 2013; Daszkiewicz and Luczkiewicz 2021; Fu et al. 2022; Mohout et al. 2023). Gait also involves lower flexion than the other two activities – lunge and stair ascent (as shown in Table 4-2),

resulting in less extreme changes from the initial MRI position of the structures, increasing the likelihood the model would be able to solve.

Table 4-2 – Maximum measured flexion angle calculated for each activity for the participant used for the FEM and the whole cohort presented in this thesis (Taken from the results in Chapter 2).

	Gait	Stair ascent	Lunge
Maximum flexion angle for HV004	7.8°	56.6°	67.0°
Maximum flexion of the whole cohort	20.2°	60.4°	111°

An overview of the main modelling steps can be found in Figure 4-2, with more detail on for these steps in Section 0.

The geometries in the model were initially separated (Step 1) to account for any potential mesh overlap caused when smoothing the MRI segmentations (in Simpleware, ScanIP) before importing them into FEBio. Then, the soft tissues were brought into contact and allowed to compress and settle into their starting kinematic position (Step 2). The contact position at the end of Step 2 was the first frame of BVR kinematic motion, ready for the joint to be driven through the rest of the kinematic frames of level gait (Step 3). All motion during the simulation was applied to the tibia bone rigid body and the femur was fixed in all 6 DOFs throughout.

Along with the constraints used to drive the model through each step, Figure 4-2 also provides a summary of the contacts applied during each step. These contacts determined the soft tissue interactions between surfaces during the simulation. More information on the constraints and contacts (including contact penalty values) can be found in Section 0.

Initialised constraints
- Femur fixed in all 6 DOFs.
- Femoral and tibial cartilage welded to femur and tibia, respectively.

Step 1: Separate

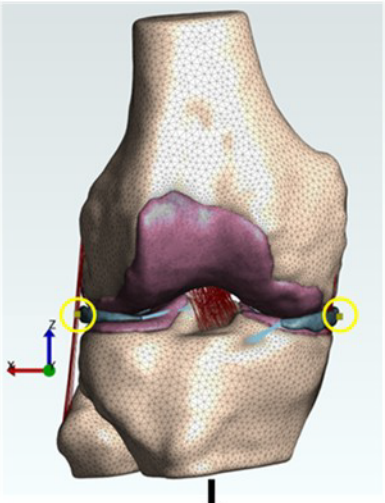

All geometries were separated by moving the tibia (and attached tissues) downwards away from the femur. The meniscus was moved half the distance of the tibia, so it was not contacting either cartilage surface.

Constraints
- Tibia: -2 mm z-displacement, fixed in all 5 other DOFs.
- Rigid body blocks[1] (circled in yellow): -1 mm z-displacement (to constrain meniscus movement)

Contacts
- Tied-facet-on-facet between rigid body block faces adjacent to the menisci outer edges.

Step 2: Initial Contact

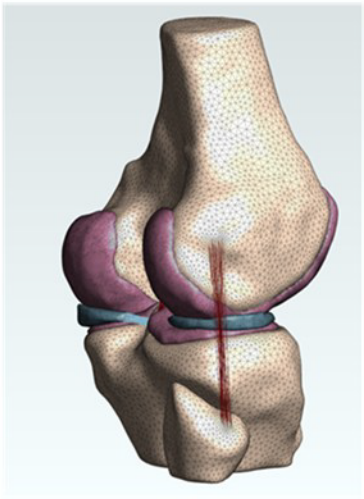

Tibia moved into first frame position, allowing the soft tissues to compress and settle.

Constraints
- Tibia: 6 DOFs moved into positions for first frame of BVR kinematics.

Contacts
- Sliding-facet-on-facet between femoral and tibial cartilage.
- Sliding-facet-on-facet between femoral cartilage and superior menisci surfaces.
- Sliding-facet-on-facet between tibial cartilage and inferior menisci surfaces.

Step 3: Kinematic-driven

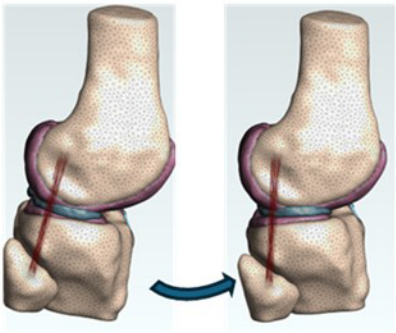

Knee joint constrained using BVR-derived kinematics of the stance phase of level gait.

Constraints
- Tibia: 6 DOFs moved through all frames of BVR kinematics.

Contacts
- Sliding-facet-on-facet between femoral and tibial cartilage.
- Sliding-facet-on-facet between femoral cartilage and superior menisci surfaces.
- Sliding-facet-on-facet between tibial cartilage and inferior menisci surfaces.

Figure 4-2 – Overview of FE modelling steps to achieve kinematically-driven motion.

[1]See Figure 4-12 in Section 0 for a clearer image of the rigid body blocks.

4.2.2 KNEE STRUCTURES GEOMETRIC REPRESENTATIONS AND MATERIAL MODELS

The following sections describe in more detail the generation of each structure within the model, including the material model used to represent it.

All the personalised geometries segmented from the T1-VIBE MRI scan (Chapter 2, Section 2.2) were meshed using the in-built ***+FE free*** algorithm in Simpleware ScanIP (Synopsis, United States). The parameter values used by the algorithm to generate the meshes of each 3D structure in the model are given in Table 4-3.

The ***+FE free*** algorithm uses adaptive meshing to generate tetrahedral elements automatically sized based on geometry, progressively refining the mesh based on image resolution (Synopsys 2022). It can generate meshes representing complex geometries, as well as allowing the user to adjust the mesh coarseness of individual regions, making it useful for meshing human tissue structures.

The material models and parameter values used for this model were taken from literature due to time constraints as the comprehensive sensitivity analysis required to fully determine the suitability of the models and parameters was outside the scope of this project. As it was an exploration of potential use of kinematic-driven modelling, example parameters from literature were deemed suitable.

*Table 4-3 – Mesh generation parameters used by the **+FE free** algorithm for each 3D structure in the model.*

	Parameter	**Femur**	**Tibia/Fibula**	**Femoral cartilage**	**Tibial cartilage**	**Medial & Lateral Meniscus**
Adaptive surface remeshing	Target minimum edge length (mm)	1.44	1.44	0.454	0.454	0.410
	Target maximum error (mm)	0.0640	0.0640	0.0640	0.0640	0.0640
	Maximum edge length (mm)	3.52	3.52	0.986	0.986	0.870
	Surface change rate *(1 = slow, 100 = fast)*	50	50	6	6	4
	Target number of elements across a layer	0.75	0.75	0.97	0.97	0.98
	Self-intersection checks	Partial	Partial	Partial	Partial	Partial
	Volume mesh generation internal change rate *(1 = slow, 100 = fast)*	30	30	30	30	30
Mesh Quality	Quality optimisation cycles	5	5	5	5	5
	Quality metric	Jacobian, in-out ratio and edge length ratio				
	Quality target	0.1	0.1	0.1	0.1	0.1
	Allow off-surface	Yes	Yes	Yes	Yes	Yes
	Maximum off-surface distance *(local edge length fraction)*	0.2	0.2	0.2	0.2	0.2
	Maximum off-surface distance (mm)	1000	1000	1000	1000	1000

Bones

The femur and tibia segmentations from the T1-VIBE scan (Section 2.2) were used to form the basis of the personalised model. The proximal fibula was also segmented for the model, as it is the attachment site for the lateral collateral ligament (LCL). The fibula model was exported with the tibia geometry, so they formed a single rigid body in the model. Therefore, the kinematic relationship between them remained constant throughout, and the constraints that prescribed tibial movement simultaneously moved the fibula.

The bones (Figure 4-3) were set as rigid bodies as bone is much stiffer than the surrounding soft tissues (Donahue et al. 2002; Adouni et al. 2012; Liu et al. 2022; Steineman et al. 2022; Uzuner et al. 2022; Yan et al. 2024). This had the added benefit of being able to directly prescribe their kinematics (using prescribed rigid body constraints); driving the bone motion using kinematics is described in more detail below (Section 4.2.3).

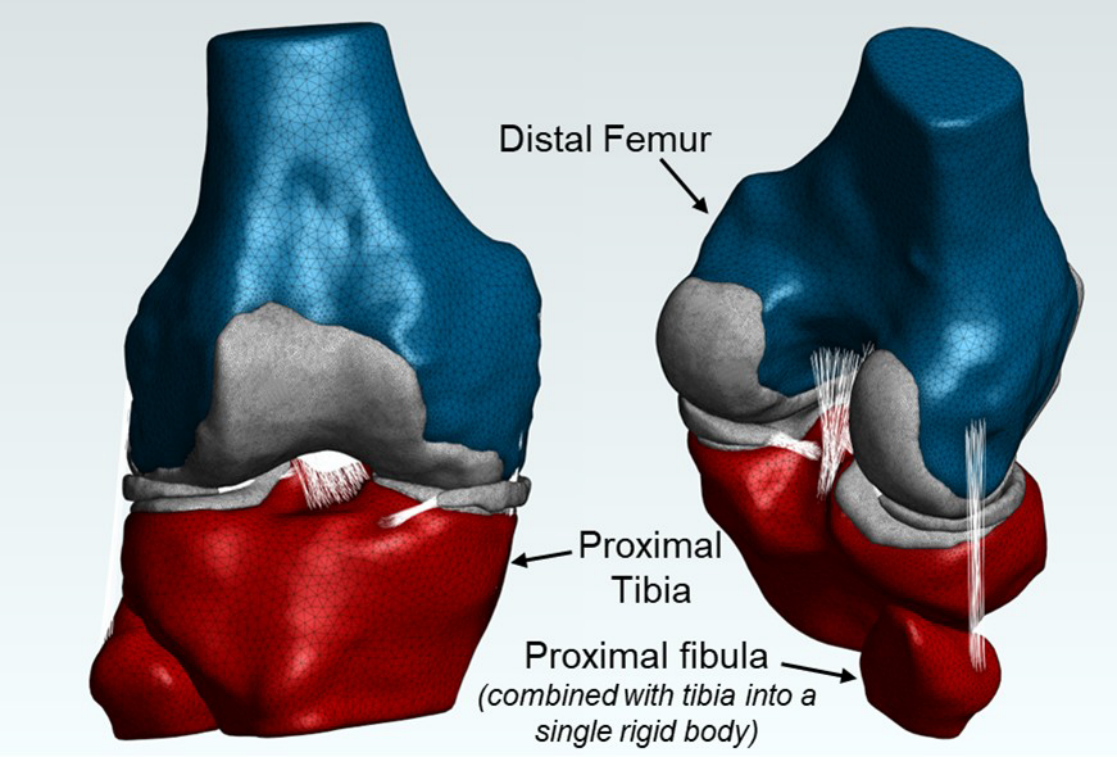

Figure 4-3 – Bone geometries included in the FEM. The femur is shown in blue and the combined tibia and fibula rigid body is shown in red.

The bones were meshed using the default mesh generation settings (Table 4-3). As no deformation occurs to rigid objects, the number of elements does not affect model outputs and a smaller number of elements reduces the computational cost, therefore

the default settings were used. The final number of elements was 266,920 for the femur and 131,182 for the combined tibia and fibula (Table 4-1).

Using rigid bodies for the bones removed the possibility of getting internal bone mechanics results, including individual element changes across the bone structure. However, it did reduce the computational time for the model as all elements in each rigid bodies were considered as one, not needing individual calculations. This also meant that the kinematics were able to be replicated from the measured bone movements from BVR as they were not affected by deformations of the bone meshes. As the model was designed to investigate soft tissue mechanics, and bone is relatively incompressible compared to the other tissues in the knee (Uzuner et al. 2022), it was decided this compromise was appropriate for this application.

It was chosen not to include the patella in this model, due to the need to add extra structures which would increase the complexity of the model without affecting the outputs from the TF joint. As the focus of this study was TF joint contact and soft tissue mechanics, adding the patella was not required.

Articular cartilage

The femoral and tibial articular cartilage (Figure 4-4) was also segmented from the T1-VIBE scan as part of the work in Chapter 3. The personalised 3D geometries were then exported, along with their bone-counterparts, so that each bone and cartilage pair was exported as a single object with two parts. This meant that when the objects were meshed in Simpleware ScanIP (Synopsis, United States), the contacting surfaces between the bone and the cartilage were produced with coincident nodes. These coincident nodes were welded together once the geometries were imported into FEBio using the *Weld nodes* tool; this ensured that the femur and femoral cartilage, and tibia and tibial cartilage, remained connected at all times in the simulation, replacing the need for a tied contact and reducing model complexity.

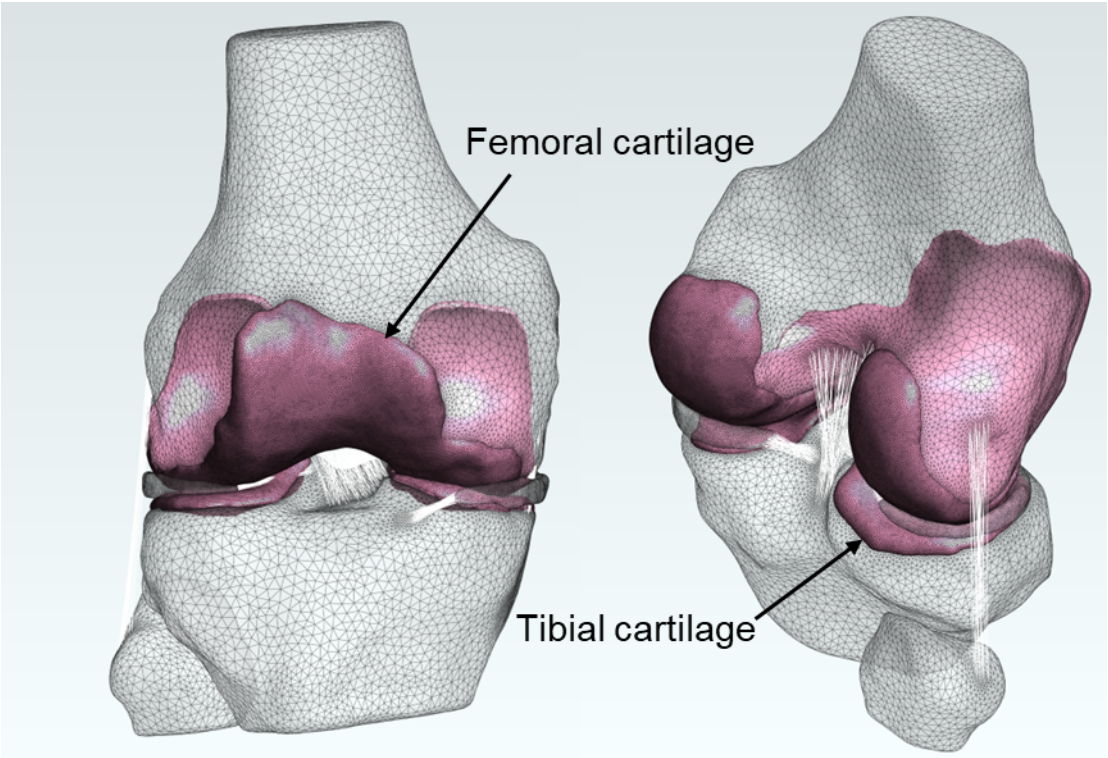

Figure 4-4 – Articular cartilage geometries in the model shown in pink.

A mesh convergence analysis was not performed for this model as this was an exploratory study. However, since a large number of elements are necessary to accurately capture the complex geometry of the structures within the knee, the mesh density was assumed to exceed the requirements for convergence.

For this model, the articular cartilage meshes were generated (Table 4-3) so there were around ten elements across the thickness of the cartilage to capture internal cartilage mechanics. As the bone mesh was set to generate at a different mesh coarseness, the elements were generated on a gradient near to the cartilage mesh so that the nodes were coincident at the points where they met (Figure 4-5). This resulted in 312,696 elements for the femoral cartilage and 103,383 elements for the tibial cartilage (Table 4-1).

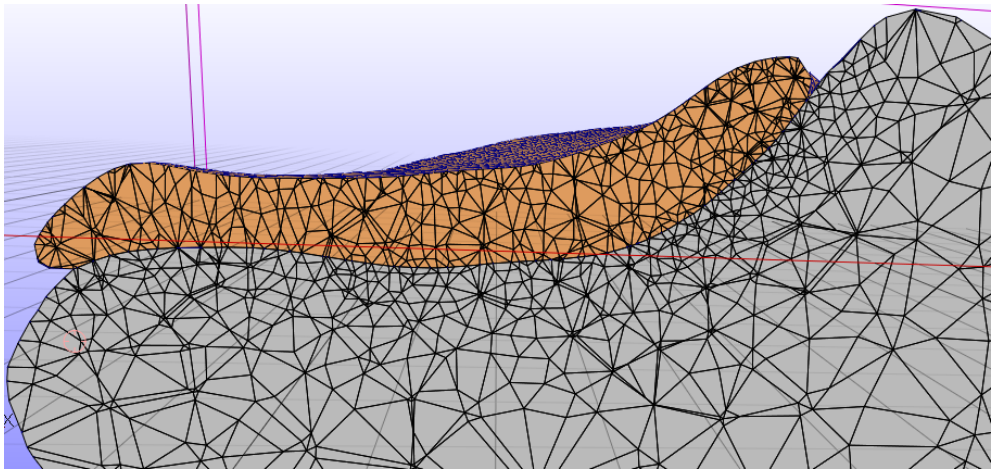

Figure 4-5 – Close up of the mesh generated of a section of the tibial cartilage and tibia bone boundary, showing the gradient change between the mesh densities.

The articular cartilage was modelled as an isotropic, linear elastic, nearly incompressible Neo-Hookean material (Besier et al. 2018), based on the OpenKnee(s) material model definition (Chokhandre et al. 2023b). This was achieved by setting the C2 parameter of FEBio's Mooney-Rivlin (uncoupled) material to 0 to reduce the model to an uncoupled version of the Neo-Hookean constitutive model (FEBio 2022a). This was done to avoid element locking that may occur when modelling nearly incompressible materials, like articular cartilage (FEBio 2022c).

The material properties used to represent cartilage using the Mooney-Rivlin model are found in Table 4-4.

Table 4-4 – Articular cartilage Mooney-Rivlin material parameters taken from Chokhandre et al. (2023b).

Parameter	Definition	Value
C1	Coefficient of the first invariant term (associated with shear stress)	2.54 MPa
C2	Coefficient of the second invariant term (reduces the model to Neo-Hookean when set to 0).	0 MPa
K	Bulk modulus (resistance to volume change).	100 MPa

Together these material coefficients cause this model to behave like a simplified version of cartilage mechanical behaviour that assumes isotropic behaviour, with an elastic modulus of 15 MPa and Poisson's ratio of 0.475 (Donahue et al. 2002; Zielinska and Donahue 2006; Guess et al. 2010; Kiapour et al. 2014b). This was

adequate for understand local cartilage mechanics at this level, whilst not being too computationally intensive (Chokhandre et al. 2023a).

Meniscus and meniscal horns

Because the meniscus plays a key role in tibiofemoral joint contact mechanics, helping to evenly distribute pressure (Yan et al. 2024), it was included in the FEM. The meniscal movement was constrained by the meniscal horns which were modelled as springs (Figure 4-6).

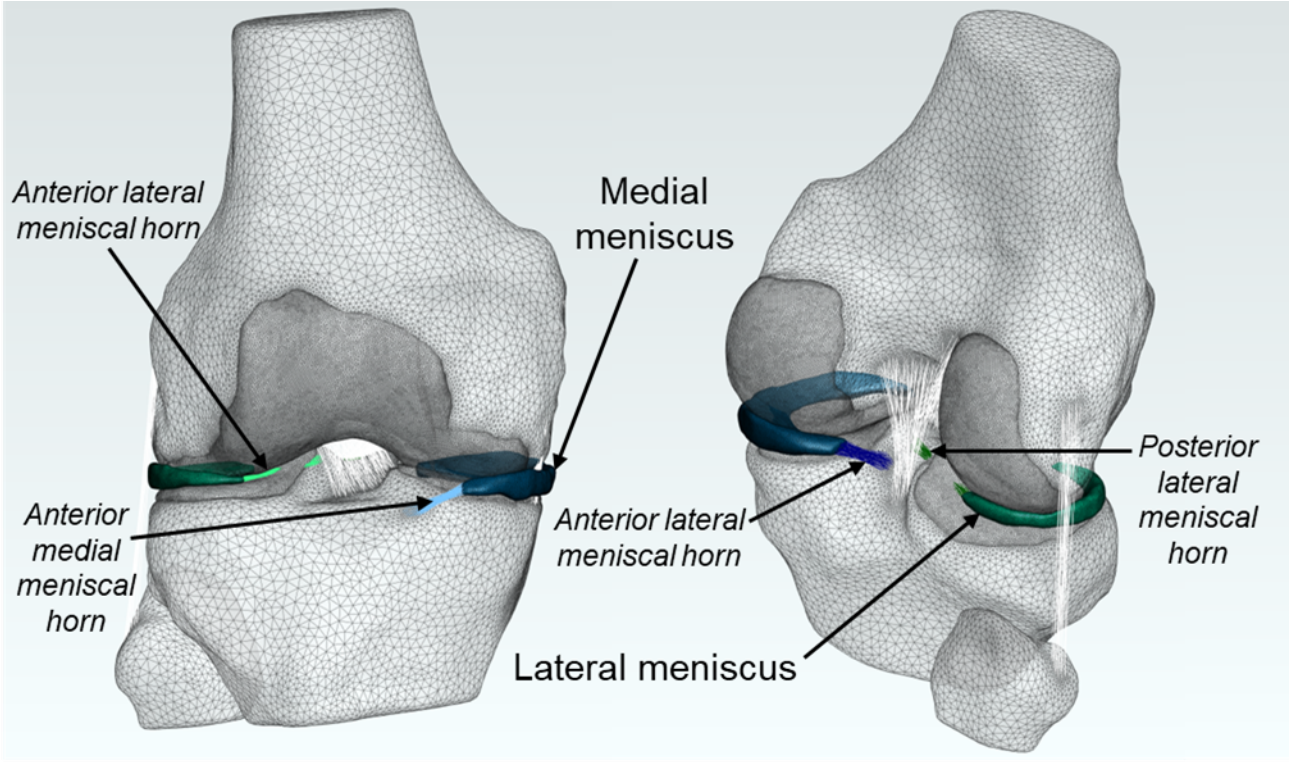

Figure 4-6 – Meniscus and meniscal horns. The medial meniscus is in blue, and the lateral meniscus is in green.

Like the articular cartilage, the geometries of the medial and lateral menisci were segmented from the T1-VIBE scan sequence, meshed (with the settings given in Table 4-3) and exported.

As it was difficult to determine the exact boundary between the meniscus body and the meniscal horns from the MRI scan, the ends of the menisci were truncated manually in Simpleware, using a similar approach to Gu and Pandy (2020), to form a flat surface for the springs to be attached to.

The meniscus body was modelled as a nearly incompressible, transversely isotropic, hyperelastic Mooney-Rivlin material (Chokhandre et al. 2023a). The material

parameters used to represent the meniscus can be found in Table 4-5 (FEBio 2022b; Chokhandre et al. 2023a). Like with the articular cartilage model, the meniscus model utilised a Mooney-Rivlin (Equation 1-1) ground substance, converted to a Neo-Hookean material by setting the constant c2 to 0 (Equation 1-3), again to avoid element locking of nearly incompressible elements (FEBio 2022c).

Table 4-5 – Meniscus transversely isotropic Mooney-Rivlin material parameters taken from Chokhandre et al. (2023a)

Parameter	Definition	Value
C1	Coefficient of the first invariant term (associated with shear stress)	4.61 MPa
C2	Coefficient of the second invariant term (reduces the model to Neo-Hookean when set to 0).	0 MPa
K	Bulk modulus (resistance to volume change).	92.16 MPa
C3	Exponential stress coefficient	0.1197 MPa
C4	Fibre uncrimping coefficient	150
C5	Modulus of straightened fibres	400 MPa
λ_m	Fibre stretch for straightened fibres	1.019

This material choice allowed for the circumferential fibres in the meniscus to be modelled using FEBio's *fiber generator* tool (FEBio 2021b) and was a convenient way to model the meniscus' capacity for compressive loading largely dictated by its circumferential stiffness which, in turn, is dictated by fibre alignment (Chokhandre et al. 2023a). To apply the circumferential fibres, a small region of faces on each truncated end of the meniscus were selected (Figure 4-7). One end was given a value of one and the other zero to define boundary conditions for a Poisson-type boundary value problem, used to generate a smooth scalar field throughout the object (FEBio 2021b). The gradient of the scalar field was then used to calculate the fibre vectors (FEBio 2021b).

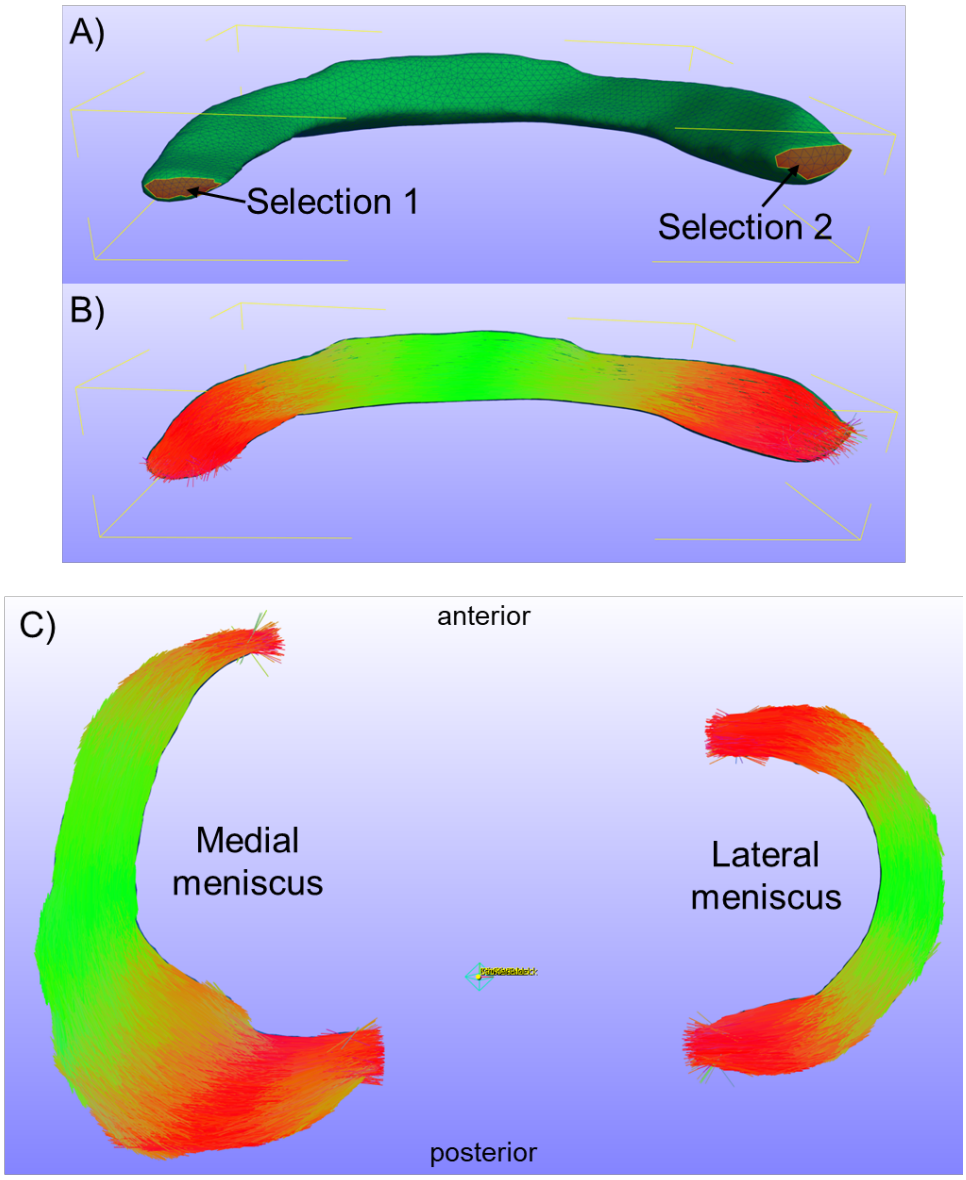

Figure 4-7 – Automatically generated circumferential fibres.
A) selection of faces on the truncated ends of the meniscal body.
B) fibres applied using those selections.
C) Superior view of the two menisci with the fibres generated.
The coloured fibres in B) and C) indicate the change in fibre direction.

Having the ends of the meniscus truncated not only helped with defining the circumferential fibre directions but also allowed for the easy attachment of springs to represent the meniscal horns, ensuring the springs followed the path of the horn geometry.

Each meniscal horn was modelled as a 1D linear spring bundle (Gu and Pandy 2020) attached from the truncated end of the meniscus to its corresponding attachment region on the tibia bone model. The attachment regions were defined where the 3D meniscal horn segmentation intersected the tibia bone model, and that

area on the tibia was given a denser mesh by remeshing the attachment region surface with a target mesh size of 1 mm. This made it easy to find the correct attachment regions on the tibia bone mesh once imported into FEBio, as well as creating more nodes to attach the springs too. This allowed the number of springs in each bundle to be defined in a way that represented the overall meniscal horn geometry with good coverage of the attachment site. Defining the meniscal horn as a bundle with a larger number of springs helps to spread the load to make a more realistic attachment between the two structures, as well as reducing the likelihood of elements or nodes deforming badly at a single attachment point.

The stiffness of each spring within the meniscal horn bundle was calculated by taking the total stiffness value of a meniscal horn – 2000 N/mm (Gu and Pandy 2020) – and dividing it by the number of springs in the bundle (Table 4-6).

Table 4-6 – Meniscal horn number and stiffness of springs in each bundle.

Meniscal horn	**Number of springs**	**Stiffness per spring (N/mm)**
Anterior medial	50	40
Posterior medial	49	40.816
Anterior lateral	37	50.054
Posterior lateral	25	80

Ligaments

The ligaments included were the four main ligaments connecting the femur and tibia (Figure 4-8): anterior cruciate ligament (ACL), posterior cruciate ligament (PCL), medial collateral ligament (MCL), and the lateral collateral ligament (LCL). These ligaments were added for the potential to leave one or more DOFs unconstrained, as seen in other kinematic-driven FEMs in literature (Halonen et al. 2013; Carey et al. 2014; Kwon et al. 2014; Bolcos et al. 2018; Gu and Pandy 2020), to account for errors in the input kinematics. However, due to the added complexity of requiring a correctly applied force to leave one DOF unconstrained, it was outside of the scope of this project. The ligaments were left in the model to allow for future potential to

implement this, or to use this model to investigate ligament elongation and forces during in-vivo motion.

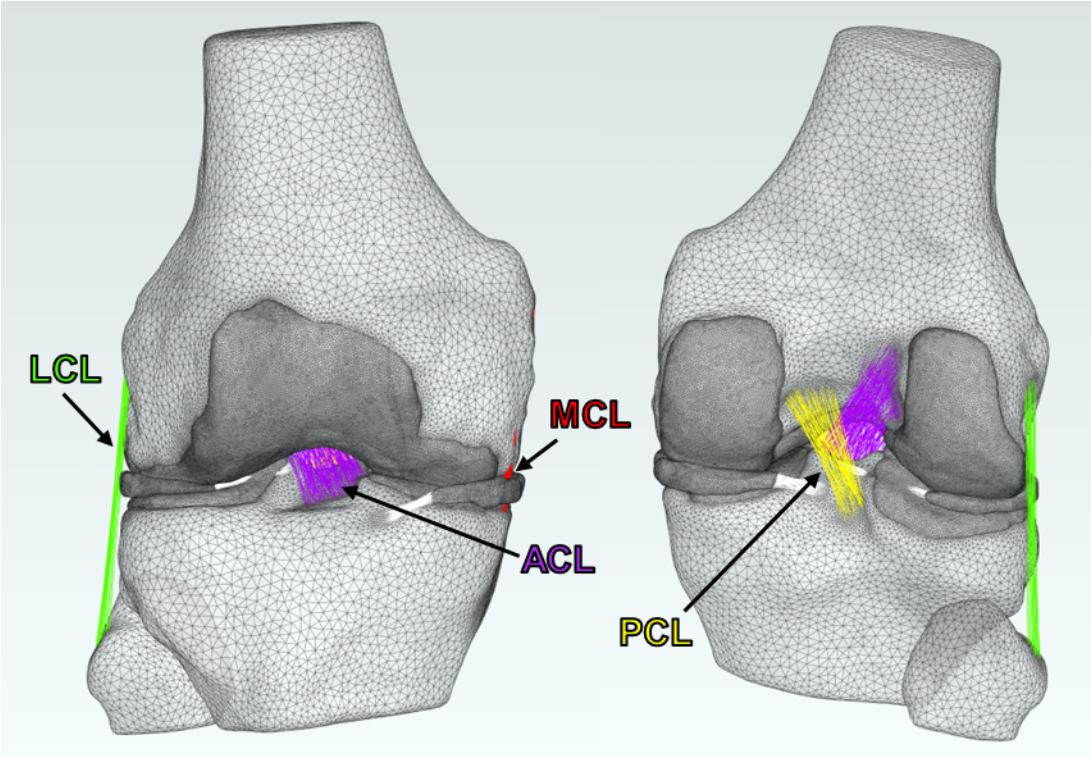

Figure 4-8 – The four main knee ligaments represented by spring bundles. The ACL is shown in purple, the PCL is in yellow, the MCL is in red and the LCL is in green.

No other ligaments were included in the model as the four main ligaments were considered substantial enough to constrain the bone movements without the need for adding extra structures. The transverse ligament (TL) of the knee (also known as the anterior inter-meniscal ligament) was not included as it was not seen on the participant's MRI scan. The reported incidence in literature of the TL varies from 31-94% (Szopinski and Adamczyk 2018) so it is not present in all individuals.

The 3D ligament geometries were roughly segmented from the T1-VIBE scan to find the attachment regions on the bones. Like with the meniscal horn attachment regions, the bone meshes were generated with a higher density of elements at the ligament attachment sites. The surface areas of the ligament attachment sites were calculated, along with the mean for each pair. The number of springs per ligament was calculated so one spring approximately represented 1 mm^2 area (Esrafilian et al. 2020). The mean area (and therefore number of springs) was rounded to the nearest 5 mm^2 to account for segmentation errors. The total number of springs used to represent each element were 145 for the ACL, 70 for the PCL, 25 for the LCL, and

65 for the MCL (Figure 4-9). The non-linear springs were then added to the model by selecting the specified number of nodes on each attachment site and attaching the springs by closest line projection.

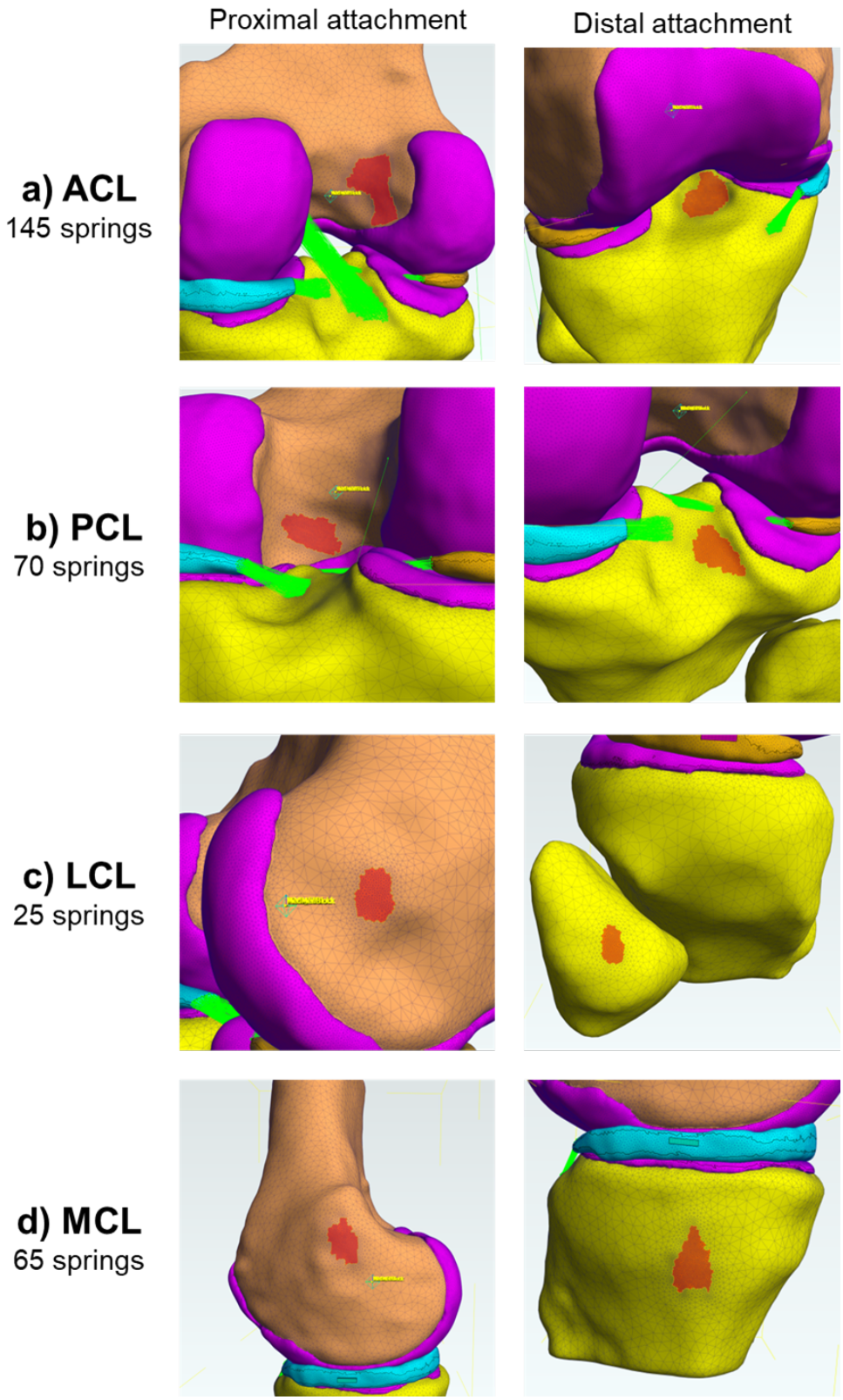

Figure 4-9 – Segmented ligament attachment regions for a) ACL, b) PCL, c) LCL and d) MCL along with the total number of springs used to represent each ligament.

The ligaments were represented in the model as non-linear Blankevoort springs (Blankevoort and Huiskes 1991). This was the same ligament model used in the MSM (Chapter 3, Section 3.2.1) and is described in more detail in Section 0.

The values of these force-strain equations for each spring in the ligament bundle were determined using the parameters in Table 1-7; this included the total stiffness (k_l) and average reference strain (ε_r) of the (anatomical) ligament bundles (Blankevoort et al. 1991) as the individual bundles could not be segmented in isolation from the MRI scan (Esrafilian et al. 2020). The force (f) was calculated for the whole ligament and then divided by the number of springs in the bundle (as given in Figure 4-9) to generate the curve for each individual spring.

Table 4-7 – Material parameters for the force-strain relationship of each ligament taken from Blankevoort et al. (1991).

Ligament	**Total stiffness/k_l [kN]**	**Reference strain/ε_r [%]**
ACL	10	8
PCL	18	-13.5
LCL	6	-7.33
MCL	8.25	3.66

For each ligament, a personalised reference length (L_r) was calculated as the distance between a central node from the defined attachment region at each end of the ligament. This distance was taken as the L_r for each ligament as the knee was approximately fully extended in the segmented position from the MRI. The L_r for each ligament is given in Table 4-8.

Table 4-8 – Ligament reference lengths (L_r) calculated.

Ligament	**Reference length/L_r [mm]**
ACL	33.5
PCL	32.0
LCL	57.1
MCL	58.4

The Blankevoort force-strain relationship curves were calculated using MATLAB for each 1D spring in the four different ligament bundles. The curves were output as text files and were imported into FEBio to define the force point curve for each discrete element set.

4.2.3 KINEMATICALLY DRIVEN MODEL

To drive the model kinematically, rigid rotations and displacements were applied to the bones (rigid bodies) within the model. In FEBio, each DOF is applied as a separate rigid constraint.

The relative TF joint motion was calculated from the object transforms (OTs) exported from the DSX Suite (HAS-Motion, Canada), so the motion of the whole joint could be applied to the tibia, whilst the femur was held still. This simplified the application of dynamic constraints in the model, improving model stability and performance.

The single OT representing each frame was then broken down into load curves representing each DOF (MATLAB), with the rotations being converted into the Euler Axis Angle convention used by FEBio to prescribe rotations to a rigid body.

Alignment of bones to the global origin

The centre of mass (COM) of a rigid body in FEBio is important as this is the point where any rigid rotations and translations are applied relative to. By default, this point is automatically calculated as the COM of the rigid body object. However, as the rigid rotations and translations applied here were not defined around the COM, but the anatomical coordinate systems (ACSs) used during image registration, it was important to set the rigid body COM to a consistent, mathematically relevant point. For ease of implementation, both rigid body COMs were set to the global coordinate system (GCS) origin. Therefore, it was important to align the OT definitions with the same origin point so the kinematics could be correctly applied.

To do this, all the geometries (bones, cartilage, meniscus) were transformed from their positions in the MRI coordinate space by the inverse of the femoral ACS definition to align the joint with the femoral ACS coincident with the GCS origin (Figure 4-10). The relationships between the geometries in 3D space remained

consistent, allowing for the springs representing the meniscal horns and ligaments to be added.

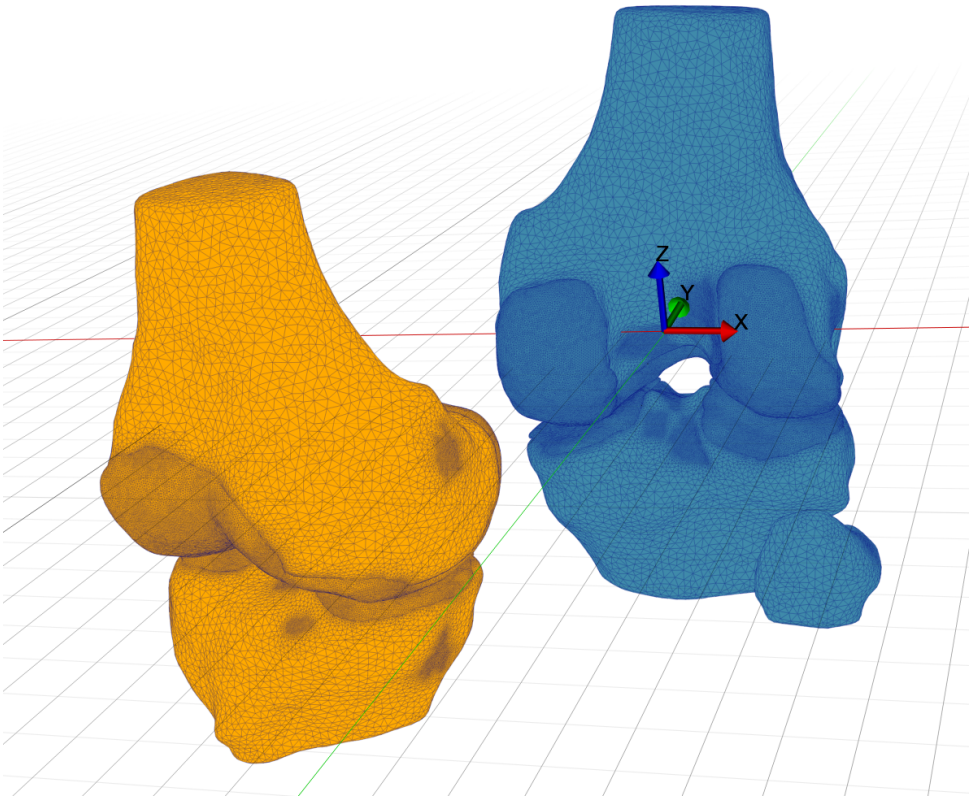

Figure 4-10 – The geometries from their original location relative from the MRI scan (orange) transformed by the inverse of the femoral ACS (blue) to align all geometries with the GCS origin in FEBio.

The tibia OTs were converted to be defined using the femoral ACS, instead of the original tibia ACS used for image registration so all motion was defined from a coincident starting point; this was the same definition used to look at the kinematics with coincident axes in Section 2.4.3, and is the same way they are defined in the MSM model. This meant the whole TF joint movement was applied to the tibia around the GCS – coincident with the femoral ACS.

Testing the kinematic inputs

To test that the OTs were correctly converted into the six rigid constraint load curves, their resulting motion was compared to the output of FEBio's Kinemat tool (FEBio 2021a). This was done using a simplified model of two identical cylinders to represent the two bones and BVR kinematics from a randomly selected lunge trial (Figure 4-11). The centre of the distal face of the 'femur' cylinder and the centre of

the proximal face of the ‘tibia’ cylinder were aligned with the GCS origin in FEBio. The generated load curves were applied to the ‘tibia’ cylinder, and the 4-point angle between the central line of the two cylinders and the point distance between the central nodes at each end were calculated at every five frames. The same kinematics were applied to the two bodies using the *Kinemat* tool (which applied the bone transforms separately to each object) and the same angles and distances were calculated.

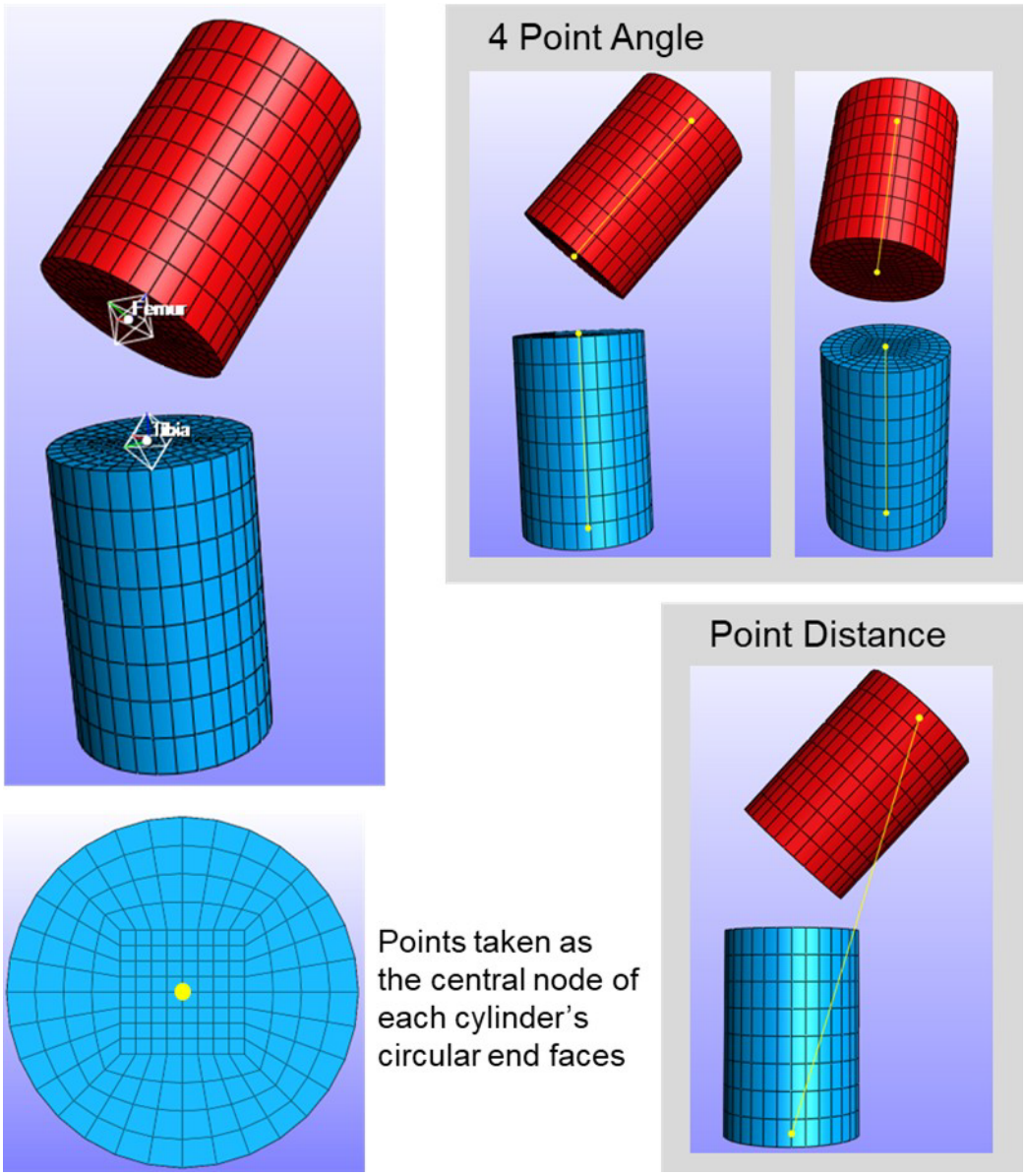

Figure 4-11 – Simple cylinder model to test rigid rotation and translation constraints were applied correctly. The red object represents the femur and the blue the tibia. Grey boxes show the two measurements taken using the central nodes of the cylinder’s circular faces.

The results were compared to ensure they were identical (Table 4-9) and that the six DOF load curves were representing the TF joint movement correctly. As the difference between the two methods was zero at all frames for both the 4-point angle

and the point distance, the load curves were shown to correctly represent the combined joint kinematics.

Table 4-9 – Results from comparison of the generated load curves and Kinemat tool results at every five frames of motion.

4 Point Angle (°)				Point Distance (mm)			
Frame	**Load curves**	**Kinemat tool**	**Difference**	**Frame**	**Load curves**	**Kinemat tool**	**Difference**
1	29.02	29.02	0.00	1	29.08	29.08	0.00
5	39.52	39.52	0.00	5	28.93	28.93	0.00
10	49.27	49.27	0.00	10	29.72	29.72	0.00
15	57.58	57.58	0.00	15	30.61	30.61	0.00
20	62.07	62.07	0.00	20	30.15	30.15	0.00
25	64.82	64.82	0.00	25	30.02	30.02	0.00
30	67.11	67.11	0.00	30	30.41	30.41	0.00
35	68.34	68.34	0.00	35	30.32	30.32	0.00
40	68.30	68.30	0.00	40	30.09	30.09	0.00
45	68.03	68.03	0.00	45	30.56	30.56	0.00
50	66.25	66.25	0.00	50	30.46	30.46	0.00
55	60.93	60.93	0.00	55	29.89	29.89	0.00
60	54.03	54.03	0.00	60	29.40	29.40	0.00
65	40.25	40.25	0.00	65	28.77	28.77	0.00

Model steps, contacts and constraints

Before running the model through the BVR-derived kinematics, two steps were needed: an initial separation to ensure no mesh overlap, and a step to bring the soft tissues in the model into contact in their first kinematic frame position. The femur and femoral cartilage were fixed using a rigid constraint in all six DOFs throughout the whole simulation; all prescribed displacements were applied to the tibia.

Separation step

For the separation, the tibia was moved inferiorly from its initial MRI position using a negative rigid z displacement control (from 0 mm to -2 mm); the other five tibial DOFs were fixed for this step. To move the meniscus so that it was not in contact

with either cartilage surface, two blocks were added next to each meniscus and a tied-facet-on-facet contact was used to connect the blocks to the faces on the edge of each meniscus (Figure 4-12). These blocks were set as rigid bodies so a rigid z displacement of -1 mm could be applied, pulling the meniscus into a position halfway between the two cartilage meshes. The blocks were inactive for the remainder of the simulation.

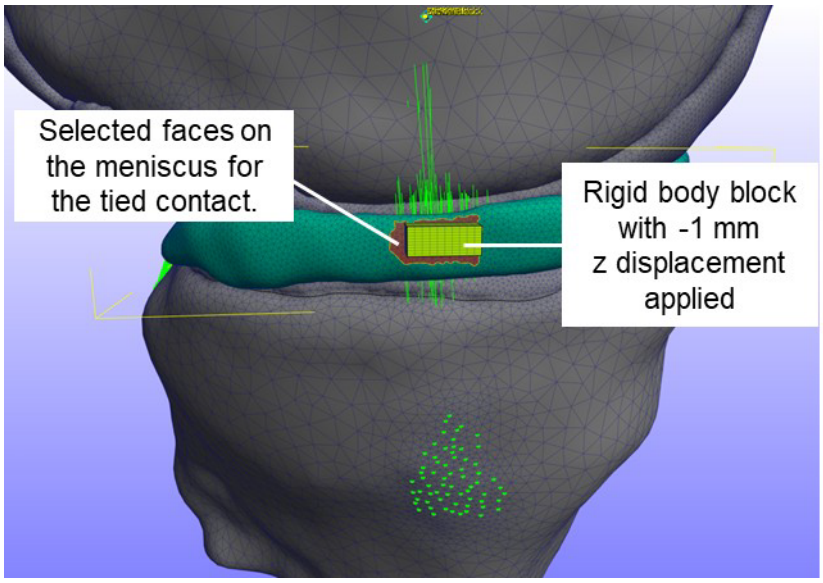

Figure 4-12 – Rigid body block with the corresponding faces on the meniscal wall for the tied contact.

Contact step

Once separated, the geometries were then brought back into contact by moving the tibia into its position of the first frame of kinematic motion using rigid constraints that varied from 0 (or -2 mm for the z-displacement) to the initial frame values. This allowed the soft tissues to be bought into contact and compress, ready to run the kinematic trial data.

Kinematics step

Once in its starting position, the tibia was moved through the TF joint motion calculated using BVR via the six DOF prescribed rigid constraints. In total there were 24 frames of BVR data corresponding to 17% through 76% of stance phase of level gait. To help the model solve, the frame rate was reduced from 60 Hz (the original frequency the BVR data was collected in) to 10 Hz by increasing the time between frames. The results were only analysed at the frames which corresponded with a BVR input frame, and no time-dependent model elements were included, so the

frame rate reduction only made it easier for the model to solve by decreasing the gradient of the load curves between frames.

A summary of the contacts and contact penalties applied during each modelling step can be found in Table 4-10. These penalties were the highest values that allowed the model to solve all kinematic steps and run to full termination.

Table 4-10 – Contacts included in each step of the model. (Identical contacts were used in Steps 2 & 3.)

Step	Primary contact surface	Secondary contact surface	Contact type	Contact penalty	Two-pass
1. Separate	Medial meniscus	Medial rigid body block	Tied-facet-on-facet	1	n/a
	Lateral meniscus	Lateral rigid body block	Tied-facet-on-facet	1	n/a
2. Initial Contact & 3. Kinematics-driven	Femoral cartilage	Tibial cartilage	Sliding-facet-on-facet	120	on
	Femoral cartilage	Medial meniscus	Sliding-facet-on-facet	60	on
	Tibial cartilage	Medial meniscus	Sliding-facet-on-facet	75	on
	Femoral cartilage	Lateral meniscus	Sliding-facet-on-facet	1	off
	Tibial cartilage	Lateral meniscus	Sliding-facet-on-facet	1	off

A low contact penalty value was required between the lateral meniscus and both cartilage surfaces in order for the model to solve for all timesteps due to an issue arising toward the end of the motion.

4.2.4 RESULTS OUTPUT AND ANALYSIS

Results were extracted from the final model at each timepoint that corresponded to a tracked BVR frame of data during the *kinematic* step.

Firstly, the contact pressures between the femoral cartilage and tibial cartilage surfaces were analysed within FEBio with screenshots of the tibial cartilage contact maps at each timepoint. The maximum contact pressure between the two cartilage surfaces was also found at each timepoint. The contact maps and maximum pressure values were compared to results from literature, as well as the corresponding contact maps for this participant from the MSM work in Chapter 3.

To analyse the stresses within the femoral, medial tibial and lateral tibial cartilage, the Cauchy stress tensor (Equation 4-11) for each element was exported at each frame. This was then used to calculate the normal (axial) stress by taking the Z component (σ_{zz}) of the stress tensor. The principal stresses were determined by calculating the eigenvalues of each stress tensor. The maximum principal stress was defined as the eigenvalue with the greatest absolute magnitude, since compressive stresses are represented by negative values. The von Mises stress was also calculated using Equation 4-12. For each stress measure, the maximum value of any element at each frame was found, along with the overall maximum at any point of the motion.

$$\sigma = \begin{bmatrix} \sigma_{xx} & \sigma_{xy} & \sigma_{xz} \\ \sigma_{yx} & \sigma_{yy} & \sigma_{yz} \\ \sigma_{zx} & \sigma_{zy} & \sigma_{zz} \end{bmatrix} \quad \textit{(Eq. 4-8)}$$

Where σ is the Cauchy stress tensor.

$$\sigma_{VM} = \quad \textit{(Eq. 4-9)}$$

$$\sqrt{\frac{1}{2}\left[\left(\sigma_{xx}-\sigma_{yy}\right)^2+\left(\sigma_{yy}-\sigma_{zz}\right)^2+\left(\sigma_{zz}-\sigma_{xx}\right)^2\right]+3\left(\sigma_{xy}^2+\sigma_{yz}^2+\sigma_{zx}^2\right)}$$

Where σ_{VM} = von Mises stress and all other stress (σ) values are components of the Cauchy stress tensor in Equation 4-11.

The maximum principal, axial and von Mises strains at each frame were calculated in a similar manner using the Cauchy strain tensor (Equation 4-13).

$$\varepsilon = \begin{bmatrix} \varepsilon_{xx} & \varepsilon_{xy} & \varepsilon_{xz} \\ \varepsilon_{yx} & \varepsilon_{yy} & \varepsilon_{yz} \\ \varepsilon_{zx} & \varepsilon_{zy} & \varepsilon_{zz} \end{bmatrix} \quad \textit{(Eq. 4-10)}$$

The maximum stresses and strains were plotted against percentage stance and compared to other FEMs modelling walking from literature.

4.3 RESULTS AND DISCUSSION

As discussed in Chapter 1, understanding how the articular cartilage behaves under joint loading is important as altered loading and the weakening of its mechanical properties are common indicators of OA (Sinusas 2012; Mukherjee et al. 2020; Katz et al. 2021; Mohout et al. 2023). Commonly used parameters to assess altered knee mechanics include contact pressure, stress and strain. In particular, articular cartilage stresses and strains are key outputs from a knee FEM as they are unmeasurable parameters in-vivo and cannot be obtained through a standard MSM pipeline (such as the one in Chapter 3).

To understand how the kinematic-driven model has performed, the outputs were compared to the magnitudes found in literature from other FEMs of the healthy human knee. This aimed to evaluate if this model has produced results of a similar magnitude to force-driven FEMs, however due to all the models using different material models and parameters, as well as being driven differently, comparison between model outputs is limited. As tissue stresses and strains are unmeasurable in-vivo, all FEMs must estimate these magnitudes so their accuracy cannot be directly confirmed.

As shown in literature, peak magnitudes of pressure, stress and strain within the articular cartilage generally corresponded to the first and second peaks of force during the stance phase of gait (Adouni et al. 2012; Halonen et al. 2013; Mononen et al. 2015; Daszkiewicz and Luczkiewicz 2021; Fu et al. 2022). For the trial used to drive this model, the peaks of the Z-component of the ground reaction force (GRF) measured by the force plate during the stance phase of gait were found to occur at 23% and 75.4% stance phase respectively. These points were both within the part of stance phase captured by BVR (17-76%) so were able to be used for comparison with the results from literature.

4.3.1 CONTACT PRESSURE

As discussed in Section 1.7.1, contact pressure is a commonly used output from FEM when investigating altered knee mechanics due to OA. The contact pressure maps of the femoral-tibial cartilage contact pressures visualised on the tibial cartilage at 10% intervals of stance phase are presented in Figure 4-13, along with the contact

map from the first and last frames analysed within FEBio. It is important to note that although the meniscus was included in the model, the cartilage contact with the meniscus is not visualised here.

The contact pressure was found to be higher on the medial plateau at the start and the end portions of the collected motion, with contact shifting to the lateral plateau during mid-stance leaving central portions of the medial plateau with no contact. This disagrees with literature where the medial plateau was found to consistently have a greater contact area than the lateral plateau throughout the same portion of stance phase modelled here (~20-75% stance) (Liu et al. 2010; Adouni et al. 2012), so no contact on the medial plateau during any part of stance is unexpected. This may be due to inaccuracies in image registration occurring during mid-stance as the contralateral limb occluded the imaged knee during its swing-phase. This highlights the potential sensitivity of the model to small kinematic errors on contact area prediction.

The maximum articular cartilage contact pressure was found to peak at 28.9 MPa, occurring on the medial plateau at 76% stance phase (the final frame of BVR data collected). This value is higher than those typically reported in the literature for healthy knees during gait, where peak contact pressures during stance phase range from 8-17 MPa (Adouni et al. 2012; Halonen et al. 2013; Daszkiewicz and Luczkiewicz 2021; Fu et al. 2022). However, some studies, such as Mononen et al. (2015), have reported local medial compartment pressures up to 35 MPa, demonstrating that large variation exists depending on model setup and driving data choices. The studies compared here differ from the present model in several key aspects that may explain the higher peak contact pressure observed.

Firstly, all of these models were at least partially force-driven, rather than purely kinematically prescribed. Adouni et al. (2012) and Daszkiewicz and Luczkiewicz (2021) applied mean, population-based joint loads and moments rather than subject-specific data, which may underestimate contact magnitudes by smoothing individual variability. Halonen et al. (2013) and Mononen et al. (2015) incorporated kinematic inputs derived from experimental data but not subject-specific geometries, while Fu et al. (2022) drove their model using MSM outputs from experimental gait data.

Differences in the applied boundary conditions and input data can strongly influence the magnitude and location of cartilage contact pressures.

Secondly, variations in mesh quality likely contributed to differences in pressure magnitude. Some models used relatively coarse hexahedral meshes (Adouni et al. 2012; Halonen et al. 2013), which are less suited to capturing complex cartilage morphologies and typically yield lower pressure magnitudes. The model presented here used a denser tetrahedral mesh, which provides more accurate surface representation but may lead to higher localised pressures.

Finally, local contact patterns were consistent with previous findings, with peak pressures located on the medial tibial plateau (Haut Donahue et al. 2003; Adouni et al. 2012; Halonen et al. 2013; Mononen et al. 2015; Daszkiewicz and Luczkiewicz 2021; Fu et al. 2022). The peak pressure corresponded with the second loading peak of stance phase (76% stance), agreeing with some other models (Daszkiewicz and Luczkiewicz 2021; Fu et al. 2022), but disagreeing with others that found peak pressures occurring at the first peak of stance (Adouni et al. 2012; Halonen et al. 2013; Mononen et al. 2015). The highest pressure from this model was located anteriorly on the medial edge of the tibial cartilage, consistent with findings by Mononen et al. (2015).

Overall, while small registration errors could have contributed to the high local value observed, the differences in model formulation, mesh resolution, and input data across studies may also contribute to the higher contact pressures obtained.

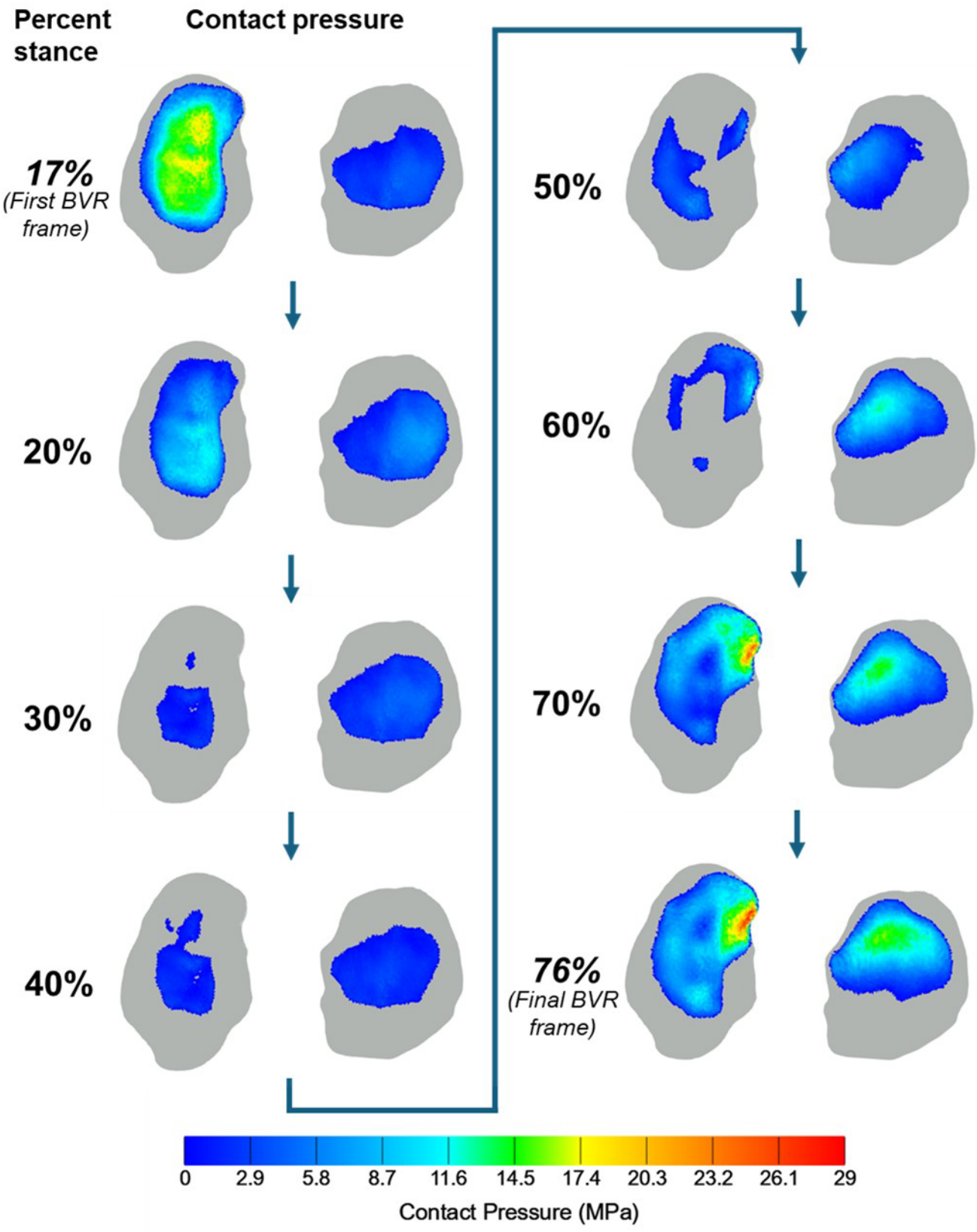

Figure 4-13 – Tibial cartilage contact pressure distributions at 10% intervals of stance phase of level gait where BVR data were obtained. Also included are the first and last frames as these involved high pressure magnitudes (with the highest pressure at 76%).

Comparison to MSM and BVR-EFM contact pressure maps from Chapter 3

Contact pressure maps during the stance phase of level gait were also calculated using an elastic foundation model in Chapter 3. This was done using the same BVR input object transforms used to drive the FEM (see Section 3.2.4 - this model will be referred to as BVR-EFM in this chapter) as well as using the marker-based motion capture (collected as described in Chapter 2, Section 2.3.2) as an input to an MSM pipeline (Section 3.2). The MSM pipeline was run with a model containing ‘generic’ contact geometries and one with the personalised MRI segmented geometries incorporated (Section 3.2.2).

The resulting tibial cartilage contact maps from these three versions of the elastic foundation model (Appendix D) were compared to the FEM contact pressures between the femoral and tibial cartilage surfaces (visualised on the tibial cartilage in Figure 4-13) to investigate their differences. The tibial cartilage was the focus for this comparison as this was the same focus as the results in Chapter 3.

Firstly, the maximum contact pressure of any element on the tibial cartilage contact surface at each frame was plotted for the four different methods (Figure 4-14). These results show that the FEM calculated the highest contact pressure values of all the methods, with particularly high pressures calculated at the start and end of the BVR captured activity. However, there was generally better agreement in the maximum pressure magnitude between methods from 20% to 60% stance.

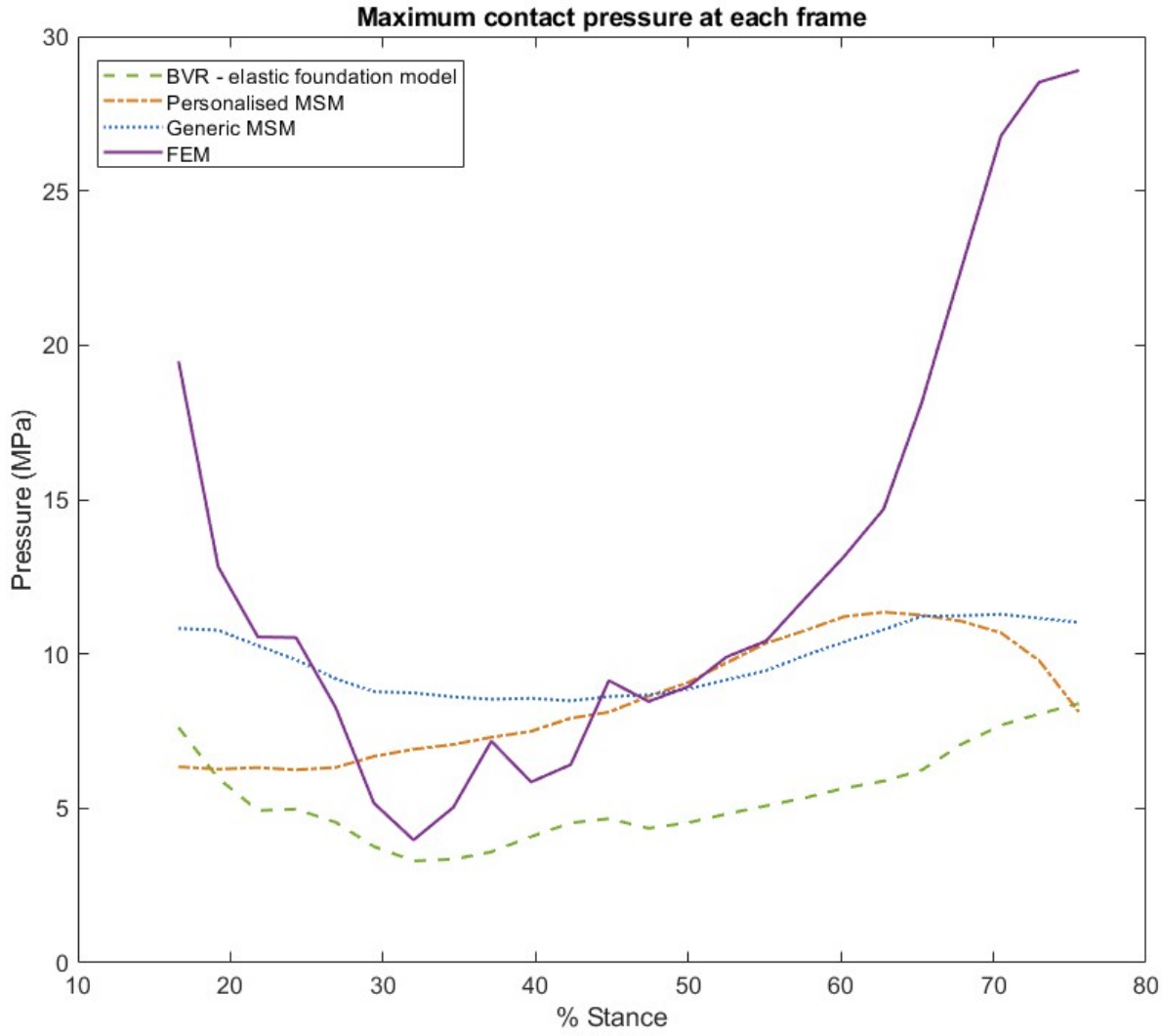

Figure 4-14 – Maximum contact pressure of any element at each frame of motion for the four methods.

The final frame of motion (which corresponds with the largest peak of z-GRF) where the highest FEM pressure (28.9 MPa) was found. This was much higher than the peak pressures found for the personalised MSM (11.35 MPa), generic MSM (11.02 MPa) and BVR-EFM (8.39 MPa). These magnitude differences could be due to the different method used to calculate pressure in FEBio and the deformation of the elements. However, this also corresponds with the larger amounts of overlap between the anterior portion of the lateral meniscus with both the femoral and tibial cartilage which could be affecting the other contacts in the model and contributing to the high pressures found between the cartilage contacts at this timepoint.

As the highest pressure values in the FEM results were generally isolated to a few elements in the final few frames of motion, to visually compare the FEM results with the three elastic foundation models, the pressure scale was set to 0-19 MPa as this was the maximum threshold used when plotting the contact maps in Appendix D. This was done to keep the visual variation between the three elastic foundation models, as when the maximum threshold was set to 29 MPa, the nuance between these three was lost. Only the visualisation of the final four frames of the FEM contact pressures were altered as all other results were below the 19 MPa threshold. An example of the visual difference is shown for 70% stance phase in Figure 4-15, showing the lower threshold is more suitable for indicating regions of high pressure.

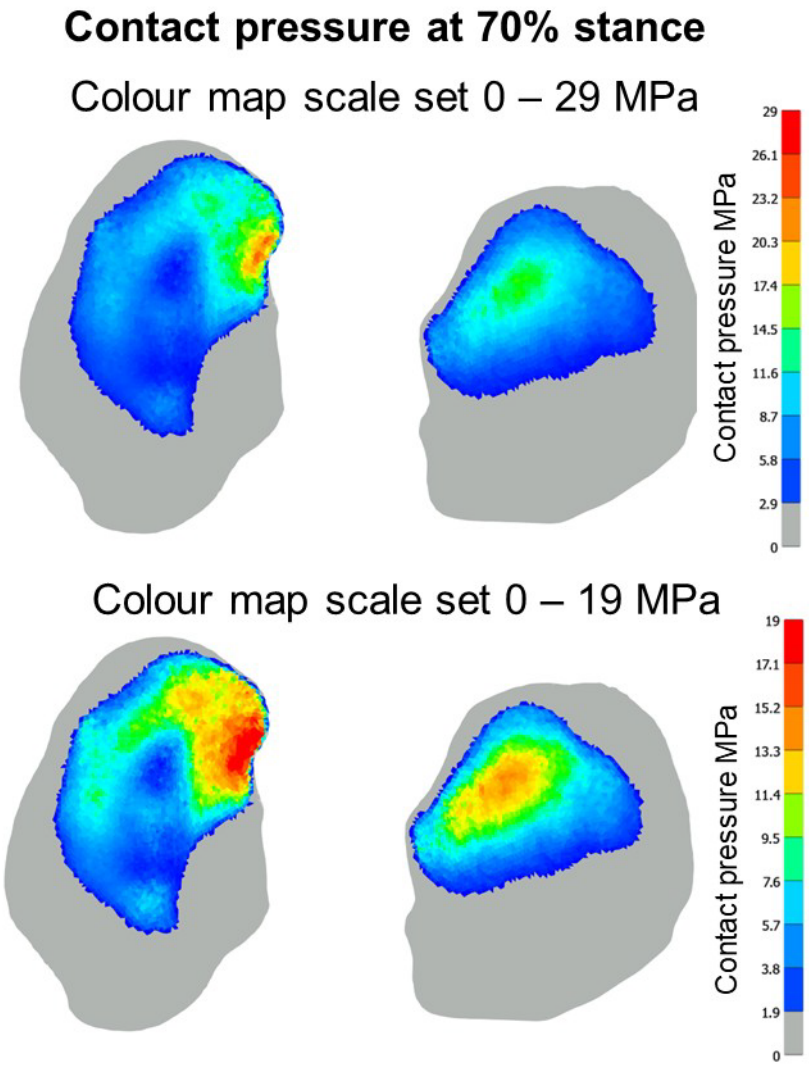

Figure 4-15 – Figure illustrating the difference in the colour map when the maximum value threshold is lowered for the FEM results.

Three main frames were chosen for comparison: 20% (Figure 4-16), 50% (Figure 4-17) and 70% stance (Figure 4-18) respectively. These three were picked for analysis as they covered the range of stance captured, representing approximately the first and second peak loading as well as mid-stance, without using the beginning and end frames of motion (which are more susceptible to image registration errors).

At 20% stance phase (Figure 4-16), all four models found higher contact pressures and larger contact areas on the medial plateau than the lateral. The contact area of the FEM and BVR-EFM maps were similar, as expected, due to using the same bone pose input data to calculate contact area. The personalised MSM showed a similar contact region to the FEM (and BVR-EFM) on the medial plateau, but not on the lateral plateau. The generic MSM showed similar pressure magnitudes to the FEM on the medial plateau, but the contact area was smaller and located more posteriorly.

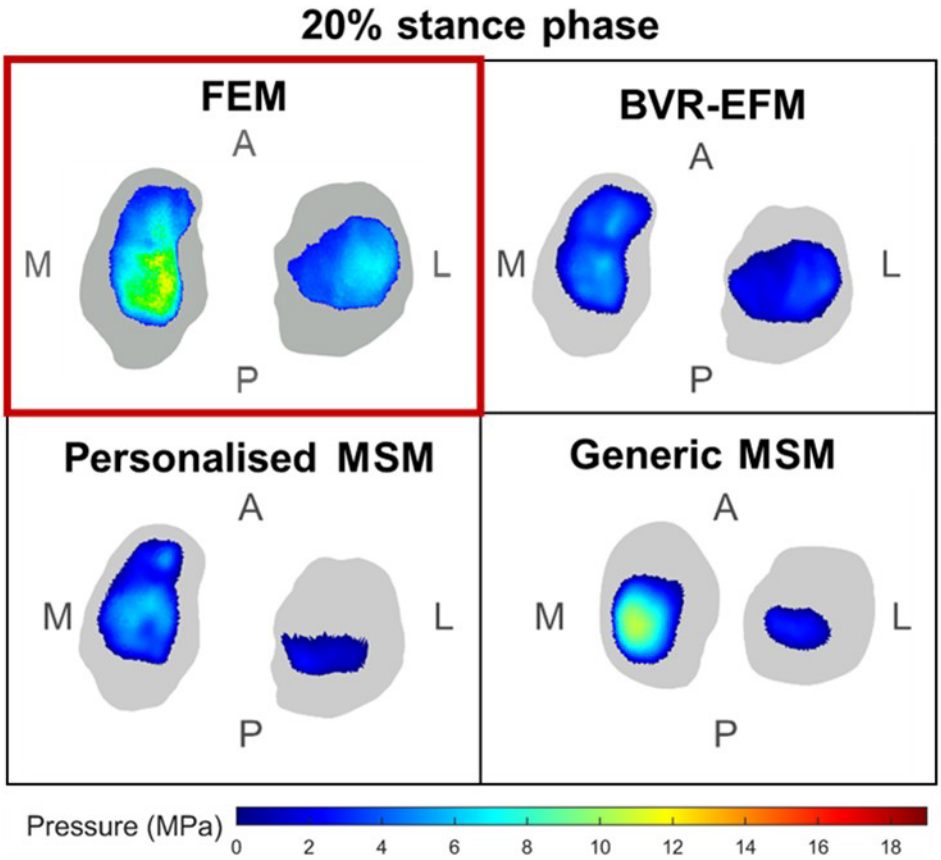

Figure 4-16 – The four tibial cartilage contact maps at 20% stance phase.

The BVR-EFM and FEM maps are likely to predict the contact area more accurately as they both use the accurate BVR bone poses as inputs, whereas the MSMs

estimate bone poses from marker-based motion capture. The FEM also has the added benefit of modelling the meniscus, making the resulting contact area between the femoral and tibial cartilage more representative of the in-vivo scenario.

At 50% stance phase (Figure 4-17), the FEM showed the smallest contact area on the medial plateau of all the contact maps, due to this, the contact pressure magnitudes were found to be higher on the lateral plateau than the medial for the FEM for mid-stance. This was not seen in the personalised and generic MSM results where the medial plateau continued to have the larger contact area and pressure magnitudes compared to the lateral plateau. The lower contact pressures and contact area 'gap' visible in both the FEM and BVR-EFM maps at 50% stance are likely due to a combination of cartilage morphology and image registration being more difficult during mid-stance due to occlusion by the contralateral limb reducing bone pose accuracy.

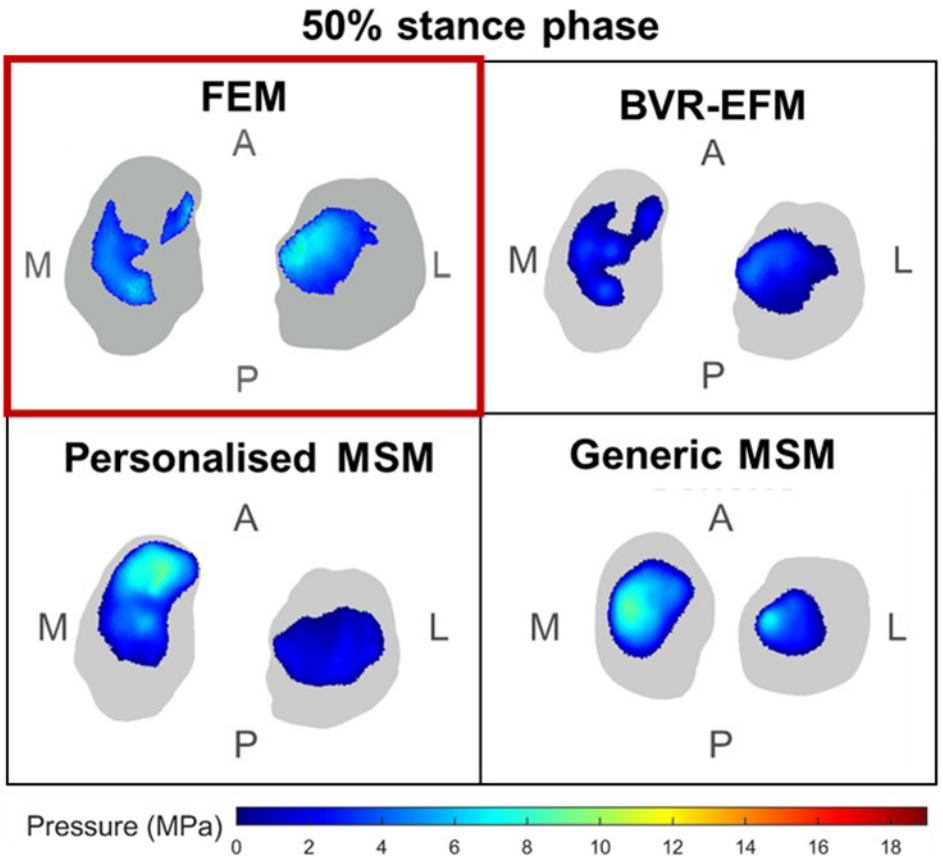

Figure 4-17 – The four tibial cartilage contact maps at 50% stance phase.

The contact maps at 70% stance phase (Figure 4-18) produced similar trends to those seen at 20% stance phase, with the FEM, BVR-EFM and personalised MSM producing similar contact regions on the medial tibial plateau with the peak contact pressure located anteriorly on the medial plateau.

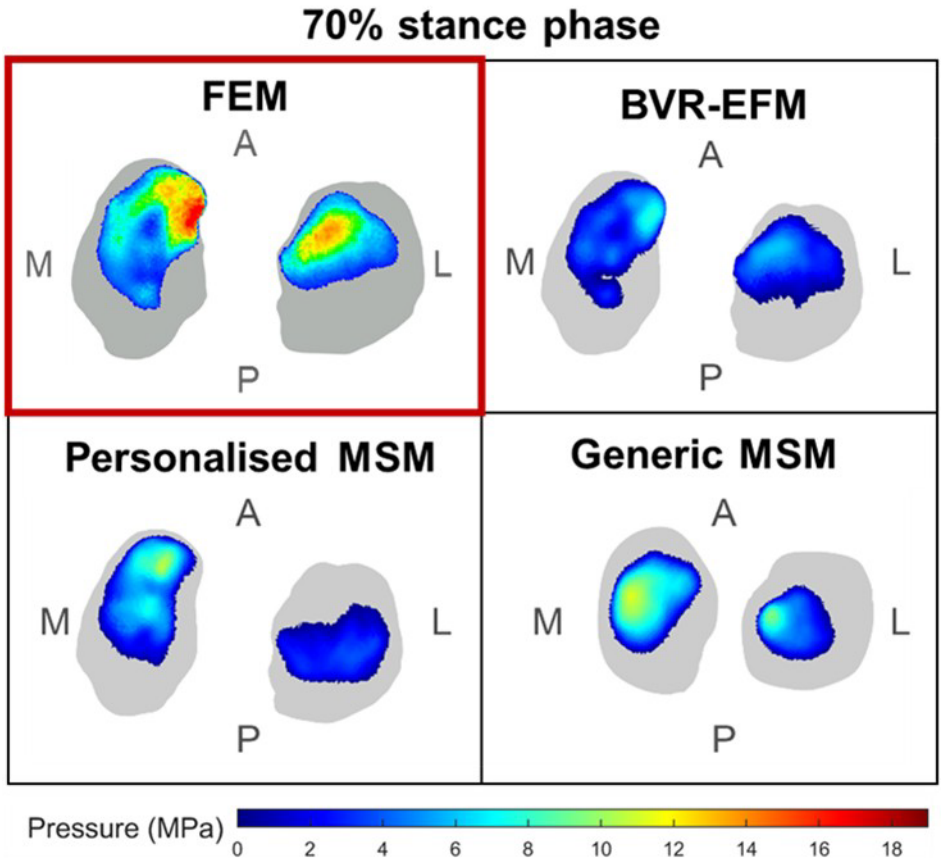

Figure 4-18 – The four tibial cartilage contact maps at 70% stance phase.

Again, the contact area on the lateral plateau was predicted to be more posteriorly located by the two MSMs, reducing their similarity. Although the generic MSM had the least similarity with predicted contact region compared to the FEM results, the contact pressure magnitudes were the most similar, with higher contact pressures also being found on the lateral plateau. In contrast, the personalised MSM had relatively low contact pressures on the lateral plateau, offloading onto the medial condyle of the knee which is not reflected in either of the BVR-based models. This suggests that the personalised model may be incorrectly distributing the load through the joint at the second peak of loading during the stance phase of gait as it has a higher ratio of medial to lateral condyle maximum contact pressure than the other three models. As altered loading distribution, such as increased medial knee loading, is associated with OA (Trad et al. 2017; Arjmand et al. 2018; Mononen et al. 2023),

this may lead to incorrect assumptions about joint function if used to model knee contact pressures and should be investigated further in the future.

4.3.2 STRESS

Unlike articular cartilage contact surfaces pressures which could be obtained through other methods, such as MSM pipelines (Chapter 3), an FEM can be used to expand the contact analysis to internal parameters such as stress within the tissue.

Maximum stress magnitudes

To understand if the model produced results comparative to literature, the maximum von Mises, principal and normal stresses were calculated across all frames of motion (Table 4-11).

The magnitudes and timing of these stress peaks (Table 4-11) showed partial agreement with previous finite element studies of the healthy knee during gait. The maximum von Mises stresses (8-13 MPa) were comparable with those reported by Halonen et al. (2013), who found a peak of approximately 10 MPa during early stance (around 20% stance). However, the maximum normal and principal stresses in the present model were lower than those from studies using more complex material formulations. For example, Halonen et al. (2013) and Mononen et al. (2015) both employed fibril-reinforced poroviscoelastic (FRPVE) cartilage models that incorporated collagen fibril orientation and depth-dependent proteoglycan and fibril distributions. Their models produced maximum principal stress magnitudes of 30-40 MPa at approximately 25% stance (Halonen et al. 2013) and 35.2 MPa at 20% stance (Mononen et al. 2015), respectively. In contrast, Yang et al. (2010) modelled cartilage as isotropic elastic and reported lower normal stresses of 13-17 MPa, closer to those found here. This demonstrates the effect of material model choice on model outputs and explains some of the differences in stress magnitude found between different FEMs. The simplified isotropic elastic model used here does not capture the depth-wise anisotropy, viscoelasticity, or fluid pressurisation represented in FRPVE models, which tend to produce higher localised stresses.

Table 4-11 – Maximum von Mises stress, normal (axial or z-) stress and compressive principal stress magnitudes in each structure and their stance-phase occurrences.

Cartilage structure	**Max. von Mises stress (MPa)**	**Occurrence (% stance)**	**Max. normal stress (MPa)**	**Occurrence (% stance)**	**Max. principal stress (MPa)**	**Occurrence (% stance)**
Femoral cartilage	12.60	16.6	11.29	16.6	2.30	16.6
Medial tibial cartilage	10.50	70.5	19.27	75.6	12.65	16.6
Lateral tibial cartilage	8.80	73.0	10.90	67.9	6.61	21.8

As well as the material model used, differences in magnitude and timing of peak pressures may also arise from the chosen mesh density and element type. The current model used a finer tetrahedral mesh than many of the earlier studies in literature, which used coarser hexahedral meshes, influencing stress concentrations and peak values. As none of the other models were solely driven by kinematics, differences in loading conditions and driving inputs would also affect stress calculations.

When comparing which cartilage structure found the highest magnitudes, the highest von Mises stresses were found in the femoral cartilage which aligns with the findings of Tarniţă et al. (2014). In contrast, the highest peak values for both maximum principal and maximum normal stress were found in the medial tibial cartilage (Table 4-11). As the medial tibial cartilage was found to have higher maximum stresses than the lateral, these results were consistent with previous findings (Yang et al. 2010; Mononen et al. 2015). The low principal and normal stresses found in the femoral cartilage were likely because of the contact mechanics between the two meshes. An artificially enlarged contact area on the femoral cartilage surface, potentially caused by segmentation or input kinematic errors or incorrectly modelled interactions with the meniscus, would spread the load across a larger area, reducing the stresses in that region.

Overall, the differences in stress magnitudes and distributions between models likely reflect a combination of factors, including variations in material models, mesh density, element type, and loading or boundary conditions. As stress cannot be directly measured in-vivo during walking, it is not possible to determine which modelling approach most accurately represents the true physiological values. Nevertheless, understanding where the present results sit compared to the range reported in literature provides useful context for evaluating model behaviour and consistency, demonstrating that the outputs are broadly comparable with those of other published FEMs of the healthy knee.

Stress variation throughout stance phase

The maximum von Mises stress of the three different regions of articular cartilage at each frame were plotted against percentage stance phase to understand how the stress varied throughout the movement (Figure 4-19). Von Mises stress was chosen

because it summarises the combined multidirectional stresses, rather than the directional loading presented by principal or normal stresses, providing a visualisation of 3D trends in cartilage loading. To reduce the influence any outliers where elements had very high stresses, the top 1% of elements under stress (where von Mises stress > 0) were averaged at each frame.

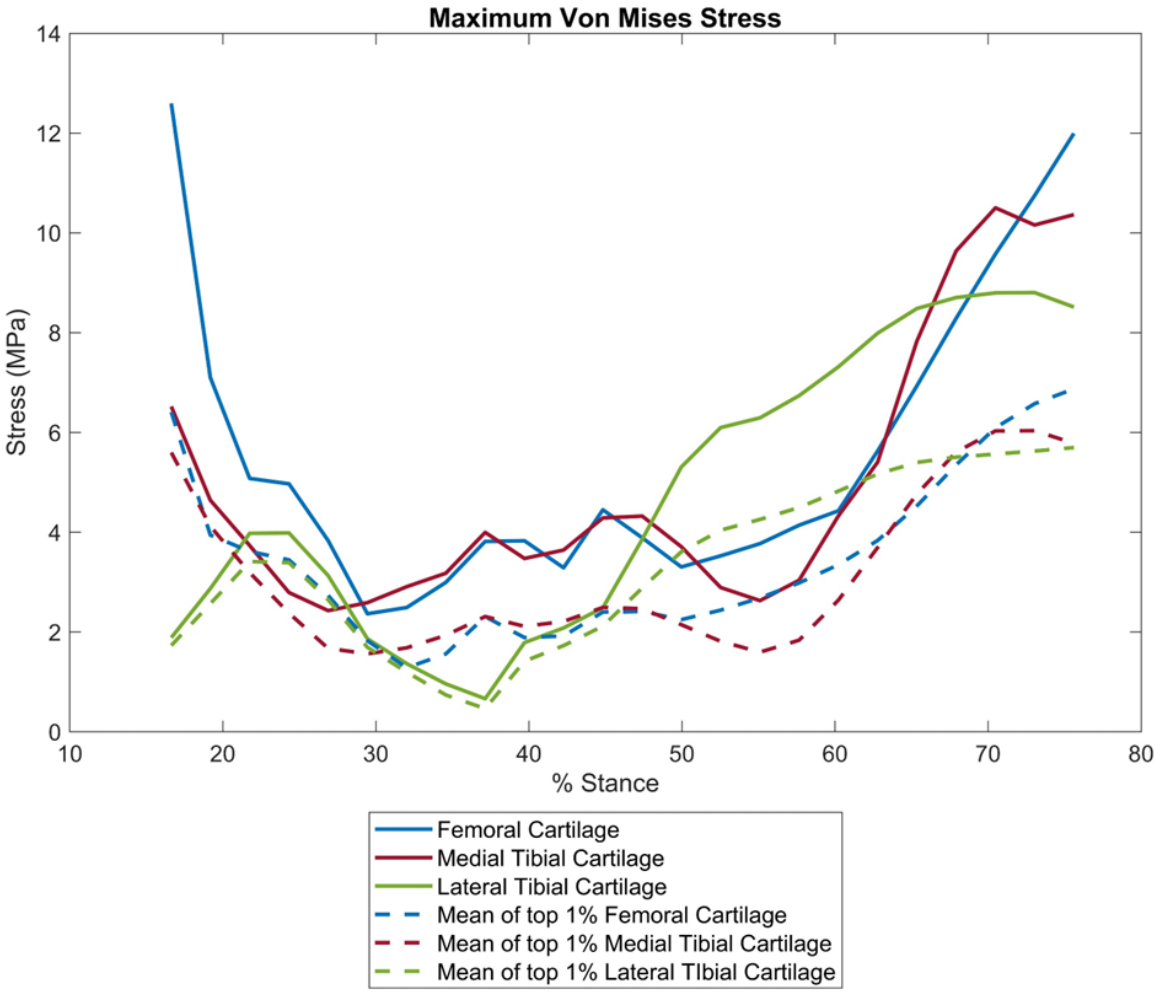

Figure 4-19 – Maximum von Mises stress in any element against percentage stance phase. The mean von Mises stress of the top 1% of elements in each cartilage structure is also included to account for any outliers.

The maximum von Mises stresses in all three structures followed a similar pattern, with higher stresses early in the collected portion of stance, a slight decrease during mid-stance, and an increase towards the end of the collected portion. The higher stresses at the start and end of stance correspond to the two loading peaks at approximately 25% and 75% of stance during level gait. A similar trend was seen in the maximum principal and normal stresses within each structure. The profiles shown in Figure 4-19 generally agree with previous literature, showing higher stresses near the loading peaks and lower stresses during mid-stance (Halonen et

al. 2013; Mononen et al. 2015). However, as the stance phase modelled was restricted to 16-76% of stance, it is more difficult to compare the overall trends, since behaviour outside the collected range cannot be confirmed. In general, the trend for the lateral tibial cartilage agreed more closely with the literature than the medial tibial cartilage. This model found the second stress peak to be higher for both the medial and lateral tibial cartilage (Figure 4-19), whereas literature reports a lower first peak and higher second peak for the lateral side (Mononen et al. 2015), and a higher initial peak for the medial side (Halonen et al. 2013; Mononen et al. 2015).

The overall maximum von Mises stress found in the femoral, medial tibial and lateral tibial cartilage structures from Table 4-11 are summarised again in Table 4-12, along with the results for the mean of the top 1% of elements.

Table 4-12 – Maximum von Mises stresses in each cartilage structure and when the maximum occurred.

Cartilage structure	**Max (MPa)**	**Occurrence (% stance)**	**Mean top 1% max (MPa)**	**Occurrence (% stance)**
Femoral cartilage	12.60	16.6	6.87	75.6
Medial tibial cartilage	10.50	70.5	6.04	73.0
Lateral tibial cartilage	8.80	73.0	5.70	75.6

As Table 4-12 shows, the maximum von Mises stress in the femoral cartilage was found at 16.6% stance, corresponding with the first frame of stance phase collected using BVR. This was not seen when the top 1% of elements were averaged, where the maximum occurred at 75.6% stance (Figure 4-20), corresponding with the second peak of loading during gait. This suggests this high initial stress was due to only a few high values, which, when investigated, were visibly concentrated at the boundary between the bone and the femoral cartilage, where the anterior, medial edge of the medial tibial cartilage contacts the femoral cartilage. This concentration of stress at the bone-cartilage boundary may be partly due to the modelling assumption of a rigid bone surface in contact with deformable cartilage. In-vivo, the bone-cartilage interface would deform slightly under load, producing a smoother stress distribution. As a result, such isolated elements of very high stress are unlikely to occur physiologically and are more likely to reflect a local numerical effect rather than a true mechanical feature.

Based on experience with BVR image registration (Chapter 2, Section 0), it is hypothesised that elevated stresses in the first frame may be linked to reduced registration accuracy when the bone was partially out of frame. This causes the early peak to occur before the first peak of loading at around 25% stance where it would

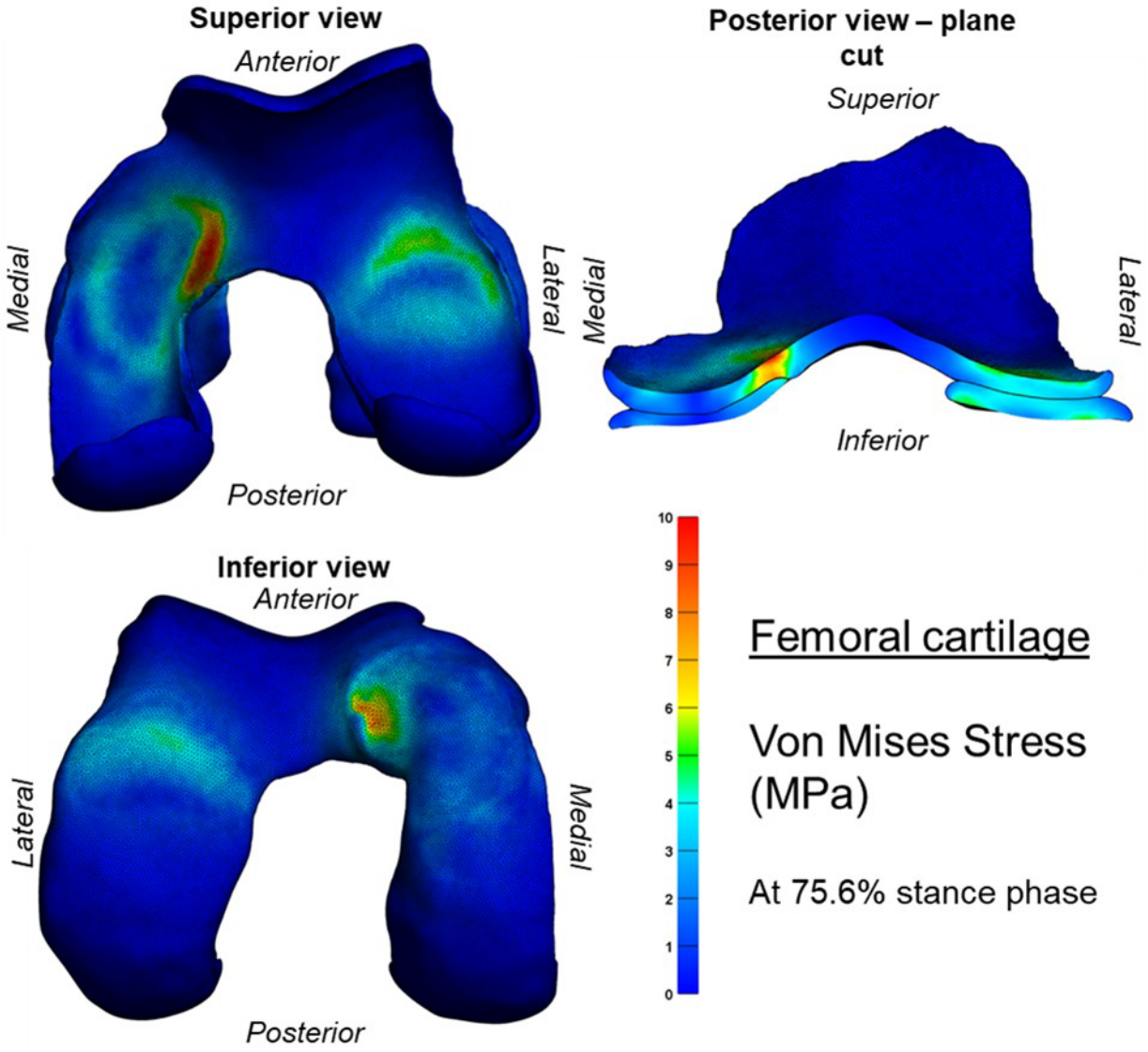

Figure 4-20 – Von Mises stress in the femoral cartilage at 75.6% when the maximum mean stress value of the top 1% of elements occurred.

be expected.

As seen clearly from the superior view (Figure 4-20), the stress patterns seen on the femoral cartilage were typically ring-shaped, likely due to the cartilage morphology resulting in larger deformation around the edges of the tibial cartilage. The stresses were higher on the medial condyle at the start of the motion, with the distribution becoming more even between the medial and lateral sides through stance phase.

The stresses moved anteriorly with increasing stance phase, consistent with the transfer of body weight during gait (Liu et al. 2010). Higher stresses were seen closer to the bone-cartilage boundary than on the cartilage-cartilage surface. This was likely due to the bones being modelled in rigid bodies so only the cartilage can deform at the bone-cartilage interface.

The von Mises stress in the tibial cartilage was also higher in the medial plateau at the start of the motion, with lower stresses in both sides during midstance, before increasing again towards the second peak of loading where the peak stresses occurred. At the peak (Figure 4-21), the von Mises stresses were generally located anteriorly, with a particularly high region of stress located anteriorly on the medial edge of the medial plateau. This may be due to a small inaccuracy in the medial-lateral (ML) translation of the tibia from image registration artificially increasing the stresses in this region where this pattern was unexpected.

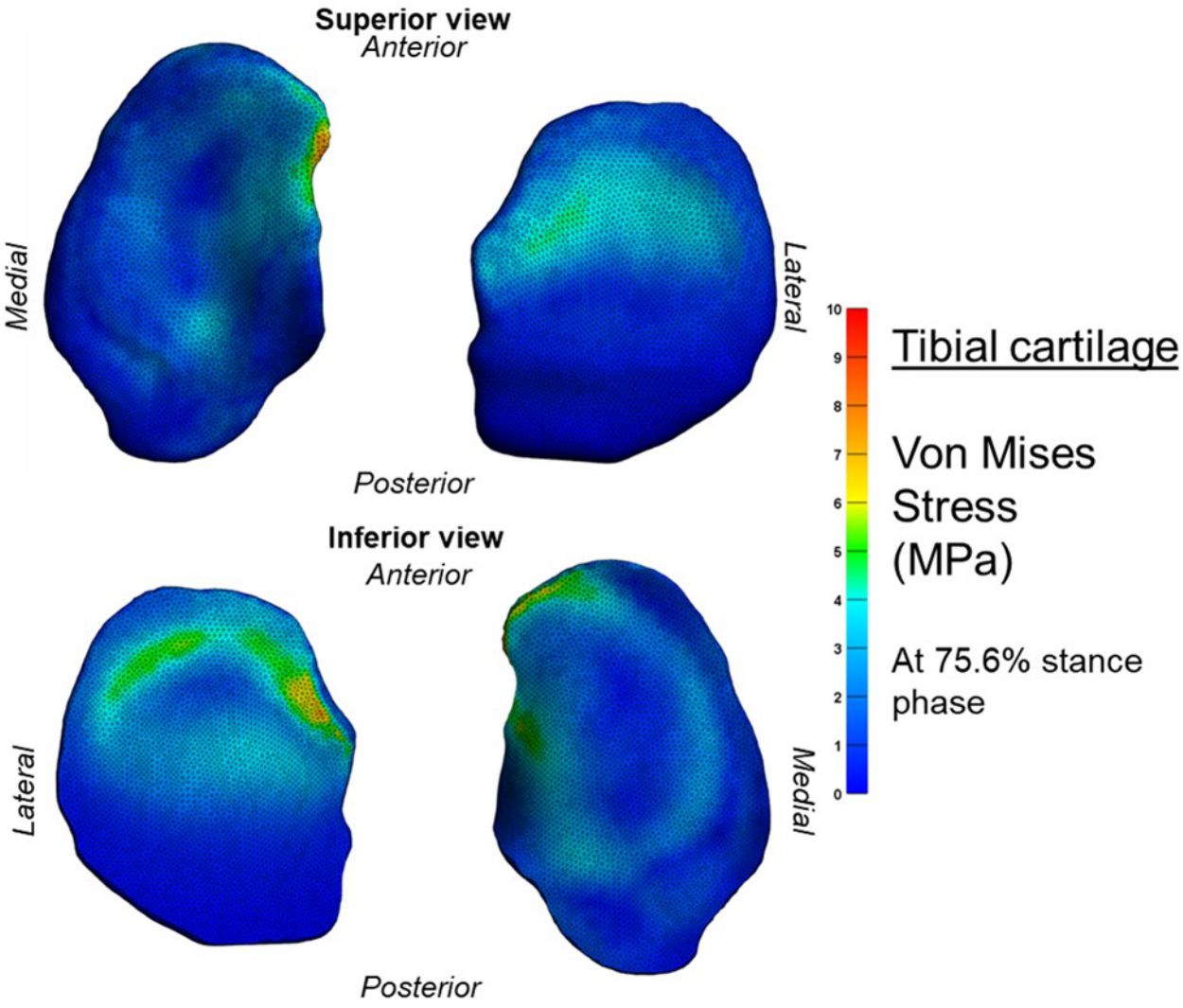

Figure 4-21 – Von Mises stress in the tibial cartilage at 75.6% stance.

4.3.3 STRAIN

Another metric of internal contact mechanics that can be extracted from an FEM simulation is strain. Increased strain within the articular cartilage has previously been shown to be linked with knee OA (Tarniţă et al. 2014; Arjmand et al. 2018; Bolcos et al. 2022; Lampen et al. 2023) and is, therefore, a key output from joint contact models used to quantify disease progression.

Maximum principal strain against percentage stance for the three cartilage structures is shown in Figure 4-22. It was chosen to analyse principal strain throughout stance as this was a commonly reported strain metric in FE models of the knee from literature (see Table 1-3, Section 1.7.1).

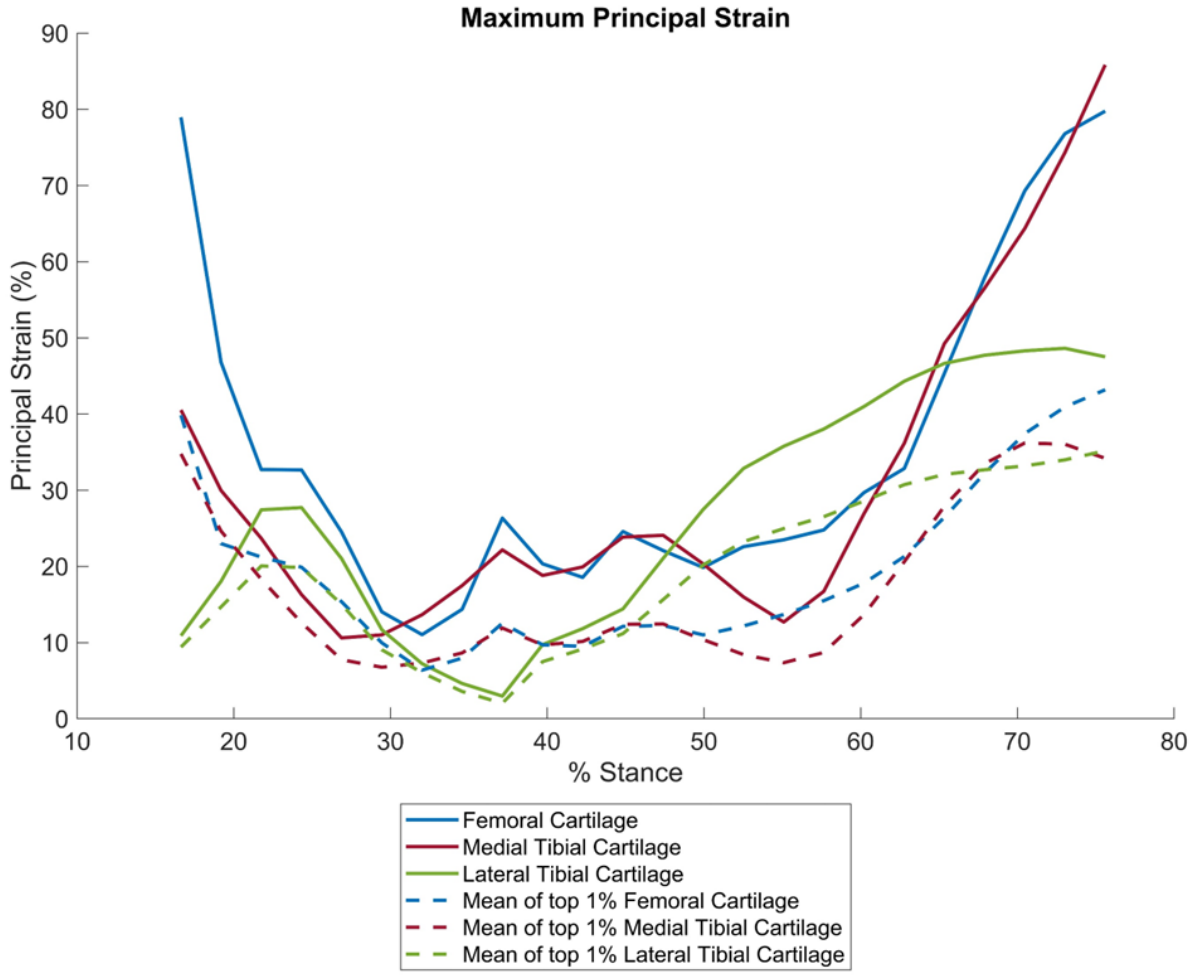

Figure 4-22 – Maximum principal strain against percentage stance. The mean principal strain of the top 1% of elements in each cartilage structure is also included to account for any outliers.

Like with von Mises stress (Figure 4-19), the highest maximum principal strains (Figure 4-22) were found at the beginning and end frames of the motion, with the

femoral cartilage and medial tibial cartilage displaying particularly large strains at the end. When the mean of the top 1% of elements was taken instead, the maximum values were much lower suggesting there were specific erroneous elements with artificially high strains at the start and end frames.

The maximum principal strains generally followed a very similar pattern to the maximum von Mises stresses in all three structures. This was expected as both stress and strain are related to element deformation.

The magnitudes of principal strain predicted by this model were much higher than those reported in literature (Table 4-13), where all maximum principal strains were reported as <30% (Adouni et al. 2012; Halonen et al. 2013; Mononen et al. 2015; Fu et al. 2022). This was also true of normal strain and shear strain magnitudes (Table 4-13). These extremely high strains highlight the need for caution when interpreting cartilage mechanics from kinematic-driven models, as FEM results can be highly sensitive to the input kinematics. Further investigation is required to better understand this sensitivity and how small variations in the kinematic inputs affect the predicted tissue strains.

Table 4-13 – Comparison of the strain results from this simulation compared with those reported in literature (Table 1-3, Section 1.7.1).

Strain metric	**Maximum value from this model**	**Maximum value reported in literature**
Principal strain	85.8%	<30%[1]
Axial strain	73%	<21%[2]
Shear strain	117%	<25%[3]

[1](Fu et al. 2022) [2](Yang et al. 2010) [3](Mohout et al. 2023)

4.4 LIMITATIONS, CHALLENGES AND RECOMMENDATIONS

4.4.1 MODEL LIMITATIONS

As this model was developed to explore the potential methodology for a fully kinematic-driven knee FEM, the material models and parameters were taken from the literature. Since material model choices can strongly influence results, the selected materials should be evaluated for their suitability and for the effect they may

have on the outputs. A sensitivity analysis of the parameter values should also be carried out before taking the model further to understand their impact on results.

Another limitation of this model is that mesh convergence was not investigated. However, as geometry has been shown to be key for knee contact simulations (even more influential than the material model chosen) (Yao et al. 2024), a fine mesh was already used to capture the geometry of the contacting surfaces with sufficient detail. Therefore, the number of elements used likely exceeded the point where further refinement would have little effect.

Although output magnitudes of the parameters of interest were compared to literature, there are limitations to this comparison. Different modelling choices – in the material models and parameters chosen – mean results are not directly comparable. Also, internal cartilage stresses and strains are unmeasurable in-vivo so all models are estimating these parameters, and their estimations will vary based on their choices and assumptions.

Another potential limitation of this model was the low contact penalties used for some of the defined contacts (given in Table 4-10 in Section 0). These were the highest values for each contact that still allowed the model to run to full termination. The contact penalties were particularly low on the lateral meniscus due to its overlap with the femoral and tibial cartilage near its anterior meniscal horn during the kinematics step. This overlap likely arose from the bone kinematics causing the anterior portion of the meniscal body to be compressed between the cartilage surfaces, creating an issue at the boundary between the meniscal body and horns. As the meniscal horns were represented by springs, they were unaffected by this overlap but also did not contribute to the contact mechanics needed to separate the articulating surfaces. Consequently, the deformation of the lateral meniscus was not accurately represented, as the overlapping geometry does not reflect the in-vivo condition where the tissues would deform under load. This limitation would affect the internal mechanical outputs (e.g. stress and strain) of both the meniscus and articular cartilage, as the meniscus would not correctly distribute load through the joint. The higher contact penalty used for cartilage-cartilage contact compared to meniscus-cartilage contacts likely influenced the results across all kinematic steps, particularly towards the end of motion when overlap was greatest and a higher

penalty would have been most beneficial. As this model focused primarily on articular cartilage behaviour, the lower meniscal contact penalties were not prohibitive for the current study, but they would need to be re-evaluated in any future work extending the analysis to meniscal mechanics.

Another future improvement to the model could be to include the PF joint in the FEM. The patella could also be prescribed using BVR-derived bone poses, extending the model's application to PF joint mechanics. As the position of the patella, and its subsequent interaction with the femoral cartilage, depends on TF kinematics, incorporating both joints would give the most comprehensive model of knee motion.

4.4.2 CHALLENGES OF THE KINEMATIC-DRIVEN FEM APPROACH

One of the main challenges of a subject-specific model using personalised geometric and kinematic inputs is the amount of time and expertise required to not only process the inputs, but also to set up the model. Due to its complexity, the pipeline is not easily scalable as every new participant or activity would require individual optimisation to allow the model to run successfully. However, highly complex, subject-specific models have the benefit of accurately capturing an individual's in-vivo joint mechanics, replicating a real-life scenario. As FEMs are sensitive to many factors, using generic model kinematics or geometries may not provide enough detail to understand in-vivo stresses and strains in the articular cartilage or other soft tissues.

Although this model has shown that a kinematically-driven FEM of the knee is possible, using this pipeline to develop models of different activities and participants would be needed to thoroughly test this methodology to confirm if this is a repeatable and useable technique for FEM.

Another challenge of kinematic-driven modelling specifically is the model's sensitivity to the kinematic inputs. This sensitivity likely caused the particularly high strains in the articular cartilage in this model, highlighting the need to investigate the sensitivity of model outputs to the input kinematic errors. Fregly et al. (2008) have shown that pose errors in input kinematics as small as 0.1 °/mm caused the maximum contact forces, pressures and area to vary by 100-200% during a gait cycle simulated using in-vivo single-plane fluoroscopy data from a knee with a TKR. They used an elastic foundation model to calculate these contact outputs (like the MSM in Chapter 3). To

understand if this sensitivity extends to the internal tissue stresses and strains in an FEM, it is recommended to perform a sensitivity analysis by altering the input kinematics by known amounts. This was not done for this model due to the time constraints, but if this model were to be utilised in the future, it should be explored to truly understand the limitations of this technique to correctly interpret the results.

The unrealistic, extreme values of stress and strain occurring at the start and end of the movement were potentially due to higher BVR kinematic errors at these frames. Image registration was likely less accurate at these frames as the bones were partially out of shot and the boundary kinematic frames cannot be placed within the trend of the other surrounding frames or filtered using the surrounding data points. This means these frames were likely less accurate, causing larger stresses and strains to occur due to the increased positional errors occurring at these frames.

4.4.3 RECOMMENDATIONS FOR KINEMATIC-DRIVEN MODELLING

One benefit of kinematic-driven modelling is the direct input of measurable data which can be used to explore the changes in the distribution of contact mechanical parameters during dynamic motion. Therefore, it is important to investigate the distributions of pressures, stresses and strains throughout the tissue, focussing more on this than the overall magnitudes.

Kinematic-driven FEMs may be useful for understanding the changes in the distributions of stresses and strains in the articular cartilage under different loading conditions or due to different pathologies. For example, they can help identify which regions of cartilage experience the highest strains, which may indicate an increased risk of wear and OA development (Griebel et al. 2013; Widmyer et al. 2013; Sutter et al. 2015). They can also be used to explore how altered loading patterns affect strain distributions and potentially influence OA progression. By relying less on the absolute magnitudes of the FEM outputs and instead comparing general patterns and trends, kinematic-driven modelling could be a useful tool for investigating articular cartilage loading.

A more suitable option may be using the accurate input BVR kinematics to drive an MSM to generate force inputs for a force-driven FEM. Hybrid MSM-FEM approaches have been developed to calculate knee contact mechanics (Besier et al. 2005; Shu et al. 2018; Navacchia et al. 2019; Ali et al. 2020; Kainz et al. 2020; Esrafilian et al.

2022; Mohout et al. 2023), but these still rely on standard marker-based motion capture inputs to drive the model. Using a similar hybrid approach, but with the higher accuracy BVR kinematics instead, some of the issues with a directly kinematic driven FEM may be overcome. For example, the contact penalty values may be able to be increased and therefore produce a more realistic contact response in the deformation of the tissues as the MSM would account for potential errors in the input kinematics through the optimisation process.

4.5 CONCLUSION

To achieve the aims set out in Section 4.1.1 and analyse articular cartilage contact mechanics in the healthy knee during the stance phase of gait, a subject-specific model was developed using personalised MRI geometries (including the bones, articular cartilage, meniscus and key ligaments) and BVR-derived bone poses to prescribe all 6 DOFs.

The cartilage pressure distributions during the prescribed stance phase of gait covered a similar area to the BVR-EFM results (as expected due to using the same kinematic inputs), however the pressure magnitudes from the FEM were found to be higher (Figure 4-14). The maximum pressure from the FEM (28.9 MPa) were also much higher than the personalised and generic MSM results, as well as the range of 8-17 MPa presented in literature (Adouni et al. 2012; Halonen et al. 2013; Mononen et al. 2015; Daszkiewicz and Luczkiewicz 2021; Fu et al. 2022). However, the highest pressures were consistently found on the medial plateau across all methods.

Stresses were successfully obtained from the model, with magnitudes comparable to literature (Table 4-11). Higher stresses were found at the start and end of the collected stance phase, corresponding with the two peaks of loading at approximately 23% and 75% of stance phase of level gait (Figure 4-19).

The strains output from the FEM (Table 4-13) were much higher than literature. This was likely due to the model's sensitivity to small kinematic errors and would require analysis before future usage of the model and pipeline.

Kinematic-driven modelling shows potential as a method for understanding TF joint contact mechanics, including the distribution of the stresses and strains throughout the 3D structures of the knee, such as the articular cartilage. This could be used to

identify regions of higher stress and strain which, if compared to OA knees, could inform on the progression of the disease and potential interventions.

By implementing a fully kinematically-driven FEM of the knee using BVR-derived 6 DOF kinematics, this chapter completes the aims for the framework set out in Section 1.8. The kinematically-driven FEM enabled detailed assessment of cartilage contact pressures, stresses, and strains during gait, providing insight into internal tissue mechanics not accessible through other methods in the framework. In this way, the FEM complements the BVR and MSM components by linking measured kinematics and joint-level loads to tissue-level mechanics. It completes the framework by demonstrating the feasibility of creating highly personalised models driven by in-vivo data, offering a new approach for evaluating knee joint mechanics that can be extended to answer clinically relevant research questions.

CHAPTER 5: DISCUSSION, CONCLUSION AND FUTURE WORK

5.1 DISCUSSION OF THE FRAMEWORK TO INVESTIGATE TIBIOFEMORAL JOINT CONTACT MECHANICS

This overall aim of this thesis, as set out in Chapter 1 (Section 1.8), was to develop a comprehensive framework to investigate tibiofemoral (TF) joint contact mechanics that integrates accurate in-vivo biplane videoradiography (BVR) kinematics into musculoskeletal models (MSM) and finite element models (FEM).

The need for such a framework was identified to provide a detailed understanding of how the knee behaves under loading during functional dynamic activities, with the future goal of informing new studies of disease progression or intervention outcomes. Understanding knee biomechanics in this context is important, as conditions such as osteoarthritis (OA) have been linked to altered joint kinematics and loading (Mills et al. 2013; Farrokhi et al. 2014; Yamagata et al. 2021), leading to pain, instability, and reduced mobility (Hunter and Bierma-Zeinstra 2019). By integrating high-fidelity imaging with personalised modelling, this work aimed to capture not only knee joint kinematics, but also contact pressures, whole-body forces, and internal cartilage mechanics. By doing so it also demonstrates that combining methodologies can provide a more comprehensive understanding of knee biomechanics than any individual method could offer.

To achieve this aim, an integrated pipeline was developed that combines high-fidelity imaging with personalised modelling techniques. The framework consists of three key components, each addressing the specific aims outlined in Section 1.8, and contributing uniquely to the overall framework.

Chapter 2 established a robust data collection and processing pipeline, acquiring MRI and BVR data to calculate accurate 6 degree of freedom (DOF) TF kinematics for comparison and validation with simultaneously collected marker-based motion capture. Implemented for the first time in a cohort of healthy participants, the feasibility of this workflow for future studies was demonstrated and it produced high-quality data to feed into the subsequent modelling stages. The BVR-

derived kinematics form the foundation of the framework, driving the FEM and providing a reference for evaluating MSM predictions.

Chapter 3 implemented the MSM pipeline using the marker-based motion capture and MRI data collected in Chapter 2. Subject-specific contact geometries from the MRI scans were incorporated to assess the benefits of personalised modelling. Outputs from both generic and personalised models were evaluated against BVR-derived kinematics and contact maps. This was the first such comparison for the OpenSim-JAM pipeline and demonstrated the potential advantages of personalised modelling. MSM complements the BVR and FEM components by providing whole-body kinetic and kinematic data, while its contact pressure maps offer a valuable reference for cross-method comparison, supporting the overarching aims of Section 1.8 to develop a robust, integrated framework for assessing knee biomechanics.

Chapter 4 implemented a fully kinematically driven FEM of the knee using the BVR-derived 6 DOF kinematics from Chapter 2. The FEM calculated internal stresses and strains within the tibial cartilage, providing insight into tissue mechanics that cannot be obtained from MSM or BVR alone, linking measured kinematics and joint-level loads to tissue-level mechanics. This completes the integrated framework and demonstrates the feasibility of highly personalised, data-driven models for evaluating knee joint mechanics.

To ensure consistency across the three framework components, the same MRI-derived personalised geometries and BVR-derived kinematics were used as the foundation. This allowed the framework to capture subject-specific variations in both kinematics and tissue mechanics. By combining these techniques into a single integrated pipeline, the framework **enables cross-validation and comparison across methods**. The integration of these techniques means that each part informs and validates the others, creating a cohesive framework for studying in-vivo knee biomechanics (Figure 5-1).

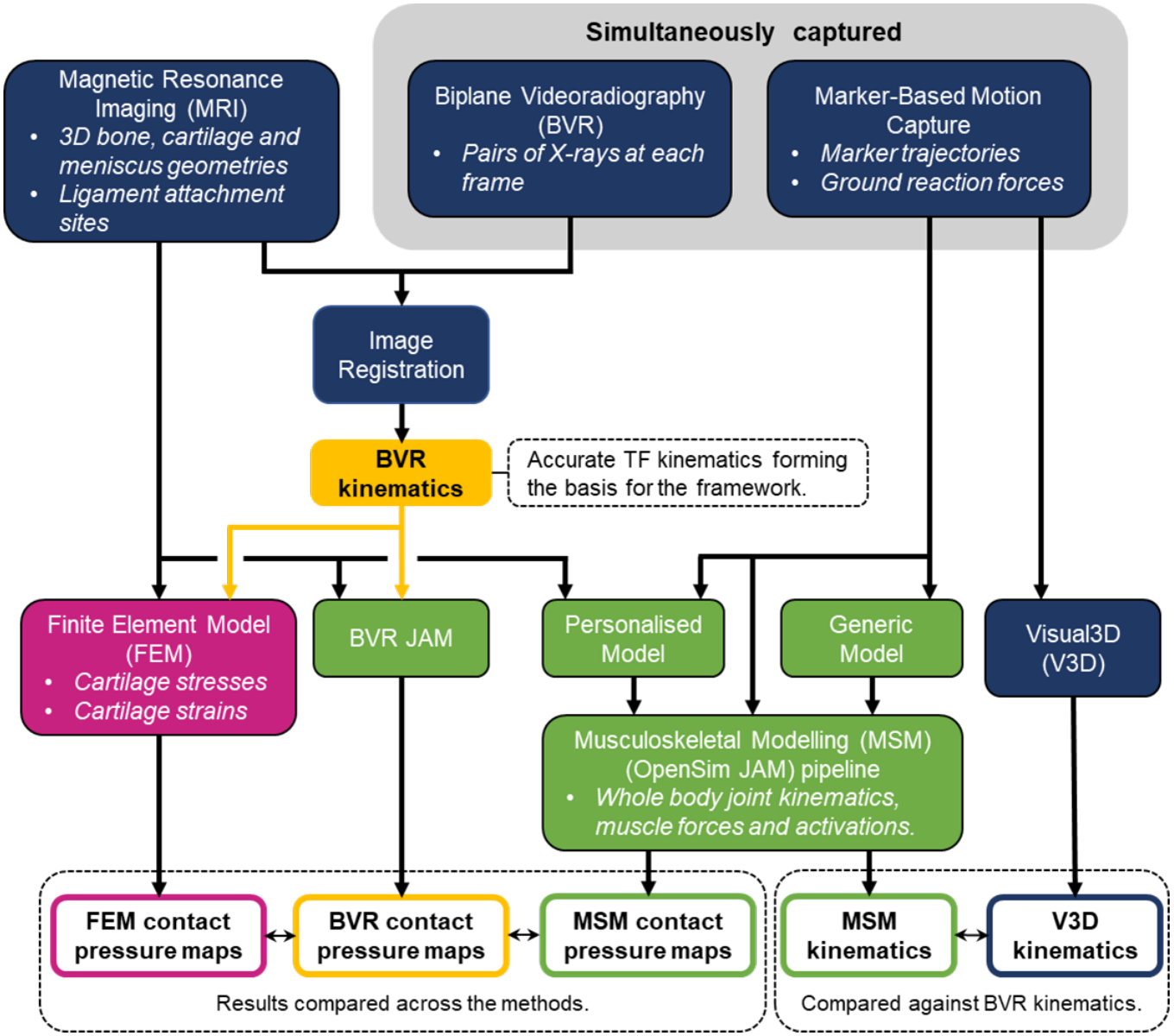

Figure 5-1 – Diagram showing the relationships between different aspects of the framework. Boxes in blue relate to work from Chapter 2, green relates to Chapter 3 and pink relates to Chapter 4.

The framework also **reveals key challenges in high-fidelity knee modelling**. Each component is technically complex, requiring extensive expertise, computational resources, and careful data processing. As collecting and analysing BVR data, segmenting MRI geometries, and running personalised MSM and FEM simulations is time consuming, scaling the pipeline would be challenging. However, detailed and highly personalised approaches can be used to assess which aspects of the model most influence the outputs. By demonstrating the sensitivity of MSM and FEM results to kinematic accuracy and geometric personalisation, this work provides practical insights for researchers who may not have access to BVR or who are using more

simplified models. In this way, the pipeline functions both as a tool for generating new biomechanical insights and as a benchmark for refining larger-scale or less detailed modelling approaches.

This framework provides both **methodological and practical contributions**, demonstrating the potential of high-fidelity, subject-specific modelling and setting a foundation for future knee biomechanics studies. Each component delivers distinct yet complementary outputs: BVR provides accurate kinematics, MSM estimates joint contact pressures and whole-body forces, and FEM quantifies internal cartilage stresses and strains. By integrating these techniques and capitalising on the strengths of each, the framework achieves the overarching aims of Section 1.8, providing a comprehensive understanding of knee biomechanics during dynamic functional activities. This approach demonstrates the value of personalised data, while guiding researchers without access to high fidelity imaging, such as BVR, highlighting the benefits and limitations of different methods. While highly personalised models and precise kinematic data are not always feasible, they can inform broader modelling strategies, emphasising the importance of developing detailed, robust pipelines. Whether applied individually or as a fully integrated system, the framework can be extended to include pathological knees, supporting clinically relevant investigations and enhancing understanding of the relationships between knee biomechanics, pain, and pathology to improve diagnosis and treatment of conditions such as OA.

As with all research, this study also had inherent limitations. Some of the main limitations are:

- A small pilot dataset.
- Patellofemoral (PF) kinematics were ignored.
- The framework was only applied to a healthy population.
- BVR imaging challenges with the current activity setups, including limited numbers of frames captured and contralateral limb occlusion, for example, during level gait.
- The BVR kinematics were not input directly into the MSM pipeline, so it was only driven by lower fidelity marker-based motion capture inputs.

- The MSM poorly predicted TF kinematics during activities involving higher flexion angles.
- No sensitivity analysis was performed on the FEM for its mesh convergence or material models and parameters.
- The sensitivity of the FEM to the kinematic inputs was not investigated.
- The contact penalties between some of the contacting surfaces in the FEM were low, for example, between the lateral meniscus and articular cartilage.

The impact of these, and the other identified limitations of each part of the framework, are discussed in more detail in Sections 2.5.8, 3.4.5, and 4.4.1. Recognising these limitations is important for contextualising the findings and identifying priorities for future research, informing the proposed areas for further development as discussed in Section 5.3.

5.2 CONCLUSION

A framework to investigate TF joint biomechanics during functional movement was developed by combining in-vivo BVR imaging with MSM and FEM, achieving the primary aims set out in Chapter 1 (Section 1.8). A robust workflow was established, linking accurate experimental data with personalised computational models to quantify and predict knee joint behaviour.

BVR data were successfully collected and processed using the newly developed acquisition and registration pipeline, providing accurate 6 DOF TF kinematics during multiple dynamic activities. The measured kinematics were consistent with prior studies, supporting the reliability of the BVR system for determining in-vivo knee motion. Compared to the BVR results, simultaneous marker-based motion capture rotations showed greater variability and an overestimated range of motion, highlighting the impact of soft tissue artefact, as well as a consistent flexion median offset of 13-14° caused by marker placement errors.

Personalising TF contact geometries within the MSM pipeline improved the prediction of knee kinematics compared to the generic model, particularly for anterior translation where the absolute median difference between MSM and BVR results was reduced by more than 7 mm. This improvement led to more accurate medial contact area predictions when benchmarked against BVR-derived contact maps. The

FEM, driven directly by BVR-derived kinematics, produced stress magnitudes comparable with literature (though strains were higher). When comparing cartilage contact pressures across methods, the FEM predicted higher peak pressures than both MSM and BVR elastic foundation models, by approximately 10 MPa and 20 MPa respectively, demonstrating how different modelling approaches offer complementary insights into joint loading mechanics.

By integrating these methods, the framework links kinematics, loading, and tissue-level responses, providing a comprehensive and highly personalised view of knee biomechanics under functional joint loading. As well as demonstrating the feasibility and value of combining in-vivo imaging with computational modelling, it highlights the strengths and limitations of each approach, providing guidance for researchers without access to BVR data. The framework's methodological advances, whether applied individually or as an integrated system, lay the foundation for personalised investigation, diagnosis, monitoring, and treatment of knee pathologies.

5.3 FUTURE WORK

As this thesis focused on methodological advancements using a small pilot cohort of five healthy participants, future work should expand these techniques to larger and more diverse cohorts, including pathological knees, to address clinically relevant questions.

The framework developed here focussed solely on the TF joint. Future work should incorporate the PF joint, as the patella is an integral part of the knee complex and important for achieving a more complete understanding of knee biomechanics.

5.3.1 DATA COLLECTION PROTOCOL IMPROVEMENTS, VALIDATION AND ITS APPLICATION TO PATIENT COHORTS

To apply the data collection protocol set out in Chapter 2 to future cohorts, it is important to consider the functional activities being imaged and the corresponding BVR X-ray configurations carefully. For level gait, only a limited number of frames could be collected due to frequent occlusion by the contralateral leg. To overcome this, a treadmill is recommended for capturing walking. Although treadmill use has been shown to alter gait patterns (Hollman et al. 2016), it enables configurations with reduced occlusion and allows a larger portion of the activity to be captured, which is

why treadmills are frequently used in BVR studies of knee kinematics (Kozanek et al. 2009; Liu et al. 2010; Barre et al. 2013; Guan et al. 2016; Guan et al. 2017; Yang et al. 2018; Gale and Anderst 2019; Koo and Koo 2019; Nagai et al. 2019; Gale and Anderst 2020; Byrapogu et al. 2022). Therefore, treadmill use is recommended to improve data quality and reduce some of the limitations associated with level gait.

As people with OA often report difficulties performing mobility-related tasks (Davis et al. 1991; Clynes et al. 2019), other activities to be considered for the pipeline include downhill walking (also on a treadmill), stair decent or step down, and sit-to-stand. Stair descent, in particular, has often been reported as the most painful activity (Gur et al. 2002; Takasaki et al. 2013; Wan et al. 2024) and is therefore important to include when investigating the effects and treatments of OA. When implementing these new activities, X-ray source–detector pairs should be positioned to minimise occlusion, ensuring at least one image without occlusion where possible. This will enhance the quality and accuracy of image registration, resulting in more reliable kinematic outputs.

To fully understand the accuracy and limitations of any BVR-derived kinematics, it is important to assess the accuracy of each specific X-ray system in each separate experimental setup used. Future work should therefore validate the system using implanted radio-opaque beads, either in-vivo or in cadaveric specimens, to quantify the accuracy of the pipeline (Section 1.4.1). This will provide a clearer and more robust understanding of its reliability.

The pipelines developed in this thesis for the collection and processing of the simultaneous BVR and marker-based motion capture data are now being adapted and used as part of an EPSRC-funded project: *‘Multi-platform pipeline for engineering human knee joint function’*. This project is in collaboration with researchers at Imperial College London and KU Leuven to link in-vivo, in-vitro and in-silico methods (including MSM) to investigate knee joint function pre- and post-total knee replacement (TKR), with a focus on knee instability after surgery. This highlights both the direction of the work presented in this thesis and the value of the developed pipelines for application to patient cohorts in addressing clinically relevant questions.

5.3.2 MUSCULOSKELETAL MODELLING PIPELINE INVESTIGATIONS

As the pipeline presented in this thesis was only an exploration using pilot data, there is scope to expand on the modelling work in the future. As discussed in Chapter 3 (Section 3.4.5), an important next step is to investigate how MSM outputs are influenced by the input kinematics. One approach would be to drive the model using BVR kinematics within the MSM pipeline. For example, inputting the BVR-measured flexion angle could help account for errors arising from femoral condyle marker misplacement, which directly affects the model-derived secondary kinematics (as these are calculated as functions of flexion). This would provide insight into how incorrect flexion angles propagate through the pipeline and impact model outputs – an important consideration when using marker-based motion capture inputs.

This could be extended further by prescribing the TF DOFs using kinematics from BVR to investigate the effect of more accurate input kinematics on contact map outputs. While the secondary kinematics would still need to settle during the COMAK step to ensure model convergence, using accurate BVR-derived inputs rather than IK results would enable solutions to be based on more realistic starting conditions. This would be particularly valuable in cases where secondary kinematics are not strongly coupled to flexion.

Inputting BVR kinematics in this way could also clarify whether accurate kinematics or personalised geometries have the greater impact on model performance. This would help identify the key limitations of the pipeline and highlight the most important considerations when only motion capture data are available. Furthermore, testing the model with accurate BVR kinematics could guide future improvements to the pipeline, supporting the generation of more accurate secondary kinematics from motion capture inputs alone. This may also include extending the model's capabilities to higher flexion angles, since this thesis demonstrated that kinematic predictions worsen during high-flexion activities. Updating the model based on the relationship between flexion and secondary kinematics derived from BVR in-vivo imaging of high-flexion activities would help the model to perform more robustly across a broader range of movements.

5.3.3 KINEMATICS-DRIVEN FINITE ELEMENT MODEL ALTERATIONS AND IMPROVEMENTS

For the FEM, as the model was primarily used to explore the feasibility of kinematic-driven modelling, further robust testing and analysis would be required before applying it to future research questions. For example, a mesh convergence study should be performed to confirm that the final model contains a sufficient number of elements, and the choice of material models and their associated parameters should be evaluated to ensure they are appropriate for the intended application.

The high contact pressures and strains observed in the model highlight the importance of understanding its sensitivity to input kinematics. Future work could explore this by systematically varying all 6 DOFs and analysing the response of each individually. Such analyses would not only clarify how kinematic errors propagate through the model but also provide guidance on optimising kinematic-driven approaches. This could inform refinement of the technique to improve robustness and reliability, bringing kinematic-driven FEM closer to practical application.

An alternative approach to the FEM step of the framework would be to drive the model using forces from the MSM pipeline. Hybrid MS-FEM approaches have been used previously (Besier et al. 2005; Shu et al. 2018; Navacchia et al. 2019; Ali et al. 2020; Kainz et al. 2020; Esrafilian et al. 2022; Mohout et al. 2023), but they still rely on marker-based motion capture inputs, increasing the number of estimated parameters. By instead inputting accurate in-vivo TF kinematics from BVR into the MSM and using those outputs to drive the FEM, the strengths of both methods could be combined. The MSM would account for small kinematic errors, while the FEM would calculate internal cartilage mechanics with reduced sensitivity to these errors. This approach would provide both whole-body kinematics and muscle forces from MSM and detailed internal cartilage mechanics from FEM, offering a cohesive, comprehensive framework for investigating multiple aspects of joint loading.

5.3.4 FUTURE OF THE FRAMEWORK

Overall, the framework developed in this thesis provides a foundation for investigating multiple aspects of knee biomechanics that can be further expanded and refined to achieve greater cohesion and integration of the various methods. By

further exploring the combined potential of the unique contributions from the BVR, MSM, and FEM components, future work could focus on creating a more seamless pipeline. For example, BVR-derived kinematics could be fed through MSM to drive FEM in a hybrid approach, enabling both whole-body and tissue-level outputs from the same data.

Expanding the framework to larger and more diverse cohorts, including pathological knees, would further enhance its value. By applying the integrated framework to clinical populations, researchers could systematically investigate how changes in joint mechanics relate to pain, disease progression, or surgical outcomes. In this way, the framework has the potential to become a versatile, translational tool, combining high-fidelity, in-vivo imaging with computational modelling to address clinically relevant questions about knee joint function and pathology.

REFERENCES

Abdel, M. P., Oussedik, S., Parratte, S., Lustig, S. and Haddad, F. S. 2014. Coronal alignment in total knee replacement. *The Bone & Joint Journal* 96-B(7), pp. 857-862.doi: 10.1302/0301-620x.96b7.33946

Adler, R. J. 2010. *The geometry of random fields*. Society for Industrial and Applied Mathematics.

Adouni, M. and Shirazi-Adl, A. 2014. Evaluation of knee joint muscle forces and tissue stresses-strains during gait in severe OA versus normal subjects. *Journal of Orthopaedic Research* 32(1), pp. 69-78.doi: https://doi.org/10.1002/jor.22472

Adouni, M., Shirazi-Adl, A. and Shirazi, R. 2012. Computational biodynamics of human knee joint in gait: from muscle forces to cartilage stresses. *J Biomech* 45(12), pp. 2149-2156.doi: 10.1016/j.jbiomech.2012.05.040

Akbarshahi, M., Schache, A. G., Fernandez, J. W., Baker, R., Banks, S. and Pandy, M. G. 2010. Non-invasive assessment of soft-tissue artifact and its effect on knee joint kinematics during functional activity. *J Biomech* 43(7), pp. 1292-1301.doi: 10.1016/j.jbiomech.2010.01.002

Akhbari, B., Morton, A. M., Moore, D. C., Weiss, A. C., Wolfe, S. W. and Crisco, J. J. 2019. Accuracy of biplane videoradiography for quantifying dynamic wrist kinematics. *J Biomech* 92, pp. 120-125.doi: 10.1016/j.jbiomech.2019.05.040

Ali, A. A., Harris, M. D., Shalhoub, S., Maletsky, L. P., Rullkoetter, P. J. and Shelburne, K. B. 2017. Combined measurement and modeling of specimen-specific knee mechanics for healthy and ACL-deficient conditions. *J Biomech* 57, pp. 117-124.doi: 10.1016/j.jbiomech.2017.04.008

Ali, A. A., Mannen, E. M., Rullkoetter, P. J. and Shelburne, K. B. 2020. Validated Computational Framework for Evaluation of In Vivo Knee Mechanics. *J Biomech Eng* 142(8).doi: 10.1115/1.4045906

Allen, K. D., Cruz-Almeida, Y. and Almarza, A. J. 2025. The osteoarthritis pain enigma and how biomechanics research can lead to new solutions. *Connect Tissue Res* 66(5), pp. 367-372.doi: 10.1080/03008207.2025.2512938

Altman, D. G. and Bland, J. M. 1983. Measurement in Medicine: the Analysis of Method Comparison Studies. *Journal of the Royal Statistical Society* 32, pp. 307-317.

Amiri, S. and Wilson, D. R. 2012. A computational modeling approach for investigating soft tissue balancing in bicruciate retaining knee arthroplasty. *Computational and mathematical methods in medicine* 2012(1), p. 652865.
Andersen, M. S. 2021. Introduction to musculoskeletal modelling. In: *Computational Modelling of Biomechanics and Biotribology in the Musculoskeletal System*. pp. 41-80. doi: 10.1016/b978-0-12-819531-4.00004-3
Anderson, A. E., Ellis, B. J., Maas, S. A., Peters, C. L. and Weiss, J. A. 2008a. Validation of finite element predictions of cartilage contact pressure in the human hip joint. *J Biomech Eng* 130(5), p. 051008.doi: 10.1115/1.2953472
Anderson, A. E., Ellis, B. J., Maas, S. A., Peters, C. L. and Weiss, J. A. 2008b. Validation of finite element predictions of cartilage contact pressure in the human hip joint.
Anderst, W., Zauel, R., Bishop, J., Demps, E. and Tashman, S. 2009. Validation of three-dimensional model-based tibio-femoral tracking during running. *Med Eng Phys* 31(1), pp. 10-16.doi: 10.1016/j.medengphy.2008.03.003
Anderst, W. J., Baillargeon, E., Donaldson, W. F., 3rd, Lee, J. Y. and Kang, J. D. 2011. Validation of a noninvasive technique to precisely measure in vivo three-dimensional cervical spine movement. *Spine (Phila Pa 1976)* 36(6), pp. E393-400.doi: 10.1097/BRS.0b013e31820b7e2f
Anderst, W. J. and Tashman, S. 2010. Using relative velocity vectors to reveal axial rotation about the medial and lateral compartment of the knee. *J Biomech* 43(5), pp. 994-997.doi: 10.1016/j.jbiomech.2009.11.014
Andriacchi, T. P., Koo, S. and Scanlan, S. F. 2009. Gait Mechanics Influence Healthy Cartilage Morphology and Osteoarthritis of the Knee. *JBJS* 91(Supplement_1), pp. 95-101.doi: 10.2106/jbjs.H.01408
Andriacchi, T. P. and Mündermann, A. 2006. The role of ambulatory mechanics in the initiation and progression of knee osteoarthritis. *Current Opinion in Rheumatology* 18(5), pp. 514-518.doi: 10.1097/01.bor.0000240365.16842.4e
Arden, N. and Nevitt, M. C. 2006. Osteoarthritis: epidemiology. *Best Pract Res Clin Rheumatol* 20(1), pp. 3-25.doi: 10.1016/j.berh.2005.09.007
Arjmand, H., Nazemi, M., Kontulainen, S. A., McLennan, C. E., Hunter, D. J., Wilson, D. R. and Johnston, J. D. 2018. Mechanical Metrics of the Proximal Tibia are Precise and Differentiate Osteoarthritic and Normal Knees: A Finite Element Study. *Sci Rep* 8(1), p. 11478.doi: 10.1038/s41598-018-29880-y

Arnold, E. M., Ward, S. R., Lieber, R. L. and Delp, S. L. 2010. A model of the lower limb for analysis of human movement. *Ann Biomed Eng* 38(2), pp. 269-279.doi: 10.1007/s10439-009-9852-5

Astephen, J. L., Deluzio, K. J., Caldwell, G. E. and Dunbar, M. J. 2008. Biomechanical changes at the hip, knee, and ankle joints during gait are associated with knee osteoarthritis severity. *J Orthop Res* 26(3), pp. 332-341.doi: 10.1002/jor.20496

Athanasiou, K. and Sanchez-Adams, J. 2009. *Engineering the knee meniscus*. Morgan & Claypool Publishers.

Bachus, K. N., DeMarco, A. L., Judd, K. T., Horwitz, D. S. and Brodke, D. S. 2006. Measuring contact area, force, and pressure for bioengineering applications: using Fuji Film and TekScan systems. *Med Eng Phys* 28(5), pp. 483-488.doi: 10.1016/j.medengphy.2005.07.022

Bakke, D. and Besier, T. 2020. Shape model constrained scaling improves repeatability of gait data. *J Biomech* 107, p. 109838.doi: 10.1016/j.jbiomech.2020.109838

Baldwin, M. A., Clary, C., Maletsky, L. P. and Rullkoetter, P. J. 2009. Verification of predicted specimen-specific natural and implanted patellofemoral kinematics during simulated deep knee bend. *Journal of biomechanics* 42(14), pp. 2341-2348.doi: https://doi.org/10.1016/j.jbiomech.2009.06.028

Baliunas, A. J., Hurwitz, D. E., Ryals, A. B., Karrar, A., Case, J. P., Block, J. A. and Andriacchi, T. P. 2002. Increased knee joint loads during walking are present in subjects with knee osteoarthritis. *Osteoarthritis and Cartilage* 10(7), pp. 573-579.doi: https://doi.org/10.1053/joca.2002.0797

Barnett, C. H. 1953. Locking at the knee joint. *J Anatomy* 87, pp. 91-95.

Barre, A., Thiran, J. P., Jolles, B. M., Theumann, N. and Aminian, K. 2013. Soft tissue artifact assessment during treadmill walking in subjects with total knee arthroplasty. *IEEE Trans Biomed Eng* 60(11), pp. 3131-3140.doi: 10.1109/TBME.2013.2268938

Bei, Y. and Fregly, B. J. 2004. Multibody dynamic simulation of knee contact mechanics. *Medical Engineering & Physics* 26(9), pp. 777-789.doi: 10.1016/j.medengphy.2004.07.004

Beidokhti, H. N., Janssen, D., Khoshgoftar, M., Sprengers, A., Perdahcioglu, E. S., Van den Boogaard, T. and Verdonschot, N. 2016. A comparison between dynamic

implicit and explicit finite element simulations of the native knee joint. *Medical Engineering & Physics* 38(10), pp. 1123-1130.
Beillas, P., Papaioannou, G., Tashman, S. and Yang, K. H. 2004. A new method to investigate in vivo knee behavior using a finite element model of the lower limb. *J Biomech* 37(7), pp. 1019-1030.doi: 10.1016/j.jbiomech.2003.11.022
Bellamy, N., Buchanan, W. W., Goldsmith, C. H., Campbell, J. and Stitt, L. W. 1988. Validation study of WOMAC: a health status instrument for measuring clinically important patient relevant outcomes to antirheumatic drug therapy in patients with osteoarthritis of the hip or knee. *J Rheumatol* 15(12), pp. 1833-1840.
Bendjaballah, M. Z., Shirazi-Adl, A. and Zukor, D. 1995. Biomechanics of the human knee joint in compression: reconstruction, mesh generation and finite element analysis. *The Knee* 2(2), pp. 69-79.
Benoit, D. L., Ramsey, D. K., Lamontagne, M., Xu, L., Wretenberg, P. and Renstrom, P. 2006. Effect of skin movement artifact on knee kinematics during gait and cutting motions measured in vivo. *Gait Posture* 24(2), pp. 152-164.doi: 10.1016/j.gaitpost.2005.04.012
Benos, L., Stanev, D., Spyrou, L., Moustakas, K. and Tsaopoulos, D. E. 2020. A Review on Finite Element Modeling and Simulation of the Anterior Cruciate Ligament Reconstruction. *Front Bioeng Biotechnol* 8, p. 967.doi: 10.3389/fbioe.2020.00967
Bensalma, F., Hagemeister, N., Cagnin, A., Ouakrim, Y., Bureau, N. J., Choinière, M. and Mezghani, N. 2022. Biomechanical markers associations with pain, symptoms, and disability compared to radiographic severity in knee osteoarthritis patients: a secondary analysis from a cluster randomized controlled trial. *BMC Musculoskeletal Disorders* 23(1).doi: 10.1186/s12891-022-05845-1
Besier, T., Schneider, M., Rooks, N. and Kazemi, M. 2018. Model Specifications ABI - Open Knee Data. Auckland, New Zealand: Auckland Bioengineering Insititute.
Besier, T. F., Gold, G. E., Beaupre, G. S. and Delp, S. L. 2005. A modeling framework to estimate patellofemoral joint cartilage stress in vivo. *Med Sci Sports Exerc* 37(11), pp. 1924-1930.doi: 10.1249/01.mss.0000176686.18683.64
Besier, T. F., Gold, G. E., Delp, S. L., Fredericson, M. and Beaupré, G. S. 2008. The influence of femoral internal and external rotation on cartilage stresses within the patellofemoral joint. *Journal of Orthopaedic Research* 26(12), pp. 1627-1635.doi: https://doi.org/10.1002/jor.20663

Bey, M. J., Zauel, R., Brock, S. K. and Tashman, S. 2006. Validation of a new model-based tracking technique for measuring three-dimensional, in vivo glenohumeral joint kinematics. *J Biomech Eng* 128(4), pp. 604-609.doi: 10.1115/1.2206199

Bingham, J. T. et al. 2008. In vivo cartilage contact deformation in the healthy human tibiofemoral joint. *Rheumatology (Oxford)* 47(11), pp. 1622-1627.doi: 10.1093/rheumatology/ken345

Blankevoort, L. and Huiskes, R. 1991. Ligament-bone interaction in a three-dimensional model of the knee. *J Biomech Eng* 113(3), pp. 263-269.doi: 10.1115/1.2894883

Blankevoort, L., Kuiper, J. H., Huiskes, R. and Grootenboer, H. J. 1991. Articular Contact in a Three-Dimensional Model of the Knee. *J Biomech* 24(11), pp. 1019-1031.

Bloemker, K. H., Guess, T. M., Maletsky, L. and Dodd, K. 2012. Computational knee ligament modeling using experimentally determined zero-load lengths. *The open biomedical engineering journal* 6, p. 33.

Bolcos, P. O. et al. 2018. Comparison between kinetic and kinetic-kinematic driven knee joint finite element models. *Sci Rep* 8(1), p. 17351.doi: 10.1038/s41598-018-35628-5

Bolcos, P. O. et al. 2022. Subject-specific biomechanical analysis to estimate locations susceptible to osteoarthritis-Finite element modeling and MRI follow-up of ACL reconstructed patients. *J Orthop Res* 40(8), pp. 1744-1755.doi: 10.1002/jor.25218

Bolcos, P. O. et al. 2020. Identification of locations susceptible to osteoarthritis in patients with anterior cruciate ligament reconstruction: Combining knee joint computational modelling with follow-up T(1rho) and T(2) imaging. *Clin Biomech (Bristol)* 79, p. 104844.doi: 10.1016/j.clinbiomech.2019.08.004

Bowd, J. 2022. *Does gait retraining have the potential to slow OA development and prolong the benefits of knee realignment surgery?* Cardiff.

Bowd, J. et al. 2023. Using musculoskeletal modelling to estimate knee joint loading pre and post high tibial osteotomy. *Clin Biomech (Bristol, Avon)* 101, p. 105855.doi: 10.1016/j.clinbiomech.2022.105855

Bragdon, C. R. et al. 2006. Comparison of Femoral Head Penetration Using RSA and the Martell Method. *Clinical Orthopaedics and Related Research*® 448, pp. 52-57.doi: 10.1097/01.blo.0000224018.88410.83
Brandon, S. C. E., Thelen, D. G., Smith, C. R., Novacheck, T. F., Schwartz, M. H. and Lenhart, R. L. 2017. The coupled effects of crouch gait and patella alta on tibiofemoral and patellofemoral cartilage loading in children. *Gait Posture* 60, pp. 181-187.doi: 10.1016/j.gaitpost.2017.12.005
Burton, W. S., Myers, C. A., Clary, C. C. and Rullkoetter, P. J. 2024. Reliable 2D-3D Registration in Dynamic Stereo-Radiography with Energy Barrier Constraints. *IEEE Transactions on Medical Imaging*, pp. 1-1.doi: 10.1109/tmi.2024.3522200
Butler, D. L., Kay, M. D. and Stouffer, D. C. 1986. Comparison of material properties in fascicle-bone units from human patellar tendon and knee ligaments. *J Biomech* 19(6), pp. 425-432.
Byrapogu, V. K., Gale, T., Hamlin, B., Urish, K. L. and Anderst, W. 2022. Medial Unicompartmental Knee Arthroplasty Restores Native Knee Kinematics During Activities of Daily Living: A Pilot Study. *Ann Biomed Eng* 51(2), pp. 308-317.doi: 10.1007/s10439-022-03021-z
Cardinale, U. et al. 2020. Knee kinematics after cruciate retaining highly congruent mobile bearing total knee arthroplasty: An in vivo dynamic RSA study. *Knee* 27(2), pp. 341-347.doi: 10.1016/j.knee.2019.11.003
Cardona, M. and Garcia Cena, C. E. 2019. Biomechanical Analysis of the Lower Limb: A Full-Body Musculoskeletal Model for Muscle-Driven Simulation. *IEEE Access* 7, pp. 92709-92723.doi: 10.1109/access.2019.2927515
Carey, R. E., Zheng, L., Aiyangar, A. K., Harner, C. D. and Zhang, X. 2014. Subject-specific finite element modeling of the tibiofemoral joint based on CT, magnetic resonance imaging and dynamic stereo-radiography data in vivo. *J Biomech Eng* 136(4), pp. 0410041-0410048.doi: 10.1115/1.4026228
Challis, J. H. 1995. A procedure for determining rigid body transformation parameters. *J Biomech* 28(7), pp. 733-737.
Checa, S., Taylor, M. and New, A. 2008. Influence of an interpositional spacer on the behaviour of the tibiofemoral joint: A finite element study. *Clinical Biomechanics* 23(8), pp. 1044-1052.doi: https://doi.org/10.1016/j.clinbiomech.2008.04.006

Chen, T., Wang, H. and Innocenti, B. 2016a. *Tekscan Measurements of Interfacial Contact Area and Stress in Articulating Joints*. Amsterdam: Academic Press. doi: 10.1016/B978-0-12-803802-4.00017-2

Chen, Z., Zhang, Z., Wang, L., Li, D., Zhang, Y. and Jin, Z. 2016b. Evaluation of a subject-specific musculoskeletal modelling framework for load prediction in total knee arthroplasty. *Med Eng Phys* 38(8), pp. 708-716.doi: 10.1016/j.medengphy.2016.04.010

Cheze, L., Moissenet, F. and Dumas, R. 2015. State of the art and current limits of musculo-skeletal models for clinical applications. *Movement & Sport Sciences* 90, pp. 7-17.

Chokhandre, S., Schwartz, A., Klonowski, E., Landis, B. and Erdemir, A. 2023a. Open Knee(s) Appendix.

Chokhandre, S., Schwartz, A., Klonowski, E., Landis, B. and Erdemir, A. 2023b. Open Knee(s): A Free and Open Source Library of Specimen-Specific Models and Related Digital Assets for Finite Element Analysis of the Knee Joint. *Ann Biomed Eng* 51(1), pp. 10-23.doi: 10.1007/s10439-022-03074-0

Cignoni, P., Callieri, M., Corsini, M., Dellepiane, M., Ganovelli, F. and Ranzuglia, G. 2008. MeshLab: an open-source mesh processing tool. In: V. Scarano, R.D.C., and U. Erra ed. *Eurographics Italian Chapter Conference.*

Clary, C. W., Fitzpatrick, C. K., Maletsky, L. P. and Rullkoetter, P. J. 2013a. The influence of total knee arthroplasty geometry on mid-flexion stability: An experimental and finite element study. *Journal of biomechanics* 46(7), pp. 1351-1357.doi: https://doi.org/10.1016/j.jbiomech.2013.01.025

Clary, C. W., Fitzpatrick, C. K., Maletsky, L. P. and Rullkoetter, P. J. 2013b. The influence of total knee arthroplasty geometry on mid-flexion stability: an experimental and finite element study. *J Biomech* 46(7), pp. 1351-1357.doi: 10.1016/j.jbiomech.2013.01.025

Cleather, D. J. and Bull, A. M. 2012. The development of lower limb musculoskeletal models with clinical relevance is dependent upon the fidelity of the mathematical description of the lower limb. Part 2: Patient-specific geometry. *Proc Inst Mech Eng H* 226(2), pp. 133-145.doi: 10.1177/0954411911432105

Clouthier, A. L., Smith, C. R., Vignos, M. F., Thelen, D. G., Deluzio, K. J. and Rainbow, M. J. 2019. The effect of articular geometry features identified using

statistical shape modelling on knee biomechanics. *Med Eng Phys* 66, pp. 47-55.doi: 10.1016/j.medengphy.2019.02.009
Clynes, M. A., Jameson, K. A., Edwards, M. H., Cooper, C. and Dennison, E. M. 2019. Impact of osteoarthritis on activities of daily living: does joint site matter? *Aging Clin Exp Res* 31(8), pp. 1049-1056.doi: 10.1007/s40520-019-01163-0
Comninou, M. and Yannas, I. V. 1976. Dependence of stress-strain nonlinearity of connective tissues on the geometry of collagen fibres. *Journal of biomechanics* 9(7), pp. 427-433.doi: https://doi.org/10.1016/0021-9290(76)90084-1
Cooper, R. J., Wilcox, R. K. and Jones, A. C. 2019. Finite element models of the tibiofemoral joint: A review of validation approaches and modelling challenges. *Med Eng Phys* 74, pp. 1-12.doi: 10.1016/j.medengphy.2019.08.002
Cowen, A. R., Davies, A. G. and Sivananthan, M. U. 2008. The design and imaging characteristics of dynamic, solid-state, flat-panel x-ray image detectors for digital fluoroscopy and fluorography. *Clin Radiol* 63(10), pp. 1073-1085.doi: 10.1016/j.crad.2008.06.002
Cui, A., Li, H., Wang, D., Zhong, J., Chen, Y. and Lu, H. 2020. Global, regional prevalence, incidence and risk factors of knee osteoarthritis in population-based studies. *EClinicalMedicine* 29-30, p. 100587.doi: 10.1016/j.eclinm.2020.100587
Curreli, C., Di Puccio, F., Davico, G., Modenese, L. and Viceconti, M. 2021. Using Musculoskeletal Models to Estimate in vivo Total Knee Replacement Kinematics and Loads: Effect of Differences Between Models. *Front Bioeng Biotechnol* 9, p. 703508.doi: 10.3389/fbioe.2021.703508
Daniel, D. M., Akeson, W. H. and O'Connor, J. J. 1990. Knee ligaments: structure, function, injury, and repair. *(No Title)*.
Dao, T. T. and Pouletaut, P. 2015. A Hertzian Integrated Contact Model of the Total Knee Replacement Implant for the Estimation of Joint Contact Forces. *Journal of Computational Medicine* 2015, pp. 1-9.doi: 10.1155/2015/945379
Daszkiewicz, K. and Luczkiewicz, P. 2021. Biomechanics of the medial meniscus in the osteoarthritic knee joint. *PeerJ* 9, p. e12509.doi: 10.7717/peerj.12509
Davico, G., Lloyd, D. G., Carty, C. P., Killen, B. A., Devaprakash, D. and Pizzolato, C. 2022. Multi-level personalization of neuromusculoskeletal models to estimate physiologically plausible knee joint contact forces in children. *Biomech Model Mechanobiol* 21(6), pp. 1873-1886.doi: 10.1007/s10237-022-01626-w

Davis, M. A., Ettinger, W. H., Neuhaus, J. M. and Mallon, K. P. 1991. Knee osteoarthritis and physical functioning: evidence from the NHANES I Epidemiologic Followup Study. *J Rheumatol* 18(4), pp. 591-598.
Dawson, J., Fitzpatrick, R., Murray, D. and Carr, A. 1998. Questionnaire on the perceptions of patients about total knee replacement. *J Bone Joint Surg Br* 80(1), pp. 63-69.doi: 10.1302/0301-620x.80b1.7859
Defrate, L. E., Papannagari, R., Gill, T. J., Moses, J. M., Pathare, N. P. and Li, G. 2006. The 6 degrees of freedom kinematics of the knee after anterior cruciate ligament deficiency: an in vivo imaging analysis. *Am J Sports Med* 34(8), pp. 1240-1246.doi: 10.1177/0363546506287299
Della Croce, U., Cappozzo, A. and Kerrigan, D. C. 1999. Pelvis and lower limb anatomical landmark calibration precision and its propagation to bone geometry and joint angles. *Medical & Biological Engineering & Computing* 37, pp. 155-161.doi: https://doi.org/10.1007/BF02513282
Delp, S. L. et al. 2007. OpenSim: open-source software to create and analyze dynamic simulations of movement. *IEEE Trans Biomed Eng* 54(11), pp. 1940-1950.doi: 10.1109/TBME.2007.901024
Dhaher, Y. Y., Kwon, T.-H. and Barry, M. 2010. The effect of connective tissue material uncertainties on knee joint mechanics under isolated loading conditions. *Journal of biomechanics* 43(16), pp. 3118-3125.
Di Raimondo, G., Willems, M., Killen, B. A., Havashinezhadian, S., Turcot, K., Vanwanseele, B. and Jonkers, I. 2023. Peak Tibiofemoral Contact Forces Estimated Using IMU-Based Approaches Are Not Significantly Different from Motion Capture-Based Estimations in Patients with Knee Osteoarthritis. *Sensors (Basel)* 23(9).doi: 10.3390/s23094484
Diamant, J., Keller, A., Baer, E., Litt, M. and Arridge, R. 1972. Collagen; ultrastructure and its relation to mechanical properties as a function of ageing. *Proceedings of the Royal Society of London. Series B. Biological Sciences* 180(1060), pp. 293-315.
Ding, Z., Nolte, D., Tsang, C. K., Cleather, D. J., Kedgley, A. E. and Bull, A. M. J. 2016. In Vivo Knee Contact Force Prediction Using Patient-Specific Musculoskeletal Geometry in a Segment-Based Computational Model. *J Biomech Eng* 138(2).doi: 10.1115/1.4032412

Donahue, T. L., Hull, M. L., Rashid, M. M. and Jacobs, C. R. 2002. A finite element model of the human knee joint for the study of tibio-femoral contact. *J Biomech Eng* 124(3), pp. 273-280.doi: 10.1115/1.1470171

Dumas, R., Zeighami, A. and Aissaoui, R. 2020. Knee Medial and Lateral Contact Forces Computed Along Subject-Specific Contact Point Trajectories of Healthy Volunteers and Osteoarthritic Patients. *Computer Methods, Imaging and Visualization in Biomechanics and Biomedical Engineering (CMBBE).* 01 April 2020. doi: 10.1007/978-3-030-43195-2_36

Dzialo, C. M., Mannisi, M., Halonen, K. S., de Zee, M., Woodburn, J. and Andersen, M. S. 2019. Gait alteration strategies for knee osteoarthritis: a comparison of joint loading via generic and patient-specific musculoskeletal model scaling techniques. *Int Biomech* 6(1), pp. 54-65.doi: 10.1080/23335432.2019.1629839

Erdemir, A., Besier, T. F., Halloran, J. P., Imhauser, C. W., Laz, P. J., Morrison, T. M. and Shelburne, K. B. 2019. Deciphering the "Art" in Modeling and Simulation of the Knee Joint: Overall Strategy. *J Biomech Eng* 141(7), pp. 0710021-07100210.doi: 10.1115/1.4043346

Erdemir, A., McLean, S., Herzog, W. and van den Bogert, A. J. 2007. Model-based estimation of muscle forces exerted during movements. *Clin Biomech (Bristol)* 22(2), pp. 131-154.doi: 10.1016/j.clinbiomech.2006.09.005

Erer, K. S. 2007. Adaptive usage of the Butterworth digital filter. *J Biomech* 40(13), pp. 2934-2943.doi: 10.1016/j.jbiomech.2007.02.019

Eskinazi, I. and Fregly, B. J. 2016. An Open-Source Toolbox for Surrogate Modeling of Joint Contact Mechanics. *IEEE Trans Biomed Eng* 63(2), pp. 269-277.doi: 10.1109/TBME.2015.2455510

Esrafilian, A., Stenroth, L., Mononen, M. E., Tanska, P., Avela, J. and Korhonen, R. K. 2020. EMG-Assisted Muscle Force Driven Finite Element Model of the Knee Joint with Fibril-Reinforced Poroelastic Cartilages and Menisci. *Sci Rep* 10(1), p. 3026.doi: 10.1038/s41598-020-59602-2

Esrafilian, A. et al. 2022. An EMG-Assisted Muscle-Force Driven Finite Element Analysis Pipeline to Investigate Joint- and Tissue-Level Mechanical Responses in Functional Activities: Towards a Rapid Assessment Toolbox. *IEEE Trans Biomed Eng* 69(9), pp. 2860-2871.doi: 10.1109/TBME.2022.3156018

Farrokhi, S., Voycheck, C. A., Klatt, B. A., Gustafson, J. A., Tashman, S. and Fitzgerald, G. K. 2014. Altered tibiofemoral joint contact mechanics and kinematics in

patients with knee osteoarthritis and episodic complaints of joint instability. *Clin Biomech* 29(6), pp. 629-635.doi: 10.1016/j.clinbiomech.2014.04.014
Farshidfar, S. S., Cadman, J., Neri, T., Parker, D., Appleyard, R. and Dabirrahmani, D. 2023. Towards a validated musculoskeletal knee model to estimate tibiofemoral kinematics and ligament strains: comparison of different anterolateral augmentation procedures combined with isolated ACL reconstructions. *Biomed Eng Online* 22(1), p. 31.doi: 10.1186/s12938-023-01094-y
FEBio. 2021a. *3.6.2 The Tools Menu*. FEBio User's Manual 1.5. Available at: https://help.febio.org/FEBioStudio/FEBioStudio_1-5-Subsection-3.2.6.html [Accessed: 24-Jul-2025].
FEBio. 2021b. *Using the Fiber Generator Tool*. Tutorials - Model Building. Available at: https://febio.org/knowledgebase/tutorials/model-building/using-the-fiber-generator-tool/
FEBio. 2022a. *4.1.2.9 Mooney-Rivlin*. FEBio User Manual 3.6.University of Utah: Available at: https://help.febio.org/docs/FEBioUser-3-6/UM36-4.1.2.9.html
FEBio. 2022b. *4.1.2.12 Transversely Isotropic Mooney-Rivlin*. FEBio User Manual 3.6.University of Utah: Available at: https://help.febio.org/FebioUser/FEBio_um_3-4-4.1.2.12.html
FEBio. 2022c. *4.1.3.17 Neo-Hookean*. FEBio User Manual 3.6.University of Utah: Available at: https://help.febio.org/docs/FEBioUser-3-6/UM36-4.1.3.17.html
Felson, D. T. 2013. Osteoarthritis as a disease of mechanics. *Osteoarthritis Cartilage* 21(1), pp. 10-15.doi: 10.1016/j.joca.2012.09.012
Fernandez, J. et al. 2023. A Narrative Review of Personalized Musculoskeletal Modeling Using the Physiome and Musculoskeletal Atlas Projects. *J Appl Biomech* 39(5), pp. 304-317.doi: 10.1123/jab.2023-0079
Fernandez, J., Zhang, J., Heidlauf, T., Sartori, M., Besier, T., Rohrle, O. and Lloyd, D. 2016. Multiscale musculoskeletal modelling, data-model fusion and electromyography-informed modelling. *Interface Focus* 6(2), p. 20150084.doi: 10.1098/rsfs.2015.0084
Fernandez, J. W., Akbarshahi, M., Kim, H. J. and Pandy, M. G. 2008. Integrating modelling, motion capture and x-ray fluoroscopy to investigate patellofemoral function during dynamic activity. *Comput Methods Biomech Biomed Engin* 11(1), pp. 41-53.doi: 10.1080/10255840701551046

Franklyn-Miller, A., Richter, C., King, E., Gore, S., Moran, K., Strike, S. and Falvey, E. C. 2017. Athletic groin pain (part 2): a prospective cohort study on the biomechanical evaluation of change of direction identifies three clusters of movement patterns. *Br J Sports Med* 51(5), pp. 460-468.doi: 10.1136/bjsports-2016-096050

Fregly, B. J., Banks, S. A., D'Lima, D. D. and Colwell, C. W., Jr. 2008. Sensitivity of knee replacement contact calculations to kinematic measurement errors. *J Orthop Res* 26(9), pp. 1173-1179.doi: 10.1002/jor.20548

Fregly, B. J., Bei, Y. and Sylvester, M. E. 2003. Experimental evaluation of an elastic foundation model to predict contact pressures in knee replacements. *J Biomech* 36(11), pp. 1659-1668.doi: 10.1016/s0021-9290(03)00176-3

Fregly, B. J., Besier, T. F., Lloyd, D. G., Delp, S. L., Banks, S. A., Pandy, M. G. and D'Lima, D. D. 2012. Grand challenge competition to predict in vivo knee loads. *J Orthop Res* 30(4), pp. 503-513.doi: 10.1002/jor.22023

Fregly, B. J., Rahman, H. A. and Banks, S. A. 2005. Theoretical accuracy of model-based shape matching for measuring natural knee kinematics with single-plane fluoroscopy. *J Biomech Eng* 127(4), pp. 692-699.doi: 10.1115/1.1933949

Frese, T., Peyton, L., Mahlmeister, J. and Sandholzer, H. 2013. Knee pain as the reason for encounter in general practice. *ISRN Family Med* 2013, p. 930825.doi: 10.5402/2013/930825

Fu, P., Liu, G., Zhang, L., Yan, Y., Wang, Y. and Li, H. 2022. Contact Characteristics of Knee-joint Cartilage During Gait Based on

Finite Element Analysis. *Current Mechanics and Advanced Materials* 2(1).doi: 10.2174/2666184502666221130111007

Galbusera, F. et al. 2014. Material models and properties in the finite element analysis of knee ligaments: a literature review. *Front Bioeng Biotechnol* 2, p. 54.doi: 10.3389/fbioe.2014.00054

Gale, T. and Anderst, W. 2019. Asymmetry in healthy adult knee kinematics revealed through biplane radiography of the full gait cycle. *J Orthop Res* 37(3), pp. 609-614.doi: 10.1002/jor.24222

Gale, T. and Anderst, W. 2020. Knee Kinematics of Healthy Adults Measured Using Biplane Radiography. *J Biomech Eng* 142(10).doi: 10.1115/1.4047419

Galvin, C. R., Perriman, D. M., Newman, P. M., Lynch, J. T., Smith, P. N. and Scarvell, J. M. 2018. Squatting, lunging and kneeling provided similar kinematic profiles in healthy knees-A systematic review and meta-analysis of the literature on deep knee flexion kinematics. *Knee* 25(4), pp. 514-530.doi: 10.1016/j.knee.2018.04.015

Ganapam, P. N., Guan, S., Gray, H. A., Sujatha, S. and Pandy, M. G. 2022. Anterior-cruciate-ligament reconstruction does not alter the knee-extensor moment arm during gait. *Gait Posture* 98, pp. 330-336.doi: 10.1016/j.gaitpost.2022.09.074

Ghazwan, A., Wilson, C., Holt, C. A. and Whatling, G. M. 2022. Knee osteoarthritis alters peri-articular knee muscle strategies during gait. *PLoS One* 17(1), p. e0262798.doi: 10.1371/journal.pone.0262798

Giarmatzis, G., Fotiadou, S., Giannakou, E., Tsiptsios, D., Vadikolias, K. and Aggelousis, N. 2022. Using musculoskeletal modelling to evaluate effect of exercise on chronic post stroke gait. *Gait & Posture* 97, pp. S57-S58.doi: 10.1016/j.gaitpost.2022.07.044

Giphart, J. E., Zirker, C. A., Myers, C. A., Pennington, W. W. and LaPrade, R. F. 2012. Accuracy of a contour-based biplane fluoroscopy technique for tracking knee joint kinematics of different speeds. *J Biomech* 45(16), pp. 2935-2938.doi: 10.1016/j.jbiomech.2012.08.045

Gorton, G. E., 3rd, Hebert, D. A. and Gannotti, M. E. 2009. Assessment of the kinematic variability among 12 motion analysis laboratories. *Gait Posture* 29(3), pp. 398-402.doi: 10.1016/j.gaitpost.2008.10.060

Gray, H., Guan, S., Loan, P. and Pandy, M. 2018. Measurement of 3D Dynamic Joint Motion Using Biplane Videoradiography. In: *Handbook of Human Motion*. pp. 101-115. doi: 10.1007/978-3-319-14418-4_154

Gray, H. A., Guan, S. and Pandy, M. G. 2017. Accuracy of mobile biplane X-ray imaging in measuring 6-degree-of-freedom patellofemoral kinematics during overground gait. *J Biomech* 57, pp. 152-156.doi: 10.1016/j.jbiomech.2017.04.009

Gray, H. A., Guan, S., Thomeer, L. T. and Pandy, M. G. 2021. Moment arm of the knee-extensor mechanism measured in vivo across a range of daily activities. *J Biomech* 123, p. 110484.doi: 10.1016/j.jbiomech.2021.110484

Gray, H. A., Guan, S., Thomeer, L. T., Schache, A. G., de Steiger, R. and Pandy, M. G. 2019. Three-dimensional motion of the knee-joint complex during normal walking

revealed by mobile biplane x-ray imaging. *J Orthop Res* 37(3), pp. 615-630.doi: 10.1002/jor.24226
Gray, H. A., Guan, S., Young, T. J., Dowsey, M. M., Choong, P. F. and Pandy, M. G. 2020. Comparison of posterior-stabilized, cruciate-retaining, and medial-stabilized knee implant motion during gait. *J Orthop Res* 38(8), pp. 1753-1768.doi: 10.1002/jor.24613
Griebel, A. J., Trippel, S. B. and Neu, C. P. 2013. Noninvasive dualMRI-based strains vary by depth and region in human osteoarthritic articular cartilage. *Osteoarthritis Cartilage* 21(2), pp. 394-400.doi: 10.1016/j.joca.2012.11.009
Griffin, T. M. and Guilak, F. 2005. The Role of Mechanical Loading in the Onset and Progression of Osteoarthritis. *Exercise and Sport Sciences Reviews* 33(4), pp. 195-200.
Grood, E. S. and Suntay, W. J. 1983. A Joint Coordinate System for the Clinical Description of Three-Dimensional Motions: Application to the Knee. *J Biomechanical Engineering* 105(2), pp. 136-144.
Gu, W. and Pandy, M. G. 2020. Direct Validation of Human Knee-Joint Contact Mechanics Derived From Subject-Specific Finite-Element Models of the Tibiofemoral and Patellofemoral Joints. *J Biomech Eng* 142(7).doi: 10.1115/1.4045594
Guan, S., Dumas, R. and Pandy, M. G. 2024. Tibiofemoral Slip Velocity in Total Knee Arthroplasty is Design-Invariant but Activity-Dependent. *Ann Biomed Eng* 52(6), pp. 1779-1794.doi: 10.1007/s10439-024-03490-4
Guan, S., Gray, H. A., Keynejad, F. and Pandy, M. G. 2016. Mobile Biplane X-Ray Imaging System for Measuring 3D Dynamic Joint Motion During Overground Gait. *IEEE Trans Med Imaging* 35(1), pp. 326-336.doi: 10.1109/TMI.2015.2473168
Guan, S., Gray, H. A., Schache, A. G., Feller, J., de Steiger, R. and Pandy, M. G. 2017. In vivo six-degree-of-freedom knee-joint kinematics in overground and treadmill walking following total knee arthroplasty. *J Orthop Res* 35(8), pp. 1634-1643.doi: 10.1002/jor.23466
Guess, T. M. and Stylianou, A. 2012. Simulation of anterior cruciate ligament deficiency in a musculoskeletal model with anatomical knees. *The open biomedical engineering journal* 6, p. 23.
Guess, T. M., Thiagarajan, G., Kia, M. and Mishra, M. 2010. A subject specific multibody model of the knee with menisci. *Med Eng Phys* 32(5), pp. 505-515.doi: 10.1016/j.medengphy.2010.02.020

Guo, N. et al. 2024. Posterior tibial slope influences joint mechanics and soft tissue loading after total knee arthroplasty. *Front Bioeng Biotechnol* 12, p. 1352794.doi: 10.3389/fbioe.2024.1352794
Gur, H., Cakin, N., Akova, B., Okay, E. and Kucukoglu, S. 2002. Concentric versus combined concentric-eccentric isokinetic training: effects on functional capacity and symptoms in patients with osteoarthrosis of the knee. *Arch Phys Med Rehabil* 83(3), pp. 308-316.doi: 10.1053/apmr.2002.30620
Gustafson, J. A., Elias, J. J., Fitzgerald, G. K., Tashman, S., Debski, R. E. and Farrokhi, S. 2021. Combining advanced computational and imaging techniques as a quantitative tool to estimate patellofemoral joint stress during downhill gait: A feasibility study. *Gait Posture* 84, pp. 31-37.doi: 10.1016/j.gaitpost.2020.11.016
Gustafson, J. A., Robinson, M. E., Fitzgerald, G. K., Tashman, S. and Farrokhi, S. 2015. Knee motion variability in patients with knee osteoarthritis: The effect of self-reported instability. *Clin Biomech* 30(5), pp. 475-480.doi: 10.1016/j.clinbiomech.2015.03.007
Haemer, J. M., Carter, D. R. and Giori, N. J. 2012. The low permeability of healthy meniscus and labrum limit articular cartilage consolidation and maintain fluid load support in the knee and hip. *Journal of biomechanics* 45(8), pp. 1450-1456.
Hallen, L. G. and Lindahl, O. 1966. The "screw-home" movement in the knee-joint. *Acta Orthop Scand* 37(1), pp. 97-106.doi: 10.3109/17453676608989407
Halloran, J. P., Petrella, A. J. and Rullkoetter, P. J. 2005. Explicit finite element modeling of total knee replacement mechanics. *Journal of biomechanics* 38(2), pp. 323-331.doi: https://doi.org/10.1016/j.jbiomech.2004.02.046
Halonen, K., Dzialo, C. M., Mannisi, M., Venäläinen, M., de Zee, M. and Andersen, M. S. 2017. Workflow assessing the effect of gait alterations on stresses in the medial tibial cartilage-combined musculoskeletal modelling and finite element analysis. *Scientific reports* 7(1), p. 17396.
Halonen, K. S., Mononen, M. E., Jurvelin, J. S., Toyras, J., Klodowski, A., Kulmala, J. P. and Korhonen, R. K. 2016. Importance of Patella, Quadriceps Forces, and Depthwise Cartilage Structure on Knee Joint Motion and Cartilage Response During Gait. *J Biomech Eng* 138(7).doi: 10.1115/1.4033516
Halonen, K. S., Mononen, M. E., Jurvelin, J. S., Toyras, J. and Korhonen, R. K. 2013. Importance of depth-wise distribution of collagen and proteoglycans in articular

cartilage--a 3D finite element study of stresses and strains in human knee joint. *J Biomech* 46(6), pp. 1184-1192.doi: 10.1016/j.jbiomech.2012.12.025
Hamai, S., Moro-oka, T. A., Dunbar, N. J., Miura, H., Iwamoto, Y. and Banks, S. A. 2013. In vivo healthy knee kinematics during dynamic full flexion. *Biomed Res Int* 2013, p. 717546.doi: 10.1155/2013/717546
Hamilton, L. D., Andreassen, T. E., Myers, C., Shelburne, K. B., Clary, C. and Rullkoetter, P. J. 2022. Supine leg press as an alternative to standing lunge in high-speed stereo radiography. *J Biomech* 138, p. 111118.doi: 10.1016/j.jbiomech.2022.111118
Hamilton, L. D., Andreassen, T. E., Myers, C. A., Shelburne, K. B., Clary, C. W. and Rullkoetter, P. J. 2023. Knee pivot location in asymptomatic older adults. *J Biomech* 149, p. 111487.doi: 10.1016/j.jbiomech.2023.111487
HAS-Motion. 2024a. *CalibrateDSX Overview*. HAS-Motion Software Documentation. Available at: https://wiki.has-motion.com/doku.php?id=other:dsx:calibratedsx:calibratedsx_overview [Accessed: 07/02/2024].
HAS-Motion. 2024b. *Coda Pelvis*. HAS-Motion Software Documentation. Available at: https://wiki.has-motion.com/doku.php?id=visual3d:documentation:modeling:segments:coda_pelvis&s[]=coda&s[]=pelvis [Accessed: 06/02/2025].
HAS-Motion. 2024c. *X4D Overview*. HAS-Motion Software Documentation. Available at: https://wiki.has-motion.com/doku.php?id=other:dsx:x4d:x4d_overview [Accessed: 07/02/2025].
Hausdorff, J. M., Lertratanakul, A., Cudkowicz, M. E., Peterson, A. L., Kaliton, D. and Goldberger, A. L. 2000. Dynamic markers of altered gait rhythm in amyotrophic lateral sclerosis. *J Appl Physiol* 88, pp. 2045-2053.
Haut Donahue, T. L., Hull, M. L., Rashid, M. M. and Jacobs, C. R. 2003. How the stiffness of meniscal attachments and meniscal material properties affect tibio-femoral contact pressure computed using a validated finite element model of the human knee joint. *J Biomech* 36, pp. 19-34.
Heesen, C., Böhm, J., Reich, C., Kasper, J., Goebel, M. and Gold, S. M. 2008. Patient perception of bodily functions in multiple sclerosis: gait and visual function are the most valuable. *Multiple Sclerosis* 14, pp. 988-991.doi: 10.1177/1352458508088916

Henak, C. R., Anderson, A. E. and Weiss, J. A. 2013. Subject-specific analysis of joint contact mechanics: application to the study of osteoarthritis and surgical planning. *J Biomech Eng* 135(2), p. 021003.doi: 10.1115/1.4023386

Hermens, H. J. and Freriks, B. 1997. The State of the Art on Sensors and Sensor Placement Procedures for Surface ElectroMyoGraphy: A proposal for sensor placement procedures. *SENIAM* 5.

Hermens, H. J., Freriks, B., Disselhorst-Klug, C. and Rau, G. 2000. Development of recommendations for SEMG sensors and sensor placement procedures. *J Electromyography and Kinesiology* 10, pp. 361-374.

Heyse, T. J. et al. 2017. Kinematics of a bicruciate-retaining total knee arthroplasty. *Knee Surg Sports Traumatol Arthrosc* 25(6), pp. 1784-1791.doi: 10.1007/s00167-016-4414-5

Hicks, J. L. 2013. *OpenSim Documentation: OpenSim's Capabilities*. Available at: https://opensimconfluence.atlassian.net/wiki/spaces/OpenSim/pages/53087561/OpenSim+s+Capabilities [Accessed: 12 March 2025].

Hingwala, D., Chatterjee, S., Kesavadas, C., Thomas, B. and Kapilamoorthy, T. R. 2011. Applications of 3D CISS sequence for problem solving in neuroimaging. *Indian J Radiol Imaging* 21(2), pp. 90-97.doi: 10.4103/0971-3026.82283

Hollander, M., Chicken, E. and Wolfe, D. A. 2014. *Nonparametric statistical methods*. Wiley series in probability and statistics. Third edition. ed. Hoboken, New Jersey: John Wiley & Sons, Inc.

Hollman, J. H., Watkins, M. K., Imhoff, A. C., Braun, C. E., Akervik, K. A. and Ness, D. K. 2016. A comparison of variability in spatiotemporal gait parameters between treadmill and overground walking conditions. *Gait Posture* 43, pp. 204-209.doi: 10.1016/j.gaitpost.2015.09.024

Holzapfel, G. A. 2000. *Nonlinear solid mechanics : a continuum approach for engineering*. Chichester: Wiley.

Hoshino, Y., Fu, F. H., Irrgang, J. J. and Tashman, S. 2013. Can joint contact dynamics be restored by anterior cruciate ligament reconstruction? *Clin Orthop Relat Res* 471(9), pp. 2924-2931.doi: 10.1007/s11999-012-2761-1

Hoshino, Y. and Tashman, S. 2012. Internal tibial rotation during in vivo, dynamic activity induces greater sliding of tibio-femoral joint contact on the medial compartment. *Knee Surg Sports Traumatol Arthrosc* 20(7), pp. 1268-1275.doi: 10.1007/s00167-011-1731-6

Hosseini, A., Van de Velde, S., Gill, T. J. and Li, G. 2012. Tibiofemoral cartilage contact biomechanics in patients after reconstruction of a ruptured anterior cruciate ligament. *J Orthop Res* 30(11), pp. 1781-1788.doi: 10.1002/jor.22122

Huddleston, J. I., Scarborough, D. M., Goldvasser, D., Freiberg, A. A. and Malchau, H. 2009. 2009 Marshall Urist Young Investigator Award: How Often Do Patients with High-Flex Total Knee Arthroplasty Use High Flexion? *Clinical Orthopaedics and Related Research®* 467(7), pp. 1898-1906.doi: 10.1007/s11999-009-0874-y

Hume, D. R., Kefala, V., Harris, M. D. and Shelburne, K. B. 2018. Comparison of Marker-Based and Stereo Radiography Knee Kinematics in Activities of Daily Living. *Ann Biomed Eng* 46(11), pp. 1806-1815.doi: 10.1007/s10439-018-2068-9

Hunter, D. J. and Bierma-Zeinstra, S. 2019. Osteoarthritis. *Lancet* 393(10182), pp. 1745-1759.doi: 10.1016/S0140-6736(19)30417-9

Hutchison, L., Grayson, J., Hiller, C., D'Souza, N., Kobayashi, S. and Simic, M. 2022. Is There a Relationship between Knee Biomechanics and Pain in People with Knee Osteoarthrisis? A Systematic Review and Meta-Analysis. *Osteoarthritis and Cartilage* 30, pp. S142-S143.doi: 10.1016/j.joca.2022.02.180

Hutchison, L., Grayson, J., Hiller, C., D'Souza, N., Kobayashi, S. and Simic, M. 2023. Relationship Between Knee Biomechanics and Pain in People With Knee Osteoarthritis: A Systematic Review and Meta-Analysis. *Arthritis Care Res (Hoboken)* 75(6), pp. 1351-1361.doi: 10.1002/acr.25001

Imani Nejad, Z. et al. 2020. The Capacity of Generic Musculoskeletal Simulations to Predict Knee Joint Loading Using the CAMS-Knee Datasets. *Ann Biomed Eng* 48(4), pp. 1430-1440.doi: 10.1007/s10439-020-02465-5

Imeni, M., Seyfi, B., Fatouraee, N. and Samani, A. 2020. Constitutive modeling of menisci tissue: a critical review of analytical and numerical approaches. *Biomech Model Mechanobiol* 19(6), pp. 1979-1996.doi: 10.1007/s10237-020-01352-1

Irrgang, J. J., Snyder-Mackler, L. M., Wainner, R. S., Fu, F. and Harner, C. D. 1998. Development of a Patient-Reported Measure of Function of the Knee*. *JBJS* 80(8), pp. 1132-1145.

Jacobs, R. and van de Bogert, T. [no date]. *soder.m*. Available at: https://www.isbweb.org/software/movanal/soder.m

Jilani, A., Shirazi-Adl, A. and Bendjaballah, M. 1997. Biomechanics of human tibio-femoral joint in axial rotation. *The Knee* 4(4), pp. 203-213.

Johnson, K. L. 1985. Normal contact of elastic solids – Hertz theory. In: *Contact Mechanics*. Vol. 1.Cambridge University Press, pp. 84-106. doi: 10.1017/cbo9781139171731.005
Kadaba, M. P., Ramakrishnan, H. K. and Wootten, M. E. 1990. Measurement of lower extremity kinematics during level walking. *J Orthop Res* 8(3), pp. 383-392.doi: 10.1002/jor.1100080310
Kainz, H. et al. 2020. A multi-scale modelling framework combining musculoskeletal rigid-body simulations with adaptive finite element analyses, to evaluate the impact of femoral geometry on hip joint contact forces and femoral bone growth. *PLoS One* 15(7), p. e0235966.doi: 10.1371/journal.pone.0235966
Kainz, H., Wesseling, M. and Jonkers, I. 2021. Generic scaled versus subject-specific models for the calculation of musculoskeletal loading in cerebral palsy gait: Effect of personalized musculoskeletal geometry outweighs the effect of personalized neural control. *Clin Biomech (Bristol)* 87, p. 105402.doi: 10.1016/j.clinbiomech.2021.105402
Kärrholm, J., Herberts, P., Hultmark, P., Malchau, H., Nivbrant, B. and Thanner, J. 1997. Radiostereometry of hip prostheses. Review of methodology and clinical results. *Clin Orthop Relat Res* (344), pp. 94-110.
Katz, J. N., Arant, K. R. and Loeser, R. F. 2021. Diagnosis and treatment of hip and knee osteoarthritis: a review. *Jama* 325(6), pp. 568-578.
Kazemi, M. and Li, L. 2014. A viscoelastic poromechanical model of the knee joint in large compression. *Medical Engineering & Physics* 36(8), pp. 998-1006.
Kazemi, M., Li, L. P., Savard, P. and Buschmann, M. D. 2011. Creep behavior of the intact and meniscectomy knee joints. *J Mech Behav Biomed Mater* 4(7), pp. 1351-1358.doi: 10.1016/j.jmbbm.2011.05.004
Kefala, V., Cyr, A. J., Harris, M. D., Hume, D. R., Davidson, B. S., Kim, R. H. and Shelburne, K. B. 2017. Assessment of Knee Kinematics in Older Adults Using High-Speed Stereo Radiography. *Med Sci Sports Exerc* 49(11), pp. 2260-2267.doi: 10.1249/MSS.0000000000001350
Kernkamp, W. A. et al. 2019. The Medial Patellofemoral Ligament Is a Dynamic and Anisometric Structure: An In Vivo Study on Length Changes and Isometry. *Am J Sports Med* 47(7), pp. 1645-1653.doi: 10.1177/0363546519840278
Khatib, N. 2018. *The Biomechanical and Biological Pathways of Tibiofemoral*

Focal Cartilage Defect Pathogenesis and Shortfalls of Microfracture Surgery. Cardiff.
Khoshgoftar, M., Vrancken, A., van Tienen, T., Buma, P., Janssen, D. and Verdonschot, N. 2015. The sensitivity of cartilage contact pressures in the knee joint to the size and shape of an anatomically shaped meniscal implant. *Journal of biomechanics* 48(8), pp. 1427-1435.
Khot, S. and Guttal, R. 2021. Contact mechanics of human knee joint: Analytical approach. *Journal of Computational Applied Mechanics* 52(4), pp. 553-569.doi: 10.22059/jcamech.2021.326466.633
Kiapour, A. et al. 2014a. Finite element model of the knee for investigation of injury mechanisms: development and validation. *J Biomech Eng* 136(1), p. 011002.doi: 10.1115/1.4025692
Kiapour, A. M. et al. 2014b. The Effect of Ligament Modeling Technique on Knee Joint Kinematics: A Finite Element Study. *Appl Math (Irvine)* 4(5A), pp. 91-97.doi: 10.4236/am.2013.45A011
Killen, B. A., Brito da Luz, S., Lloyd, D. G., Carleton, A. D., Zhang, J., Besier, T. F. and Saxby, D. J. 2020. Automated creation and tuning of personalised muscle paths for OpenSim musculoskeletal models of the knee joint. *Biomech Model Mechanobiol* 20(2), pp. 521-533.doi: 10.1007/s10237-020-01398-1
Killen, B. A., Willems, M. and Jonkers, I. 2024. An open-source framework for the generation of OpenSim models with personalised knee joint geometries for the estimation of articular contact mechanics. *J Biomech* 177.doi: 10.1016/j.jbiomech.2024.112387
Kim, H. J., Fernandez, J. W., Akbarshahi, M., Walter, J. P., Fregly, B. J. and Pandy, M. G. 2009. Evaluation of predicted knee-joint muscle forces during gait using an instrumented knee implant. *J Orthop Res* 27(10), pp. 1326-1331.doi: 10.1002/jor.20876
Kim, Y., Kim, K. I., Choi, J. and Lee, K. 2011. Novel methods for 3D postoperative analysis of total knee arthroplasty using 2D-3D image registration. *Clin Biomech* 26(4), pp. 384-391.doi: 10.1016/j.clinbiomech.2010.11.013
Kinney, A. L., Besier, T. F., D'Lima, D. D. and Fregly, B. J. 2013. Update on grand challenge competition to predict in vivo knee loads. *J Biomech Eng* 135(2), p. 021012.doi: 10.1115/1.4023255
Klets, O., Mononen, M. E., Tanska, P., Nieminen, M. T., Korhonen, R. K. and Saarakkala, S. 2016. Comparison of different material models of articular cartilage in

3D computational modeling of the knee: Data from the Osteoarthritis Initiative (OAI). *Journal of biomechanics* 49(16), pp. 3891-3900.
Knörlein, B. J., Baier, D. B., Gatesy, S. M., Laurence-Chasen, J. D. and Brainerd, E. L. 2016. Validation of XMALab software for marker-based XROMM. *J Exp Biol* 219(Pt 23), pp. 3701-3711.doi: 10.1242/jeb.145383
Kobayashi, K., Hosseini, A., Sakamoto, M., Qi, W., Rubash, H. E. and Li, G. 2013. In vivo kinematics of the extensor mechanism of the knee during deep flexion. *J Biomech Eng* 135(8), p. 81002.doi: 10.1115/1.4024284
Koh, T., Grabiner, M. D. and De Swart, R. J. 1992. In-vivo Tracking of the Human Patella. *J Biomech* 25(6), pp. 637-643.
Koo, Y. J. and Koo, S. 2019. Three-Dimensional Kinematic Coupling of the Healthy Knee During Treadmill Walking. *J Biomech Eng* 141(8).doi: 10.1115/1.4043562
Kour, R. Y. N., Guan, S., Dowsey, M. M., Choong, P. F. and Pandy, M. G. 2022. Kinematic function of knee implant designs across a range of daily activities. *J Orthop Res* 41(6), pp. 1217-1227.doi: 10.1002/jor.25476
Kozanek, M., Hosseini, A., Liu, F., Van de Velde, S. K., Gill, T. J., Rubash, H. E. and Li, G. 2009. Tibiofemoral kinematics and condylar motion during the stance phase of gait. *J Biomech* 42(12), pp. 1877-1884.doi: 10.1016/j.jbiomech.2009.05.003
Kumar, D., Manal, K. T. and Rudolph, K. S. 2013. Knee joint loading during gait in healthy controls and individuals with knee osteoarthritis. *Osteoarthritis Cartilage* 21(2), pp. 298-305.doi: 10.1016/j.joca.2012.11.008
Kwon, O. R. et al. 2014. Biomechanical comparison of fixed- and mobile-bearing for unicomparmental knee arthroplasty using finite element analysis. *J Orthop Res* 32(2), pp. 338-345.doi: 10.1002/jor.22499
Lafortune, M. A., Cavanagh, P. R., Sommer, H. J. and Kalenak, A. 1992a. Three-Dimensional Kinematics of the Human Knee During Walking. *J Biomech* 25(4), pp. 347-357.
Lafortune, M. A., Cavanagh, P. R., Sommer, H. J. and Kalenak, A. 1994. Foot inversion-eversion and knee kinematics during walking. *J Orthop Res* 12, pp. 412-420.doi: 10.1002/jor.1100120314
Lafortune, M. A., Cavanagh, P. R. and Sommer, H. J. K., A. 1992b. Three-Dimensional Kinematics of the Human Knee During Walking. *J Biomech* 25(4), pp. 347-357.

Lampen, N., Su, H., Chan, D. D. and Yan, P. 2023. Finite element modeling with subject-specific mechanical properties to assess knee osteoarthritis initiation and progression. *J Orthop Res* 41(1), pp. 72-83.doi: 10.1002/jor.25338
Lee, Y. S., Seon, J. K., Shin, V. I., Kim, G. H. and Jeon, M. 2008. Anatomical evaluation of CT-MRI combined femoral model. *Biomed Eng Online* 7, p. 6.doi: 10.1186/1475-925X-7-6
Lenhart, R. L. 2015. *Influence of Surgery on Musculoskeletal Mechanics in Children with Crouch Gait.* Wisconsin-Madison.
Lenhart, R. L., Kaiser, J., Smith, C. R. and Thelen, D. G. 2015. Prediction and Validation of Load-Dependent Behavior of the Tibiofemoral and Patellofemoral Joints During Movement. *Ann Biomed Eng* 43(11), pp. 2675-2685.doi: 10.1007/s10439-015-1326-3
LeRoux, M. A. and Setton, L. A. 2002. Experimental and biphasic FEM determinations of the material properties and hydraulic permeability of the meniscus in tension. *J. Biomech. Eng.* 124(3), pp. 315-321.
Leszko, F., Hovinga, K. R., Lerner, A. L., Komistek, R. D. and Mahfouz, M. R. 2011. In vivo normal knee kinematics: is ethnicity or gender an influencing factor? *Clin Orthop Relat Res* 469(1), pp. 95-106.doi: 10.1007/s11999-010-1517-z
Levens, A. S., Inman, V. T. and Blosser, J. A. 1948. TRANSVERSE ROTATION OF THE SEGMENTS OF THE LOWER EXTREMITY IN LOCOMOTION. *JBJS* 30(4), pp. 859-872.
Li, G., Gil, J., Kanamori, A. and Woo, S.-Y. 1999. A validated three-dimensional computational model of a human knee joint.
Li, G., Sakamoto, M. and Chao, Y. S. 1997. A comparison of different methods in predicting static pressure distribution in articulating joints. *J Biomech* 30(6), pp. 635-638.
Li, G., Van de Velde, S. K. and Bingham, J. T. 2008. Validation of a non-invasive fluoroscopic imaging technique for the measurement of dynamic knee joint motion. *J Biomech* 41(7), pp. 1616-1622.doi: 10.1016/j.jbiomech.2008.01.034
Li, J. S., Hosseini, A., Cancre, L., Ryan, N., Rubash, H. E. and Li, G. 2013. Kinematic characteristics of the tibiofemoral joint during a step-up activity. *Gait Posture* 38(4), pp. 712-716.doi: 10.1016/j.gaitpost.2013.03.004

Li, K., Zheng, L., Tashman, S. and Zhang, X. 2012. The inaccuracy of surface-measured model-derived tibiofemoral kinematics. *J Biomech* 45(15), pp. 2719-2723.doi: 10.1016/j.jbiomech.2012.08.007
Li, L., Herzog, W., Korhonen, R. and Jurvelin, J. 2005. The role of viscoelasticity of collagen fibers in articular cartilage: axial tension versus compression. *Medical Engineering & Physics* 27(1), pp. 51-57.
Li, L., Yang, L., Zhang, K., Zhu, L., Wang, X. and Jiang, Q. 2020. Three-dimensional finite-element analysis of aggravating medial meniscus tears on knee osteoarthritis. *Journal of orthopaedic translation* 20, pp. 47-55.
Lin, C. C., Li, J. D., Lu, T. W., Kuo, M. Y., Kuo, C. C. and Hsu, H. C. 2018. A model-based tracking method for measuring 3D dynamic joint motion using an alternating biplane x-ray imaging system. *Med Phys*.doi: 10.1002/mp.13042
Lin, C. C., Lu, T. W., Wang, T. M., Hsu, C. Y. and Shih, T. F. 2014. Comparisons of surface vs. volumetric model-based registration methods using single-plane vs. bi-plane fluoroscopy in measuring spinal kinematics. *Med Eng Phys* 36(2), pp. 267-274.doi: 10.1016/j.medengphy.2013.08.011
Lin, Z. and Yan, T. 2011. Long-term effectiveness of neuromuscular electrical stimulation for promoting motor recovery of the upper extremity after stroke. *J Rehabil Med* 43(6), pp. 506-510.doi: 10.2340/16501977-0807
Liu, F., Kozanek, M., Hosseini, A., Van de Velde, S. K., Gill, T. J., Rubash, H. E. and Li, G. 2010. In vivo tibiofemoral cartilage deformation during the stance phase of gait. *J Biomech* 43(4), pp. 658-665.doi: 10.1016/j.jbiomech.2009.10.028
Liu, W., Sun, X., Liu, W., Liu, H., Zhai, H., Zhang, D. and Tian, F. 2022. Finite element study of a partial meniscectomy of a complete discoid lateral meniscus in adults. *Med Eng Phys* 107, p. 103855.doi: 10.1016/j.medengphy.2022.103855
Lloyd, D. G. and Besier, T. F. 2003. An EMG-driven musculoskeletal model to estimate muscle forces and knee joint moments in vivo. *J Biomech* 36(6), pp. 765-776.doi: 10.1016/s0021-9290(03)00010-1
Lloyd, D. G., Jonkers, I., Delp, S. L. and Modenese, L. 2023. The History and Future of Neuromusculoskeletal Biomechanics. *J Appl Biomech* 39(5), pp. 273-283.doi: 10.1123/jab.2023-0165
Long, H. et al. 2022. Prevalence Trends of Site-Specific Osteoarthritis From 1990 to 2019: Findings From the Global Burden of Disease Study 2019. *Arthritis Rheumatol* 74(7), pp. 1172-1183.doi: 10.1002/art.42089

Luis, I., Afschrift, M., De Groote, F. and Gutierrez-Farewik, E. M. 2022. Evaluation of musculoskeletal models, scaling methods, and performance criteria for estimating muscle excitations and fiber lengths across walking speeds. *Front Bioeng Biotechnol* 10, p. 1002731.doi: 10.3389/fbioe.2022.1002731

Maas, S. A., Ellis, B. J., Ateshian, G. A. and Weiss, J. A. 2012. FEBio: finite elements for biomechanics. *J Biomech Eng* 134(1), p. 011005.doi: 10.1115/1.4005694

Mackey, A. H., Walt, S. E., Lobb, G. A. and Stott, N. S. 2005. Reliability of upper and lower limb three-dimensional kinematics in children with hemiplegia. *Gait Posture* 22(1), pp. 1-9.doi: 10.1016/j.gaitpost.2004.06.002

Mahesh, M. 2001. Fluoroscopy: Patient Radiation Exposure Issues. *RadioGraphics* 21(4), pp. 1033-1045.

Marouane, H., Shirazi-Adl, A. and Adouni, M. 2016. Alterations in knee contact forces and centers in stance phase of gait: A detailed lower extremity musculoskeletal model. *J Biomech* 49(2), pp. 185-192.doi: 10.1016/j.jbiomech.2015.12.016

Marra, M. A. 2019. *Personalized musculoskeletal modeling of the knee joint.*

Marra, M. A., Vanheule, V., Fluit, R., Koopman, B. H., Rasmussen, J., Verdonschot, N. and Andersen, M. S. 2015. A subject-specific musculoskeletal modeling framework to predict in vivo mechanics of total knee arthroplasty. *J Biomech Eng* 137(2), p. 020904.doi: 10.1115/1.4029258

McCarthy, I., Hodgins, D., Mor, A., Elbaz, A. and G., S. 2013. Analysis of knee flexion characteristics and how the alter with onset knee osteoarthritis: a case control study. *BMC Musculoskelet Disord* 14, p. 169.doi: 10.1186/1471-2474-14-169

McClay, I. S. 1990. *A comparison of tibiofemoral and patellofemoral joint motion in runners with and without patellofemoral pain.* Ph.D., The Pennsylvania State University.

Meireles, S., Wesseling, M., Smith, C. R., Thelen, D. G., Verschueren, S. and Jonkers, I. 2017. Medial knee loading is altered in subjects with early osteoarthritis during gait but not during step-up-and-over task. *PLoS One* 12(11), p. e0187583.doi: 10.1371/journal.pone.0187583

Meng, Q., Jin, Z., Wilcox, R. and Fisher, J. 2014. Computational investigation of the time-dependent contact behaviour of the human tibiofemoral joint under body weight. *Proc Inst Mech Eng H* 228(11), pp. 1193-1207.doi: 10.1177/0954411914559737

Mesfar, W. and Shirazi-Adl, A. 2006. Knee joint mechanics under quadriceps–hamstrings muscle forces are influenced by tibial restraint. *Clinical Biomechanics* 21(8), pp. 841-848.doi: https://doi.org/10.1016/j.clinbiomech.2006.04.014
Messner, K. and Gao, J. 1998. The menisci of the knee joint. Anatomical and functional characteristics, and a rationale for clinical treatment. *The Journal of Anatomy* 193(2), pp. 161-178.
Millard, M., Uchida, T., Seth, A. and Delp, S. L. 2013. Flexing computational muscle: modeling and simulation of musculotendon dynamics. *J Biomech Eng* 135(2), p. 021005.doi: 10.1115/1.4023390
Miller, R. H. 2018. Hill-based muscle modelling. In: *Handbook of Human Motion*. Vol. 1-3.Springer International Publishing, pp. 373-394. doi: 10.1007/978-3-319-14418-4_203
Mills, K., Hunt, M. A. and Ferber, R. 2013. Biomechanical deviations during level walking associated with knee osteoarthritis: a systematic review and meta-analysis. *Arthritis Care Res (Hoboken)* 65(10), pp. 1643-1665.doi: 10.1002/acr.22015
Minns, R. J. 2005. The role of gait analysis in the management of the knee. *Knee* 12(3), pp. 157-162.doi: 10.1016/j.knee.2004.12.009
Miranda, D. L., Rainbow, M. J., Crisco, J. J. and Fleming, B. C. 2013. Kinematic differences between optical motion capture and biplanar videoradiography during a jump-cut maneuver. *J Biomech* 46(3), pp. 567-573.doi: 10.1016/j.jbiomech.2012.09.023
Miranda, D. L., Rainbow, M. J., Leventhal, E. L., Crisco, J. J. and Fleming, B. C. 2010. Automatic determination of anatomical coordinate systems for three-dimensional bone models of the isolated human knee. *J Biomech* 43(8), pp. 1623-1626.doi: 10.1016/j.jbiomech.2010.01.036
Miranda, D. L., Schwartz, J. B., Loomis, A. C., Brainerd, E. L., Fleming, B. C. and Crisco, J. J. 2011. Static and dynamic error of a biplanar videoradiography system using marker-based and markerless tracking techniques. *J Biomech Eng* 133(12), p. 121002.doi: 10.1115/1.4005471
Miyazaki, T., Wada, M., Kawahara, H., Sato, M., Baba, H. and Shimada, S. 2002. Dynamic load at baseline can predict radiographic disease progression in medial compartment knee osteoarthritis. *Annals of the Rheumatic Diseases* 61(7), pp. 617-622.doi: 10.1136/ard.61.7.617

Mo, F., Jean, A. P., Dominique, C. and and Masson, C. 2012. The failure modelling of knee ligaments in the finite element model. *International Journal of Crashworthiness* 17(6), pp. 630-636.doi: 10.1080/13588265.2012.704194
Modenese, L., Ceseracciu, E., Reggiani, M. and Lloyd, D. G. 2016. Estimation of musculotendon parameters for scaled and subject specific musculoskeletal models using an optimization technique. *J Biomech* 49(2), pp. 141-148.doi: 10.1016/j.jbiomech.2015.11.006
Modenese, L. and Renault, J. B. 2021. Automatic generation of personalised skeletal models of the lower limb from three-dimensional bone geometries. *J Biomech* 116, p. 110186.doi: 10.1016/j.jbiomech.2020.110186
Moglo, K. and Shirazi-Adl, A. 2003. Biomechanics of passive knee joint in drawer: load transmission in intact and ACL-deficient joints. *The Knee* 10(3), pp. 265-276.
Moglo, K. E. and Shirazi-Adl, A. 2005. Cruciate coupling and screw-home mechanism in passive knee joint during extension--flexion. *J Biomech* 38(5), pp. 1075-1083.doi: 10.1016/j.jbiomech.2004.05.033
Mohout, I., Elahi, S. A., Esrafilian, A., Killen, B. A., Korhonen, R. K., Verschueren, S. and Jonkers, I. 2023. Signatures of disease progression in knee osteoarthritis: insights from an integrated multi-scale modeling approach, a proof of concept. *Front Bioeng Biotechnol* 11, p. 1214693.doi: 10.3389/fbioe.2023.1214693
Moissenet, F., Modenese, L. and Dumas, R. 2017. Alterations of musculoskeletal models for a more accurate estimation of lower limb joint contact forces during normal gait: A systematic review. *J Biomech* 63, pp. 8-20.doi: 10.1016/j.jbiomech.2017.08.025
Mononen, M., Julkunen, P., Töyräs, J., Jurvelin, J., Kiviranta, I. and Korhonen, R. 2011. Alterations in structure and properties of collagen network of osteoarthritic and repaired cartilage modify knee joint stresses. *Biomechanics and modeling in mechanobiology* 10, pp. 357-369.
Mononen, M. E., Jurvelin, J. S. and Korhonen, R. K. 2015. Implementation of a gait cycle loading into healthy and meniscectomised knee joint models with fibril-reinforced articular cartilage. *Comput Methods Biomech Biomed Engin* 18(2), pp. 141-152.doi: 10.1080/10255842.2013.783575
Mononen, M. E., Paz, A., Liukkonen, M. K. and Turunen, M. J. 2023. Atlas-based finite element analyses with simpler constitutive models predict personalized

progression of knee osteoarthritis: data from the osteoarthritis initiative. *Sci Rep* 13(1), p. 8888.doi: 10.1038/s41598-023-35832-y
Mononen, M. E., Tanska, P., Isaksson, H. and Korhonen, R. K. 2016. A Novel Method to Simulate the Progression of Collagen Degeneration of Cartilage in the Knee: Data from the Osteoarthritis Initiative. *Scientific reports* 6(1), p. 21415.doi: 10.1038/srep21415
Mooney, M. 1940. A Theory of Large Elastic Deformation. *Journal of applied physics* 11(9), pp. 582-592.doi: 10.1063/1.1712836
Moore, D. S., Notz, W. and Fligner, M. A. 2015. *The basic practice of statistics*. Seventh edition / David S. Moore, William I. Notz, Michael A. Fligner. ed. New York: W.H. Freeman and Company.
Mootanah, R. et al. 2014. Development and validation of a computational model of the knee joint for the evaluation of surgical treatments for osteoarthritis. *Comput Methods Biomech Biomed Engin* 17(13), pp. 1502-1517.doi: 10.1080/10255842.2014.899588
Morejon, A., Dalbo, P. L., Best, T. M., Jackson, A. R. and Travascio, F. 2023. Tensile energy dissipation and mechanical properties of the knee meniscus: relationship with fiber orientation, tissue layer, and water content. *Front Bioeng Biotechnol* 11, p. 1205512.doi: 10.3389/fbioe.2023.1205512
Moro-oka, T. A. et al. 2007. Can magnetic resonance imaging-derived bone models be used for accurate motion measurement with single-plane three-dimensional shape registration? *J Orthop Res* 25(7), pp. 867-872.doi: 10.1002/jor.20355
Mow, V. C., Gibbs, M., Lai, W. M., Zhu, W. and Athanasiou, K. A. 1989. Biphasic indentation of articular cartilage—II. A numerical algorithm and an experimental study. *Journal of biomechanics* 22(8-9), pp. 853-861.
Mow, V. C. and Huiskes, R. 2005. *Basic orthopaedic biomechanics & mechano-biology*. Lippincott Williams & Wilkins.
Mukherjee, S., Nazemi, M., Jonkers, I. and Geris, L. 2020. Use of Computational Modeling to Study Joint Degeneration: A Review. *Front Bioeng Biotechnol* 8, p. 93.doi: 10.3389/fbioe.2020.00093
Myers, C. A. et al. 2011. Measurements of tibiofemoral kinematics during soft and stiff drop landings using biplane fluoroscopy. *Am J Sports Med* 39(8), pp. 1714-1722.doi: 10.1177/0363546511404922

Myers, C. A., Torry, M. R., Shelburne, K. B., Giphart, J. E., LaPrade, R. F., Woo, S. L. and Steadman, J. R. 2012. In vivo tibiofemoral kinematics during 4 functional tasks of increasing demand using biplane fluoroscopy. *Am J Sports Med* 40(1), pp. 170-178.doi: 10.1177/0363546511423746

Nagai, K., Gale, T., Chiba, D., Su, F., Fu, F. and Anderst, W. 2019. The Complex Relationship Between In Vivo ACL Elongation and Knee Kinematics During Walking and Running. *J Orthop Res* 37(9), pp. 1920-1928.doi: 10.1002/jor.24330

Nagai, K., Gale, T., Irrgang, J. J., Tashman, S., Fu, F. H. and Anderst, W. 2018. Anterior Cruciate Ligament Reconstruction Affects Tibiofemoral Joint Congruency During Dynamic Functional Movement. *The American Journal of Sports Medicine* 46(7), pp. 1566-1574.doi: 10.1177/0363546518764675

Navacchia, A., Hume, D. R., Rullkoetter, P. J. and Shelburne, K. B. 2019. A computationally efficient strategy to estimate muscle forces in a finite element musculoskeletal model of the lower limb. *J Biomech* 84, pp. 94-102.doi: 10.1016/j.jbiomech.2018.12.020

Neubert, A. et al. 2017. Comparison of 3D bone models of the knee joint derived from CT and 3T MR imaging. *Eur J Radiol* 93, pp. 178-184.doi: 10.1016/j.ejrad.2017.05.042

Nha, K. W., Papannagari, R., Gill, T. J., Van de Velde, S. K., Freiberg, A. A., Rubash, H. E. and Li, G. 2008. In vivo patellar tracking: clinical motions and patellofemoral indices. *J Orthop Res* 26(8), pp. 1067-1074.doi: 10.1002/jor.20554

Nilsson, K. G., Karrholm, J. and Ekelund, L. 1990. Knee Motion in Total Knee Arthroplasty: A Roentgen Stereophotogrammetric Analysis of the Kinematics of the Tricon-M Knee Prosthesis. *Clinical Orthopaedics and Related Research* 256, pp. 147-161.

Oka, T., Wada, O., Asai, T., Maruno, H. and Mizuno, K. 2020. Importance of knee flexion range of motion during the acute phase after total knee arthroplasty. *Phys Ther Res* 23(2), pp. 143-148.doi: 10.1298/ptr.E9996

Pandy, M. G. and Andriacchi, T. P. 2010. Muscle and joint function in human locomotion. *Annu Rev Biomed Eng* 12, pp. 401-433.doi: 10.1146/annurev-bioeng-070909-105259

Pataky, T. C. 2012. One-dimensional statistical parametric mapping in Python. *Comput Methods Biomech Biomed Engin* 15(3), pp. 295-301.doi: 10.1080/10255842.2010.527837

Pavao, S. L., dos Santos, A. N., Woollacott, M. H. and Rocha, N. A. 2013. Assessment of postural control in children with cerebral palsy: a review. *Res Dev Disabil* 34(5), pp. 1367-1375.doi: 10.1016/j.ridd.2013.01.034

Paz, A., Orozco, G. A., Korhonen, R. K., García, J. J. and Mononen, M. E. 2021. Expediting Finite Element Analyses for Subject-Specific Studies of Knee Osteoarthritis: A Literature Review. *Applied Sciences* 11(23).doi: 10.3390/app112311440

Peloquin, J. M., Santare, M. H. and Elliott, D. M. 2016. Advances in quantification of meniscus tensile mechanics including nonlinearity, yield, and failure. *Journal of Biomechanical Engineering* 138(2), p. 021002.

Peña, E., Calvo, B., Martinez, M. and Doblare, M. 2006. A three-dimensional finite element analysis of the combined behavior of ligaments and menisci in the healthy human knee joint. *Journal of biomechanics* 39(9), pp. 1686-1701.

Peña, E., Calvo, B., Martínez, M. and Doblaré, M. 2008. Computer simulation of damage on distal femoral articular cartilage after meniscectomies. *Computers in Biology and Medicine* 38(1), pp. 69-81.

Peña, E., Pérez del Palomar, A., Calvo, B., Martínez, M. and Doblaré, M. 2007. Computational modelling of diarthrodial joints. Physiological, pathological and post-surgery simulations. *Archives of Computational Methods in Engineering* 14, pp. 47-91.

Périé, D. and Hobatho, M. 1998. In vivo determination of contact areas and pressure of the femorotibial joint using non-linear finite element analysis. *Clinical Biomechanics* 13(6), pp. 394-402.

Peters, A. E., Akhtar, R., Comerford, E. J. and Bates, K. T. 2018. Tissue material properties and computational modelling of the human tibiofemoral joint: a critical review. *PeerJ* 6, p. e4298.doi: 10.7717/peerj.4298

Petersen, W. and Tillmann, B. 1998. Collagenous fibril texture of the human knee joint menisci. *Anatomy and embryology* 197(4), pp. 317-324.

Petrucci, M. 2024. *OpenSim Documentation: See the Work*. Available at: https://opensimconfluence.atlassian.net/wiki/spaces/OpenSim/pages/100139009/See+the+Work [Accessed: 11 March 2025].

Pitcairn, S., Kromka, J., Hogan, M. and Anderst, W. 2020. Validation and application of dynamic biplane radiography to study in vivo ankle joint kinematics during high-demand activities. *J Biomech* 103, p. 109696.doi: 10.1016/j.jbiomech.2020.109696

Pitcairn, S., Lesniak, B. and Anderst, W. 2018. In vivo validation of patellofemoral kinematics during overground gait and stair ascent. *Gait Posture* 64, pp. 191-197.doi: 10.1016/j.gaitpost.2018.06.028
Postolka, B., Schutz, P., Fucentese, S. F., Freeman, M. A. R., Pinskerova, V., List, R. and Taylor, W. R. 2020. Tibio-femoral kinematics of the healthy knee joint throughout complete cycles of gait activities. *J Biomech* 110, p. 109915.doi: 10.1016/j.jbiomech.2020.109915
Potocnik, B., Zazula, D., Cigale, B., Heric, D., Cibula, E. and Tomazic, T. 2008. A Patient-specific Knee Joint Computer Model Using MRI Data and 'in vivo' Compressive Load from the Optical Force Measuring System. *Journal of Computing and Information Technology* 16(3).doi: 10.2498/cit.1001126
Price, P. D. B., Gissane, C. and Cleather, D. J. 2020. The influence of pain on tibiofemoral joint contact force and muscle forces in knee osteoarthritis patients during stair ascent. *Engineering Reports* 2(9).doi: 10.1002/eng2.12227
Prieto-Alhambra, D., Judge, A., Javaid, M. K., Cooper, C., Diez-Perez, A. and Arden, N. K. 2014. Incidence and risk factors for clinically diagnosed knee, hip and hand osteoarthritis: influences of age, gender and osteoarthritis affecting other joints. *Annals of the Rheumatic Diseases* 73(9), pp. 1659-1664.doi: 10.1136/annrheumdis-2013-203355
Qi, W., Hosseini, A., Tsai, T. Y., Li, J. S., Rubash, H. E. and Li, G. 2013. In vivo kinematics of the knee during weight bearing high flexion. *J Biomech* 46(9), pp. 1576-1582.doi: 10.1016/j.jbiomech.2013.03.014
Rainbow, M. J., Miranda, D. L., Cheung, R. T., Schwartz, J. B., Crisco, J. J., Davis, I. S. and Fleming, B. C. 2013. Automatic determination of an anatomical coordinate system for a three-dimensional model of the human patella. *J Biomech* 46(12), pp. 2093-2096.doi: 10.1016/j.jbiomech.2013.05.024
Ramsey, D. K. and Wretenberg, P. 1999. Biomechanics of the knee: methodological considerations in the in vivo kinematic analysis of the tibiofemoral and patellofemoral joint. *Clinical Biomechanics* 14, pp. 595-611.
Ramsey, D. K., Wretenberg, P. F., Benoit, D. L., Lamontagne, M. and Nemeth, G. 2003. Methodological concerns using intra-cortical pins to measure tibiofemoral kinematics. *Knee Surg Sports Traumatol Arthrosc* 11(5), pp. 344-349.doi: 10.1007/s00167-003-0388-1

Rathnayaka, K., Momot, K. I., Noser, H., Volp, A., Schuetz, M. A., Sahama, T. and Schmutz, B. 2012. Quantification of the accuracy of MRI generated 3D models of long bones compared to CT generated 3D models. *Med Eng Phys* 34(3), pp. 357-363.doi: 10.1016/j.medengphy.2011.07.027

Reinschmidt, C., van de Bogert, A. J., Nigg, B. M., Lundberg, A. and Murphy, N. 1997a. Effect of skin movement on the analysis of skeletal knee joint motion during running. *J Biomech* 30, pp. 729-732.

Reinschmidt, C., van den Bogert, A. J., Lundberg, A., Nigg, B. M., Murphy, N. and Stacoff, A. S., A. 1997b. Tibiofemoral and tibiocalcaneal motion during walking: external vs. skeletal markers. *Gait & Posture* 6, pp. 98-109.

Richards, R. E., Andersen, M. S., Harlaar, J. and van den Noort, J. C. 2018. Relationship between knee joint contact forces and external knee joint moments in patients with medial knee osteoarthritis: effects of gait modifications. *Osteoarthritis Cartilage* 26(9), pp. 1203-1214.doi: 10.1016/j.joca.2018.04.011

Ridhma, Kaur, M., Sofat, S. and Chouhan, D. K. 2020. Review of automated segmentation approaches for knee images. *IET Image Processing* 15(2), pp. 302-324.doi: 10.1049/ipr2.12045

Rivlin, R. S. 1948. Large elastic deformations of isotropic materials. II. Some uniqueness theorems for pure, homogeneous deformation. *Philosophical Transactions of the Royal Society of London, Series A: Mathematical and Physical Sciences* 240, p. 459.

Rivlin, R. S. 1949a. Large elastic deformations of isotropic materials. V. The problem of flexure. *Proceedings of the Royal Society of London. Series A, Mathematical and physical sciences* 195(1043), pp. 463-473.doi: 10.1098/rspa.1949.0004

Rivlin, R. S. 1949b. Large Elastic Deformations of Isotropic Materials. VI. Further Results in the Theory of Torsion, Shear and Flexure. *Philosophical transactions of the Royal Society of London. Series A: Mathematical and physical sciences* 242(845), pp. 173-195.doi: 10.1098/rsta.1949.0009

Roos, E. M., Roos, H. P., Lohmander, L. S., Ekdahl, C. and Beynnon, B. D. 1998. Knee Injury and Osteoarthritis Outcome Score (KOOS)--development of a self-administered outcome measure. *J Orthop Sports Phys Ther* 28(2), pp. 88-96.doi: 10.2519/jospt.1998.28.2.88

Rudin, S., Bednarek, D. R. and Wong, R. 1991. Accurate characterization of image intensifier distortion. *Medical Physics* 18(6), pp. 1145-1151.

Rullkoetter, P. J., Fitzpatrick, C. K. and Clary, C. W. 2017. How Can We Use Computational Modeling to Improve Total Knee Arthroplasty? Modeling Stability and Mobility in the Implanted Knee. *J Am Acad Orthop Surg* 25 Suppl 1, pp. S33-S39.doi: 10.5435/JAAOS-D-16-00640

Russakoff, D. B., Rohlfing, T., Mori, K., Rueckert, D., Ho, A., Adler, J. R., Jr. and Maurer, C. R., Jr. 2005. Fast generation of digitally reconstructed radiographs using attenuation fields with application to 2D-3D image registration. *IEEE Trans Med Imaging* 24(11), pp. 1441-1454.doi: 10.1109/TMI.2005.856749

Salarian, A., Russmann, H., Vingerhoets, F. J., Dehollain, C., Blanc, Y., Burkhard, P. R. and Aminian, K. 2004. Gait assessment in Parkinson's disease: toward an ambulatory system for long-term monitoring. *IEEE Trans Biomed Eng* 51(8), pp. 1434-1443.doi: 10.1109/TBME.2004.827933

Sati, M., de Guise, J. A., Larouche, S. and Drouin, G. 1996. Quantitative assessment of skin-bone movement at the knee. *The Knee* 3, pp. 121-138.

Sawacha, Z. et al. 2012. Biomechanical assessment of balance and posture in subjects with ankylosing spondylitis. *Journal of NeuroEngineering and Rehabilitation* 9, p. 63.doi: 10.1186/1743-0003-9-63

Schwechter, E. M. and Fitz, W. 2012. Design rationale for customized TKA: a new idea or revisiting the past? *Curr Rev Musculoskelet Med* 5(4), pp. 303-308.doi: 10.1007/s12178-012-9143-x

Scovil, C. Y. and Ronsky, J. L. 2006. Sensitivity of a Hill-based muscle model to perturbations in model parameters. *J Biomech* 39(11), pp. 2055-2063.doi: 10.1016/j.jbiomech.2005.06.005

Seeley, M. K., Lee, H., Son, S. J., Timmerman, M., Lindsay, M. and Hopkins, J. T. 2022. A Review of the Relationships Between Knee Pain and Movement Neuromechanics. *Journal of Sport Rehabilitation* 31(6), pp. 684-693.doi: 10.1123/jsr.2021-0020

Segal, N. A. et al. 2009. Baseline articular contact stress levels predict incident symptomatic knee osteoarthritis development in the MOST cohort. *J Orthop Res* 27(12), pp. 1562-1568.doi: 10.1002/jor.20936

Seth, A. et al. 2018. OpenSim: Simulating musculoskeletal dynamics and neuromuscular control to study human and animal movement. *PLoS Comput Biol* 14(7), p. e1006223.doi: 10.1371/journal.pcbi.1006223

Setliff, J. C. and Anderst, W. J. 2024. A scoping review of human skeletal kinematics research using biplane radiography. *J Orthop Res* 42(5), pp. 915-922.doi: 10.1002/jor.25806
Sharma, L., Song, J., Felson, D. T., Cahue, S., Shamiyeh, E. and Dunlop, D. D. 2001. The Role of Knee Alignment in Disease Progression and Functional Decline in Knee Osteoarthritis. *Jama* 286(2), pp. 188-195.doi: 10.1001/jama.286.2.188
Shih, K. S., Lin, C. C., Lu, H. L., Fu, Y. C., Lin, C. K., Li, S. Y. and Lu, T. W. 2020. Patient-specific instrumentation improves functional kinematics of minimally-invasive total knee replacements as revealed by computerized 3D fluoroscopy. *Comput Methods Programs Biomed* 188, p. 105250.doi: 10.1016/j.cmpb.2019.105250
Shirazi, R. and Shirazi-Adl, A. 2009. Computational biomechanics of articular cartilage of human knee joint: Effect of osteochondral defects. *Journal of biomechanics* 42(15), pp. 2458-2465.doi: https://doi.org/10.1016/j.jbiomech.2009.07.022
Shriram, D., Praveen Kumar, G., Cui, F., Lee, Y. H. D. and Subburaj, K. 2017. Evaluating the effects of material properties of artificial meniscal implant in the human knee joint using finite element analysis. *Scientific reports* 7(1), p. 6011.
Shu, L., Yamamoto, K., Yao, J., Saraswat, P., Liu, Y., Mitsuishi, M. and Sugita, N. 2018. A subject-specific finite element musculoskeletal framework for mechanics analysis of a total knee replacement. *J Biomech* 77, pp. 146-154.doi: 10.1016/j.jbiomech.2018.07.008
Shu, L., Yao, J., Yamamoto, K., Sato, T. and Sugita, N. 2021. In vivo kinematical validated knee model for preclinical testing of total knee replacement. *Comput Biol Med* 132, p. 104311.doi: 10.1016/j.compbiomed.2021.104311
Sinusas, K. 2012. Osteoarthritis: diagnosis and treatment. *American family physician* 85(1), pp. 49-56.
Smith, C. R. 2017. *Simulating the effects of Anterior Cruciate Ligament Injury and Treatment on Cartilage Loading during Walking.* Wisconsin-Madison.
Smith, C. R., Choi, K. W., Negrut, D. and Thelen, D. G. 2018. Efficient Computation of Cartilage Contact Pressures within Dynamic Simulations of Movement. *Comput Methods Biomech Biomed Eng Imaging Vis* 6(5), pp. 491-498.doi: 10.1080/21681163.2016.1172346

Smith, C. R., Lenhart, R. L., Kaiser, J., Vignos, M. F. and Thelen, D. G. 2016. Influence of Ligament Properties on Tibiofemoral Mechanics in Walking. *J Knee Surg* 29(2), pp. 99-106.doi: 10.1055/s-0035-1558858

Söderkvist, I. and Wedin, P. A. 1993. Determining the movements of the skeleton using well-configured markers. *J Biomech* 26(12), pp. 1473-1477.

Stagni, R., Fantozzi, S., Cappello, A. and Leardini, A. 2005. Quantification of soft tissue artefact in motion analysis by combining 3D fluoroscopy and stereophotogrammetry: a study on two subjects. *Clin Biomech* 20(3), pp. 320-329.doi: 10.1016/j.clinbiomech.2004.11.012

Standring, S. M. B. E. P. D. F. K. C. H. F. A. S. H. F. 2021. Knee and leg. In: Standring, S.M.B.E.P.D.F.K.C.H.F.A.S.H.F. ed. *Gray's Anatomy*. pp. 1395-1429.e1392. Available at: https://www.clinicalkey.com/student/content/book/3-s2.0-B9780702077050000781doi: http://dx.doi.org/10.1016/B978-0-7020-7705-0.00078-1

Steineman, B. D., LaPrade, R. F. and Haut Donahue, T. L. 2022. Loosening of Posteromedial Meniscal Root Repairs Affects Knee Mechanics: A Finite Element Study. *J Biomech Eng* 144(5).doi: 10.1115/1.4053100

Sutter, E. G., Widmyer, M. R., Utturkar, G. M., Spritzer, C. E., Garrett, W. E., Jr. and DeFrate, L. E. 2015. In vivo measurement of localized tibiofemoral cartilage strains in response to dynamic activity. *Am J Sports Med* 43(2), pp. 370-376.doi: 10.1177/0363546514559821

Suzuki, T., Hosseini, A., Li, J. S., Gill, T. J. t. and Li, G. 2012. In vivo patellar tracking and patellofemoral cartilage contacts during dynamic stair ascending. *J Biomech* 45(14), pp. 2432-2437.doi: 10.1016/j.jbiomech.2012.06.034

Sylvester, A. D., Lautzenheiser, S. G. and Kramer, P. A. 2021. A review of musculoskeletal modelling of human locomotion. *Interface Focus* 11(5), p. 20200060.doi: 10.1098/rsfs.2020.0060

Synopsys. 2022. Simpleware FE Technical Datasheet. *Release Version U-2022.12*.

Synopsys. 2024. Simpleware Reference Guide: Recursive Gaussian.

Szopinski, K. T. and Adamczyk, P. 2018. Interposition of the transverse ligament of the knee into a fracture of the tibial plateau: a case report. *Skeletal Radiol* 47(7), pp. 1011-1014.doi: 10.1007/s00256-018-2883-y

Takasaki, H., Hall, T. and Jull, G. 2013. Immediate and short-term effects of Mulligan's mobilization with movement on knee pain and disability associated with

knee osteoarthritis--a prospective case series. *Physiother Theory Pract* 29(2), pp. 87-95.doi: 10.3109/09593985.2012.702854
Tanaka, T., Gale, T., Nishida, K., Xu, C., Fu, F. and Anderst, W. 2023. Posterior tibial slope and meniscal slope correlate with in vivo tibial internal rotation during running and drop jump. *Knee Surg Sports Traumatol Arthrosc* 31(6), pp. 2366-2373.doi: 10.1007/s00167-022-07163-4
Tarniţă, D., Catana, M. and Tarnita, D. N. 2014. Modeling and Finite Element Analysis of the Human Knee Joint Affected by Osteoarthritis. *Key Engineering Materials* 601, pp. 147-150.doi: 10.4028/www.scientific.net/KEM.601.147
Tashman, S., Collon, D., Anderson, K., Kolowich, P. and Anderst, W. 2004. Abnormal rotational knee motion during running after anterior cruciate ligament reconstruction. *Am J Sports Med* 32(4), pp. 975-983.doi: 10.1177/0363546503261709
Tashman, S., Kolowich, P., Collon, D., Anderson, K. and Anderst, W. 2007. Dynamic function of the ACL-reconstructed knee during running. *Clin Orthop Relat Res* 454, pp. 66-73.doi: 10.1097/BLO.0b013e31802bab3e
Taylor, K. D., Mottier, F. M., Simmons, D. W., Cohen, W., Pavlak, R., Jr., Cornell, D. P. and Hankins, G. B. 1982. An automated motion measurement system for clinical gait analysis. *J Biomech* 15(7), pp. 505-516.
Thakkar, R. S., Flammang, A. J., Chhabra, A., Padua, A. and Carrino, J. A. 2011. 3T MR Imaging of Cartilage using 3D Dual Echo Steady State (DESS). *Orthopedic Imaging Clinical*, pp. 33-36.
Thelen, D. G., Won Choi, K. and Schmitz, A. M. 2014. Co-simulation of neuromuscular dynamics and knee mechanics during human walking. *J Biomech Eng* 136(2), p. 021033.doi: 10.1115/1.4026358
Thienkarochanakul, K., Javadi, A. A., Akrami, M., Charnley, J. R. and Benattayallah, A. 2020. Stress Distribution of the Tibiofemoral Joint in a Healthy Versus Osteoarthritis Knee Model Using Image-Based Three-Dimensional Finite Element Analysis. *Journal of Medical and Biological Engineering* 40(3), pp. 409-418.doi: 10.1007/s40846-020-00523-w
Thomeer, L., Guan, S., Gray, H., Schache, A., de Steiger, R. and Pandy, M. 2021. Six-Degree-of-Freedom Tibiofemoral and Patellofemoral Joint Motion During Activities of Daily Living. *Ann Biomed Eng* 49(4), pp. 1183-1198.doi: 10.1007/s10439-020-02646-2

Thomeer, L. T., Guan, S., Gray, H. A. and Pandy, M. G. 2022. Articular contact motion at the knee during daily activities. *J Orthop Res* 40(8), pp. 1756-1769.doi: 10.1002/jor.25222

Thomeer, L. T., Lin, Y. C. and Pandy, M. G. 2020. Load Distribution at the Patellofemoral Joint During Walking. *Ann Biomed Eng* 48(12), pp. 2821-2835.doi: 10.1007/s10439-020-02672-0

Thorhauer, E. and Tashman, S. 2015. Validation of a method for combining biplanar radiography and magnetic resonance imaging to estimate knee cartilage contact. *Med Eng Phys* 37(10), pp. 937-947.doi: 10.1016/j.medengphy.2015.07.002

Torry, M. R. et al. 2011a. Relationship of knee shear force and extensor moment on knee translations in females performing drop landings: a biplane fluoroscopy study. *Clin Biomech* 26(10), pp. 1019-1024.doi: 10.1016/j.clinbiomech.2011.06.010

Torry, M. R. et al. 2011b. Knee kinematic profiles during drop landings: a biplane fluoroscopy study. *Med Sci Sports Exerc* 43(3), pp. 533-541.doi: 10.1249/MSS.0b013e3181f1e491

Trad, Z., Barkaoui, A. and Chafra, M. 2017. A Three Dimensional Finite Element Analysis of Mechanical Stresses in the Human Knee Joint: Problem of Cartilage Destruction. *Journal of Biomimetics, Biomaterials and Biomedical Engineering* 32, pp. 29-39.doi: 10.4028/www.scientific.net/jbbbe.32.29

Tranberg, R., Saari, T., Zugner, R. and Karrholm, J. 2011. Simultaneous measurements of knee motion using an optical tracking system and radiostereometric analysis (RSA). *Acta Orthop* 82(2), pp. 171-176.doi: 10.3109/17453674.2011.570675

Treloar, L. R. G. 1943a. The elasticity of a network of long-chain molecules—II. *Transactions of the Faraday Society* 39, pp. 241-246.doi: 10.1039/TF9433900241

Treloar, L. R. G. 1943b. The elasticity of a network of long-chain molecules. I. *Transactions of the Faraday Society* 39, pp. 36-41.doi: 10.1039/tf9433900036

Trent, P. S., Walker, P. S. and Wolf, B. 1976. Ligament length patterns, strength, and rotational axes of the knee joint. *Clinical Orthopaedics and Related Research (1976-2007)* 117, pp. 263-270.

Tsai, T. Y., Lu, T. W., Kuo, M. Y. and Lin, C. C. 2011. Effects of soft tissue artifacts on the calculated kinematics and kinetics of the knee during stair-ascent. *J Biomech* 44(6), pp. 1182-1188.doi: 10.1016/j.jbiomech.2011.01.009

Ulbricht, H., Hou, M., Wang, X., He, J. and Zhang, Y. 2020. The Effect of Correction Algorithms on Knee Kinematics and Kinetics during Gait of Patients with Knee Osteoarthritis. *Appl Bionics Biomech* 2020, p. 8854124.doi: 10.1155/2020/8854124

Uzuner, S., Kuntze, G., Li, L. P., Ronsky, J. L. and Kucuk, S. 2022. Creep behavior of human knee joint determined with high-speed biplanar video-radiography and finite element simulation. *J Mech Behav Biomed Mater* 125, p. 104905.doi: 10.1016/j.jmbbm.2021.104905

Valstar, E. R., Gill, R., Ryd, L., Flivik, G., Börlin, N. and Kärrholm, J. 2005. Guidelines for standardization of radiostereometry (RSA) of implants. *Acta Orthop* 76(4), pp. 563-572.doi: 10.1080/17453670510041574

Van de Velde, S. K., Bingham, J. T., Hosseini, A., Kozanek, M., DeFrate, L. E., Gill, T. J. and Li, G. 2009a. Increased tibiofemoral cartilage contact deformation in patients with anterior cruciate ligament deficiency. *Arthritis Rheum* 60(12), pp. 3693-3702.doi: 10.1002/art.24965

Van de Velde, S. K., Gill, T. J. and Li, G. 2009b. Dual fluoroscopic analysis of the posterior cruciate ligament-deficient patellofemoral joint during lunge. *Med Sci Sports Exerc* 41(6), pp. 1198-1205.doi: 10.1249/MSS.0b013e3181981eb5

Van de Velde, S. K., Kernkamp, W. A., Hosseini, A., LaPrade, R. F., van Arkel, E. R. and Li, G. 2016. In Vivo Length Changes of the Anterolateral Ligament and Related Extra-articular Reconstructions. *Am J Sports Med* 44(10), pp. 2557-2562.doi: 10.1177/0363546516651431

van Rossom, S., Smith, C. R., Thelen, D. G., Vanwanseele, B., Van Assche, D. and Jonkers, I. 2018. Knee Joint Loading in Healthy Adults During Functional Exercises: Implications for Rehabilitation Guidelines. *J Orthop Sports Phys Ther* 48(3), pp. 162-173.doi: 10.2519/jospt.2018.7459

van Tunen, J. A. C., Dell'Isola, A., Juhl, C., Dekker, J., Steultjens, M., Thorlund, J. B. and Lund, H. 2018. Association of malalignment, muscular dysfunction, proprioception, laxity and abnormal joint loading with tibiofemoral knee osteoarthritis - a systematic review and meta-analysis. *BMC Musculoskelet Disord* 19(1), p. 273.doi: 10.1186/s12891-018-2202-8

Vaziri, A., Nayeb-Hashemi, H., Singh, A. and Tafti, B. A. 2008. Influence of meniscectomy and meniscus replacement on the stress distribution in human knee joint. *Annals of Biomedical Engineering* 36, pp. 1335-1344.

Veerkamp, K., Kainz, H., Killen, B. A., Jonasdottir, H. and van der Krogt, M. M. 2021. Torsion Tool: An automated tool for personalising femoral and tibial geometries in OpenSim musculoskeletal models. *J Biomech* 125, p. 110589.doi: 10.1016/j.jbiomech.2021.110589

Vincent, K. R., Conrad, B. P., Fregly, B. J. and Vincent, H. K. 2012. The pathophysiology of osteoarthritis: a mechanical perspective on the knee joint. *PM R* 4(5 Suppl), pp. S3-9.doi: 10.1016/j.pmrj.2012.01.020

Wade, L., Needham, L., McGuigan, P. and Bilzon, J. 2022. Applications and limitations of current markerless motion capture methods for clinical gait biomechanics. *PeerJ* 10, p. e12995.doi: 10.7717/peerj.12995

Walker, P. S. and Erkiuan, M. J. 1975. The role of the menisci in force transmission across the knee. *Clinical Orthopaedics and Related Research*® 109, pp. 184-192.

Wan, Y., McGuigan, P., Bilzon, J. and Wade, L. 2024. The effect of foot orientation modifications on knee joint biomechanics during daily activities in people with and without knee osteoarthritis. *Clin Biomech (Bristol)* 117, p. 106287.doi: 10.1016/j.clinbiomech.2024.106287

Wang, F. et al. 2024. Detection of kinematic abnormalities in persons with knee osteoarthritis using markerless motion capture during functional movement screen and daily activities. *Front Bioeng Biotechnol* 12, p. 1325339.doi: 10.3389/fbioe.2024.1325339

Wang, R. et al. 2022. Clarify Sit-to-Stand Muscle Synergy and Tension Changes in Subacute Stroke Rehabilitation by Musculoskeletal Modeling. *Front Syst Neurosci* 16, p. 785143.doi: 10.3389/fnsys.2022.785143

Weiss, J. A. and Gardiner, J. C. 2001. Computational modeling of ligament mechanics. *Critical Reviews™ in Biomedical Engineering* 29(3).

Weiss, J. M. et al. 2002. What functional activities are important to patients with knee replacements? *Clin Orthop Relat Res* 404, pp. 172-188.doi: 10.1097/00003086-200211000-00030

Welte, L., Dickinson, A., Arndt, A. and Rainbow, M. J. 2022. Biplanar Videoradiography Dataset for Model-based Pose Estimation Development and New User Training. *J Vis Exp* (183).doi: 10.3791/63535

Whatling, G. M., Biggs, P. R., Elson, D. W., Metcalfe, A., Wilson, C. and Holt, C. 2020. High tibial osteotomy results in improved frontal plane knee moments, gait

patterns and patient-reported outcomes. *Knee Surg Sports Traumatol Arthrosc* 28(9), pp. 2872-2882.doi: 10.1007/s00167-019-05644-7
Widmyer, M. R. et al. 2013. High body mass index is associated with increased diurnal strains in the articular cartilage of the knee. *Arthritis Rheum* 65(10), pp. 2615-2622.doi: 10.1002/art.38062
Williams, D. E. 2018. *Development and Validation of a Biplane Fluoroscopy System to Quantify In-Vivo Knee Kinematics.* Cardiff.
Williams, D. E., Rainbow, M. J., Yoon, D., Criso, J. J. and Welte, L. 2026. Less is more: downsampling x-ray images improves pose estimation accuracy. *Medical Engineering & Physics* 147(2).doi: 10.1088/1873-4030/ae2909
Willing, R. T., Lalone, E. A., Shannon, H., Johnson, J. A. and King, G. J. 2013. Validation of a finite element model of the human elbow for determining cartilage contact mechanics. *J Biomech* 46(10), pp. 1767-1771.doi: 10.1016/j.jbiomech.2013.04.001
Wilson, W., Van Rietbergen, B., Van Donkelaar, C. and Huiskes, R. 2003. Pathways of load-induced cartilage damage causing cartilage degeneration in the knee after meniscectomy. *Journal of biomechanics* 36(6), pp. 845-851.
Wu, G. et al. 2002. ISB recommendation on definitions of joint coordinate system of various joints for the reporting of human joint motion—part I: ankle, hip, and spine. *J Biomech* 35, pp. 543-548.
Wyndow, N., Collins, N., Vicenzino, B., Tucker, K. and Crossley, K. 2016. Is There a Biomechanical Link Between Patellofemoral Pain and Osteoarthritis? A Narrative Review. *Sports Medicine* 46(12), pp. 1797-1808.doi: 10.1007/s40279-016-0545-6
Xiao, Y., Ling, M., Liang, Z., Ding, J., Zhan, S., Hu, H. and Chen, B. 2021. Dual fluoroscopic imaging and CT-based finite element modelling to estimate forces and stresses of grafts in anatomical single-bundle ACL reconstruction with different femoral tunnels. *Int J Comput Assist Radiol Surg* 16(3), pp. 495-504.doi: 10.1007/s11548-021-02307-2
Yamagata, M., Taniguchi, M., Tateuchi, H., Kobayashi, M. and Ichihashi, N. 2021. The effects of knee pain on knee contact force and external knee adduction moment in patients with knee osteoarthritis. *J Biomech* 123, p. 110538.doi: 10.1016/j.jbiomech.2021.110538

Yan, M., Liang, T., Zhao, H., Bi, Y., Wang, T., Yu, T. and Zhang, Y. 2024. Model Properties and Clinical Application in the Finite Element Analysis of Knee Joint: A Review. *Orthop Surg* 16(2), pp. 289-302.doi: 10.1111/os.13980

Yanez, R. et al. 2024. Finite element graft stress for anteromedial portal, transtibial, and hybrid transtibial femoral drillings under anterior translation and medial rotation: an exploratory study. *Sci Rep* 14(1), p. 11922.doi: 10.1038/s41598-024-61061-y

Yang, C., Tashiro, Y., Lynch, A., Fu, F. and Anderst, W. 2018. Kinematics and arthrokinematics in the chronic ACL-deficient knee are altered even in the absence of instability symptoms. *Knee Surg Sports Traumatol Arthrosc* 26(5), pp. 1406-1413.doi: 10.1007/s00167-017-4780-7

Yang, N. H., Nayeb-Hashemi, H., Canavan, P. K. and Vaziri, A. 2010. Effect of frontal plane tibiofemoral angle on the stress and strain at the knee cartilage during the stance phase of gait. *J Orthop Res* 28(12), pp. 1539-1547.doi: 10.1002/jor.21174

Yao, J., Crockett, J., D'Souza, M., G, A. D., R, K. W., A, C. J. and Mengoni, M. 2024. Effect of meniscus modelling assumptions in a static tibiofemoral finite element model: importance of geometry over material. *Biomech Model Mechanobiol* 23(3), pp. 1055-1065.doi: 10.1007/s10237-024-01822-w

Yao, J., Funkenbusch, P. D., Snibbe, J., Maloney, M. and Lerner, A. L. 2006. Sensitivities of medial meniscal motion and deformation to material properties of articular cartilage, meniscus and meniscal attachments using design of experiments methods.

Yao, J., Salo, A. D., Lee, J. and Lerner, A. L. 2008. Sensitivity of tibio-menisco-femoral joint contact behavior to variations in knee kinematics. *J Biomech* 41(2), pp. 390-398.doi: 10.1016/j.jbiomech.2007.08.015

Yeo, S. H., Verheul, J., Herzog, W. and Sueda, S. 2023. Numerical instability of Hill-type muscle models. *J R Soc Interface* 20(199), p. 20220430.doi: 10.1098/rsif.2022.0430

Yu, C.-H., Walker, P. S. and Dewar, M. E. 2001. The effect of design variables of condylar total knees on the joint forces in step climbing based on a computer model. *Journal of biomechanics* 34(8), pp. 1011-1021.doi: https://doi.org/10.1016/S0021-9290(01)00060-4

Zajac, F. 1989. Muscle and tendon: properties, models, scaling, and application to biomechanics and motor control. *Critical reviews in biomedical engineering* 17(4).

Zajec, F. 1989. Muscle and tendon properties, models, scaling, and application to biomechanics and motor control. *Critical reviews in biomedical engineering* 17(4), pp. 359-411.
Zdero, R., Brzozowski, P. and Schemitsch, E. H. 2023. Experimental Methods for Studying the Contact Mechanics of Joints. *Biomed Res Int* 2023, p. 4914082.doi: 10.1155/2023/4914082
Zdero, R., Mahboob, Z. and Bougherara, H. 2016. *Fujifilm Measurements of Interfacial Contact Area and Stress in Articulating Joints*. Amsterdam: Academic Press. doi: 10.1016/B978-0-12-803802-4.00016-0
Zelle, J., van de Groes, S. A. W., de Waal Malefijt, M. C. and Verdonschot, N. 2014. Femoral loosening of high-flexion total knee arthroplasty: The effect of posterior cruciate ligament retention and bone quality reduction. *Medical Engineering & Physics* 36(3), pp. 318-324.doi: https://doi.org/10.1016/j.medengphy.2013.11.015
Zhang, J. et al. 2014. The MAP Client: User-Friendly Musculoskeletal Modelling Workflows. In: *Biomedical Simulation*. pp. 182-192. doi: 10.1007/978-3-319-12057-7_21
Zhao, Y., Ding, S. and Todoh, M. 2022. Validate the force-velocity relation of the Hill's muscle model from a molecular perspective. *Front Bioeng Biotechnol* 10, p. 1006571.doi: 10.3389/fbioe.2022.1006571
Zielinska, B. and Donahue, T. L. 2006. 3D finite element model of meniscectomy: changes in joint contact behavior. *J Biomech Eng* 128(1), pp. 115-123.doi: 10.1115/1.2132370
Zink, J. V. et al. 2015. Standardized quantitative measurements of wrist cartilage in healthy humans using 3T magnetic resonance imaging. *World J Orthop* 6(8), pp. 641-648.doi: 10.5312/wjo.v6.i8.641

APPENDIX A: SYNCHRONISED BIPLANE X-RAY AND MOTION CAPTURE PROTOCOL

KNEE

SYNCHRONISED BIPLANE X-RAY & MOTION CAPTURE PROTOCOL

VERSION 1.1

05 AUGUST 2022

T0.15/T0.16 • MSKBRF • CARDIFF SCHOOL OF ENGINEERING

Table of Contents

1 SET UP - PRIOR TO PARTICIPANT

Print off the following forms before the participant arrives:

- **Participant information sheet and consent form (x2)** (*BBRCVA - Fluoroscopy - HVIS.CF - v12.1 clean.doc)* – just consent form needed for second copy.
- **Fluoroscopy screening form** *(ARUKBBC – Fluoroscopy – screening form PRB – v10 – CLEAN.docx)*
- **Informed consent checklist** *(BBRCVA CRF Informed Consent Checklist – v1.1.doc)*
- **Data collection visit form** *(BBRCVA CRF Visit – v2.doc)*
- **Knee X-ray Protocol Computer Sheet Checklist** (*KneeFluoroComputerSheet0.2.docm)* – update Participant ID and select relevant leg before printing.
- **Questionnaires:**
    - ***Knee Outcome Survey***
    - ***KOOS***
    - ***Oxford Knee Score***
    - ***PACS proforma***
    - ***WOMAC***

1.1 Motion Capture

1.1.1 Camera Positioning

12 motion capture cameras and 6 Miqus video cameras required. The same motion capture camera setup is used for left or right knee.

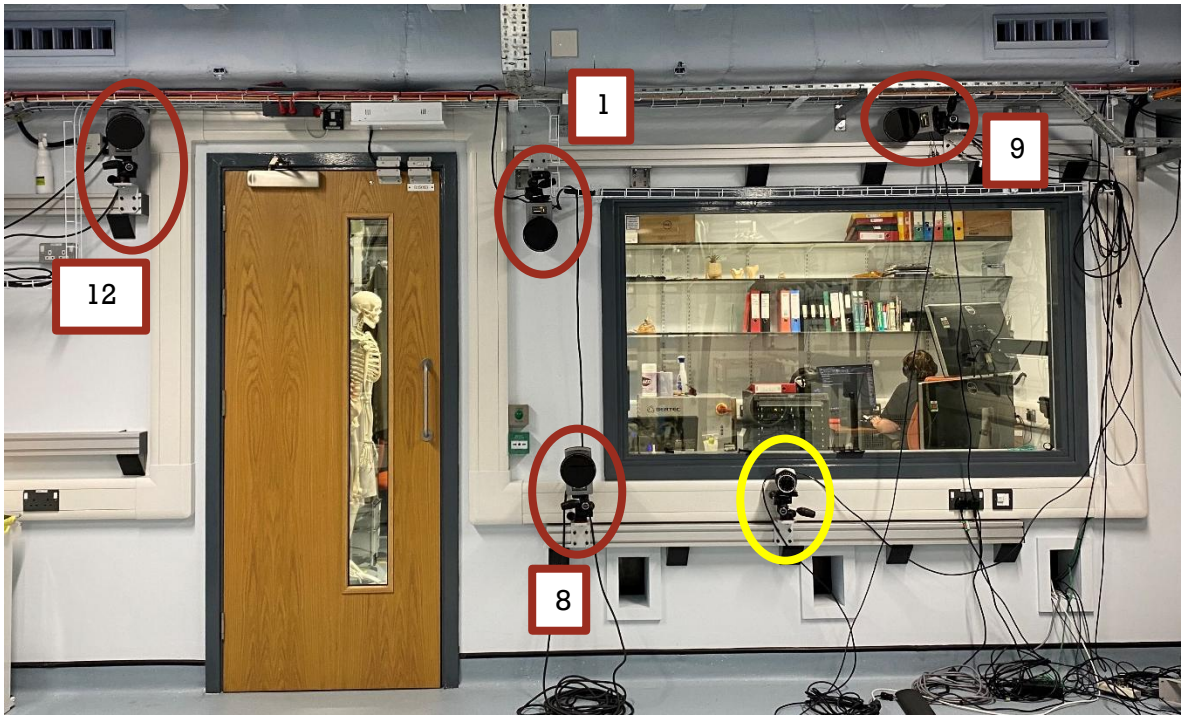

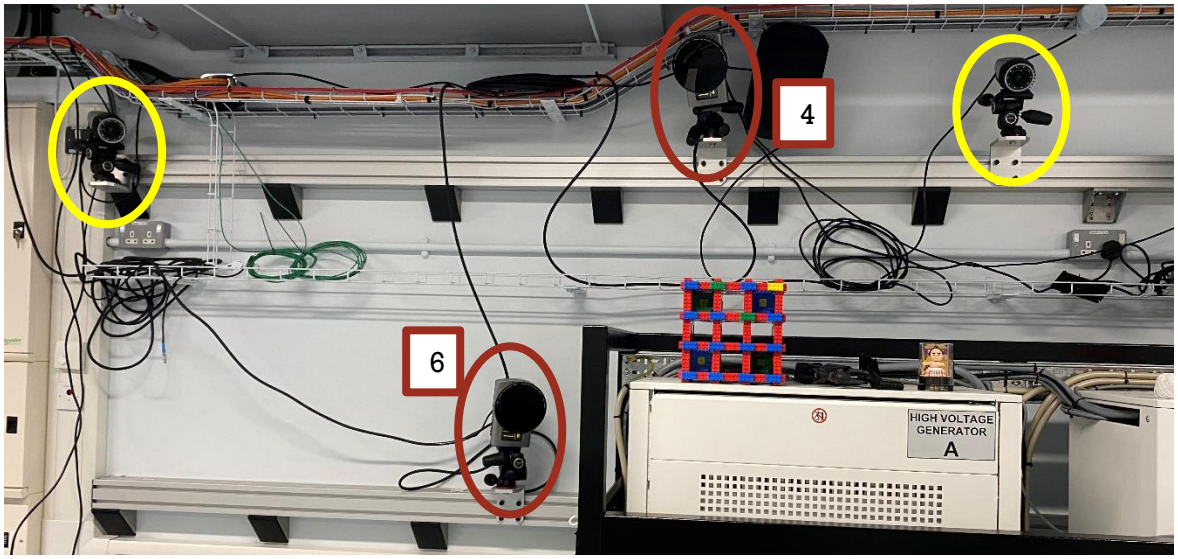
4
6
HIGH VOLTAGE
GENERATOR
A

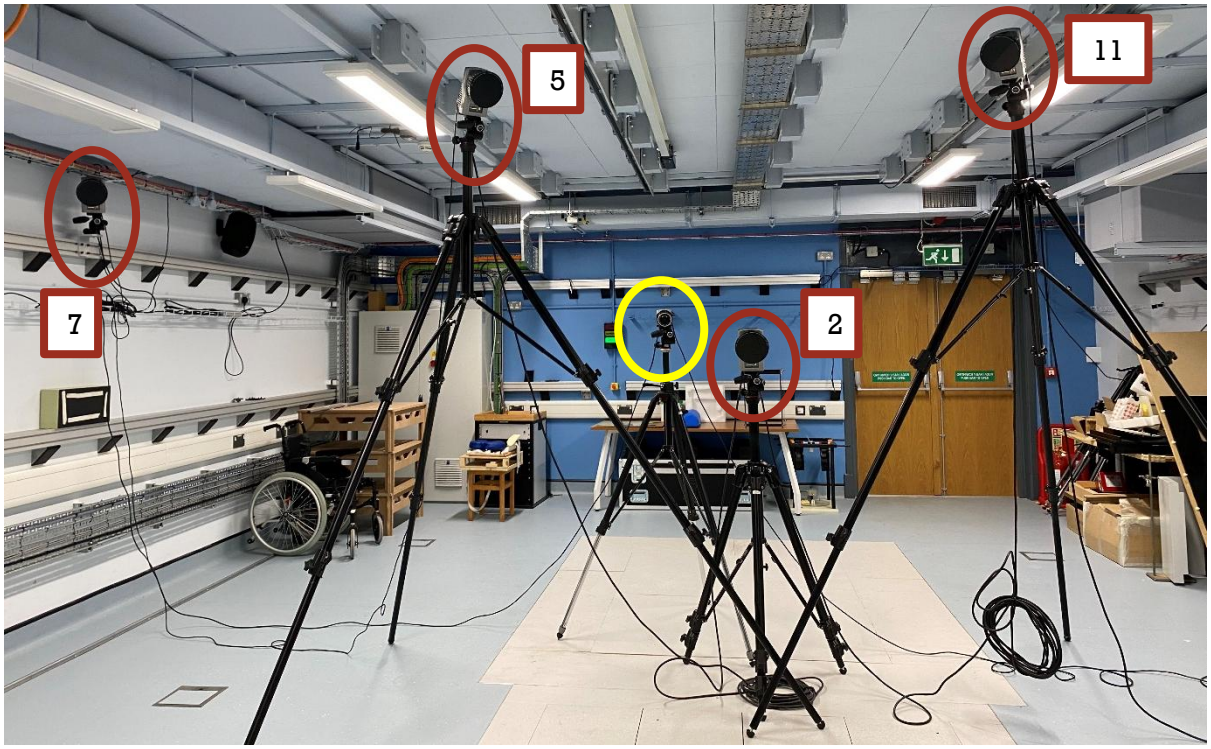
5
11
7
2

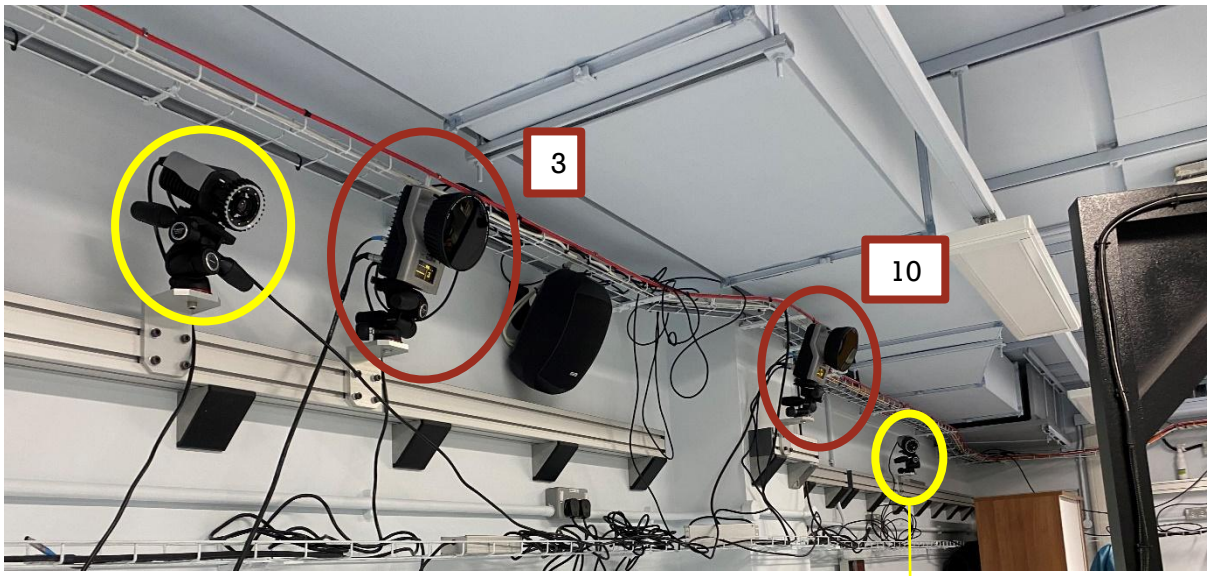
3
10

The diagram shows a floorplan of the lab with the camera positions (black circles) with their camera number from Qualisys and their cabling. Yellow = data and power, red = mains power, blue = data cable. (L) denotes a camera on the lower rail. 5, 2 and 11 are on tripods. The numbers in white boxes show the force plates.

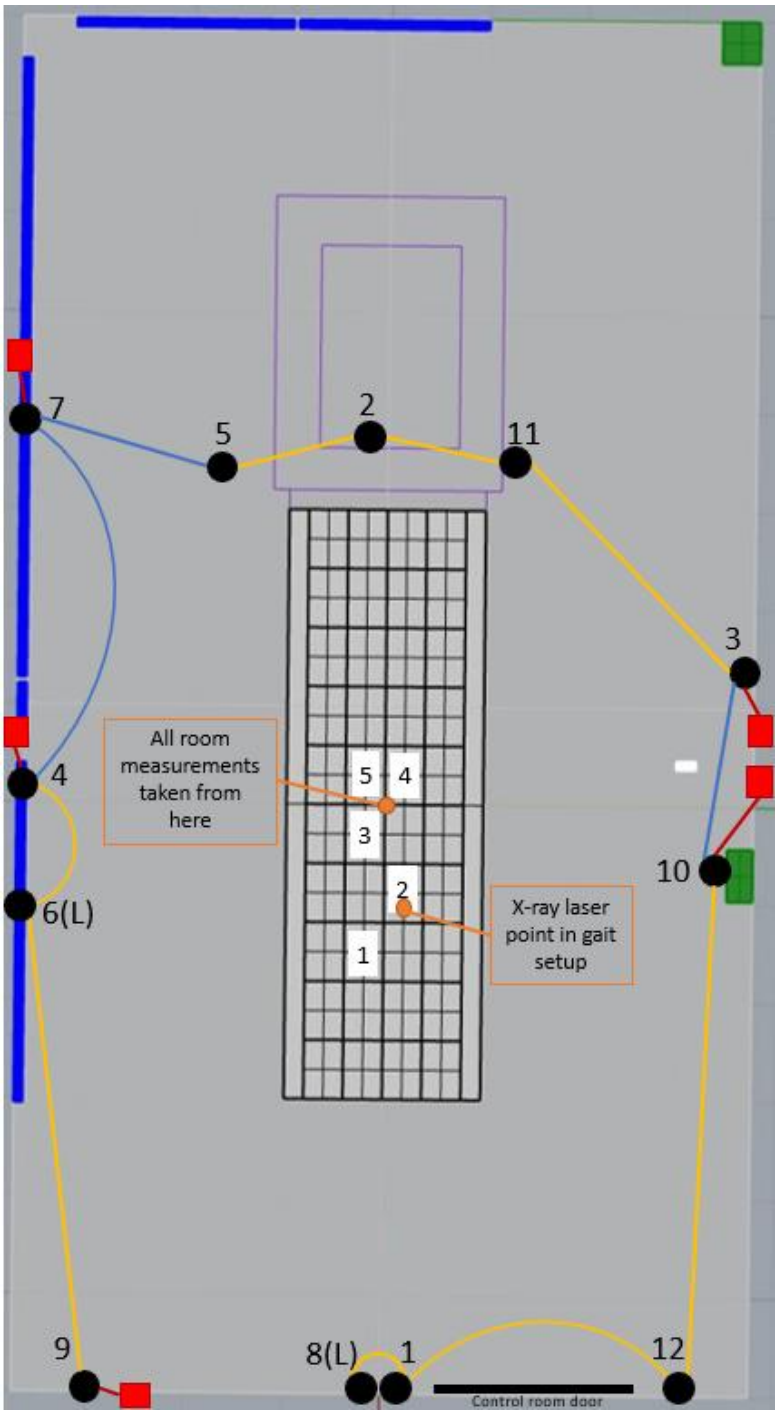

For wall mounted cameras:

Camera Info	Camera Serial No.	16697	16704	16641	16712	16709	16715	16648	16644	16711	16697	16704	16641
	Camera Number in Qualisys	3	10	12	1	8	9	6	4	7	3	10	12
	Exposure and flash time (us)	58	128	249	537	93	171	23	607	180	58	128	249
	Marker Threshold (%)	15	42	56	14	21	22	26	38	42	15	42	56
	Camera Focus (m)	10	10	10	Infinity	10	10	10	4.6	10.5	10	10	10
	Camera Aperture (f)	5.6	2.8	5	11	9	7.1	2.8	11	7.1	5.6	2.8	5
Tripod Head	Tripod Head Style (Hex or Rect)	Rect	Rect	Rect	Rect	Rect	Rect	Rect	Rect	Rect	Rect	Rect	Rect
	Tripod Head α angle (Flex)	20	20	30	10	10	0	10	30	15	20	20	30
	Tripod Head β angle (adduction)	25	0	5	0	0	90	5	5	10	25	0	5
	Tripod Head γ angle (internal Rotation)	5	60	25	75	65	40	15	40	55	5	60	25
Wall mounted	Wall.Rail.Distance.Side	E.UC.1215.R	E.UD.46.L	S.UB.13.R	S.UC.65.L	S.LC.10.R	S.UC.556.R	W.LA.1255.L	W.UA.1846.R	W.UC.2240.L	E.UC.1215.R	E.UD.46.L	S.UB.13.R
	Camera mount up or down	Up	Up	Up	Down	Up	Up	Up	Up	Up	Up	Up	Up

Where the wall mount key is:

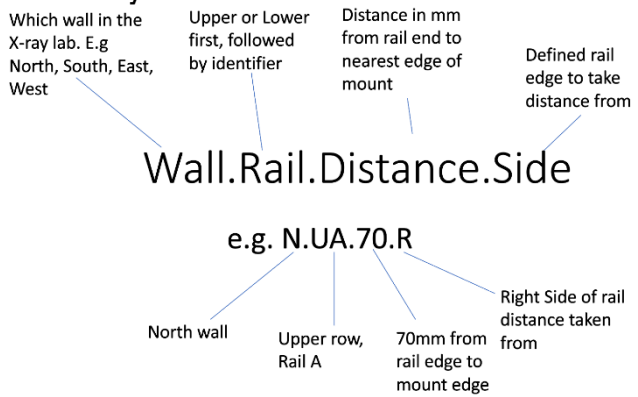

For cameras on tripods:

Camera Info	Camera Serial No.	16710	16700	16694
	Camera Number in Qualisys	5	2	11
	Exposure and flash time (us)	128	258	58
	Marker Threshold (%)	15	23	15
	Camera Focus (m)	17.6	13.6	10
	Camera Aperture (f)	7.1	11	5.6
Tripod Head	Tripod Head Style (Hex or Rect)	Rect	Rect	Rect
	Tripod Head α angle (Flex)	30	15	25
	Tripod Head β angle (adduction)	0	10	0
	Tripod Head γ angle (internal Rotation)	40	0	70
Tripod	Tripod Serial Number	NT002	NT005	NT004
	Tripod Vertical Column Height (mm)	258	254	258
	Tripod to floor centre (mm)	1803	611	1800
	Tripod centre X position in room (mm)	-2992	-3377	-3475
	Tripod Centre Y position in room (mm)	-1095	148	1067
	Leg 1 X (mm)	-1999	-2934	-2592
	Leg 1 Y (mm)	-1509	97	-34
	Leg 2 X (mm)	-3652	-3607	-4646
	Leg 2 Y (mm)	-1507	-222	1428
	Leg 3 X (mm)	-2808	-2999	-2626
	Leg 3 Y (mm)	82	550	1996
	Leg 1 length (mm)	2206	900	2275
	Leg 2 length (mm)	2205	905	2331
	Leg 3 length (mm)	2329	915	2338

(See pictures above for placement of tripods in room)

1.1.2 Calibration

To initialise and calibrate the motion capture camera system:

1. Turn on Qualisys cameras and force plates
2. Turn on HDBX computer and open InstaCal and Qualisys Track Manager (QTM) in that order.
3. Load up the "Knee Miqus Stairs" Qualisys project folder HDBX
4. Calibrate the volume with the L-Frame on force plate 2, with the long axis pointing in the direction of travel. *Make sure to calibrate whole volume for all three activities.*

5. Locate each of the force plates individually by using the metal corner markers and saving the file: 'FP_1' etc.

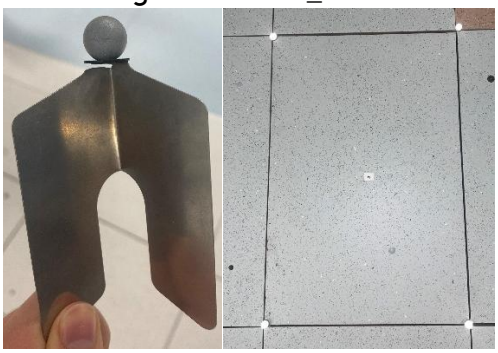

Locate each step of the stairs by placing a marker on the four corners.

6. Zero the force plates and then test by visualising the force arrows during real-time.

1.2 EMG

Ensure EMG box is plugged in and EMGs are charged ahead of time. On InstaCal, check EMGs are visible and sufficiently charged.

1.3 Biplane X-ray

To initialise the biplane X-ray system:

1. From the keys safe in T0.16, put the key labelled 'Emergency Stop Reset Key' and place it into the C1 X-Ray Safety Interface.
2. Turn on the C1 X-Ray Safety Interface by rotating the red control clockwise. The emergency alarm will sound and is deactivated by turning the emergency alarm reset key clockwise.
3. Ensure all required dosimeter badges are being worn.
4. Turn on the C3 manipulator Control Panel by rotating the red control clockwise to power the manipulator.
5. Login to the Manipulator HMI to allow manipulation of the machine.
6. Turn on both Epsilon Generator interfaces labelled 'High Voltage Generator A and B' by pressing the power button.

1.3.1 System Positioning

The X-ray machine must be moved into the correct position for the data collection. The following parameters must be changed:

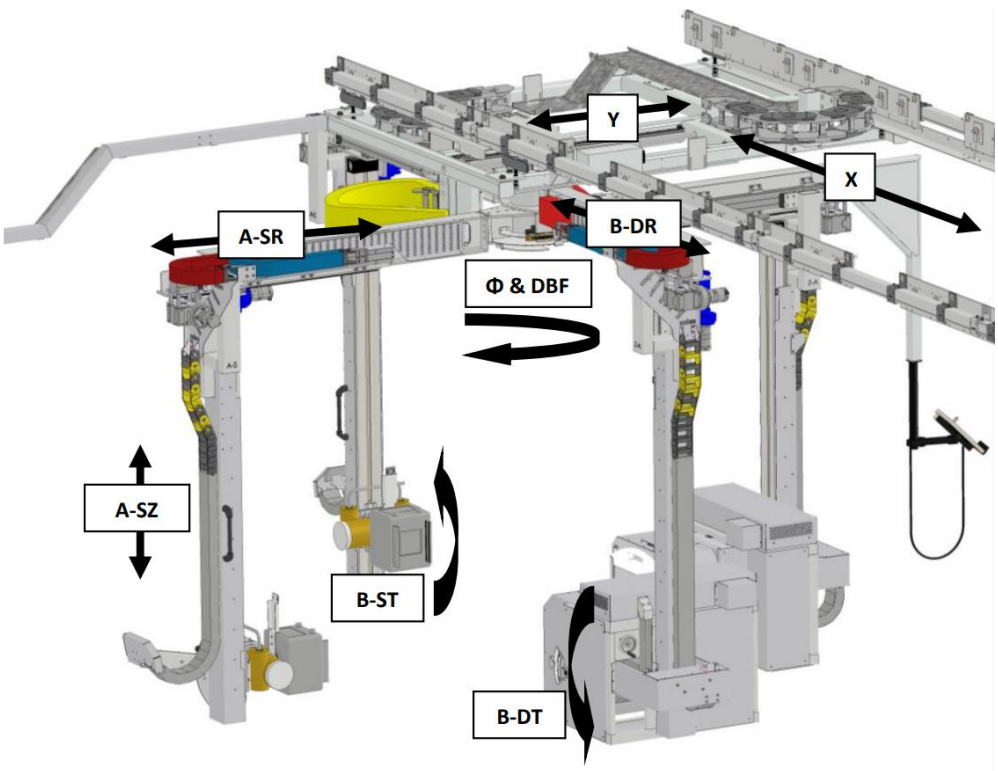

Axis ID	Description
X	Longitudinal axis along direction of walking
Y	Lateral axis perpendicular to X
A-Φ	Rotate Axis – set A
A-DT	Tilt Axis – set A detector
A-S T	Tilt Axis – set A x-ray source
A-DR	Radial Axis - set A detector
A-SR	Radial Axis - set A x-ray source
A-DZ	Vertical Axis – set A detector
A-SZ	Vertical Axis – set A x-ray source
B-Φ	Rotate Axis – set B
B-DT	Tilt Axis – set B detector
B-ST	Tilt Axis – set B x-ray source
B-DR	Radial Axis - set B detector
B-SR	Radial Axis - set B x-ray source
B-DZ	Vertical Axis – set B detector
B-SZ	Vertical Axis – set B x-ray source

Before the participant arrives, the X-ray system should be set to the **stairs** configuration with the instrumented staircase in-situ.

For the **right** leg setup:
(The front edge of the bottom step of the staircase should be aligned with FP4 and FP5 – but not touching the force plates).

Gait:

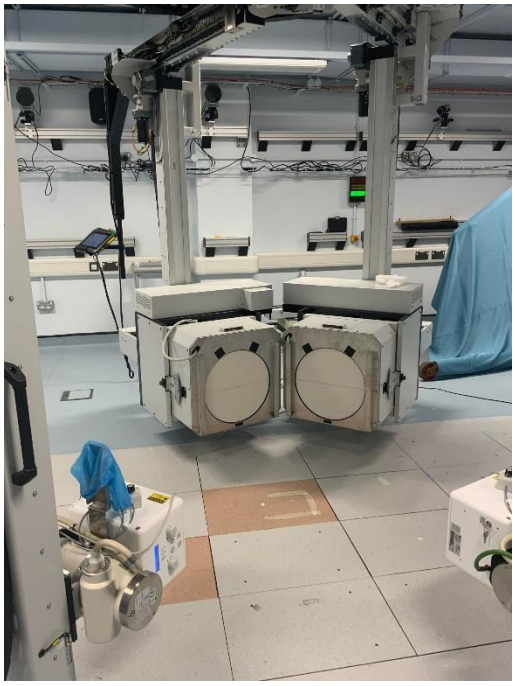

Lunge:

The first set up required will be stairs followed by gait, then lunge. The values for all parameters for each X-ray set up can be found in Appendix A.

1.3.2 X-ray Warmup

To warmup the X-ray tubes:

1. Place lead aprons in front of image intensifier.
2. Select the **warmup** protocol.

3. Enable the Neutral Density filter by pressing the F1 Button.

4. Perform 2 rounds of preparing the system:
    a. Press PREP on both systems
    b. Hold the PREP buttons until the indicator light begins blinking
    c. Continue to hold the PREP button while pressing the X-Ray button
    d. Hold all buttons until the system automatically stops firing
    e. The HU should be above 5% after both exposures

5. Remove the lead aprons and replace on the hangers in control room (T0.16)

Software:

1. Open PFV4 and load the camera settings 50FPS test
2. Adjust the frame rate to **60 FPS**, pulse width **1.25ms**
3. Press the calibrate button in PV4 each time the settings are changed
4. Select the appropriate settings on the Epsilon Generators:
    - Stair ascent = **80kV, 160mA** (first setup)
    - Gait = **80kV, 160mA**
    - Lunge = **70kV, 125mA**

2 SET UP – WITH PARTICIPANT

2.1 Initial Participant Interactions

When the participant arrives:

1. Turn on intercom system.
2. Meet participant at entrance to MSKBRF and take them to T0.15/16.
3. Ask the participant to change into shorts and T-shirt.

4. Confirm identity of volunteer.
5. Carry out informed consent. Ensure both copies of the form are filled.
6. Record **participant ID, date of birth, height, and weight** on the computer sheet checklist.
7. Adjust X-ray machine Z-height to match participant.

2.2 EMG Placement

14 EMGs are used.

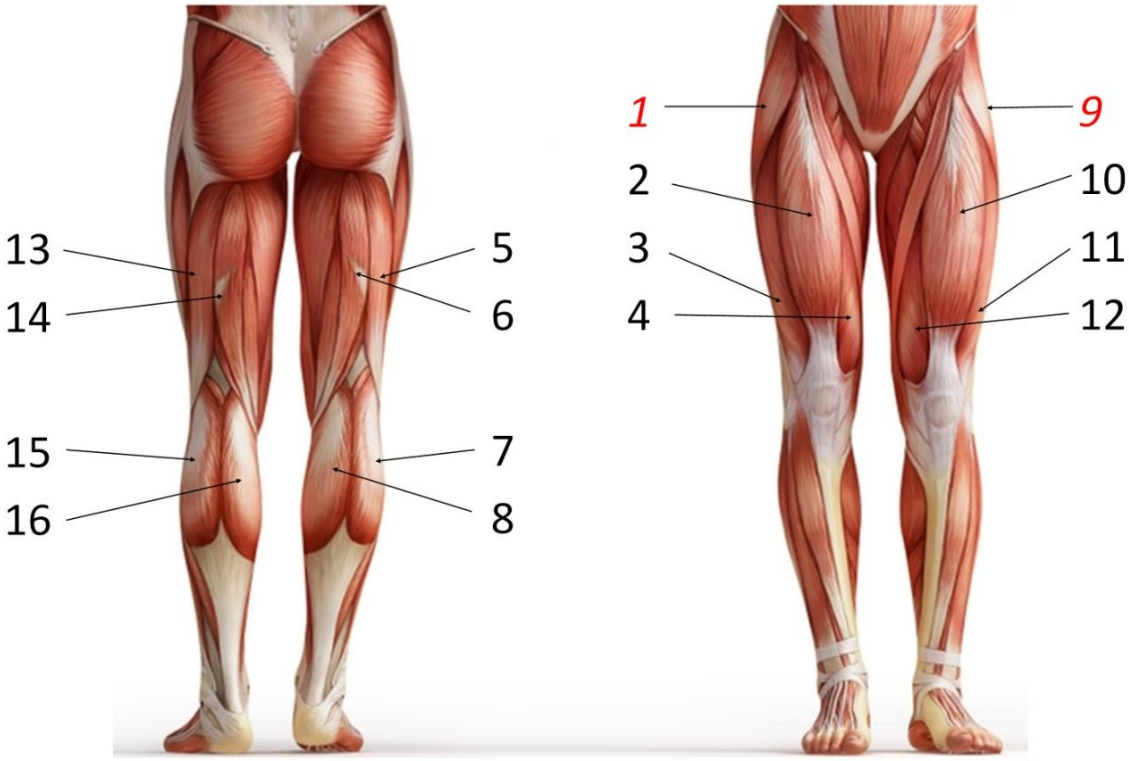

Once EMGs are placed, secure with Tubigrip. Carry out the following tests (as on the computer sheet checklist):

- EMGTest
- MVCRight[1] – Maximum Voluntary Contractions (right leg).
- MVCLeft[1] – Maximum Voluntary Contractions (left leg).

[1]MVC tests: get participant to stand on tiptoes for 3 seconds, flex leg behind them (pushing up) while you resist for 3 seconds, sit on chair and extend leg (pushing upwards) while you resist for 3 seconds.

2.3 Motion Capture Markers

2.3.1 Marker Set

54 are needed for the modified Cleveland Clinic marker set.

*Note: Separate L & R PSIS markers are not included. Instead, a single **PSIS** marker is included.*

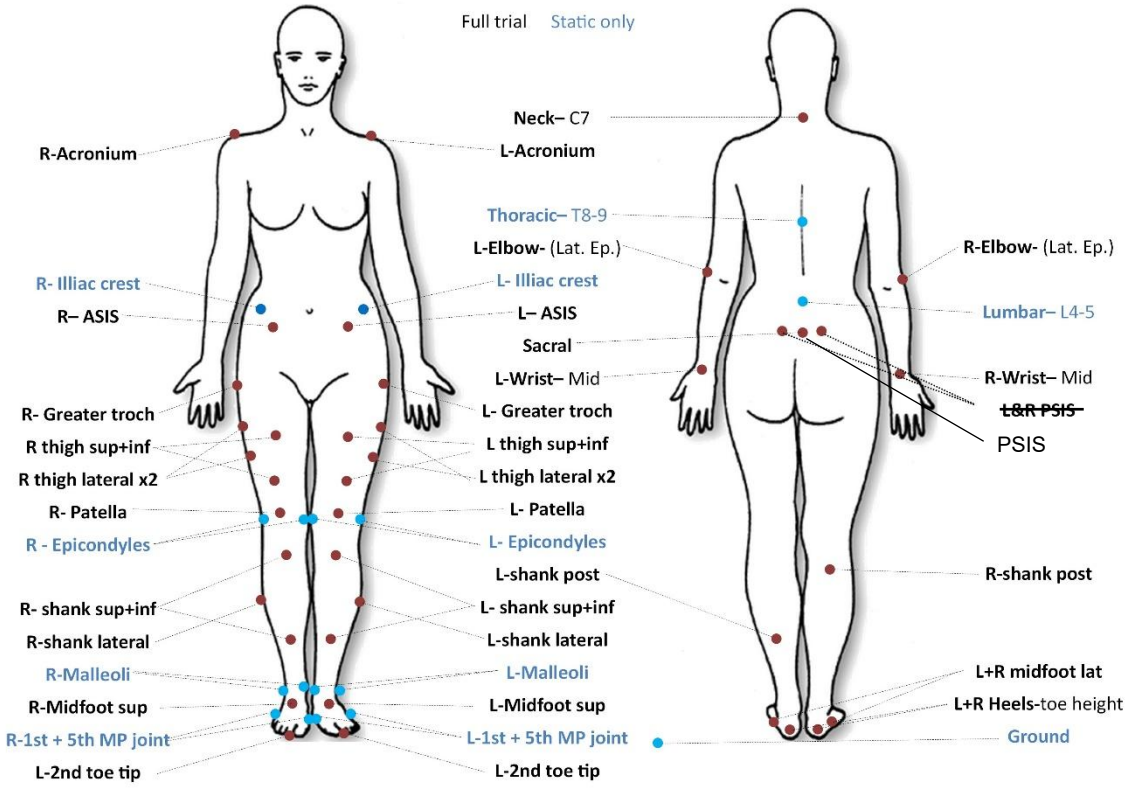

2.3.2 Motion Capture Statics

Collect (at least) two motion-capture-only statics (see computer sheet checklist). These should be in a position that is as neutral as possible (with hands down by sides, feet roughly shoulder width apart).

1. Standing with one leg on force plate 2 facing away from the south wall (towards control room).
2. Standing with both feet on force plate 1 facing the west wall (towards the door to the corridor).

Check: once statics are complete, apply marker list on QTM to check all markers are visible. Repeat statics if necessary.

3 X-RAY CALIBRATION

The following calibration steps should be carried out at the start and end of each set of measurements using a different set up.

The X-rays should be saved using this format: **Particpant_Setup_Time_Calibration** (e.g. 'HV001_Stairs_Start_White')

3.1 White

Capture plain biplane screens with nothing in front of them (see setup photos from Section 1.3.1).
Used for uniformity correction in post-processing.

3.2 Grids

Place the two metal grids on the detector faces. Collect an X-ray exposure.

Used for image distortion correction in post-processing.

3.3 Lego Cube

Creates grid of metal beads with four wire shapes. Place on other objects to get correct height (this may differ based on participant height) and collect an X-ray exposure.

Examples of the orientation and placement of the cube for each of the three setups:

1. STAIRS

2. GAIT

3. LUNGE

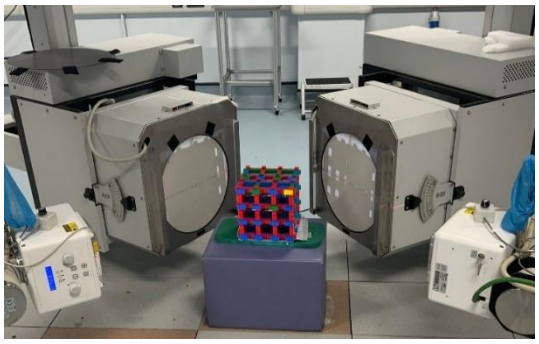

Ensure both images of the cube show the beads clearly (with minimal overlap) and the four shapes should be identifiable for post-processing.

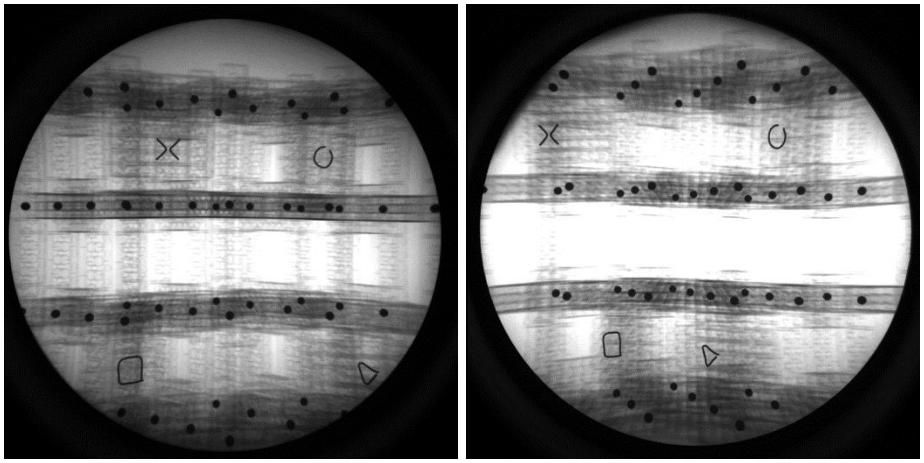

3.4 Cone

Cone with motion capture markers. Place into view, align top of cone with red laser, and collect capture.

Used to synchronise bi-plane X-ray and motion capture systems.

4 DATA COLLECTION

For each setup, complete a motion-capture-only static, an X-ray static, a couple of repeats of the activity with only motion-capture and then X-ray captures of the activity.

Ensure DIAMENTOR dose printer is turned on before beginning captures involving participant.

4.1 Stair Ascent

Participant will climb stairs with their desired imaging leg landing on the first step (in-line with the X-rays).
Watch out for height limit when climbing stairs – warn participant to be careful not to hit their head

Setup photo

1. 'Start_Stairs_' X-ray calibration set

2. Motion capture static:

3. X-ray static (standing at bottom of stairs with leg on first step):

4. Activity captures (motion capture only & with X-rays).
5. 'End_Stairs_' X-ray calibration set

4.2 Gait

Participant will walk down the lab with their desired leg hitting force plate 2. Do test walks to get correct starting location using the tape markers on the floor.

Change QTM project to "Knee Miqus" (not KneeMiqusStairs) before collecting gait and lunge or turn off the stairs in the settings.

1. 'Start_Gait_' X-ray calibration set
2. Motion capture static:

3. X-ray static:

4. Activity captures (motion capture only & with X-rays).
5. ‘End_Gait_’ X-ray calibration set

4.3 Lunge

Participant will stand facing the X-ray detectors and lunge forward onto the desired leg.

1. ‘Start_Gait_’ X-ray calibration set
2. Motion capture static/X-ray static:

3. Activity captures (motion capture only & with X-rays).

4. ‘End_Gait_’ X-ray calibration set

5 POST-PARTICIPANT STEPS

After the participant has left:

1. Print dosage labels and stick on the dosage sheets.
2. Upload data to NAS.
3. Scan and upload participant sheet.
4. Check relevant paperwork is all signed.
5. File documents.

6 APPENDICIES

6.1 Appendix A – X-ray System Setups

Axis ID	Unit	Description	Stair Ascent Right	Stair Ascent Left	Gait	Lunge
X	mm	Longitudinal axis along direction of walking	3799	2611	2077	2201
Y	mm	Lateral axis perpendicular to X	-294	-294	-312	-312
A-Φ	°	Rotate Axis – set A	115	130	112	150
A-DT	°	Tilt Axis – set A detector	0	0	0	0
A-S T	°	Tilt Axis – set A x-ray source	0	0	0	0
A-DR	mm	Radial Axis - set A detector	550	550	485	370
A-SR	mm	Radial Axis - set A x-ray source	1150	1150	1300	980
A-DZ	mm	Vertical Axis – set A detector	750	750	460	550
A-SZ	mm	Vertical Axis – set A x-ray source	771	771	457	539
B-Φ	°	Rotate Axis – set B	63	63	61	115
B-DT	°	Tilt Axis – set B detector	0	0	0	0
B-ST	°	Tilt Axis – set B x-ray source	0	0	0	0
B-DR	mm	Radial Axis - set B detector	550	550	485	370
B-SR	mm	Radial Axis - set B x-ray source	1150	1150	1300	980
B-DZ	mm	Vertical Axis – set B detector	750	750	466	550
B-SZ	mm	Vertical Axis – set B x-ray source	773	773	485	543

APPENDIX B: QUESTIONNAIRES

KNEE OUTCOME SURVEY
Activities of Daily Living Scale

SYMPTOMS:

1. **To what degree does pain in your knee affect your daily activity level?**

L	R	
☐	☐	I never have pain in my knee.
☐	☐	I have pain in my knee, but it does not affect my daily activity.
☐	☐	Pain affects my activity slightly.
☐	☐	Pain affects my activity moderately.
☐	☐	Pain affects my activity severely.
☐	☐	Pain in my knee prevents me from performing all daily activities.

2. **To what degree does grinding or grating of your knee affect your daily activity level?**

L	R	
☐	☐	I never have grinding or grating in my knee.
☐	☐	I have grinding or grating in my knee, but it does not affect my daily activity.
☐	☐	Grinding or grating affects my activity slightly.
☐	☐	Grinding or grating affects my activity moderately.
☐	☐	Grinding or grating affects my activity severely.
☐	☐	Grinding or grating in my knee prevents me from performing all daily activities.

3. **To what degree does stiffness in your knee affect your daily activity level?**

L	R	
☐	☐	I never have stiffness in my knee.
☐	☐	I have stiffness in my knee, but it does not affect my daily activity.
☐	☐	Stiffness affects my activity slightly.
☐	☐	Stiffness affects my activity moderately.
☐	☐	Stiffness affects my activity severely.
☐	☐	Stiffness in my knee prevents me from performing all daily activities.

Subject: ID: Date:

4. To what degree does swelling in your knee affect your daily activity level?

L R

☐☐ I never have swelling in my knee.
☐☐ I have swelling in my knee, but it does not affect my daily activity.
☐☐ Swelling affects my activity slightly.
☐☐ Swelling affects my activity moderately.
☐☐ Swelling affects my activity severely.
☐☐ Swelling in my knee prevents me from performing all daily activities.

5. **To what degree does slipping of your knee affect your daily activity level?**

L R

☐☐ I never have slipping of my knee.
☐☐ I have slipping in my knee, but it does not affect my daily activity.
☐☐ Slipping affects my activity slightly.
☐☐ Slipping affects my activity moderately.
☐☐ Slipping affects my activity severely.
☐☐ Slipping of my knee prevents me from performing all daily activities.

6. To what degree does buckling of your knee affect your daily activity level?

L R

☐☐ I never have buckling of my knee.
☐☐ I have buckling of my knee, but it does not affect my daily activity.
☐☐ Buckling affects my activity slightly.
☐☐ Buckling affects my activity moderately.
☐☐ Buckling affects my activity severely.
☐☐ Buckling of my knee prevents me from performing all daily activities.

7. To what degree does weakness or lack of strength of your leg affect your daily activity level?

L R

☐☐ My leg never feels weak.
☐☐ My leg feels weak, but it does not affect my daily activity.
☐☐ Weakness affects my activity slightly.
☐☐ Weakness affects my activity moderately.
☐☐ Weakness affects my activity severely.
☐☐ Weakness of my leg prevents me from performing all daily activities.

Subject: ID: Date:

FUNCTIONAL DISABILITY WITH ACTIVITIES OF DAILY LIVING:

8. How does your knee affect your ability to walk?

L R

- ☐☐ My knee does not affect my ability to walk.
- ☐☐ I have pain in my knee when walking, but it does not affect my ability to walk.
- ☐☐ My knee prevents me from walking more than 1 mile.
- ☐☐ My knee prevents me from walking more than 1/2 mile.
- ☐☐ My knee prevents me from walking more than 1 block.
- ☐☐ My knee prevents me from walking.

9. Because of your knee, do you walk with crutches or a cane?

L R

- ☐☐ I can walk without crutches or a cane.
- ☐☐ My knee causes me to walk with 1 crutch or a cane.
- ☐☐ My knee causes me to walk with 2 crutches.
- ☐☐ Because of my knee, I cannot walk even with crutches.

10. Does your knee cause you to limp when you walk?

L R

- ☐☐ I can walk without a limp.
- ☐☐ Sometimes my knee causes me to walk with a limp.
- ☐☐ Because of my knee, I cannot walk without a limp.

11. How does your knee affect your ability to go up stairs?

L R

- ☐☐ My knee does not affect my ability to go up stairs.
- ☐☐ I have pain in my knee when going up stairs, but it does not limit my ability to go up stairs.
- ☐☐ I am able to go up stairs normally, but I need to rely on use of a railing.
- ☐☐ I am able to go up stairs one step at a time with use of a railing.
- ☐☐ I have to use crutches or a cane to go up stairs.
- ☐☐ I cannot go up stairs.

Subject: ID: Date:

12. How does your knee affect your ability to go down stairs?

L	R	
☐	☐	My knee does not affect my ability to go down stairs.
☐	☐	I have pain in my knee when going down stairs, but it does not limit my ability to go down stairs.
☐	☐	I am able to go down stairs normally, but I need to rely on use of a railing.
☐	☐	I am able to go down stairs one step at a time with use of a railing.
☐	☐	I have to use crutches or a cane to go down stairs.
☐	☐	I cannot go down stairs.

13. How does your knee affect your ability to stand?

L	R	
☐	☐	My knee does not affect my ability to stand, I can stand for unlimited amounts of time.
☐	☐	I have pain in my knee when standing, but it does not limit my ability to stand.
☐	☐	Because of my knee I cannot stand for more than 1 hour.
☐	☐	Because of my knee I cannot stand for more than 1/2 hour.
☐	☐	Because of my knee I cannot stand for more than 10 minutes.
☐	☐	I cannot stand because of my knee.

14. How does your knee affect your ability to kneel on the front of your knee?

L	R	
☐	☐	My knee does not affect my ability to kneel on the front of my knee. I can kneel for unlimited amounts of time.
☐	☐	I have pain when kneeling on the front of my knee, but it does not limit my ability to kneel.
☐	☐	I cannot kneel on the front of my knee for more than 1 hour.
☐	☐	I cannot kneel on the front of my knee for more than 1/2 hour.
☐	☐	I cannot kneel on the front of my knee for more than 10 minutes.
☐	☐	I cannot kneel on the front of my knee.

Subject: ID: Date:

15. How does your knee affect your ability to squat?

L	R	
☐	☐	My knee does not affect my ability to squat, I can squat all the way down.
☐	☐	I have pain in my knee when squatting, but I can still squat all the way down.
☐	☐	I cannot squat more than3/4 of the way down.
☐	☐	I cannot squat more than 1/2 of the way down.
☐	☐	I cannot squat more than 1/4 of the way down.
☐	☐	I cannot squat because of my knee.

16. How does your knee affect your ability to sit with your knee bent?

L	R	
☐	☐	My knee does not affect my ability to sit with my knee bent, I can sit for unlimited amounts of time.
☐	☐	I have pain in my knee when sitting with my knee bent, but it does not limit my ability to sit.
☐	☐	I cannot sit with my knee bent for more than 1 hour.
☐	☐	I cannot sit with my knee bent for more than 1/2 hour.
☐	☐	I cannot sit with my knee bent for more than 10 minutes.
☐	☐	I cannot sit with my knee bent.

17. How does your knee affect your ability to rise from a chair?

L	R	
☐	☐	My knee does not affect my ability to rise from a chair.
☐	☐	I have pain when rising from a seated position, but it does not affect my ability to rise from a seated position.
☐	☐	Because of my knee I can only rise from a chair if I use my hands and arms to assist.
☐	☐	Because of my knee I cannot rise from a chair.

KOOS KNEE SURVEY

Today's date: _____/_____/_____ Date of birth: _____/_____/_____

Name: _____

INSTRUCTIONS: This survey asks for your view about your knee. This information will help us keep track of how you feel about your knee and how well you are able to perform your usual activities.
Answer every question by ticking the appropriate box, only one box for each question. If you are unsure about how to answer a question, please give the best answer you can.

Symptoms

These questions should be answered thinking of your knee symptoms during the **last week**.

S1. Do you have swelling in your knee?

Never	Rarely	Sometimes	Often	Always
☐	☐	☐	☐	☐

S2. Do you feel grinding, hear clicking or any other type of noise when your knee moves?

Never	Rarely	Sometimes	Often	Always
☐	☐	☐	☐	☐

S3. Does your knee catch or hang up when moving?

Never	Rarely	Sometimes	Often	Always
☐	☐	☐	☐	☐

S4. Can you straighten your knee fully?

Always	Often	Sometimes	Rarely	Never
☐	☐	☐	☐	☐

S5. Can you bend your knee fully?

Always	Often	Sometimes	Rarely	Never
☐	☐	☐	☐	☐

Stiffness

The following questions concern the amount of joint stiffness you have experienced during the **last week** in your knee. Stiffness is a sensation of restriction or slowness in the ease with which you move your knee joint.

S6. How severe is your knee joint stiffness after first wakening in the morning?

None	Mild	Moderate	Severe	Extreme
☐	☐	☐	☐	☐

S7. How severe is your knee stiffness after sitting, lying or resting **later in the day**?

None	Mild	Moderate	Severe	Extreme
☐	☐	☐	☐	☐

Pain

P1. How often do you experience knee pain?

Never	Monthly	Weekly	Daily	Always
☐	☐	☐	☐	☐

What amount of knee pain have you experienced the **last week** during the following activities?

P2. Twisting/pivoting on your knee

None	Mild	Moderate	Severe	Extreme
☐	☐	☐	☐	☐

P3. Straightening knee fully

None	Mild	Moderate	Severe	Extreme
☐	☐	☐	☐	☐

P4. Bending knee fully

None	Mild	Moderate	Severe	Extreme
☐	☐	☐	☐	☐

P5. Walking on flat surface

None	Mild	Moderate	Severe	Extreme
☐	☐	☐	☐	☐

P6. Going up or down stairs

None	Mild	Moderate	Severe	Extreme
☐	☐	☐	☐	☐

P7. At night while in bed

None	Mild	Moderate	Severe	Extreme
☐	☐	☐	☐	☐

P8. Sitting or lying

None	Mild	Moderate	Severe	Extreme
☐	☐	☐	☐	☐

P9. Standing upright

None	Mild	Moderate	Severe	Extreme
☐	☐	☐	☐	☐

Function, daily living

The following questions concern your physical function. By this we mean your ability to move around and to look after yourself. For each of the following activities please indicate the degree of difficulty you have experienced in the **last week** due to your knee.

A1. Descending stairs

None	Mild	Moderate	Severe	Extreme
☐	☐	☐	☐	☐

A2. Ascending stairs

None	Mild	Moderate	Severe	Extreme
☐	☐	☐	☐	☐

For each of the following activities please indicate the degree of difficulty you have experienced in the **last week** due to your knee.

A3. Rising from sitting

None	Mild	Moderate	Severe	Extreme
☐	☐	☐	☐	☐

A4. Standing

None	Mild	Moderate	Severe	Extreme
☐	☐	☐	☐	☐

A5. Bending to floor/pick up an object

None	Mild	Moderate	Severe	Extreme
☐	☐	☐	☐	☐

A6. Walking on flat surface

None	Mild	Moderate	Severe	Extreme
☐	☐	☐	☐	☐

A7. Getting in/out of car

None	Mild	Moderate	Severe	Extreme
☐	☐	☐	☐	☐

A8. Going shopping

None	Mild	Moderate	Severe	Extreme
☐	☐	☐	☐	☐

A9. Putting on socks/stockings

None	Mild	Moderate	Severe	Extreme
☐	☐	☐	☐	☐

A10. Rising from bed

None	Mild	Moderate	Severe	Extreme
☐	☐	☐	☐	☐

A11. Taking off socks/stockings

None	Mild	Moderate	Severe	Extreme
☐	☐	☐	☐	☐

A12. Lying in bed (turning over, maintaining knee position)

None	Mild	Moderate	Severe	Extreme
☐	☐	☐	☐	☐

A13. Getting in/out of bath

None	Mild	Moderate	Severe	Extreme
☐	☐	☐	☐	☐

A14. Sitting

None	Mild	Moderate	Severe	Extreme
☐	☐	☐	☐	☐

A15. Getting on/off toilet

None	Mild	Moderate	Severe	Extreme
☐	☐	☐	☐	☐

For each of the following activities please indicate the degree of difficulty you have experienced in the **last week** due to your knee.

A16. Heavy domestic duties (moving heavy boxes, scrubbing floors, etc)

None	Mild	Moderate	Severe	Extreme
☐	☐	☐	☐	☐

A17. Light domestic duties (cooking, dusting, etc)

None	Mild	Moderate	Severe	Extreme
☐	☐	☐	☐	☐

Function, sports and recreational activities

The following questions concern your physical function when being active on a higher level. The questions should be answered thinking of what degree of difficulty you have experienced during the **last week** due to your knee.

SP1. Squatting

None	Mild	Moderate	Severe	Extreme
☐	☐	☐	☐	☐

SP2. Running

None	Mild	Moderate	Severe	Extreme
☐	☐	☐	☐	☐

SP3. Jumping

None	Mild	Moderate	Severe	Extreme
☐	☐	☐	☐	☐

SP4. Twisting/pivoting on your injured knee

None	Mild	Moderate	Severe	Extreme
☐	☐	☐	☐	☐

SP5. Kneeling

None	Mild	Moderate	Severe	Extreme
☐	☐	☐	☐	☐

Quality of Life

Q1. How often are you aware of your knee problem?

Never	Monthly	Weekly	Daily	Constantly
☐	☐	☐	☐	☐

Q2. Have you modified your life style to avoid potentially damaging activities to your knee?

Not at all	Mildly	Moderately	Severely	Totally
☐	☐	☐	☐	☐

Q3. How much are you troubled with lack of confidence in your knee?

Not at all	Mildly	Moderately	Severely	Extremely
☐	☐	☐	☐	☐

Q4. In general, how much difficulty do you have with your knee?

None	Mild	Moderate	Severe	Extreme
☐	☐	☐	☐	☐

Thank you very much for completing all the questions in this questionnaire.

The Oxford Knee Score

During the past four weeks:

1. **How would you describe the pain you usually have from your knee**

L	R	
☐	☐	None
☐	☐	Very mild
☐	☐	Mild
☐	☐	Moderate
☐	☐	Severe

2. **Have you had any trouble with washing and drying yourself (all over) because of your knee?**

L	R	
☐	☐	No trouble at all
☐	☐	Very little trouble
☐	☐	Moderate trouble
☐	☐	Extreme difficulty
☐	☐	Impossible to do

3. **Have you had any trouble getting in and out of a car or using public transport because of your knee? (whichever you tend to use)**

L	R	
☐	☐	No trouble at all
☐	☐	Very little trouble
☐	☐	Moderate trouble
☐	☐	Extreme difficulty
☐	☐	Impossible to do

4. **For how long have you been able to walk before the pain from your knee becomes severe? (with or without a stick)**

L	R	
☐	☐	No Pain/ > 30min
☐	☐	16 to 30 min
☐	☐	5 to 15 min
☐	☐	Around the house only
☐	☐	Not at all – severe on walking

5. **After a meal (sat at table), how painful has it been for you to stand up from a chair because of your knee?**

L	R	
☐	☐	Not at all painful
☐	☐	Slightly painful
☐	☐	Moderately painful
☐	☐	Very painful
☐	☐	Unbearable

6. **Have you been limping when walking, because of your knee?**

L	R	
☐	☐	Rarely/never
☐	☐	Sometimes or just at first
☐	☐	Often, not just at first
☐	☐	Most of the time
☐	☐	All of the time

7. **Could you kneel down and get up again afterwards?**

L	R	
☐	☐	Yes, easily
☐	☐	With a little difficulty
☐	☐	With moderate difficulty
☐	☐	With extreme difficulty
☐	☐	No, impossible

8. **Have you been troubled by pain from your knee in bed at night?**

L	R	
☐	☐	No nights
☐	☐	Only 1 or 2 nights
☐	☐	Some nights
☐	☐	Most nights
☐	☐	Every night

9. How much has pain from your knee interfered with your usual work (including housework)

L	R	
☐	☐	Not at all
☐	☐	A little bit
☐	☐	Moderately
☐	☐	Greatly
☐	☐	Totally

10. Have you felt that your knee might suddenly "give way" or let you down?

L	R	
☐	☐	Rarely/never
☐	☐	Sometimes or just at first
☐	☐	Often, not just at first
☐	☐	Most of the time
☐	☐	All of the time

11. Could you do the household shopping on your own?

L	R	
☐	☐	Yes, easily
☐	☐	With little difficulty
☐	☐	With moderate difficulty
☐	☐	With extreme difficulty
☐	☐	No, impossible

12. Could you walk down a flight of stairs?

L	R	
☐	☐	Yes, easily
☐	☐	With little difficulty
☐	☐	With moderate difficulty
☐	☐	With extreme difficulty
☐	☐	No, impossible

NEW PATIENT

PACS

CLINICAL INFORMATION SPECIAL INTEREST GROUP (CISIG) of the Pain Society

PACS (pain audit collection system) is a database for collecting information from pain clinics on diagnosis, treatment and outcome for the purposes of clinical governance and audit

Pain intensity, impact of pain on the patient's life, and the outcomes achieved from treatment are measured using the Brief Pain Inventory (BPI). The BPI uses a numeric rating scale to score pain, pain relief and interference with function

Different tear-off BPI forms are available for 'new' or 'follow-up' patients. Completion of these will aid data entry into PACS

By using the form each time your patient attends the clinic, response to treatment can be followed and, if requested, compared with other clinics

Please see User's Manual for Instructions

Clinical Information Special Interest Group
The Pain Society
The English & Irish Chapter of the International Association for the Study of Pain

PACS is supported by an educational grant from Pharmacia

PHARMACIA

PACS/BPI ASSESSMENT FORM

Hospital

Date

Registration number

Patient's name

Year of birth

Diagnosis

1.

2.

Duration of symptoms

Treatment

Consultant

Source: Pain Research Group, Department of Neurology, University of Wisconsin-Madison

This data is collected for assessment of your pain. In addition, the information is entered into a national database for audit and research. This is anonymous. If you do not wish it to be used, then please inform pain clinic staff.

PHARMACIA

BRIEF PAIN INVENTORY

Please circle your response or ask for help if you are having problems

1. Please rate your pain by circling the one number that best describes your pain at its WORST in the past week.

0 1 2 3 4 5 6 7 8 9 10
NO PAIN — PAIN AS BAD AS YOU CAN IMAGINE

2. Please rate your pain by circling the one number that best describes your pain at its LEAST in the past week.

0 1 2 3 4 5 6 7 8 9 10
NO PAIN — PAIN AS BAD AS YOU CAN IMAGINE

3. Please rate your pain by circling the one number that best describes your pain on the AVERAGE.

0 1 2 3 4 5 6 7 8 9 10
NO PAIN — PAIN AS BAD AS YOU CAN IMAGINE

4. Please rate your pain by circling the one number that tells how much pain you have RIGHT NOW.

0 1 2 3 4 5 6 7 8 9 10
NO PAIN — PAIN AS BAD AS YOU CAN IMAGINE

5. Circle the one number that describes how during the past week, PAIN HAS INTERFERED with your:

A. General activity

0 1 2 3 4 5 6 7 8 9 10
DOES NOT INTERFERE — COMPLETELY INTERFERES

B. Mood

0 1 2 3 4 5 6 7 8 9 10
DOES NOT INTERFERE — COMPLETELY INTERFERES

C. Walking ability

0 1 2 3 4 5 6 7 8 9 10
DOES NOT INTERFERE — COMPLETELY INTERFERES

D. Normal work (includes work both outside the home and housework)

0 1 2 3 4 5 6 7 8 9 10
DOES NOT INTERFERE — COMPLETELY INTERFERES

E. Relationships with other people

0 1 2 3 4 5 6 7 8 9 10
DOES NOT INTERFERE — COMPLETELY INTERFERES

F. Sleep

0 1 2 3 4 5 6 7 8 9 10
DOES NOT INTERFERE — COMPLETELY INTERFERES

G. Enjoyment of life

0 1 2 3 4 5 6 7 8 9 10
DOES NOT INTERFERE — COMPLETELY INTERFERES

PACS

CLINICAL INFORMATION SPECIAL INTEREST GROUP (CISIG) of the Pain Society

PACS (pain audit collection system) is a database for collecting information from pain clinics on diagnosis, treatment and outcome for the purposes of clinical governance and audit

Pain intensity, impact of pain on the patient's life, and the outcomes achieved from treatment are measured using the Brief Pain Inventory (BPI). The BPI uses a numeric rating scale to score pain, pain relief and interference with function

Different tear-off BPI forms are available for 'new' or 'follow-up' patients. Completion of these will aid data entry into PACS

By using the form each time your patient attends the clinic, response to treatment can be followed and, if requested, compared with other clinics

Please see User's Manual for Instructions

Clinical Information Special Interest Group
The Pain Society
The English & Irish Chapter of the International Association for the Study of Pain

PACS is supported by an educational grant from Pharmacia

PHARMACIA

PACS/BPI ASSESSMENT FORM

Hospital

Date

Registration number

Patient's name

Year of birth

Treatment

Consultant

BRIEF PAIN INVENTORY

Please circle your response or ask for help if you are having problems

1. How much RELIEF have pain treatments or medications FROM THIS CLINIC provided? Please circle the one percentage that shows how much.

100% 90% 80% 70% 60% 50% 40% 30% 20% 10% 0%
COMPLETE RELIEF NO RELIEF

2. Please rate your pain by circling the one number that best describes your pain at its WORST in the past week.

0 1 2 3 4 5 6 7 8 9 10
NO PAIN PAIN AS BAD AS YOU CAN IMAGINE

3. Please rate your pain by circling the one number that best describes your pain at its LEAST in the past week.

0 1 2 3 4 5 6 7 8 9 10
NO PAIN PAIN AS BAD AS YOU CAN IMAGINE

4. Please rate your pain by circling the one number that best describes your pain on the AVERAGE.

0 1 2 3 4 5 6 7 8 9 10
NO PAIN PAIN AS BAD AS YOU CAN IMAGINE

5. Please rate your pain by circling the one number that tells how much pain you have RIGHT NOW.

0 1 2 3 4 5 6 7 8 9 10
NO PAIN PAIN AS BAD AS YOU CAN IMAGINE

6. Circle the one number that describes how during the past week, PAIN HAS INTERFERED with your:

A. General activity

0 1 2 3 4 5 6 7 8 9 10
DOES NOT INTERFERE COMPLETELY INTERFERES

B. Mood

0 1 2 3 4 5 6 7 8 9 10
DOES NOT INTERFERE COMPLETELY INTERFERES

C. Walking ability

0 1 2 3 4 5 6 7 8 9 10
DOES NOT INTERFERE COMPLETELY INTERFERES

D. Normal work (includes work both outside the home and housework)

0 1 2 3 4 5 6 7 8 9 10
DOES NOT INTERFERE COMPLETELY INTERFERES

E. Relationships with other people

0 1 2 3 4 5 6 7 8 9 10
DOES NOT INTERFERE COMPLETELY INTERFERES

F. Sleep

0 1 2 3 4 5 6 7 8 9 10
DOES NOT INTERFERE COMPLETELY INTERFERES

G. Enjoyment of life

0 1 2 3 4 5 6 7 8 9 10
DOES NOT INTERFERE COMPLETELY INTERFERES

Source: Pain Research Group, Department of Neurology, University of Wisconsin-Madison

This data is collected for assessment of your pain. In addition, the information is entered into a national database for audit and research. This is anonymous. If you do not wish it to be used, then please inform pain clinic staff.

PHARMACIA

The Western Ontario and McMaster Universities Osteoarthritis Index

(WOMAC)

Name:_____ Date:_____

Instructions: Please rate the activities in each category according to the following scale of difficulty: 0 = None, 1 = Slight, 2 = Moderate, 3 = Very, 4 = Extremely

Circle **one number** for each activity

Pain	1. Walking	0	1	2	3	4
	2. Stair Climbing	0	1	2	3	4
	3. Nocturnal	0	1	2	3	4
	4. Rest	0	1	2	3	4
	5. Weight bearing	0	1	2	3	4
Stiffness	1. Morning stiffness	0	1	2	3	4
	2. Stiffness occurring later in the day	0	1	2	3	4
Physical Function	1. Descending stairs	0	1	2	3	4
	2. Ascending stairs	0	1	2	3	4
	3. Rising from sitting	0	1	2	3	4
	4. Standing	0	1	2	3	4
	5. Bending to floor	0	1	2	3	4
	6. Walking on flat surface	0	1	2	3	4
	7. Getting in / out of car	0	1	2	3	4
	8. Going shopping	0	1	2	3	4
	9. Putting on socks	0	1	2	3	4
	10. Lying in bed	0	1	2	3	4
	11. Taking off socks	0	1	2	3	4
	12. Rising from bed	0	1	2	3	4
	13. Getting in/out of bath	0	1	2	3	4
	14. Sitting	0	1	2	3	4
	15. Getting on/off toilet	0	1	2	3	4
	16. Heavy domestic duties	0	1	2	3	4
	17. Light domestic duties	0	1	2	3	4

Total Score: _____ / 96 = _____%

Comments / Interpretation (to be completed by therapist only):

APPENDIX C: BVR, GENERIC MSM & PERSONALISED MSM KINEMATICS PRESENTED PER PARTICIPANT

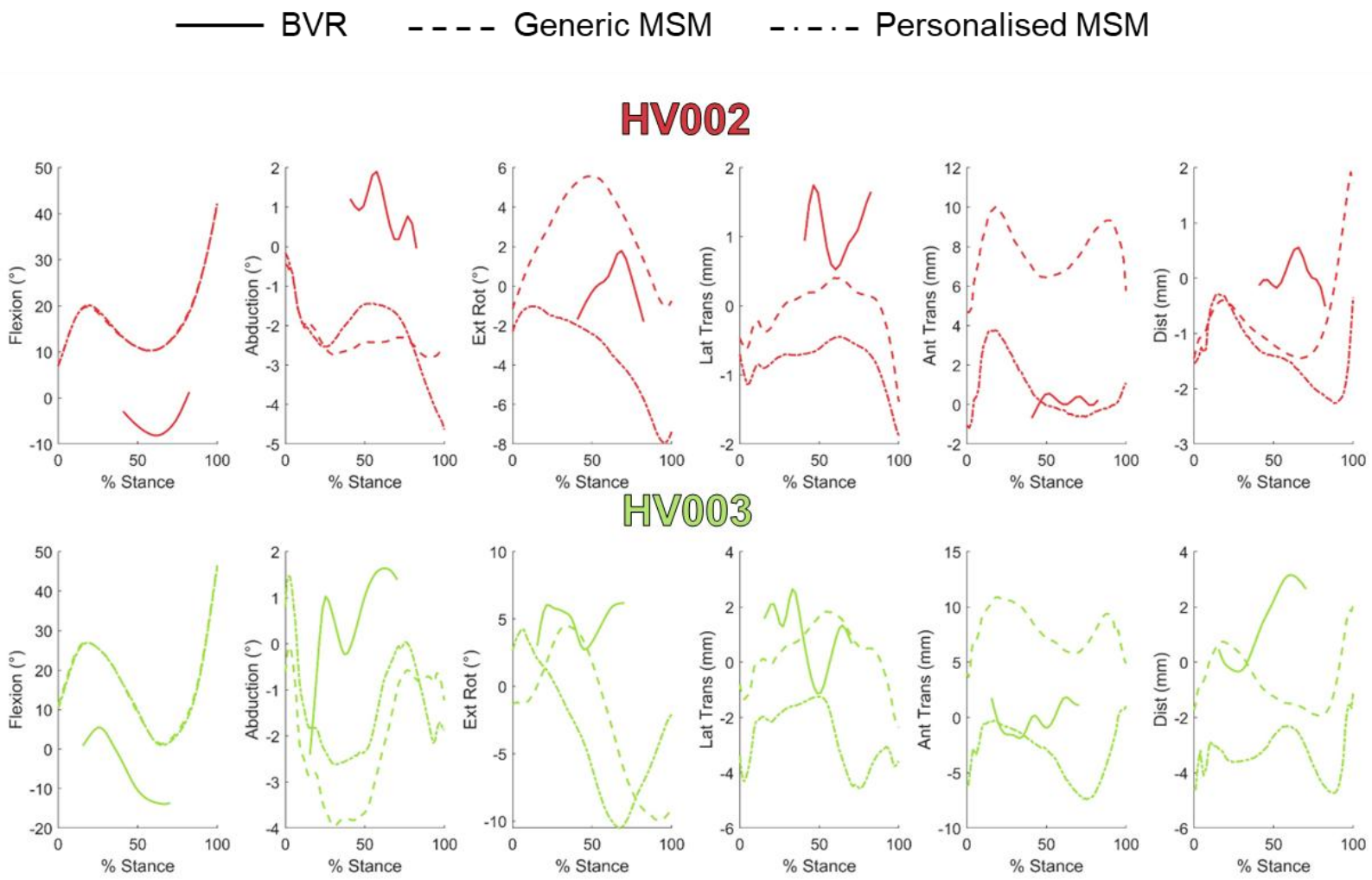
BVR
Generic MSM
Personalised MSM
HV002
HV003
Flexion (°)
Abduction (°)
Ext Rot (°)
Lat Trans (mm)
Ant Trans (mm)
Dist (mm)
% Stance

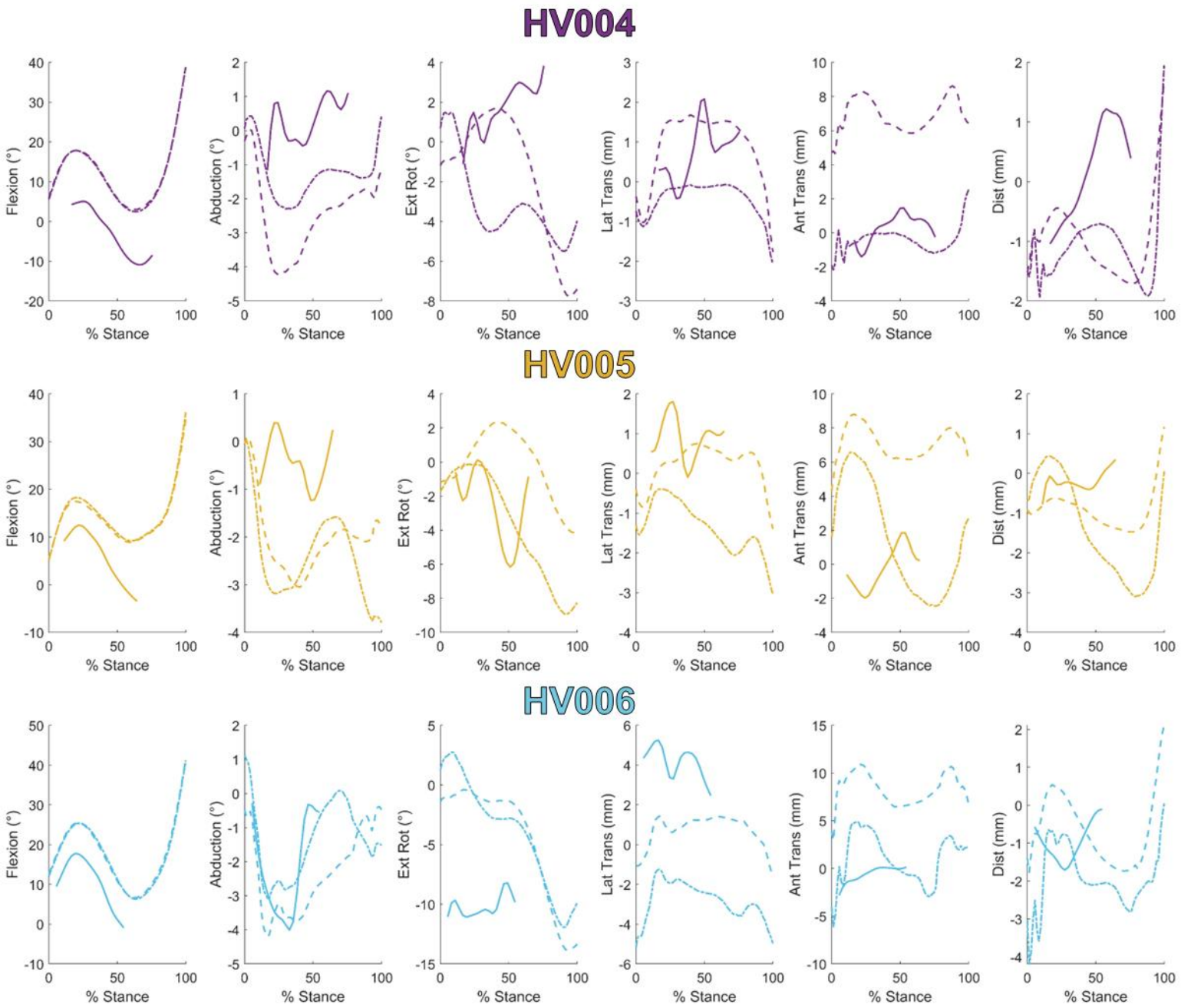
HV004
HV005
HV006
Flexion (°)
Abduction (°)
Ext Rot (°)
Lat Trans (mm)
Ant Trans (mm)
Dist (mm)
% Stance

APPENDIX D: CONTACT PRESSURE MAPS PER PARTICIPANT FOR THE THREE ACTIVITIES

Contact map results during level gait

Contact pressure maps from the generic MSM, personalised MSM, and BVR-JAM equivalent at **10% intervals of stance phase** of level gait where data were available for each individual participant.

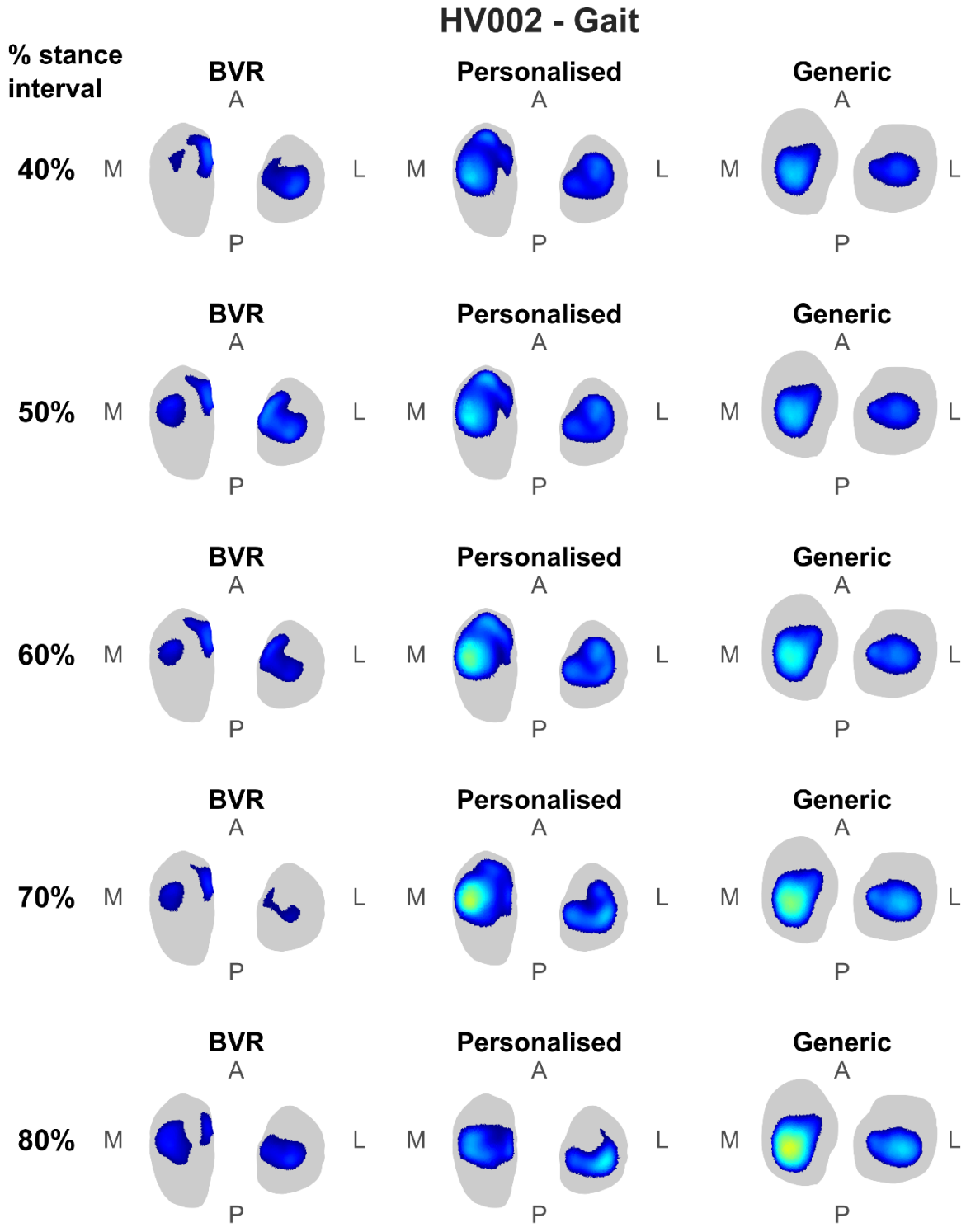
HV002 - Gait
% stance interval
BVR
Personalised
Generic
40%
50%
60%
70%
80%
A
P
M
L
Pressure (MPa)
0
2
4
6
8
10
12
14
16
18

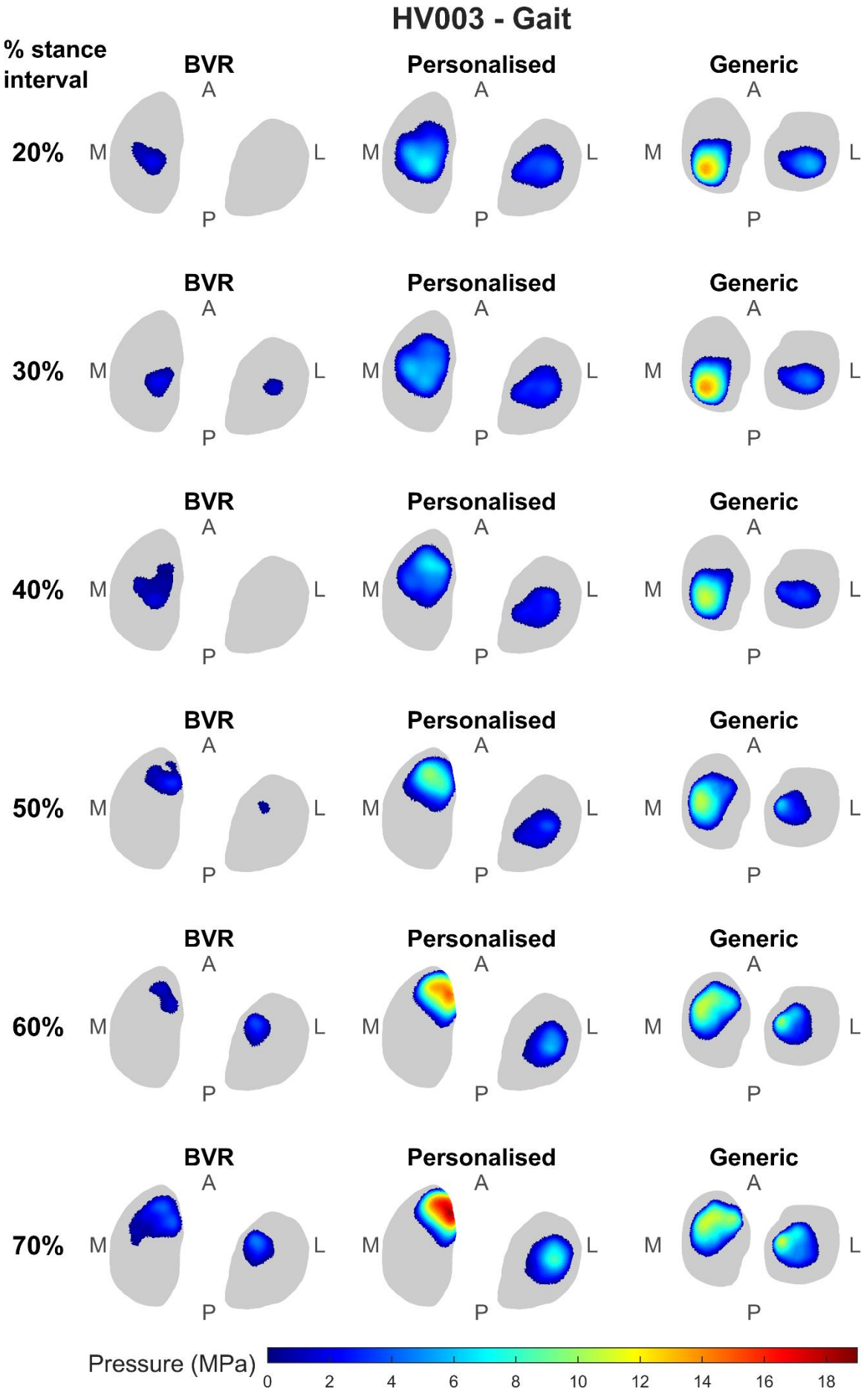
HV003 - Gait
% stance interval
BVR
Personalised
Generic
20%
30%
40%
50%
60%
70%
A
P
M
L
Pressure (MPa)
0
2
4
6
8
10
12
14
16
18

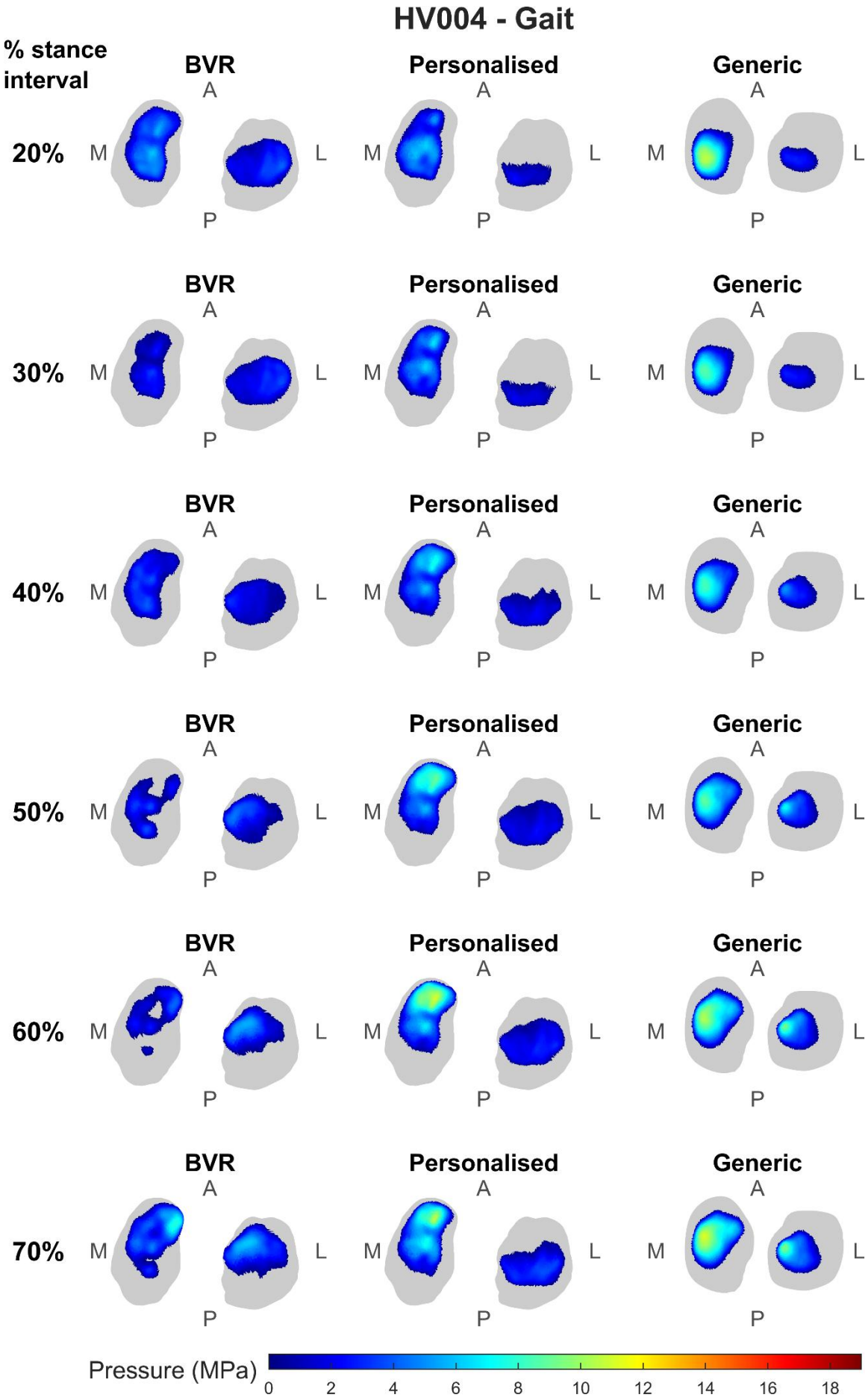
HV004 - Gait
% stance interval
BVR
Personalised
Generic
20%
30%
40%
50%
60%
70%
A
P
M
L
Pressure (MPa)
0
2
4
6
8
10
12
14
16
18

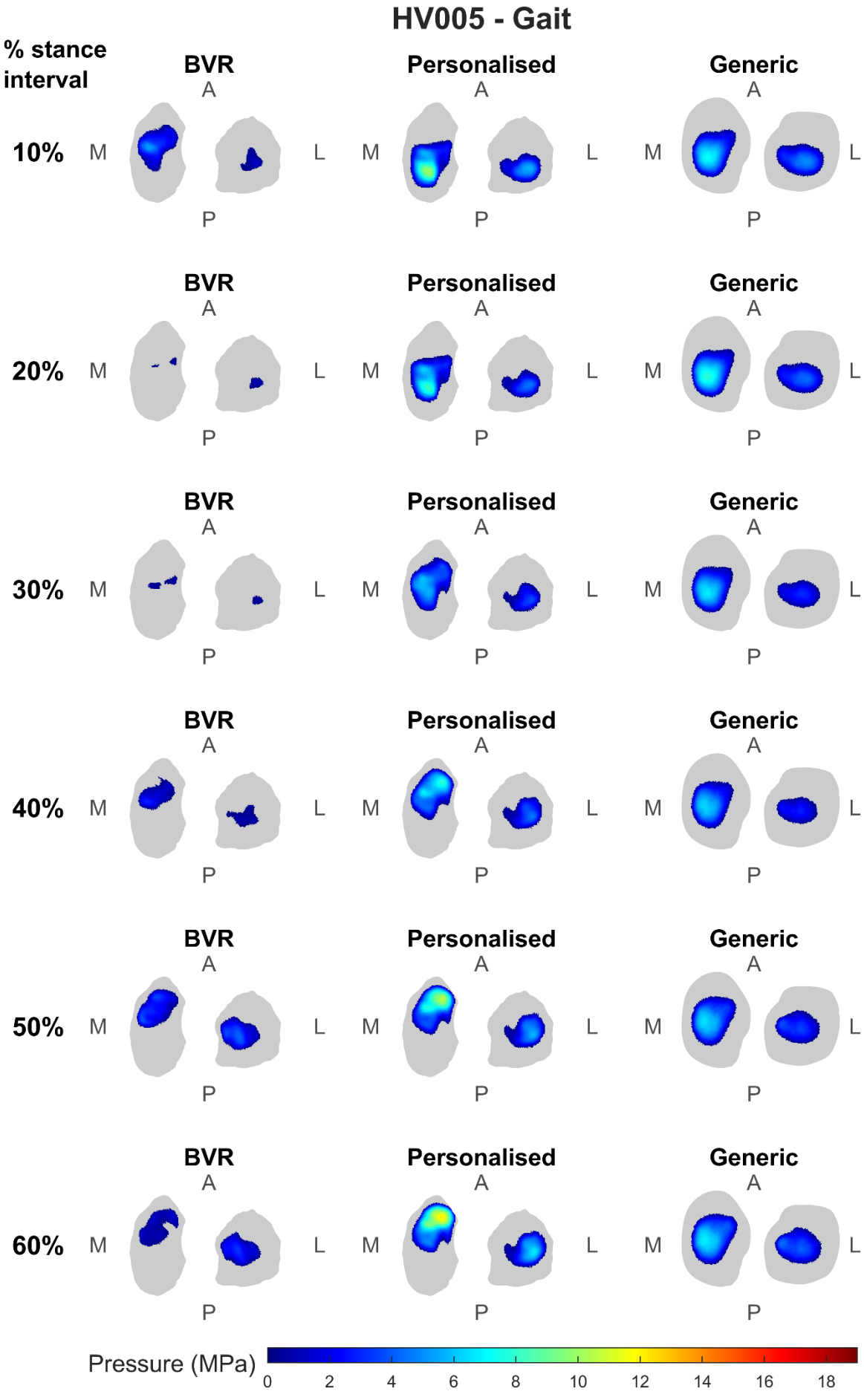
HV005 - Gait
% stance interval
BVR
Personalised
Generic
10%
20%
30%
40%
50%
60%
A
P
M
L
Pressure (MPa)
0
2
4
6
8
10
12
14
16
18

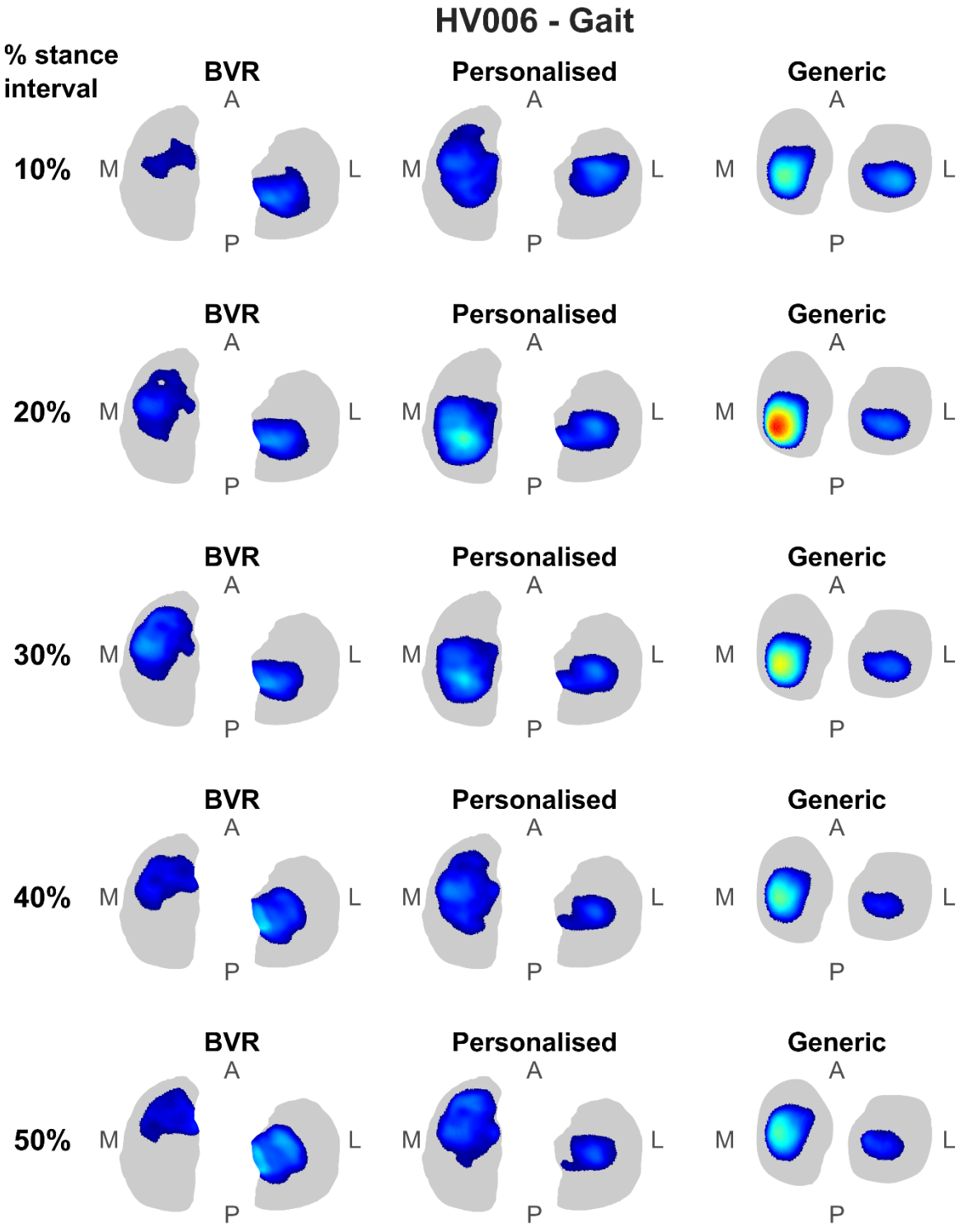
HV006 - Gait
% stance interval
BVR
Personalised
Generic
10%
20%
30%
40%
50%
A
P
M
L
Pressure (MPa)
0
2
4
6
8
10
12
14
16
18

Contact map results during stair ascent

Contact pressure maps from the generic MSM, personalised MSM, and BVR-JAM equivalent at **10% intervals of stance phase** of stair ascent where data were available for each individual participant.

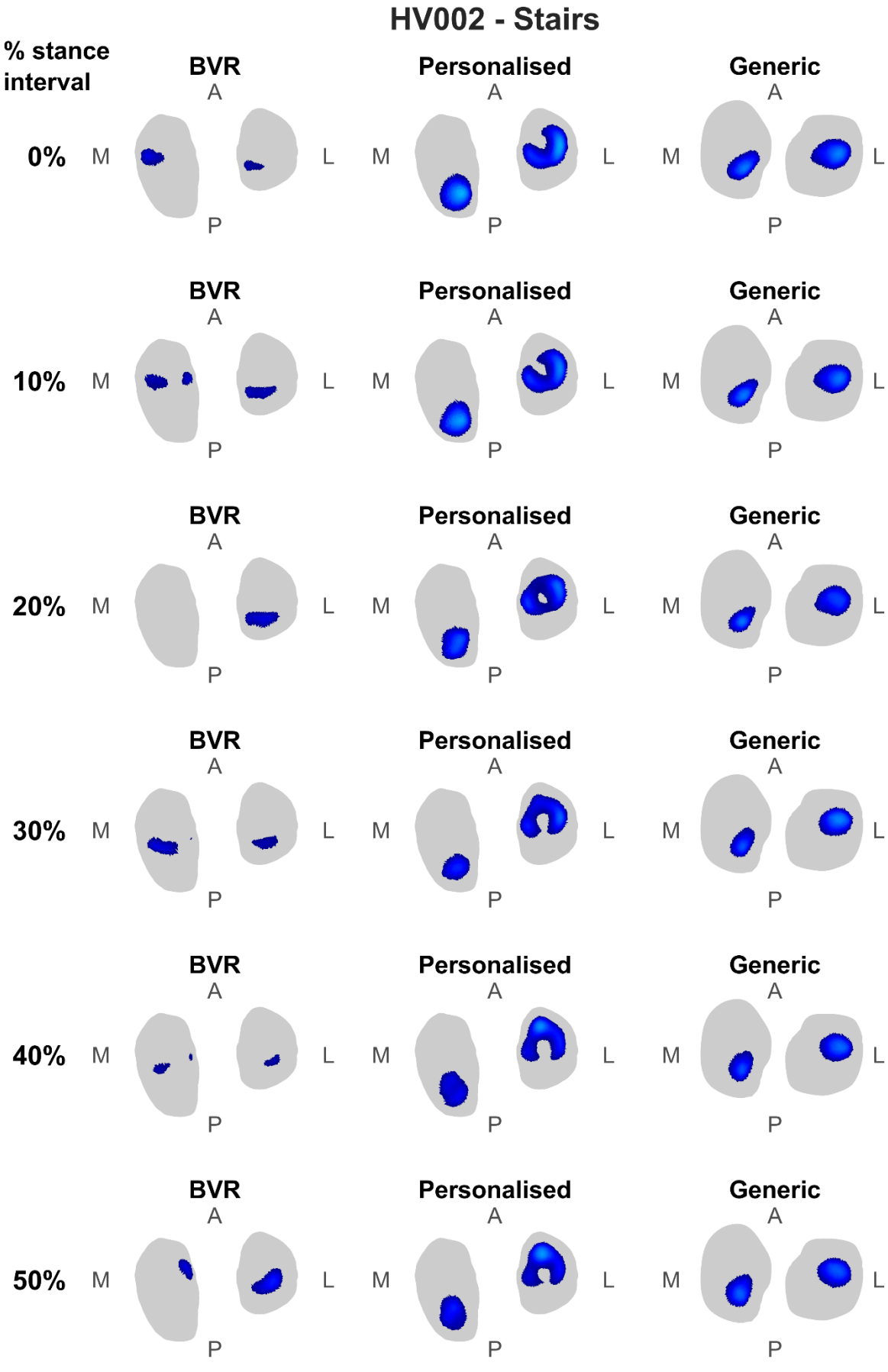
HV002 - Stairs
% stance interval
BVR
Personalised
Generic
A
P
M
L
0%
10%
20%
30%
40%
50%
Pressure (MPa)
0
2
4
6
8
10
12
14
16
18

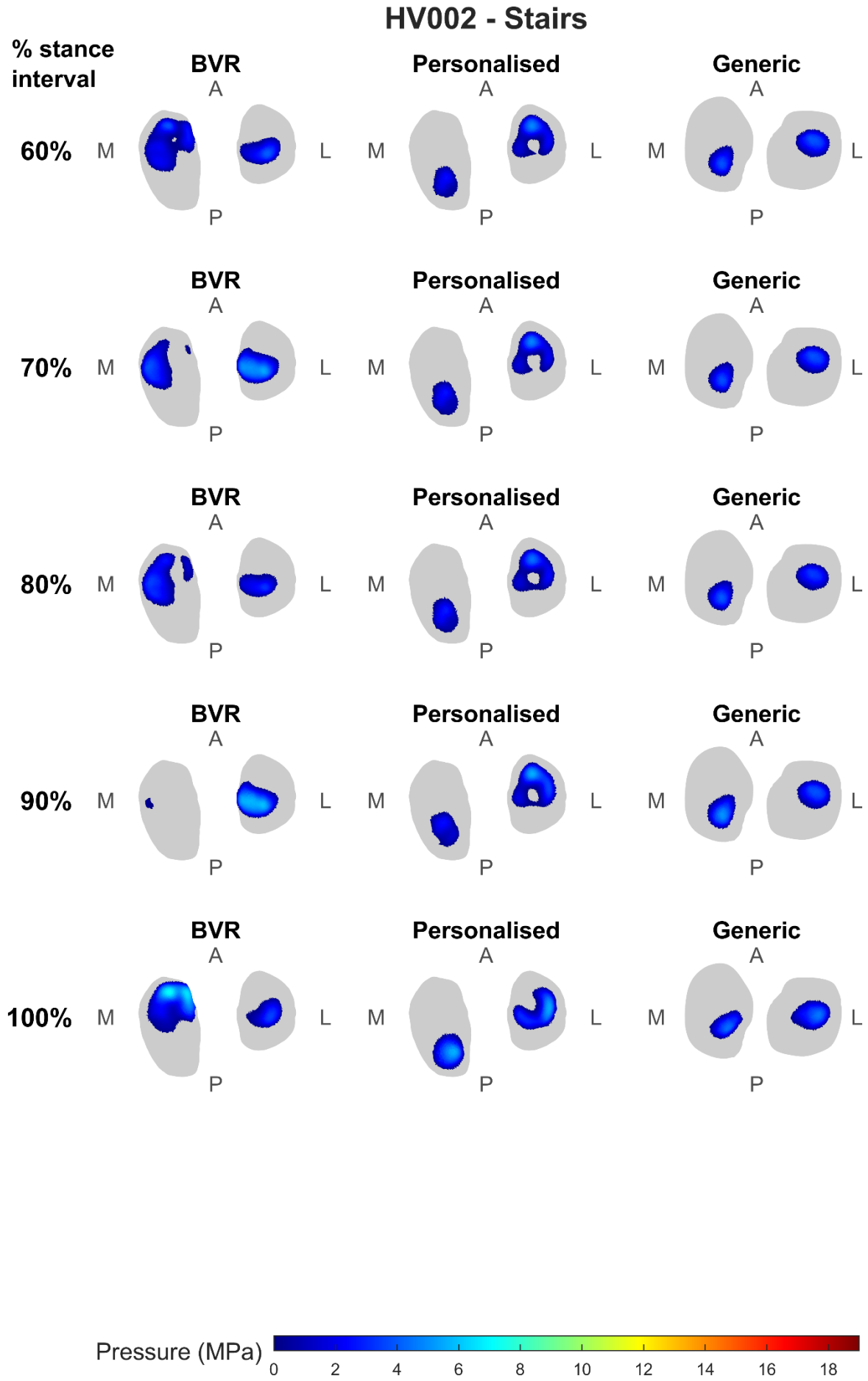
HV002 - Stairs
% stance interval
BVR
Personalised
Generic
60%
70%
80%
90%
100%
A
P
M
L
Pressure (MPa)
0
2
4
6
8
10
12
14
16
18

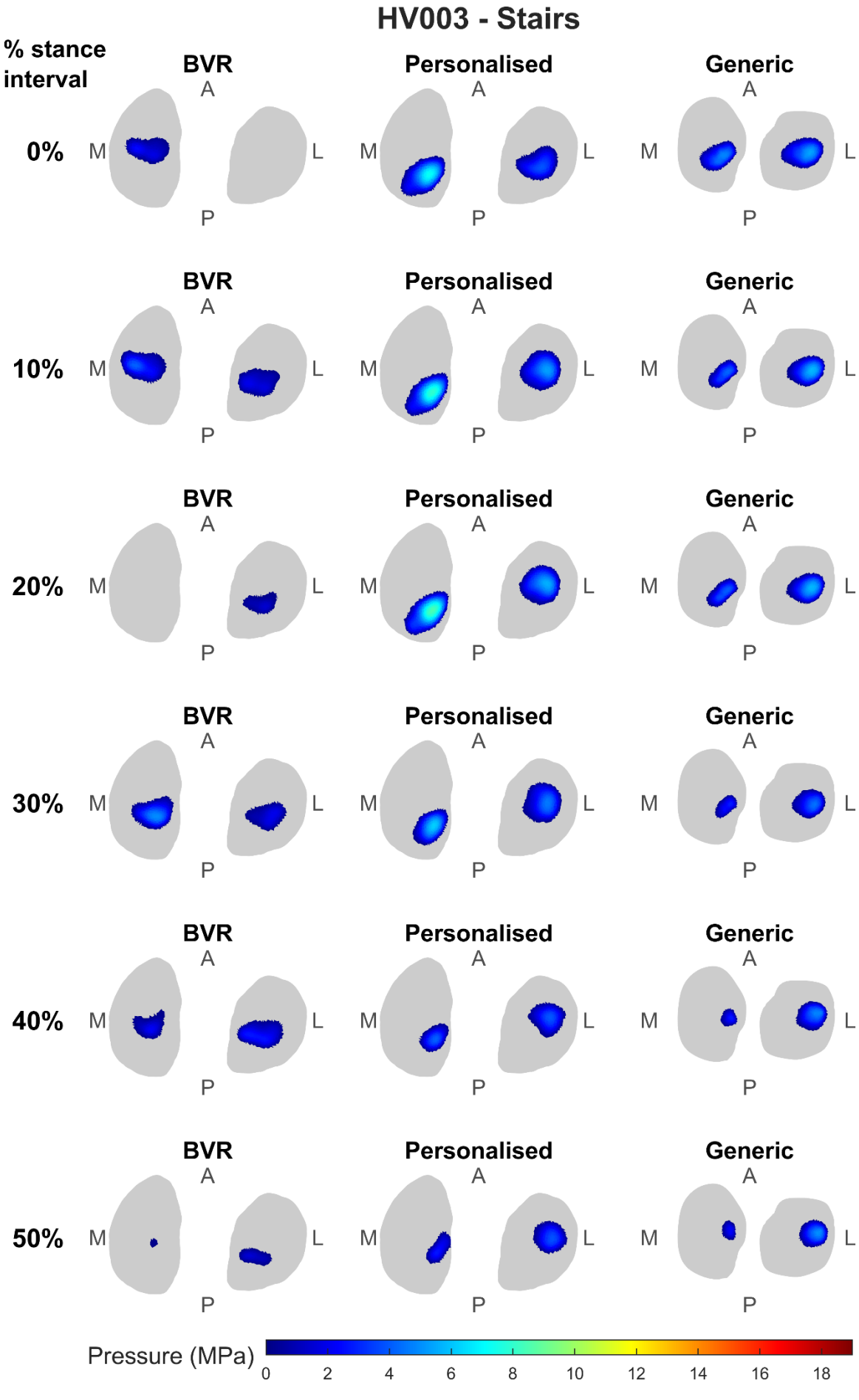
HV003 - Stairs
% stance interval
BVR
Personalised
Generic
0%
10%
20%
30%
40%
50%
A
P
M
L
Pressure (MPa)
0
2
4
6
8
10
12
14
16
18

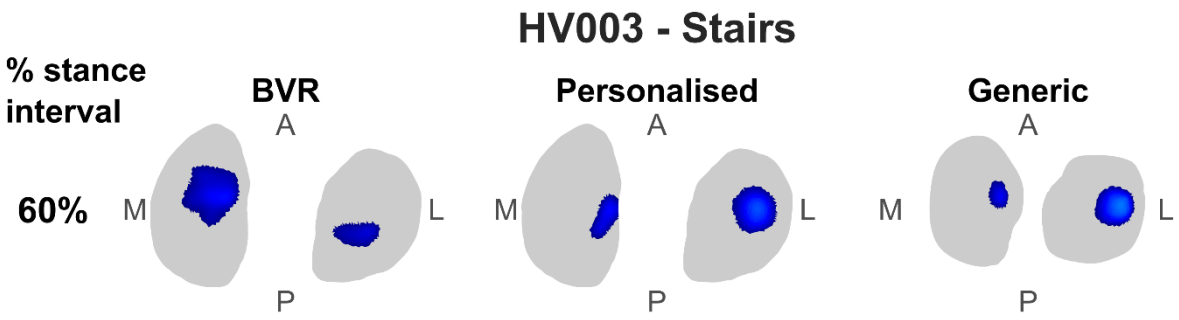
HV003 - Stairs
% stance interval
60%
BVR
Personalised
Generic
A
M
L
P
Pressure (MPa)
0
2
4
6
8
10
12
14
16
18

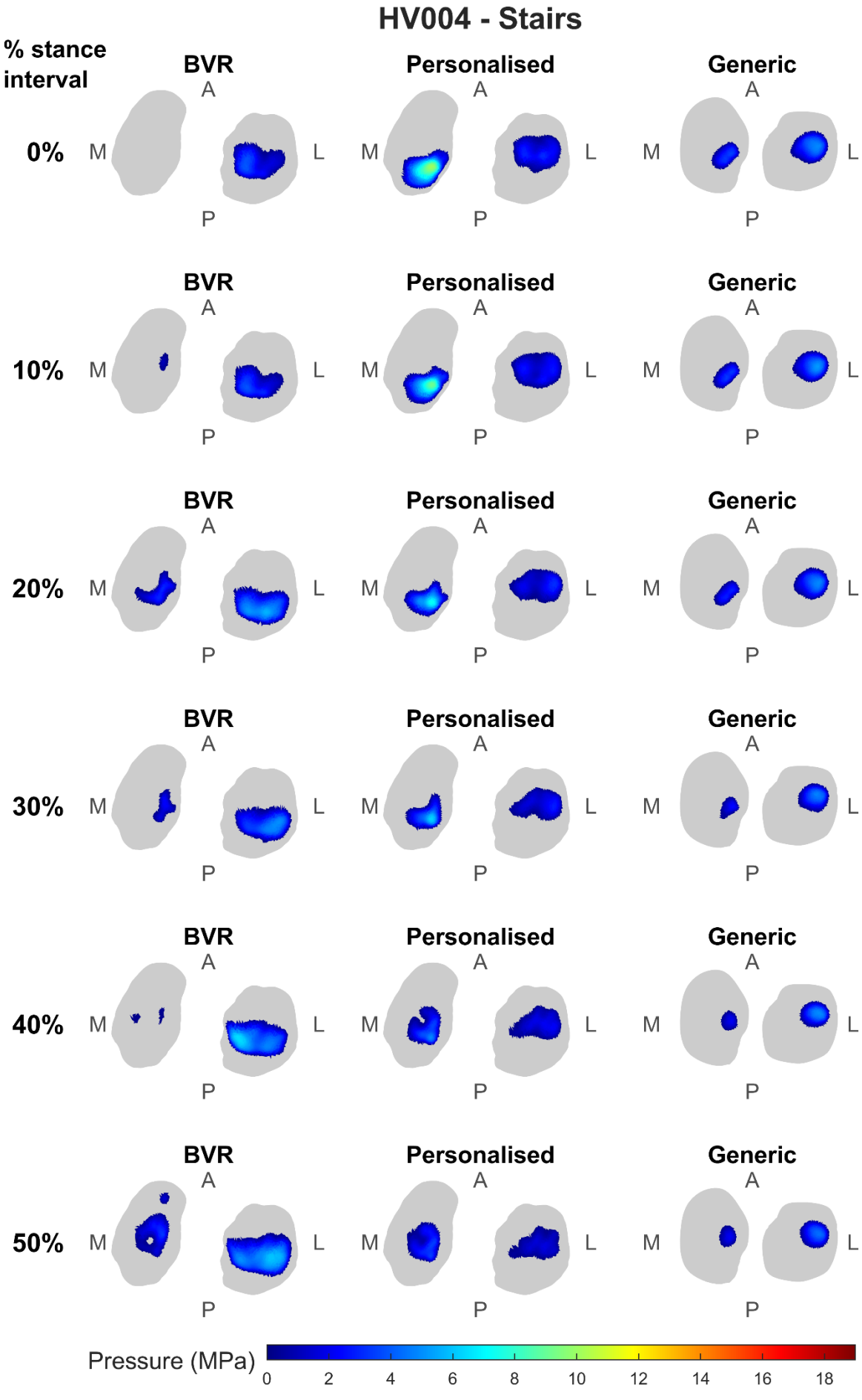
HV004 - Stairs
% stance interval
BVR
Personalised
Generic
0%
10%
20%
30%
40%
50%
A
P
M
L
Pressure (MPa)
0
2
4
6
8
10
12
14
16
18

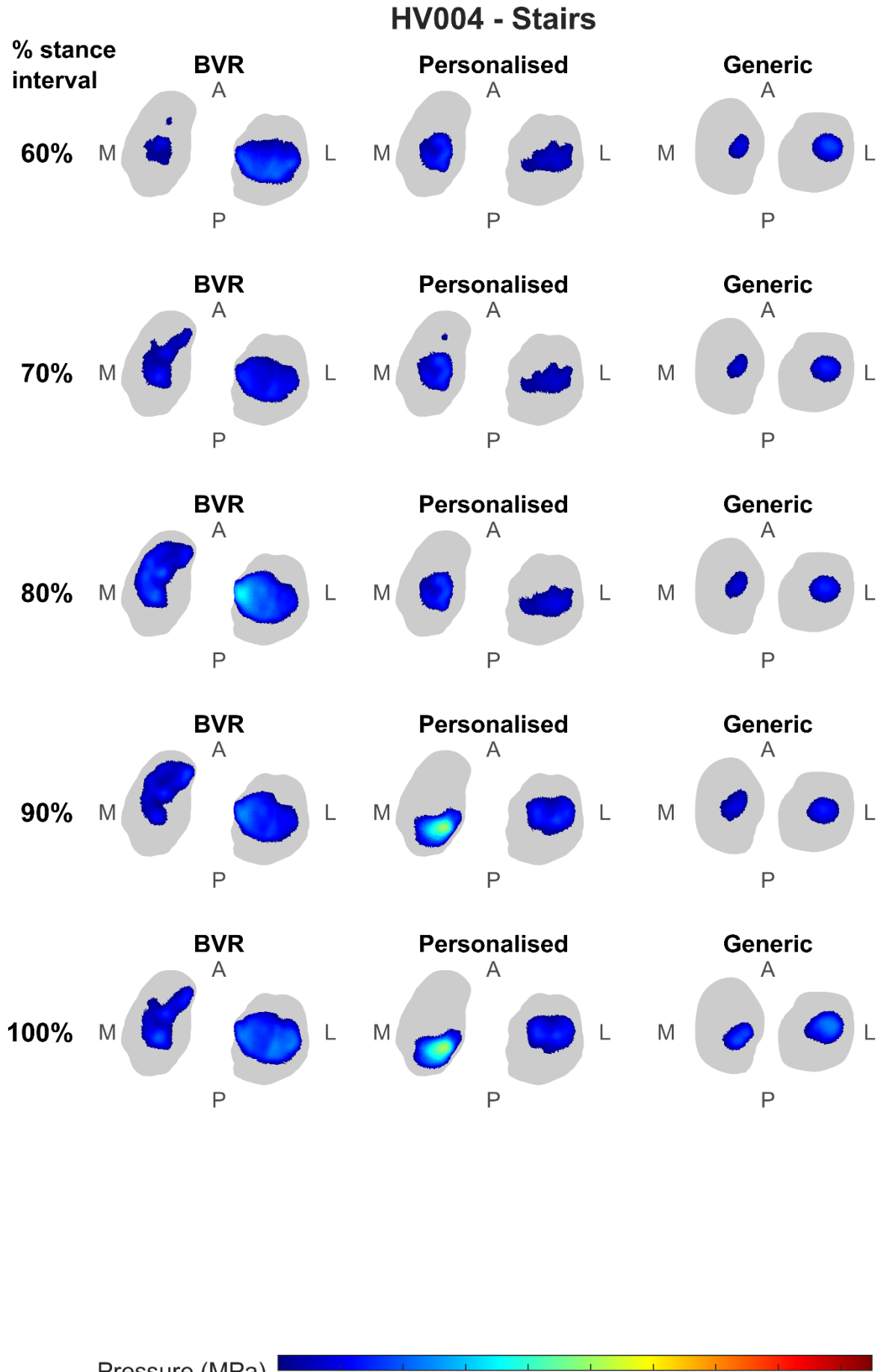
HV004 - Stairs
% stance interval
BVR
Personalised
Generic
60%
70%
80%
90%
100%
A
M
L
P
Pressure (MPa)
0
2
4
6
8
10
12
14
16
18

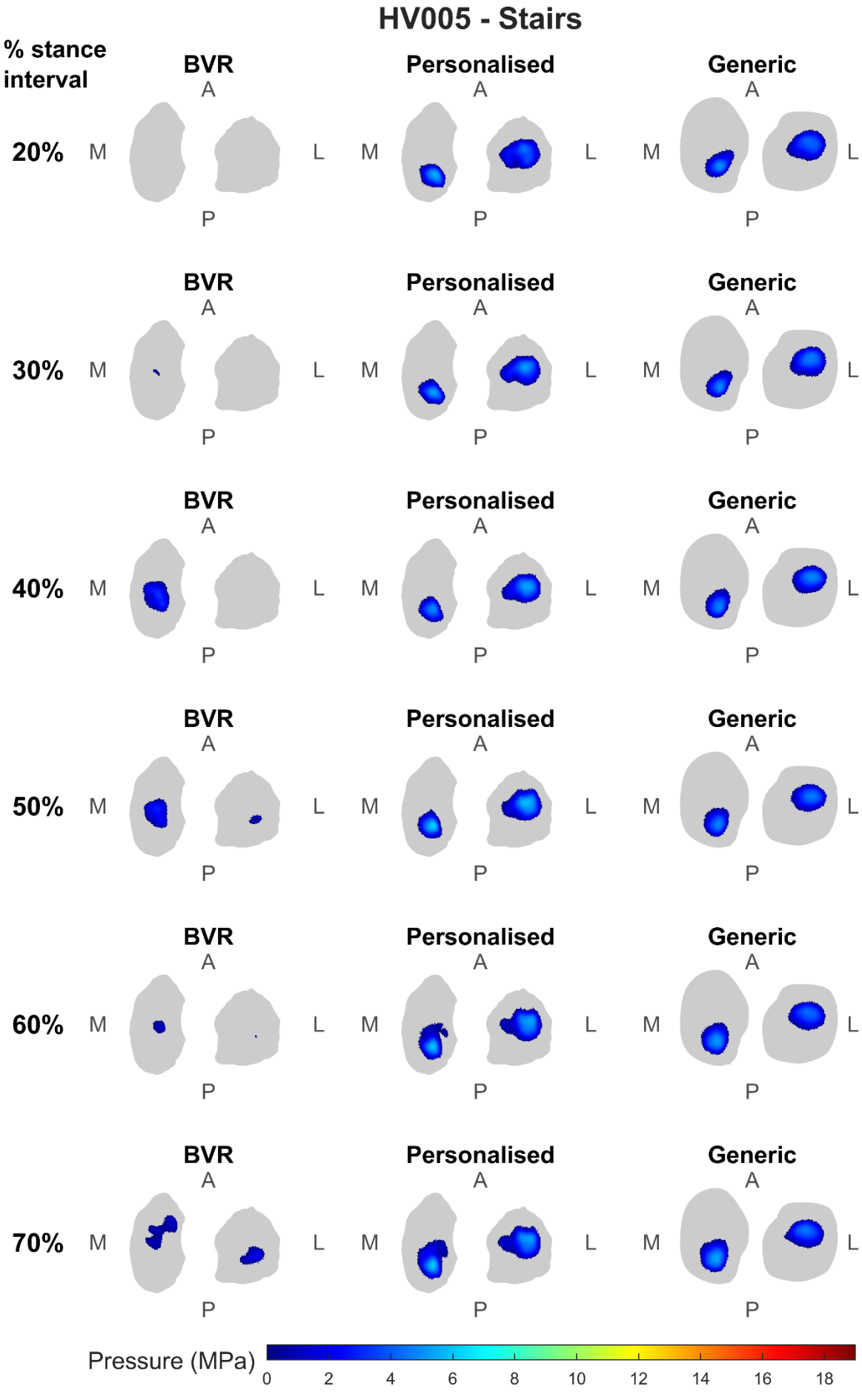
HV005 - Stairs
% stance interval
BVR
Personalised
Generic
20%
30%
40%
50%
60%
70%
A
P
M
L
Pressure (MPa)
0
2
4
6
8
10
12
14
16
18

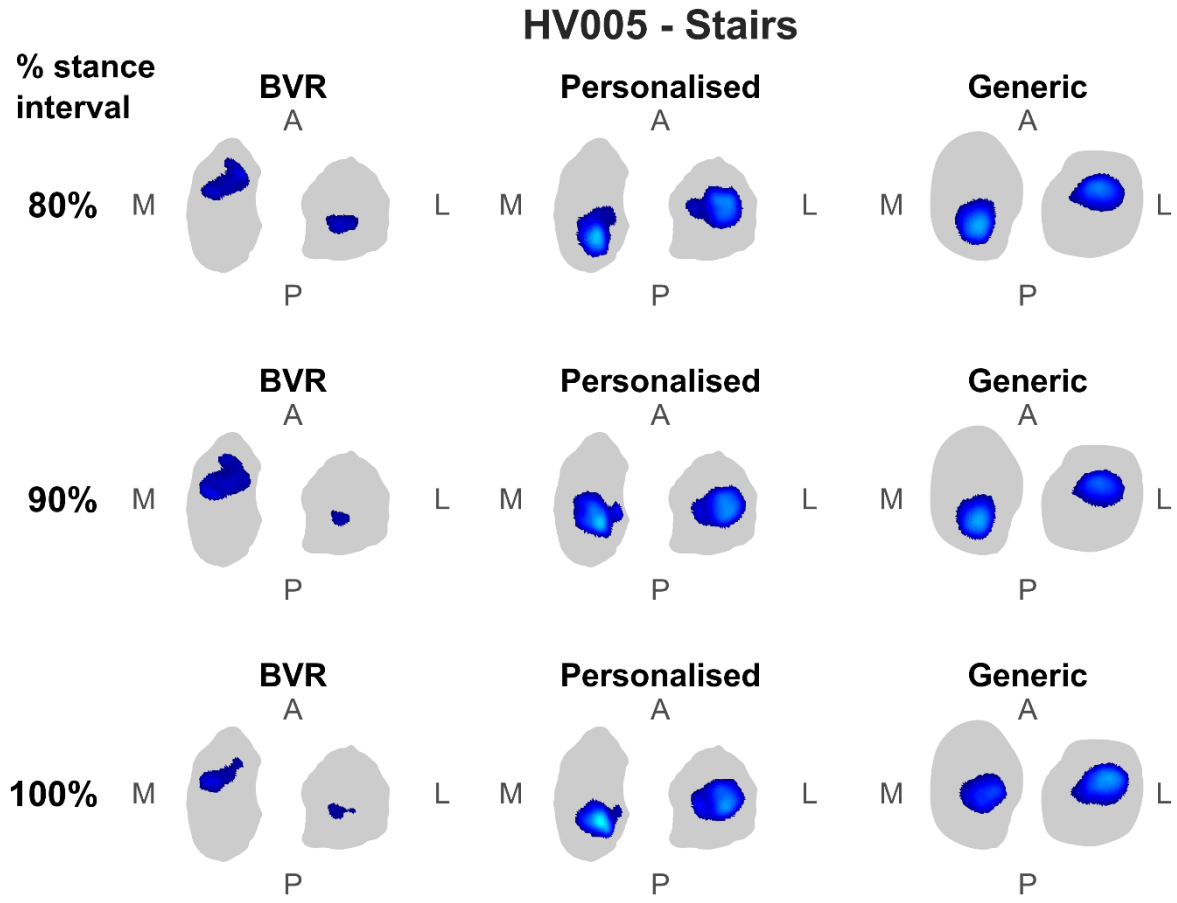
HV005 - Stairs
% stance interval
BVR
Personalised
Generic
80%
90%
100%
A
P
M
L

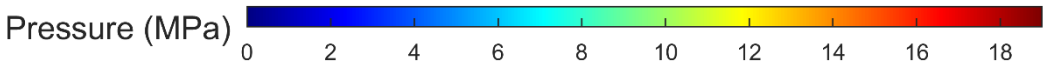
Pressure (MPa)
0
2
4
6
8
10
12
14
16
18

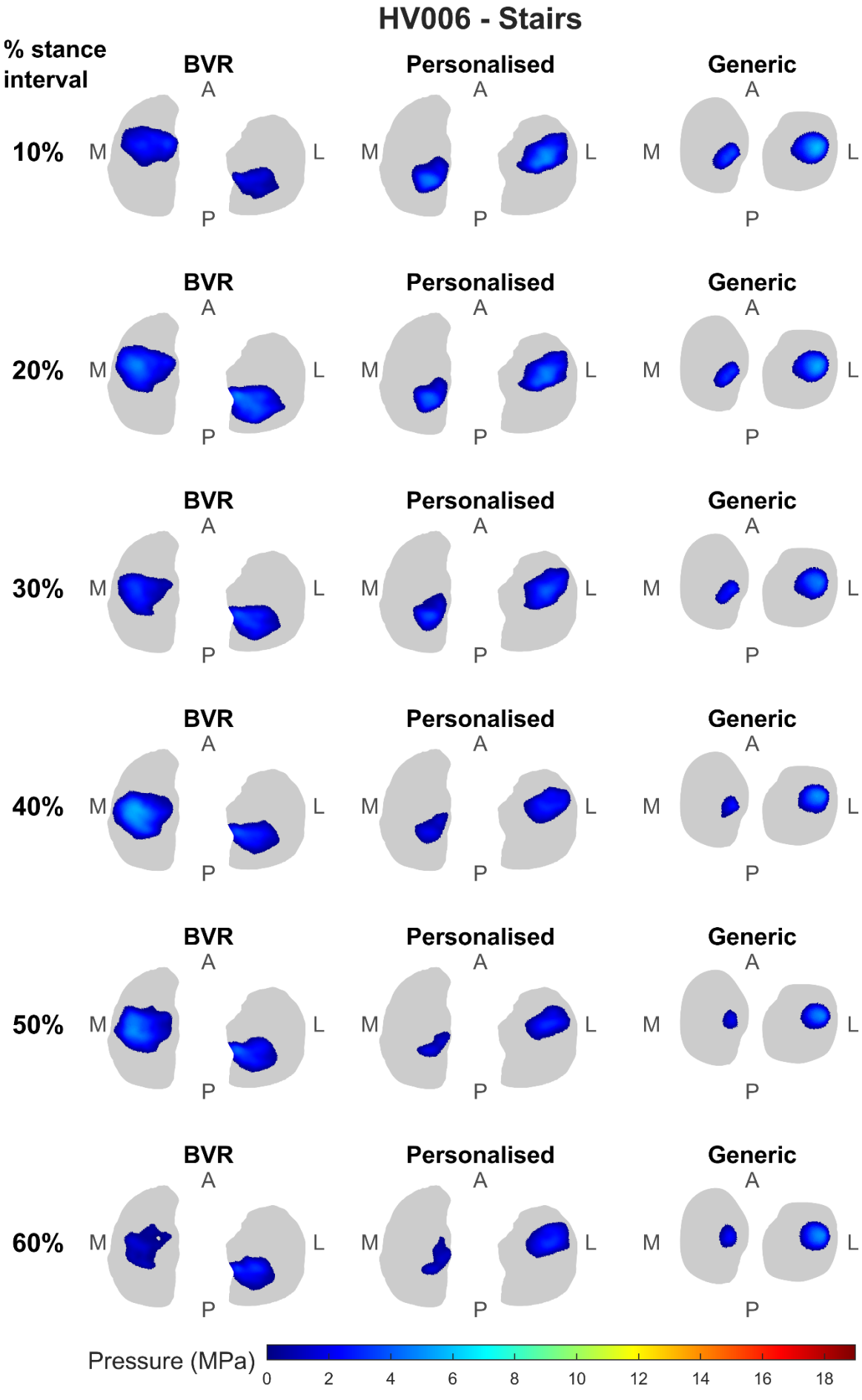
HV006 - Stairs
% stance interval
BVR
Personalised
Generic
10%
20%
30%
40%
50%
60%
A
P
M
L
Pressure (MPa)
0
2
4
6
8
10
12
14
16
18


HV006 - Stairs
% stance interval
BVR
Personalised
Generic
70%
A
M
L
P
Pressure (MPa)
0
2
4
6
8
10
12
14
16
18

Contact map results during lunging

Contact pressure maps from the generic MSM, personalised MSM, and BVR-JAM equivalent at **10% intervals of lunge** (defined as heel-strike to toe-off) where data were available for each individual participant.

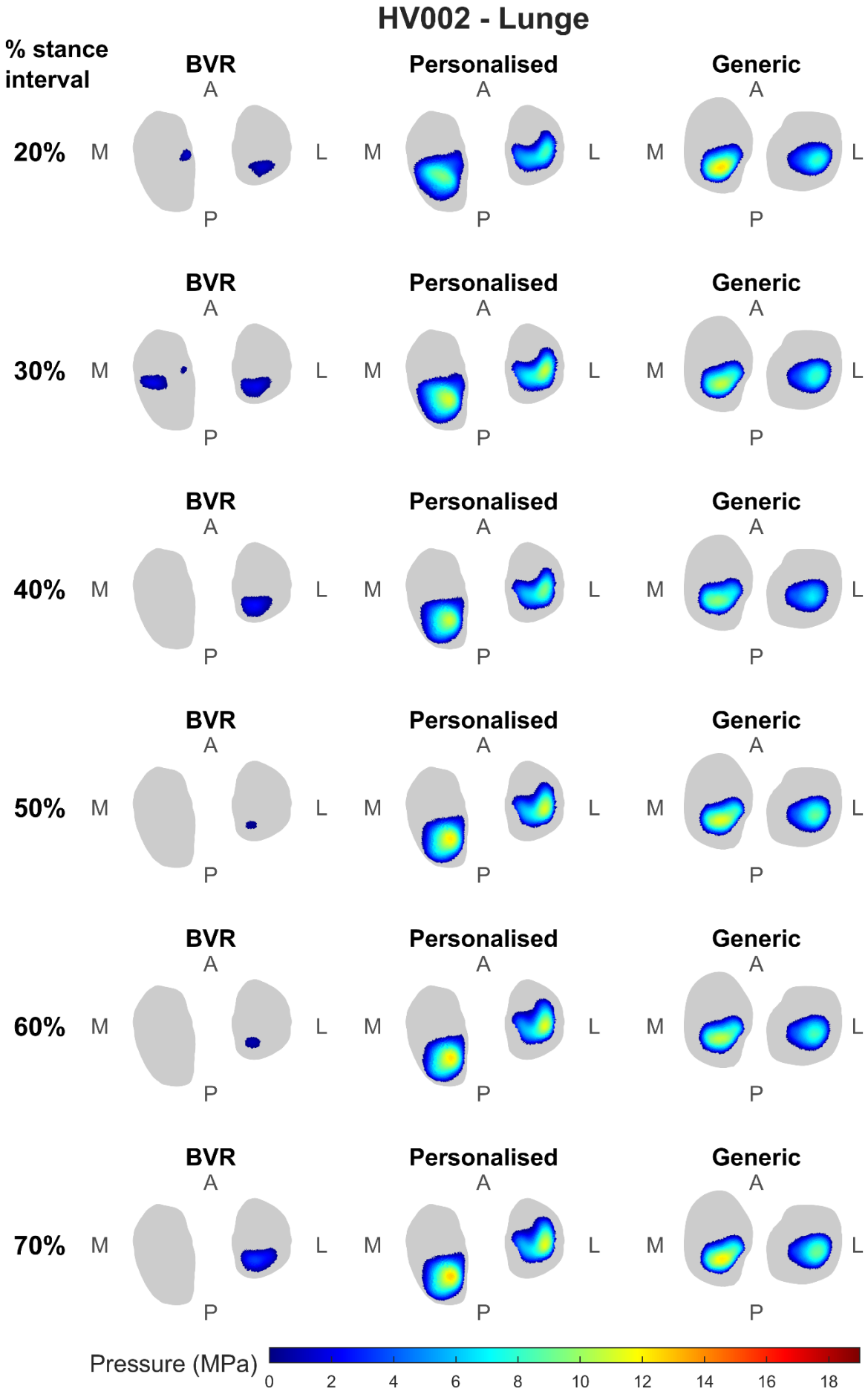
HV002 - Lunge
% stance interval
BVR
Personalised
Generic
20%
30%
40%
50%
60%
70%
A
P
M
L
Pressure (MPa)
0
2
4
6
8
10
12
14
16
18

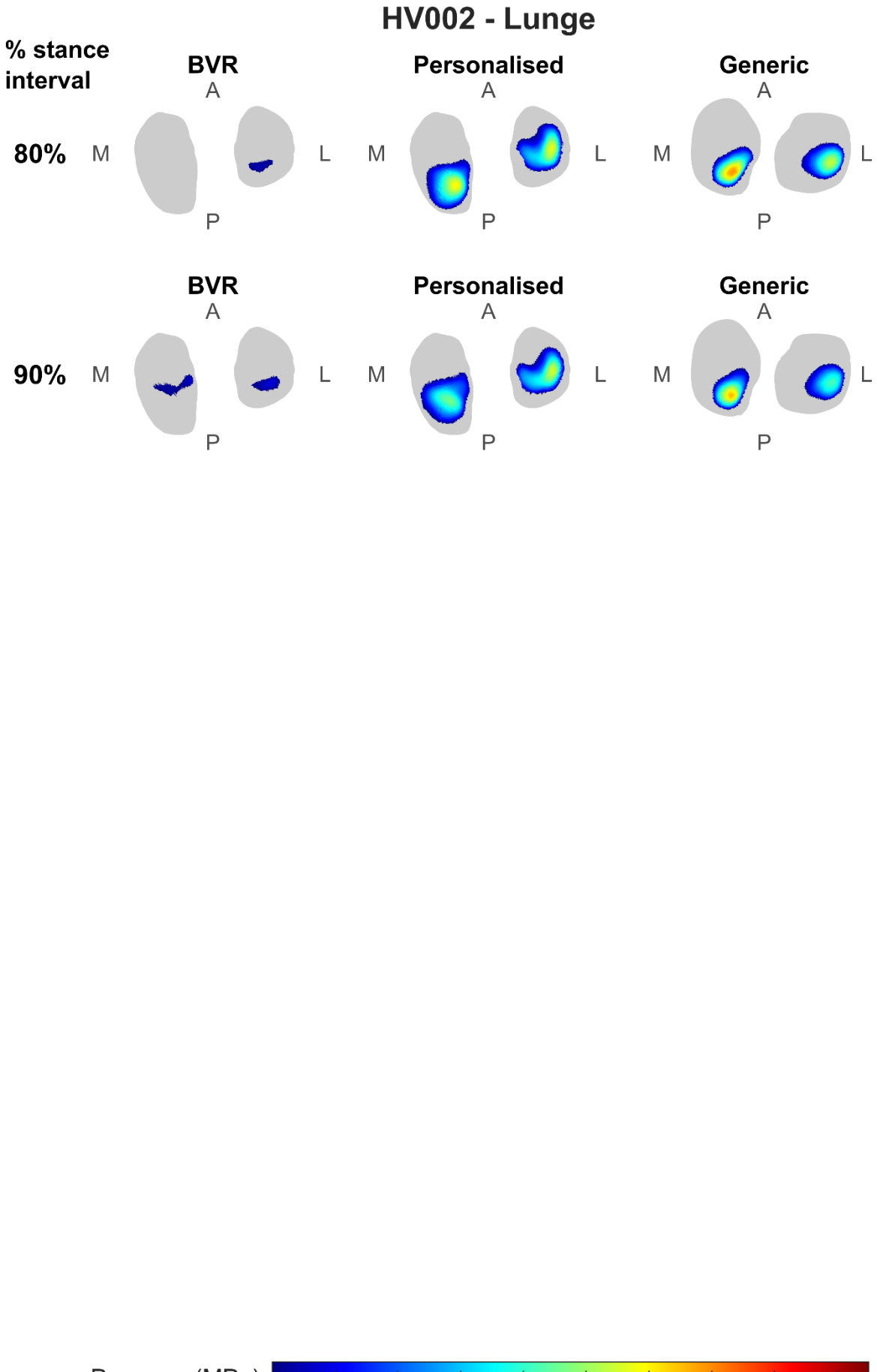
HV002 - Lunge
% stance interval
BVR
Personalised
Generic
80%
90%
A
P
M
L
Pressure (MPa)
0
2
4
6
8
10
12
14
16
18

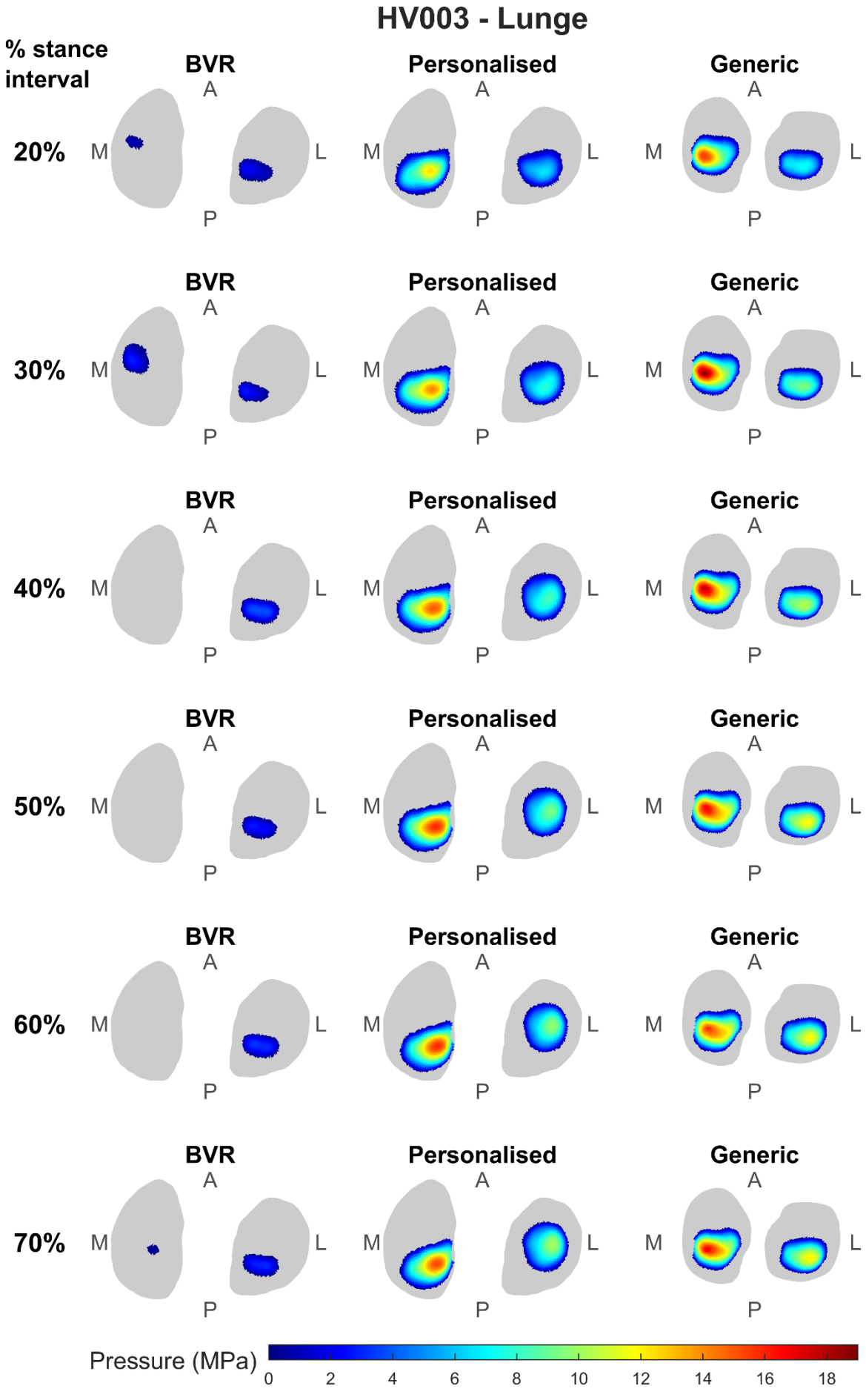
HV003 - Lunge
% stance interval
BVR
Personalised
Generic
20%
30%
40%
50%
60%
70%
A
P
M
L
Pressure (MPa)
0
2
4
6
8
10
12
14
16
18


HV003 - Lunge
% stance interval
80%
BVR
Personalised
Generic
A
M
L
P
Pressure (MPa)
0
2
4
6
8
10
12
14
16
18

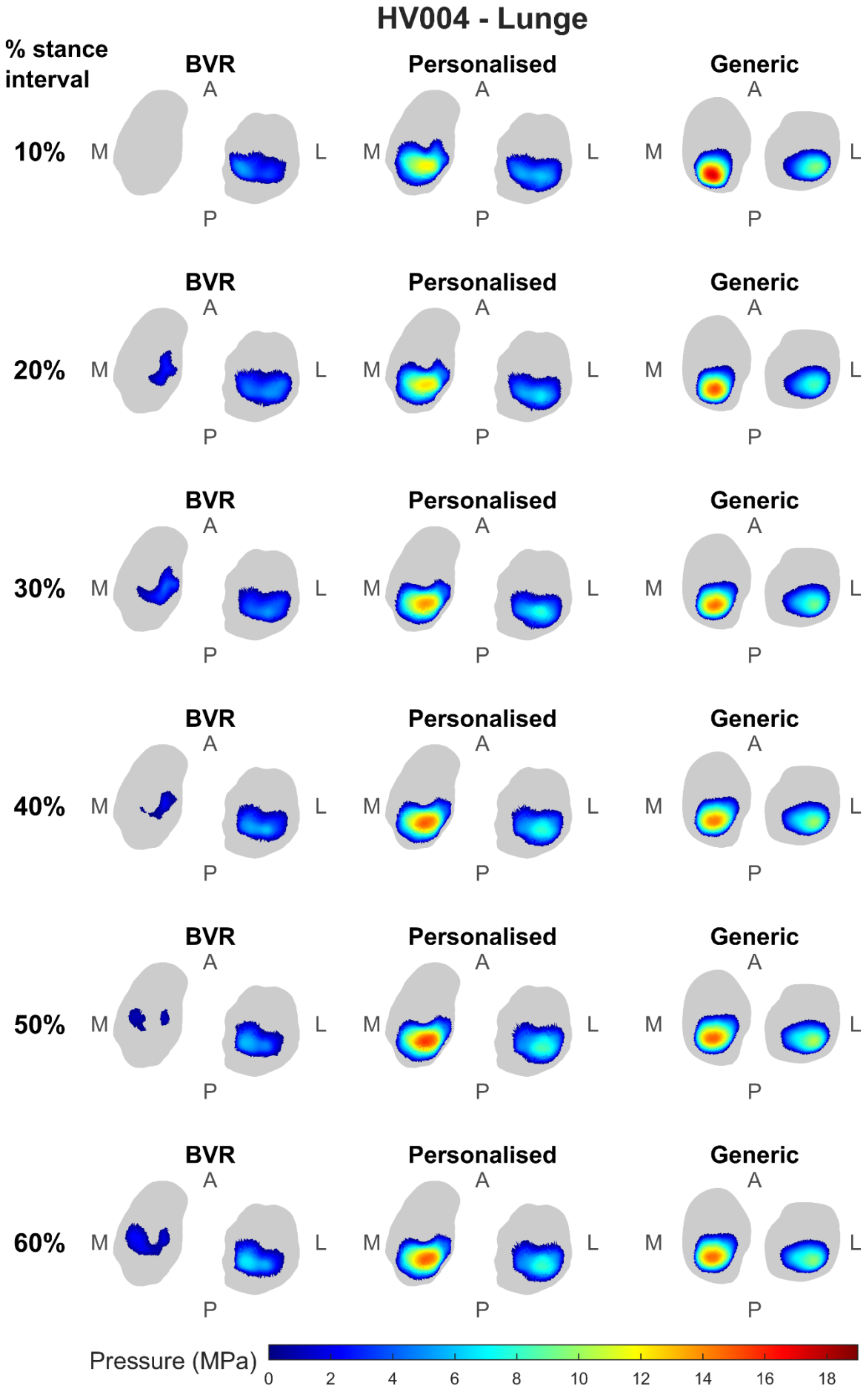
HV004 - Lunge
% stance interval
BVR
Personalised
Generic
10%
20%
30%
40%
50%
60%
A
P
M
L
Pressure (MPa)
0
2
4
6
8
10
12
14
16
18

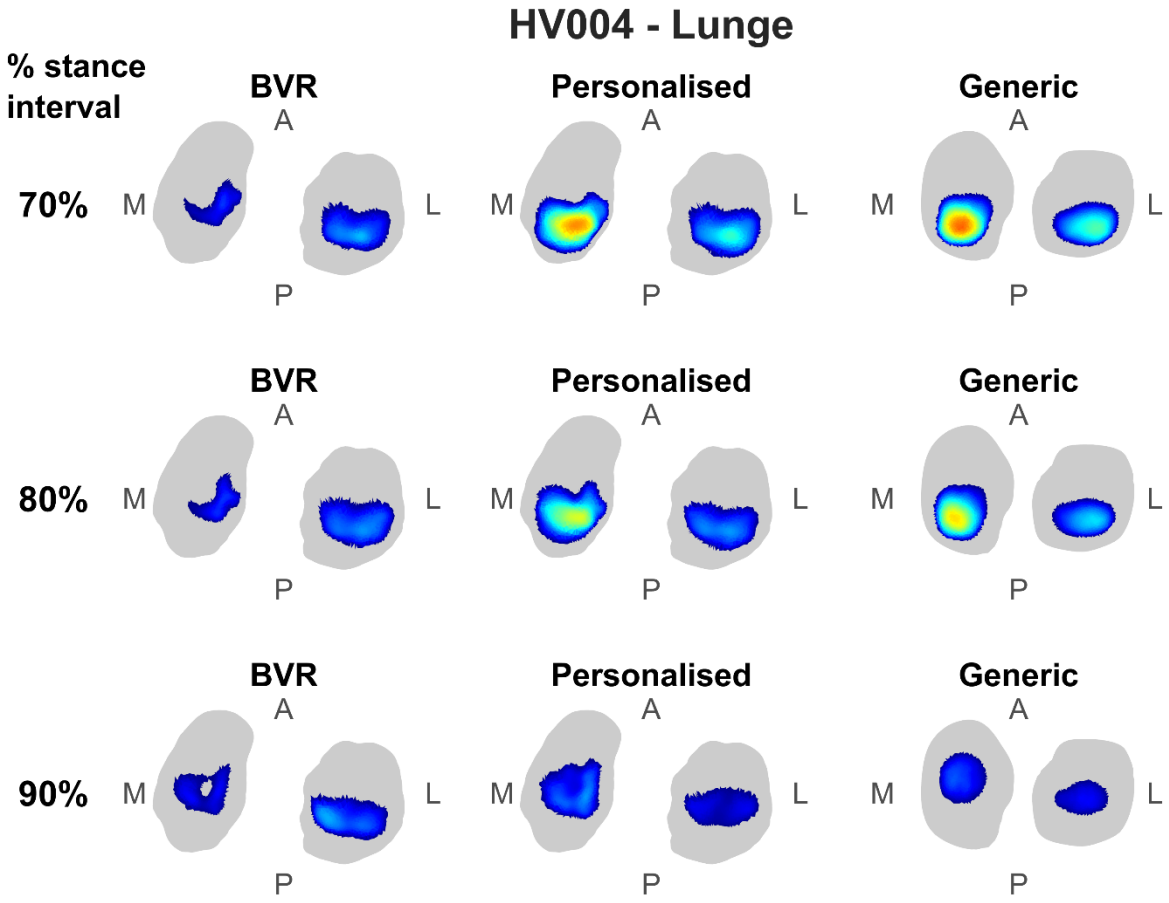
HV004 - Lunge
% stance interval
BVR
Personalised
Generic
70%
80%
90%
A
P
M
L

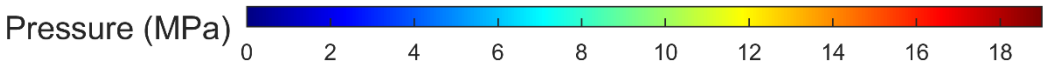
Pressure (MPa)
0
2
4
6
8
10
12
14
16
18

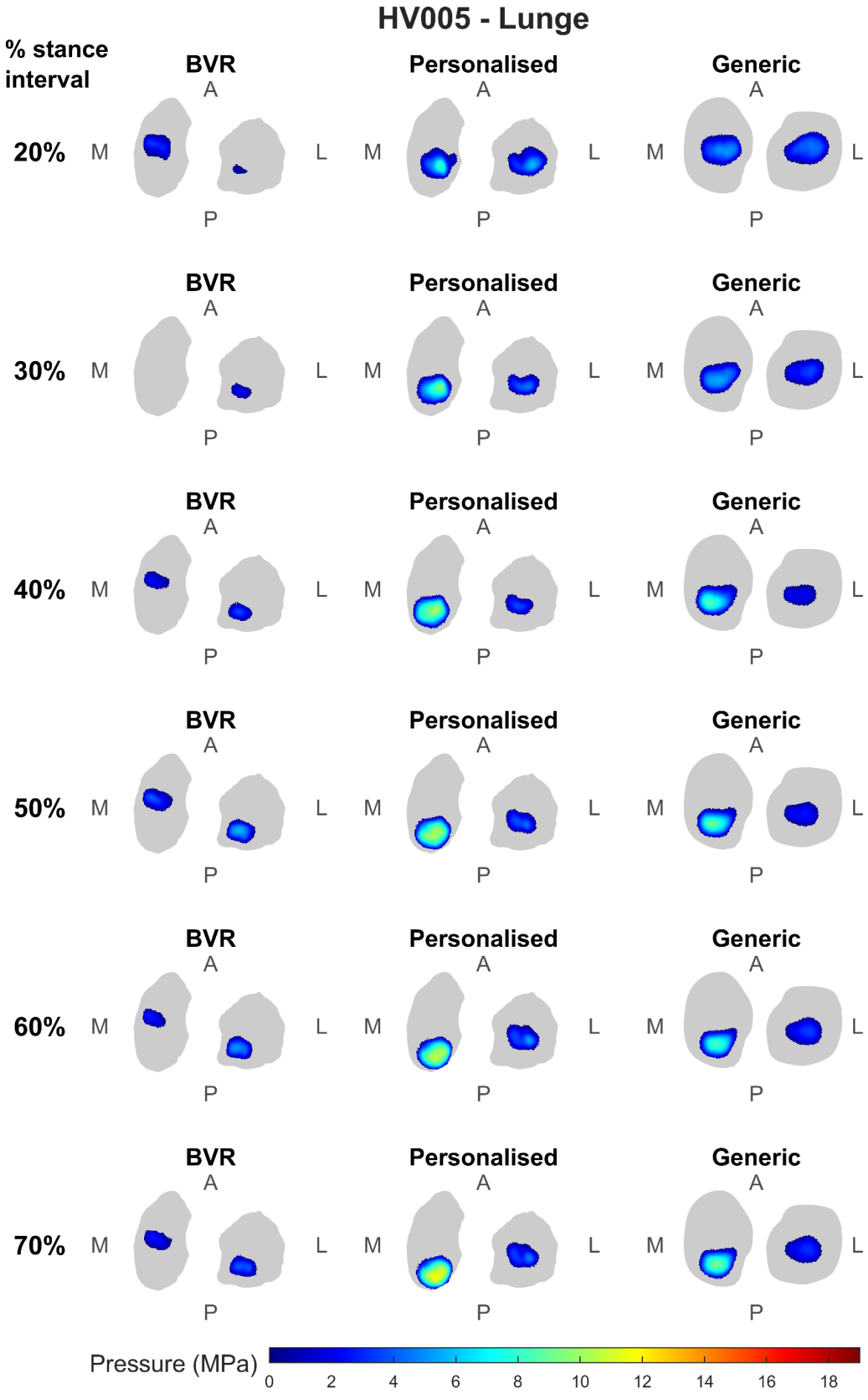
HV005 - Lunge
% stance interval
BVR
Personalised
Generic
20%
30%
40%
50%
60%
70%
A
P
M
L
Pressure (MPa)
0
2
4
6
8
10
12
14
16
18

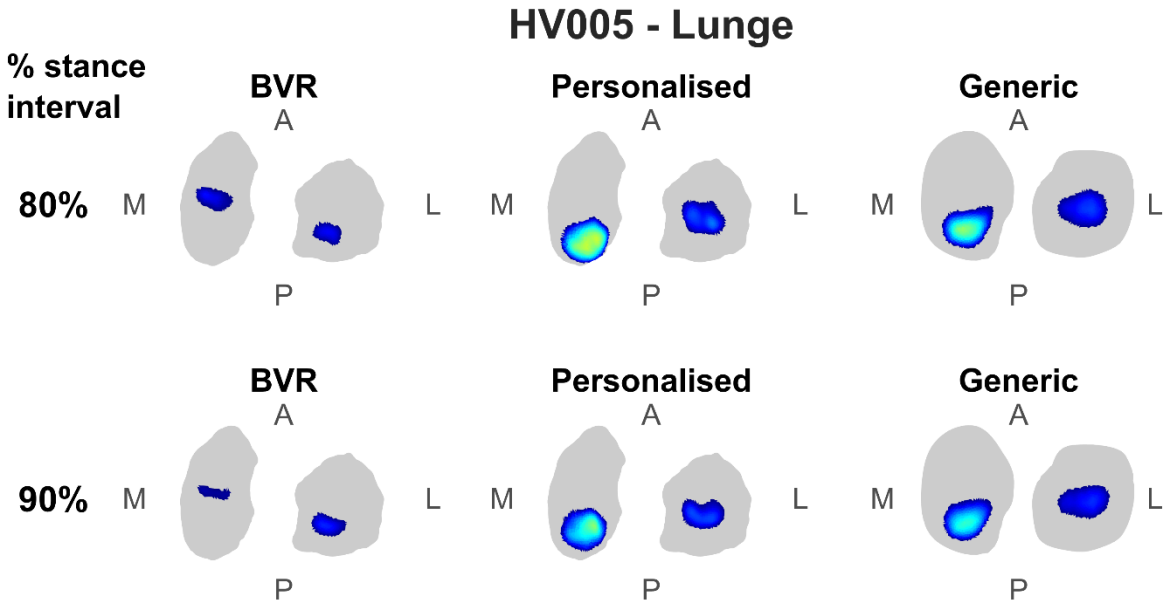
HV005 - Lunge
% stance interval
BVR
Personalised
Generic
80%
90%
A
P
M
L

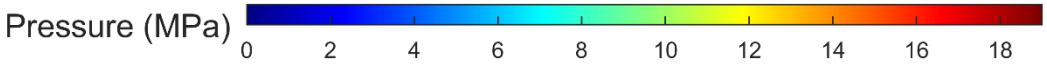
Pressure (MPa)
0
2
4
6
8
10
12
14
16
18

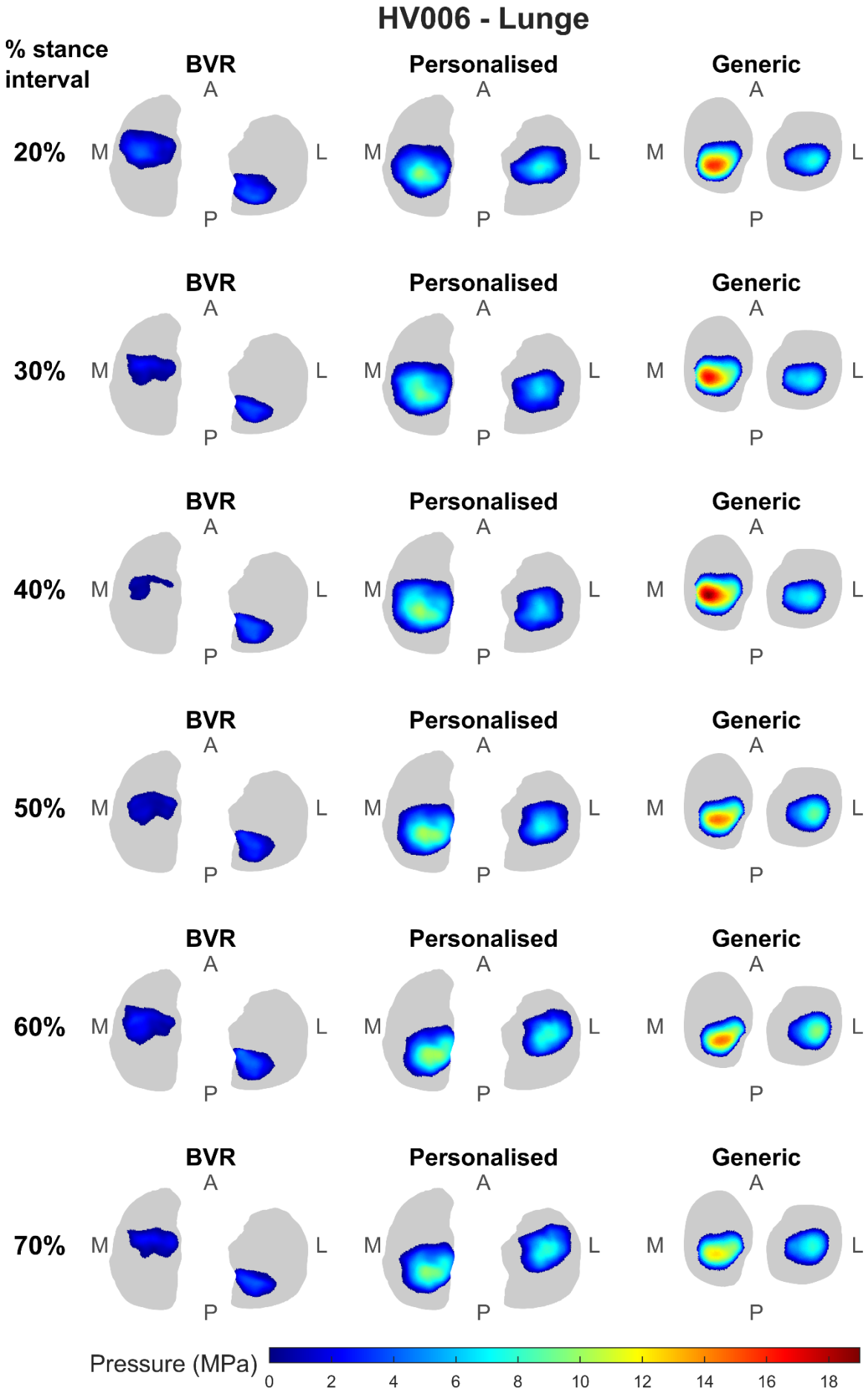
HV006 - Lunge
% stance interval
BVR
Personalised
Generic
20%
30%
40%
50%
60%
70%
A
P
M
L
Pressure (MPa)
0
2
4
6
8
10
12
14
16
18

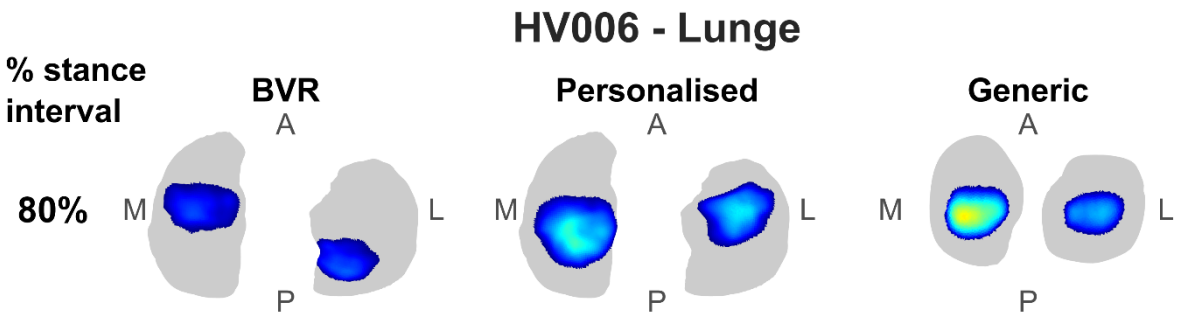
HV006 - Lunge
% stance interval
80%
BVR
Personalised
Generic
A
M
L
P
Pressure (MPa)
0
2
4
6
8
10
12
14
16
18